UAB
Universitat Autònoma de Barcelona

Top-Down Approaches for the De-Reticulation and Synthesis of Metal-Organic Frameworks

Borja Ortín Rubio

ADVERTIMENT. L'accés als continguts d'aquesta tesi queda condicionat a l'acceptació de les condicions d'ús establertes per la següent llicència Creative Commons: https://creativecommons.org/licenses/?lang=ca

ADVERTENCIA. El acceso a los contenidos de esta tesis queda condicionado a la aceptación de las condiciones de uso establecidas por la siguiente licencia Creative Commons: https://creativecommons.org/licenses/?lang=es

WARNING. The access to the contents of this doctoral thesis it is limited to the acceptance of the use conditions set by the following Creative Commons license: https://creativecommons.org/licenses/?lang=en

UAB
Universitat Autònoma de Barcelona

Top-Down Approaches for the De-Reticulation and Synthesis of Metal-Organic Frameworks

Borja Ortín Rubio

Doctoral Thesis
PhD in Chemistry

Supervisors

Prof. Dr. Daniel Maspoch

Dr. Inhar Imaz

Catalan Institute of Nanoscience and Nanotechnology (ICN2)
Department of Chemistry – Faculty of Sciences

2024

Memòria presentada per aspirar al Grau de Doctor per Borja Ortín Rubio

Borja Ortín Rubio

vist-i-plau

Prof. Dr. Daniel Maspoch

ICREA Research Professor & Group Leader
Supramolecular NanoChemistry & Materials Group
Catalan Institute of Nanoscience and Nanotechnology

Dr. Inhar Imaz

CSIC Research Scientist
Supramolecular NanoChemistry & Materials Group
Catalan Institute of Nanoscience and Nanotechnology

Bellaterra, 10 de gener de 2024

"Nothing exists except atoms and empty space;
everything else is opinion."

Democritus

ca. 460 BC-370 BC

Table of contents

Abstract XI

Resum XIII

Acknowledgements XV

Glossary XIX

Chapter 1. Introduction to reticular chemistry: Design and post-design approaches and their related applications 25

1.1. Introduction: From serendipity to the rational design 27

1.2. Historical overview: From coordination chemistry to its extension to Coordination Polymers (CPs) 29

1.3. Reticular Chemistry 38

1.3.1. General concepts: Requisites, secondary building units (SBUs), and isoreticular principle 38

1.3.2. Linker design: Metal-Organic Polyhedra (MOPs) and Zeolitic Imidazolate Frameworks (ZIFs) 41

1.3.3. The impact of the metal-based building unit 44

1.3.4. Covalent Organic Frameworks (COFs) 49

1.3.5. Heterogeneity in reticular materials 51

1.4. Terminology 55

1.5. Topological classification 57

1.6. Simplification 63

1.7. Design approaches 65

1.7.1. Differences between Molecular Building Block (MBB) and SBU 65

1.7.2. Modulated synthesis 66

1.7.3. Supermolecular approaches 67

1.7.4. Merged nets 68

1.7.5. Net-coded building units (**net**-cBUs) 69

1.8. Post-synthetic strategies 70

1.8.1. Chemical modification of pre-formed CPs 70

1.8.2. Post-Synthetic Modification (PSM) of organic ligands 71

1.8.2.1. PSM of pendant and backbone functional groups 71

1.8.2.2. Solvent-Assisted Linker Exchange (SALE) 72

1.8.2.3. Linker insertion: bond formation 73
1.8.2.4. Linker elimination: bond cleavage 75
1.8.3. PSM of metal species 79
1.8.4. PSM of nano- and micro-particles 81

1.9. Tailor-made reticular materials for specific applications 82

1.10. References 88

Chapter 2. Objectives 129

Chapter 3. Desymmetrization of MBBs in reticular chemistry 133

3.1. Introduction 135
3.1.1. Limits of reticular chemistry 135
3.1.2. Introduction of missing parameters for the description of reticular materials 138
3.1.3. Desymmetrization of organic ligands 139
3.1.3.1. Types of desymmetrization 139
3.1.3.2. Symmetric elongation 140
3.1.3.3. Dissymmetric elongation 142
3.1.3.4. Asymmetric elongation 145
3.1.3.5. Non-conventional operations: out-of-plane rotations and translations 147
3.1.3.6. Multiple desymmetrizations 148

3.2. Results and discussion 148
3.2.1. Influence of desymmetrization of organic MBBs in MOFs constructed with high-connected clusters 148
3.2.1.1. Zr-clusters combined with 4-c square/rectangular organic MBBs 148
3.2.1.2. RE-clusters combined with 4-c square/rectangular organic MBBs 170
3.2.1.3. Zr-clusters combined with 4-c tetrahedral organic MBBs 175
3.2.1.4. RE-clusters combined with 4-c tetrahedral organic MBBs 185
3.2.1.5. Zr-clusters combined with 3-c triangular organic MBBs 189
3.2.1.6. RE-clusters combined with 3-c triangular organic MBBs 195
3.2.1.7. Zr- and RE-clusters combined with 6-c organic MBBs 200
3.2.2. Exploring the desymmetrization effect of 4-c linkers in Zr- and RE-MOFs 203
3.2.3. Exploring the desymmetrization effect of 8-c ligand in Zr-MOFs 212

3.3. Experimental section 219
3.3.1. Materials, methods and characterization 219
3.3.1.1. Materials 219
3.3.1.2. Methods 220
3.3.1.3. Synthesis 221
3.3.1.4. Characterization 228
3.3.2. ^{1}H and ^{13}C Nuclear Magnetic Resonance 231

3.3.3. Single-Crystal X-Ray Diffraction 235
3.3.4. BETSI analysis 239

3.4. Conclusions 241

3.5. References 242

Chapter 4. Net-clipping: Theoretical de-reticulation of nets 275

4.1. Introduction 277
4.1.1. Limits of the "bottom-up" approaches 277
4.1.2. A top-down approach for the prediction of topologies in the assembly of less-symmetric MBBs 278

4.2. Results and discussion 280
4.2.1. Theoretical deduction: design strategy for net-clipping 280
4.2.1.1. Identification of the target MBBs 280
4.2.1.2. Generation of clipped nets from less-symmetric derived nets 282
4.2.2. Experimental validation: Synthesis of MOFs based on less-symmetric linkers 286
4.2.2.1. Net-clipping of 4-c squares 286
4.2.2.2. Net-clipping of 4-c tetrahedra 294
4.2.2.3. Net-clipping of 6-c hexagons 298
4.2.2.4. Net-clipping of 8-c cubes 300
4.2.2.5. Net-clipping of 12-c hexagonal prisms 306
4.2.2.6. Net-clipping out of edge-transitive nets 308

4.3. Experimental section 314
4.3.1. Materials, methods and characterization 314
4.3.1.1. Materials 314
4.3.1.2. Methods 315
4.3.1.3. Synthesis 316
4.3.1.4. Characterization 325
4.3.2. ^{1}H and ^{13}C Nuclear Magnetic Resonance 326
4.3.3. Single-Crystal X-Ray Diffraction 334

4.4. Conclusions 340

4.5. References 342

Chapter 5. Clip-off chemistry: Programmed de-reticulation of nets 353

5.1. Introduction 355
5.1.1. Limits of post-synthetic methods 355
5.1.2. Controlled breaking: Cleavable bonds at specific positions 356

5.2. Results and discussion 358
5.2.1. Topological analysis of the disassembly: Erasing edges or nodes 358
5.2.2. Clip-off synthesis of new reticular materials 363
5.2.2.1. From Zr-**scu**-MOF to Zr-**pcu**-MOF 363
5.2.2.2. From Sc-**soc**-MOF to Sc-**pcu**-MOF 371

5.3. Experimental section 378
5.3.1. Materials, methods and characterization 378
5.3.1.1. Materials 378
5.3.1.2. Methods 378
5.3.1.3. Synthesis 379
5.3.1.4. Characterization 380
5.3.2. ^{1}H Nuclear Magnetic Resonance 382
5.3.3. Single-Crystal X-Ray Diffraction 390

5.4. Conclusions 394

5.5. References 395

Chapter 6. General conclusions 401

Annex 405

List of publications 407
Net-Clipping: An Approach to Deduce the Topology of Metal-Organic Frameworks Built with Zigzag Ligands 409
Clipp-off Chemistry: Synthesis by Programmed Disassembly of Reticular Materials 415
A Mesoporous Zr-Based Metal–Organic Framework Driven by the Assembly of an Octatopic Linker 425
Net-Clipping as a Top-Down Approach for the Prediction of Topologies of MOFs Built from Reduced-Symmetry Linkers 429
Engineering Covalent Organic Frameworks in the Modulation of Photocatalytic Degradation of Pollutants Under Visible Light Conditions 441
Photoredox Heterobimetallic Dual Catalysis Using Engineered Covalent Organic Frameworks 453
Multicomponent, Functionalized HKUST-1 Analogues Assembled via Reticulation of Prefabricated Metal-Organic Polyhedral Cavities 465
Isoreticular Constraction of Metal-Organic Frameworks Induced by Cleavage of Covalent Bonds 475
Metal- and Covalent-Organic Framework Mixed Matrix Membranes for CO_2 Separation: A Perspective on Stability and Scalability 483

Abstract

The present PhD Thesis has been devoted to the study, understanding and implementation of novel top-down approaches for the rational design of reticular materials built with less-symmetric molecular building blocks (MBBs). Two strategies are proposed based on the de-reticulation of nets to accomplish this objective. The first approach, *net-clipping*, is based on the theoretical clipping of more-symmetric MBBs for the topological prediction of nets constructed with less-symmetric MBBs. The second approach, *Clip-off Chemistry*, is based on the programmed disassembly of reticular materials by bond cleavage at specific, controlled positions.

Chapter 1 encompasses a general introduction and the development of the reticular chemistry field, from their discoveries and conception to their rationalization and classification. Additionally, we focus on the most relevant synthetic and post-synthetic methodologies used for designing reticular materials to contextualize the reader to the significance of the presented work in this Thesis.

Chapter 2 introduces the general and specific objectives of this Thesis.

In Chapter 3, we review the state of the art of the effect of desymmetrization of organic MBBs on the assembly of metal-organic frameworks (MOFs) based on high-connected Zr- and rare-earth (RE)-clusters. We study the most important desymmetrizations performed in literature and how these affects to the connectivity and geometry of the cluster, and therefore, to the net. Moreover, less-symmetric MBBs are designed for the synthesis of novel MOFs to understand the different chemical behaviour of similar high-connected inorganic MBBs.

Chapter 4 describes the first top-down approach, *net-clipping*, based on the de-reticulation of MOFs and edge-transitive nets by clipping MBBs or nodes of higher connectivity and symmetry by half. We select the clippable MBBs with 4-connected (4-c) square/rectangular, 4-c tetrahedral, 6-c hexagonal, 8-c cubic, and 12-c

hexagonal prismatic linkers to decrease its symmetry into less-regular MBBs. By applying net-clipping to all the nets constructed with nodes with these connectivities and shapes, 141 derived and 56 clipped nets are anticipated, being 39 of them described for the first time. We validate our strategy with the synthesis of 6 novel MOFs constructed with less-symmetric MBBs and several literature examples that confirm our predictions.

Chapter 5 describes a new synthetic methodology, *Clip-off Chemistry*, based on the de-reticulation of MOFs *via* bond breaking for the obtention of novel molecules or materials. We validate our strategy with the synthesis of two topologically different tridimensional (3D) MOFs (Zr-**pcu**-MOF and Sc-**pcu**-MOF) from other two different 3D MOFs as precursors (Zr-**scu**-MOF and Sc-**soc**-MOF, respectively). Using the ozonolysis reaction and double bonds as our cleavable reaction/groups, respectively, we demonstrate that this transformation can be performed quantitively, selectively, and periodically, occurring in a single-crystal-to-single-crystal fashion.

Resum

La present Tesi Doctoral ha estat dedicada a l'estudi, comprensió i implementació de noves aproximacions de dalt a baix per al disseny racional de materials reticulars construïts amb blocs de construcció moleculars (MBBs) menys simètrics. Es proposen dues estratègies basades en la desreticulació de xarxes per a aconseguir aquest objectiu. La primera aproximació, *net-clipping*, es basa en el tall teòric de MBBs més simètrics per a la predicció topològica de xarxes construïdes amb MBBs menys simètrics. La segona aproximació, *Clip-off Chemistry*, es basa en el desmuntatge programat de materials reticulars per la ruptura d'enllaços en posicions específiques i controlades.

El capítol 1 abasta una introducció general i el desenvolupament del camp de la química reticular, des dels seus descobriments i concepció fins a la seua racionalització i classificació. A més a més, ens centrem en les metodologies sintètiques i post-sintètiques més rellevants utilitzades per al disseny de nous materials reticulars per a contextualitzar al lector sobre la importància del treball presentat en aquesta Tesi.

El capítol 2 presenta els objectius generals i específics d'aquesta Tesi.

En el capítol 3, es revisa l'estat de l'art de l'efecte de desimetrització de MBBs orgànics en l'assemblatge de xarxes metal·loorgàniques (MOFs) basats en clústers de Zr i terres rares (RE). Estudiem les desimetritzacions més importants realitzades en la literatura i com aquestes afecten a la connectivitat i geometria del clúster, i per tant, de la xarxa. Altrament, es dissenyen MBBs menys simètrics per a la síntesi de nous MOFs per comprendre el diferent comportament químic de MBBs inorgànics similars altament connectats.

El capítol 4 descriu la primera aproximació de dalt a baix, *net-clipping*, basat en la desreticulació de MOFs i xarxes transitives d'eix per retallar MBBs o nodes de connectivitat i simetria més altes a la meitat. Seleccionem els MBBs retallables amb

connectors quadrats/rectangulars 4-connectats (4-c), tetraèdrics 4-c, hexagonals 6-c, cúbics 8-c i prismàtics hexagonals 12-c per a disminuir la seua simetria en MBBs menys regulars. Aplicant net-clipping en totes les xarxes construïdes amb nodes amb aquestes connectivitats i formes, s'anticipen 141 xarxes derivades i 56 retallades, sent 39 d'elles descrites per primera vegada. Validem la nostra estratègia amb la síntesi de 6 nous MOFs construïts amb MBBs menys simètrics i diversos exemples de la literatura que confirmen les nostres prediccions.

El capítol 5 descriu una nova metodologia sintètica, *Clip-off Chemistry*, basada en la desreticulació de MOFs mitjançant la ruptura d'enllaços per a l'obtenció de noves molècules o materials. Validem la nostra estratègia amb la síntesi de dos MOFs tridimensionals (3D) topològicament diferents (Zr-**pcu**-MOF i Sc-**pcu**-MOF) a partir d'altres dos MOFs 3D diferents com a precursors (Zr-**scu**-MOF i Sc-**soc**-MOF, respectivament). Fent servir la reacció d'ozonòlisi i els enllaços dobles com a reacció/grups retallables, respectivament, demostrem que aquesta transformació es pot realitzat de manera quantitativa, selectiva i periòdica, ocorrent de forma monocristall-a-monocristall.

Acknowledgements

A continuació, trobareu les 4 pàgines més llegides (i menys avorrides) d'aquesta Tesi que resumeixen la contribució més important dels últims 5 anys on he tingut el plaer de treballar i conviure amb molta gent que m'ha ajudat, no només científicament, a crèixer.

Sense cap dubte, començaré donant les gràcies a la meua família: a ma mare, *a mi padre*, a Claudia, als iaios i *a la abuela*, per tot el suport emocional rebut durant tants anys. Malgrat no ser una gran distància, els 350 km que separen l'ICN2 de casa s'han fet durs, sobretot als moments més difícils. Gràcies per donar suport a les meues decisions i per la confiança tot i que sempre he sigut un desastre. En especial, a la meua mare i *a mi padre*, que han sigut el millor exemple a seguir, especialment quan parlem d'esforç. A mesura que passaven els anys, he entès la sort que he tingut amb els pares que em van tocar. També els he d'agrair l'herència que m'han transmès per gaudir la química, encara no està clar si ve de la increïble dedicació de ma mare a la divulgació, *o de aquella matrícula que sacó mi padre de joven en el instituto*.

Com no, voldria agrair al professor Daniel Maspoch l'oportunitat de treballar en un camp tan fascinant i de formar-me com a científic amb les millors condicions possibles. Estar sota la teua supervisió m'ha fet aprendre de la teua passió per la recerca, exigència, creativitat i la constant dedicació que transmets. Sense la teua ajuda i consells no estaria a aquest punt i aquesta Tesi no tindria la qualitat que es mereixia.

También me gustaría agradecer al Dr. Inhar Imaz además de su guía, su extremada paciencia y tolerancia conmigo. Poca gente habrá sufrido mi cabezonería con tanta intensidad. Es difícil recordar algún momento en el que las cosas no fueran bien sin que esté constantemente apoyando y preocupándose a mi lado. Para mí has sido todo un ejemplo de cómo debe ser un investigador. Gracias por toda tu ayuda.

El següent grup de persones per agrair són tots els components de NanoUp. Tots ells, tant al laboratori com a l'oficina, han descobert que soc un pesat. Ja siga en algun projecte, experiment o només compartint espai, he gaudit molt de la seua companyia al llarg d'aquests anys. Als antics membres amb qui vaig treballar tant i em van ajudar quan començava aquesta etapa: Vincent, Hosein, Ceren, Javier Troyano, Javier Pérez, Najmeh, Luis Carlos, Asier, Farnoosh, Sergi, Civan, Mateusz, Jordi, Jiemin, Marta Ruiz, Leyre, Carlos i Thais, *a quien recuerdo con especial cariño en nuestros viajes de vuelta a València*. Als companys que més temps m'han patit recentment: Yang, Susana, Lingxin, Mary, Arnau, Akim, Alba, Sara, Jorge, Sonia, Cornelia, Xu, Funda, Libni, Kornel, Sofia, Javier Fonseca, Juan Pablo i Anna, amb qui he treballat en tants projectes des que vaig arribar al grup. També a les noves incorporacions al grup amb qui lamentablement no he coincidit tant com voldria: Pilar, Roberto, Gerard Pena, Xiang, Partha i Dongsik. Estic molt agraït d'haver compartit tants moments, ja siga treballant o amb unes cerveses, els dies eren més divertits amb cadascun de vosaltres. *Among them, a special thanks to Michele and Marcel, who made that year one of the best I can remember in our sub-group. Otro agradecimiento especial va dedicado a Xulián, autodenominado como summer-love (le gusta hablar...), que su corta estancia marcó a todos en el grupo*. A Marta Sanmartí i a José els he d'agrair tota l'ajuda que m'han ofert, *en especial a José, que siempre me ha ayudado y soportado cuando a última hora intentaba negociar sus planes.*

D'entre tot el grup, voldria especialment agrair a Laura, Gerard i Yunhui aquest extra de calidesa que m'aportaven. Recorde amb tendresa las llargues converses a qualsevol hora i lloc amb Laura que al final es convertien en necessàries. Un dels millors moments del dia era arribar ben prompte per poder comentar amb Gerard les notícies de política (més ben dit els comentaris de les notícies), ho he trobat a faltar des que marxares del grup. *Of course, no one else but Yunhui can receive the biggest part of my appreciation. These 5 long years working with you have been special thanks to your extremely loud laugh, motivation, and friendship. I am grateful for sharing so many*

hours together in the lab, office, and synchrotron together as you made the journey really fun.

Per descomptat, voldria agrair a la Dra. Judith Juanhuix tot el que m'ha ensenyat i ajudat al sincrotró i també disculpar-me per les trucades de matinada que ràpidament ha contestat quan teníem un problema. *A Jessica le quiero agradecer toda la ayuda y compañía durante tantas medidas en el difractómetro, espero que mi charla fuera más agradable que el olor que alguna de mis muestras impregnaba en la sala.*

Otra de mis suertes fue llegar a una casa en la que coincidí con un grupo de gente que se convirtió en una segunda familia. Estaré eternamente agradecido a Jaime, Marc y Javi por haberme hecho más feliz con solo un silbidito después de cada día en el laboratorio. Llegar a casa y hacer deporte juntos, salir a tomar algo los viernes y planear los *findes* y viajes era el respiro que necesitaba y me daba más vida. Aunque ya suene lejano, el confinamiento era más llevadero con una paella (probablemente las mejores paellas que se habrán hecho en Sabadell en la historia) con vosotros todos los sábados. Esta sección también se extiende a Iris y Jaime (el bueno) que, aunque no compartíamos techo, siempre formaron parte de la familia.

Tornar a València sempre ha sigut un moment de descans i punt de trobada amb tanta gent que estime, incloent aquells que també viuen fora: Paules, Marc, Rafa, Altea, Tapy, Cris, Rubén, Camús, César i Pablo. Gràcies per traure sempre temps cada cap de setmana que baixe, simplement fer una volta, esmorzar o fer alguna cervesa amb vosaltres em dona molta alegria. *He de hacer una mención especial a Paules por, aunque nunca lo haya pedido, priorizarme como regla sistemática poniéndome como una de sus prioridades. Nunca tendré suficiente tiempo para devolverle tanto cariño.*

Als meus companys i amics de carrera: Jaume, Carles i Héctor, per tantes hores fent partidetes entre classes i laboratoris. Especialment a Jaume, per esperar-me tants matins enfadat quan feia tard per anar a classe junts. *Aquí debo dar especialmente las gracias a Camús otra vez porque, además de darme una gran amistad, me ha acompañado*

durante tantos años estudiando juntos. Probablemente me guste tanto la química por haberla estudiado contigo.

También me gustaría agradecer a mis compañeros del máster aquel intenso año y, en especial, a todos los integrantes del laboratorio de Quino que me acogisteis y me hicisteis sentir uno más desde el primer día. Guardo muchos recuerdos y bromas de mi época en ese laboratorio en el que aprendí mucha química y se me contagió una pequeña parte de la pasión que sentían Quino, José, Simón y José.

Para acabar, los agradecimientos más importantes son para Cristina, que ha decidido acompañarme y convivir conmigo durante estos últimos años cuando empezaba la peor parte de esta etapa. Gracias por tu infinita paciencia con mi forma de ser, por adaptarte a mí cuando lo he necesitado y por ayudarme con mi agobio y estrés. Tu capacidad de esfuerzo y superación continua ha sido la mejor fuente de inspiración para obligarme a mejorar. Gracias por aguantar todos mis cambios de humor y sobre todo por hacer que cualquier cosa sea más divertida, siempre consigues sacarme una sonrisa.

Glossary

1,3,5,7-ATC	1,3,5,7-Adamantanetetracarboxylate
1,3-ADA	1,3-Adamantanediacetate
1,3-ADC	1,3-Adamantanedicarboxylate
1,5-NDC	1,5-Naphthalenedicarboxylate
2,6-DFBA	2,6-Difluorobenzoid acid
2D, 3D	Two-dimensional, three-dimensional
2-FBA	2-Fluorobenzoic acid
3,3',5,5'-ABTC	3,3',5,5'-Azobenzene-tetracarboxylate
3,3',5,5'-BPTC	3,3',5,5'-Biphenyl-tetracarboxylate
3,3',5,5'-EBTC	5-[2-(3,5-Dicarboxyphenyl)ethenyl]benzene-1,3-dicarboxylate
3,3'-ABDC	3,3'-Azobenzene-dicarboxylate
3,3'-BPDC	3,3'-Biphenyl-dicarboxylate
3-c	3-Connected
Å	Angstrom
AcOEt	Ethyl acetate
AcOH	Acetic acid
AFM	Atomic Force Microscopy
APT	Atom Probe Tomography
BCN	Barcelona Material
BCPB	1,2,3,4,5,6-Hexakis[3,5-bis(4-carboxyl-phenyl)phenoxymethyl]benzene
BDC	1,4-Benzenedicarboxylate/Terephthalate
BET	Brunauer-Emmet-Teller
BHB	3,3',3'',5,5',5''-Benzene-1,3,5-triyl-hexabenzoate
BHEB	1,2,3,4,5,6-Benzene-hexaethynylbenzoate
BINOL	Binaphthol
bipy	4,4'-Bipyridine
BPDC	Biphenyldicarboxylate
BTB	4,4',4''-Benzene-1,3,5-triyl-trisbenzoate
BTC	1,3,5-Benzenetricarboxylate/Trimesate

BTE	4,4',4''-(Benzene-1,3,5-triyl-tris(ethyne-2,1-diyl))-trisbenzoate
BTEB	1,3,5-Benzene-trisethynylbenzoate
BUT	Beijing University of Technology
CBPB	1,2,3,4,5,6-Hexakis(4-carboxybiphenyl)benzene
CCDC	Cambridge Crystallographic Data Centre
CN	Coordination Network
COF	Covalent-Organic Framework
CP	Coordination Polymer
CPB	1,2,3,4,5,6-Hexakis(4-carboxyphenyl)benzene
CPTTA	5'-(4-Carboxyphenyl)-[1,1':3',1''-terphenyl]-3,4'',5-tricarboxylate
CU	Concordia University
DCM	Dichloromethane
DIFP	Diisopropyilfluorophosphate
DIP	Diisopropylphosphate
DMA	*N,N*-Dimethylacetamide
DMF	*N,N*-Dimethylformamide
DMSO	Dimethyl sulfoxide
DMTIB	3,6-Dimethyl-tetra(5'-isophthalate)benzene
DPDS	4,4'-Dipyridyl disulfide
DUT	Dresden University of Technology
δ	Chemical shift
EPINET	Euclidean Patterns in Non-Euclidean Tilings
ESI-MS	Electrospray Ionization Mass Spectrometry
Et_2O	Diethyl ether
EtOH	Ethanol
FESEM	Field-Emission Scanning Electron Microscopy
FT-IR	Fourier Transform Infrared
GC	Gas Chromatography
h/w	Height-to-width ratio
HFPB	Hexaformylphenylbenzene
HIAM	Hoffmann Institute of Advanced Material
HKUST	Hong-Kong University of Science and Technology
HSAB	Hard and Soft Acids and Bases

θ	Torsion angle
icn	Institut Català de Nanociència i Nanotecnologia
INA	Isonicotinate
InOF	Indium-Organic Framework
IRMOF	Isoreticular Metal-Organic Framework
IRMOP	Isoreticular Metal-Organic Polyhedra
IUPAC	International Union of Pure and Applied Chemistry
J	Coupling constant
LIFM	Lehn Institute of Functional Materials
m/z	Mass-to-charge ratio
MAF	Metal Azolate Framework
MBB	Molecular Building Block
MbioF	Metal-Biomolecule Framework
MCP	Microporous Coordination Polymers
MeCN	Acetonitrile
MeOH	Methanol
MIL	Material Institute Lavoisier
mip	Methyl-isophthalate
mmen	*N,N'*-Dimethylehtylenediamine
MMM	Mixed-Matrix Membrane
MOCN	Metal-Organic Coordination Network
MOF	Metal-Organic Framework
MOM	Metal-Organic Material
MOP	Metal-Organic Polyhedra
MT	Minimal Transitivity
MTB	4,4',4'',4'''-Methanetetraylbenzoate
MTBC	4,4',4'',4'''-Methanetetrayltetrabiphenyl-4-carboxylate
MTV	Multivariate
NDI	Naphthalenediimide
net-cBU	net-coded Building Blocks Unit
NMR	Nuclear Magnetic Resonance
NOTT	Nottingham
NRG	Net Relation Graph

NU	Northwestern University
PCN	Porous Coordination Network
PCP	Porous Coordination Polymer
PDVQTC	5'',5''''''-((1*E*,1'*E*)-1,4-phenylenebis(ethene-2,1-diyl))bis(2',2''',5',5'''-tetramethyl-[1,1':4',1'':3'',1''':4''',1''''-quinquephenyl]-4,4''''-dicarboxylate)
PDVTTC	5',5''''-((1*E*,1'*E*)-1,4-phenylenebis(ethene-2,1-diyl))bis(([1,1':3',1''-terphenyl]-4,4''-dicarboxylate))
PSM	Post-Synthetic Modification
PSP	Post-Synthetic Polymerization
PTMTI	5,5',5'',5'''-[1,2,4,5-Phenyltetramethoxy]tetraisophthalate
PXRD	Powder X-Ray Diffraction
ρ	Density
RCSR	Reticular Chemistry Structure Resource
RE	Rare-earth
REDOR	Rotational-Echo Double-Resonance
rt	Room temperature
SALE	Solvent-Assisted Linker Exchange
SBB	Supermolecular Building Block
SBC	Supermolecular Building Chain
SBL	Supermolecular Building Layer
SCXRD	Single-Crystal X-Ray Diffraction
SPINOL	1,1'-Spirobiindane-7,7'-diol
σ	Single bond
TAPB	4,4',4''-(Triazine-2,4,6-triyl-tris(benzene-4,1-diyl))tribenzoate
TAPB	1,3,5-Tris(*p*-aminophenyl)benzene
TATB	4,4',4''-*s*-Triazine-2,4,6-triyl-tribenoate
TBCPB	1,2,4,5-Tetrakis[3,5-bis(4-carboxyphenyl)phenoxymethyl]benzene
TBU	Tertiary Building Unit
TCM	Trinity College Material
4-TCPB	1,2,4,5-Tetrakis(4-carboxyphenyl)-benzene
3-TCPB	1,2,4,5-Tetrakis(3-carboxyphenyl)-benzene
TCPP	Tetrakis(4-carboxyphenyl)porphyrin

TCPT	3,3'',5,5''-Tetrakis(4-carboxyphenyl)-*p*-terphenyl
TEM	Transmission Electron Microscopy
TFA	Trifluoroacetic acid
TFPB	1,3,5-Tris(4-formylphenyl)benzene
TGA	Thermogravimetric Analysis
THA	Triptycene-hexaacetate
THF	Tetrahydrofuran
TMBPDC	2,2',6,6'-Tetramethoxy-[1,1'-biphenyl]-3,3'-dicarboxylate
TMBPTC	2,2',6,6'-Tetramethoxy-[1,1'-biphenyl]-3,3',5,5'-tetracarboxylate
TMEDA	*N,N,N',N'*-Tetramethylethylenediamine
TMP	Trimethylphosphine
TMTA	4,4',4''-(2,4,6-Trimethylbenzene-1,3,5-triyl)tribenzoate
TMTB	3,3',3'',3'''-[1,2,4,5-Phenyltetramethoxy]tetrabenzoate
TPE	Tetraphenylethylene
TRUMOF	Truchet-tile Metal-Organic Framework
TTATTDC	5',5'''',5''''''-((1,3,5-Triazine-2,4,6-triyl)tris(azanediyl))tris-(([1,1':3,1''-terphenyl]-4,4''dicarboxylate))
TTF	Tetrathiafulvalene
TTFTB	Tetrathiafulvalene tetrabenzoate
UiO	Universitetet i Oslo
UMCM	University of Michigan Crystalline Material
UTSA	University of Texas at San Antonio
WSU	Washington State University
wt.	Weight
φ	Twisting angle
ψ	Bending angle
ZIF	Zeolitic Imidazolate Frameworks
ZJNU	Zhejiang Normal University

Chapter 1

Introduction to reticular chemistry: Design and post-design approaches and their related applications

1.1. Introduction: From serendipity to the rational design

The scientific endeavour in synthetic chemistry has been directed to control and understand the behaviour of matter. Over the last three centuries, researchers such as Friedrich August Kekulé,[1] Gilbert N. Lewis,[2,3] Linus Pauling[4–6] or Roald Hoffmann[7,8] deepening in chemical bonding, disentangled the meaning of control in chemical reactions by means of geometry, length, angles, strength, or electron density, shedding light on the important parameters governing control over molecules and materials. These tools together with the accumulated knowledge in reactivity, allowed the evolution of chemical science to a discipline able to synthesize tailor-made compounds, no matter existed or created. It should be noted that, the process of understanding reactivity has emerged by product of randomly mix components for obtaining an unexpected result. Originally, trial and error methodologies permitted the successful synthesis of molecules. In fact, the term synthesis comes back to the times of Aristotle in the 4th century BC, from the Greek σύνθεσις "*súnthesis*" (σύν "*sun*" - together; τίθημι "*títhēmí*" - put; and σις "*sis*" - forms nouns of action), which means putting together.[9]

It is the further step of analysing the reaction, proposing potential intermediates, and slightly modifying the reaction conditions what gave them information about what was going on in a vial or flask. Rationalization of the chemical transformations enabled the design in chemistry, modifying molecules at demand, predicting (or deducing) the results. The emergence of design in reactions divided researchers in two main approaches: (i) to set a plan of the target molecule by a chemical, controlled path of well-known modifications; or (ii) explore the unprecedent combination of substances, which cannot be anticipated. The first approach has been historically related to molecular chemists, more specifically to organic chemists, while the second one to inorganic or materials chemists. Specially, the methodology for exercising control in two- or three-dimensional structures has been considered as a synthetic wasteland until the end of the 20th century.[10–12]

Nevertheless, theoretical predictions were suggested for finding new materials.[13] The division in synthetic chemistry into organic and inorganic (organised and non-organised) was firstly proposed by Torbern Olof Bergman in Uppsala, in 1777.[14] However, it was not until 1786 when Antoine Lavoisier described organic compounds containing C, H and O atoms, as well as N according to Claude Louis Berthollet experiments.[15] Later, Jöns Jakob Berzelius determined by chemical analysis that S, P and other elements were also present in organic materials. For all the rest, it was packed in the broad range of inorganic chemistry.[16]

While Nature has been inspiring scientists for the design of natural molecules more efficiently or making molecules mimicking its processes, there has been always another side looking for the discovery of new structures. The earliest synthesis reported of an unnatural molecule was Cadet's fuming liquid, a mixture of cacodyl and cacodyl oxide, date to 1757. It was prepared by Louis Claude Cadet de Gassicourt while he was investigating about arsenic-containing cobalt ores ($CoAs_2$ and $CoAsS_2$) and various acids for the preparation of invisible inks.[17] By serendipitous, he created the first organometallic compound. It was not until 1830 when the second organometallic compound, Zeise's salt, was discovered by William Christopher Zeise, during his studies of boiling $PtCl_4$ in ethanol (EtOH).[18] However, it was not until 1954 that its structure was elucidated thanks to the single-crystal X-ray diffraction (SCXRD).[19] Besides, serendipity has also been presented in the synthesis of natural molecules, as in the obtention of urea from inorganic components (ammonia and lead oxycianate).[20] But the first unnatural organic molecule was not reported until 1853-54 (100 years later than the first inorganic molecule) by Pierre Eugène Marcellin Berthelot, who performed the deliberate esterification of fatty acids with glycerol.[21] This is an example of how the evolution of design and logic was applied from the serendipitous synthesis of urea to the intentioned unnatural esters in organic molecules.

1.2. Historical overview: From coordination chemistry to its extension to Coordination Polymers (CPs)

In the case of inorganic molecules, the process of rationalizing synthetic process could not be applied until 1893 when Alfred Werner laid the foundations of a new field, coordination chemistry, capable of explaining the linkage involving metal centres and surrounding ligands.[22] He introduced geometric concepts for rationalizing these interactions, the definition of coordination bonds, as well as the isomerism of coordination compounds with two ligands by measuring the conductivity of its dissociation. This field paved the way for the development of many new fields such as supramolecular, cluster and transition-metal carboxylate cluster chemistries.[23] In fact, compounds from the latest one were already described 200 years ago, in 1823,[24] but their molecular arrangement were not elucidated until the middle of the 20th century with the help of the SCXRD.[25] At this point, the field erupted thanks to the contribution of extended studies from Yoshihiko Saito, or later, from Frank Albert Cotton and others.[26–35]

Until then, inorganic chemistry was mostly related to metal-based structures from materials science that could not be anticipated or rationalized. Their discovery was the result of serendipity, observation, and properties for many kinds of compounds such as salts, metal oxides, nitrides or sulfides and zeolites, among others. These later compounds were microporous structures that were already known since Axel Fredrick Bronsted discovered stilbite in 1756, which could release water upon heating, naming them as zeolites from the Greek ζέωλίθος "zéōlíthos" (ζέω "zéō" - to boil; λίθος "líthos" - stone). In contrast to the prior materials, their composition was purely inorganic composed of tetrahedral $[SiO_4]^{4-}$ and $[AlO_4]^{5-}$ units, where tetrahedra are joined by corner sharing (oxygen atoms). The presence of Al^{3+} metals in the framework makes it negatively charged, balanced by the counterion metals in the pores (usually, from the first and second column of the periodic table). Despite being present in nature, R. M. Barrer synthesized the first unnatural zeolite in 1948,

mimicking the alkaline and high thermal natural conditions.[36,37] Instead of metallic counterions, it was reported that organic cations, commonly quaternary amines, led to the discovery of new networks while were remaining in the pores, as a template effect growing around them. The tuning of the organic counterion could be tuned to unveil the synthesis of specific catalyst for a particular reaction, using a template with a similar size than the intermediate formed during the reaction, directing to just one product.[38] Moreover, these templates could be removed by calcination due to the high thermal stability of the materials. Despite exhibiting a limited variety of chemical functionalization due to the inorganic nature, restricted to forming new structures by tuning the synthetic conditions, their microporosity and thermal stability have made them as perfect candidates in some applications such as ion exchange, catalysis in oil-cracking or molecular sieves.[39–41]

The implementation of X-ray diffraction in materials science unlocked the spatial arrangement of the atoms in the structures. Crystallography was a developing field since its first apparition by descripting the shape of different crystal compounds pioneered by René Just Haüy.[42] This technique was key in the first steps towards the rational design of inorganic materials once understood the chemical behavior and organization of each atom under different synthetic conditions; as well as the different kind of interactions and bonds. In fact, the elucidation of crystalline compounds dramatically affected the evolution of these fields, as new structures were exponentially discovered in the subsequent decades.

The barrage of new metal-organic systems in the field of solid-state made traditional porous crystalline materials, such as zeolites, no match for them. Certainly, it was the group of Yoshihiko Saito again who for the first time attempted to extend the coordination bond into two directions for linking distinct metal sites in a coordination polymer (CP) in 1957.[43] But it was not until 1959 when he successfully created three examples of the first rationalized CPs, combining Cu(I) metal ions and ditopic hydrocarbon ligands of different length with terminal nitrile groups. The length of the linker influenced on the dimensionality of the polymer,

obtaining a monodimensional chain with succinonitrile,[44] a bidimensional square lattice layer with glutaronitrile,[45] and a tridimensional diamond-like structure with adiponitrile (Figure 1.1).[46]

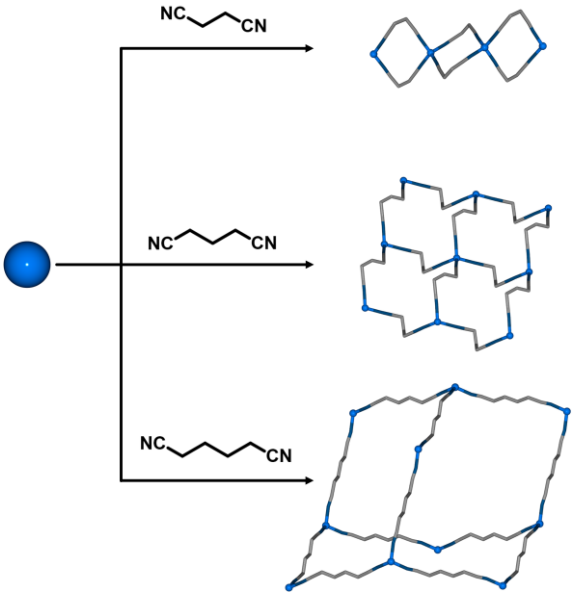


Figure 1.1. First coordination polymers reported based on the assembly of tetrahedral Cu(II) with succinonitrile, glutaronitrile and adiponitrile resulting in a 1D chain, a 2D layer and a 3D framework, respectively.

It is true that before this, purely inorganic CPs were known since 1707, such as ferric hexacyanoferrate(II) (also called Prussian Blue), a synthetic blue pigment discovered by serendipity by Diesbach and Dippel in Berlin.[47] Curiously, Diesbach was looking for synthesizing Florentine Lake, a red pigment based on cochineal red. When he ran out of potash, he borrowed from Dippel's contaminated with hexacyanoferrate, so the addition to the iron sulfate-containing solution produced a blue precipitate, due to the coordination of the molecular complex hexacyanoferrate(II) to iron(III), forming $Fe[Fe(CN)_6]_3{\cdot}xH_2O$ (x = 14-16). Once more, the crystal structure remained unknown until 1977 when A. Ludi elucidated by SCXRD.[48] Another similar structure, known as Hofmann clathrate, was reported

much later, in 1897. These structures were extended tetracyanonickelate(II) in a square conformation coordinated to octahedral Ni(II), capped by ammonia in the axial position.[49] Its structure, $[Ni(CN)_2(NH)_3]\cdot C_6H_6$, was elucidated in 1949 by H. M. Powell by X-ray crystallography, showing a two-dimensional (2D) square grid network (**sql**).[50] The packing of these layers generated some potential voids between the axial positions where benzene molecules were trapped. These clathrates were studied to form mixed-metal analogues by combining two charged complexes,[51,52] or even the pillaring of the layers by diamine linkers such as ethylenediamine.[53] However, the problem with these structures is the limited chemistry that cyanide linkers presents because they are not functionalizable, compared to the metal-organic networks reported by Saito. It must be said that, by using the neutral linkers, the resulting frameworks were charged, where nitrates balancing the charge were located inside the pores of the structure.

The following advance can be attributed to the organic research group of Siegfried Hünig, who crystallized an isostructural Cu(I)-based network linked by the *N,N'*-dicyanoquinonediimines while they were looking to construct an organic conductor in 1986.[54] In this case, the corresponding framework was neutral. Even so, the major contribution to the field of CPs started in 1989 with B. F. Hoskins and R. Robson. One of the first important works was the synthesis of a binodal diamond-like structure (**dia**), with both tetrahedral Cu(I) and 4,4',4",4"'-tetracyanotetraphenylmethane, where the BF_4^- anions fit in the pores (Figure 1.2, left).[55] For the first time, they used a rigid organic ligand with higher connectivity, to be used as a node instead of an edge. They studied the chemistry of extending transition metal clusters with nitrile functional groups, forming a plethora of diamond-like networks, or the exchange of the counterion in the pores without structural collapse.[56] In addition, they also reported the first structure with two different nodes with different geometry: a porphyrin-based linker with a square conformation joined by the tetrahedral Cu(I) metal centers, mimicking the well-known PtS net (**pts**) (Figure 1.2, right).[57] All their work was inspired by the control

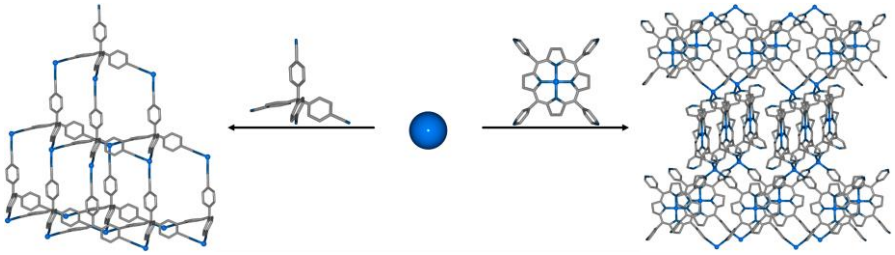


Figure 1.2. Representative examples of two pioneering CPs based on rigid linkers with different geometry. Tetrahedral Cu(II) metal ions are reticulated with a tetrahedral linker into a diamond-like network (left), or with a square linker into a PtS-like net (right).

of weak bonds presented in supramolecular systems and the design of solid-state supramolecular structures in a subfield named as crystal engineering, which studies the packing of molecules (generally organic) by hydrogen, halogen or intermolecular interactions. These strategies enable the prediction of solid-state suprastructures by fixing molecules in specific crystallographic positions, crystallizing them. Hoskins and Robson translated these concepts to metal-organic networks through the coordination bonds.

The description and classification of these networks was based on the prior work provided by Wells in 1977.[58] He studied the most relevant nets presented in chemical systems, such as zeolites and ionic salts, or in classical inorganic compounds, such as pure metallic or metal oxides, nitrides, and sulfides. His approach is based on the simplification of the atoms in a network according to their connectivity, resulting in different topologies due to their circuits of connections. Essentially, it is the most suitable way to describe and differentiate materials, reducing them to an abstract mathematical entity such a net. Some of the most common nets that were described are the 2D square and hexagonal grids (**sql** and **hcb**), and the 3D α-polonium/NaCl (**pcu**), diamond (**dia**), Lonsdaleite (**lon**), quartz (**qtz**), feldspar-related and zeolite-related (**fel**, **sod**, **fau**, **ana**, **rho**, etc.), PtS (**pts**), NbO (**nbo**), cubic (10,3)a (**srs**), rutile (**rtl**), Pt_3O_4 (**pto**), and Ge_3N_4 (**sln**) nets.

It was Robson who pioneered the translation of these concepts from pure inorganic solids to coordination framework solids with the net-based approach as well as the introduction of the concept of molecular building blocks (MBBs) by deconstructing the components of the net according to the functionality, stereochemistry, and connectivity.[59,60] This could help to predict the resulting structures by selecting the appropriates pre-organized MBBs and assemble them for affording the target net. At that point, the approach was based on experimental, far less predicting the potential wide range of structures to come. However, it was the beginning of the rational design of networks based on coordinate bonds, a convenient interaction due to their reversibility, crucial for the crystal growth. But, as they suggested, could be translated to reversible C-O or C-N bonds to engineer 2D or 3D covalently bonded organic polymers in single-crystals.

The design of CPs based on N-donors bridging linkers was exploited by many researchers such as M. J. Zaworotko,[61–64] S. Kitagawa[65–67], and M. Fujita[68,69], among others.[70–74] However, we can attribute one of the most significant contributions to the field to the group of O. M. Yaghi in 1995. This year they discovered a $ThSi_2$-like (**ths**) net constructed with the rigid 4,4'-bipyridine (bipy) and Cu(I) ions in a trigonal coordination environment (Figure 1.3, left).[75] This study was very important because: (i) it was the first time that the term "metal-organic framework (MOF)" was employed; and (ii) it was proposed the solvothermal synthesis as a viable route to accessing transition metal-based frameworks.

Some drawbacks that these monodentate metal-binding linkers represented was that: (i) the coordination environment is relatively uncertain, exemplified by the competition between ligands and solvent modifying the geometrical arrangement, what makes them not designable; (ii) these structures generally collapsed upon solvent removal or counterion exchange; and (iii) the resulting structures are not chemically stable owing to their weaker bonds. All these features moved researchers to explore the use of anionic chelating ligands rather than monodentate, ones to enhance the framework stability because of the high thermodynamic association in

metal-chelating ligand due to the potent entropy-related chelate effect, protecting from solvent or anion competitors. Moreover, the number of ligands surrounding the metal can be reduced, consequently reducing the possible outcomes for a better design and prediction on the network assembly. This is the case of the simplest oxalate or 2,2'-bipyrimidine linkers combined with octahedral transition metals on 2D or 3D assemblies, developed by researchers coming from the field of coordination complexes and molecular magnetism.[67,76–81] Another example is the use of organic carboxylates, as firstly introduced by Yaghi in a 2D MOF capable of developing host-guest chemistry with pyridines, despite not being all the carboxylates deprotonated and chelating metals.[82]

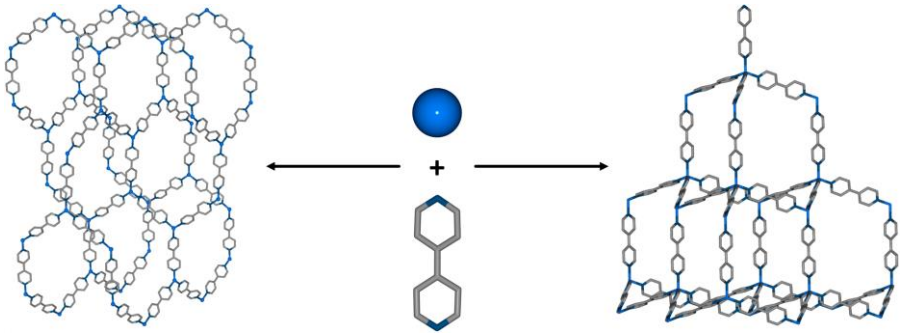


Figure 1.3. Two different structures obtained by the group of Yaghi when assembling the same building units. The Cu metal ions can be bridged by rigid, ditopic linkers into a ThS-like net if the metal adopts a triangular coordination geometry (left); or into a diamond-like network if the metal adopts a tetrahedral coordination geometry (right).

Another problem that the group of Yaghi noticed is the poor predictability of the coordination environment of single metal ions as vertex in networks. For example, the previous MOF was reported both with bipy and Cu(I) in a trigonal[75] or tetrahedral[74] coordination environment, affording the corresponding **ths** or **dia** nets, respectively (Figure 1.3). This motivated them to fix the metal in a specific coordination environment, so they were inspired by the well-known chemistry of transition-metal carboxylate clusters, known since the 40s and 50s after their structural arrangement elucidation. Based on the simplest bimetallic unit known

surrounded by 4 carboxylates and two available axial positions, also called as "paddlewheel", they synthesized the first MOF (MOF-2) by extending Zn(II) pyramidal metals presented in the paddlewheel unit with terephthalic acid (H_2BDC) under diffusion conditions (Figure 1.4, top).[83] The main advantages of this revolutionary strategy were: (i) the control on the metallic building unit, displaying rigidity, directionality and a fixed coordination geometry; (ii) the presence of the anionic binding moiety, providing an electrostatic contribution to the coordination bond and therefore, increasing the bond strength; (iii) the resulting framework was neutral, without any need of counterions in the pores to compensate the charge; and (iv) the generation of a new inorganic unit that, considering their points of extension including the carboxylates, could define a geometry and connectivity. All these reasons certified why this MOF became the cornerstone of design of new metal-organic materials (MOMs).

Another important fact that all these features contributed to was for the establishment of microporosity in a MOM. Gas sorption isotherm measurements had been confirmed and studied in crystalline and amorphous porous inorganic solids, such as zeolites, activated carbon and related molecular sieves. The first attempt to study porosity in metal-organic species was performed by R. Barrer in 1969, demonstrating that Werner complexes, β-[M(γ-picoline)$_4$(NCS)$_2$] (where M is Co(II) and Ni(II)), can adsorb gases reversibly.[84] However, the complexes became non-porous upon cycling, breaking their packing. Since then, the adsorption of gases was frustrated due to the network collapsing after removing counterions in the pores until 1997, when Susumu Kitagawa reported the adsorption of CH_4, N_2 and O_2 carried out at 298K from 1 to 36 atm for a $Co_2(bipy)_3(NO_3)_4{\cdot}xH_2O$ CP.[85] In this case, the structure could remain stable after desolvation and vacuum. But, according to Yaghi, the real measurement to confirm microporosity should be performed at low pressure, measuring the adsorption isotherm at 77K, known as the "*gold standard for measuring porosity*". If not, you are forcing the gas molecules

into the material. This was firstly demonstrated with MOF-2, exhibiting a Langmuir surface area of 275 m^2/g.

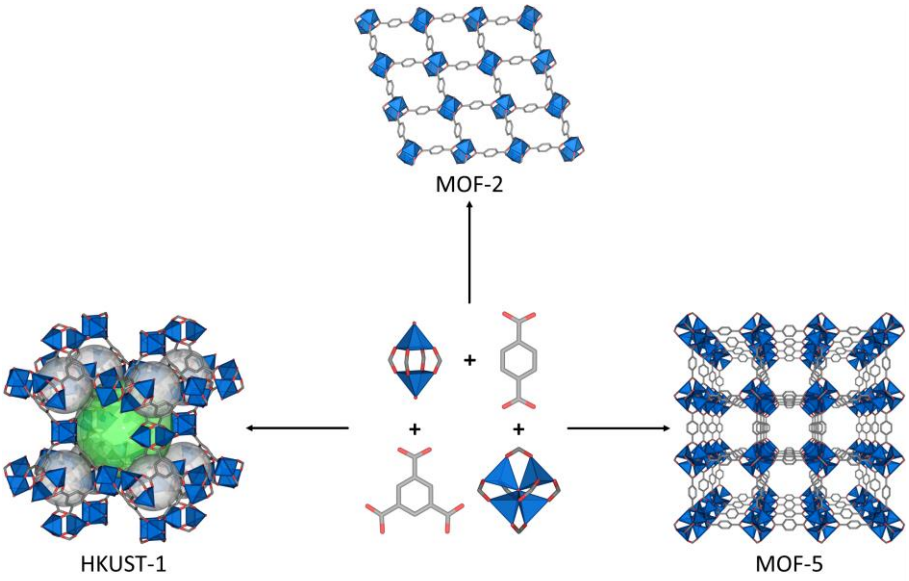


Figure 1.4. Representation of the most significant first MOFs based on basic unit components. The combination of ditopic organic linkers and 4-c M(II)-paddlewheel clusters formed MOF-2 (top). Increasing the connectivity of the ditopic linker to a tritopic while maintaining the same inorganic MBB built HKUST-1 (left). Increasing the connectivity of the cluster to a 6-c Zn(II)-based cluster while maintaining the same organic MBB yielded MOF-5 (right). Note that here and in the following figures, the metal ions are represented by their coordination figure in the clusters, and some structures displayed big spheres with different colours that are stand for the empty space of the porous structures.

The appearance of MOF-2 inspired researchers to expand the chemistry of using metal carboxylate clusters. The next year, by increasing the connectivity of the organic MBB BDC to trimesic acid (H_3BTC, 3-connected, 3-c), an isostructural dimer carboxylate-cluster based on Cu(II) was extended to yield the first 3D framework under solvothermal conditions, $[Cu_3(TMA)_2(H_2O)_2]$, known as HKUST-1 (Figure 1.4, left).[86] This MOF crystallized in a twisted boracite-like topology (**tbo**), showing a Brunauer-Emmet-Teller (BET) surface area of 692.2 m^2/g (which could be improved later up to 1800 m^2/g). A few months later, Yaghi

reported a new MOF by increasing the connectivity of the inorganic MBB instead of the organic one. By using the same components of MOF-2 but sightly modifying the conditions, they found that Zn(II) ions changed their coordination from pyramidal to tetrahedral in the well-known tetranuclear oxyhexacarboxylate cluster, displaying an octahedral conformation according to their points of extension (6-c).[87] This 3D framework with formula $Zn_4O(BDC)_3$ (named as MOF-5) exhibited an α-polonium-like topology (**pcu**) and a high Langmuir surface area of 2900 m^2/g (which later was optimized to 4000 m^2/g) (Figure 1.4, right). At this point, MOFs represented a superior control and broader chemical functionality in the field of materials science and a competitor of traditional zeolite in many applications, which could not surpass such a high surface area values (usually, between 300 and 1000 m^2/g). These pioneering studies at the end of the 20th century stablished the beginning of the reticular chemistry field.

1.3. Reticular Chemistry

1.3.1. General concepts: Requisites, secondary building units (SBUs), and isoreticular principle

Reticular chemistry is defined as the chemistry of linking MBBs by strong bonds to make crystalline open frameworks.[88,89] The term reticular comes from the Latin *reticulum*, which means net-like. It consists in the prior analysis of MBBs according to their points of extension and chemical functionality. The points of extension are defined by the connectivity and geometry when simplifying to a node in a net. The chemical functionality determine which kind of interaction can be formed to produce the linkage and the directionality they govern over the reticulation. These two basic aspects are essential for linking molecules to make larger discrete and extended structures. This strategy became a turning-point in chemical synthesis

because permitted to transfer the precision and control, which is applied modifying molecules in molecular chemistry to extended chemical structures.

One of the most attractive and beautiful points is that the design in both organic and inorganic chemistry come together to this new field since its division in 1777. Containing both chemistries joined by strong interactions in a crystalline phase can open up to a myriad of applications or even the combination of some of them. Crystallization of this phase helps the subsequent study of the orientation, geometry, and connections between the MBBs for their topological classification. However, one of the drawbacks is the dilemma of creating strong bonds in a periodic fashion, known as the *crystallization problem* (Figure 1.5). The difficulty in crystallizing something is almost proportional to how strongly they are interacting. This contrasts with the supramolecular chemistry, which is based on the control of weak bonds such as Van der Waals, hydrogen-bonds or neutral donor-linkers

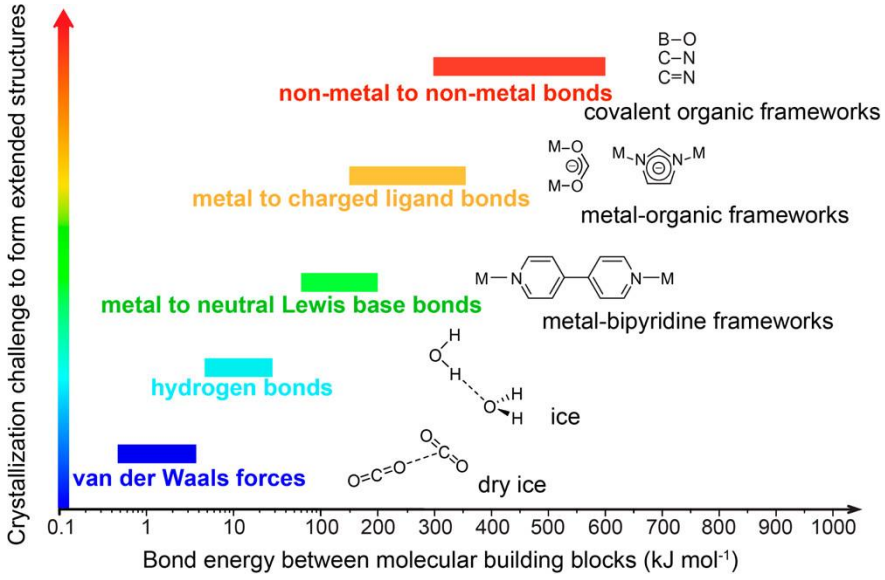


Figure 1.5. Schematic diagram of the *crystallization problem*. The more increased the bond energy of linkages between the MBBs, the most difficult to extend them in a crystalline structure. The selection of the MBBs should balance its facility to create reversible bonds, to self-repaired and correct defects formed during the crystal growth, and the rigidity and directionality of their points of extension.

bonded to metal. Reticular chemistry aims on controlling strong bonds such as charged linkers bonded to metals or covalent bonds.[89]

Another prerequisite in reticular chemistry is the use of judiciously-designed, rigid and geometrically well-defined building units to form extended framework structures. The geometric constraint inherent to these MBBs limits the number of possible resulting net topologies. However, under appropriate reaction conditions, other topologies than the default ones can be targeted. The geometry of the MBBs is related to their metrics, such as length, width, size, and angles, which can affect to direct the synthesis to a specific structure. It is fundamental that these characteristics in both MBBs remain unaltered during synthetic conditions to introduce a degree of predictability and control the chemistry of the metal ion used. This makes a difference from retrosynthesis; inasmuch as reticular synthesis demands to remain unaltered the structural integrity and rigidity of the building blocks.

The central core in reticular chemistry is the rationalization of complex structures according to their connections (Figure 1.6a). The introduction of transition metal carboxylate clusters in MOFs required its simplification into a unit with a specific geometry. Partial subunits in periodic structures have been already coined as secondary building units (SBUs) for the representation of cavities or fragments in zeolites, which was translated for the first time in a reticular material in HKUST-1, considering as SBU an octahedral cage respect to the position of the paddlewheel clusters.[86] However, a few months later Yaghi used this term to represent the geometry of the inorganic MBB from their points of extension, such as the carboxylate C atoms in most carboxylate MOFs.[87] This approach for SBU has been the most used in reticular materials, being the target "blueprint" cluster *in-situ* formed under the proper conditions or preformed in a two-steps synthesis.

By following this approach, the same group studied the limits of expanding the organic linker in terms of its length, therefore increasing the spacing between

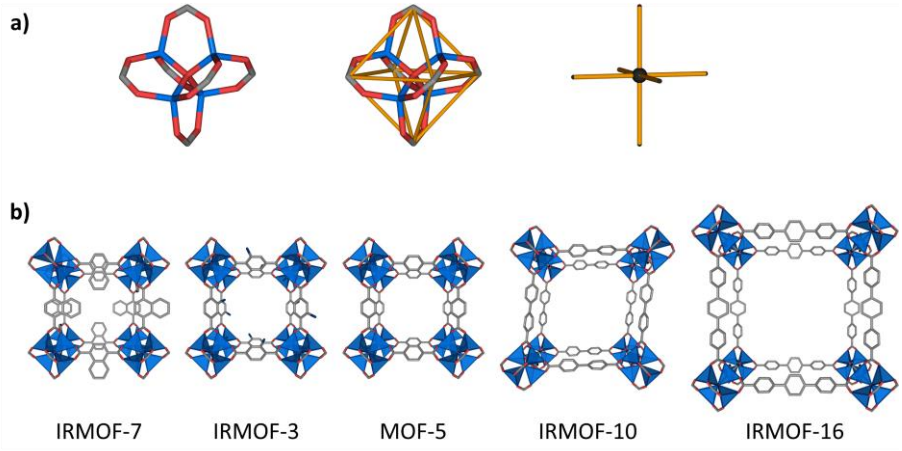


Figure 1.6. a) Simplification of an inorganic SBU (Zn-tetramer oxyhexacarboxylate) according to the geometrical figure representing its points of extension (octahedron) or into a 6-c vertex. b) Isoreticular frameworks of MOF-5 by introducing pendant groups in the organic linker (amine, IRMOF-3; benzene, IRMOF-7) or by expanding the metrics with additional benzene rings (IRMOF-10 and IRMOF-16).

vertices in a network. This concept, named as *isoreticular principle*, led the discovery of 16 MOFs with the same underlying topology, which confirmed the predictable pore shape and metrics by tuning linkers from 3.8 to 28.8 Å or by decorating pendant functionalities (Figure 1.6b). Some isoreticular MOFs (IRMOFs) presented interpenetration when the linker size increase, as nature does not like vacuum and tend to occupy this space with additional nets. However, by tuning the synthetic conditions, the single nets could also be achieved.[90]

1.3.2. Linker design: Metal-Organic Polyhedra (MOPs) and Zeolitic Imidazolate Frameworks (ZIFs)

The imminent expansion of reticular chemistry made researchers study the scope of ligands with different functionalities and connectivities. Investigating the useful metric information that linkers hold, more sophisticated effects were explored, such as bending or twisting of the connecting groups respect each other (Figure 1.7a).

The simplest bending, where binding groups are co-planar and bent by an angle (θ), gave rise to the discovery of a metal-organic polyhedron (MOP). By using isophthalate, the 120º between both carboxylates promoted the isolation of a discrete macromolecule, exhibiting 12 Cu(II)-paddle-wheel in a cuboctahedral fashion joined by 24 isophthalates (Figure 1.7b).[91] This cage, which resulted porous, neutral and robust, represented an alternative to classic supramolecular cages, often encountered through the assembly of Pd-N weaker bonds and positively charged. In these materials, it could be studied how the bending angle of the organic linkers impact in the assembly of cages, as 90º between carboxylates yielded a different cage, with 6 Cu(II)-paddlewheels in an octahedral conformation,[92] and a mixture of both yielded a tricapped trigonal prism MOP with 9 Cu(II)-paddlewheels.[93]

Another kind of change can prompt structures with different dimensionality due to guiding MBBs in thermodynamically favoured conformations. This was confirmed in the assembly of square building blocks, mostly M(II)-paddlewheels, with

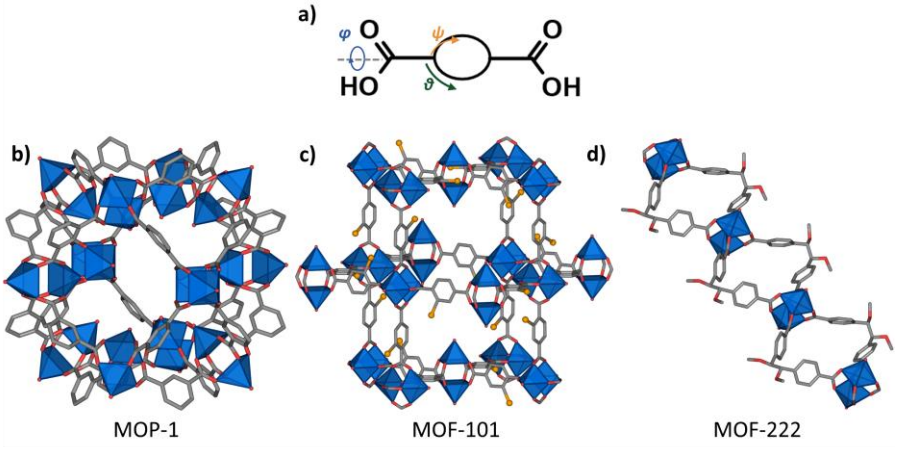


Figure 1.7. a) Bending and torsion angles studied for ditopic linkers. The functionalities can be redirected by bending in the plane while carboxylates remain coplanar (θ); by twisting one of the planes with a torsion angle about the linker axis relative to the other (φ); or by bending out of the plane towards each other and breaking the coplanarity. b) Structure of the first MOP when bonding the θ angle in 120º. c) Structure of MOF-101 when twisting the φ angle in 90º. d) Structure of MOF-222 when bending the ψ angle in 70º.

different organic linkers. The exhaustive study of ligand conformations confirmed that steric hindrance or electronic repulsion can change other angles and favor new phases.[94,95] This is the case of introducing a single functional group in the *ortho*-position of one of the carboxylates in the BDC linker, producing the twisting (φ) of the neighboring carboxylate plane respect to the other in 90º. The assembly of this linker with Cu(II)-paddlewheels forms the tridimensional NbO-type framework (**nbo**) rather than the bidimensional square lattice (**sql**) (Figure 1.7c).[96] Another possible torsion can be driven by the bending (ψ) of both planes of the carboxylate groups toward each other, which resulted in the assembly of Zn(II)-paddlewheels in a 1D ladder structure (Figure 1.7d).[95]

Perhaps the most studied effect has been the bending angle thanks to the discovery of frameworks able to mimic zeolite-like nets. The most significant example is the use of imidazolate, which forms an angle of 145º similar to Si-O-Si bonds. The earliest example was reported in 2002 using Co(II) single-metal-ions adopting a not common zeolitic topology (**nog**).[97] One year later, Zn(II) was coordinated by four benzimidazolate ligands to mimic, for the first time, a well-known topology related to zeolitic-materials such as the sodalite (**sod**).[98] The steric hindrance produced by the benzyl side group forced the orientation of the linkers to afford this specific topology. The same group pioneered this field for understanding how influenced tuning the side groups in different azolates or the choice of metals, discovering many different structures.[99] The main advantage of these nets was the obtention of high surface areas having the same underlying topology than their relative zeolites. One of the most famous structures, built with Zn(II) and 2-methylimidazole, showed high thermal and chemical stabilities. However, they did not name this family after a while as metal azolate frameworks (MAFs),[100–102] and the same year the group of Yaghi reported a similar study about the scope of zeolitic imidazolate frameworks (ZIFs), terminology that was adopted and stablished in the reticular community, naming this compound as ZIF-8 (Figure 1.8).[103]

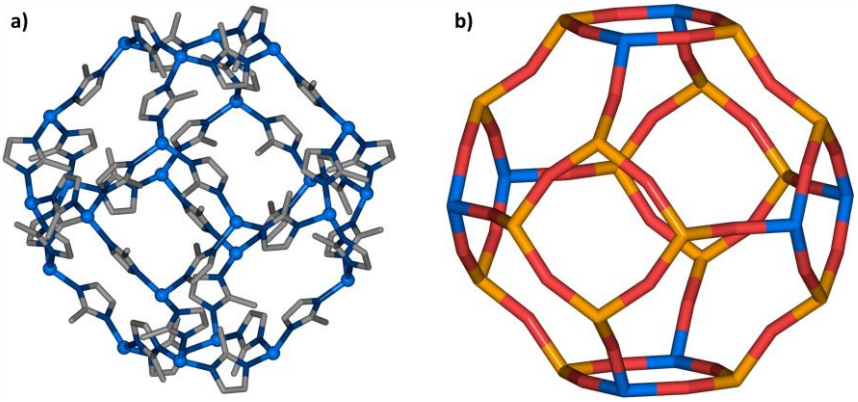


Figure 1.8. Comparison of the structures based on the same underlying net constructed with a) metal and organic components (ZIF-8), or with b) purely inorganic components (sodalite). Note the difference in the cavity size, obtaining bigger pores in the case of MOFs.

The scope of linkers was increased in terms of connectivity and size. Some examples are the use of tetrahedral (4-c),[104] square (4-c)[105] and the dendritic trigonal prism (6-c) MBBs.[106] Moreover, the expansion of the metrics in the linkers unveiled new materials, most of them on account of the chemical information of the linker when the orientation of the carboxylates is slightly modified, producing the overall structural rearrangement into a new net because of the cluster directionality.[107–110]

1.3.3. The impact of the metal-based building unit

After this point, the control of structure metrics and functionality was later expanded by exploring different inorganic MBBs of different connectivity and shapes simultaneously. In the case of the metal-based component, one of the first achievements was to move from M(II)-based clusters, which usually formed weaker coordination bonds, to M(III)-based carboxylate clusters, able to form strong M-O bonds, as in the case of Cr(III), Fe(III), V(III), In(III) or Al (III) or rare earth metals (RE). The first appearance of these metals in MOF chemistry was performed by the group of G. Ferey, usually obtaining metal-oxo chains as an SBU.[111–113] In fact, the discovery of linking metal-based chains was crucial for expanding the scope of

inorganic MBBs as well as for the subsequent discovery of the breathing effect, a structural transformation according to the flexibility of the net, being still connected but compressed in one direction and stretched in the perpendicular direction, affecting to the channels, pore sizes and apertures of the framework.[114–118] The swelling of the structure can be triggered by the solvent removal or exchange by changing the host interactions with solvents or gases.

A few years later, in 2002, the same group reported the introduction of the trimer cluster in a MOF.[119] The metals (V^{3+}) displayed an octahedral coordination, with a central triple bridged O atom, 6 carboxylates in a trigonal prism conformation, and 3 open metal sites with OH^-/H_2O molecules, one for each metal. Curiously, the combination of this cluster with the isophthalic acid formed a structure with the same underlying topology as MOF-5, being a trigonal prism instead of an octahedron (Figure 1.9). This 60º difference between both planes in the MBBs was

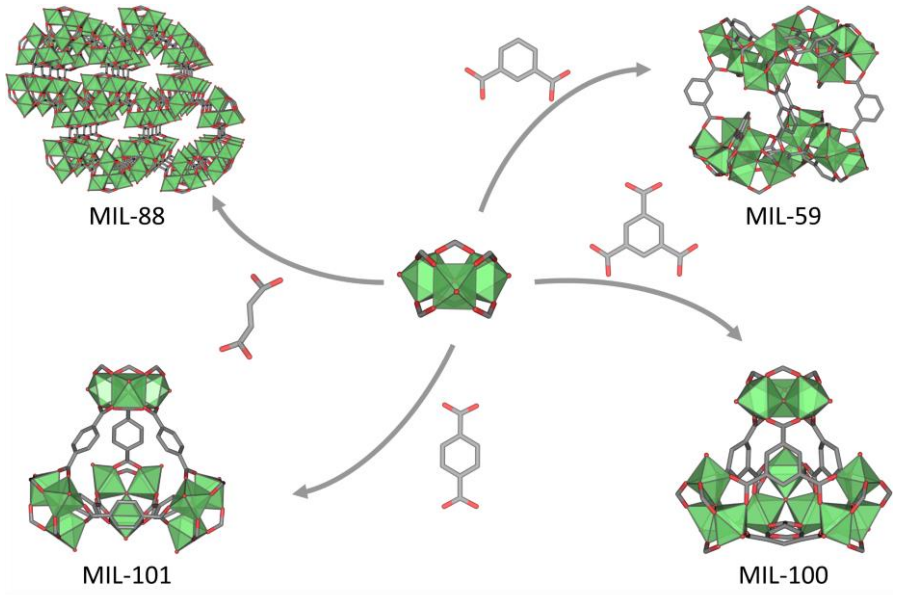


Figure 1.9. Assembly of the trimer M(III)-cluster into different MOFs according to the symmetry and connectivity into MIL-88 (fumarate), MIL-59 (isophthalate), MIL-101 (BDC) and MIL-100 (BTC).

avoided by the effect of the bent linker. This structure paved the way for the synthesis of the "default" net by combining trigonal prismatic MBBs with rigid linear linkers, in the well-known MIL-88[120] (which underlying topology was later named as **acs** due to MOF- 235).[121] This MOF stood out for its synthesis, which was firstly performed in a two-steps procedure by using the preformed cluster acetate, and for its breathing unveiled by the solvent-host interactions in an isoreticular analogue, which was the first case in a cluster-based MOF, and the largest swelling ever observed by SCXRD (Figure 1.9).[122,123] The trimeric cluster increased the repertoire accessible to chemists for the discovery of new structures based on this MBB, leading to two of the most famous mesoporous MOFs such as MIL-100[124] and MIL-101 (Figure 1.9).[125]

The fruitful results obtained with M^{3+}-based SBUs in terms of connectivity, porosity, and stability inspired researchers to move to stronger bonds, such as those resulting from the M^{4+}-carboxylates. The higher the oxidation state of a metal, the smaller the atomic radius, resulting in a more concentrated charge/radius ratio, which make them hard acids and match with the hard carboxylate moiety, according to the hard and soft acids and bases (HSAB) principle.[126,127] The first case disengaged the use of the highly-connected, hexanuclear Zr-based cluster in MOF chemistry, which exhibited a cuboctahedral arrangement of 12 BDC around it in UiO-66 (Figure 1.10).[128] This cluster represented an important milestone for the development of reticular chemistry, unveiling new nets with nodes with a different and higher coordination geometry than those previously reported, as the 12-c **fcu** topology. This framework was demonstrated to be able to expand the linker metrics with the isoreticular UiO-67 and UiO-68. One of the most interesting features of this cluster is its high-stability produced by the strong Zr-O-C bond, which enable the synthesis of a myriad of structures by tuning ligand connectivity and symmetry, producing defaults of connectivity in a cubic (8-c),[129,130] hexagonal (6-c),[131] octahedral (6-c),[132] trigonal prismatic (6-c)[133] or square (4-c) shapes,[134,135] among the most regular ones. This specific characteristic of the Zr-hexamer cluster allowed the

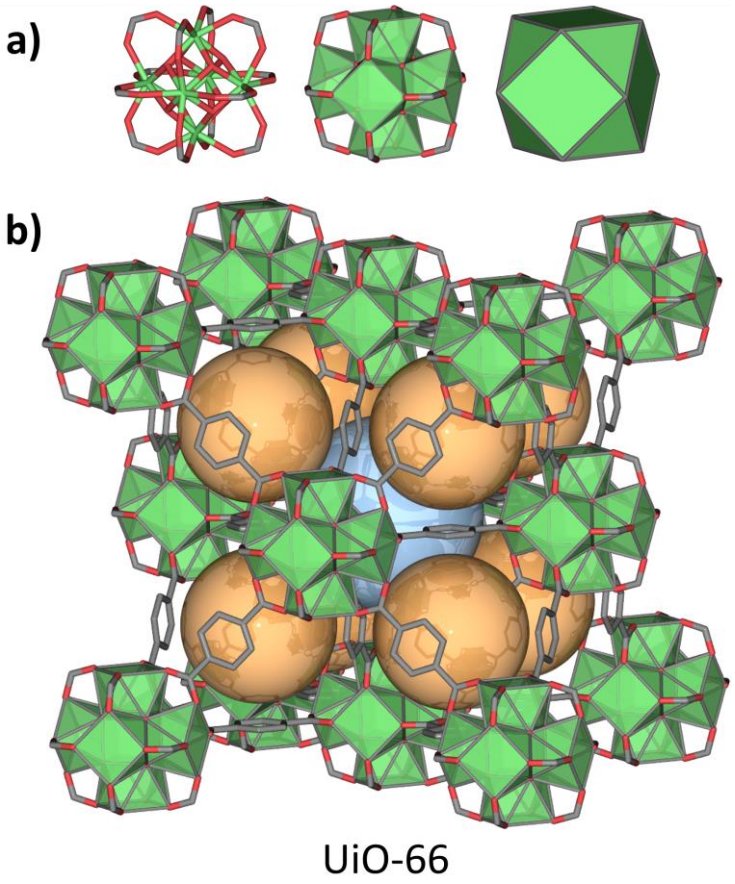


Figure 1.10. a) Zr-hexamer oxo/hydroxo-cluster with 12 carboxylates represented in their atomic arrangement (left), coordination geometry of the tetragonal antiprism Zr atoms (center), and cuboctahedral geometry according to its points of extension (right). b) Crystal structure of UiO-66.

discovery of new regular nets, which were not accessible due to the connectivity or geometry required. Isoreticular clusters were able to replicate the hexamer conformation with Hf^{4+},[136] and 5 years, later with RE metals such as Y^{3+}, Tb^{3+}, Ce^{3+}, Eu^{3+}, Dy^{3+}, Ho^{3+}, Er^{3+}, Yb^{3+}, Sm^{3+}, Gd^{3+} or Th^{4+}, displaying a different coordination environment and chemical versatility represented by the presence of clusters with different nuclearity.[137] In addition, the **fcu** topology was also achieved when Ti^{4+}

was incorporated in porous frameworks with an octanuclear wheel-like cluster in MIL-125.[138]

The rich chemical diversity of metal species was not limited to discrete carboxylate clusters. As mentioned before in literature, it is common to find examples of 1D metal-oxo chains as SBUs for the construction of MOFs. These structures are based on cylinder packings, where the most common are the ones constructed with parallel rods, and the rod axes intersect a perpendicular plane in a pattern of the nodes of a 2-periodic net. The most common structures are based on square (**sql**), hexagonal (**hcb**), triangular (**hxl**) and a combination of the last two (**kgm**) channels.[139] While the first one was earlier discovered in structures related to MIL-53 (Figure 1.11a), the second one represented an ideal platform for exercising reticular chemistry. MOF-74, synthesized in 2005 by decorating hydroxyl groups in the symmetrical ortho positions of BDC, direct Zn(II) atoms to form the rod SBU connecting the atoms through both hydroxides and carboxylates (Figure 1.11b).[140] This stable MOF was demonstrated as an excellent platform of the isoreticular chemistry, by substituting the metals (or mixed metals) and expanding the linker metrics up to eleven benzene rings, increasing the pore aperture from 14 to 98 Å, the biggest ever reported.[141] Periodic SBUs are not limited to rods, as metal-oxo layers have been reported pillared by ditopic linkers such as BDC (Figure 1.11c).[142]

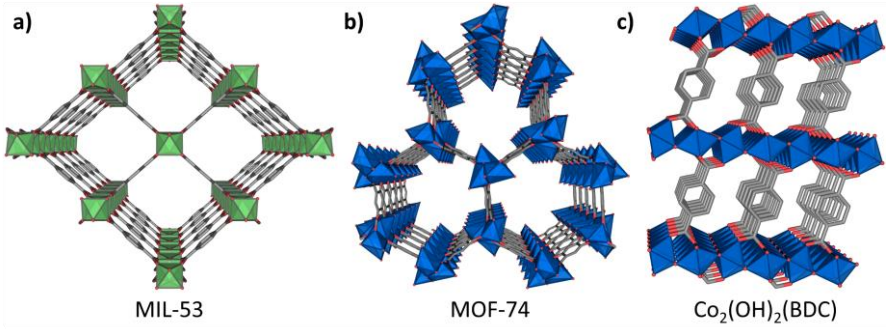


Figure 1.11. Structures based on the extension of metal-oxo chains in a) Cr(III)-MIL-53 and b) Zn(II)-MOF-74 in square and hexagonal channels, respectively; or in the extension of metal-oxo layers in c) $Co_2(OH)_2(BDC)$.

Both cases can merge properties of traditional metal oxides and novel porous frameworks. However, it is known the difficulty in synthesizing big enough single-crystals suitable for SCXRD of MOFs based on this periodic SBUs, as all of their structures have been elucidated by powder X-ray refinements, probably due to the fast creation of the non-reversible metal-oxygen bond, preventing the crystal growth.

1.3.4. Covalent Organic Frameworks (COFs)

The other direction in which reticular chemistry has been growing is in the combination or purely organic MBBs, as a counterpart to traditional purely inorganic materials. However, the strong linkage often generates amorphous, disordered materials as stated by the *crystallization problem* (Figure 1.15). The control of these polymers has been restricted to one dimension over the last century, still not periodic. The two first porous, crystalline covalent organic frameworks (COFs) were reported in 2005 through the reversible condensation of boronic acid moieties to form boroxines.[143] These porous materials crystallized in 2D planar layers of hexagonal pores in a honeycomb-like (**hcb**) by joining linear diboronic acids to form 3-c boraxine MBBs or by joining 3-c cathecholes with linear diboronic to form

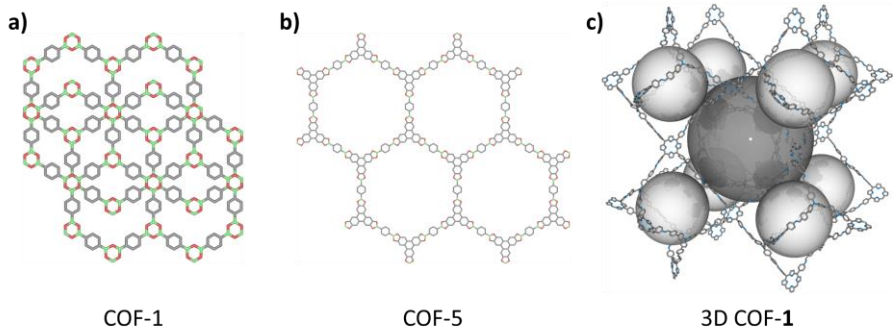


Figure 1.12. 2D COFs based on the condensation of a) boronic acid and b) boroxines to form COF-1 and COF-5, respectively. c) 3D COF based on the assembly of an imine-linked porphirine-based tetratopic linker and a tritopic linker.

boronate linkages (Figure 1.12). Moreover, the isoreticular principle was demonstrated in these new materials with a systematic variation of metrics by linking progressively larger triangles and struts.[144] By using the same chemistry, the same group reported two years later the introduction of tridimensional MBBs (with tetrahedral geometry) that induced the formation of the first four 3D COFs by self-condensation or when combining with triangular-shape MBBs, obtaining carbon nitride-like (**ctn**) and boracite-like (**bor**) nets.[145]

The chemistry of COFs has been developed focusing on the scope of finding new linkages able to produce crystalline phases. New frameworks were reported based on triazine,[146] imine,[147] hydrazone,[148] borazine,[149] phenazine,[150] *trans*-azodioxy,[151] polyimide,[152] dioxin,[153] and so on. However, all attempts to crystallize them in a single-crystal failed for more than 20 years,[151,154] until the first single-crystal of a COF could be determined by SCXRD.[155]

As in the case of MOFs, COF chemistry was expanded to a higher valency, not just driven by a polytopic linker, but though the formation of an organic SBU. By mimicking the well-known inorganic cubic siloxane, the group of Yaghi substituted the Si atoms by B and P, which are known to form discrete B-O-P cubes, and they linked them to form polycubane COFs.[156] The strategy was based on introducing in a single organic MBB both functionalities that can self-condense in single-crystals of 8-c cubic borophosphonates or an infinite 1D B-O-P rod, being the last one isolated in single-crystals suitable for x-ray analysis. One of the most complex designs in reticular materials has been as a consequence of introducing supramolecular interactions in their frameworks. The concept of mechanical bond was exemplified in discrete molecules such as catenanes, rotaxanes or molecular knots, among others. Mechanically-bonded structures were planned to construct based on this chemistry, by extending the aldehyde functionalized Cu(I)-bisphenanthroline with benzine to yield a diamond-like framework (**dia**).[157] This weaving COF could be dematalated, being based on purely helical organic threads after using the metal as a template (Figure 1.13a). By extending the same

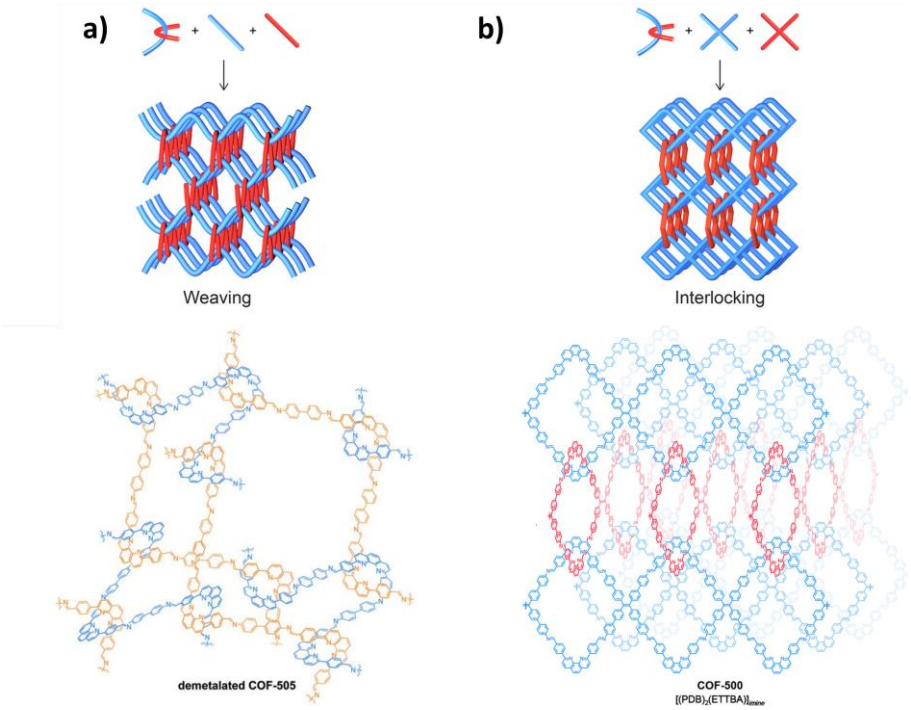


Figure 1.13. a) Weaving and b) interlocking COF structures by using supramolecular design strategies.

supermolecular SBU with a square 4-c MBB, the resulting framework consisted of interlocked 1D square ribbons in a PtS-like structure (**pts**), as a new mode of mechanical entanglement (Figure 1.13b).[158]

1.3.5. Heterogeneity in reticular materials

The increasing complexity of reticular materials was enriched by introducing multicomponent and multivariate systems, which comprise materials built with two or more ligands or metals, being ternary with three components, quaternary with four components, etc. The use of two ligands has been studied since the beginning of the 21st century, finding examples in pillared 2D layers or multicomponent cages from Kitagawa and Fujita groups, respectively.[159,160]

Aromatic N-donor linkers have been extensively studied for bridging metal-organic layers as well as MOPs through coordination of the open metal sites. This was exemplified by MOF-500,[161] the first one based on tetrahedral cages (IRMOP-51)[162] linked to form a β-crystobalite-like framework (**crs**). Later, the glossary was expanded with different cages, which can form 12-c (**fcu**) or 6-c (**pcu**) nets depending on the points of extension of the MOP.[163,164] However, the ligands are based on different coordination chemistry, and therefore different bond strength. The first time that both linkers with carboxylate functionalization were used was reported in 2003, using the simplest 2-c BDC and 3-c BTC linkers with Zn(II).[165] Surprisingly, none of the clusters found in MOF-5 or HKUST-1 were found, but the well-known trinuclear hour-glass crystallized increasing the structural diversity. Expanding BTC linker but maintaining BDC enabled the discovery of a new MOF by Matzger group, UMCM-1, which exhibited the 6-c octahedral tetranuclear Zn-cluster, surrounded by 2 BDC and 4 4,4',4''-benzene-1,3,5-triyl-trisbenzoates (BTBs).[166] In this case, the structural diversity pointed the obtention of new topologies according to the substituents in the cluster (Figure 1.14).

One of the main drawbacks of using two linkers is that requires an excellent control of synthetic conditions, being the ratio of linkers crucial for obtaining a different MOF. If not, MOFs with single linkers such as MOF-5 or MOF-177 could be found under different molar ratio, or even mixtures of different phases. In fact, by extending the linker into the 2,6-naphthalenedicarboxylate or both linkers to 4,4',4''-(benzene-1,3,5-triyl-tris(ethyne-2,1-diyl))-trisbenzoate (BTE) and biphenyl dicarboxylate (BPDC) resulted in two new nets with different topologies, resulting in DUT-6 and MOF-210, respectively (Figure 1.14).[167,168] These findings had shed light on the polymorphism unlocked by introducing multiple polycarboxylate linkers in MOFs. Another clearly example of the topological diversity of new nets can be subjected to the number of substituents in the cluster. This is the case of the mixed-linker systems based on the 6-c Fe-trimer: MIL-142, MIL-143 and MOF-907.[169,170] The three nets are related, but differ on the linker distribution, being MIL-

142 connected through two ditopic and four tritopic ligands, MIL-143 connected through three ditopic and three tritopic ligands, and MOF-907 connected through four ditopic and two tritopic ligands (Figure 1.14).

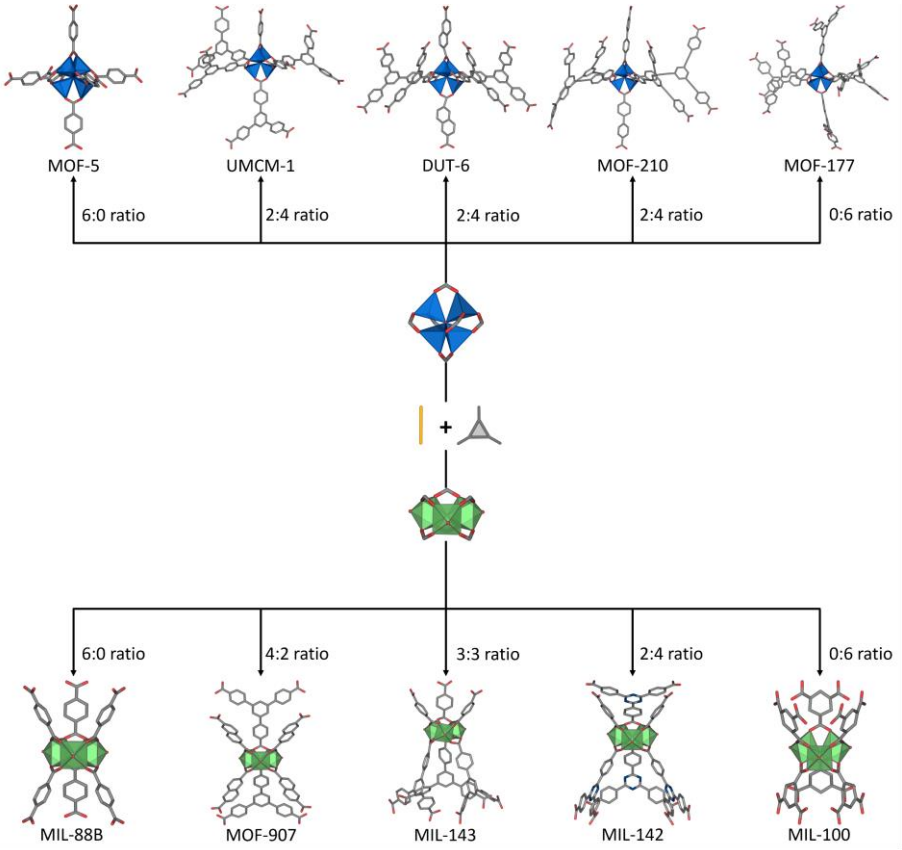


Figure 1.14. Structural diversity in mixed-linker systems according to the ratio used or their arrangement in the different positions of the cluster exemplified by the 6-c octahedral Zn-tetramer and the 6-c trigonal prism M(III)-trimer.

To date, the most complex systems based on this approach was performed by use of the isoreticular principle in the same system, creating multivariate (MTV) MOFs constructed of different linkers (up to 8) with the same size in terms of connectivity but decorated with different functional groups.[171] The single phases (isoreticular forms of MOF-5) could be determined by SCXRD, but the functionalities along the

MOF backbone were disordered in the complex pores. In fact, later these functionalities could be determined in their spatial arrangement using solid-state rotational-echo double-resonance (REDOR) nuclear magnetic resonance combined with molecular simulations, which can discern between random, alternating, and various cluster forms domains.[172] Translating multivariety to tritopic BTB-like linkers in MOF-177 unveiled the formation of more regular nets based on pyrite (**pyr**) and rutile (**rtl**) topologies depending on the functional groups decorating in ortho positions.[173]

Finally, the introduction of more than one metal in CPs was reported since the beginning of the field of reticular chemistry, often presented in single-metal-ion-based structures.[174–176] The first time that two metals were presented in the same SBU was in a 1D rod described by the group of Ferey.[177] This was further increased ten years later to 4, 6, 8, and 10 different metals in a series of isoreticular MOF-74.[178] However, the control or determination of the position remains challenging, being consider as heterogeneity within order. The first sequencing determined in the last example was by using the atom probe tomography (APT), determining the most probable scenarios in random, duplicates (long and short) and insertion configurations.[179]



Figure 1.15. Multivariate-MOFs constructed with different a) linker functionalities in the MOF-5 framework and b) metals in the 1D-SBUs of MOF-74.

Mixed-metal MOFs have also been reported with other SBUs using different strategies. One of them is based on encoding a metal in a determined cluster, and then extending it in a two steps methodology, as reported with the trimer and a

hexanuclear wheel cluster.[180,181] Another strategy has been introducing two metals that would guide to two different SBUs in a one-pot synthesis. The first case was reported by Matzger group in 2010, using a mixture of Cu/Co and Cu/Fe where the Cu(II) atoms preferred to form a paddlewheel cluster, and Co(II) or Fe(III) atoms preferred to form trimer clusters. The last strategy is based on a retrosynthetic approach for a multi-step synthesis.[182] Taking advantage of a 6-c hexanuclear cluster in a MOF with defaults of connectivity, it was incorporated a ligand that fit in that position having a non-coordinated functional group. These free functionalities directed for the incorporation of single-metals (such as Ni(II) or Cu(I)) or the formation of a new 12-c hexanuclear Hf-based cluster.

1.4. Terminology

The rapid expansion of these materials that came from different fields (solid state, inorganic and coordination chemistry) merged with different nomenclature, which divide researchers according to the sub-discipline they were working. This situation faced the necessity to determine some guidelines for differentiate CPs and MOFs.[183] According to the international union of pure and applied chemistry (IUPAC), coordination polymer is defined as "a coordination compound with repeating coordination entities extending in 1, 2, or 3 dimensions".[184] They do not need to be crystalline, so the prefix 1D-, 2D-, or 3D- is acceptable for the indicating the degree of extension. Another extensively used term that is a subset of CP, coordination network (CN), is defined as "a coordination compound extending, through repeating coordination entities, in 1 dimension, but with cross-links between two or more individual chains, loops, or spiro-links, or a coordination compound extending through repeating coordination entities in 2 or 3 dimensions". Thus, CN encompasses all the members of the CP excluding the 1D polymers. This concept is important as it is included in the IUPAC definition of metal-organic framework, defined as "a coordination network with organic ligands

containing potential voids". This fact reflected the overall idea of needed proven porosity by experimental adsorption isotherms, which was refused for the many dynamic systems able to change in structure and therefore potential porosity or solvent and/or guest filled voids through external stimuli. Moreover, this criterion was extended for not requiring crystallinity, as in the case of CPs or CNs.

Albeit the terms CP and CN were widely accepted by the scientific community, the term MOF generated a great controversy. The major discrepancy was related to the needed crystallinity, which should be achieved by growing single-crystals suitable for SCXRD or defined X-ray diffraction patterns. In fact, this is in keeping with the ordinary meaning of "framework" and is consistent with the use of the term in COFs, which are attributed for describing materials extended in two or three dimensions. Another controversy was related to the porosity attributed to the "potential voids", being nonporous MOFs with high density a representative example. Some researchers believed that porosity should not be employed as a parameter to judge because it is not an absolute property and can depend on the size and chemical nature of the guest or an arbitrary pore size. This was reflected on an alternative proposed definition for MOF: "a class of CPs comprising organic linkers

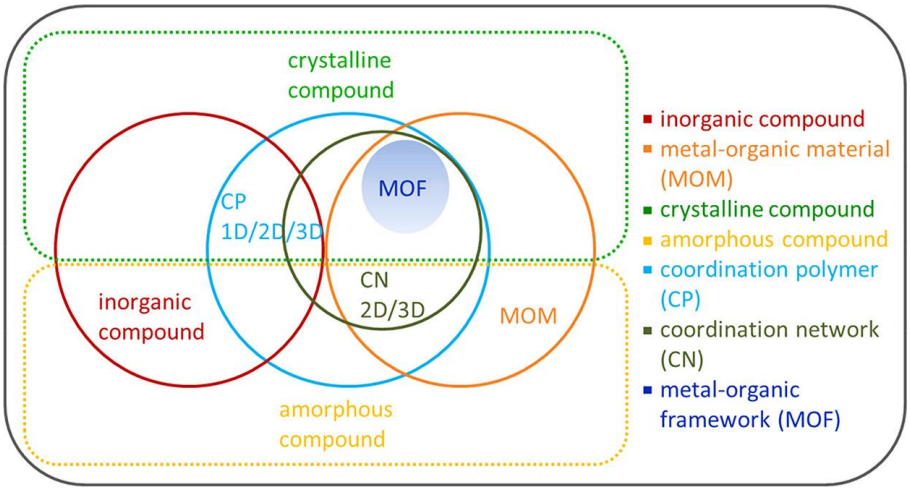


Figure 1.16. Venn diagram representation to illustrate the relationship between the different kind of inorganic, metal-organic, amorphous, or crystalline materials.

wherein metal-ligand interaction/bonding leads to 2D or 3D crystalline network structures".[185]

According to the authors, Figure 1.16 represents a diagram of the relationship among all definitions. Note that the term metal-organic material refers to any discrete and/or polymeric coordination compound, no matter its crystallinity. As previously mentioned, the nature of a CP or CN can by purely inorganic or hybrid, whereas a MOF is restricted to organic-bridging-based materials. Additional terms as porous coordination polymers (PCPs), porous coordination networks (PCNs), microporous coordination polymers (MCPs) or metal-organic coordination networks (MOCN) are often used in literature and can refer to subclass of the terms defined by the IUPAC, which do not create any discrepancy. In the same way, there has been a trend to classify MOFs according to the composition, properties or structural features (ZIFs, MbioF, etc.), as well as the common practice of naming these materials based on their institution (HKUST, UiO, MIL, DUT, UMCM, NOTT, etc.).

1.5. Topological classification

In crystal chemistry, structures or frameworks are extended through weak or strong chemical bonds in a motif. The atoms or group of atoms can be simplified to nodes/vertices in a net that are connected through edges, the chemical bonds. Most of these nets are based on sphere or cylindrical packings, where their circuits of connections reveal the kind of faces, and the remaining space in the circuits of connections reveal the kind of tilings.[186] Considerable and pioneering efforts by Wells has been devoted to relating the underlying net of crystal structures with a determined topology.[58,187] These findings created some bridges between chemists, crystallographers and mathematicians, which their contributions have been ignored between them during the 20th century.[188] The growing field of reticular

chemistry demanded a unified nomenclature and classification for the almost infinite variety of topologies.[189]

The first descriptors for nets were based on their circuits of connections, thus the cycles of the net. One example is the *Schläfli symbol* {*p*,*q*,*r*} for 3D nets, in which "*p*" is a circuit of connections, "*q*" means the number of {*p*}'s that meet at a vertex, and "*r*" means the number of {*p*,*q*}'s meet at an edge; or the *vertex symbol* (*A*.*B*.*C*…) to describe the local topology of vertex in polyhedral and 2-periodic tilings. Later, Wells introduced the *point symbol* ($A^a.B^b$…) for 2D nets, which indicates that there are "*a*" angles with shortest cycles that are *A*-cycles, etc. Other terms such as *face symbol* or *Delaney-Dress symbol* for describing the tilings were also implemented. However, the complexity of these descriptors increases simultaneously with the complexity of some nets, which decrease in regularity or symmetry. In addition, all these terms have been unfortunately confused and misused between them in literature.[190]

Inspired by the codes used to specify a zeolite framework type, O'Keeffe and co-workers developed the *RCSR symbols* (Reticular Chemistry Structure Resource), a three-letters code in lower case and bold.[191] Usually, the name of the nets is related to the name of the materials, the chemical composition, the polyhedra representing the shape of the vertices, or the name of the institution of researchers that discovered them (i.e. **dia** stands for diamond, **sod** stands for sodalite, **srs** for $SrSi_2$, **pcu** stands for primitive cubic unit, **ftw** stands for four and twelve, **acs** stands for Andrea C. Sudik, etc.). The generation of databases with all nets helped researchers to design the starting MBBs for assembling these possible structures and to develop conceptual strategies to rationalize and predict new ones.

Even though the RCSR database is the most common and widely known in the field of MOFs, it must be said that it is not complete and do not contain all possible nets. Theoretical and experimental nets are found in other databases with different nomenclatures, such as the EPINET (Euclidean Patterns in Non-Euclidean Tilings)

with the symbol sqc*N*, where "s" stands for Systre, "q" stands for cubic, "c" stands for Coxeter orbitold family, and "*N*" is derived from the systre-key ranking; the international zeolite association database (IZA) with capital three-letter symbols; the TOPOS database with N*D*n TOPOS symbols, where "N" is a sequence of coordination numbers of all independent nodes, "*D*" in one of the letters *C*, *L* o *T* (stands for chain, layer or three-periodic, respectively), and "n" enumerates non-isomorphic nets with a given N*D* sequence; or the data on supernet-subnet relations and transformations, with the subnet **s**-d-*G*-n symbols, where "**s**" is a conventional name of the initial net, "d" is a set of coordination numbers of all inequivalent nodes, "*G*" is the space group for the most symmetrical embedding and "n" enumerates non-isomorphic subnets.

Some extensions can be added to the name to give more information: "**a**" refers of the *augmented* net, where the vertices are replaced by a polygon or polyhedra with the shape of the original one; "**b**" refers to *binary* version of a net with just one kind of vertex (uninodal); "**c**" refers to *catenated* nets intergrown; "**d**" refers to the *dual* net; "**e**" refers to the *edge* net by putting new vertices in the middle of the edges; "**w**" refers to weaving; "**x**" refers to *extended* coordination when the coordination of a node is extended to the second sphere of coordination; "**y**" refers to polycatenane, etc.

Nets can be classified according to their connectivity, symmetry (space group) or D-symbol size. Still, any of these parameters can distinguished between regular nets. A regular net is defined as that with symmetry that requires the coordination figure to be a regular polygon or polyhedron. Regularity can be measured by the array [*pqrs*], which is defined as transitivity, according to the number of kinds of vertices (*p*), edges (*q*), faces (*r*) and tiles (*s*).[192] Based on this criteria, regular nets are those with transitivity [1111], represented by just 5 topologies: **srs** (3-c, triangle), **nbo** (4-c, square), **dia** (4-c tetrahedron), **pcu** (6-c, octahedron) and **bcu** (8-c, cube).[193] Among them, the only net with D-symbol size equal to 1 is the **pcu**, which is the most regular one. If the coordination figure in a net is a quasiregular polyhedron

(with one kind of vertex and edges, but two kind of faces), then is a quasiregular net. This is the case for the cuboctahedron in the **fcu** net, with transitivity [1112], which is the only net complying [111*s*] criteria. When the regularity is decreased into [11*rs*], these nets are called semiregular nets, unique for just 14 nets (**lvt**, **sod**, **lcs**, **lcv**, **qtz**, **hxg**, **lcy**, **crs**, **bcs**, **acs**, **reo**, **thp**, **rhr** and **ana**).[194] To identify the regularity in a specific parameter in a set of nets, when this parameter is the most regular (1), it is called as transitive (i.e. if $p = 1$, then is vertex-transitive). Accordingly, the last 20 nets described are vertex- and edge-transitive. These nets are of prime interest, as described the most regular and symmetric nets that can be formed upon the assembly of MBBs with that determined geometry. Coincidentally, their occurrences are higher in reticular materials than less-regular topologies according to the Cambridge Crystallographic Data Centre (CCDC) Database,[195] in agreement with Pauling's fifth rule of parsimony.[4] Therefore, the topologies of these nets are known as the default nets when the MBB match with the geometric parameters to their vertices, ergo the formation of structures based on non-default nets requires the introduction of some complexity into the components of the synthesis, such as directional information, size, length or width.

Another group of nets with prime importance in reticular chemistry are those in which all the links are the same (edge-transitive).[196–198] These nets should have transitivities [11] (the last 20 nets) or [21]. These topologies are the most regular for uninodal and binodal nets, hence the target (and most probable to form) for chemist when using regular MBBs connected through linear connections. Note that these nets can be formed by combining both polytopic organic and inorganic MBB, adopting the position of the vertices in the case of binodal, or the inorganic MBB as a vertex and the organic MBB as an edge if the latter is ditopic in the case of uninodal. As most of these nets have been reported in experimental findings, there is an increasing interest in minimal edge-transitive nets.[199–201] Minimal transitivity (MT) refers to the smallest possibility to form nets by joining vertices. If the number of nodes increases to three (A, B and C), the minimal possible transitivity is [32] (A

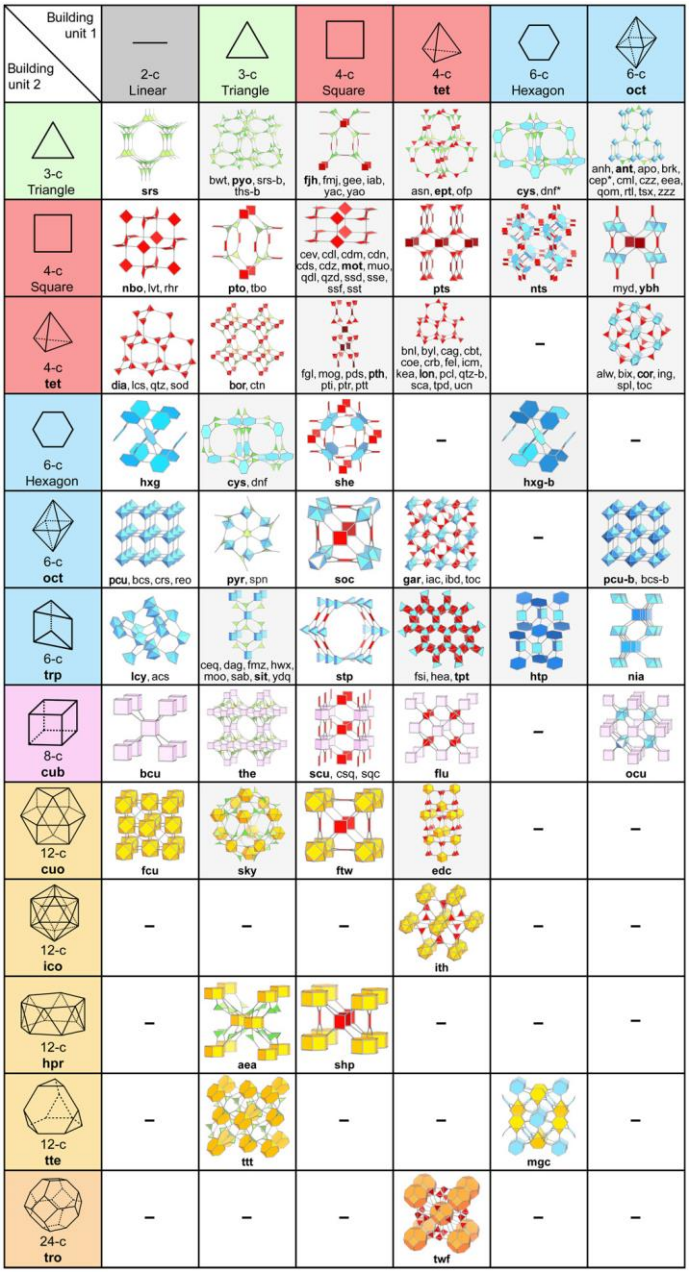


Figure 1.17. Representation of the "*reticular table*", exhibiting some binodal nets (in augmented form) that can be constructed when combining regular MBBs. If there are more than one possible net, the one in bold indicated the net drawn.

connects to B, and B also connects to C). Recently, the number of MOFs with minimal edge-transitivity is growing, in accordance with the direction in complexity of the field.

Some nets present an interesting relation between each other, as one net can grow inside another one by placing a new vertex inside each tile and connecting them by edges through the face common to the two tiles. This characteristic is known as a dual net, which is transformed by inverting the [*pqrs*] values for [*srqp*]. The most regular binodal net is formed by transforming the transitivity of the **fcu** topology [1112], which must have two vertices and a [2111] transitivity. This is the net of the CaF_2 structure, which was named as **flu** topology, and formed by the packing of rhombic dodecahedral tilings (a space-filling polyhedron). For example, the **bcu** topology is the dual net of the **nbo** topology and viceversa, as the dual of the dual is the original net. Some nets are self-dual, as the case of **srs**, **dia** or **pcu**, which is in close relationship with the presence of interpenetration, being these three nets the most frequent to observe this phenomenon.

By analysing the augmented form of the nets, MBBs that match the geometry of the nodes can be used for building them as a "default topology". A simple reticular table can be constructed by showing the possibilities of combining two building units (Figure 1.17).[202] For some cases, it is impossible to combine those building units in the most symmetrical and regular way, as well as some combinations yield more than one possible nets with different maximum symmetry and angles between the building units. Recently, a review classify them according to their coordination number and figure (Figure 1.18).[203] Additionally, they catalogue them into three types of nets: those topologies which have unique coordination figures, and therefore, just one edge-transitive net can be build (Type I); those topologies which their coordination figures afford two or three distinct nets, requiring additional information for affording an specific net such as torsion angles (Type II); and those topologies which are difficult to predict structures based on their building units

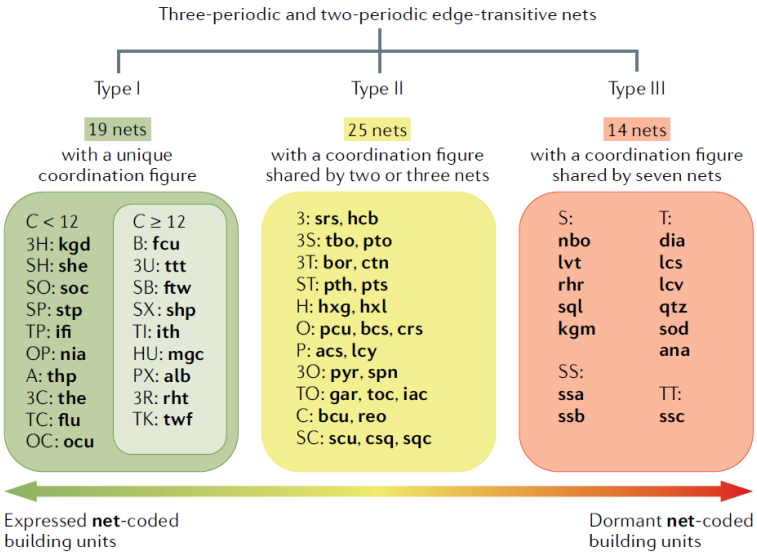


Figure 1.18. Categories of 2D (5 nets) and 3D (53 nets) edge-transitive nets into three different types according to their combined building units. Type I nets have unique coordination figures. Type II nets have two or three nets coded by the same coordination figure. Type III nets are the rest of nets based on square or tetrahedral building units, coded in seven nets for each case. Coordination figures: 3, triangle; A, square antiprism; B, cuboctahedron; C, cube; H, hexagon; I, icosahedron; K, truncated octahedron; O, octahedron; P, trigonal prism; R, rhombicuboctahedron; S, square; T, tetrahedron; U, truncated tetrahedron; X, hexagonal prism.

assembly due to their high occurrence, existing seven nets for each square and tetrahedral coordination figure (Type III).

1.6. Simplification

The successful implementation of the reticular approach to metal-organic and pure organic materials is based on the simplification of the MBBs into a middle point that represents a node in a net (or graph), and that underlying net of the structure corresponds to a specific topology.[89,204] When the MBB has a regular geometry, there is a unique way of simplifying it. However, when the MBB is desymmetrized and has a connectivity higher than 3, it can be replaced in a group of edges and less-

connected nodes which corresponds to more regular coordination figures (i.e. the elongation or torsion of an MBB), according to the recommendations.[205–207] The substitution of the former coordination figure for the new group of coordination figures in a net generates a *derived net* (Figure 1.19a).[205] Note that, due to the geometric arrangement of the MBBs in 3-periodic nets, some nets can have more derived nets with the same building units inasmuch as different circuits of connections can be formed. The derived nets represent a more precise description of the structure with the complete topological information, corresponding to the same windows as the ones formed in the structures. Meanwhile, the parent net provides information about the most probable nets to form as are more reliable design targets. Thus, some MOFs or COFs with branched or dendritic linkers can express different underlying nets and both should be described as provide useful information.[207]

More intricate variants can be formed using the same methodology. If the

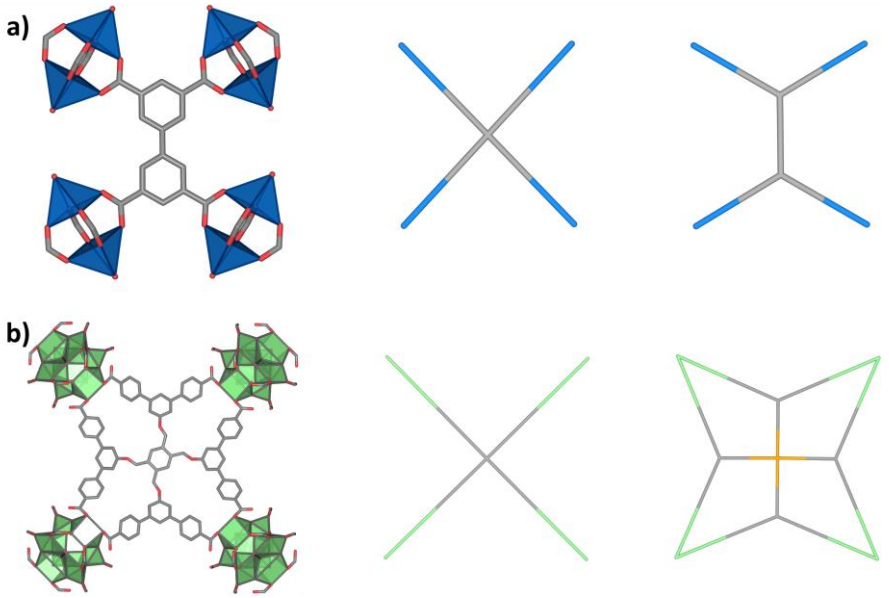


Figure 1.19. a) Simplification of a tetratopic ligand into a central 4-c rectangular node or into two more regular 3-c triangular nodes. b) Simplification of an octatopic ligand into a central 4-c square node or into a set of more regular 3-c triangular and central 4-c square nodes.

substitution of the node with a new group of nodes increases the coordination number of unreplaced nodes, it generates a *related net* (Figure 1.19b).[199–201] In this case, structures should be described just in this form, as the relation between the parent and related nets indicates the regularity of the net but does not correspond with the coordination figure of the MBBs. As in the last example, different related nets can be generated depending on the coordination figures that substitute the former vertex.[200]

The relation between nets was extensively studied by the net relation graph (NRG) approach.[208,209] This approach generated new nets by transforming regular and symmetric supernets by deleting or changing edges and nodes and decreasing its symmetry. This process unveiled more than 5278 uninodal and 38304 binodal new nets and subnets, which some of them are derived nets.

The identification of bigger units in crystal structures enable its simplification according to pores or cages.[210,211] The packing of the cages can be associated with a net if a node is generated in the middle of the tiling and joined to the neighboring tiles. Additionally, nets can also be deconstructed as the pillaring of 2D nets.[212–216] These approximations can be useful for relating the structures with some properties or phenomena characteristics of the specific net. However, this deconstruction should always be followed by the real topology of the net for completing the description of the structure and not as a substitute.

1.7. Design approaches

1.7.1. Differences between Molecular Building Block (MBB) and SBU

Structural design approaches are generally based on three main strategies: the use of building blocks, the quest for a target net and the isoreticular concept for increase structural diversity.[203] The concept of building unit has been used for a century.[4] It was used as a model for understanding the geometry and packing in crystal

structures. This approach led to the introduction of both MBB and SBU concepts in MOMs. Despite being used indistinctly in literature, the MBB referred to the molecular entity as a unit for constructing solid-state architectures, while the SBU referred to the geometry and points of extension of that MBB. However, SBU was defined as a structural second level of complexity for the metal centers in carboxylate-based clusters, and not for the use of polytopic linkers.[87] In fact, polybranched dendritic ligands were coined as the tertiary building units (TBUs) to make a distinction, because SBUs contained bond sequences that converge to form rings whereas TBUs branch.[106] Nowadays, most of the researchers used the term SBU for referring an in-situ formed carboxylate cluster and MBB for both inorganic and organic units. Note that the inorganic MBBs presenting open metal sites can accept more ligands to increase its connectivity.

1.7.2. Modulated synthesis

One of the first synthetic approaches was the use of modulators to control the self-assembly of reticular materials.[217,218] A modulator is a monotopic organic linker that compete with the organic linker for constructing the framework, decreasing the growth rate, and improving the crystallinity of the material due to the reversibility of the substitution. In the case of MOFs based on transition metal carboxylate clusters, modulators that are usually used are monocarboxylates (formic acid, acetic acid, trifluoroacetic acid, benzoic acid, etc.) for slowing down the formation of the cluster. For COFs, monoamines (e.g. aniline) are used as modulators for the formation of imine-based linkages. First reports used the modulated synthesis for controlling the particle size and shape.[219,220] Later, it was demonstrated that can also favor the formation of certain clusters, phases with different topologies or to modulate the formation of defects in the structure and the functionalization of the surface.[136,221–226] The most significant case was the discovery of rare-earth (RE) fluoro-bridged hexanuclear clusters analogous to Zr-based clusters,[137] as well as

more high-connected new clusters that permitted the synthesis of new MOFs based on unprecedented nets by functionalizing the *ortho*-position of benzoic acid with fluor groups (2-FBA).[227,228]

1.7.3. Supermolecular approaches

In order to access more connected and complex MOFs, researchers developed new design approaches based on larger building blocks formed by multiple MBBs that generate polyhedral or layers.[229] The introduction of supermolecular building blocks (SBBs) relies on the use of MOPs as building units in the assembly of MOFs.[161,210,211,229,230] Both *in-situ* and two steps assembly has been already demonstrated.[163,164] This approach allowed the synthesis of MOFs based on the highest-connected edge-transitive **rht** 3,24-c net (Figure 1.20a).[211] Their mathematical simplification to a vertex according to its geometry and points of extension is well-known considered as a TBU, despite its first definition.[202,203] The

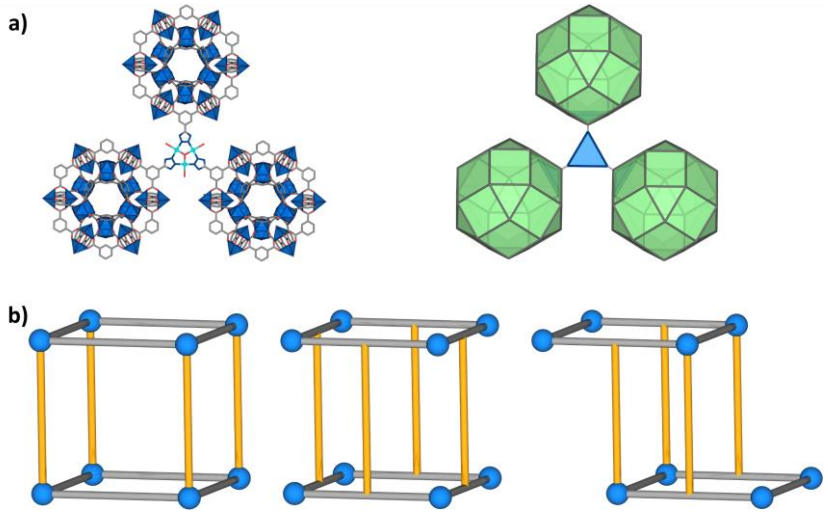


Figure 1.20. a) SBB strategy based on the assembly of a MOP with 24 points of extension with rhombicuboctahedral shape with triangular MBBs into the **rht** net. b) SBL strategies for the pillaring of **sql** nets through vertex-to-vertex, edge-to-edge and vertex to edge (from left to right).

analogous supermolecular building layer (SBL) approach permitted the interpretation of 3D MOFs as the pillaring of layers.[212–216,231] The pillaring is based on the edge-transitive 2-periodic **hcb**, **sql**, **kgm**, **hxl** and **kgd** lattices and can be pillared in three main ways: vertex-to-vertex, edge-to-edge and vertex-to-edge (Figure 1.20b).[229] The SBL approach has been demonstrated both with pillaring axial linkers and with structural polytopic ligands. Both approaches successfully illustrated that bigger units could direct to a specific net and can explain the origin of some complicated assemblies.

1.7.4. Merged nets

Recently, a new strategy enabled the rational design of mixed-linker structures based on the merged-net approach, which consists of merging two edge-transitive nets (transitivity [21 or [11]]) into a minimal edge-transitive net (transitivity [32]).[232] For MOFs, each linker forms independent nets, and both meet at the inorganic MBB. To date, this is the only strategy for building multi-component frameworks with two linkers in different crystallographic positions, which were associated to poorly controlled trial-and-error methodologies. The most extensive group of merged nets studied (140 novel nets) are those termed as "three-periodic and thee periodic" (3p-3p). To them, we can find some MOFs corroborating this approach as in the 3,6,12-c **sph** net (merging 3,6-c **spn** and 6,6-c **hxg-b** topologies), constructed with 3-c tritopic and 6-c hexagonal organic linkers, and the 12-c RE-hexanuclear cluster (Figure 1.21);[232] or the 4,12 **tam** net (merging 6-c **pcu** and 4,6-c **she** topologies), constructed with 2-c linear and 4-c square organic linkers, and the 12-c Zr-hexanuclear cluster.[182] Additionally, nets with different dimensionality can also be merged. This is the case for merging three- and two-periodic nets (3p-2p), three- and one-periodic nets (3p-1p) and three- and zero-periodic nets (3p-0p).[203] Note that, for building merged-nets, it is essential to maintain a ratio constant

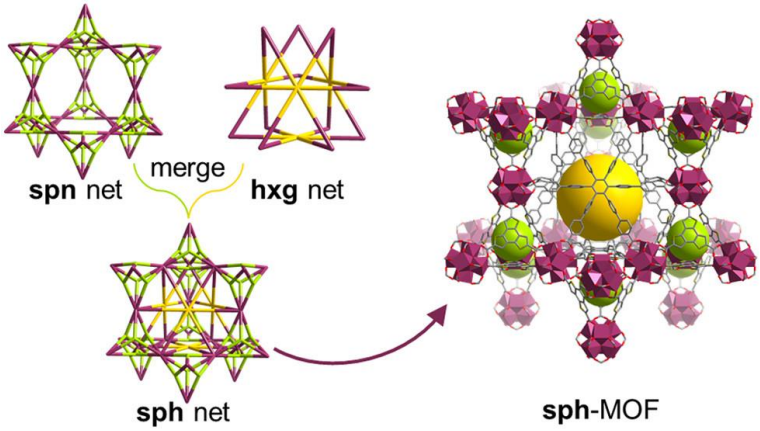


Figure 1.21. Schematic showing the design concept of merged nets by combining the **spn** and **hxg** nets into the **sph** net.

between both linkers in case of expansion or contraction, otherwise nets with single linkers or less-regular topologies will rather be formed.

1.7.5. Net-coded building units (net-cBUs)

One of the most recent strategies was to access specific nets through the building units or a set of linked building units that embed their unique geometrical code. This includes the vertex coordination figure, dihedral angles between them or bigger units that direct to a single net, coined as net-coded building blocks unit (**net**-cBU).[199–201,203,233,234] This idea was previously introduced for some target nets based on SBBs and SBLs without an exhaustive analysis of all their possible outcomes.[229] By following the previous mentioned classification (Figure 1.18), Type I nets represent expressed net-coded building units exclusive to reticulate them, dictating the requisite geometrical information. The MBBs that possess essential information as shape, connectivity and vertex-centre-vertex angle for the points of extension will yield the target net. In Type II and III nets, their net-coded building units are dormant as more information is required to distinguish multiple nets based on same coordination figures. For affording the expressed building units, it is

necessary to code slight differences as desymmetrized building units, or fixed dihedral angles between connected building units, SBBs or SBLs.[203] For example, expressed **alb**-cBU and **shp**-cBU were used for directing the reticulation of **alb** and **shp** nets by combining 12-c hexagonal prism MBBs with 6-c trigonal prism and 4-c square MBBs, respectively.[234] Also, expressed **tbo**-cBU were used for constructing a **tbo**-MOF by using a cuboid TBU of an octatopic linker simplified as square node joined to four triangular nodes.[212]

1.8. Post-synthetic strategies

1.8.1. Chemical modification of pre-formed CPs

The chemical complexity of reticular materials can further be tuned *a posteriori* of the material synthesis as in a molecular chemistry perspective. The post-synthetic modification (PSM) is a process that involves the chemical modification of a preformed structure into a new one without substantial alteration of its crystallinity.[235–239] It is possible the functionalization of certain groups that are limited to the assembly process due to harsh solvothermal conditions such as high temperature or pressure, the presence of metal salts or the extreme acid or basic media that some MOFs, COFs or MOPs require. These functionalities can tune the properties of the materials and enrich the chemical versatility for further potential applications. As it was already applied to other organic, inorganic or hybrid materials, it was conceived to extend the PSM to CPs in 1990 by Hoskins and Robson, where the authors stated that "Relatively unimpeded migration of species throughout the lattice may allow chemical functionalization of the rods subsequent to the construction of the framework. The introduction of one or more catalytic centers per rod may thereby be straightforward".[56]

The earliest examples of applying this concept were reported a decade later in a covalent PSM of a CP with pendant alcohol groups that reacted to form esters or

cross-linked siloxanes;[240,241] and the alkylation of pendant pyridines in a homochiral MOF.[242] However, this strategy remained ignored for a decade until Cohen revived this strategy in 2007.[243] They successfully functionalized the amino pendant group of IRMOF-3 into amides by suspending the material into a solution in the presence of acetic anhydride.

PSM can be generally divided into three main groups:

- Modifications affecting the organic components.
- Modifications affecting the metal-based component.
- Modifications affecting the microscopic particle characteristics.

1.8.2. Post-Synthetic Modification (PSM) of organic ligands

1.8.2.1. PSM of pendant and backbone functional groups

Organic ligands possess a wide range of functionalities able to react in a myriad range of varieties. Since the first condensation reported, the scope of the reaction according to the bulkiness of the substituent group has been studied. The bigger the size, the lower the yield due to the difficulty of diffusion through the windows of the framework. Additionally, the scope was also expanded to other kind of reactions. For example, in COF chemistry, it is known the difficulty of crystallizing materials by the formation of certain bonds. PSM allowed the introduction of these groups by first synthesizing a more feasible imine-based COF and then performing different reactions to transform it to amide, thiazole, oxazole, amine and quinoline, among others.[244–248] Unfortunately, it is hard to achieve complete conversion through PSM. This feature can be exploited by introducing multiple functional groups for affording MTV-materials by sequential PSMs. Instead, if the sequential steps focus on the new introduced group, the process led to tandem PSM. This strategy was exploited to reach seven sequential tandem reactions in an isoreticular

expanded MOF-74 (IRMOF-74-III) to mimic the chemical environment of the active site of an enzyme, thus forming an MTV peptide-based MOF (Figure 1.22).[249]

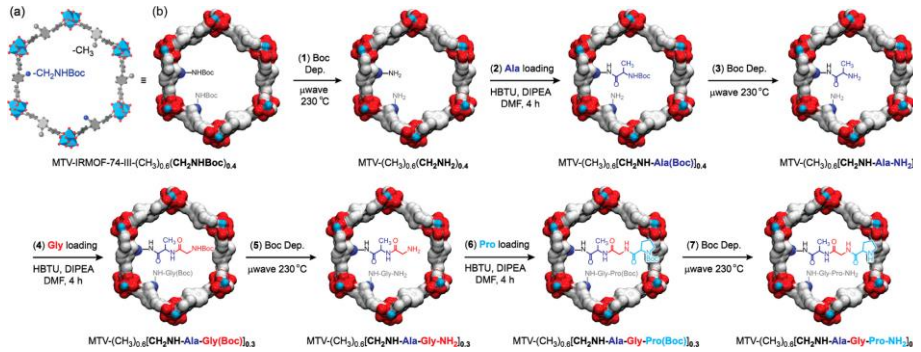


Figure 1.22. Schematic drawing of the seven post-synthetic reactions performed in the pores of MTV-IRMOF-74-III.

1.8.2.2. Solvent-Assisted Linker Exchange (SALE)

Another target to modify in a matrix is the coordination bond. Both N-donor and carboxylate were demonstrated to be exchanged with an additional linker that permit to introduce new functionalities, and contract or expand the framework, some of them even in a single-crystal to single-crystal manner.[250–255] We refer a single-crystal to single-crystal process when the size of the crystals is enough to characterize by SCXRD and not the bulk in powder X-ray diffraction (PXRD). This process has been termed as "solvent-assisted ligand exchange" (SALE) to highlight the importance of the solvent during the exchange process.[256] While mostly all N-donor linkers (generally pillaring MOF layers) can be completely substituted, the yield of exchange with carboxylate-linkers scarcely reaches high values. However, it has been demonstrated to be an impressive strategy to introduce ligands in mild-conditions that cannot resists solvothermal synthesis, as imine-based linkers. [257]

1.8.2.3. Linker insertion: bond formation

While the substitution does not affect to the framework's connectivity, adding or removing some pieces can dramatically affect to the framework. On one side, the insertion of additional molecules to the structure requires the capability of accepting them by an open metal site or a linker vacancy presented in the network. On the other side, the elimination of some linkers in the overall structure while avoiding the structure collapse remains challenging and demands a high reticular control. The first report that combine both strategies and indeed, the first controlled removal of linkers was reported by Qiaowei Li *et al.* in 2014.[258] They reported a MOF based on two different octahedral Zn-based SBUs product of the assembly of an asymmetric linear linker combining carboxylate and pyrazole functionalities.

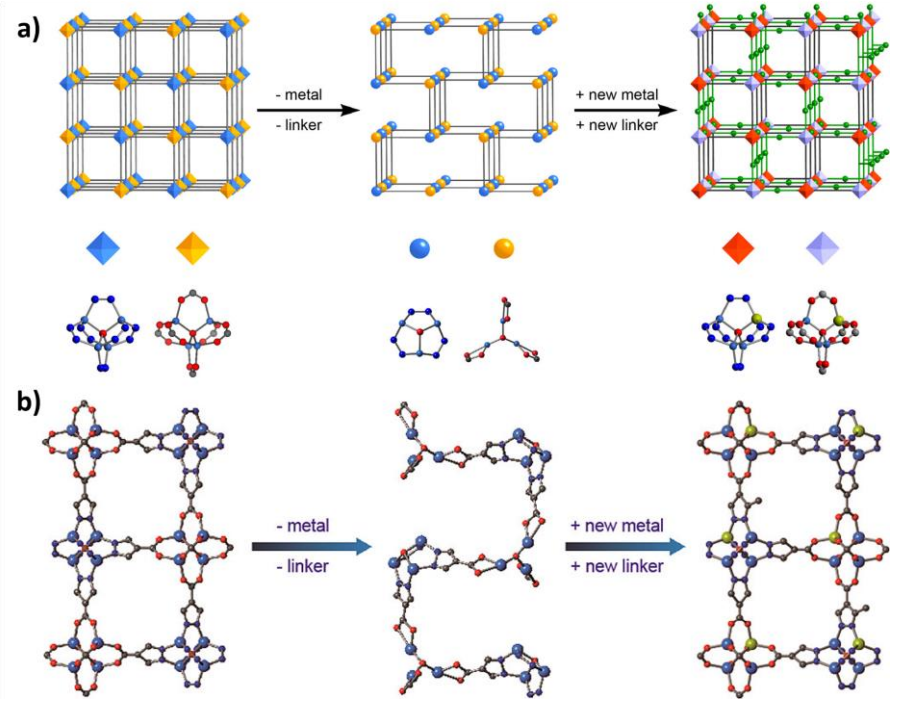


Figure 1.23. a) Schematic illustration of a framework undergoing metal and linker elimination reactions and new metal and linker addition reactions. b) Single-crystal to single-crystal transformation of the elimination and addition steps in a MOF.

The immersion of the MOF in water undergoes an ordered elimination of half of the linkers and transformed the tetranuclear octahedral clusters in trinuclear triangular clusters, generating an **srs**-MOF. The latter vacancies could be used as a template for inserting the former or new linkers and metals for reconstructing the **pcu**-MOF and generate a multicomponent heterometallic and heteroleptic MOF (Figure 1.23).

Additional insertion strategies have been reported so far. The use of the axial positions in paddlewheels was studied long time ago affording pillaring structures and increasing the dimensionality of the materials. Finding tridimensional vacancies that fit molecular entities of a predetermined size requires more intricate strategies or a flexible matrix able to adapt a wide range of linkers. One example is to use high-connected clusters that present open metal sites or decrease of connectivity due to the desymmetrization of the linker. This strategy was exploited by the group of Hong-Cai Zhou, reporting a linear linker twisted by the steric hindrance of two methyl groups and driving to an 8-c cubic Zr-cluster instead of the 12-c cuboctahedral present in the UiO-66, and therefore assembling in a **bcu** net instead of the most symmetric **fcu** net.[259] This effect produced the presence of two pockets of different size, where can be filled by measuring its vacancies and introducing organic linkers that match in size by sequential linker installation. This strategy was further developed with a huge variety of linkers[260–262] and, in more complicated systems as in the 4,8-c **scu**-MOFs, able to create 2 or 3 rational vacancies depending on the symmetry of the linker used, allowing the synthesis of ternary, quaternary and quinary MOF systems (Figure 1.24a).[263–265] More examples illustrated the feasibility of introducing capping linkers to the missing positions in the Zr-cluster with different functionalities in NU-1000,[266] or the coordination tritopic pyridine-based linkers in the open metal sites of the trimer cluster presented in the isoreticular Mg_3-MIL-88, changing the topology from the 6-c **acs** to the 3,9-c **nia-d**.[267] This strategy was further developed to introduce a series of tritopic linkers with different functionalities in the MIL-88B structure by

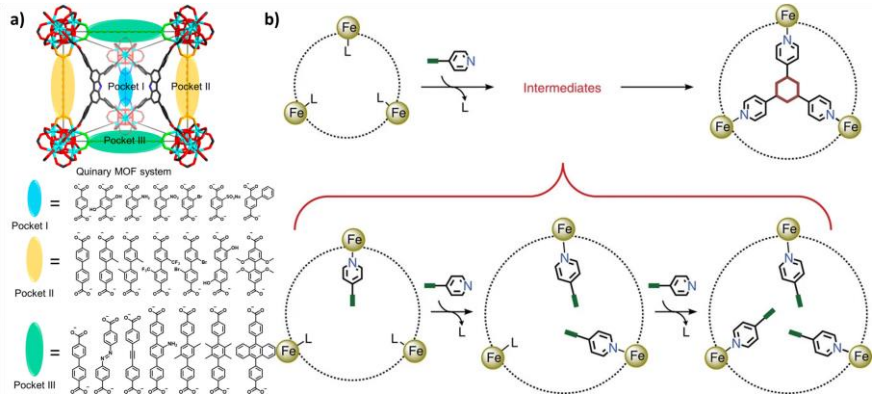


Figure 1.24. a) Linker insertion strategy applied to a **scu**-MOF with three different pockets due to the use of a symmetry-reduced linker. b) Linker insertion strategy applied to an **acs**-MOF and subsequent post-synthetic cyclotrimerization to form a new tritopic linker that modify the topology of the structure.

combining the linker insertion and a post-synthetic cyclotrimerization of cyanides, alkynes and alkenes monomers into *s*-triazine, benzene and cyclohexane derivatives, respectively (Figure 1.24b).[268]

1.8.2.4. Linker elimination: bond cleavage

Finally, bond cleavage can be used as a top-down strategy to modify the chemical environment of reticular materials as well as to destroy them. If the cleavage is produced in ligands that belong to the framework's backbone, the degree of control lies on the percentage of ligand removal. The cleavage can be originated under external chemical or physical stimuli and must be selective to a specific bond for keeping the crystalline character of the materials.[269] The first strategy reported was the hydrolysis of imine bonds in a Zr-MOF triggered by acetic acid. As imine bonds cannot be introduce by direct synthesis in solvothermal conditions, Zhou *et al.* reported the linker exchange of azobenzene-4,4'-dicarboxylate for 4-carboxybenzylidene-4-aminobenzate, which can be hydrolized into 4-amino benzoic acid and 4-formylbenzoic acid (Figure 1.25). A systematic study of

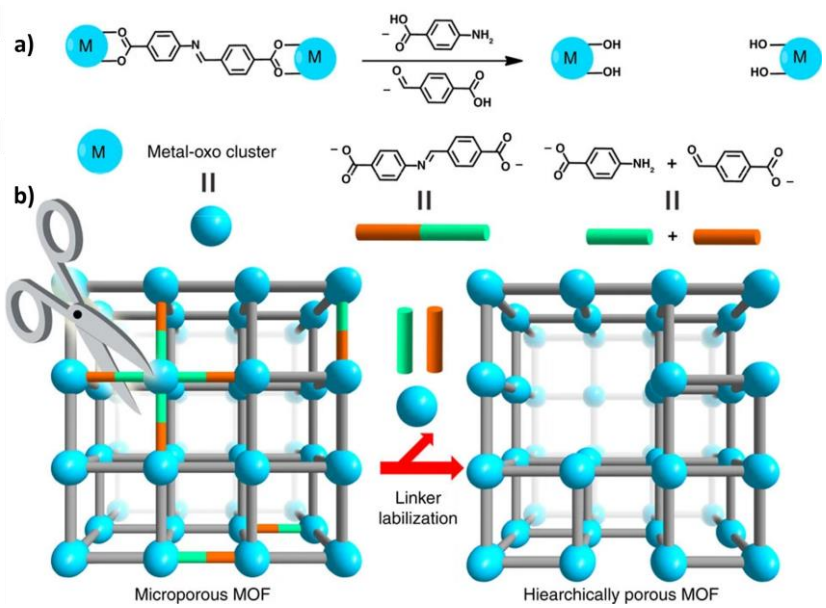


Figure 1.25. a) Linker labilization of the imine bond *via* hydrolysis. b) Production of a hierarchically porous MOF by the cleavage of covalent bonds in a mixed-linker system with random positions.

exchanging different percentage of linkers up to 43% and their subsequent labilization demonstrating the production of hierarchical pores.[257] Indeed, this strategy was further implemented for introducing additional weaker linkers that are not able to exchange strongly bonded linkers, as isonicotinate (INA) or $M(INA)_2$, where M can be Ni^{2+}, Cu^{2+}, Mn^{2+}, Fe^{2+}, Co^{2+} and Pd^{2+}.[270]

The same concept was applied generating hierarchical pores by controlled linker thermolysis. In this case, the same group could directly synthesis mixed-linker MTV-MOFs combining thermolabile and thermostable ligands. Some of them, as 2-amino-1,4-benzenedicarboxylate ($BDC\text{-}NH_2$) could be easily removed at 300 °C by thermal decomposition through a decarboxylation, producing the aggregation of decarboxylated Zr-clusters in ultrasmall metal oxide (Figure 1.26). Additionally, the terminal ligands were removed by increasing the temperature or by treating the material with diluted acid solution.[271] Thermolysis has also been demonstrated to cleave ester bonds in cross-linkers expanded analogues of MOF-74 and introducing

free carboxylic groups in a MOF, which has proven to be difficult.[272] In this case, the strategy modified the connectivity of the net and not the porosity of the material.

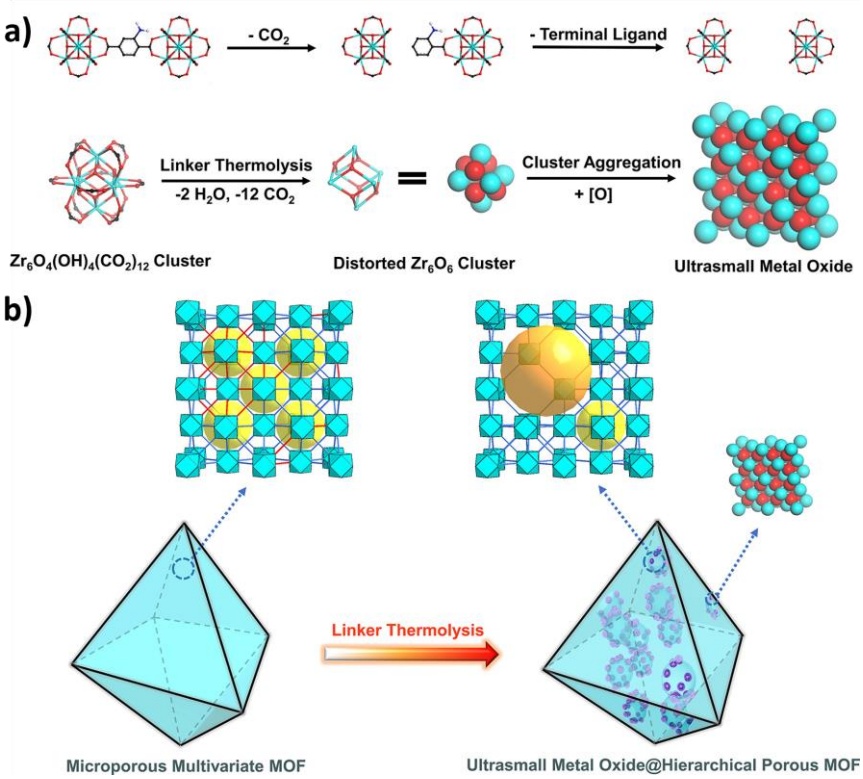


Figure 1.26. a) Linker termolysis of the carbon-carbon bond *via* decarboxylation, producing the aggregation of the free Zr-clusters produced in metal oxide nanoparticles. b) Production of a hierarchically porous MOF and metal oxide nanoparticles aggregated in the pores of the structure by the cleavage of covalent bonds in a mixed-linker system with random positions.

The introduction of free high reactive functional groups remains challenging. Another reaction that has been proven to introduce them in MOFs is *via* ozonolysis. Maspoch *et al.* reported that pendant olefin groups in UiO-like structures can be cleaved by using ozone, the first solid-gas phase covalent PSM of a MOF in a single-crystal to single-crystal fashion. Both reductive and oxidative work-ups were proven to be suitable for incorporating both aldehydes and carboxylic acids,

respectively.[273] Translating the pendant group to a backbone functionality in the matrix, the removal of the ligands could fuse micropores into mesopores in MOFs (Figure 1.27). To do so, MTV-**fcu**-MOFs with pairs of ligands of similar length were prepared in different ratios, being one of the linkers active and the other inert to ozone. It must be mentioned that no linker exchange was needed to introduce both functionalities, as double bonds, azo bonds and aromatic rings are strong functionalities that resist solvothermal conditions. In this case, the ozonolysis generated both aldehyde and carboxylic acid products, which could be washed with an acetic acid solution to remove the fragments and increase the pore width. The overall surface areas of the systems were reduced due to the partial collapse of the

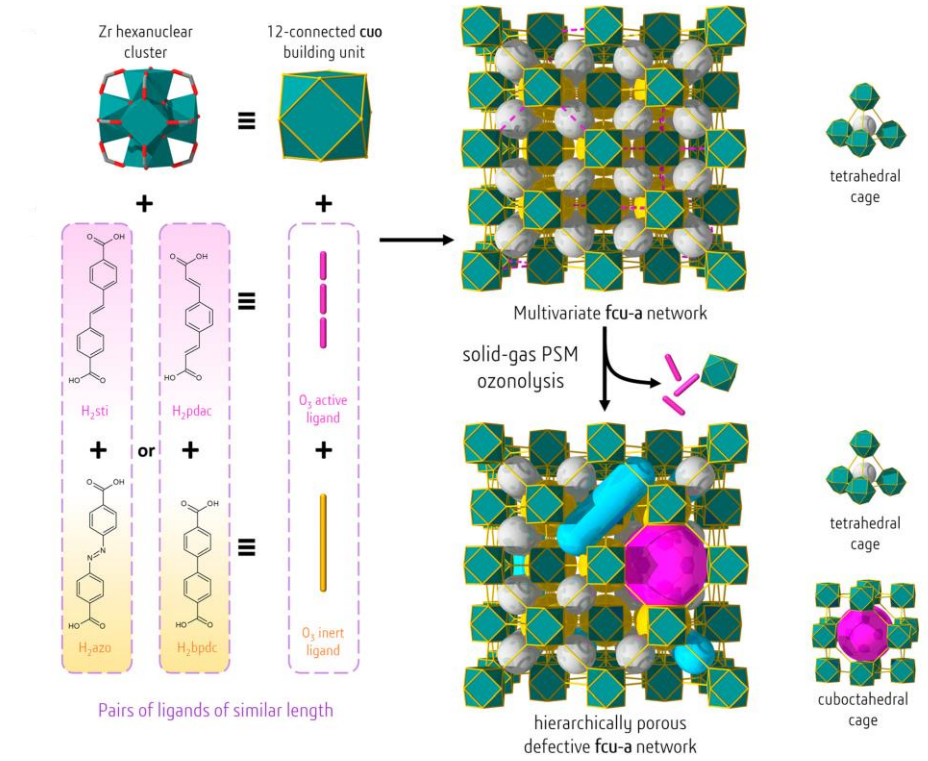


Figure 1.27. Schematic illustration of a mixed-linker system for the production of a hierarchically porous MOF by the cleavage of covalent double bonds in random positions and fusing micropores into mesopores.

frameworks when increasing the active linkers to ozone, inversely proportional to the presence of mesopores.[274]

By controlling the position of the chemical cleavage instead of a random position in the framework, the dimensionality can be modified by selective cleavage of desired bonds. This strategy was performed by first intercalating a 2D Cu-based MOF with 4,4'-dipyridyl disulfide (DPDS) for constructing a new 3D crystal structure. As the disulfide functionality was introduced in the pillaring pyridine-based ligand, the reduction of this bond using trimethylphosphine (TMP) allowed the exfoliation of the tridimensional structure into single 2D MOF nanosheets.[275]

The last destructive technique of MOFs was reported using light. Introducing an incompatible tetratopic linker in UiO-66 dictated the defects of the **fcu** structure. The porphyrine-based linker undergoes a decomposition by first a decarboxylation and then successive oxidative destruction or dissociations. The photolytic removal of the linker in the missing-cluster defects generates mesopores by applying a continuous 405 nm laser, engineering hierarchical mesopores but in a less-controlled manner.

1.8.3. PSM of metal species

Metal exchange in inorganic materials is a well-known process that occurs in nature. It is based on the substitution of a labile metal for another one according to the HSAB principle.[276] The first metal exchange in a MOF was reported by the group of Long, partially substituting the Mn^{2+} metals for Li^{+}, Cu^{+}, Fe^{2+}, Co^{2+}, Ni^{2+}, Cu^{2+} or Zn^{2+} in the SBU without altering its conformation or geometry but modifying the electronic charge when adding monovalent metals.[277] It is believed that, as in SALE, solvent is a key factor to change the coordination environment of the metal in a transition state facilitating the transmetallation. This strategy can force a determined metal to adopt a non-conventional geometry imposed by the lattice given by the MOF. This was illustrated by Carl K. Brozek and Mircea Dincă

substituting the tetrahedral Zn^{2+} in MOF-5 by Ni^{2+} (Figure 1.28). Here, two *N,N*-dimethylformamide (DMF) molecules coordinated the Ni^{2+} in an octahedral coordination and, after heating, both can subsequently lose for affording a square pyramidal and tetrahedral conformations.[278] The same authors were able to introduce later Ti^{3+}, V^{2+}, V^{3+}, Cr^{2+}, Cr^{3+}, Mn^{2+}, and Fe^{3+} in the same SBU. For those trivalent metals, an additional chloride in the coordination sphere stabilized the metal adopting a pseudo-trigonal bipyramide.[279] Additionally, both ligand and metal exchanges have been performed on the same MOF simultaneously or in tandem.[280,281]

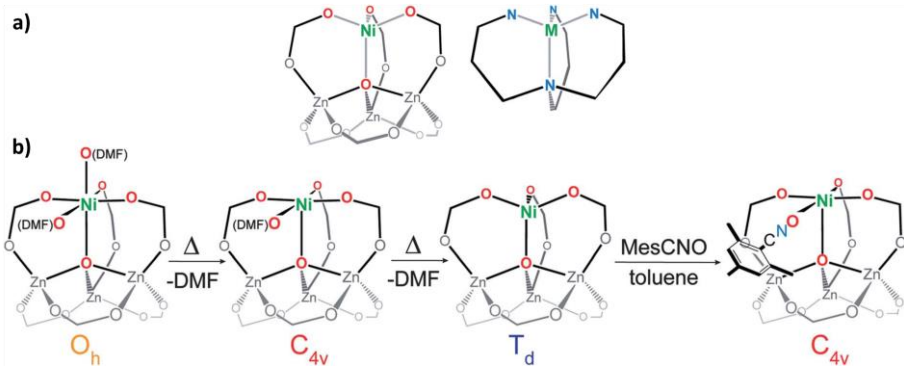


Figure 1.28. a) Illustration of the $Zn_3O(CO_2)$ SBU of MOF-5 acting as a tripodal support that reinforces a tetrahedral geometry of Ni(II), similar to the chelating tetra-amine ligands. b) Modification of the symmetry and coordination geometry of the Ni(II) after different chemical processes.

Another strategy to introduce new metal units in a MOF is by taking advantage of free functional groups or open metal sites able to coordinate single metal ions. Some examples of anchoring transition metal in the ligands of the MOF are the use of binaphthol (BINOL) or bipyridines units able to chelate Ti^{4+} or Pd^{2+} and Cu^{2+}, respectively.[282,283] This method allowed the successfully loading of metals by PSM, as the organometallic complexes can be degraded during the synthetic process in the one-step direct synthesis.

1.8.4. PSM of nano- and micro-particles

Beyond the metal and ligand, PSM can also affect to the weak interactions of the structures, the microscopic crystal shape and morphology and the polymerization of new materials in the pores of the MOF. One example of breaking them is through the mechanical exfoliation in 2D systems that are packed for the isolation of single nanosheets. The delamination process was reported by sonication of a Cd-MOF for 60 min, or either by applying pressure grinding the material for 30 min.[284] Exercising control over the particles can indeed modify the crystal morphology *via* PSM. The chemical etching can shape materials at the nano- and micro-scale. This process occurs at preferential crystal faces by the anisotropic wet etching driven by

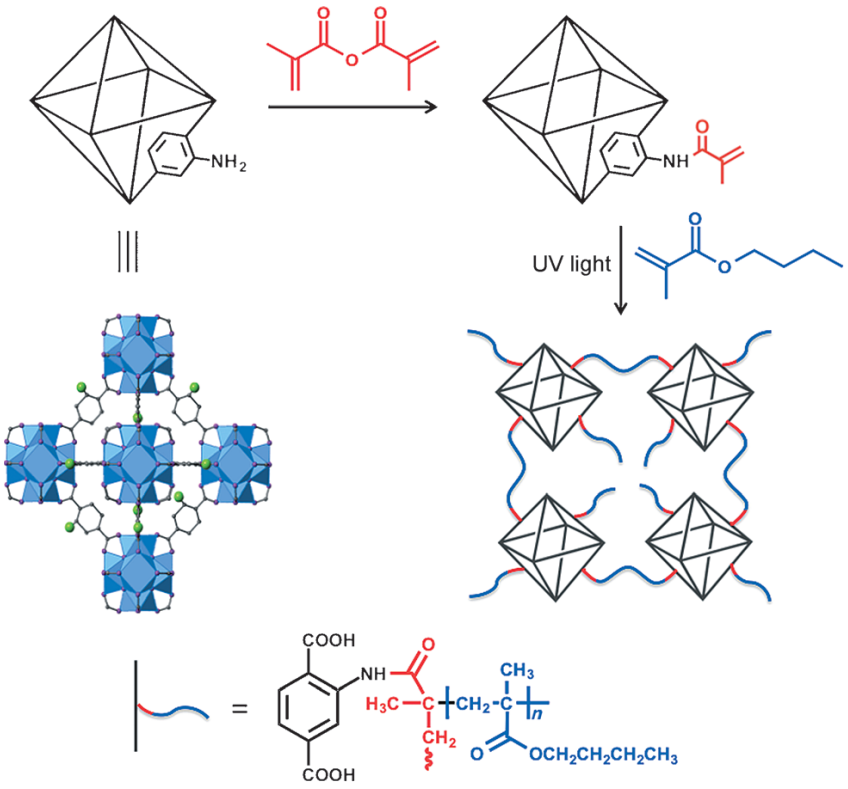


Figure 1.29. PSM of UiO-NH_2 with methacrylic anhydride and subsequent PSP by irradiation with UV light.

acid-base reactions, breaking the coordination bonds. Maspoch *et al.* reported the change in crystal morphology of ZIF-8 and ZIF-67 (cubes, tetrahedra, truncated and non-truncated rhombic dodecahedra, and hollow box) by simply adjusting the pH of the etchant solution.[285] MOFs can also serve as templates for other materials, which can be transformed into polymer materials or polymer-MOF composites. Pendant groups able to polymerize can cross-link inside the pores of the MOF lattice creating a polymer monoliths. The post-synthetic polymerization (PSP) was reported using click reactions of azides and triple bonds,[286] and radical polymerization of doble bonds (Figure 1.29).[287,288]

1.9. Tailor-made reticular materials for specific applications

The most noticeable advantage of reticular materials is the high degree of control of the chemical composition, phase and structural arrangement that can be predicted. This advantage can be used for building materials for specific applications with determined requirements, a unique characteristic in these tailor-made materials compared to other traditional purely inorganic or organic materials.[289] Conventionally, the possible applications to use those materials were exploited after characterizing all the properties or after trial-and-error experiments. The combination of both organic and inorganic MBBs permit benefit from both chemistries, even simultaneously. The main applications that can be targeted are gas storage/separation, catalysis, sensing, molecular removal/delivery, magnetism, conductivity, or structural resolution, which relied on two main factors: the capability to create any kind of strong or weak interaction and the porosity of the material.

As we previously explained, stablishing microporosity was one of the key cornerstones to profit MOFs and COFs in many applications. Since its first measurements, researchers have been developing and improving different methods for optimize the activation of the materials.[290] Obtaining frameworks that exhibit

high surface areas are one of the great challenges and goals designing CPs. The main strategies used for achieve it is by using lighter transition metals (first row), extending the organic struts by using the isoreticular concept in order to enlarge the cavities, and using mixed-linkers MOFs that are able to create wider pores.[110,168,291] To date, the highest BET specific surface area has reached up to 7839 m^2/g in DUT-60, a Zn-based mixed-linker MOF.[292]

Gas separation, production and storage consume a high quantity of resources, energy and currency. There is a global awareness about the necessity of reduce the production and release of greenhouse gases and move to greener options. The fact that porous materials are used as molecular sieves and adsorbents of many different gases is not surprising, as is the main focus in zeolites, MOFs and COFs. Several studies demonstrated the feasibility of MOFs for the H_2 and CH_4 storage,[293–296] CO_2 and NH_3 capture,[297–300] and H_2O adsorption.[132,301,302] Molecules presenting dipoles can be chemically attached by enhancing their reactivity in matrix designed for these interactions. A particular example of the rational selection of MOFs for specific applications is the use of Mg-MOF-74 for the CO_2 capture. As it is constructed upon the assembly of infinite inorganic metal-oxo rods, displays a high number of open metal sites able to attack to the electrophile carbon in CO_2.[303] This interaction was further improved by precisely designing the interior cavities by introducing amine groups both coordinatively and covalently attached to the framework, which can react with carbon dioxide forming carbamates. This was implemented by the introduction of *N,N'*-dimethylehtylenediamine (mmen) in an isoreticular expanded Mg-MOF-74 (Figure 1.30a),[304] and also by using isoreticular expanded linkers with free amino groups after its deprotection in a series of differently functionalized IRMOF-74-III, demonstrating a high selectivity even in the presence of water (Figure 1.30b).[305]

One of the main industrial interests is the chemical separation of molecules. Zeolites have been being used for decades in this area. However, the richer chemistry that MOFs and COFs display make them ideal candidates for improving some

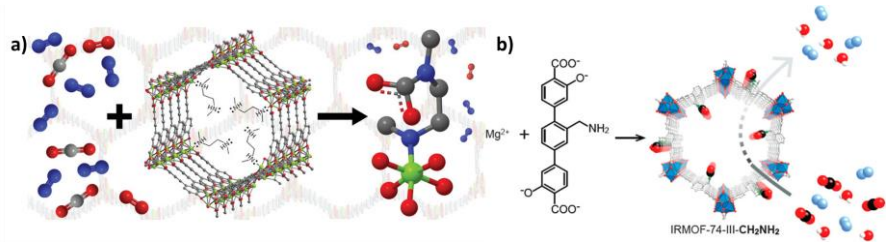


Figure 1.30. PSM of MOF-74-like structures with amine groups in the a) open metal sites and b) organic struts for the capture of CO_2 forming carbamates.

performances and selectivities. Their applications as stationary phases for the separation of alkanes and alkenes have been already reported based on structural design on the windows sizes.[306,307] Beyond this level, some materials have been developed to efficiently separate most difficult molecules such as enantiomers or even isotopes.[308–311] A step below, some small molecules as methane (CH_4) are of special interest in industry and requires their purification and complete separation. As natural gas contains corrosive impurities such as acid gases and CO_2, upgrading through the use of combined organic polymers and MOFs in mixed-matrix membranes (MMMs) demonstrated exceptional high separations.[312,313] Perhaps one the most difficult molecules to separate after isotopes and enantiomers according to their size, shape and physical properties is N_2 from O_2 or CH_4. The presence of nitrogen in natural gas dilutes its heating values, however, its inertness turned their separation into a big challenge. To do it, the group of Eddaoudi reported a mixed-linker Zr-based MOF based on fumarate and mesaconate in a 2:1 ratio. The difference of the methyl group in both linkers produced an asymmetric pore window on the triangular faces of the structure, which blocked the access of tetrahedral methane and led linear nitrogen to diffuse, obtaining the highest record in N_2/CH_4 selectivity and removing both CO_2 and N_2 from natural gas (Figure 1.31). The use of the MOF membrane is expected to reduce the purification cost in a 66% compared to traditional methods.[314]

Host-guest chemistry can be conducted in the pores or surface of reticular materials, allowing the possibility of applying them in very important fields such as catalysis,

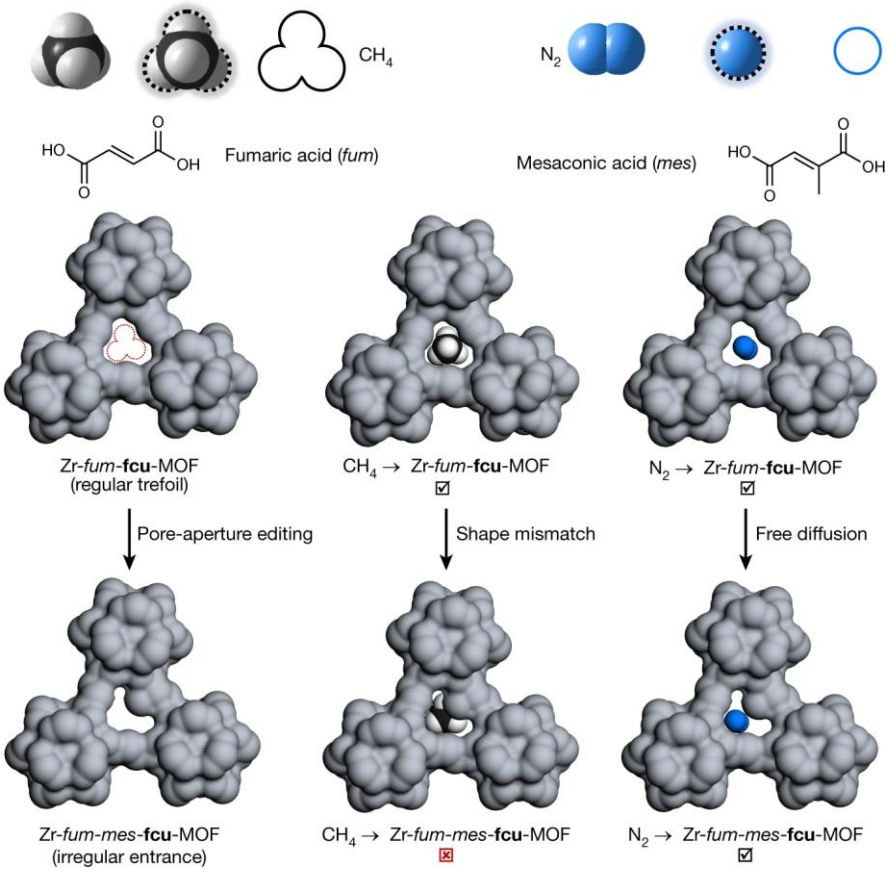


Figure 1.31. Design of a mixed-linker **fcu**-MOF with an asymmetric pore aperture for the exclusion of tetrahedral CH_4 molecules due to the shape mismatch and the free diffusion of linear N_2 molecules for natural gas valorization.

sensing, molecular removal and delivery. The main advantage of reticular materials for catalysis is that they combine the best features of homogeneous and heterogeneous catalysis: they can use the same mechanisms and greater interaction of homogeneous systems and also these catalytic centers are spread along the pores of the material to increase its activity and can be reused and easy to separate, as belongs to the homogeneous systems. The first catalysis was reported by Fujita in 1998, a 2D Cd-based CP clathrate benzaldehyde in the pores and enabled its cyanosilylation.[69] Since then, reticular materials have been applied to many catalytic

processes, with a special emphasis on carbon dioxide reduction due to the needed on reducing weather emergencies (Figure 1.32a).[315–317] The ideal chemical environment for performing the catalysis has been performed in both metal and organic MBBs. From one hand, the deliberate introduction of organic ligands with free functional chelating centres for the metal complexation was illustrated by bipyridine and binaphthol units for Pd and Ti, respectively, which can be involved in catalytic cycles involving couplings and asymmetric catalysis.[282,283] From the other hand, the presence of open metal sites can provide materials able to react in the pores avoiding extra PSM that can decrease the crystallinity. Some interesting examples have been exemplified by high-connected and high-valent Zr- and Ti-based MOFs, able to detoxify chemical warfare by hydrolysing the P-F and P-O bonds in nerve agents and their simulants as a Lewis acid or the photocatalytic oxidation of benzyl alcohol to benzaldehyde, respectively (Figure 1.32b).[138,318–322]

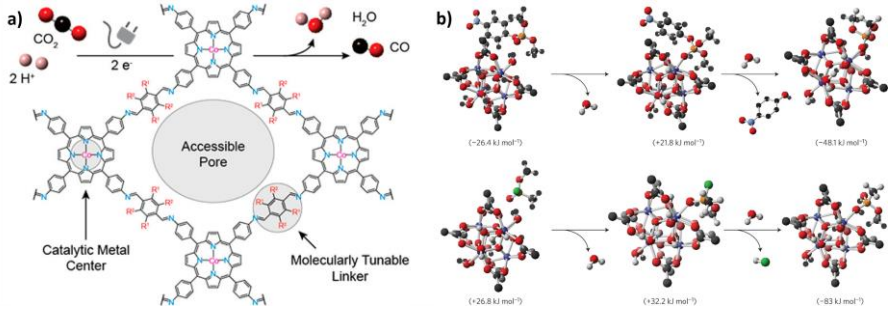


Figure 1.32. a) Electrocatalytic CO_2 reduction in a porphyrin-based COF. b) Destruction of P-O and P-F containing chemical warfare agents in the Zr-sites of NU-1000.

Controlling the weak interactions when guests occupy the empty space in close proximity to the framework have been studied since the first MOFs reported.[82] When the interaction of the framework with a guest produce any kind of change of electrical, photophysical or mechanical properties, the material can be used as a chemical sensor.[323] Stronger interactions can also be controlled in MOFs exhibiting open metal sites. This can be used for attaching in a coordinative alignment of chiral molecules to a chiral framework which allow their structural resolution.[324] This

approach represented a breakthrough, as many natural products are difficult to crystallize and the chiral matrix can enantioselectively crystallized from racemic mixtures (Figure 1.33).[325] Nevertheless, the control of interaction with guests has been exploited for the molecular removal or delivery as they presented much more

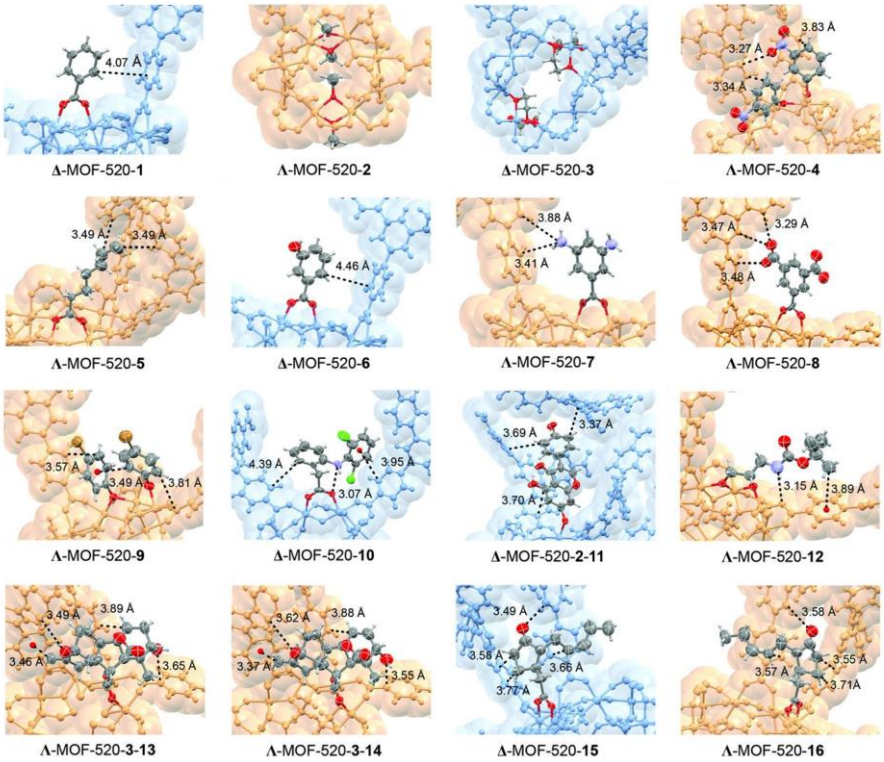


Figure 1.33. Refined structures of 16 different molecules coordinatively aligned in the different chiral MOF-520.

fruitful applications. Molecular removal has notable contributions for water remediation, especially in metal or dye pigments sequestration.[326,327] Molecular delivery has focused on biomedicine applications with the controlled release of drugs.[328–332]

1.10. References

(1) Kekulé, A. Ueber Die s. g. Gepaarten Verbindungen Und Die Theorie Der Mehratomigen Radicale. *Justus Liebigs Ann. Chem.* **1857**, *104*, 129–150.

(2) Lewis, G. N. Valence and Tautomerism. *J. Am. Chem. Soc.* **1913**, *35*, 1448–1455.

(3) Lewis, G. N. The Atom and the Molecule. *J. Am. Chem. Soc.* **1916**, *38*, 762–785.

(4) Pauling, L. The Principles Determining the Structure of Complex Ionic Crystals. *J. Am. Chem. Soc.* **1929**, *51*, 1010–1026.

(5) Linus Pauling, B. THE NATURE OF THE CHEMICAL BOND. APPLICATION OF RESULTS OBTAINED FROM THE QUANTUM MECHANICS AND FROM A THEORY OF PARAMAGNETIC SUSCEPTIBILITY TO THE STRUCTURE OF MOLECULES. *J. Am. Chem. Soc.* **1931**, *53*, 1367–1400.

(6) Pauling, L. Nature of Forces between Large Molecules of Biological Interest. *Nature* **1948**, *161*, 707–709.

(7) Woodward, R. B.; Hoffmann, R. The Conservation of Orbital Symmetry. *Angew. Chem. Int. Ed.* **1969**, *8*, 781–853.

(8) Hoffmann, R. Building Bridges Between Inorganic and Organic Chemistry (Nobel Lecture). *Angew. Chem. Int. Ed.* **1982**, *21*, 711–724.

(9) Wentrup, C. Origins of Organic Chemistry and Organic Synthesis. *Eur. J. Org. Chem.* **2022**, *2022*, e202101492.

(10) Hoffmann, R. How Should Chemists Think? *Sci. Am.* **1993**, *268*, 66–73.

(11) Maddox, J. Crystals from First Principles. *Nature* **1988**, *335*, 201.

(12) Hawthorne, F. C. Crystals from First Principles. *Nature*. **1990**, *345*, 297.

(13) Cohen, M. L. Novel Materials from Theory. *Nature* **1989**, *338*, 291–292.

(14) Bergman, T. Tal om chemiens nyaste framsteg : hållet i Kongl. Maj:ts Höga Nävaro för dess vetenskaps-academie vid præsidii nedläggande den, GoogleBooks, Uppsala, **1**777.

(15) Lavoisier, A. Réflexions Sur la décomposition de l'eau par les substances végetales et animales, *Histoire de l'Academie Royale des Sciences* **1786**, 590-605.

(16) Berzelius, J. J. Föreläsningar i Djurkemien, Förra Delen (Part1), Carl Delén, Stockholm, **1806**.

(17) Seyferth, D. Cadet's Fuming Arsenical Liquid and the Cacodyl Compounds of Bunsen. *Organometallics* **2001**, *20*, 1488–1498.

(18) Zeise, W. C. Von Der Wirkung Zwischen Platinchlorid Und Alkohol, Und von Den Dabei Entstehenden Neuen Substanzen. *Ann. Phys.* **1831**, *97*, 497–541.

(19) Wunderlich, J. A.; Mellor, D. P. A Note on the Crystal Structure of Zeise's Salt. *Acta Cryst.* **1954**, *7*, 130–130.

(20) Wöhler, F. Ueber Künstliche Bildung Des Harnstoffs. *Ann. Phys.* **1828**, *88*, 253–256.

(21) Berthelot, M. Sur les combinasions de la glycérine avec les acides. *Comptes rendus* **1853**, *36*, 27-29.

(22) Werner, A. Beitrag Zur Konstitution Anorganischer Verbindungen. *Zeitschrift für anorganische Chemie* **1893**, *3*, 267–330.

(23) Diercks, C. S.; Kalmutzki, M. J.; Diercks, N. J.; Yaghi, O. M. Conceptual Advances from Werner Complexes to Metal-Organic Frameworks. *ACS Cent. Sci.* **2018**, *4*, 1457–1464.

(24) Brooke, H. J. On the Crystalline Forms of Artificial Salts. *Annals of Philosophy (London)* **1823**, *6*, 38-43.

(25) van Niekerk, J. N.; Schoening, F. R. L.; IUCr. A New Type of Copper Complex as Found in the Crystal Structure of Cupric Acetate, $Cu_2(CH_3COO)_4{\cdot}2H_2O$. *Acta Cryst.* **1953**, *6*, 227–232.

(26) KoyamaHirozo; SaitoYoshihiko. The Crystal Structure of Zinc Oxyacetate, $Zn_4O(CH_3COO)_6$. *Bull. Chem. Soc. Jpn.* **1953**, *27*, 112–114.

(27) Watanabe, T.; Saito, Y.; Koyama, H. Order-Disorder Transition in Beryllium Oxyacetate Crystals. *Nature* **1949**, *164*, 1046.

(28) Niekerk, J. N. Van; Schoening, F. R. L.; Wet, J. F. De. The Structure of Crystalline Chromous Acetate Revealing Paired Chromium Atoms. *Acta Cryst.* **1953**, *6*, 501–504.

(29) Cotton, F. A.; Rice, C. E.; Rice, G. W. Crystal and Molecular Structure of Anhydrous Tetraacetatodichromium. *J. Am. Chem. Soc.* **1977**, *99*, 4704–4707.

(30) van Niekerk, J. N.; Schoening, F. R. L. A New Type of Copper Complex as Found in the Crystal Structure of Cupric Acetate, $Cu_2(CH_3COO)_4{\cdot}2H_2O$. *Acta Cryst.* **1953**, *6*, 227–232.

(31) Cotton, F. A.; DeBoer, B. G.; LaPrade, M. D.; Pipal, J. R.; Ucko, D. A. The Crystal and Molecular Structures of Dichromium Tetraacetate Dihydrate and Dirhodium Tetraacetate Dihydrate. *Acta Cryst. B* **1971**, *27*, 1664–1671.

(32) Porai-Koshits, M. A.; Antsyshkina, A. S. The structure of rhodium acetate complexes, *Dokl. Akad. Nauk SSSR* **1962**, *146, 1102–1105.*

(33) Cotton, F. A.; DeBoer, B. G.; LaPrade, M. D.; Pipal, J. R.; Ucko, D. A. Multiple Chromium(II)-Chromium(II) and Rhodium(II)-Rhodium(II) Bonds. *J. Am. Chem. Soc.* **1970**, *92*, 2926–2927.

(34) Catterick, J.; Hursthouse, M. B.; New, D. B.; Thornton, P. Preparation, X-Ray Crystal Structure, and Magnetic Properties of a Trinuclear Cobalt(II) Carboxylate. *J. Chem. Soc. Chem. Commun.* **1974**, *20*, 843–844.

(35) Orgel, L. E. Structure of the Trinuclear Basic Acetates. *Nature* **1960**, *187*, 504–505.

(36) Barrer, R. M. 33. Synthesis of a Zeolitic Mineral with Chabazite-like Sorptive Properties. *J. Chem. Soc.* **1948**, 127–132.

(37) Barrer, R. M. 435. Syntheses and Reactions of Mordenite. *J. Chem. Soc.* **1948**, 2158–2163.

(38) Gallego, E. M.; Portilla, M. T.; Paris, C.; León-Escamilla, A.; Boronat, M.; Moliner, M.; Corma, A. "Ab Initio" Synthesis of Zeolites for Preestablished Catalytic Reactions. *Science* **2017**, *355*, 1051–1054.

(39) Huber, G. W.; Iborra, S.; Corma, A. Synthesis of Transportation Fuels from Biomass: Chemistry, Catalysts, and Engineering. *Chem. Rev.* **2006**, *106*, 4044–4098.

(40) Arambiy, P.; Angel, S. H. J.; Vitaly, K. In Zeolites and Their Applications, Intech, **2018**.

(41) Moshoeshoe, M.; Nadiye-Tabbiruka, M. S.; Obuseng, V. A Review of the Chemistry, Structure, Properties and Applications of Zeolites. *Am. J. Mater. Sci.* **2017**, *7*, 196–221.

(42) Haüy, R.-J. Traité de Cristallographie, Paris, **1822**.

(43) KandaSeiichi; SaitoYoshihiko. Synthesis of Co-Ordination Compounds of High Molecular Weight. *Bull. Chem. Soc. Jpn.* **1957**, *30*, 192–193.

(44) KinoshitaYukio; MatsubaraIkuo; SaitoYoshihiko. The Crystal Structure of Bis(Succinonitrilo)Copper(I) Nitrate. *Bull. Chem. Soc. Jpn.* **1959**, *32*, 741–747.

(45) KinoshitaYukio; MatsubaraIkuo; SaitoYoshihiko. The Crystal Structure of Bis(Glutaronitrilo)Copper(I) Nitrate. *Bull. Chem. Soc. Jpn.* **1959**, *32* (11), 1216–1221.

(46) KinoshitaYukio; MatsubaraIkuo; HiguchiTaiichi; SaitoYoshihiko. The Crystal Structure of Bis(Adiponitrilo)Copper(I) Nitrate. *Bull. Chem. Soc. Jpn.* **1959**, *32* (11), 1221–1226.

(47) Kraft, A. On the Discovery and History of Prussian Blue. *Bull. Hist. Chem.* **2008**, *33*, 61-67.

(48) Buser, H. J.; Schwarzenbach, D.; Petter, W.; Ludi, A. The Crystal Structure of Prussian Blue: $Fe_4[Fe(CN)_6]_3 \cdot xH_2O$. *Inorg. Chem.* **1977**, *16*, 2704–2710.

(49) Hofmann, K. A.; Küspert, F. Verbindungen von Kohlenwasserstoffen Mit Metallsalzen. *Zeitschrift für Anorganische Chemie* **1897**, *15*, 204–207.

(50) Powell, H. M.; Rayner, J. H. Clathrate Compound Formed by Benzene with an Ammonia–Nickel Cyanide Complex. *Nature* **1949**, *163*, 566–567.

(51) IwamotoToschitake; MiyoshiTadahiko; MiyamotoTakeshi; SasakiYukiyoshi; FujiwaraShizuo. The Metal Ammine Cyanide Aromatics Clathrates. I. The Preparation and Stoichiometry of the Diamminemetal(II) Tetracyano-Niccolate(II) Dibenzene and Dianiline. *Bull. Chem. Soc. Jpn.* **1967**, *40*, 1174–1178.

(52) Iwamoto, T.; Nakano, T.; Morita, M.; Miyoshi, T.; Miyamoto, T.; Sasaki, Y. The Hofman-Type Clathrate: $M(NH_3)_2M'(CN)_4$. 2G. *Inorg. Chim. Acta* **1968**, *2*, 313–316.

(53) Miyoshi, T.; Iwamoto, T.; Sasaki, Y. The Structure of Catena-μ-Ethylenediaminecadmium(II) Tetracyanoniccolate(II) Dibenzene Clathrate: $Cd(en)Ni(CN)_4.2C_6H_6$. *Inorg. Chim. Acta* **1972**, *6*, 59–64.

(54) Aumüller, A.; Erk, P.; Klebe, G.; Hünig, S.; von Schütz, J. U.; Werner, H. -P. A Radical Anion Salt of 2,5-Dimethyl-*N,N'*-Dicyanoquinonediimine with Extremely High Electrical Conductivity. *Angew. Chem. Int. Ed.* **1986**, *25*, 740–741.

(55) Hoskins, B. F.; Robson, R. Infinite Polymeric Frameworks Consisting of Three Dimensionally Linked Rod-like Segments. *J. Am. Chem. Soc.* **1989**, *111*, 5962–5964.

(56) Hoskins, B. F.; Robson, R. Design and Construction of a New Class of Scaffolding-like Materials Comprising Infinite Polymeric Frameworks of 3D-Linked Molecular Rods. A Reappraisal of the $Zn(CN)_2$ and $Cd(CN)_2$ Structures and the Synthesis and Structure of the Diamond-Related Frameworks $[N(CH_3)_4][Cu^{I}Zn^{II}(CN)_4]$ and Cu^{I}[4,4',4",4"'-Tetracyanotetraphenylmethane]$BF_4{\cdot}xC_6H_5NO_2$. *J. Am. Chem. Soc.* **1990**, *112*, 1546–1554.

(57) Abrahams, B. F.; Hoskins, B. F.; Michail, D. M.; Robson, R. Assembly of Porphyrin Building Blocks into Network Structures with Large Channels. *Nature* **1994**, *369*, 727–729.

(58) Wells, A. F. Three-Dimensional Nets and Polyhedral, Wiley, Hoboke, **19**77.

(59) Batten, S. R.; Robson, R. Interpenetrating Nets: Ordered, Periodic Entanglement. *Angew. Chem. Int. Ed.* **1998**, *37*, 1460-1494.

(60) Robson, R. A Net-Based Approach to Coordination Polymers. *J. Chem. Soc., Dalton Trans.* **2000**, *21*, 3735–3744.

(61) Copp, S. B.; Subramanian, S.; Zaworotko, M. J. Formation of Interwoven 2-D Networks by the Spontaneous Strict Self-Assembly of $[\{M(CO)_3(M_3\text{-}OH)\}_4]$ (M = Mn, Re) and Complementary Angular Spacer Molecules. *Angew. Chem. Int. Ed.* **1993**, *32*, 706–709.

(62) MacGillivray, L. R.; Subramanian, S.; Zaworotko, M. J. Interwoven Two- and Three-Dimensional Coordination Polymers through Self-Assembly of Cu^{I} Cations with Linear Bidentate Ligands. *J. Chem. Soc. Chem. Commun.* **1994**, *11*, 1325–1326.

(63) Robinson, F.; Zaworotko, M. J. Triple Interpenetration in [Ag(4,4'-Bipyridine)][NO_3], a Cationic Polymer with a Three-Dimensional Motif Generated by Self-Assembly of 'T-Shaped' Building Blocks. *J. Chem. Soc. Chem. Commun.* **1995**, *23*, 2413–2414.

(64) Subramanian, S.; Zaworotko, M. J. Porous Solids by Design: $[Zn(4,4'\text{-}Bpy)_2(SiF_6)]_N \cdot xDMF$, a Single Framework Octahedral Coordination Polymer with Large Square Channels. *Angew. Chem. Int. Ed.* **1995**, *34*, 2127–2129.

(65) Munakata, M.; Kuroda-Sowa, T.; Maekawa, M.; Nakamura, M.; Akiyama, S.; Kitagawa, S. Architecture of 2D Sheets with Six-Membered Rings of Coppers Interconnected by 2,1,3-Benzothiadiazoles and a Layered Structure Composed of the 2D Sheets. *Inorg. Chem.* **1994**, *33*, 1284–1291.

(66) Munakata, M.; Kuroda-Sowa, T.; Maekawa, M.; Honda, A.; Kitagawa, S. Building a Two-Dimensional Co-Ordination Polymer Having a Multilayered Arrangement. A Molecular Assembly Comprising Hanging Phenazine Molecules between Polymeric Stair Frameworks of Copper(I) Halides. *J. Chem. Soc., Dalton Trans.* **1994**, *19*, 2771–2775.

(67) Kitagawa, S.; Okubo, T.; Kawata, S.; Kondo, M.; Katada, M.; Kobayashi, H. An Oxalate-Linked Copper(II) Coordination Polymer, $[Cu_2(Oxalate)_2(Pyrazine)_3]_n$, Constructed with Two Different Copper Units: X-Ray Crystallographic and Electronic Structures. *Inorg. Chem.* **1995**, *34*, 4790–4796.

(68) Fujita, M.; Kwon, Y. J.; Sasaki, O.; Ogura, K.; Yamaguchi, K. Interpenetrating Molecular Ladders and Bricks. *J. Am. Chem. Soc.* **1995**, *117*, 7287–7288.

(69) Fujita, M.; Washizu, S.; Ogura, K.; Kwon, Y. J. Preparation, Clathration Ability, and Catalysis of a Two-Dimensional Square Network Material Composed of Cadmium(II) and 4, 4′-Bipyridine. *J. Am. Chem. Soc.* **1994**, *116*, 1151–1152.

(70) Real, J. A.; De Munno, G.; Muñoz, M. C.; Julve, M. Crystal Structure and Magnetic Properties of $[Fe(Pyz)_2(NCS)_2]_n$ (Pyz = Pyrazine), a 2D Sheetlike Polymer. *Inorg. Chem.* **1991**, *30*, 2701–2704.

(71) Santoro, A.; Mighell, A. D.; Reimann, C. W. The Crystal Structure of a 1:1 Cupric Nitrate–Pyrazine Complex $Cu(NO_3)_2.(C_4N_2H_4)$. *Acta Cryst. B* **1970**, *26*, 979–984.

(72) Darriet, J.; Haddad, M. S.; Duesler, E. N.; Hendrickson, D. N.; Haddad, M. S.; Hendrickson, D. N. Crystal Structure and Magnetic Properties of Bis(Pyrazine)Copper(II) Perchlorate, $Cu(Pyz)2_(ClO_4)_2$, a Two-Dimensional Heisenberg Antiferromagnet. *Inorg. Chem.* **1979**, *18*, 2679–2682.

(73) Carlucci, L.; Ciani, G.; Proserpio, D. M.; Sironi, A. Novel Networks of Unusually Coordinated Silver(I) Cations: The Wafer-Like Structure of $[Ag(Pyz)_2][Ag_2(Pyz)_5](PF_6)_3 \cdot 2G$ and the Simple Cubic Frame of $[Ag(Pyz)_3](SbF_6)$. *Angew. Chem. Int. Ed.* **1995**, *34*, 1895–1898.

(74) Yaghi, O. M.; Richardson, D. A.; Li, G.; Davis, C. E.; Groy, T. L. Open-Framework Solids with Diamond-like Structures Prepared from Clusters and Metal-Organic Building Blocks. *MRS Online Proceedings Symposium* **1995**, *371*, 15–19.

(75) Yaghi, O. M.; Li, H. Hydrothermal Synthesis of a Metal-Organic Framework Containing Large Rectangular Channels. *J. Am. Chem. Soc.* **1995**, *117*, 10401–10402.

(76) Munno, G. De; Ruiz, R.; Lloret, F.; Faus, J.; Sessoli, R.; Julve, M. Oxalate and 2,2′-Bipyrimidine as Useful Tools in Designing Layered Compounds. *Inorg. Chem.* **1995**, *34*, 408–411.

(77) Pellaux, R.; Schmalle, H. W.; Huber, R.; Fischer, P.; Hauss, T.; Ouladdiaf, B.; Decurtins, S. Molecular-Based Magnetism in Bimetallic Two-Dimensional Oxalate-Bridged Networks. An X-Ray and Neutron Diffraction Study. *Inorg. Chem.* **1997**, *36*, 2301–2308.

(78) Mathonière, C.; Nuttall, C. J.; Carting, S. G.; Day, P. Ferrimagnetic Mixed-Valency and Mixed-Metal Tris(Oxalato)Iron(III) Compounds: Synthesis, Structure, and Magnetism. *Inorg. Chem.* **1996**, *35*, 1201–1206.

(79) Larionova, J.; Mombelli, B.; Sanchiz, J.; Kahn, O. Magnetic Properties of the Two-Dimensional Bimetallic Compounds $(NBu_4)[M^{II}Ru^{III}(Ox)_3]$ (NBu_4 = Tetra-n-Butylammonium; M = Mn, Fe, Cu; Ox = Oxalate). *Inorg. Chem.* **1998**, *37*, 679–684.

(80) De Munno, G.; Julve, M.; Nicolo, F.; Lloret, F.; Faus, J.; Ruiz, R.; Sinn, E. 2,2′-Bipyrimidineoxalatocopper(II) Complexes: From the Mononuclear Complex to the 2D Sheetlike Polymer. *Angew. Chem. Int. Ed.* **1993**, *32*, 613–615.

(81) Decurtins, S.; Schmalle, H. W.; Schneuwly, P.; Oswald, H. R. Photochemical Synthesis and Structure of a 3-Dimensional Anionic Polymeric Network of an Iron(II) Oxalato Complex with Tris(2,2′-Bipyridine)Iron(II) Cations. *Inorg. Chem.* **1993**, *32*, 1888–1892.

(82) Yaghi, O. M.; Li, G.; Li, H. Selective Binding and Removal of Guests in a Microporous Metal–Organic Framework. *Nature* **1995**, *378*, 703–706.

(83) Li, H.; Eddaoudi, M.; Groy, T. L.; Yaghi, O. M. Establishing Microporosity in Open Metal-Organic Frameworks: Gas Sorption Isotherms for Zn(BDC) (BDC = 1,4-Benzenedicarboxylate) [28]. *J. Am. Chem. Soc.* **1998**, *120*, 8571–8572.

(84) Allison, S. A.; Barrer, R. M. Sorption in the β-Phases of Transition Metal(II) Tetra-(4-Methylpyridine) Thiocyanates and Related Compounds. *J. Chem. Soc. A* **1969**, 1717–1723.

(85) Kondo, M.; Yoshitomi, T.; Seki, K.; Matsuzaka, H.; Kitagawa, S. Three-Dimensional Framework with Channeling Cavities for Small Molecules: $\{[M_2(4,4'\text{-Bpy})_3(NO_3)_4]\cdot xH_2O\}_n$ (M = Co, Ni, Zn). *Angew. Chem. Int. Ed.* **1997**, *36*, 1725–1727.

(86) Chui, S. S.-Y.; Lo, S. M.-F.; Charmant, J. P. H.; Orpen, A. G.; Williams, I. D. A Chemically Functionalizable Nanoporous Material $[Cu_3(TMA)_2(H_2O)_3]_n$. *Science* **1999**, *283*, 1148–1150.

(87) Li, H.; Eddaoudi, M.; O'Keeffe, M.; Yaghi, O. M. Design and Synthesis of an Exceptionally Stable and Highly Porous Metal-Organic Framework. *Nature* **1999**, *402*, 276–279.

(88) Yaghi, O. M.; Kalmutzki, M. J.; Diercks, C. S. *Introduction to Reticular Chemistry*; Wiley, **2019**.

(89) Yaghi, O. M.; O'Keeffe, M.; Ockwig, N. W.; Chae, H. K.; Eddaoudi, M.; Kim, J. Reticular Synthesis and the Design of New Materials. *Nature* **2003**, *423*, 705–714.

(90) Eddaoudi, M.; Kim, J.; Rosi, N.; Vodak, D.; Wachter, J.; O'Keeffe, M.; Yaghi, O. M. Systematic Design of Pore Size and Functionality in Isoreticular MOFs and Their Application in Methane Storage. *Science* **2002**, *295*, 469–472.

(91) Eddaoudi, M.; Kim, J.; Wachter, J. B.; Chae, H. K.; O'Keeffe, M.; Yaghi, O. M. Porous Metal–Organic Polyhedra: 25 Å Cuboctahedron Constructed from 12 $Cu_2(CO_2)_4$ Paddle-Wheel Building Blocks. *J. Am. Chem. Soc.* **2001**, *123*, 4368–4369.

(92) Ni, Z.; Yassar, A.; Antoun, T.; Yaghi, O. M. Porous Metal-Organic Truncated Octahedron Constructed from Paddle-Wheel Squares and Terthiophene Links. *J. Am. Chem. Soc.* **2005**, *127*, 12752–12753.

(93) Li, J. R.; Zhou, H. C. Metal–Organic Hendecahedra Assembled from Dinuclear Paddlewheel Nodes and Mixtures of Ditopic Linkers with 120 and 90° Bend Angles. *Angew. Chem. Int. Ed.* **2009**, *48*, 8465–8468.

(94) Eddaoudi, M.; Kim, J.; Vodak, D.; Sudik, A.; Wachter, J.; O'Keeffe, M.; Yaghi, O. M. Geometric Requirements and Examples of Important Structures in the Assembly of Square Building Blocks. *Proc. Nat. Acad. Sci. U. S. A.* **2002**, *99*, 4900–4904.

(95) Furukawa, H.; Kim, J.; Ockwig, N. W.; O'Keeffe, M.; Yaghi, O. M. Control of Vertex Geometry, Structure Dimensionality, Functionality, and Pore Metrics in the Reticular Synthesis of Crystalline Metal-Organic Frameworks and Polyhedra. *J. Am. Chem. Soc.* **2008**, *130*, 11650–11661.

(96) Eddaoudi, M.; Kim, J.; O'Keeffe, M.; Yaghi, O. M. Cu2[o-$BrC_6H_3(CO_2)_2]_2(H_2O)_2$·$(DMF)_8(H_2O)_2$: A Framework Deliberately Designed to Have the NbO Structure Type. *J. Am. Chem. Soc.* **2002**, *124*, 376–377.

(97) Tian, Y.-Q.; Cai, C.-X.; Ji, Y.; You, X.-Z.; Peng, S.-M.; Lee, G.-H.; You, -Z; Tian, Y.-Q.; Cai, C.-X.; Ji, Y.; Peng, S.-M.; Lee, G.-H. $Co_5(Im)_{10}{\cdot}2\ MB]_\infty$: A Metal-Organic Open-Framework with Zeolite-Like Topology. *Angew. Chem. Int. Ed* **2002**, *41*, 1384-1386.

(98) Huang, X.; Zhang, J.; Chen, X. $[Zn(Bim)_2]{\cdot}(H_2O)_{1.67}$: A Metal-Organic Open-Framework with Sodalite Topology. *Chin. Sci. Bull.* **2003**, *48*, 1531–1534.

(99) Huang, X.-C.; Lin, Y.-Y.; Zhang, J.-P.; Chen, X.-M.; Huang, X.-C.; Lin, Y.-Y.; Zhang, J.-P.; Chen, X.-M. Ligand-Directed Strategy for Zeolite-Type Metal–Organic Frameworks: Zinc(II) Imidazolates with Unusual Zeolitic Topologies. *Angew. Chem. Int. Ed.* **2006**, *45*, 1557–1559.

(100) Zhang, J. P.; Zhu, A. X.; Lin, R. B.; Qi, X. L.; Chen, X. M. Pore Surface Tailored SOD-Type Metal-Organic Zeolites. *Adv. Mater.* **2011**, *23*, 1268–1271.

(101) Zhang, J. P.; Zhang, Y. B.; Lin, J. Bin; Chen, X. M. Metal Azolate Frameworks: From Crystal Engineering to Functional Materials. *Chem. Rev.* **2012**, *112*, 1001–1033.

(102) Zhu, A. X.; Lin, J. Bin; Zhang, J. P.; Chen, X. M. Isomeric Zinc(Il) Triazolate Frameworks with 3-Connected Networks: Syntheses, Structures, and Sorption Properties. *Inorg. Chem.* **2009**, *48*, 3882–3889.

(103) Park, K. S.; Ni, Z.; Côté, A. P.; Choi, J. Y.; Huang, R.; Uribe-Romo, F. J.; Chae, H. K.; O'Keeffe, M.; Yaghi, O. M. Exceptional Chemical and Thermal Stability of Zeolitic Imidazolate Frameworks. *Proc. Nat. Acad. Sci. U. S. A.* **2006**, *103*, 10186–10191.

(104) Chen, B.; Eddaoudi, M.; Reineke, T. M.; Kampf, J. W.; O'Keeffe, M.; Yaghi, O. M. $Cu_2(ATC){\cdot}6H_2O$: Design of Open Metal Sites in Porous Metal-Organic Crystals (ATC: 1,3,5,7-Adamantane Tetracarboxylate). *J. Am. Chem. Soc.* **2000**, *122*, 11559–11560.

(105) Chen, B.; Ockwig, N. W.; Fronczek, F. R.; Contreras, D. S.; Yaghi, O. M. Transformation of a Metal-Organic Framework from the NbO to PtS Net. *Inorg. Chem.* **2005**, *44*, 181–183.

(106) Chae, H. K.; Eddaoudi, M.; Kim, J.; Hauck, S. I.; Hartwig, J. F.; Yaghi, O. M. Tertiary Building Units: Synthesis, Structure, and Porosity of a Metal-Organic Dendrimer Framework (MODF-1). *J. Am. Chem. Soc.* **2001**, *123*, 11482–11483.

(107) Kim, J.; Chen, B.; Reineke, T. M.; Li, H.; Eddaoudi, M.; Moler, D. B.; O'Keeffe, M.; Yaghi, O. M. Assembly of Metal-Organic Frameworks from Large Organic and Inorganic Secondary Building Units: New Examples and Simplifying Principles for Complex Structures. *J. Am. Chem. Soc.* **2001**, *123*, 8239–8247.

(108) Chen, B.; Eddaoudi, M.; Hyde, S. T.; O'Keeffe, M.; Yaghi, O. M. Interwoven Metal-Organic Framework on a Periodic Minimal Surface with Extra-Large Pores. *Science* **2001**, *291*, 1021–1023.

(109) Chae, H. K.; Kim, J.; Friedrichs, O. D.; O'Keeffe, M.; Yaghi, O. M. Design of Frameworks with Mixed Triangular and Octahedral Building Blocks Exemplified by the Structure of $[Zn_4O(TCA)_2]$ Having the Pyrite Topology. *Angew. Chem. Int. Ed.* **2003**, *42*, 3907–3909.

(110) Chae, H. K.; Siberio-Pérez, D. Y.; Kim, J.; Go, Y. B.; Eddaoudi, M.; Matzger, A. J.; O'Keeffe, M.; Yaghi, O. M. A Route to High Surface Area, Porosity and Inclusion of Large Molecules in Crystals. *Nature* **2004**, *427*, 523–527.

(111) Serpaggi, F.; Férey, G. Hybrid Open Frameworks (MIL-*n*). Part 4 Synthesis and Crystal Structure of MIL-8, a Series of Lanthanide Glutarates with an Open Framework, $[Ln(H_2O)]_2[O_2C(CH_2)_3CO_2]_3{\cdot}4H_2O$. *J. Mater. Chem.* **1998**, *8*, 2737–2741.

(112) Serpaggi, F.; Férey, G. Hybrid Open Frameworks (MIL-*n*): Synthesis and Crystal Structure of MIL-17 — a Rare-Earth Dicarboxylate with a Relatively Open Framework, $[Pr(H_2O)]_2[O_2C(CH_2)_2CO_2]_3{\cdot}H_2O$. *Micropor. Mesopor. Mater.* **1999**, *32*, 311–318.

(113) Millange, F.; Serre, C.; Férey, G. Synthesis, Structure Determination and Properties of MIL-53as and MIL-53ht: The First Cr^{III} Hybrid Inorganic–Organic Microporous Solids: $Cr^{III}(OH)\cdot\{O_2C–C_6H_4–CO_2\}\cdot\{HO_2C–C_6H_4–CO_2H\}_x$. *Chem. Commun.* **2002**, *2*, 822–823.

(114) Barthelet, K.; Marrot, J.; Riou, D.; Férey, G. A Breathing Hybrid Organic-Inorganic Solid with Very Large Pores and High Magnetic Characteristics. *Angew. Chem. Int. Ed.* **2002**, *41*, 281-284.

(115) Serre, C.; Millange, F.; Thouvenot, C.; Noguès, M.; Marsolier, G.; Louër, D.; Férey, G. Very Large Breathing Effect in the First Nanoporous Chromium(III)-Based Solids: MIL-53 or $Cr^{III}(OH)\cdot\{O_2C\text{-}C_6H_4\text{-}CO_2\}\cdot\{HO_2C\text{-}C_6H_4\text{-}CO_2H\}_x\cdot H_2O_y$. *J. Am. Chem. Soc.* **2002**, *124*, 13519–13526.

(116) Férey, G.; Latroche, M.; Serre, C.; Millange, F.; Loiseau, T.; Percheron-Guégan, A. Hydrogen Adsorption in the Nanoporous Metal-Benzenedicarboxylate $M(OH)(O_2C–C_6H_4–CO_2)$($M = Al^{3+}$, Cr^{3+}), MIL-53. *Chem. Commun.* **2003**, *3*, 2976–2977.

(117) Loiseau, T.; Serre, C.; Huguenard, C.; Fink, G.; Taulelle, F.; Henry, M.; Bataille, T.; Férey, G. A Rationale for the Large Breathing of the Porous Aluminum Terephthalate (MIL-53) Upon Hydration. *Chem. Eur. J.* **2004**, *10*, 1373–1382.

(118) Bourrelly, S.; Llewellyn, P. L.; Serre, C.; Millange, F.; Loiseau, T.; Férey, G. Different Adsorption Behaviors of Methane and Carbon Dioxide in the Isotypic Nanoporous Metal Terephthalates MIL-53 and MIL-47. *J. Am. Chem. Soc.* **2005**, *127*, 13519–13521.

(119) Barthelet, K.; Riou, D.; Férey, G. $[V^{III}(H_2O)]_3O(O_2CC_6H_4CO_2)_3\cdot$(Cl, $9H_2O$) (MIL-59): A Rare Example of Vanadocarboxylate with a Magnetically Frustrated Three-Dimensional Hybrid Framework. *Chem. Commun.* **2002**, *2*, 1492–1493.

(120) Serre, C.; Millange, F.; Surblé, S.; Férey, G. A Route to the Synthesis of Trivalent Transition-Metal Porous Carboxylates with Trimeric Secondary Building Units. *Angew. Chem. Int. Ed.* **2004**, *43*, 6285–6289.

(121) Sudik, A. C.; Côté, A. P.; Yaghi, O. M. Metal-Organic Frameworks Based on Trigonal Prismatic Building Blocks and the New "acs" Topology. *Inorg. Chem.* **2005**, *44*, 2998–3000.

(122) Serre, C.; Mellot-Draznieks, C.; Surblé, S.; Audebrand, N.; Filinchuk, Y.; Férey, G. Role of Solvent-Host Interactions That Lead to Very Large Swelling of Hybrid Frameworks. *Science* **2007**, *315*, 1828–1831.

(123) Surblé, S.; Serre, C.; Mellot-Draznieks, C.; Millange, F.; Férey, G. A New Isoreticular Class of Metal-Organic-Frameworks with the MIL-88 Topology. *Chem. Commun.* **2006**, *3*, 284–286.

(124) Férey, G.; Serre, C.; Mellot-Draznieks, C.; Millange, F.; Surblé, S.; Dutour, J.; Margiolaki, I. A Hybrid Solid with Giant Pores Prepared by a Combination of Targeted Chemistry, Simulation, and Powder Diffraction. *Angew. Chem. Int. Ed.* **2004**, *43*, 6296–6301.

(125) Férey, C.; Mellot-Draznieks, C.; Serre, C.; Millange, F.; Dutour, J.; Surblé, S.; Margiolaki, I. Chemistry: A Chromium Terephthalate-Based Solid with Unusually Large Pore Volumes and Surface Area. *Science* **2005**, *309*, 2040–2042.

(126) Pearson, R. G. Hard and Soft Acids and Bases. *J. Am. Chem. Soc.* **1963**, *85*, 3533–3539.

(127) Pearson, R. G. Hard and Soft Acids and Bases, HSAB, Part II: Underlying Theories. *J. Chem. Educ.* **1968**, *45*, 643–648.

(128) Cavka, J. H.; Jakobsen, S.; Olsbye, U.; Guillou, N.; Lamberti, C.; Bordiga, S.; Lillerud, K. P. A New Zirconium Inorganic Building Brick Forming Metal Organic Frameworks with Exceptional Stability. *J. Am. Chem. Soc.* **2008**, *130*, 13850–13851.

(129) Morris, W.; Volosskiy, B.; Demir, S.; Gándara, F.; McGrier, P. L.; Furukawa, H.; Cascio, D.; Stoddart, J. F.; Yaghi, O. M. Synthesis, Structure, and Metalation of Two New Highly Porous Zirconium Metal–Organic Frameworks. *Inorg. Chem.* **2012**, *51*, 6443–6445.

(130) Feng, D.; Gu, Z. Y.; Li, J. R.; Jiang, H. L.; Wei, Z.; Zhou, H. C. Zirconium-Metalloporphyrin PCN-222: Mesoporous Metal–Organic Frameworks with Ultrahigh Stability as Biomimetic Catalysts. *Angew. Chem. Int. Ed.* **2012**, *51*, 10307–10310.

(131) Feng, D.; Chung, W. C.; Wei, Z.; Gu, Z. Y.; Jiang, H. L.; Chen, Y. P.; Darensbourg, D. J.; Zhou, H. C. Construction of Ultrastable Porphyrin Zr Metal-Organic Frameworks through Linker Elimination. *J. Am. Chem. Soc.* **2013**, *135*, 17105–17110.

(132) Furukawa, H.; Gándara, F.; Zhang, Y.-B.; Jiang, J.; Queen, W. L.; Hudson, M. R.; Yaghi, O. M. Water Adsorption in Porous Metal–Organic Frameworks and Related Materials. *J. Am. Chem. Soc.* **2014**, *136*, 4369–4381.

(133) Nguyen, P. T. K.; Nguyen, H. T. D.; Nguyen, H. N.; Trickett, C. A.; Ton, Q. T.; Gutiérrez-Puebla, E.; Monge, M. A.; Cordova, K. E.; Gándara, F. New Metal-Organic Frameworks for Chemical Fixation of CO_2. *ACS Appl. Mater. Interfaces* **2018**, *10*, 733–744.

(134) Zhang, Y.; Zhang, X.; Lyu, J.; Otake, K. I.; Wang, X.; Redfern, L. R.; Malliakas, C. D.; Li, Z.; Islamoglu, T.; Wang, B.; Farha, O. K. A Flexible Metal-Organic Framework with 4-Connected Zr_6 Nodes. *J. Am. Chem. Soc.* **2018**, *140*, 11179–11183.

(135) Wang, H.; Dong, X.; Lin, J.; Teat, S. J.; Jensen, S.; Cure, J.; Alexandrov, E. V.; Xia, Q.; Tan, K.; Wang, Q.; Olson, D. H.; Proserpio, D. M.; Chabal, Y. J.; Thonhauser, T.; Sun, J.; Han, Y.; Li, J. Topologically Guided Tuning of Zr-MOF Pore Structures for Highly Selective Separation of C6 Alkane Isomers. *Nat. Commun.* **2018**, *9*, 1–11.

(136) Bon, V.; Senkovskyy, V.; Senkovska, I.; Kaskel, S. Zr(IV) and Hf(IV) Based Metal–Organic Frameworks with reo-Topology. *Chem. Commun.* **2012**, *48*, 8407–8409.

(137) Xue, D. X.; Cairns, A. J.; Belmabkhout, Y.; Wojtas, L.; Liu, Y.; Alkordi, M. H.; Eddaoudi, M. Tunable Rare-Earth fcu-MOFs: A Platform for Systematic Enhancement of CO_2 Adsorption Energetics and Uptake. *J. Am. Chem. Soc.* **2013**, *135*, 7660–7667.

(138) Dan-Hardi, M.; Serre, C.; Frot, T.; Rozes, L.; Maurin, G.; Sanchez, C.; Férey, G. A New Photoactive Crystalline Highly Porous Titanium(IV) Dicarboxylate. *J. Am. Chem. Soc.* **2009**, *131*, 10857–10859.

(139) Schoedel, A.; Li, M.; Li, D.; O'Keeffe, M.; Yaghi, O. M. Structures of Metal-Organic Frameworks with Rod Secondary Building Units. *Chem. Rev.* **2016**, *116*, 12466–12535.

(140) Rosi, N. L.; Kim, J.; Eddaoudi, M.; Chen, B.; O'Keeffe, M.; Yaghi, O. M. Rod Packings and Metal-Organic Frameworks Constructed from Rod-Shaped Secondary Building Units. *J. Am. Chem. Soc.* **2005**, *127*, 1504–1518.

(141) Deng, H.; Grunder, S.; Cordova, K. E.; Valente, C.; Furukawa, H.; Hmadeh, M.; Gándara, F.; Whalley, A. C.; Liu, Z.; Asahina, S.; Kazumori, H.; O'Keeffe, M.; Terasaki, O.; Stoddart, J. F.; Yaghi, O. M. Large-Pore Apertures in a Series of Metal-Organic Frameworks. *Science* **2012**, *336* , 1018–1023.

(142) Huang, Z. L.; Drillon, M.; Masciocchi, N.; Sironi, A.; Zhao, J. T.; Rabu, P.; Panissod, P. Ab-Initio XRPD Crystal Structure and Giant Hysteretic Effect (H(c) = 5.9 T) of a New Hybrid Terephthalate-Based Cobalt(II) Magnet. *Chem. Mater.* **2000**, *12*, 2805–2812.

(143) Côté, A. P.; Benin, A. I.; Ockwig, N. W.; O'Keeffe, M.; Matzger, A. J.; Yaghi, O. M. Porous, Crystalline, Covalent Organic Frameworks. *Science* **2005**, *310*, 1166–1170.

(144) Côté, A. P.; El-Kaderi, H. M.; Furukawa, H.; Hunt, J. R.; Yaghi, O. M. Reticular Synthesis of Microporous and Mesoporous 2D Covalent Organic Frameworks. *J. Am. Chem. Soc.* **2007**, *129*, 12914–12915.

(145) El-Kaderi, H. M.; Hunt, J. R.; Mendoza-Cortés, J. L.; Côté, A. P.; Taylor, R. E.; O'Keeffe, M.; Yaghi, O. M. Designed Synthesis of 3D Covalent Organic Frameworks. *Science* **2007**, *316*, 268–272.

(146) Kuhn, P.; Antonietti, M.; Thomas, A. Porous, Covalent Triazine-Based Frameworks Prepared by Ionothermal Synthesis. *Angew. Chem. Int. Ed.* **2008**, *47*, 3450–3453.

(147) Uribe-Romo, F. J.; Hunt, J. R.; Furukawa, H.; Klöck, C.; O'Keeffe, M.; Yaghi, O. M. A Crystalline Imine-Linked 3-D Porous Covalent Organic Framework. *J. Am. Chem. Soc.* **2009**, *131*, 4570–4571.

(148) Uribe-Romo, F. J.; Doonan, C. J.; Furukawa, H.; Oisaki, K.; Yaghi, O. M. Crystalline Covalent Organic Frameworks with Hydrazone Linkages. *J. Am. Chem. Soc.* **2011**, *133*, 11478–11481.

(149) Jackson, K. T.; Reich, T. E.; El-Kaderi, H. M. Targeted Synthesis of a Porous Borazine-Linked Covalent Organic Framework. *Chem. Commun.* **2012**, *48*, 8823–8825.

(150) Guo, J.; Xu, Y.; Jin, S.; Chen, L.; Kaji, T.; Honsho, Y.; Addicoat, M. A.; Kim, J.; Saeki, A.; Ihee, H.; Seki, S.; Irle, S.; Hiramoto, M.; Gao, J.; Jiang, D. Conjugated Organic Framework with Three-Dimensionally Ordered Stable Structure and Delocalized π Clouds. *Nat. Commun.* **2013**, *4*, 1–8.

(151) Beaudoin, D.; Maris, T.; Wuest, J. D. Constructing Monocrystalline Covalent Organic Networks by Polymerization. *Nat. Chem.* **2013**, *5*, 830–834.

(152) Fang, Q.; Zhuang, Z.; Gu, S.; Kaspar, R. B.; Zheng, J.; Wang, J.; Qiu, S.; Yan, Y. Designed Synthesis of Large-Pore Crystalline Polyimide Covalent Organic Frameworks. *Nat. Commun.* **2014**, *5*, 1–8.

(153) Zhang, B.; Wei, M.; Mao, H.; Pei, X.; Alshmimri, S. A.; Reimer, J. A.; Yaghi, O. M. Crystalline Dioxin-Linked Covalent Organic Frameworks from Irreversible Reactions. *J. Am. Chem. Soc.* **2018**, *140*, 12715–12719.

(154) Zhang, Y. B.; Su, J.; Furukawa, H.; Yun, Y.; Gándara, F.; Duong, A.; Zou, X.; Yaghi, O. M. Single-Crystal Structure of a Covalent Organic Framework. *J. Am. Chem. Soc.* **2013**, *135*, 16336–16339.

(155) Ma, T.; Kapustin, E. A.; Yin, S. X.; Liang, L.; Zhou, Z.; Niu, J.; Li, L. H.; Wang, Y.; Su, J.; Li, J.; Wang, X.; Wang, W. D.; Wang, W.; Sun, J.; Yaghi, O. M. Single-Crystal X-Ray Diffraction Structures of Covalent Organic Frameworks. *Science* **2018**, *361*, 48–52.

(156) Gropp, C.; Ma, T.; Hanikel, N.; Yaghi, O. M. Design of Higher Valency in Covalent Organic Frameworks. *Science* **2020**, *370*, eabd6406.

(157) Liu, Y.; Ma, Y.; Zhao, Y.; Sun, X.; Gándara, F.; Furukawa, H.; Liu, Z.; Zhu, H.; Zhu, C.; Suenaga, K.; Oleynikov, P.; Alshammari, A. S.; Zhang, X.; Terasaki, O.; Yaghi, O. M. Weaving of Organic Threads into a Crystalline Covalent Organic Framework. *Science* **2016**, *351*, 365–369.

(158) Liu, Y.; Diercks, C. S.; Ma, Y.; Lyu, H.; Zhu, C.; Alshmimri, S. A.; Alshihri, S.; Yaghi, O. M. 3D Covalent Organic Frameworks of Interlocking 1D Square Ribbons. *J. Am. Chem. Soc.* **2019**, *141*, 677–683.

(159) Kitaura, R.; Fujimoto, K.; Noro, S.-I.; Kondo, M.; Kitagawa, S. A Pillared-Layer Coordination Polymer Network Displaying Hysteretic Sorption: $[Cu_2(Pzdc)_2(Dpyg)]_n$ (Pzdc = Pyrazine-2,3-Dicarboxylate; Dpyg = 1,2-Di(4-Pyridyl)-Glycol). *Angew. Chem. Int. Ed.* **2002**, *41*, 133-135.

(160) Kumazawa, K.; Biradha, K.; Kusukawa, T.; Okano, T.; Fujita, M. Multicomponent Assembly of a Pyrazine-Pillared Coordination Cage That Selectively Binds Planar Guests by Intercalation. *Angew. Chem. Int. Ed.* **2003**, *42*, 3909–3913.

(161) Sudik, A. C.; Côté, A. P.; Wong-Foy, A. G.; O'Keeffe, M.; Yaghi, O. M. A Metal–Organic Framework with a Hierarchical System of Pores and Tetrahedral Building Blocks. *Angew. Chem. Int. Ed.* **2006**, *118*, 2590–2595.

(162) Sudik, A. C.; Millward, A. R.; Ockwig, N. W.; Côté, A. P.; Kim, J.; Yaghi, O. M. Design, Synthesis, Structure, and Gas (N_2, Ar, CO_2, CH_4, and H_2) Sorption Properties of Porous Metal-Organic Tetrahedral and Heterocuboidal Polyhedra. *J. Am. Chem. Soc.* **2005**, *127*, 7110–7118.

(163) Chun, H. Low-Level Self-Assembly of Open Framework Based on Three Different Polyhedra: Metal-Organic Analogue of Face-Centered Cubic Dodecaboride. *J. Am. Chem. Soc.* **2008**, *130*, 800–801.

(164) Li, J. R.; Timmons, D. J.; Zhou, H. C. Interconversion between Molecular Polyhedra and Metal-Organic Frameworks. *J. Am. Chem. Soc.* **2009**, *131*, 6368–6369.

(165) Chen, W.; Wang, J. Y.; Chen, C.; Yue, Q.; Yuan, H. M.; Chen, J. S.; Wang, S. N. Photoluminescent Metal-Organic Polymer Constructed from Trimetallic Clusters and Mixed Carboxylates. *Inorg. Chem.* **2003**, *42*, 944–946.

(166) Koh, K.; Wong-Foy, A. G.; Matzger, A. J. A Crystalline Mesoporous Coordination Copolymer with High Microporosity. *Angew. Chem. Int. Ed.* **2008**, *47*, 677–680.

(167) Klein, N.; Senkovska, I.; Gedrich, K.; Stoeck, U.; Henschel, A.; Mueller, U.; Kaskel, S. A Mesoporous Metal–Organic Framework. *Angew. Chem. Int. Ed.* **2009**, *48*, 9954–9957.

(168) Furukawa, H.; Ko, N.; Go, Y. B.; Aratani, N.; Choi, S. B.; Choi, E.; Yazaydin, A. Ö.; Snurr, R. Q.; O'Keeffe, M.; Kim, J.; Yaghi, O. M. Ultrahigh Porosity in Metal-Organic Frameworks. *Science* **2010**, *329*, 424–428.

(169) Chevreau, H.; Devic, T.; Salles, F.; Maurin, G.; Stock, N.; Serre, C. Mixed-Linker Hybrid Superpolyhedra for the Production of a Series of Large-Pore Iron(III) Carboxylate Metal–Organic Frameworks. *Angew. Chem. Int. Ed.* **2013**, *52*, 5056–5060.

(170) Nguyen, H. L.; Vu, T. T.; Nguyen, D. K.; Trickett, C. A.; Doan, T. L. H.; Diercks, C. S.; Nguyen, V. Q.; Cordova, K. E. A Complex Metal-Organic Framework Catalyst for Microwave-Assisted Radical Polymerization. *Commun. Chem.* **2018**, *1*, 1–7.

(171) Deng, H.; Doonan, C. J.; Furukawa, H.; Ferreira, R. B.; Towne, J.; Knobler, C. B.; Wang, B.; Yaghi, O. M. Multiple Functional Groups of Varying Ratios in Metal-Organic Frameworks. *Science* **2010**, *327*, 846–850.

(172) Kong, X.; Deng, H.; Yan, F.; Kim, J.; Swisher, J. A.; Smit, B.; Yaghi, O. M.; Reimer, J. A. Mapping of Functional Groups in Metal-Organic Frameworks. *Science* **2013**, *341*, 882–885.

(173) Zhang, Y. B.; Furukawa, H.; Ko, N.; Nie, W.; Park, H. J.; Okajima, S.; Cordova, K. E.; Deng, H.; Kim, J.; Yaghi, O. M. Introduction of Functionality, Selection of Topology, and Enhancement of Gas Adsorption in Multivariate Metal-Organic Framework-177. *J. Am. Chem. Soc.* **2015**, *137*, 2641–2650.

(174) Baggio, R.; Garland, M. T.; Perec, M. Synthesis and X-Ray Crystal Determination of Four Novel Lanthanide (III) Oxydiacetate Complexes. *Inorg. Chim. Acta* **1998**, *281*, 18–24.

(175) Pardo, E.; Ruiz-García, R.; Lloret, F.; Faus, J.; Julve, M.; Journaux, Y.; Delgado, F.; Ruiz-Pérez, C. Cobalt(II)–Copper(II) Bimetallic Chains as a New Class of Single-Chain Magnets. *Adv. Mater.* **2004**, *16*, 1597–1600.

(176) Zeng, M. H.; Wang, B.; Wang, X. Y.; Zhang, W. X.; Chen, X. M.; Gao, S. Chiral Magnetic Metal-Organic Frameworks of Dimetal Subunits: Magnetism Tuning by Mixed-Metal Compositions of the Solid Solutions. *Inorg. Chem.* **2006**, *45*, 7069–7076.

(177) Serre, C.; Millange, F.; Thouvenot, C.; Gardant, N.; Pellé, F.; Férey, G. Synthesis, Characterisation and Luminescent Properties of a New Three-Dimensional Lanthanide Trimesate: $M((C_6H_3)–(CO_2)_3)$ (M = Y, Ln) or MIL-78. *J. Mater. Chem.* **2004**, *14*, 1540–1543.

(178) Wang, L. J.; Deng, H.; Furukawa, H.; Gándara, F.; Cordova, K. E.; Peri, D.; Yaghi, O. M. Synthesis and Characterization of Metal-Organic Framework-74 Containing 2, 4, 6, 8, and 10 Different Metals. *Inorg. Chem.* **2014**, *53*, 5881–5883.

(179) Ji, Z.; Li, T.; Yaghi, O. M. Sequencing of Metals in Multivariate Metal-Organic Frameworks. *Science* **2020**, *369*, 674–680.

(180) Feng, D.; Wang, K.; Wei, Z.; Chen, Y. P.; Simon, C. M.; Arvapally, R. K.; Martin, R. L.; Bosch, M.; Liu, T. F.; Fordham, S.; Yuan, D.; Omary, M. A.; Haranczyk, M.; Smit, B.; Zhou, H. C. Kinetically Tuned Dimensional Augmentation as a Versatile Synthetic Route towards Robust Metal–Organic Frameworks. *Nat. Commun.* **2014**, *5*, 1–9.

(181) López-García, C.; Canossa, S.; Hadermann, J.; Gorni, G.; Oropeza, F. E.; De La Peña O'Shea, V. A.; Iglesias, M.; Angeles Monge, M.; Gutiérrez-Puebla, E.; Gándara, F. Heterometallic Molecular Complexes Act as Messenger Building Units to Encode Desired Metal-Atom Combinations to Multivariate Metal-Organic Frameworks. *J. Am. Chem. Soc.* **2022**, *144*, 16262–16266.

(182) Yuan, S.; Qin, J. S.; Li, J.; Huang, L.; Feng, L.; Fang, Y.; Lollar, C.; Pang, J.; Zhang, L.; Sun, D.; Alsalme, A.; Cagin, T.; Zhou, H. C. Retrosynthesis of Multi-Component Metal–organic Frameworks. *Nat. Commun.* **2018**, *9*, 1–11.

(183) Batten, S. R.; Champness, N. R.; Chen, X. M.; Garcia-Martinez, J.; Kitagawa, S.; Öhrström, L.; O'Keeffe, M.; Suh, M. P.; Reedijk, J. Coordination Polymers, Metal–Organic Frameworks and the Need for Terminology Guidelines. *CrystEngComm* **2012**, *14*, 3001–3004.

(184) Batten, S. R.; Champness, N. R.; Chen, X. M.; Garcia-Martinez, J.; Kitagawa, S.; Öhrström, L.; O'Keeffe, M.; Suh, M. P.; Reedijk, J. Terminology of Metal-Organic Frameworks and Coordination Polymers (IUPAC Recommendations 2013). *Pure Appl. Chem.* **2013**, *85*, 1715–1724.

(185) Seth, S.; Matzger, A. J. Metal-Organic Frameworks: Examples, Counterexamples, and an Actionable Definition. *Cryst. Growth Des.* **2017**, *17*, 4043–4048.

(186) O'Keeffe, M.; Hyde, B. G. Crystal Structures – Patterns and Symmetry, Dover Publications Inc., New York, **1996**.

(187) Wells, A. F. Structural Inorganic Chemistry, Oxford University Press, Croydon, **1945**.

(188) Delgado-Friedrichs, O.; O'Keeffe, M. Crystal Nets as Graphs: Terminology and Definitions. *J. Solid State Chem.* **2005**, *178*, 2480–2485.

(189) O'Keeffe, M.; Eddaoudi, M.; Li, H.; Reineke, T.; Yaghi, O. M. Frameworks for Extended Solids: Geometrical Design Principles. *J. Solid State Chem.* **2000**, *152*, 3–20.

(190) Blatov, V. A.; O'Keeffe, M.; Proserpio, D. M. Vertex-, Face-, Point-, Schläfli-, and Delaney-Symbols in Nets, Polyhedra and Tilings: Recommended Terminology. *CrystEngComm* **2009**, *12*, 44–48.

(191) O'Keeffe, M.; Peskov, M. A.; Ramsden, S. J.; Yaghi, O. M. The Reticular Chemistry Structure Resource (RCSR) Database of, and Symbols for, Crystal Nets. *Acc. Chem. Res.* **2008**, *41*, 1782–1789.

(192) Delgado-Friedrichs, O.; O'Keeffe, M.; Yaghi, O. M. Taxonomy of Periodic Nets and the Design of Materials. *Phys. Chem. Chem. Phys.* **2007**, *9*, 1035–1043.

(193) Delgado Friedrichs, O.; O'Keeffe, M.; Yaghi, O. M. Three-Periodic Nets and Tilings: Regular and Quasiregular Nets. *Acta Cryst. A* **2003**, *59*, 22–27.

(194) Friedrichs, O. D.; O'Keeffe, M.; Yaghi, O. M. Three-Periodic Nets and Tilings: Semiregular Nets. *Acta Cryst. A* **2003**, *59*, 515–525.

(195) Ockwig, N. W.; Delgado-Friedrichs, O.; O'Keeffe, M.; Yaghi, O. M. Reticular Chemistry: Occurrence and Taxonomy of Nets and Grammar for the Design of Frameworks. *Acc. Chem. Res.* **2005**, *38*, 176–182.

(196) Delgado-Friedrichs, O.; O'Keeffe, M.; Yaghi, O. M. Three-Periodic Nets and Tilings: Edge-Transitive Binodal Structures. *Acta Cryst. A* **2006**, *62*, 350–355.

(197) Delgado-Friedrichs, O.; O'Keeffe, M. Three-Periodic Tilings and Nets: Face-Transitive Tilings and Edge-Transitive Nets Revisited. *Acta Cryst. A* **2007**, *63*, 344–347.

(198) Li, M.; O'Keeffe, M.; Proserpio, D. M.; Proserpio, D. M.; Zhang, H. F. A New Group of Edge-Transitive 3-Periodic Nets and Their Derived Nets for Reticular Chemistry. *Cryst. Growth Des.* **2020**, *20*, 4062–4068.

(199) Chen, Z.; Jiang, H.; O'Keeffe, M.; Eddaoudi, M. Minimal Edge-Transitive Nets for the Design and Construction of Metal–Organic Frameworks. *Faraday Discuss.* **2017**, *201*, 127–143.

(200) Chen, Z.; Jiang, H.; Li, M.; O'Keeffe, M.; Eddaoudi, M. Reticular Chemistry 3.2: Typical Minimal Edge-Transitive Derived and Related Nets for the Design and Synthesis of Metal-Organic Frameworks. *Chem. Rev.* **2020**, *120*, 8039–8065.

(201) Chen, Z.; Thiam, Z.; Shkurenko, A.; Weselinski, L. J.; Adil, K.; Jiang, H.; Alezi, D.; Assen, A. H.; O'Keeffe, M.; Eddaoudi, M. Enriching the Reticular Chemistry Repertoire with Minimal Edge-Transitive Related Nets: Access to Highly

Coordinated Metal-Organic Frameworks Based on Double Six-Membered Rings as Net-Coded Building Units. *J. Am. Chem. Soc.* **2019**, *141*, 20480–20489.

(202) Kalmutzki, M. J.; Hanikel, N.; Yaghi, O. M. Secondary Building Units as the Turning Point in the Development of the Reticular Chemistry of MOFs. *Sci. Adv.* **2018**, *4*, eaat9180.

(203) Jiang, H.; Alezi, D.; Eddaoudi, M. A Reticular Chemistry Guide for the Design of Periodic Solids. *Nat. Rev. Mat.* **2021**, *6*, 466–487.

(204) O'Keeffe, M.; Yaghi, O. M. Deconstructing the Crystal Structures of Metal-Organic Frameworks and Related Materials into Their Underlying Nets. *Chem. Rev.* **2012**, 112, 675–702.

(205) Li, M.; Li, D.; O'Keeffe, M.; Yaghi, O. M. Topological Analysis of Metal-Organic Frameworks with Polytopic Linkers and/or Multiple Building Units and the Minimal Transitivity Principle. *Chem. Rev.* **2014**, *114*, 1343–1370.

(206) Eubank, J. F.; Walsh, R. D.; Poddar, P.; Srikanth, H.; Larsen, R. W.; Eddaoudi, M. Metal-Organic Framework Diversity via Heterocoordination of a Multifunctional Ligand: $SrAl_2$ and a Novel (3,4)-Connected Network. Cryst. Growth Des. **2006**, *6*, 1453-1457.

(207) Bonneau, C.; O'Keeffe, M.; Proserpio, D. M.; Blatov, V. A.; Batten, S. R.; Bourne, S. A.; Lah, M. S.; Eon, J. G.; Hyde, S. T.; Wiggin, S. B.; Öhrström, L. Deconstruction of Crystalline Networks into Underlying Nets: Relevance for Terminology Guidelines and Crystallographic Databases. *Cryst. Growth Des.* **2018**, *18*, 3411–3418.

(208) Blatov, V. A. Topological Relations between Three-Dimensional Periodic Nets. I. Uninodal Nets. *Acta Cryst. A* **2007**, *63*, 329–343.

(209) Blatov, V. A.; Proserpio, D. M. Topological Relations between Three-Periodic Nets. II. Binodal Nets. *Acta Cryst. A* **2009**, *65*, 202–212.

(210) Cairns, A. J.; Perman, J. A.; Wojtas, L.; Kravtsov, V. C.; Alkordi, M. H.; Eddaoudi, M.; Zaworotko, M. J. Supermolecular Building Blocks (SBBs) and Crystal Design: 12-Connected Open Frameworks Based on a Molecular Cubohemioctahedron. *J. Am. Chem. Soc.* **2008**, *130*, 1560–1561.

(211) Nouar, F.; Eubank, J. F.; Bousquet, T.; Wojtas, L.; Zaworotko, M. J.; Eddaoudi, M. Supermolecular Building Blocks (SBBs) for the Design and Synthesis of Highly Porous Metal-Organic Frameworks. *J. Am. Chem. Soc.* **2008**, *130*, 1833–1835.

(212) Eubank, J. F.; Mouttaki, H.; Cairns, A. J.; Belmabkhout, Y.; Wojtas, L.; Luebke, R.; Alkordi, M.; Eddaoudi, M. The Quest for Modular Nanocages: tbo-MOF as an Archetype for Mutual Substitution, Functionalization, and Expansion of Quadrangular Pillar Building Blocks. *J. Am. Chem. Soc.* **2011**, *133*, 14204–14207.

(213) Eubank, J. F.; Wojtas, L.; Hight, M. R.; Bousquet, T.; Kravtsov, V. C.; Eddaoudi, M. The next Chapter in MOF Pillaring Strategies: Trigonal Heterofunctional Ligands to Access Targeted High-Connected Three Dimensional Nets, Isoreticular Platforms. *J. Am. Chem. Soc.* **2011**, *133*, 17532–17535.

(214) Ma, B. Q.; Mulfort, K. L.; Hupp, J. T. Microporous Pillared Paddle-Wheel Frameworks Based on Mixed-Ligand Coordination of Zinc Ions. *Inorg. Chem.* **2005**, *44*, 4912–4914.

(215) Chen, B.; Ockwig, N. W.; Millward, A. R.; Contreras, D. S.; Yaghi, O. M.; Chen, B.; Contreras, D. S.; Ockwig, N. W.; Millward, A. R.; Yaghi, O. M. High H_2 Adsorption in a Microporous Metal–Organic Framework with Open Metal Sites. *Angew. Chem. Int. Ed.* **2005**, *44*, 4745–4749.

(216) Lin, X.; Jia, J.; Zhao, X.; Thomas, K. M.; Blake, A. J.; Walker, G. S.; Champness, N. R.; Hubberstey, P.; Schröder, M. High H_2 Adsorption by Coordination-Framework Materials. *Angew. Chem. Int. Ed.* **2006**, *45*, 7358–7364.

(217) Forgan, R. S. Modulated Self-Assembly of Metal–Organic Frameworks. *Chem. Sci.* **2020**, *11*, 4546–4562.

(218) Jiang, D.; Huang, C.; Zhu, J.; Wang, P.; Liu, Z.; Fang, D. Classification and Role of Modulators on Crystal Engineering of Metal Organic Frameworks (MOFs). *Coord. Chem. Rev.* **2021**, *444*, 214064.

(219) Hermes, S.; Witte, T.; Hikov, T.; Zacher, D.; Bahnmüller, S.; Langstein, G.; Huber, K.; Fischer, R. A. Trapping Metal-Organic Framework Nanocrystals: An in-Situ Time-Resolved Light Scattering Study on the Crystal Growth of MOF-5 in Solution. *J. Am. Chem. Soc.* **2007**, *129*, 5324–5325.

(220) Tsuruoka, T.; Furukawa, S.; Takashima, Y.; Yoshida, K.; Isoda, S.; Kitagawa, S. Nanoporous Nanorods Fabricated by Coordination Modulation and Oriented Attachment Growth. *Angew. Chem. Int. Ed.* **2009**, *48*, 4739–4743.

(221) Schaate, A.; Roy, P.; Godt, A.; Lippke, J.; Waltz, F.; Wiebcke, M.; Behrens, P. Modulated Synthesis of Zr-Based Metal–Organic Frameworks: From Nano to Single Crystals. *Chem. Eur. J.* **2011**, *17*, 6643–6651.

(222) Wu, H.; Chua, Y. S.; Krungleviciute, V.; Tyagi, M.; Chen, P.; Yildirim, T.; Zhou, W. Unusual and Highly Tunable Missing-Linker Defects in Zirconium Metal-Organic Framework UiO-66 and Their Important Effects on Gas Adsorption. *J. Am. Chem. Soc.* **2013**, *135*, 10525–10532.

(223) Øien, S.; Wragg, D.; Reinsch, H.; Svelle, S.; Bordiga, S.; Lamberti, C.; Lillerud, K. P. Detailed Structure Analysis of Atomic Positions and Defects in Zirconium Metal-Organic Frameworks. *Cryst. Growth Des.* **2014**, *14*, 5370–5372.

(224) Cliffe, M. J.; Wan, W.; Zou, X.; Chater, P. A.; Kleppe, A. K.; Tucker, M. G.; Wilhelm, H.; Funnell, N. P.; Coudert, F. X.; Goodwin, A. L. Correlated Defect Nanoregions in a Metal–Organic Framework. *Nat. Commun.* **2014**, *5*, 1–8.

(225) Trickett, C. A.; Gagnon, K. J.; Lee, S.; Gándara, F.; Bürgi, H. B.; Yaghi, O. M. Definitive Molecular Level Characterization of Defects in UiO-66 Crystals. *Angew. Chem. Int. Ed.* **2015**, *54*, 11162–11167.

(226) Bon, V.; Senkovska, I.; Weiss, M. S.; Kaskel, S. Tailoring of Network Dimensionality and Porosity Adjustment in Zr- and Hf-Based MOFs. *CrystEngComm* **2013**, *15*, 9572–9577.

(227) Vizuet, J. P.; Mortensen, M. L.; Lewis, A. L.; Wunch, M. A.; Firouzi, H. R.; McCandless, G. T.; Balkus, K. J. Fluoro-Bridged Clusters in Rare-Earth Metal-Organic Frameworks. *J. Am. Chem. Soc.* **2021**, *143*, 17995–18000.

(228) Bicalho, H. A.; Saraci, F.; Velazquez-Garcia, J. de J.; Titi, H. M.; Howarth, A. J. Unravelling the Synthesis of a Rare-Earth Cluster-Based Metal–Organic Framework with spn Topology. *Chem. Commun.* **2022**, *58*, 10925–10928.

(229) Guillerm, V.; Kim, D.; Eubank, J. F.; Luebke, R.; Liu, X.; Adil, K.; Lah, M. S.; Eddaoudi, M. A Supermolecular Building Approach for the Design and Construction of Metal-Organic Frameworks. *Chem. Soc. Rev.* **2014**, *43*, 6141–6172.

(230) Perry VI, J. J.; Perman, J. A.; Zaworotko, M. J. Design and Synthesis of Metal-Organic Frameworks Using Metal-Organic Polyhedra as Supermolecular Building Blocks. *Chem. Soc. Rev.* **2009**, *38*, 1400–1417.

(231) Chun, H.; Dybtsev, D. N.; Kim, H.; Kim, K. Synthesis, X-Ray Crystal Structures, and Gas Sorption Properties of Pillared Square Grid Nets Based on Paddle-Wheel Motifs: Implications for Hydrogen Storage in Porous Materials. *Chem. Eur. J.* **2005**, *11*, 3521–3529.

(232) Jiang, H.; Jia, J.; Shkurenko, A.; Chen, Z.; Adil, K.; Belmabkhout, Y.; Weselinski, L. J.; Assen, A. H.; Xue, D. X.; O'Keeffe, M.; Eddaoudi, M. Enriching the Reticular Chemistry Repertoire: Merged Nets Approach for the Rational Design of Intricate Mixed-Linker Metal-Organic Framework Platforms. *J Am Chem Soc* **2018**, *140* (28), 8858–8867.

(233) Alezi, D.; Peedikakkal, A. M. P.; Weseliński, Ł. J.; Guillerm, V.; Belmabkhout, Y.; Cairns, A. J.; Chen, Z.; Wojtas, Ł.; Eddaoudi, M. Quest for Highly Connected

Metal-Organic Framework Platforms: Rare-Earth Polynuclear Clusters Versatility Meets Net Topology Needs. *J. Am. Chem. Soc.* **2015**, *137*, 5421–5430.

(234) Chen, Z.; Weseliński, Ł. J.; Adil, K.; Belmabkhout, Y.; Shkurenko, A.; Jiang, H.; Bhatt, P. M.; Guillerm, V.; Dauzon, E.; Xue, D. X.; O'Keeffe, M.; Eddaoudi, M. Applying the Power of Reticular Chemistry to Finding the Missing alb-MOF Platform Based on the (6,12)-Coordinated Edge-Transitive Net. *J. Am. Chem. Soc.* **2017**, *139*, 3265–3274.

(235) Cohen, S. M. Postsynthetic Methods for the Functionalization of Metal-Organic Frameworks. *Chem. Rev.* **2012**, *112*, 970–1000.

(236) Wang, Z.; Cohen, S. M. Postsynthetic Modification of Metal–Organic Frameworks. *Chem. Soc. Rev.* **2009**, *38*, 1315–1329.

(237) Tanabe, K. K.; Cohen, S. M. Postsynthetic Modification of Metal–Organic Frameworks—a Progress Report. *Chem. Soc. Rev.* **2011**, *40*, 498–519.

(238) Kalaj, M.; Cohen, S. M. Postsynthetic Modification: An Enabling Technology for the Advancement of Metal-Organic Frameworks. *ACS Cent. Sci.* **2020**, *6*, 1046–1057.

(239) Cohen, S. M. The Postsynthetic Renaissance in Porous Solids. *J. Am. Chem. Soc.* **2017**, *139*, 2855–2863.

(240) Kiang, Y. H.; Gardner, G. B.; Lee, S.; Xu, Z. Porous Siloxane Linked Phenylacetylene Nitrile Silver Salts from Solid State Dimerization and Low Polymerization. *J. Am. Chem. Soc.* **2000**, *122*, 6871–6883.

(241) Kiang, Y. H.; Gardner, G. B.; Lee, S.; Xu, Z.; Lobkovsky, E. B. Variable Pore Size, Variable Chemical Functionality, and an Example of Reactivity within Porous Phenylacetylene Silver Salts. *J. Am. Chem. Soc.* **1999**, *121*, 8204–8215.

(242) Seo, J. S.; Whang, D.; Lee, H.; Jun, S. I.; Oh, J.; Jeon, Y. J.; Kim, K. A Homochiral Metal–Organic Porous Material for Enantioselective Separation and Catalysis. *Nature* **2000**, *404*, 982–986.

(243) Wang, Z.; Cohen, S. M. Postsynthetic Covalent Modification of a Neutral Metal-Organic Framework. *J. Am. Chem. Soc.* **2007**, *129*, 12368–12369.

(244) Waller, P. J.; Lyle, S. J.; Osborn Popp, T. M.; Diercks, C. S.; Reimer, J. A.; Yaghi, O. M. Chemical Conversion of Linkages in Covalent Organic Frameworks. *J. Am. Chem. Soc.* **2016**, *138*, 15519–15522.

(245) Waller, P. J.; Alfaraj, Y. S.; Diercks, C. S.; Jarenwattananon, N. N.; Yaghi, O. M. Conversion of Imine to Oxazole and Thiazole Linkages in Covalent Organic Frameworks. *J. Am. Chem. Soc.* **2018**, *140*, 9099–9103.

(246) Haase, F.; Troschke, E.; Savasci, G.; Banerjee, T.; Duppel, V.; Dörfler, S.; Grundei, M. M. J.; Burow, A. M.; Ochsenfeld, C.; Kaskel, S.; Lotsch, B. V. Topochemical Conversion of an Imine- into a Thiazole-Linked Covalent Organic Framework Enabling Real Structure Analysis. *Nat. Commun.* **2018**, *9*, 1–10.

(247) Liu, H.; Chu, J.; Yin, Z.; Cai, X.; Zhuang, L.; Deng, H. Covalent Organic Frameworks Linked by Amine Bonding for Concerted Electrochemical Reduction of CO_2. *Chem* **2018**, *4*, 1696–1709.

(248) Li, X.; Zhang, C.; Cai, S.; Lei, X.; Altoe, V.; Hong, F.; Urban, J. J.; Ciston, J.; Chan, E. M.; Liu, Y. Facile Transformation of Imine Covalent Organic Frameworks into Ultrastable Crystalline Porous Aromatic Frameworks. *Nat. Commun.* **2018**, *9*, 1–8.

(249) Fracaroli, A. M.; Siman, P.; Nagib, D. A.; Suzuki, M.; Furukawa, H.; Toste, F. D.; Yaghi, O. M. Seven Post-Synthetic Covalent Reactions in Tandem Leading to Enzyme-like Complexity within Metal-Organic Framework Crystals. *J. Am. Chem. Soc.* **2016**, *138*, 8352–8355.

(250) Kim, M.; Cahill, J. F.; Su, Y.; Prather, K. A.; Cohen, S. M. Postsynthetic Ligand Exchange as a Route to Functionalization of 'Inert' Metal–Organic Frameworks. *Chem. Sci.* **2011**, *3*, 126–130.

(251) Karagiaridi, O.; Bury, W.; Sarjeant, A. A.; Stern, C. L.; Farha, O. K.; Hupp, J. T. Synthesis and Characterization of Isostructural Cadmium Zeolitic Imidazolate Frameworks via Solvent-Assisted Linker Exchange. *Chem. Sci.* **2012**, *3*, 3256–3260.

(252) Karagiaridi, O.; Bury, W.; Tylianakis, E.; Sarjeant, A. A.; Hupp, J. T.; Farha, O. K. Opening Metal-Organic Frameworks Vol. 2: Inserting Longer Pillars into Pillared-Paddlewheel Structures through Solvent-Assisted Linker Exchange. *Chem. Mater.* **2013**, *25*, 3499–3503.

(253) Karagiaridi, O.; Lalonde, M. B.; Bury, W.; Sarjeant, A. A.; Farha, O. K.; Hupp, J. T. Opening ZIF-8: A Catalytically Active Zeolitic Imidazolate Framework of Sodalite Topology with Unsubstituted Linkers. *J. Am. Chem. Soc.* **2012**, *134*, 18790–18796.

(254) Burnett, B. J.; Barron, P. M.; Hu, C.; Choe, W. Stepwise Synthesis of Metal - Organic Frameworks: Replacement of Structural Organic Linkers. *J. Am. Chem. Soc.* **2011**, *133*, 9984–9987.

(255) Li, T.; Kozlowski, M. T.; Doud, E. A.; Blakely, M. N.; Rosi, N. L. Stepwise Ligand Exchange for the Preparation of a Family of Mesoporous MOFs. *J. Am. Chem. Soc.* **2013**, *135*, 11688–11691.

(256) Deria, P.; Mondloch, J. E.; Karagiaridi, O.; Bury, W.; Hupp, J. T.; Farha, O. K. Beyond Post-Synthesis Modification: Evolution of Metal–Organic Frameworks via Building Block Replacement. *Chem. Soc. Rev.* **2014**, *43*, 5896–5912.

(257) Yuan, S.; Zou, L.; Qin, J. S.; Li, J.; Huang, L.; Feng, L.; Wang, X.; Bosch, M.; Alsalme, A.; Cagin, T.; Zhou, H. C. Construction of Hierarchically Porous Metal–Organic Frameworks through Linker Labilization. *Nat. Commun.* **2017**, *8*, 1–10.

(258) Tu, B.; Pang, Q.; Wu, D.; Song, Y.; Weng, L.; Li, Q. Ordered Vacancies and Their Chemistry in Metal-Organic Frameworks. *J. Am. Chem. Soc.* **2014**, *136*, 14465–14471.

(259) Yuan, S.; Lu, W.; Chen, Y. P.; Zhang, Q.; Liu, T. F.; Feng, D.; Wang, X.; Qin, J.; Zhou, H. C. Sequential Linker Installation: Precise Placement of Functional Groups in Multivariate Metal-Organic Frameworks. *J. Am. Chem. Soc.* **2015**, *137*, 3177–3180.

(260) Yuan, S.; Chen, Y. P.; Qin, J. S.; Lu, W.; Zou, L.; Zhang, Q.; Wang, X.; Sun, X.; Zhou, H. C. Linker Installation: Engineering Pore Environment with Precisely Placed Functionalities in Zirconium MOFs. *J. Am. Chem. Soc.* **2016**, *138*, 8912–8919.

(261) Kim, H.; Kim, D.; Moon, D.; Choi, Y. N.; Baek, S. Bin; Lah, M. S. Symmetry-Guided Syntheses of Mixed-Linker Zr Metal–Organic Frameworks with Precise Linker Locations. *Chem. Sci.* **2019**, *10*, 5801–5806.

(262) Chen, C. X.; Wei, Z. W.; Jiang, J. J.; Zheng, S. P.; Wang, H. P.; Qiu, Q. F.; Cao, C. C.; Fenske, D.; Su, C. Y. Dynamic Spacer Installation for Multirole Metal-Organic Frameworks: A New Direction toward Multifunctional MOFs Achieving Ultrahigh Methane Storage Working Capacity. *J. Am. Chem. Soc.* **2017**, *139*, 6034–6037.

(263) Zhang, X.; Frey, B. L.; Chen, Y. S.; Zhang, J. Topology-Guided Stepwise Insertion of Three Secondary Linkers in Zirconium Metal-Organic Frameworks. *J. Am. Chem. Soc.* **2018**, *140*, 7710–7715.

(264) Hu, Y.; Zhang, X.; Shu, R.; Khoo, H.; Fiankor, C.; Zhang, X.; Zhang, J. Stepwise Assembly of Quinary Multivariate Metal–Organic Frameworks via Diversified Linker Exchange and Installation. *J. Am. Chem. Soc.* **2023**, *145*, 13929–13937.

(265) Pang, J.; Yuan, S.; Qin, J.; Wu, M.; Lollar, C. T.; Li, J.; Huang, N.; Li, B.; Zhang, P.; Zhou, H. C. Enhancing Pore-Environment Complexity Using a Trapezoidal

Linker: Toward Stepwise Assembly of Multivariate Quinary Metal-Organic Frameworks. *J. Am. Chem. Soc.* **2018**, *140*, 12328–12332.

(266) Deria, P.; Bury, W.; Hod, I.; Kung, C. W.; Karagiaridi, O.; Hupp, J. T.; Farha, O. K. MOF Functionalization via Solvent-Assisted Ligand Incorporation: Phosphonates vs Carboxylates. *Inorg. Chem.* **2015**, *54*, 2185–2192.

(267) Zhai, Q. G.; Bu, X.; Mao, C.; Zhao, X.; Daemen, L.; Cheng, Y.; Ramirez-Cuesta, A. J.; Feng, P. An Ultra-Tunable Platform for Molecular Engineering of High-Performance Crystalline Porous Materials. *Nat. Commun.* **2016**, *7*, 1–9.

(268) Wei, Y. S.; Zhang, M.; Liao, P. Q.; Lin, R. B.; Li, T. Y.; Shao, G.; Zhang, J. P.; Chen, X. M. Coordination Templated [2+2+2] Cyclotrimerization in a Porous Coordination Framework. *Nat. Commun.* **2015**, *6* , 1–7.

(269) Feng, L.; Wang, K. Y.; Day, G. S.; Ryder, M. R.; Zhou, H. C. Destruction of Metal-Organic Frameworks: Positive and Negative Aspects of Stability and Lability. *Chem. Rev.* **2020**, *120*, 13087–13133.

(270) Yuan, S.; Zhang, P.; Zhang, L.; Garcia-Esparza, A. T.; Sokaras, D.; Qin, J. S.; Feng, L.; Day, G. S.; Chen, W.; Drake, H. F.; Elumalai, P.; Madrahimov, S. T.; Sun, D.; Zhou, H. C. Exposed Equatorial Positions of Metal Centers via Sequential Ligand Elimination and Installation in MOFs. *J. Am. Chem. Soc.* **2018**, *140*, 10814–10819.

(271) Feng, L.; Yuan, S.; Zhang, L. L.; Tan, K.; Li, J. L.; Kirchon, A.; Liu, L. M.; Zhang, P.; Han, Y.; Chabal, Y. J.; Zhou, H. C. Creating Hierarchical Pores by Controlled Linker Thermolysis in Multivariate Metal-Organic Frameworks. *J. Am. Chem. Soc.* **2018**, *140*, 2363–2372.

(272) Geary, J.; Wong, A. H.; Xiao, D. J. Thermolabile Cross-Linkers for Templating Precise Multicomponent Metal-Organic Framework Pores. *J. Am. Chem. Soc.* **2021**, *143*, 10317–10323.

(273) Albalad, J.; Xu, H.; Gándara, F.; Haouas, M.; Martineau-Corcos, C.; Mas-Ballesté, R.; Barnett, S. A.; Juanhuix, J.; Imaz, I.; Maspoch, D. Single-Crystal-to-Single-Crystal Postsynthetic Modification of a Metal–Organic Framework via Ozonolysis. *J. Am. Chem. Soc.* **2018**, *140*, 2028–2031.

(274) Guillerm, V.; Xu, H.; Albalad, J.; Imaz, I.; Maspoch, D. Postsynthetic Selective Ligand Cleavage by Solid–Gas Phase Ozonolysis Fuses Micropores into Mesopores in Metal–Organic Frameworks. *J. Am. Chem. Soc.* **2018**, *140*, 15022–15030.

(275) Ding, Y.; Chen, Y. P.; Zhang, X.; Chen, L.; Dong, Z.; Jiang, H. L.; Xu, H.; Zhou, H. C. Controlled Intercalation and Chemical Exfoliation of Layered Metal-Organic Frameworks Using a Chemically Labile Intercalating Agent. *J. Am. Chem. Soc.* **2017**, *139*, 9136–9139.

(276) Brozek, C. K.; Dincă, M. Cation Exchange at the Secondary Building Units of Metal–Organic Frameworks. *Chem. Soc. Rev.* **2014**, *43*, 5456–5467.

(277) Dincă, M.; Long, J. R. High-Enthalpy Hydrogen Adsorption in Cation-Exchanged Variants of the Microporous Metal-Organic Framework $Mn_3[(Mn_4Cl)_3(BTT)_8(CH_3OH)_{10}]_2$. *J. Am. Chem. Soc.* **2007**, *129*, 11172–11176.

(278) Brozek, C. K.; Dinca, M. Lattice-Imposed Geometry in Metal–Organic Frameworks: Lacunary Zn_4O Clusters in MOF-5 Serve as Tripodal Chelating Ligands for Ni^{2+}. *Chem. Sci.* **2012**, *3*, 2110–2113.

(279) Brozek, C. K.; Dincă, M. Ti^{3+}-, $V^{2+/3+}$-, $Cr^{2+/3+}$-, Mn^{2+}-, and Fe^{2+}-Substituted MOF-5 and Redox Reactivity in Cr- and Fe-MOF-5. *J. Am. Chem. Soc.* **2013**, *135*, 12886–12891.

(280) Kim, M.; Cahill, J. F.; Fei, H.; Prather, K. A.; Cohen, S. M. Postsynthetic Ligand and Cation Exchange in Robust Metal-Organic Frameworks. *J. Am. Chem. Soc.* **2012**, *134*, 18082–18088.

(281) Fei, H.; Cahill, J. F.; Prather, K. A.; Cohen, S. M. Tandem Postsynthetic Metal Ion and Ligand Exchange in Zeolitic Imidazolate Frameworks. *Inorg. Chem.* **2013**, *52*, 4011–4016.

(282) Wu, C. De; Hu, A.; Zhang, L.; Lin, W. A Homochiral Porous Metal-Organic Framework for Highly Enantioselective Heterogeneous Asymmetric Catalysis. *J. Am. Chem. Soc.* **2005**, *127*, 8940–8941.

(283) Bloch, E. D.; Britt, D.; Lee, C.; Doonan, C. J.; Uribe-Romo, F. J.; Furukawa, H.; Long, J. R.; Yaghi, O. M. Metal Insertion in a Microporous Metal-Organic Framework Lined with 2,2′-Bipyridine. *J. Am. Chem. Soc.* **2010**, *132*, 14382–14384.

(284) Tamuly, P.; Sama, F.; Moorthy, J. N. Metal–Organic Nanosheets (MONs): Exfoliation by Mechanical Grinding and Iodine Capture. *Adv. Mater. Interfaces* **2022**, *9*, 2200337.

(285) Avci, C.; Ariñez-Soriano, J.; Carné-Sánchez, A.; Guillerm, V.; Carbonell, C.; Imaz, I.; Maspoch, D. Post-Synthetic Anisotropic Wet-Chemical Etching of Colloidal Sodalite ZIF Crystals. *Angew. Chem. Int. Ed.* **2015**, *54*, 14417–14421.

(286) Ishiwata, T.; Furukawa, Y.; Sugikawa, K.; Kokado, K.; Sada, K. Transformation of Metal-Organic Framework to Polymer Gel by Cross-Linking the Organic Ligands Preorganized in Metal-Organic Framework. *J. Am. Chem. Soc.* **2013**, *135*, 5427–5432.

(287) McDonald, K. A.; Feldblyum, J. I.; Koh, K.; Wong-Foy, A. G.; Matzger, A. J. Polymer@MOF@MOF: "Grafting from" Atom Transfer Radical Polymerization for the Synthesis of Hybrid Porous Solids. *Chem. Commun.* **2015**, *51*, 11994–11996.

(288) Zhang, Y.; Feng, X.; Li, H.; Chen, Y.; Zhao, J.; Wang, S.; Wang, L.; Wang, B. Photoinduced Postsynthetic Polymerization of a Metal–Organic Framework toward a Flexible Stand-Alone Membrane. *Angew. Chem. Int. Ed.* **2015**, *54*, 4259–4263.

(289) Furukawa, H.; Cordova, K. E.; O'Keeffe, M.; Yaghi, O. M. The Chemistry and Applications of Metal-Organic Frameworks. *Science* **2013**, *341*, 1230444.

(290) Rowsell, J. L. C.; Spencer, E. C.; Eckert, J.; Howard, J. A. K.; Yaghi, O. M. Chemistry: Gas Adsorption Sites in a Large-Pore Metal-Organic Framework. *Science* **2005**, *309*, 1350–1354.

(291) Farha, O. K.; Eryazici, I.; Jeong, N. C.; Hauser, B. G.; Wilmer, C. E.; Sarjeant, A. A.; Snurr, R. Q.; Nguyen, S. T.; Yazaydin, A. Ö.; Hupp, J. T. Metal-Organic Framework Materials with Ultrahigh Surface Areas: Is the Sky the Limit? *J. Am. Chem. Soc.* **2012**, *134*, 15016–15021.

(292) Hönicke, I. M.; Senkovska, I.; Bon, V.; Baburin, I. A.; Bönisch, N.; Raschke, S.; Evans, J. D.; Kaskel, S. Balancing Mechanical Stability and Ultrahigh Porosity in Crystalline Framework Materials. *Angew. Chem. Int. Ed.* **2018**, *57*, 13780–13783.

(293) Wong-Foy, A. G.; Matzger, A. J.; Yaghi, O. M. Exceptional H_2 Saturation Uptake in Microporous Metal-Organic Frameworks. *J. Am. Chem. Soc.* **2006**, *128*, 3494–3495.

(294) Kaye, S. S.; Dailly, A.; Yaghi, O. M.; Long, J. R. Impact of Preparation and Handling on the Hydrogen Storage Properties of Zn_4O(1,4-Benzenedicarboxylate)$_3$ (MOF-5). *J. Am. Chem. Soc.* **2007**, *129*, 14176–14177.

(295) Rowsell, J. L. C.; Yaghi, O. M. Effects of Functionalization, Catenation, and Variation of the Metal Oxide and Organic Linking Units on the Low-Pressure Hydrogen Adsorption Properties of Metal-Organic Frameworks. *J. Am. Chem. Soc.* **2006**, *128*, 1304–1315.

(296) Chen, Z.; Li, P.; Anderson, R.; Wang, X.; Zhang, X.; Robison, L.; Redfern, L. R.; Moribe, S.; Islamoglu, T.; Gómez-Gualdrón, D. A.; Yildirim, T.; Stoddart, J. F.; Farha, O. K. Balancing Volumetric and Gravimetric Uptake in Highly Porous Materials for Clean Energy. *Science* **2020**, *368*, 297–303.

(297) Millward, A. R.; Yaghi, O. M. Metal-Organic Frameworks with Exceptionally High Capacity for Storage of Carbon Dioxide at Room Temperature. *J. Am. Chem. Soc.* **2005**, *127*, 17998–17999.

(298) Snyder, B. E. R.; Turkiewicz, A. B.; Furukawa, H.; Paley, M. V.; Velasquez, E. O.; Dods, M. N.; Long, J. R. A Ligand Insertion Mechanism for Cooperative NH_3 Capture in Metal–Organic Frameworks. *Nature* **2023**, *613*, 287–291.

(299) Doonan, C. J.; Tranchemontagne, D. J.; Glover, T. G.; Hunt, J. R.; Yaghi, O. M. Exceptional Ammonia Uptake by a Covalent Organic Framework. *Nat. Chem.* **2010**, *2*, 235–238.

(300) Lin, J. Bin; Nguyen, T. T. T.; Vaidhyanathan, R.; Burner, J.; Taylor, J. M.; Durekova, H.; Akhtar, F.; Mah, R. K.; Ghaffari-Nik, O.; Marx, S.; Fylstra, N.; Iremonger, S. S.; Dawson, K. W.; Sarkar, P.; Hovington, P.; Rajendran, A.; Woo, T. K.; Shimizu, G. K. H. A Scalable Metal-Organic Framework as a Durable Physisorbent for Carbon Dioxide Capture. *Science* **2021**, *374*, 1464–1469.

(301) Kim, H.; Yang, S.; Rao, S. R.; Narayanan, S.; Kapustin, E. A.; Furukawa, H.; Umans, A. S.; Yaghi, O. M.; Wang, E. N. Water Harvesting from Air with Metal-Organic Frameworks Powered by Natural Sunlight. *Science* **2017**, *356*, 430–434.

(302) Towsif Abtab, S. M.; Alezi, D.; Bhatt, P. M.; Shkurenko, A.; Belmabkhout, Y.; Aggarwal, H.; Weseliński, Ł. J.; Alsadun, N.; Samin, U.; Hedhili, M. N.; Eddaoudi, M. Reticular Chemistry in Action: A Hydrolytically Stable MOF Capturing Twice Its Weight in Adsorbed Water. *Chem* **2018**, *4*, 94–105.

(303) Britt, D.; Furukawa, H.; Wang, B.; Glover, T. G.; Yaghi, O. M. Highly Efficient Separation of Carbon Dioxide by a Metal-Organic Framework Replete with Open Metal Sites. *Proc. Natl. Acad. Sci. U. S. A.* **2009**, *106*, 20637–20640.

(304) McDonald, T. M.; Lee, W. R.; Mason, J. A.; Wiers, B. M.; Hong, C. S.; Long, J. R. Capture of Carbon Dioxide from Air and Flue Gas in the Alkylamine-

Appended Metal-Organic Framework Mmen-Mg_2(Dobpdc). *J. Am. Chem. Soc.* **2012**, *134*, 7056–7065.

(305) Fracaroli, A. M.; Furukawa, H.; Suzuki, M.; Dodd, M.; Okajima, S.; Gándara, F.; Reimer, J. A.; Yaghi, O. M. Metal-Organic Frameworks with Precisely Designed Interior for Carbon Dioxide Capture in the Presence of Water. *J. Am. Chem. Soc.* **2014**, *136*, 8863–8866.

(306) Chen, B.; Liang, C.; Yang, J.; Contreras, D. S.; Clancy, Y. L.; Lobkovsky, E. B.; Yaghi, O. M.; Dai, S. A Microporous Metal–Organic Framework for Gas-Chromatographic Separation of Alkanes. *Angew. Chem. Int. Ed.* **2006**, *45*, 1390–1393.

(307) Cadiau, A.; Adil, K.; Bhatt, P. M.; Belmabkhout, Y.; Eddaoudi, M. A Metal-Organic Framework-Based Splitter for Separating Propylene from Propane. *Science* **2016**, *353*, 137–140.

(308) Muhammad, R.; Jee, S.; Jung, M.; Park, J.; Kang, S. G.; Choi, K. M.; Oh, H. Exploiting the Specific Isotope-Selective Adsorption of Metal-Organic Framework for Hydrogen Isotope Separation. *J. Am. Chem. Soc.* **2021**, *143*, 8232–8236.

(309) Su, Y.; Otake, K. ichi; Zheng, J. J.; Horike, S.; Kitagawa, S.; Gu, C. Separating Water Isotopologues Using Diffusion-Regulatory Porous Materials. *Nature* **2022**, *611*, 289–294.

(310) Jiang, H.; Yang, K.; Zhao, X.; Zhang, W.; Liu, Y.; Jiang, J.; Cui, Y. Highly Stable Zr(IV)-Based Metal-Organic Frameworks for Chiral Separation in Reversed-Phase Liquid Chromatography. *J. Am. Chem. Soc.* **2021**, *143*, 390–398.

(311) Bondorf, L.; Fiorio, J. L.; Bon, V.; Zhang, L.; Maliuta, M.; Ehrling, S.; Senkovska, I.; Evans, J. D.; Joswig, J. O.; Kaskel, S.; Heine, T.; Hirscher, M. Isotope-Selective Pore Opening in a Flexible Metal-Organic Framework. *Sci. Adv.* **2022**, *8*, 7035.

(312) Liu, Y.; Liu, G.; Zhang, C.; Qiu, W.; Yi, S.; Chernikova, V.; Chen, Z.; Belmabkhout, Y.; Shekhah, O.; Eddaoudi, M.; Koros, W.; Liu, Y.; Liu, G.; Zhang, C.; Qiu, W.; Yi, S.; Koros, W.; Chernikova, V.; Chen, Z.; Belmabkhout, Y.; Shekhah, O.; Eddaoudi, M. Enhanced CO_2/CH_4 Separation Performance of a Mixed Matrix Membrane Based on Tailored MOF-Polymer Formulations. *Adv. Sci.* **2018**, *5*, 1800982.

(313) Datta, S. J.; Mayoral, A.; Srivatsa Bettahalli, N. M.; Bhatt, P. M.; Karunakaran, M.; Carja, I. D.; Fan, D.; Mileo, P. G. M.; Semino, R.; Maurin, G.; Terasaki, O.; Eddaoudi, M. Rational Design of Mixed-Matrix Metal-Organic Framework Membranes for Molecular Separations. *Science* **2022**, *376*, 1080–1087.

(314) Zhou, S.; Shekhah, O.; Ramírez, A.; Lyu, P.; Abou-Hamad, E.; Jia, J.; Li, J.; Bhatt, P. M.; Huang, Z.; Jiang, H.; Jin, T.; Maurin, G.; Gascon, J.; Eddaoudi, M. Asymmetric Pore Windows in MOF Membranes for Natural Gas Valorization. *Nature* **2022**, *606*, 706–712.

(315) Nam, D. H.; De Luna, P.; Rosas-Hernández, A.; Thevenon, A.; Li, F.; Agapie, T.; Peters, J. C.; Shekhah, O.; Eddaoudi, M.; Sargent, E. H. Molecular Enhancement of Heterogeneous CO_2 Reduction. *Nat. Mater.* **2020**, *19*, 266–276.

(316) Lin, S.; Diercks, C. S.; Zhang, Y. B.; Kornienko, N.; Nichols, E. M.; Zhao, Y.; Paris, A. R.; Kim, D.; Yang, P.; Yaghi, O. M.; Chang, C. J. Covalent Organic Frameworks Comprising Cobalt Porphyrins for Catalytic CO_2 Reduction in Water. *Science* **2015**, *349*, 1208–1213.

(317) Diercks, C. S.; Lin, S.; Kornienko, N.; Kapustin, E. A.; Nichols, E. M.; Zhu, C.; Zhao, Y.; Chang, C. J.; Yaghi, O. M. Reticular Electronic Tuning of Porphyrin Active Sites in Covalent Organic Frameworks for Electrocatalytic Carbon Dioxide Reduction. *J. Am. Chem. Soc.* **2018**, *140*, 1116–1122.

(318) Katz, M. J.; Mondloch, J. E.; Totten, R. K.; Park, J. K.; Nguyen, S. T.; Farha, O. K.; Hupp, J. T.; Katz, M. J.; Mondloch, J. E.; Totten, R. K.; Park, J. K.; Nguyen,

S. T.; Farha, O. K.; Hupp, J. T. Simple and Compelling Biomimetic Metal–Organic Framework Catalyst for the Degradation of Nerve Agent Simulants. *Angew. Chem. Int. Ed.* **2014**, *53*, 497–501.

(319) Mondloch, J. E.; Katz, M. J.; Isley, W. C.; Ghosh, P.; Liao, P.; Bury, W.; Wagner, G. W.; Hall, M. G.; Decoste, J. B.; Peterson, G. W.; Snurr, R. Q.; Cramer, C. J.; Hupp, J. T.; Farha, O. K. Destruction of Chemical Warfare Agents Using Metal–Organic Frameworks. *Nat. Mater.* **2015**, *14*, 512–516.

(320) López-Maya, E.; Montoro, C.; Rodríguez-Albelo, L. M.; Aznar Cervantes, S. D.; Lozano-Pérez, A. A.; Cenís, J. L.; Barea, E.; Navarro, J. A. R. Textile/Metal–Organic-Framework Composites as Self-Detoxifying Filters for Chemical-Warfare Agents. *Angew. Chem. Int. Ed.* **2015**, *54*, 6790–6794.

(321) Islamoglu, T.; Chen, Z.; Wasson, M. C.; Buru, C. T.; Kirlikovali, K. O.; Afrin, U.; Mian, M. R.; Farha, O. K. Metal-Organic Frameworks against Toxic Chemicals. *Chem. Rev.* **2020**, *120*, 8130–8160.

(322) Chambers, M. B.; Wang, X.; Ellezam, L.; Ersen, O.; Fontecave, M.; Sanchez, C.; Rozes, L.; Mellot-Draznieks, C. Maximizing the Photocatalytic Activity of Metal-Organic Frameworks with Aminated-Functionalized Linkers: Substoichiometric Effects in MIL-125-NH_2. *J. Am. Chem. Soc.* **2017**, *139*, 8222–8228.

(323) Kreno, L. E.; Leong, K.; Farha, O. K.; Allendorf, M.; Van Duyne, R. P.; Hupp, J. T. Metal-Organic Framework Materials as Chemical Sensors. *Chem. Rev.* **2012**, *112*, 1105–1125.

(324) Lee, S.; Kapustin, E. A.; Yaghi, O. M. Coordinative Alignment of Molecules in Chiral Metal-Organic Frameworks. *Science* **2016**, *353*, 808–811.

(325) Öhrström, L. Now You See Me Too. *Science* **2016**, *353*, 754–755.

(326) Boix, G.; Troyano, J.; Garzón-Tovar, L.; Camur, C.; Bermejo, N.; Yazdi, A.; Piella, J.; Bastus, N. G.; Puntes, V. F.; Imaz, I.; Maspoch, D. MOF-Beads Containing

Inorganic Nanoparticles for the Simultaneous Removal of Multiple Heavy Metals from Water. *ACS Appl. Mater. Interfaces* **2020**, *12*, 10554–10562.

(327) Haque, E.; Jun, J. W.; Jhung, S. H. Adsorptive Removal of Methyl Orange and Methylene Blue from Aqueous Solution with a Metal-Organic Framework Material, Iron Terephthalate (MOF-235). *J. Hazard. Mater.* **2011**, *185*, 507–511.

(328) Horcajada, P.; Chalati, T.; Serre, C.; Gillet, B.; Sebrie, C.; Baati, T.; Eubank, J. F.; Heurtaux, D.; Clayette, P.; Kreuz, C.; Chang, J. S.; Hwang, Y. K.; Marsaud, V.; Bories, P. N.; Cynober, L.; Gil, S.; Férey, G.; Couvreur, P.; Gref, R. Porous Metal–Organic-Framework Nanoscale Carriers as a Potential Platform for Drug Delivery and Imaging. *Nat. Mater.* **2009**, *9*, 172–178.

(329) Dong, Z.; Sun, Y.; Chu, J.; Zhang, X.; Deng, H. Multivariate Metal-Organic Frameworks for Dialing-in the Binding and Programming the Release of Drug Molecules. *J. Am. Chem. Soc.* **2017**, *139*, 14209–14216.

(330) Horcajada, P.; Gref, R.; Baati, T.; Allan, P. K.; Maurin, G.; Couvreur, P.; Férey, G.; Morris, R. E.; Serre, C. Metal-Organic Frameworks in Biomedicine. *Chem. Rev.* **2012**, *112*, 1232–1268.

(331) Horcajada, P.; Serre, C.; Vallet-Regí, M.; Sebban, M.; Taulelle, F.; Férey, G. Metal–Organic Frameworks as Efficient Materials for Drug Delivery. *Angew. Chem. Int. Ed.* **2006**, *118*, 6120–6124.

(332) Horcajada, P.; Serre, C.; Maurin, G.; Ramsahye, N. A.; Balas, F.; Vallet-Regí, M.; Sebban, M.; Taulelle, F.; Férey, G. Flexible Porous Metal-Organic Frameworks for a Controlled Drug Delivery. *J. Am. Chem. Soc.* **2008**, *130*, 6774–6780.

Chapter 2

Objectives

Having illustrated the evolution of reticular chemistry, its rationalization, and its main synthetic and post-synthetic design strategies in Chapter 1, we observed that most of the regular organic and inorganic MBBs have been used for the assembly of edge-transitive nets. However, when decreasing the symmetry of the building bricks complicates the rational design of the desired product, obtaining unexpected frameworks far away from the default nets that beforehand were planned to obtain. This fact is related to the commonly used bottom-up strategies, which are restricted for regular MBBs and cannot anticipate the outcomes when deviating from ideal geometries. Indeed, these strategies will always face limits on the prediction, as its simplification into nodes or edges are not considering more information metrics that are encoded in the MBBs. The increasing interest of symmetry effects for deducing new underlying nets points out the demand in this field to give more tools for the repertoire of reticular chemistry.

In this context, the main goal of this Thesis is to develop new top-down design strategies for the prediction and understanding of the assembly of MOFs based on less-symmetric ligands. To achieve this goal, the present Thesis will be divided according to three fundamental objectives:

- Identify the different operations that can reduce the symmetry of organic MBBs and study its effect in the assembly of MOFs. Specifically, we will focus on exploring and explaining the desymmetrization effect of organic MBBs that affect to the inorganic MBBs; concretely, high-connected Zr- and RE-based clusters. To do so, we will compare the assembly of linkers with different metrics in Zr- and RE-MOFs reported in literature, and then apply these concepts for the synthesis of novel MOFs based on less-symmetric linkers.

- Develop a new top-down approach, which we have called net-clipping, for the prediction and deduction of reticular materials based on the theoretical de-reticulation of edge-transitive nets. Specifically, we will rationalize that

MOFs constructed with less-symmetric ligands could be derived from MOFs constructed with more-symmetric ligands by simply reducing by half the connectivity of the latter. To this end, we will firstly focus on the theoretical deduction of the possible nets constructed with less-symmetric linkers. Then, we will validate our new strategy with experimental structures based on literature examples and novel MOFs that will corroborate our approach.

- Develop a new synthetic methodology, which we called Clip-off Chemistry, for the prediction and synthesis of novel reticular materials based on a top-down approach by de-reticulating a net erasing nodes or edges in a controlled manner. We will locate cleavable bonds at precise positions in a MOF structure for the topological transformation into novel MOFs without altering the dimensionality/periodicity. In particular, we will use a polytopic linker containing different circuits of connections in the MOF, where some of them contains cleavable bonds. In this case, the cleavable bond will be olefines, and the cleavable reaction will be ozonolysis.

Chapter 3

Desymmetrization of MBBs in reticular chemistry

This Chapter is based on the following publications:

- Ortín-Rubio, B.; Perona-Bermejo, C.; Suárez del Pino, J. A.; Carmona, F. J.; Gándara, F.; Navarro, J. A. R.; Juanhuix, J.; Imaz, I.; Maspoch, D. A Mesoporous Zr-Based Metal–Organic Framework Driven by the Assembly of an Octatopic Linker *Chem. Commun.* **2023**, *59*, 7803-7806.

- Ortín-Rubio, B.;[‡] Yang, Y.;[‡] Rostoll-Berenguer, J.; Vila, C.; Juanhuix, J.; Imaz, I.; Maspoch, D. Exploring the Effect of Linker Desymmetrization in Zr and Rare Earth Metal-Organic Frameworks Unveils New Topologies with Defective Clusters *In preparation.* ([‡] = co-first authorship)

- Ortín-Rubio, B.; Imaz, I.; Maspoch, D. Desymmetrization of Organic Molecular Building Blocks in Metal-Organic Frameworks Constructed with High-Connected Clusters *In preparation.*

3.1. Introduction

3.1.1. Limits of reticular chemistry

Despite the successful implementation of the net-based approach for coordination and organic crystalline polymers, still remains difficult to completely understand or direct the formation of some nets. Perhaps the most glaring example is the presence of polymorphism in structures constructed with the same or similar MBBs. The simplest case is the presence of **sql** and **kgm** MOFs and COFs built with identical chemical composition. While the **kgm** net is a more thermodynamically favoured topology, the kinetical **sql** product is based on more regular MBBs with 90º angles between their connections, representing a more regular square.[1,2] Other examples can be found in literature as the **tbo** and **pto** topologies in Cu-based MOFs,[3] the **scu**, **sqc** and **csq** topologies in Zr-based MOFs,[4] or the **dia** and zeolite-like topologies formed with tetrahedral single metal ions difficult to predict. This problem has been widely explored by researchers, which can tune the synthetic conditions to obtain different phases. Indeed, even when the phases can be attributed to a thermodynamic/kinetic product or with a specific range of concentration or modulator in the procedure, it remains almost impossible to predict the orientation of linkers when they form derived nets. Some examples have been illustrated over the years: the **nbo-b** topology has three different derived nets with the underlying **fof**, **fog** and **tfb** topologies (Figure 3.1a). The group of Zhou reported that the **fof** net can be constructed upon the assembly of Cu(II)-paddlewheels and a tetratopic azobenzene linker.[5] However, by using a stilbene derivative, they constructed a MOF based on the **fog** topology.[5] Curiously, the group of Zaworotko reported that the assembly of the azobenzene tetracarboxylic linker with Ni(II) yields a MOF that exhibited the underlying **tfb** derived net.[6] Another example was reported by the group of Eddaoudi with tetratopic linkers and 12-c RE-based clusters building two different MOFs based on the same parent **ftw** net (Figure 3.1b). The same azobenzene linker resulted in the derived **kxe** net, while

the MOF obtained using a shorter biphenyl tetracarboxylate ligand presented the **kle** underlying topology.[7]

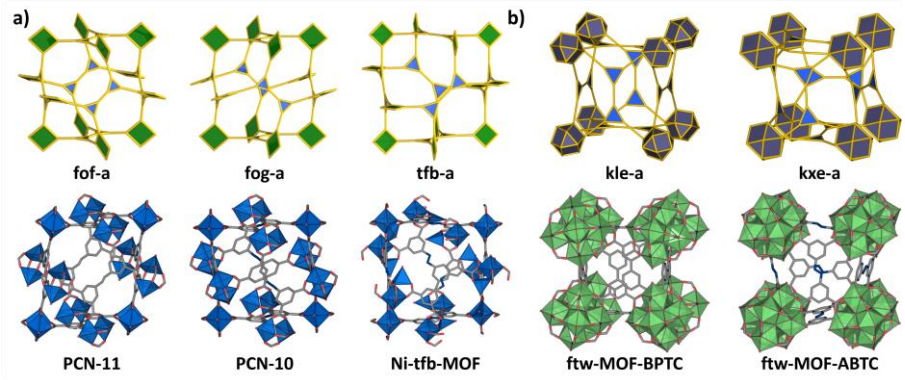


Figure 3.1. Comparison of different derived nets from the same parent a) **nbo** and b) **ftw** nets and the respective MOFs reported with these underlying derived nets, frustrating the topological prediction due to the linker orientation in the space.

Polymorphism has also been reported with MOFs exhibiting different connectivity. The presence of high-connected MBBs that enable defaults on coordination sites opened the door to this phenomenon. The most clear example is represented by the ubiquitous Zr-based oxo-hydroxo-cluster, which adopt different shapes (cuboctahedral, cubic, trigonal prismatic, hexagonal or square, among the most regulars), and the tetratopic porphyrin ligand, reported in the **fcu** (4,12)-c, **shp** (4,12)-c, **csq** (4,8)-c, **scq** (4,8)-c, **csq** (4,8)-c and **she** (4,6)-c topologies. This fact underlines the difficulty in predicting the net that will be formed when regular and rigid MBBs are used for constructing these nets. Still, some researchers identified the proper synthetic conditions to obtain different phases, which are difficult to understand without knowing the supramolecular interactions in the crystal growth for each case.

Some other limitations are attributed to the mismatch between the geometry of certain MBBs and the geometry of the nodes that they represent in the underlying net of the structure. The interconversion is given by MBBs with the same

connectivity but different geometry (tetrahedron and square, octahedron, trigonal prism and hexagon, etc.) that can be caused by the angular distortion induced by the adjacent MBB. The most noticeable example is the trimer cluster with a trigonal prism shape, which can be reticulated in MOFs with nets that require octahedral nodes. This has been illustrated in MIL-59 or the **soc**-MOFs with the underlying **pcu** and **soc** topologies, respectively.[8,9] Note that both nets can be afforded upon proper distortion of the other component, with bent linkers for the **pcu** net instead of the default **acs** net that is afforded with linear linkers (Figure 3.2a);[10] or rectangular ligands for the **soc** net instead of the default **stp** net that is afforded with regular square ligands (Figure 3.2b).[11] The opposite case is also presented using a tetranuclear Zn-based cluster and a bent linker to construct a MOF with the underlying **lcy** topology, which should be constructed with trigonal prismatic MBBs (Figure 3.2c).[12] More examples are illustrated by tetrahedral MBBs that afford

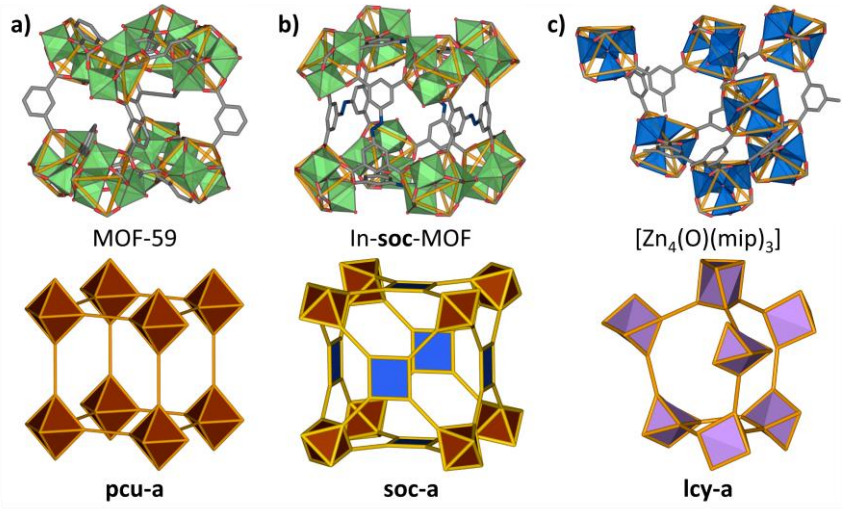


Figure 3.2. Mismatch generated between the geometry of the inorganic MBB used and the augmented form of the nodes in: a) MOF-59 constructed with trigonal prismatic SBUs to afford the **pcu** net that should be constructed with octahedral nodes; b) In-**soc**-MOF constructed with trigonal prismatic SBUs to afford the **soc** net that should be constructed with octahedral nodes; and c) $[Zn_4(O)(mip)_3]$ constructed with octahedral SBUs to afford the **lcy** net that should be constructed with trigonal prismatic nodes.

nets based on square nodes, hexagonal MBBs that afford nets based on octahedral nodes, and so on.

Lastly, there is a general unawareness of the effect of desymmetrizating molecules in the assembly of reticular materials. As the principles of reticular chemistry are based on regular, rigid, and geometrically well-defined building blocks, the use of molecules that do not exhibit ideal shapes can dramatically affect on the cluster formation or net result. Moreover, the incompatibility of assembling certain regular MBBs in a net can produce a mismatch that result in the torsion and symmetry, or connectivity decreased of the MBBs.

3.1.2. Introduction of missing parameters for the description of reticular materials

Progress broadening the scope of new organic ligands, SBUs or nets unmasked the restrictions of the topological approach to predict the reticulation of molecular components. Nowadays the criterion for anticipating the assembly is based on the connectivity of the MBBs, their geometry respect to their points of extension and the linkage they form, but all of them are not sufficient. In fact, the clearest example has been pinpointed in linear linkers that exhibited angular torsions. Three types of angles can be controlled in linkers related to their in-plane, out-of-plane and torsion rotations (Figure 1.7a). In each type, there is an angular range that determines certain assemblies, so the angular torsion between the MBBs should be provided to distinguish between the assemblies and perform a superior design. Some examinations already measured these angles in topologies and/or MOFs for a more comprehensive understanding of the angular effect.[13]

Moving away from standard metrics can also deviate from default nets. In non-coplanar linkers, the width that separates both functional groups can preclude some MOFs formation. Ligand width results in a different spatial distribution of the

surrounding clusters and therefore, a different dihedral angle between them, creating a mismatch. In polytopic linkers, altering the height/width (h/w) ratio can dramatically affect to MOF structure or direct to a different kind of net as we will later see.

Other kind of parameters can be related to the introduction of bulky groups that create a steric hindrance with neighbouring components but do not affect to the orientation of the directionality or the symmetry of the linker; the relative size of both inorganic and organic MBBs, as some linkers with similar metrics can form specific nets that upon expansion without altering the directionality or h/w ratio cannot form isoreticular structures, deviating from the isoreticular principle; or the use of more than 2 components as mixed-linkers or mixed-metals systems, that their different nets formed are just related to the synthetic conditions (Figure 1.14).

3.1.3. Desymmetrization of organic ligands

3.1.3.1. Types of desymmetrization

Deviations from standard metrics were found crucial when the organic ligands experienced some kind of desymmetrizations. The different changes in position of the end groups in the organic MBBs resulting from the desymmetrizations of the ideal shapes can be summarized in eight fundamental operations: identity, expansion, contraction, torsion, in-plane rotation, out-of-plane rotation, in-plane translation and out-of-plane translation (Figure 3.3).[14] The effects of the identity, angular torsion and in-plane rotation operations were already previously discussed. This Section will cover the design of organic MBBs with more intricate desymmetrizations, with a special emphasis in the different kinds of elongations reported so far.

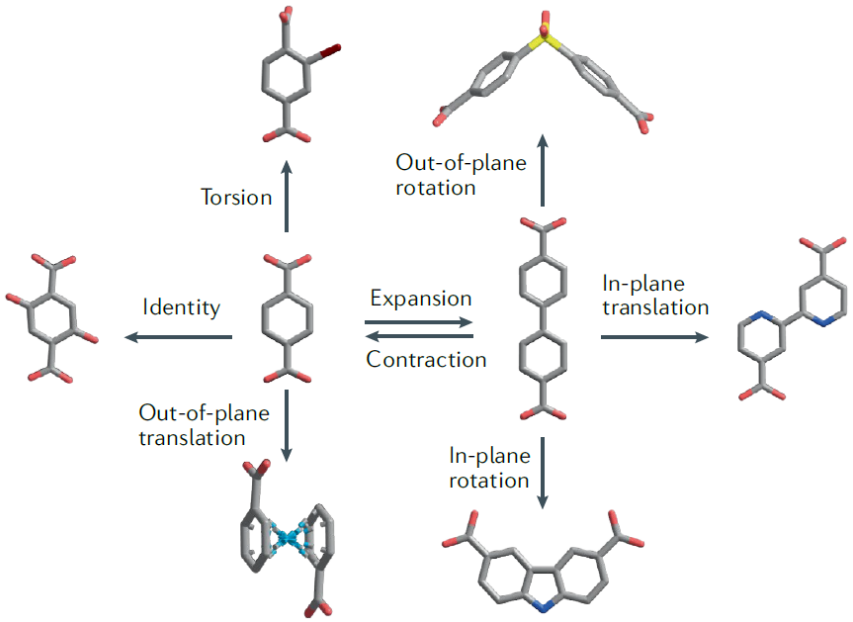


Figure 3.3. Illustration of the eight different operations applied to the simplest ditopic linker and their corresponding transformation into linkers with different shapes.

3.1.3.2. Symmetric elongation

Ligand expansion has been extensively studied since the appearance of the former MOF structures with the aim of obtaining isoreticular structures with higher surface areas.[15] The design of the linkers relies on increasing the length (in the case of 2-c linear ligands) or size (considering length, width or angles in the case of polytopic ligands) in a symmetrical way in order to not disturb the parameters for obtaining such a concrete structure. For example, MOF-2[16] has been expanded up to five phenyl rings from terephthalic acid by increasing the length, confirming the isoreticular principle obtaining the same underlying net.[17] Therefore, the size of the square windows increases in the periodic compound. In the case of MOF-5, use of the same approach gave birth to the first interpenetrated MOFs.[15] The empty and

accessible space created by the high surface area of the structure permits the formation of an additional net in the pores. Actually, interpenetration has been correlated to linker expansion for some specific nets, such as those who are self-dual (**srs**, **dia**, **lcy**, **pcu**, **ftw**, **ctn**, **mgc**, **pyr**, **pto**, etc.) as in the case of the isoreticular **pcu** structures.[18] In this case, the symmetry of the linkers has been maintained, without altering the cluster symmetry or environment and therefore, the symmetry of the net.

Moving to the HKUST-1 platform,[19] enlargement of BTC by adding an extra phenyl ring leads to a topologically distinct **pto** net.[20] Again, the resulting net exhibits a 2-fold interwoven network. As explained before, this is the other possibility when combining triangles and squares with just one kind of edges. In the case of the **tbo** net, the triangular MBB is twisted in a torsion angle of 90º respect to the square MBB. For achieving this conformation, the carboxylate groups of the linker must be completely planar respect to the center of the linker. BTC perfectly match for adopting this conformation due to the conjugation of the carboxylate groups with the phenyl ring, keeping the planarity. In this case, BTB moiety suffers a torsion angle of 55º due to the steric hindrance of the phenyl rings, preventing the planarity of the carboxylate groups with the central ring.[3,14] The steric hindrance allows the desymmetrization of the ligand because of the torsion angle produced, decreasing the symmetry of the linker and therefore, the symmetry of the resulting net. In fact, **pto** net has a lower symmetry (*Pm-3n*) than the **tbo** net (*Fm-3m*), but in the last case, a slight bending of the organic moiety is needed for affording the higher symmetric **tbo** net. Ligand modification of BTB into 4,4',4''-*s*-triazine-2,4,6-triyl-tribenoate (TATB) erase the steric hindrance between phenyl rings because of the disappearance of the three hydrogen atoms. This fact avoids frustrating the planarity of the linker, inducing the formation of an interpenetrated **tbo**.[21] Increasing more the size of the linker unveils polymorphism of both nets due to two possible conformations according to the σ-bond rotation,[3,22] or even the introduction of different functional groups can tune the formation of each net.[23]

3.1.3.3. Dissymmetric elongation

The first rationalized desymmetrization of a linker was performed by Matzger and coworkers, expanding a tritopic linker just in one direction by adding a phenyl ring.[24] This unsymmetrical substitution drives to the formation of two types of clusters when combining with a Cu salt. On one side, the isophthalate moiety produces the well-known paddlewheel dimer, connected between them in a 2D **kgm** fashion. On the other side, the carboxyphenyl part led to the formation of a Cu trimer cluster, $Cu_3(RCO_2)_6$, with a trigonal prismatic shape. This cluster was already discovered in its isolated form, but this was the first time that was reported in a MOF structure.[25] The trigonal prismatic cluster acts in the structure as a pillaring of the **kgm** lattices, unveiling a new **agw** topology with (3,4,6)-connected nodes. So, the dissymmetric elongation of the linker decreases it symmetry (C_{2v}), preventing the formation of the Cu-dimer (D_{4h}) and evolving to the Cu-trimer (D_{3h}), a less-symmetric cluster, and resulting in a net with symmetry decreased ($P6_3/mmc$). Topologically, the desymmetrization of this 3-c regular vertex can be viewed as a 3-c less-symmetric vertex, which is connected via two edges instead of one, as in the case of BTC (Figure 3.4a). Further investigation of the use of this linker reveals that a mixture of Cu with another metal salts (such as Co^{II}, Mn^{II} or Fe^{III}) can produce heterobimetallic MOFs, where the new metals replaced Cu^{II} in the trimer cluster, with an extra μ_3-O^{2-} in the center of the cluster and H_2O/OH^- surrounding ligands for accomplish an octahedral coordination environment in the case of Fe^{III}.[26] Conversely, the total substitution of Cu^{II} salt with Co^{II}, Mn^{II} or Mg^{II} when using this linker unveils a new 3,6-c net (with an underlying 3,6T51 topology) with a linear trinuclear cluster that shows an octahedral fashion.[26,27] This cluster, known as hour-glass SBU,[28–30] was already reported in the case of linear linkers for adopting the underlying **pcu** net due to its octahedral connectivity.[31,32]

Successive efforts by the same group reported a novel Cu-based MOF joint by the elongation of two points of extension of BTC.[33] In this case, the linker has the same symmetry (C_{2v}) but with different metrics (without an isophthalate unit). Due to the

different types of carboxylate groups, a new **fmj** net is formed with two types of paddlewheel units in UMCM-151. The elongated arms of the linker are connected between them in a 2D **sql** fashion, which are pillared by the paddlewheel constructed with the shorter carboxylate groups, resulting in a non-interpenetrated $(3^2,4^3)$-c net. Topologically, the desymmetrization of this 3-c regular vertex is similar as in the latter case, reversing the length of the edges (Figure 3.4a). Curiously, the simplest way to desymmetrize a 3-c vertex (elongation of one or two points of extension) evolves in the production of pillaring nets, both of them (**sql** and **kgm**) 2D layers comprised of 4-c square-like nodes joint by the same symmetrically edges.

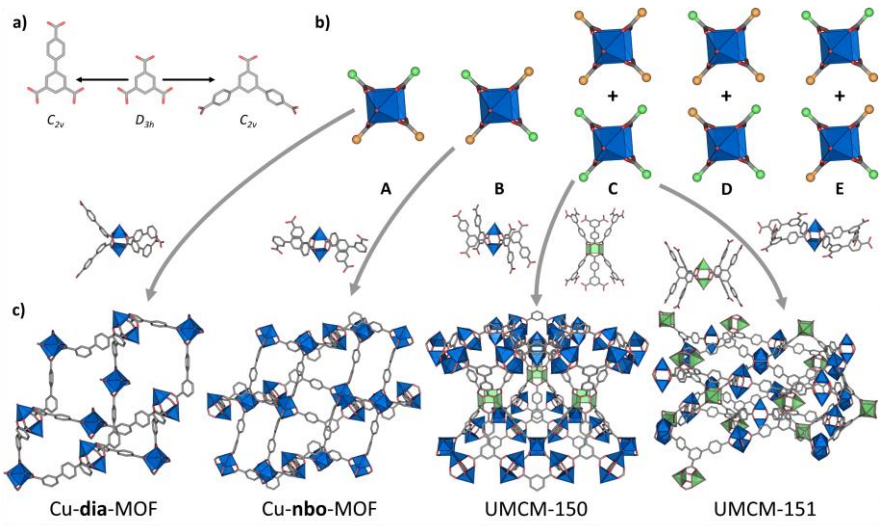


Figure 3.4. a) Desymmetrization of BTC linker by elongating one (left) and two (right) arms into less symmetric linkers, and therefore, two different edges. b) Possible combinations of a Cu(II)-paddlewheel and a linker with two different binding sites (green and orange): A, 2:2-substituted *cis*-cluster; B, 2:2-substituted *trans*-cluster; C, a mixture of both 4:0- and 0:4-substituted clusters; D, a mixture of both 3:1- and 1:3-substituted clusters; and E, a mixture of both 2:2-substituted *cis*- and *trans*-clusters. c) Representation of some MOFs with the most probable scenarios when assembling less-symmetric clusters with two different binding sites: MOFs based on one kind of 2:2-substituted clusters (A and B) or based on two different 4:0-substituted clusters (C).

The same strategy was used for designing the first desymmetrized bent ligand with an extra phenyl ring, showing two distinct binding sites.[34] In this case, the use of this unsymmetrically substituted carboxylate groups allowed the formation of two different polymorphs based on paddlewheel units when mixing with Cu^{II}. This effect is also known as "*supramolecular isomerism*". A careful analysis of both structures revealed that, in each case, there is just one kind of vertex: Cu-dimer units chelated by the two distinct binding sites in two different arrangements; a *cis* or *trans* conformation. In the first case, two carboxylate groups *meta*-substituted are adjacent, and on the other side, there are two carboxylate groups that are *para*-substituted. This conformation of the cluster is extended in a 3-fold interpenetrated $I4_1$ net with an underlying **dia** topology. Surprisingly, the desymmetrization of the linker generates a less-symmetric paddlewheel, resulting in a **dia** net with lower symmetry (default symmetry for **dia** net is *Fd-3m*), a net based on the assembly of tetrahedra. The tetrahedral orientation/geometry can be achieved because of the bending angle of the linkers in the square-planar MBB, shifting 90º two points of the square (an edge) needed for increasing the dimensionality of the MBB (Figure 1.7c). In the second case, the carboxylate groups *meta*- and *para*-substituted are opposite. This conformation of the cluster is extended in a 2-fold interpenetrated *R-3* net with an underlying **nbo** topology. Here, the less-symmetric linker generates a less-symmetric paddlewheel, resulting in a **nbo** net with lower symmetry (default symmetry for **nbo** net is *Im-3m*). In this case, the topological simplification of the linker makes no difference from the default bent or linear linker. The difference in the chemical environment of 2-c MBBs can be considered as a blind spot in the mathematical discipline of topology, because of the straightforward consideration as an edge in a net.

From these last examples, we can summarize the effect of having dissymmetric linkers when mixing with the simplest dimer cluster (Figure 3.4b). In the case of the 2-c linker, the two different chemical environments of the linker provide vertex-transitive (one kind of vertex) structures with the two possible cluster

diastereomers (A and B). This is the case of obtaining less symmetric clusters for achieving more symmetric networks (with MT). For the 3-c linkers, the structures found show two different clusters, fully substituted with the same chemical environment (C) in a ratio according to the different branches of the linker. This is the case of obtaining more symmetric clusters but in a less regular binodal net. The structures found show the most symmetrical combinations that can be obtained with dissymmetric linkers, but these are not the unique possibilities. Another combination of two possible clusters in an equal ratio is possible, with a 3:1 substitution in each cluster (D), or even a mixture of A and B clusters can be achieved (E), yet to be discovered.

3.1.3.4. Asymmetric elongation

The desymmetrization of linkers can be induced asymmetrically by elongating them in different axis, distorting their geometry. In order to increase the degree of desymmetrization, the connectivity of the MBB should increase (at least to 4-c) because there is just one possible asymmetric elongation in the case of triangles (Figure 3.4a). The first reported cases were UMCM-152 and UMCM-153,[33] MOFs based on a 4-c trapezoidal linker and Cu(II)-paddlewheels. This linker was derived from a 3-c BTB, by the replacement of a *p*ara-benzoate by an isophthalate (Figure 3.5). For UMCM-152, the less-symmetric (C_{2v}) linker guide to the formation of a less-symmetric cluster resulting in a **fof**/**nbo** net with lower symmetry (*R3m*, when the default symmetry for **fof** is *R-3m*), which can be observed as the pillaring of 2D **kgm** layers (Figure 3.5a). For UMCM-153, the linker adopts a torsion angle between the two central cores due to a σ-bond rotation that produces a less symmetric cluster (C_{2h}), resulting in a different underlying *Fddd* net with 3^2,4T65 topology. Interestingly, this net can also be described as the pillaring of **sql** 2D nets (Figure 3.5b).

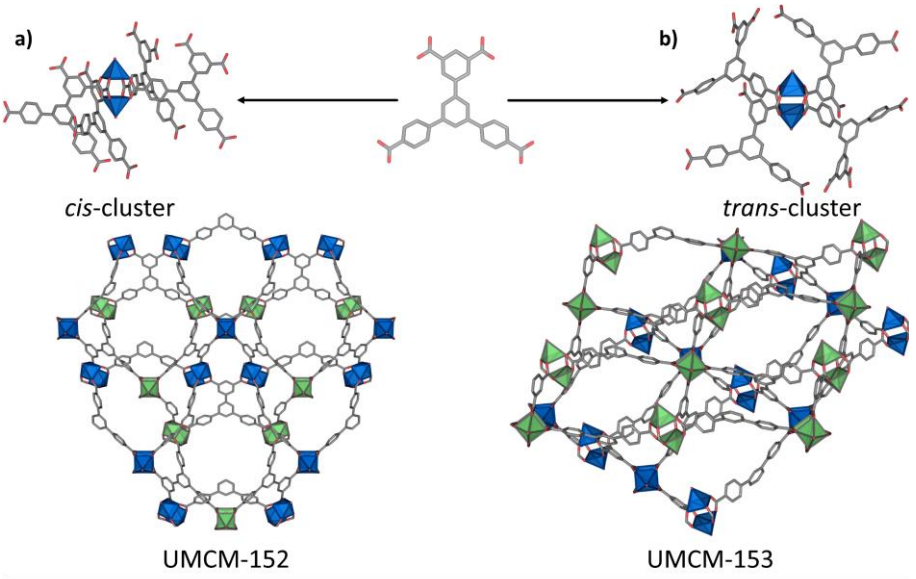


Figure 3.5. Assembly of a less-symmetric 4-c linker with Cu(II)-paddlewheels in two different polymorphs according to the *cis*- or *trans*-substitution in the 4-c cluster into a) UMCM-152 based on edge-to-edge pillaring of **kgm** layers; and b) UMCM-153 based on the edge-to-edge pillaring of **sql** layers.

Moreover, the distortion of 5-c linkers has been studied with a triphenylbenzene core with an unsymmetrical distribution of the carboxylate groups.[33] In this case, the linker possesses a C_2 symmetry with two different chemical environments. When mixing with Zn^{II}, an uncommon three-bladed paddlewheel with tetrahedral coordination was found with axial mono-coordination of carboxylates, giving a 5-c vertex in a 3,3,5T34 topology. In fact, this net can also be described as a pillaring of **bex** layers. Coincidentally, a similar cluster (C_2) has been recently found with a more regular 5-c linker (pyrrole core) in a Cu-based pentaMOF-3,[35] mixed with distorted 4-c paddlewheels in a $Pna2_1$ net with underlying 4^2,5,8^2T4 topology. Alternatively, this net can also be described as the pillaring of distorted **sql** nets with the rod-like SBUs in a sqc54 topology. By using another synthetic conditions, the same linker can form a more symmetric **lvt** net with regular 4-c paddlewheels in pentaMOF-2 (*C2/c*). In these two cases, the geometric frustration of 4-c and 5-c

nodes cannot result in any topology. For that reason, the linker decrease its connectivity to 4. Simplifying the effect of the linker on the cluster and net, we can consider that the effect of using a 5-c linker drives to a 5-c cluster.

3.1.3.5. Non-conventional operations: out-of-plane rotations and translations

Beyond the most common strategies for tuning the shape of organic units, some creative pieces of work explored different geometries with potential structural guidance to new materials. One case is the rotation of the connecting groups that can also result in a dihedral angle when it is applied out of the plane.[1] This configuration can lock some clusters via multiple-bridging when the operation is applied to 2-c linkers,[36,37] but also can be exhibited in branched linkers when the central core direct to a certain conformation, which can be key for the success when targeting some nets considering the dihedral angle formed by the nodes.[38,39]

Despite being used in conventional linkers without intention, the translation operations are the most recent additions when studying the effects of organic MBBs in the reticulation of periodic structures. When this operation is applied in the plane to ditopic linkers results in zigzag linkers, losing the coplanarity of the connecting groups and appearing a width parameter. Some common linkers that exhibited this zigzag effect are fumarate, 2,6-naphthalenedicarboxylate, and 4,4'-azobenzene-dicarboxylate. The most comprehensive study was reported by our group affording isoreticular Zr-MOFs exhibiting defaults of connectivity in the cluster due to the length mismatch because of the width of the linker, resulting in the **bcu** net rather than the more connected **fcu** net.[40] It must be mentioned that linkers exhibiting a small width parameter can result on both polymorphs, acting as linear and zigzag in each structure.

Out-of-plane translation occurs in linkers that translate the directionality of the binding site and brings a tridimensional character to the organic MBB. As the out-

of-plane rotation, this translation has been less explored due to the difficulty of controlling the spatial distribution during the synthetic conditions. Nonetheless, some examples were achieved via paracyclophane or metallocene-based units, which can tune the properties of the materials compared to the linear equivalents.[41,42]

3.1.3.6. Multiple desymmetrizations

In the last decade, several organic MBBs presented the combination of different desymmetrizations. The most common (and feasible) operations to combine are the expansion/contraction with the identity, in-plane rotation, in-plane translation, and torsion, which resulted in polymorph structures or non-default topologies. In addition, recent publications have explored sophisticated designs that combined the expansion of linkers with an out-of-plane translation with the central paracyclophane core, which can result in a new cluster environment and net topologies;[43] or the combination of both common angular effects (in-plane rotation and torsion), which can adopt a similar conformation as the out-of-plane rotation but in a more controlled fashion, locking the orientation and position of the clusters via multiple-bridging.[37]

3.2. Results and discussion

3.2.1. Influence of desymmetrization of organic MBBs in MOFs constructed with high-connected clusters

3.2.1.1. Zr-clusters combined with 4-c square/rectangular organic MBBs

Highly connected clusters have been one of the targets in the last decade in the field of MOF chemistry. Their use as building blocks enables the construction of high connected nets, which is one of the key features for synthesizing robust and highly

stable structures. In addition, the more connected nodes, the less possible nets can be formed. As mentioned above, the discovery of the $Zr_6O_4(OH)_4$ cluster permitted the access to high-connected nets with 12-c nodes with cuboctahedral shape.[44] Among the uninodal and binodal edge-transitive nets, the **fcu** and **ftw** topologies can be built. For the 2-c linkers, linear shapes were able to construct MOFs with the underlying **fcu** net. However, when introducing a desymmetrization factor due to the steric hindrance produced by the bulkiness of functional groups, a twisted conformation promotes the formation of PCN-700, which exhibits an underlying **bcu** topology.[45] The σ-bond rotation in the twisted linker drives to a change of directionality of one cluster respect to the other, incompatible with the orientation of the clusters in the **fcu** topology. However, this 90º shift match with the orientation of cubes in the case of the **bcu** topology, producing a decrease of connectivity in the cluster. Despite the decrease of connectivity, the resulting **bcu** [1111] is one of the regular nets, compared to the default semi-regular **fcu** [1112]. The decrease of symmetry of the linker (C_1) produce a less-symmetric cluster (D_{4h}) instead of the symmetric 12-c hexamer (O_h), resulting in a less-symmetric $P4_2/mmc$ net (Figure 3.6).

The same topology could be achieved thanks to the disruption of the collinearity in the case of zigzag linkers (C_{2h}), obtaining isoreticular **bcu** structures.[40] In fact, in the case of zigzag linkers that the width parameter is smaller, **fcu** structures can also be obtained.[46] Also, the combination of zigzag and steric effects via introduction of a bulky group yields a **reo** MOF, with an underlying net of 8-c cubic clusters in a *Pm-3* system.[47] The steric hindrance produced by the functional groups cannot allow the **bcu** phase, generating the corresponding polymorph. In fact, this **reo** topology was previously achieved by the effect of bent linkers,[48] a less common and less regular net [1122] compared to **bcu**, according to Pauling's principle.[49] Further elongation and torsion of linkers can produce less-symmetric 8 coordinated clusters with pairs of linkers bridging the Zr-clusters in a 4-c **dia**-MOF that crystallized in an $I4_1/a$ system.[50] By breaking the coplanarity of the carboxylate groups but in different

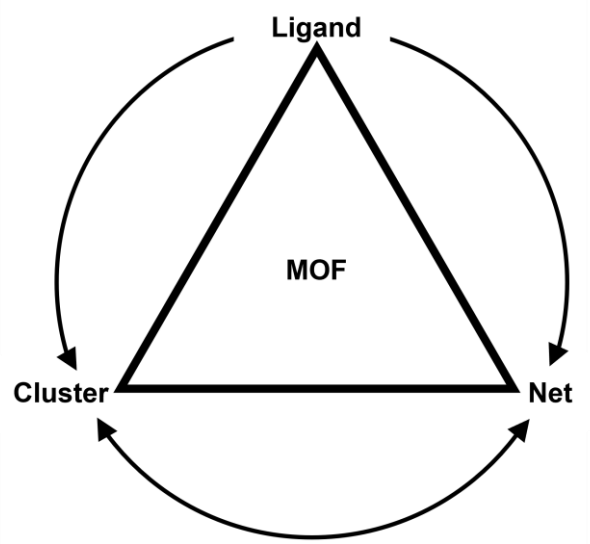


Figure 3.6. Symmetry triad of MOFs based on their components and characteristics. The selection of the metrics and symmetry of the ligands direct to specific clusters or nets. Some clusters can force to assembly with ligands in nets with unusual topologies; or some specific nets can force to adopt clusters uncommon geometries and/or connectivities.

planes, a 9-c triangular cupola Zr-cluster is formed in a 2D MOF when assembled with paracyclophanes.[43] Moreover, a decrease of the degree to 120º in bent linkers (C_2) promotes the formation of a 6-c **pcu** net (*R-3*), exhibiting a 12 coordinated cluster with pairs of linkers bridging to the same neighboring clusters.[51] If the bending occurs out-of-the plane, the Zr-cluster tend to further decrease its connectivity and dimensionality to a 4-c **sql** 2D net (*I4/mmm*), exhibiting an 8 coordinated cluster with pairs of linkers bridging again to the same neighboring clusters.[52]

The other possible net to construct is based on the 4,12-c **ftw** topology, which was achieved with the corresponding square-like organic MBBs based on porphyrin and cruciform ligands.[53] The use of the high symmetric tetrakis(4-carboxyphenyl)porphyrin (TCPP) linker (D_{4h}) promotes the formation of the high symmetric cluster (O_h) in a 4,12-c **ftw** net (*Pm-3m*). Its discovery was parallel to a polymorph exhibiting a less-connecter cluster with cubic shape, achieving a 4,8-c

csq underlying topology (Figure 3.7). Here, a σ-bond rotation (~56.08º) in the arms of the ligand produces a decrease of the symmetry (C_{2v}), inducing the decrease of connectivity and symmetry in the cluster (D_{4h}) and resulting in a less-symmetric *P6/mmm* net. In this structure, we can notice two main features that promotes the formation of the **csq** net via desymmetrization: i) the σ-bond rotation between the phenyl ring and the porphyrin center; and ii) the geometry transformation of the square conformation of the linker into a more rectangular shape, obtaining a 0.95 h/w ratio (Figure 3.8). This last characteristic was already pointed by Matzger *et al.*, justifying the possible distortion of a square into a rectangular shape of the organic linkers, which cannot be reached from a rectangle to a square.[54] Here, the authors suggested a map for the prediction of net topologies of MOFs based on Zr-clusters and tetratopic linkers according to the symmetry and ratio of the linker. Recently, a more complete scheme for Zr-MOFs has been reported according to the linker connectivity and geometry and cluster connectivity.[55] In this map, the topologies reported with 2-, 3- and 4-c linkers are described as well as those nets yet to be discovered. However, these maps just explain the possible outcomes considering the combinations of the MBBs, but there is no explanation on why the cluster connectivity changes or the difference between topologies of the same connectivity. Neither there is a symmetry or ratio aspect for explaining the influence in the structures.

Other two porphyrin-MOF polymorphs with an 8-c Zr-cluster were successively discovered based on other edge-transitive nets, the **sqc** and **scu** topologies (Figure 3.7).[56,57] MOFs based on these underlying topologies are kinetical products compared to the most symmetric and thermodynamic **csq** net, with $I4_1/amd$ and *Cmmm* symmetries in the **sqc** and **scu** nets, respectively. Interestingly, the rotation of the phenyl ring in the **scu** net (56.06º) is similar to the **csq** net, but in different directions respect to the center, which guide to a different symmetry (C_{2h}). This is not surprising, as the **csq** and **scu** are nets that are related to each other by their spatial distribution, as the **sql** and **kgm** 2D nets. However, the h/w ratio of the

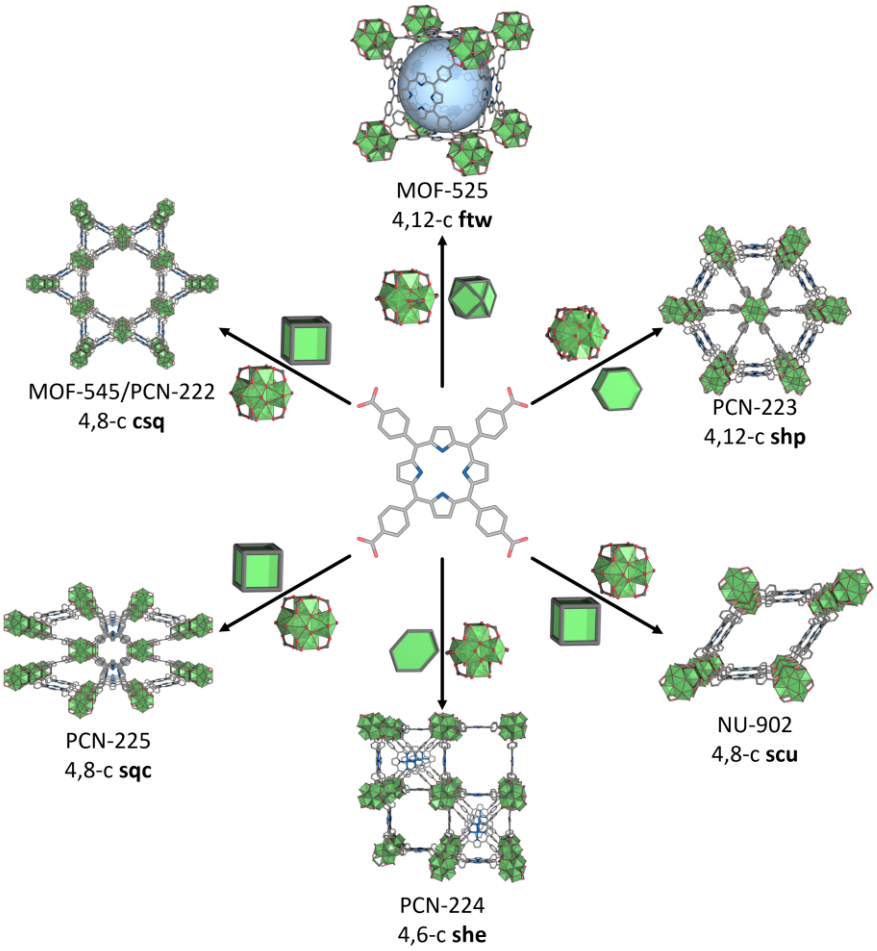


Figure 3.7. The six polymorph Zr-MOFs based on the assembly of TCPP linker for constructing six different edge-transitive nets. The connectivity and geometry of the Zr_6-cluster change to afford them: a 12-c cuboctahedral SBU to form the **ftw** net, a 12-c hexagonal prismatic SBU to form the **shp** net, an 8-c cubic SBU to form the **csq**, **sqc** and **scu** nets, and a 6-c hexagonal SBU to form the **she** net.

porphyrin is slightly decreased to 0.88, which match with the assignment to a kinetical product. On the other hand, the porphyrin in the **sqc** net displays a lower rotation of the phenyl rings (39.43). Curiously, all arms rotate in the same direction (C_{2h}), obtaining the three most symmetric conformations of the porphyrin. Also, the porphyrin is desymmetrized in a more rectangular shape (0.87 h/w) to achieve

the topology of this net. To the best of our knowledge, this is the first time that such an in-depth analysis of the MBBs have been performed to understand the assembly of the different polymorphs with the rotation, symmetry, and h/w ratio of the ligands.

Two additional polymorph structures were discovered using these two MBBs which can be related to the former structures. In 2013, the group of Hong-Cai Zhou reported that the connectivity of the Zr-cluster could be further decreased to 6, exhibiting a hexagonal shape.[58] Its reticulation with the porphyrin yielded the 4,6-c **she** net exhibiting a very symmetric *Im-3m* space group. Interestingly, the linker exhibits a perfect square conformation, with an h/w ratio of 1. We attribute this factor to the perfect match of the Zr-cluster with a hexagonal conformation, which does not need to be desymmetrized in a rectangular shape to afford the **she** net, as for the **ftw** net. On the contrary, when the Zr-cluster is 8-c, its shape is elongated in a square prism rather than a perfect cube, demanding the same elongation to the organic MBB to afford the **csq**, **sqc** and **scu** nets (Figure 3.8). Another curious characteristic is that the rotation of the phenyl rings is 74.70º, close to a perpendicular orientation, and with the same overall rotation as in the **csq** net (C_{2v}). We attributed this conformation to the most stable and thermodynamic one compared to the rest, as the **she** net is highly symmetric and the **csq** net is the most symmetric among the nets constructed with the 8-c cluster. The following year, the same group discovered the last polymorph PCN-223, a rare threefold, disordered 12-c Zr-cluster exhibiting a hexagonal prism conformation.[59] The MOF exhibited the 4,12-c **shp** net, crystallizing in the *P6/m* group, with a slight distortion of the porphyrin displaying a 0.91 h/w ratio. This structure shows certain similarity with PCN-222, which has an underlying **csq** topology. The correlation can be explained if PCN-223 is considered as a threefold disordered variant of PCN-222/MOF-545. However, some authors stated that the **shp** net is better correlated as threefold twins of ordered **scu** net, which match with the disordered cluster.[60] Indeed, attending to the linker conformation (C_{2h}), the porphyrin has the same orientation

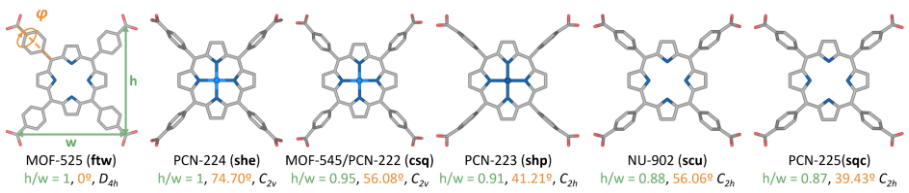


Figure 3.8. Characteristics of the same TCPP linker in different Zr-MOFs analyzed according to its rectangular aspect with the h/w ratio, the rotation of the carboxylates and the symmetry of the ligand according to the orientation of the arms rotating. Note that all structures have been measured by carbon-to-carbon distances of the carboxylate groups, and it has been considered just the rotation of the carboxylate groups respect to the plane of the core, as some phenyl rings can rotate in different angles than the carboxylate groups. These criteria will stand for all the following measurements of different kind of linkers. In addition, the h/w ratio has been considered with the longest side as the width, being the maximum ratio obtained the square conformation.

of the phenyl rings as in the porphyrin of the **scu** net, but with a different rotation (41.21º).

Disordered Zr-clusters were also found in PCN-221, first considered as a new Zr_8O_6 cluster in an underlying **ftw** net.[61] However, it was demonstrated that this cluster is a fourfold disordered hexanuclear Zr-cluster, forming the **ftw** net due to the disordered structure of PCN-224 (*d*PCN-224), which has an underlying **she** net.[62] Curiously, the aromatic rings and carboxylate groups are rotated 90º with respect to the center, which is close to the rotation appearing in the **she** net, and with the perfect square shape. This fact questioned the first **ftw** net MOF, MOF-525, which was simulated completely planar and never found in a single-crystal analysis. In fact, the repulsion between the hydrogen atoms of the phenyl ring and the porphyrin would prohibit this conformation. This was confirmed by the elongation of the porphyrin linker, where the first phenyl ring is perpendicular to the plane and the carboxylate group is parallel to the porphyrin, obtaining a series of **ftw**-MOFs.[63]

An additional structure with the lowest connectivity of a Zr-cluster reported so far was synthesized with the porphyrin unit.[64] The structure exhibits a 4-c cluster in a 2D **sql-b** net, where the clusters could be rectangular-like in a complete flat layer or intercalated with 4-c bent-coordinated clusters to form a zigzag folded layer.[65]

However, there is no evidence of any crystallographic data to support these structure, neither any simulation to confirm the crystal phase in the bulk PXRD, which was simply compared to show some differences with the **csq** PCN-222 MOF, supported by microscope images (TEM and AFM). We believe that this characterization is frankly still inadequate to determine the structural organization of this plausible phase.

Since then, many researchers have sought to expand the Zr-MOF family with new polytopic linkers to shed light on the linker-shape role in the reticulation of Zr-MOFs. The first building unit to substitute the porphyrinic core was the pyrene by the group of Farha. Although its desymmetrization in a rectangular shape is not highly pronounced (0.99 h/w ratio), the steric hindrance between the hydrogen atoms force to adopt a 52.11º rotation forming a **csq** net.[66] NU-1000 crystallized in the P6/mmm system and exhibited the same rotation of the phenyl rings as in the **csq**-like porphyrin MOF. A polymorphic NU-901 phase was also reported exhibiting a **scu** net according to PXRD studies and a simulated structure,[67] but its crystal structure have never been solved by SCXRD. In fact, its isolation is often found with NU-1000 impurities depending on the synthetic conditions, demanding detailed synthetic protocols to obtain each desired phase.[68] Another building unit related to pyrene was the biphenyl which was reported by the group of Matzger.[54] However, the flexibility of the σ-bond promoted the rotation to a more symmetric tetrahedral shape of the linker. Later, the groups of Hong and Zhou reported a huge study on the functionalization of different positions of the same linker skeleton to tune the angular torsion of their arms, obtaining three different possible underlying topologies (**flu**, **scu** and **csq**).[69] Curiously, the inner biphenyl group resulted coplanar in the MOFs when affording a rectangular shape, presumably due to conjugative effects. Although both **scu** and **csq** nets were found by modifying the synthetic conditions, their single crystals confirmed the desymmetrization into a rectangular shape (all linkers show between 0.82-0.93 h/w ratio) and similar degree of rotation in both C_{2h} and C_{2v} symmetries. Additionally, the bulkiness of the

functional group can direct to the **csq** net, as there is a higher degree of rotation and therefore, a bigger space to accommodate larger functional groups. A more recent study performed by the group of Gao showed that, replacing the biphenyl units in the central core by bipy units, inhibited the steric hindrance of neighboring hydrogens, driving to the formation of an **ftw** net without any rotation of the phenyl arms.[70] The ligand adopted a sightly distorted conformation in a D_2 symmetry, showing a 0.91 h/w ratio. As the ideal **ftw** net requires a 4-connected square shaped node, it is disordered in two perpendicular positions, which average enable to behave like a square node.

On the one hand, as in the porphyrinic units, both biphenyl and pyrene central core were expanded by increasing the arm lengths, and therefore, altering the metrics on the organic MBBs (Figure 3.9). The same scenario occurred in the Zr-MOFs, appearing the rectangular linkers (0.94 and 0.96, respectively) disordered or alternated in **ftw/kle** underlying topologies of the net, in a complete planar conformation.[71,72] The more extended the arms, the more flexible are the linkers, able to adopt a square shape in highly disordered isoreticular structures.[73–75] However, when introducing an additional desymmetrization factor as an in-plane translation,[76–80] a torsion,[78] or by simply adjusting the synthetic conditions,[77,78] the **scu**,[79] **sqc**,[80] **csq**[76–78] and **shp**[77] net resulted instead of the default **ftw** net. Curiously, using the naphthalene unit as an arm dramatically decrease the h/w ratio to 0.61, 0.74 and 0.78 in the **csq**, **sqc** and **shp** nets, respectively, depending on the orientation of the naphthalene. As expected, in the **csq** and **sqc** nets the rotation of the arms is quite similar (51.79º and 42.91º, respectively). However, in the **shp** net, the ligand is completely planar adopting a trapezoidal shape. This is quite surprising, as all the planar conformations yielded to the **ftw** net, highlighting the effect of desymmetrization from the square shaped. Trapezoidal shape linkers have also been studied by using a carbazole core, which always led to **scu** nets with the usual conformation and rotation of the arms, but with a slightly decreased C_s symmetry, which also led to decrease the Zr-cluster symmetry to C_{2v}.[77,80–82] This is

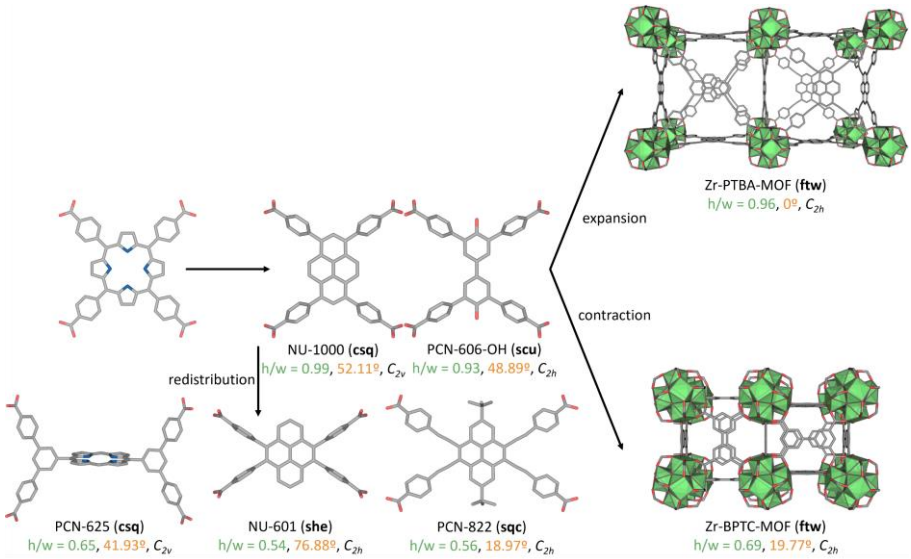


Figure 3.9. Representation of some rectangular linkers used to substitute the TCPP in the assembly of Zr-MOFs guiding to different underlying topologies according to their metrics by expansion, contraction or redistribution of the points of extension that modify the h/w ratio and rotation of the carboxylates.

in line with the proposed **shp**-**scu** disordered relationship, as both nets are the only examples when the linker exhibit a trapezoidal shape, and the desymmetrization thermodynamically favored the **scu** formation.

On the other hand, the contraction of linkers has not been extensively studied, as generally the pioneering ligands are the most basic and smaller as possible. As polytopic linkers are based on a central core extended with *para*-benzoate moieties, the phenyl ring can be erased in order to target MOFs constructed with smaller windows and cavities sizes (Figure 3.9). This strategy was developed by the group of Li, targeting an unusual **ftw**/**kle** net in a Zr-MOF constructed with a rectangular shaped linker that exhibits a 0.69 h/w ratio.[55] This MOF represented "the exception that proves the rule", as it is the only rigid linker with such a desymmetrization able to construct the default **ftw** net, which requires a square shape. By taking a closer look at the structure, the dissymmetric elongation force the linkers to alternate both orientations, requiring that Zr-clusters tilt towards shortest distance and decreasing

the overall symmetry of the system. We noticed that each position of the linker corresponds to the linker distribution in **she** and **soc** nets, as the linkers are connected to the hexagonal plane or to the trigonal antiprism conformations of the Zr-cluster, being the **ftw** a merged net of the formers (Figure 3.10). To the best of our knowledge, this observation has never been reported before. To afford this phase, the carboxylate groups in the linkers are not completely planar and rotates 2.77º in one orientation, forcing to the linker in the other orientation to rotate up to 19.70º to perfectly match into this space, as both orientations are not related by symmetry. We postulate that the exclusivity of this structure is given by the small size of the organic MBB, which in average is quite similar to the same size of the inorganic MBB (6.13 A) according to its width and height. In fact, an assembly with the analogue pyrene core yielded the isoreticular MOF.[83]

These findings suggest that, by controlling the synthetic conditions, other rectangular linkers may be used for constructing the **ftw** nets in Zr-MOFs. However, it should be noted that there is a limit in the ligand aspect ratio, the orientation and symmetry of their carboxylate groups and the linker size respect to the Zr-cluster which such a net will no longer be thermodynamically favored. An extended linker that keeps the same 0.69 h/w ratio will promote the formation of a less-connected cluster, as the size compared to the Zr-cluster will be unbalanced and the linker would require an unfavored bending to afford the underlying **ftw** topology. This is indeed confirmed for linkers with decreased ratio due to a redistribution of the points of extension (Figure 3.9). For example, a porphyrin core can be extended in just two directions and then branched into another two each one, obtaining a rectangular linker with a 0.65 h/w ratio. Its extension with the Zr-cluster yielded PCN-625, and according to its simulation, exhibits a **csq** net with 41.93º rotation of the phenyl arms.[84] Again, the strong desymmetrization into the rectangular shape deviates the rotation from 50-60º, as in the previous case of the **ftw** net. This effect is also observed for pyrene-substituted linkers, changing the common 1,3,6,8-siting to 4,5,9,10-siting of benzoates, which increase the dihedral

angle due to steric interactions up to 76.88º. As expected, this range corresponds to the formation of the **she** net, which is afforded despite the low 0.54 h/w ratio that caused the decrease of symmetry of the Zr-cluster to C_{3v}.[85] Furthermore, the extension of this linker with a triple bond slightly increase the ratio to 0.56, enabling a more planar conformation. However, the size of the linker prevents the formation of the **ftw** net and promotes the formation of a **sqc** net, where the symmetry of the cluster is distorted from the ideal cubic to D_{2d}.[86] Here, the rotation is decreased to 18.97º, which is less than in the previous **sqc** Zr-MOFs. In fact, it occurs a similar rotation to the linker than in the distorted **ftw** net.

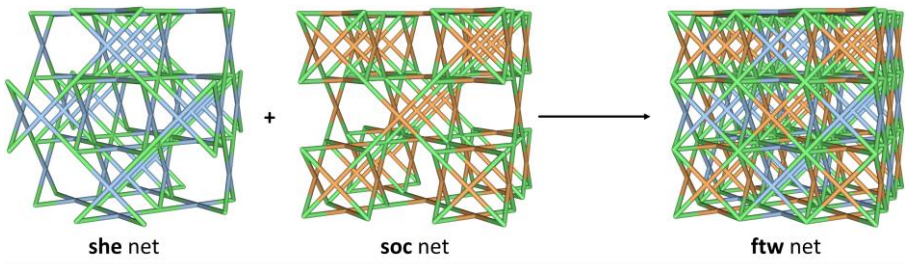


Figure 3.10. Schematic showing the merging of **she** and **soc** nets into the **ftw** net.

Beyond these units, a better core to mimic the square porphyrinic shape but barely used is the tetraphenylethylene (TPE) moiety. It was not until last year that firstly appeared in literature, which was used for constructing a **she**-type Zr-MOF which crystallized in the ideal *Im-3m* system.[87] The linker exhibited a perfect square conformation due to the disorder in two orientations of the ethylene unit, and the proximity between all the aromatic rings caused the rotation to 90º. This is not surprising, as this net is the most symmetric to obtain for regular linkers when the **ftw** is prohibited, favoring the most symmetric D_{3d} conformation of the cluster. The flexibility of the TPE moiety also unveiled a **scu** polymorph, which according to its simulation crystallized in the *Cmmm* space group and exhibited a rectangular shape (0.76 ratio) and a C_{2h} symmetry with a 53.01º rotation. The same case was observed by extending symmetrically with an additional phenyl ring in the arms: three different polymorphs were reported with the corresponding **ftw**, **csq** and **scu**

underlying topologies. The first one, PCN-94, crystallized in the *Pm-3m*, exhibiting a square-shaped, planar conformation of the linker with the disordered central core.[88] The second one, PCN-128, crystallized in the *P6/mmm*, exhibiting a rectangular 0.69 ratio and a C_{2v} symmetry with a 48.25º rotation.[89] The third one, LIFM-114/WSU-5, crystallized in the *Fmmm*, exhibiting a rectangular 0.68 ratio and a C_{2h} symmetry with a 54.59º rotation in a 2-fold interpenetrated structure.[88,90] In addition, the extension with a naphthalene here also decreased the ratio to 0.61 and a C_{2h} symmetry with two different rotations of 44.91 and 55.03º due to the transversal parameter.[91]

Recently, more rectangular shaped ligands have been developed and studied for deciphering its effect on the assembly of Zr-MOFs, such as 1,2,4,5-tetrakis(4-carboxyphenyl)benzene (4-TCPB) by using a central benzene core. It can also be regarded as the dissymmetric contraction of the biphenyl unit. Its strong rectangular form (0.56 h/w ratio) as well as the rotation of the phenyl arms (36.74º) due to the close proximity of the *ortho*-substituted rings led the linker adopt a C_{2h} symmetry, and therefore promoting the formation of a **scu** net.[92] Interestingly, the mono-substitution with a nitro group in a free position of the central core forced the linker to adopt the same conformation but reducing its symmetry to C_2 and increasing the ratio to 0.67 due to the steric hindrance.[93] This fact slightly modify the rotation up to 57.19º and produce a three-fold twinning of the **scu** net, which average resulted to be the **shp** net. Introducing bromo groups in both free positions of the 4-TCPB produced a similar effect obtaining a 0.64 ratio but modifying the symmetry to the C_{2v} due to the rotation toward the same direction in 52.19º, which directs to the **csq** net formation.[93] These studies confirmed that the effect of the steric hindrance in linker functionalization can induce a topological transformation. However, it was demonstrated that, by adjusting the synthetic conditions, a plethora of structures can be achieved similar to the case of the porphyrin Zr-MOFs, which frustrates the topology prediction of the underlying nets. By using different modulators, solvents or amount of modulator, the assembly

of Zr-clusters with the di-bromo-4-TCPB yielded four different structures: the already identified **csq** net, the **shp** net, the **she** net, and a new 4^3,5-c net.[94] This is not surprising, as many reports have been studying the effect of synthetic conditions to control the phase purity when exists other polymorphs of Zr-MOFs built with the porphyrin unit, elucidating the principles to control the kinetical or thermodynamical products.[95–97] The most symmetric **she** net was formed when the linker adopted the same C_{2v} symmetry and ratio but with a higher rotation of the carboxylate groups (71.03º).[94] Similar to the nitro-4-TCPB, the linker can adopt the C_{2h} symmetry with a 0.61 ratio to afford the isostructural three-fold disordered **scu** net.[98] Additionally, a novel 4^3,5-c topology was synthesized also when the linker adopted the C_{2h} symmetry. However, the linker exhibits three different conformations according to their crystallographic positions: the most regular adopting a very elongated rectangular shape with a 0.49 ratio and 64.65º rotation; a trapezoidal shape with 60.26º rotation, and a very desymmetrized trapezoidal shape linker with two different 69.66º and 89.18º rotations.[94]

The same phenomenon was observed by the group of Gándara when introducing a bulkier group as two phenyl rings obtaining two different MOFs.[99] Surprisingly, although the linker contains six carboxylic acids, it prefers to decrease its connectivity to four due to the impossibility of forming the **hxg-b** net because of the steric hindrance that forces to have a higher rotation compared to that net, which need a different functionality or a symmetric extension to afford it. The first MOF crystallized in the $P6_3/m$ group exhibiting a **stp** net. The ligand exhibited a not regular trapezoidal shape with the two different rotations of 85.61º and 80.77º, according to the bidentate and monodentate coordination of the carboxylate groups, respectively. The desymmetrization of the molecule forced the cluster to be desymmetrized with two independent zirconium atoms according to the coordination of each carboxylate. The overall geometry is also distorted to a trigonal prismatic geometry, which is in stark contrast to the other more symmetric hexagonal or trigonal antiprism geometries found. The second MOF crystallized in

the *C2/c* space group exhibiting the less regular **hfp** net. Here, the desymmetrization in the ligand is increased and revealed three different conformations: a regular rectangle of 0.63 ratio and 55.04º and 64.28º rotations; another rectangular shape of 0.65 ratio and 45.54º and 53.88º rotations; and a very distorted trapezoidal shape with four independent rotations (16.00º, 43.83º, 78.95º and 80.11º). This asymmetric environment led to form a Zr_6O_8 cluster core with six independent Zr atoms, in an irregular, distorted cubic shape. These contributions shed light on the effect of the rectangular shape and the rotation of the carboxylate groups in the organic MBBs for the discovery of new nets with unprecedented cluster shapes.

The last example of a rectangular organic MBB displaying the strongest elongation in the core was based on a tetrathiafulvalene (TTF) core with four pending benzoates (TTFTB), which will force the benzoates to rotate due to its proximity to each other, but less hindered since the aromatic ring is 5-membered.[100] Upon assembly with the Zr-cluster, the MOF formed a **scu** net that crystallized in the *Cmmm* system, displaying a 0.56 ratio and 50.31º rotation in a C_{2h} symmetry. In order to increase this rotation, methyl groups were introduced in the 3-position of the phenyl rings (Me-TTFTB), driving to a **she**-MOF which crystallized in the *Pm-3m*. The rotation of the linker changed to 76.52º, and the linker adopted the C_{2v} symmetry and a 0.55 ratio to afford this net. Curiously, almost simultaneously, the group of Gascón reported the same combination that yielded two different 2D Zr-MOFs with underlying **sql** net under appropriate conditions.[101] One of them also exhibits the 8-coordinated Zr-cluster, which is doubly bridged to the neighboring clusters in a bended C_{2h} symmetry form, displaying a higher 0.59 ratio and the rotations of the carboxylate groups in 36.69º and 43.57º. In contrast, the second one is 4-c in an almost square shape Zr-cluster (0.97 ratio), but the remaining four positions of the cube are occupied by TTFTB molecules that oriented perpendicular to the net, bridging a neighboring cluster. In this strange structure, the linker

exhibits an almost planar conformation due to the disorder (6.56º rotation) and a 0.62 ratio.

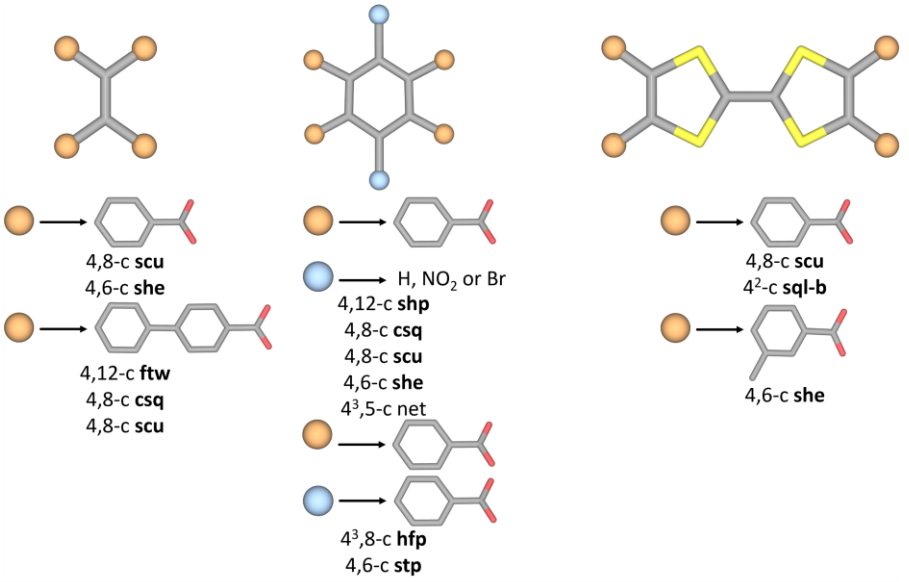


Figure 3.11. Topological diversity in Zr-MOFs assembled with linkers with different rigid cores according to the substituents in the arms modifying the linker metrics or introducing bulky groups in neighboring positions.

Beyond these examples, all the rest of reported linkers in Zr-MOFs can be considered as modified versions of the former core except for those who are based on square shape MBBs. There are just four examples: two represented by a rigid cyclopentadiene cobalt complex and a spirobifluorene that form **ftw**-MOFs due to directionality of the square cores;[102,103] and two other cases based on flexible units instead of rigid ligands. These two later MOFs are constructed with a macrocycle[104] or a palladium-based complex.[105] As both MBBs can adapt its conformation easily, they adopt the square conformation to form the **ftw** net.

The modifications of the linkers have been focused on the dissymmetric elongation. The first group studying this effect was from A. J. Matzger. They synthesized a perylene-based tetratopic linker, which can be viewed as an elongation of the

biphenyl unit.[54] The resulting Zr-MOF has the underlying **csq** net due to the rectangular shape of the linker (0.87 ratio) and the rotation of the carboxylate groups (49.99º). Then, the group of J.-R. Li elongated the biphenyl unit in the other direction by inserting an extra benzene ring in the core (Figure 3.12a). Upon assembly with Zr^{IV}, a **sqc** MOF with a distorted D_{2d} cluster and a rectangular ligand with a C_{2h} symmetry (0.75 ratio and 44.91º rotation) was observed.[106] This was also the case for the isoreticular example introducing pyridine units. However, the group of Li reported that other nets can be achieved when introducing different functionalities or adjusting the synthetic conditions. For example, the introduction of diamines or benzothiadiazoles in the central ring induced the formation of a **scu** net, in which the linker adopted a C_{2h} symmetry with a 0.76-0.79 ratios and 48.47-52.56º rotation, respectively.[107,108] But, when the linker adopted a C_{2v} symmetry with a 0.81 ratio and 51.84º rotation, the most symmetric **csq** net was synthesized.[108,109] In addition, a new 4,4,12-c **csp** net was achieved by combining both linkers in the C_{2h} and C_{2v} symmetries, with 0.76 and 0.68 ratios and 44.52 and 53.71º rotations, respectively.[108,110] This topology can be considered as a 3p-2p merged net of the 3D **sqc** and 2D **sql** nets.

Recently, the elongation in this direction has been further explored by other groups. For example, instead of a benzene core, two triple bonds were introduced by Zhang and coworkers for crystallizing a Zr-MOF in the *Cmmm* space group with an underlying **scu** net.[111] Here, the linker displays the C_{2h} symmetry with a 0.76 ratio and 49.97º rotation of the carboxylate group. Then, the group of Deria expanded this elongation by using a phenyl-ethynylene core, resulting in a Zr-MOF with a different underlying **csq** net.[112] According to its simulation, the linker exhibited a C_{2v} symmetry with a 0.60 ratio and 40.15º rotation of the carboxylates. Moreover, an anthracene derived-linker yielded the same net, as well as two other polymorphs by modification of the synthetic procedure: the **scu** and **shp** nets, both related by symmetry.[113] Another linker that yielded the **scu** net was reported by Eddaoudi and coworkers. This linker is based on a naphthalenediimide core that formed a Zr-

MOF in the *Cmmm* group.[114] Here, the linker displayed again the C_{2h} symmetry with a 0.62 ratio and 48.74º rotation. At this point, it is clear that the desymmetrization into rectangular-shaped linkers prompt the formation of nets based on the 8-c Zr-cluster. However, there is not reported any control among them, being the isolation of a determined phase just a matter of synthetic conditions. Another example that illustrates this fact has been recently published by Li and coworkers. They used a tetratopic linker with a 1,4-phenylene-diamine core to construct HIAM-402 and HIAM-403, which exhibited the **sqc** and **scu** nets, respectively.[115] In both cases, the high flexibility imparted by the two sp^3 nitrogen atoms resulted in a C_{2h} symmetry, but with 0.82 and 0.86 ratio and the twisting of the carboxylate groups in 42.43 and 50.71º, respectively. In general, both Zr-clusters are similar except for a slight distortion in the coordination environment in the **sqc** MOF from the regular cubic shape, which is in agreement with previous results.

Dissymmetric elongation of other cores has also been recently studied. For example, Farha and coworkers recently expanded the TTF moiety by introducing a phenyl ring between the two imidazoles, obtaining a Zr-MOF with also an underlying **scu** net.[116] The linker crystallized with a C_{2h} symmetry exhibiting a very elongated rectangular shape, with a 0.51 ratio and 16.18º rotation of the carboxylate groups. Another very interesting example was performed studying the elongation of a more rigid biphenyl core, which can limit the rotation of the carboxylate groups and strictly depend on the h/w ratio. This is indeed the case for two different Zr-MOFs. The first one was the azobenzene moiety, where the translation modifies its shape from rectangular to rhomboidal and decreases the aspect ratio of the organic linker, frustrating the formation of an isoreticular **ftw**-MOF.[55] As in the shorter version, the linker needs to adopt two different conformations to fit in the **scu** structure in both *trans* and *gauche* conformations: the first one presents higher rotations (10.84º, 13.38º, 13.91º and 14.02º) in a planar 0.56 ratio, whereas the other needs to slightly bent its conformation with a 0.57 ratio and almost planar carboxylate groups (1.47º, 3.30º, 6.11º and 7.30º). Due to the absence of freedom for rotating the carboxylate

groups, the linker cannot drive to the most thermodynamic **csq** net, which is limited to form subnets of the **ftw** net. Interestingly, all the previous **scu**-MOFs crystallized in the underlying derived **tty** topology, where the linkers are oriented in the same direction. However, in this structure, the linkers adopt both orientations in the underlying 3^2,8T132 topology (Figure 3.12c). The second Zr-MOF further decreases its ratio to 0.44 by replacing the azo bound with an extra phenyl ring, making impossible to assemble in the **scu** net as cannot fit due to the metrics, evolving to an **lvt-b** net.[55,117] In this structure, the cluster is forced to decrease its connectivity to four, which was never been observed before, adopting

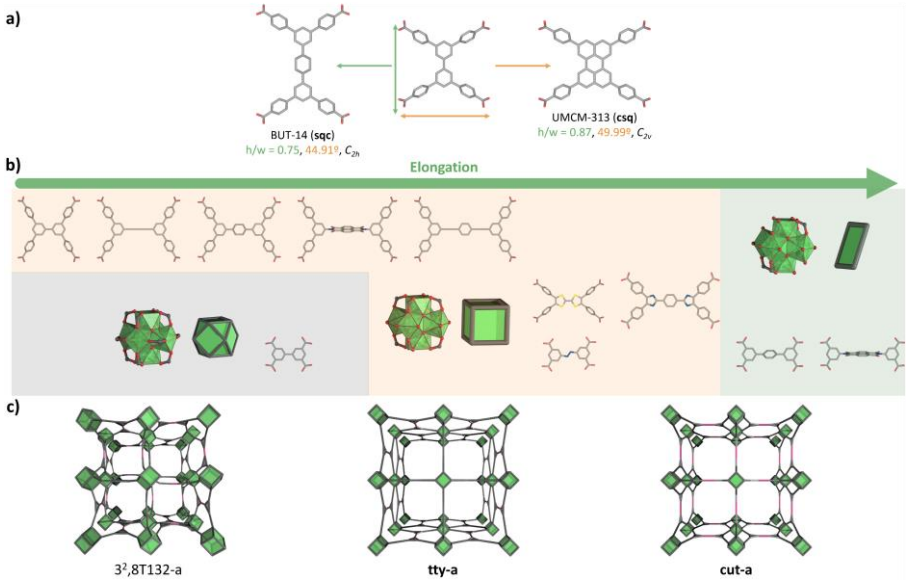


Figure 3.12. a) Illustration of the two possible directions for the dissymmetric elongation of 4-c rectangular linkers. b) Representation of the elongation of three different cores by introducing functional groups between the aromatic rings. This parameter influence in the connectivity of the Zr-cluster, decreasing from 8-c cubic (orange area) to 4-c rectangular (green area) SBUs in h/w ratios smaller than 0.5. The black area represents the exceptional case with smaller linkers that can drive to 12-c cuboctahedral Zr-SBUs if there is a smaller elongation. c) Schematic of the three derived nets of the **scu** net in augmented form when splitting the 4-c node. Note that the elongation can be performed in just one direction (**tty** and **cut**) or in both directions (3^2,8T132). Generally, the **tty** is the underlying topology in most of the scu-derived nets, but when the linker is smaller drives to the 3^2,8T132 topology.

a rectangular shape (0.55 ratio) induced by the strong rectangular shape of the linker. In fact, the 4-c SBU resembles that of the dinuclear paddlewheel cluster, as it was the only one that could yield this type of net. The carboxylate groups also rotate 21.64º in the same direction, displaying the same C_{2h} symmetry, and forming another subnet of the **ftw** topology. This study was further confirmed by Farha and coworkers, decreasing the aspect ratio to 0.33 by substituting the phenyl ring by a naphthalenediimide, obtaining the same underlying **lvt-b** net with 8.82 and 15.20º rotations in the same C_{2h} symmetry.[118] To the best of our knowledge, this linker shows the most elongated desymmetrization.

Instead of elongating symmetrically to obtain a rectangular shape, the elongation can be performed in two arms leading to a trapezoidal shape, as reported by the group of Matzger.[33] Combining this linker with the Zr-cluster yielded a **csq** MOF that crystallized in the $P6_3/mmc$ system.[119] Here, the longer arms permitted the formation of this net as they can rotate 55.13º, but forced the bending of the linker to try to accommodate the shorter arms rotating 30.91º. Another kind of desymmetrization that can drive to a trapezoidal linker is by designing a "K"-shaped MBB, combining the directionality of the terphenyl unit and the benzimidazole core.[120] This linker produced a new trinodal 4^2,8-c net, exhibiting triangular, square, and hexagonal channels where isolated Zr-clusters were found in the triangular channels. Here, two different crystallographic linkers exhibit rotations of 30.74 and 46.97º in one linker, and 33.62 and 39.40º in the other linker.

Beyond the elongation, other desymmetrizations can influence in the assembly process. For example, the out-of-plane rotation can form bent, tetratopic ligands that affect to the directionality and h/w ratio. This effect was studied by Serre *et al.* introducing a methylene unit in the rigid biphenyl unit, which imparted high flexibility to the linker for reticulate the first Zr-**soc**-MOF.[121] A slight rotation of 9.52º and a 0.64 ratio produced a linker that exhibited a C_{2v} symmetry, which decreased the connectivity to 6 in a triangular antiprism conformation of the Zr-cluster in the presence of a tetratopic ligand. The methylene groups pointed to the

1D channels of the structure, creating bigger cubic pores with a ball shape. If the linker is extended with phenyl rings at the arms, the rotation is promoted to adopt a more stable 8-c cubic Zr-cluster in an unusual **scu** net. The group of Zhou reported an SO_2-functionalized linker that, for the first time exhibited the C_{2v} symmetry in a **scu** net. In addition, PCN-901-SO_2 crystallized in a very symmetric *P4/mmm* space group exhibiting two kind of channels, one with the linkers bending inside, and the other with the linkers bending outside.[122] Surprisingly, the linker also exhibited a rotation of 85.35º, which is more common observed in **she**-MOFs, and a high 0.92 ratio.

In-plane and out-of-plane translation operations were also explored by researchers in tetratopic ligands. First, the group of Li expanded the azobenzene linker to yield another **scu** MOF, but with the **tty** derived net.[123] The linker exhibited the conventional C_{2h} symmetry, a ratio of 0.89 and rotations of 47.36 and 50.65º. Then, the group of Farha studied the out-of-plane translation effect with paracyclophane scaffolds.[43] They obtained two different Zr-MOFs: the first one displayed a linker with a ratio of 0.60 and a rotation of 49.50º in a **scu** net; and the second displayed a disordered linker with a ratio of 0.61 and a rotation of 79.24º of the carboxylate groups in a **she** net. A further elongation with triple bonds in different positions produced a linker with 0.74 ratio and carboxylate groups rotating in 1.12 and 15.47º, to form a novel 4,8-c net with a less-symmetric 8-c D_{2d} Zr-cluster.[124] Finally, the in-plane translation combined with a strong elongation have been recently studied by Schröder *et al.* They used a naphthalene unit between two isophthalates. They discovered a new Zr-MOF with an unprecedented 3,5-c binodal **mfm** net. Interestingly, the Zr-cluster shows the same coordination of the carboxylate groups as the previous 4-c Zr-MOFs but, in this case, two pairs of clusters are joined together by their open metal sites *via* two formates, with an overall distorted pyramidal geometry. This structure is induced by the rhomboidal shape of the linker, which crystallized in a C_{2h} symmetry displaying a ratio of 0.37 and rotations of the carboxylate groups of 9.66, 12.50, 14.93 and 16.77º. It is worth mentioning

that the connectivity of this cluster and the formate pair bridging have never been observed before in a Zr-MOF.

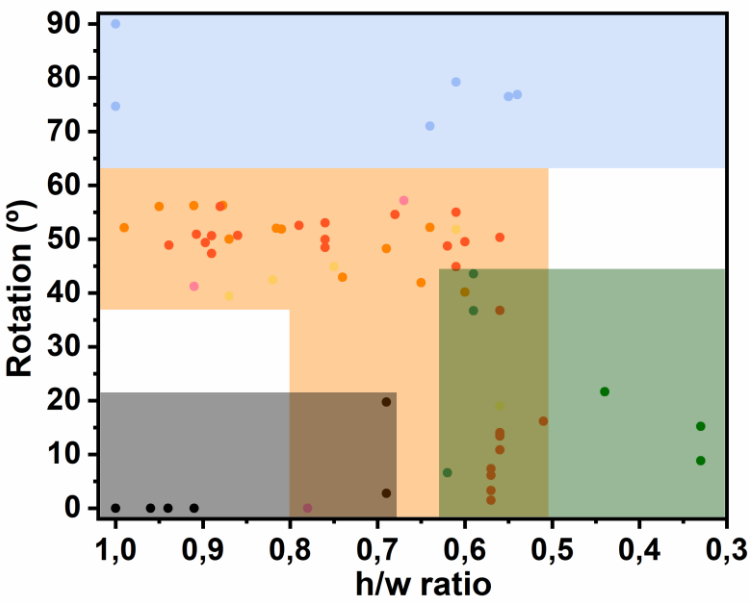


Figure 3.13. Graphic representing the square/rectangular linkers as a function of their aspect ratio and carboxylate rotation in Zr-MOFs. Four different areas can be differentiated: black (based on 12-c cuboctahedral Zr-clusters); orange (based on 8-c cubic and 12-c hexagonal prism Zr-clusters); blue (based on 6-c hexagonal Zr-clusters); and green (based on 4-c rectangular Zr-clusters). Dots represent: ftw-nets (black), **shp**-nets (pink), **csq**-nets (orange), **scu**-nets (red), **sqc**-nets (yellow), **she**-nets (blue), **lvt**- and **sql**-nets (green).

Once revisited all the Zr-MOFs constructed with square and rectangular ligands, we endeavor in understanding the formation of a specific cluster or a net guided by the symmetry and metrics of the organic MBBs. We represented the h/w ratio versus the rotation of the carboxylate groups of the linkers in the different crystal structures according to their topology (Figure 3.13). We limit the scope of the nets to those edge-transitive and most regular nets, excluding isolated examples with underlying new nets that were obtained under different conditions. Although there is not a clear explanation on the formation of a specific net, we could observe a relation between both factors and a tendency to form four different areas that match

with the four main different clusters: the 12-c cuboctahedral cluster (black), the 8-c cubic and its three-fold disordered 12-c hexagonal prism clusters (orange), the 6-c hexagonal cluster (blue), and the 4-c square and rectangular cluster (green). From the graph, we can conclude that: (i) linkers with low rotation and high ratio tend to form the default **ftw** net; (ii) linkers with rotations higher than 70º tend to form the **she** net; (iii) linkers with low rotations and low ratio tend to form structures based on the 4-c defective Zr-cluster such as **sql** or **lvt** nets, and (iv) linkers with rotations between 35 and 60º tend to form structures based on the 8-c cubic Zr-cluster, such as **csq**, **sqc**, **scu** or the disordered **shp** nets; as well as linker with lower rotations when the linker has a decreased ratio between 0.5 and 0.8 in areas overlapping the 12-c or 4-c cluster areas.

3.2.1.2. RE-clusters combined with 4-c square/rectangular organic MBBs

Similar to the Zr^{4+} and Hf^{4+}, RE-based clusters have been widely explored for the construction of high-connected nets due to its structural similarity with the Zr-cluster. However, their chemical environment is a bit different, and this fact affects to the chemical behavior, which strongly influences in the cluster and structural formation. The first reported structure assembled with a tetratopic linker was performed by the group of Eddaoudi. They reported a series of RE-**ftw**-MOFs based on square and rectangular linkers and a cuboctahedral hexanuclear RE-fluorocluster.[125] Surprisingly, both types of shapes afforded the 12-c cluster, in quite contrast to the Zr-hexanuclear (Figure 3.14). For example, the 3,3'',5,5''-tetrakis(4-carboxyphenyl)-*p*-terphenyl (TCPT) linker shows a 0.78 ratio, and the assembly of this skeleton with the Zr-cluster yielded an 8-c cubic conformation in the **scu**, **sqc** and **csq** nets. Due to the elongation, the linker exhibited two different crystallographic positions to fit in this net in alternated orientations with an underlying **kle** derived net. The same occurred in the elongated linker with an ethynyl group in the arms that increased the ratio to 0.89. To accommodate both

orientations, the RE-cluster is tilted toward the shorter connection. The same kind of structure was found when using the contracted biphenyl unit, obtaining an analogous Zr-MOF, with the same ratio and similar rotations of the carboxylate groups (2.11 and 17.44º).[7,126] However, when using the more elongated azobenzene tetracarboxylate linker, instead of forming the less-connected **scu** net, the RE-cluster remains 12-connected but changes to the **kxe** derived net to accommodate the linker in the most suitable and symmetric conformation, with a ratio of 0.55 and rotations of the carboxylate groups of 7.93 and 11.15º.[7,126] This observation was already pointed by Li and coworkers, highlighting the different effect of desymmetrization of the organic MBBs when assembling with the Zr or RE SBUs (Figure 3.14). The difference between them can be according to three possible reasons: i) the difference in the coordination environment, where Zr is 8-coordinated in an tetragonal antiprism conformation and the RE metals are 9-coordinated with an additional OH^-/H_2O; ii) the difference in the charge, as RE are 3+ and Zr 4+; iii) and the difference in the size, being RE much bigger than Zr. All these factors may contribute to the RE-cluster to behave in a more flexible conformation, remaining unaffected by the elongation ratio of the linkers.

While elongation is not deviating from the default **ftw** net when combining square/rectangular ligands and the RE-fluorocluster, we have observed that the rotation of the linker can tremendously determine the assembly of different nets, or even the evolution of the cluster into a completely different one. In fact, even though the most regular porphyrin based linker was used, its assembly with RE metals in the presence of fluorinated modulators unveiled an **shp**-MOF. The 12-c hexagonal prism conformation was adopted by a 2-fold disordered new nonanuclear cluster, exhibiting a tricapped trigonal prism conformation of the metal ions (Figure 3.14).[127,128] We believe that the formation of the **shp** net over the **ftw** net is due to the rotation of the phenyl ring into 69.10º because of the repulsion of the hydrogen atoms in the arm and core, adopting the C_{2v} symmetry needed for this net, with a slight elongation into a ratio of 0.98. In fact, this was further confirmed by

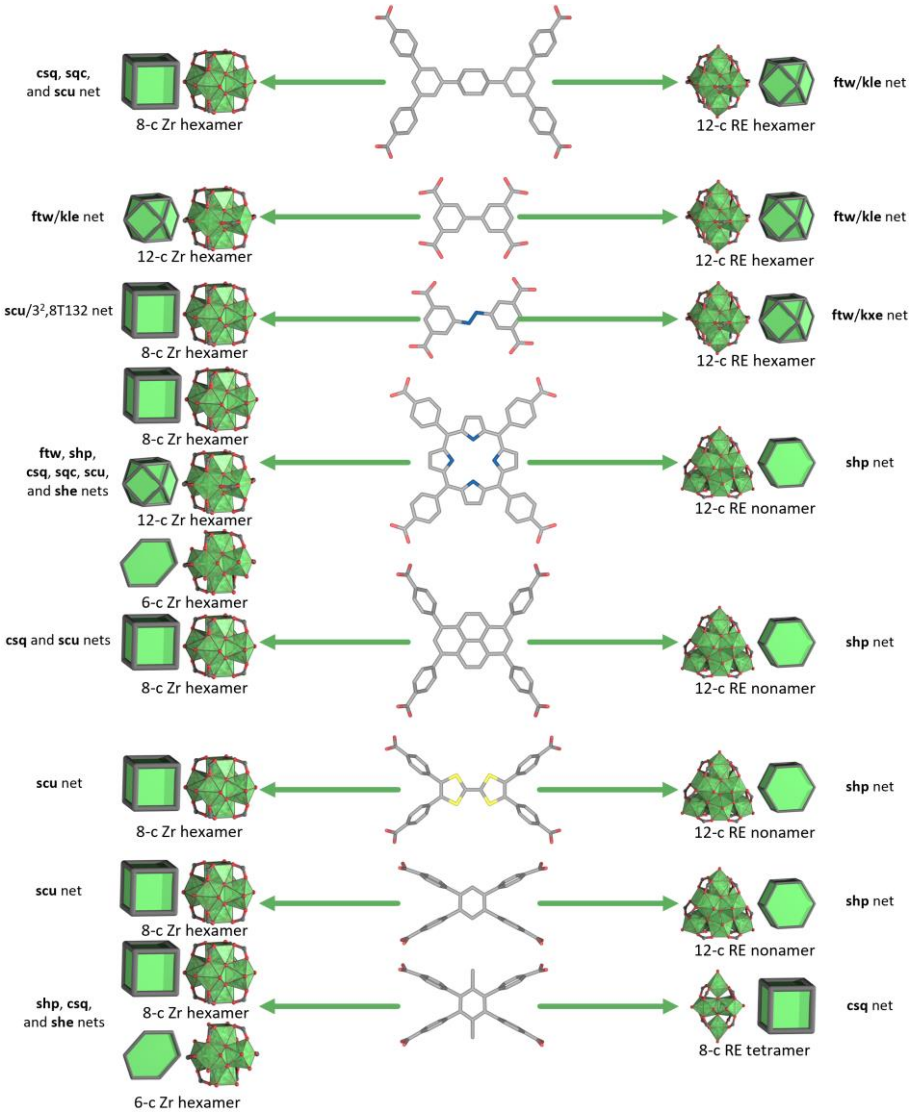


Figure 3.14. Comparison between the assembly of some 4-c square/rectangular linkers with Zr- or RE-clusters. For the Zr-case, the robust Zr-hexamer is always present fully connected or presenting defaults of connectivity; while it prefers to evolve and form different clusters without any vacancy, such as the nonamer or tetramer, for the RE-case. The default **ftw** net can be obtained in RE-MOFs despite the elongation of linkers, which is certainly difficult for Zr-MOFs. However, the rotation of the carboxylates due to the steric hindrance influences and prevents the formation of the **ftw** net and usually drives to the formation of the **shp** net with a RE_9-fluorocluster.

the groups of Sun and Zhou, reporting a mixed-linker RE-MOF with the TCPP linker and a second linear linker. As the **ftw** net cannot be constructed due to the rotation, the arms prefer to rotate and drive to the **she** net.[129] However, because of the difficulty in isolating defects in the connectivity of the RE-cluster, this structure cannot be isolated. However, introducing an extra ditopic linker stabilized the conformation of the square shaped linker in the same position of the **she** net and directing to a new underlying **tam** topology, which can be regarded as a 3p-3p merged net of the **she** and **pcu** topologies.

Regarding other central cores used in tetracarboxylate linkers for the assembly of Zr-MOFs, the only one that could drive to the assembly of **ftw**-MOFs is based on the spirobifluorene core, which exhibits some flexibility to adapt a perfect square shape and coplanar conformation of the carboxylate groups.[103,130] For those presenting a steric hindrance with the phenyl rings in the arms, the rotation promoted connectivity defects in the 8-c cluster. Nevertheless, replacing Zr- by RE-clusters induced the formation of isoreticular **shp**-MOFs with the 12-c nonanuclear cluster, as in the previous case. This was observed with the pyrene, 4-TCPB and TTF central cores, displaying different rations of 0.99, 0.64 and 0.49, respectively; and rotations of 47.28, 58.91 and 42.62 and 58.01º, respectively (Figure 3.14).[131–134] Curiously, in contrast to in the Zr-MOFs the linkers exhibited the C_{2v} symmetry, exhibiting the underlying **shp** net with the C_{2h} symmetry; due to the difference of the **scu** threefold disordered structure versus the new nonanuclear cluster. Indeed, for some specific metals (Yb and Lu) when combined with the pyrene-based tetratopic linker, an undecanuclear RE-cluster was achieved in the same **shp**-MOF, with two extra metals in the apical positions.[135]

In order to study the effect of the torsion angle produced by the steric hindrance in RE-MOFs, researchers increased the rotation by introducing functional groups in the *ortho*-position. Trikalitis *et al.* were the pioneering in this area, introducing two methyl groups into the 4-TCPB linker.[136] Surprisingly, the combination of an almost perpendicular carboxylate group (rotation of 78.02º) and a strong elongation (ratio

of 0.56) with C_{2v} symmetry promoted the evolution of the RE-cluster to a new 8-c tetranuclear cluster in a rhombic shape with planar D_{2h} symmetry, to assembly in a **csq** underlying net. This tetranuclear cluster is different from the previously reported 6-c cluster in a tetrahedral conformation reported by Rosi and coworkers in the presence of linkers or modulators with amino instead of fluoro groups in the *ortho*-position.[137] In a similar study, Li et al. introduced one or two amino groups in the TCPT linker that induced defective RE-clusters, which is quite uncommon unless an excess of modulators coordinates to stabilize the hexanuclear cluster.[138] In the presence of just one amino group, the linker adopts the C_{2h} symmetry with the rotation of 49.37º and a ratio of 0.79, forming the first RE-**scu**-MOF with six capping carboxylate groups and four open metal sites in the fluorocluster. In the presence of two amino groups, the structure evolved into a new net comprising 10-c hexanuclear clusters with an elongated octahedron geometry. In this MOF, the linkers occupy three different positions, and all of them adopts the C_{2v} symmetry: they exhibit increasing rotations of the carboxylate groups in 55.42, 77.95 and 89.74º while decreasing its ratio down to 0.85, 0.84 and 0.80, respectively.

More defective clusters have been prompted by the use of trapezoidal shaped linkers. As mentioned before, a carbazole core promoted the desymmetrization of the organic MBB and prompted the same effect observed in the Zr-cluster, obtaining 8-c hexanuclear RE-clusters. The cluster is capped in two positions by monotopic carboxylate groups and exhibits four open metal positions in a **scu**-MOF.[134] The steric hindrance between the core and arms produced two rotations in 45.49 and 55.11º. When extending the arms with the transversal naphthalene, the arms preferred to orient in a rectangular shape because of the σ-bond rotation (ratio of 0.87) and rotation of 53.02º to assembly the more thermodynamically favored **shp** net with the 12-c nonanuclear cluster. Another trapezoidal shape was afforded by Zhou and coworkers, introducing four naphthalenes in a pyrene moiety in a less-symmetric distribution of the 1,3,5 and 9 positions.[139] Due to the π-π stacking, the trapezoidal linker appeared disorder and doubly bridging 8-c RE-

clusters in a new underlying 4,8-c **cyc** net. Finally, the trapezoidal shape can also be afforded by using an in-plane rotation introducing an amino group between two isophthalates. The combination of this linker with Y salt in the presence of 2-FBA promoted the formation of a defective 8-c hexanuclear cluster and a single metal ion (SMI) chelated by four ligands in a tetrahedral geometry. The MOF exhibited a novel trinodal 4^2,8-c net, with formates capping the vacancies of the Y-cluster, and a linker with a carboxylate groups completely planar bonded to the SMI and the other slightly rotates in 9.46º to bond the hexanuclear cluster. In contrast to the Zr-clusters, a linker with a similar skeleton promoted the formation of the 6-c trigonal antiprism in a **soc**-MOF.

Finally, it has also been explored the out-of-plane rotation in the assembly of RE-MOFs in combination with the torsion angle produced by a neighboring functional group. Zhou *et al.* introduced an amino group in the *ortho*-position of the benzoate arms in the biphenyl unit, forcing to rotate 76.78º; and a SO_2 pivot group in the middle of the biphenyl unit as a hinge, producing the bending of the molecule and a 0.83 ratio with a C_{2v} symmetry. This linker favored again the formation of the 12-c hexagonal prism nonanuclear cluster, reticulating a new edge-transitive 4,12-c **dfs** net. Interestingly, these last two **cyc** and **dfs** examples formed two new edge-transitive nets, which are characteristic by the double bridging of two building units to the same MBBs.[140] In fact, these nets can be formed by the parent **pts** and **stp** nets, respectively, by splitting one of the nodes into two pairs of vertices. Therefore, RE-MOFs can unveil new high-symmetric nets when combining with desymmetrized organic MBBs that are less-common to observe.

3.2.1.3. Zr-clusters combined with 4-c tetrahedral organic MBBs

The influence of desymmetrizating tetratopic organic MBBs with tetrahedral shapes have been narrowly explored in high-connected nets compared to the square/tetrahedral linkers. Still, similar effects were found in some reported

examples when combining them with the Zr-cluster. In fact, in addition to the 4,12-c **ftw** and **shp** nets, another edge-transitive **ith** net can be constructed if the tetrahedral building unit is chosen. However, in this case, the 12-c building unit must possess an icosahedral geometry. Interestingly, Yaghi *et al.* achieved this net by using the 4,4',4'',4'''-methanetetraylbenzoate (MTB) linker, which has a tetrahedral sp^3 carbon in the core, reticulating MOF-812 that crystallized in the *C2/c* space group.[141] To afford this net, both MBBs are distorted, and the Zr-cluster displayed an unprecedented icosahedral shape. Compared to the cuboctahedral cluster that can be skewed into a trigonal antiprism and a hexagon, the carboxylate groups in the former orientation remain unaltered, whereas the hexagonal conformation is highly distorted with four carboxylate groups acting as monodentate ligands and moving from the plane. The tetrahedral linker was highly distorted in two different positions: one elongated along the *b* axis with two different rotations of 42.21 and 95.32º; and the other one very distorted and elongated along the ac plane and all different rotations of the carboxylate groups (36.19, 45.43, 76.20 and 88.64º). Despite forming a high-connected net, the high distortion of both MBBs indicated its unfavored formation, which was not observed in any other Zr-MOF. Indeed, MOF-812 was obtained as a byproduct of a polymorph MOF-841, which could be obtained as an isolated product and exhibited more regular MBBs in an underlying **flu** net.[141] MOF-841 crystallized in the *I4/m* space group, and the tetrahedral linker displayed a more regular but elongated conformation, with a D_{2d} symmetry with a ratio of 0.90 and more planar carboxylate groups with a rotation of 17.84º. This decrease in symmetry in the linker promotes a symmetry decrease in the Zr-cluster from O_h to D_{4h} in the 8-c cubic conformation, with the remaining positions occupied by water or monocoordinated formates. Here, in the case of tetrahedral linkers, we observed the same phenomenon than in the square/rectangular shapes. Indeed, by elongating the MBB, the connectivity of the Zr-cluster decreases evolving to a different topology.

The symmetric elongation of the MTB linker with a benzene unit was reported by Zhou and coworkers, obtaining an isoreticular **flu** net crystallizing in the same *I4/m* system. The elongation unveiled a more regular MBB owing to the lack of repulsion of the benzene rings of the MTB linker, adopting a more planar conformation with a rotation of the carboxylate groups of 1.86º and a D_{2d} symmetry.[142] In this structure, the flexibility of the linker causes the loss of the C_3 rotation and distorting the tetrahedra with an elongation in the *c* axis in a ratio of 0.79. In addition, an unprecedented polymorph was reported by Lin *et al.* In this structure, there are two types of clusters: a 12-c hexanuclear cluster with a cuboctahedral geometry; and a 12-c octanuclear cluster with distorted icosahedral geometry, both linked by the tetrahedral linker.[143] Therefore, its underlying net is trinodal and exhibited a $4,12^2$-c **buh** topology. However, as already reported for the *d*PCN-224 (former PCN-221), a recent examination performed by the group of Lotsch disclosed the disordered nature of the hexanuclear cluster in the wrongly elucidated octanuclear cluster, which could be attributed to a four-fold and six-fold overlapping of orientational disorder, allowing the formation of this particular topology.[144] We believe that the rotational freedom of the carboxylate groups likely play a role in the formation of this MOF, being two planar (1.65º) and two perpendicular (85.43 and 89.45º) in a C_{2v} symmetry distorted conformation. In fact, this net was reported in an isoreticular structure where the linker was further extended with a triple bond between the benzene rings but remained in the same conformation and symmetry.[145] While deciphering the disordered cluster, the group of Lotsch could isolate another polymorph with a higher degree of disorder in their building blocks. This new structure crystallized in the trigonal *P-3c1* space group with a novel, complex tetranodal net.[144] Here, there are two crystallographically independent linkers and clusters, being one of each ordered and the others disordered in two different positions. The disordered building blocks along the *c* axis comprises upshifted or downshifted positions highly correlated. Accordingly, the net can be simplified as an ordered $4^2,12^2$-c model or in an average 4^2,15,18-c model. In fact, the disordered structure complicates the conformational analysis of the linker, which

may cause the formation of this product due to geometrical frustration of the ordered variant. These examples remark the difficulty in predicting polymorphs when flexible or disordered building blocks are assembled in reticular materials. In a similar example, the group of Trikalitis explored the functionalization of this linker with a sulfone group forming a five-member ring that reduced this flexibility, prohibiting the rotation of adjacent aromatic rings. When assembling with the Zr-cluster, a different **flu** net with significantly increased symmetry ($P4_2/mnm$) was synthesized, which can be attributed to the rigidity and bending of the arms in 164.73º, leading to a reduction of the symmetry to S_4.[146] In this polymorph, the Zr-clusters are not oriented in the same direction, being the central of the cell rotated in 90º with respect to those at the corners; while the linkers are elongated in a ratio of 0.94 and the carboxylate groups rotate 60.67º.

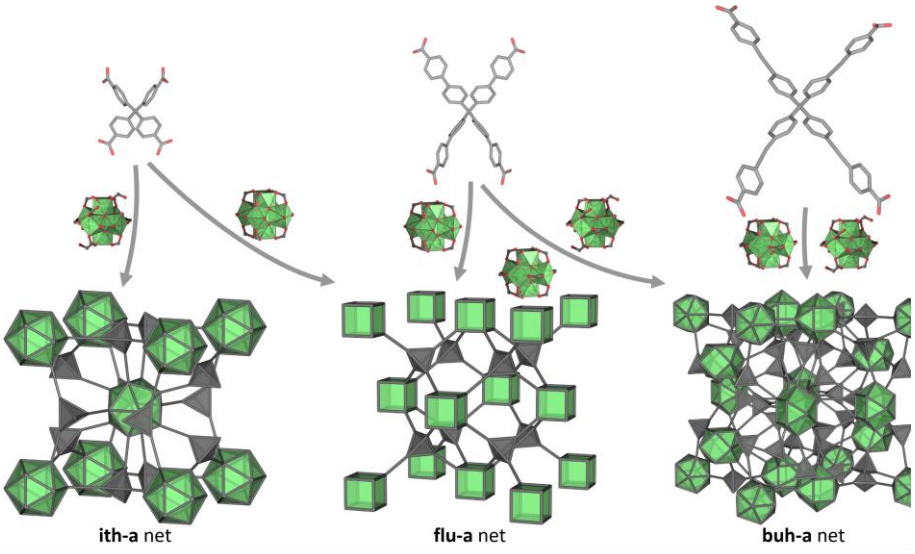


Figure 3.15. Structural evolution of Zr-MOFs when increasing the tetrahedral linker size from the 4,12-c **ith** net based on icosahedral Zr_6-SBUs, to the 4,8-c **flu** net based on cubic Zr_6-SBUs or the $4,12^2$-c **buh** net based on cuboctahedral and icosahedral Zr_6-SBUs.

Other central cores with tetrahedral shape have been explored in the quest for novel Zr-MOFs. Janiak *et al.* reported the use of an adamantane tetraphenyl-based linker

that unveiled two different polymorphs: the expected **flu** net with an elongated linker (0.94 ratio) and a slight rotation of the carboxylates (15.04º); and an intermediate phase of a novel 3,4,10-c net, exhibiting an unusual 10-c cluster, a distorted tetrahedral linker with rotations of the carboxylate groups of 64.99 and 82.52º, and a linker exhibiting a default of connectivity in a trigonal shape, with a free carboxylic pointing the pores of the structure.[147] In fact, this very interesting net is related to the **flu** topology, as can be interconverted by merging pairs of 3-c nodes into 4-c tetrahedral nodes via overlapping two out of the three edges and therefore, decreasing the connectivity of the 10-c cluster to 8. In fact, this transformation could be performed under vacuum and heating at 120-190ºC, and the extra linkers were expelled to the pores.

The biphenyl unit was firstly reported by the group of Matzger to adopt a tetrahedral conformation, where the two central aryl rings formed a distorted tetrahedral shape with a dihedral angle of 29.8º. The Zr-MOF crystallized in the *Fmmm* space group with a ratio of 0.96 and rotation of the carboxylate groups of 45.13º, exhibiting the 8-c cluster in a **flu** net.[54] Furthermore, they also predicted that, by increasing the dihedral angle up to 90º due to the introduction of bulky groups at ortho-positions to lock the C-C linkage, it would increase the rigidity and symmetry of the linker and the stability of the framework. In the following years, Zhou *et al.* demonstrated both the flexibility of the same linker and the net crystallizing in different conformations (dihedral angles 45.09-45.98º; ratio 0.96; and carboxylate groups rotating in 43.33-51.46º); and the introduction of functional groups that increases the dihedral angle, such as two hydroxy groups (47.46º) decreasing the ratio to 0.93, or four methyl groups (72.83º) further decreasing the ratio to 0.92.[69,77,148] Furthermore, they replaced the benzene arms by naphthalenes in both cores, obtaining **flu** Zr-MOFs but with different metrics. The flexible core showed a similar dihedral angle of 33.29º but the ratio of the linker decreased to 0.84 and a rotation of the carboxylate groups of 42.26º; and the rigid core crystallized in a more symmetric *P4/mnc* space group, exhibiting an almost

perpendicular dihedral angle of 85.80º in a more tetrahedral conformation (ratio of 0.98) and higher rotation of the carboxylate groups (73.58º).[77]

In a similar study, the group of Cui explored the introduction of both methyl and hydroxy groups in biphenyl units to impart chirality in the linker and therefore, in the Zr-MOF. The chiral (*S*)-biphenol scaffold also adopted a distorted tetrahedral geometry and directed to the construction of **flu** nets with benzene and naphthalene arms.[149] In both cases, the dihedral angle was increased to 60.69 and 60.11º, but the rotation of the carboxylate groups differed from 50.93 to 57.92º, respectively, despite having similar ratios of 0.89 and 0.90. Furthermore, by replacing trifluoroactic acid (TFA) by acetic acid in the synthetic conditions, they obtained two different **ith** nets according to the linker used. When assembling Zr^{IV} with the linker with benzene arms, the linker exhibited a distorted tetrahedral shape with a 76.34º dihedral angle and rotation of the carboxylate groups of 31.71 and 43.33º that drive to the formation of an unprecedented nonanuclear Zr-cluster in a distorted and elongated icosahedral geometry (Figure 3.17a). The Zr atoms are arranged in a tricapped trigonal prismatic conformation, which can be described as the packing of two hexanuclear Zr-clusters via face sharing. Notably, an isoreticular structure could be synthesized by introducing an adjacent phenyl ring in the arm that promotes the increased rotation of the dihedral angle (83.58º) and carboxylate groups (38.61 and 44.15º). When the assembly is performed with the linker exhibiting naphthalene arms, the linker showed a distorted tetrahedral shape with a 79.56º dihedral angle and rotations of the carboxylate groups of 49.79 and 56.72º that drive to the formation of an unprecedented two-fold disordered Zr-cluster in a distorted icosahedral geometry. Despite the difference structural arrangement, it is observed that a higher dihedral angle is needed to afford the **ith** nets compared to the **flu** nets. Isoreticular **flu**-MOFs were also constructed with crown ether functionalizations in the chiral pockets obtaining similar dihedral and torsion angles, even with a further extended biphenyl unit in the arms.[150]

Recently, two additional core analogues were reported mimicking the tetrahedral geometry as linkers in Zr-MOFs. The group of Zhang synthesized NPF-500, which is constructed with a *N,N'*-bicarbazole that adopts a perfect perpendicular dihedral angle of 90º and completely planar carboxylate groups in a D_{2d} symmetry, with an elongation into a ratio of 0.78.[151] The high symmetric linker promoted a more symmetric *I4/mmm* compared to the biphenyl analogues. Functionalization of the arms with an extra benzene ring yielded an isostructural **flu**-MOF. However, the methyl functionalization of these arms produced a desymmetrization of the linker with a very distorted tetrahedral shape exhibiting a dihedral angle of 77.12º and carboxylate groups rotating in 50.83 and 51.58º, guiding to the assembly of a 4,12-c rare **ith** net, showing a 12-c Zr_9-cluster with very distorted icosahedral geometry (Figure 3.17a).[152] The group of Li synthesized another **flu**-MOF, HIAM-4014, which is constructed with a saddle-shaped tetrathiophene-based tetracarboxylate that has an octagonal ring that direct to a tetrahedral conformation.[153] Here, the carboxylate groups are almost planar (1.68º) and the linker is elongated in the *c* axis (0.83 ratio), with the same D_{2d} symmetry that promotes the crystallization in a *I4/m* system.

Although there are no more examples of tetrahedral ligands that has been elongated in just one direction or controlling the rotation of the carboxylate groups, we are confident that, in the future, more defaulted clusters and MOFs exhibiting other topologies will be assembled. To date, the number of structures that differ from the default **ith** or **flu** nets is limited, but some researchers could deviate from these topologies by introducing more complicated design strategies. For example, the first structure that decrease even more the connectivity of the Zr-cluster was via using a more flexible calixarene-based linker.[154] Its 1,3-alternated conformation displayed a tetrahedral geometry with a ratio of 0.82, but the rotation of the carboxylate groups cannot be measured due to the building unit used (Figure 3.16). This linker promoted the formation of a 6-c Zr cluster with hexagonal conformation with the remaining six positions occupied by formates. However, the flexibility of the linker

drives to form a 4,6-c **gar** net, where the SBUs occupy the positions of the octahedra in the net despite its hexagonal conformation, creating a mismatch. The MOF crystallized in the highest symmetric *Ia-3d* space group, and the underlying topology is an edge-transitive net that has never been observed before in a MOF constructed with clusters.

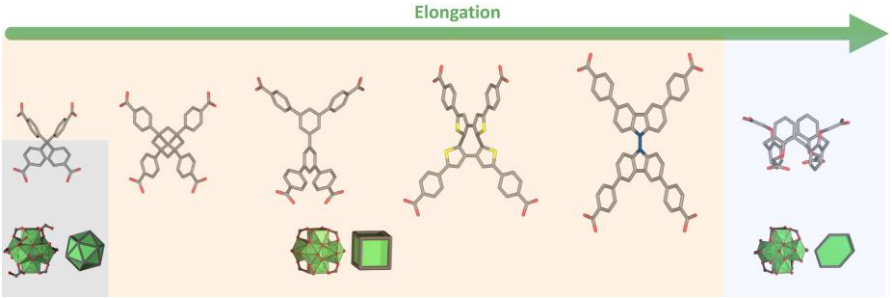


Figure 3.16. Representation of the elongation in the aspect ratio of tetrahedral ligands with different cores. This parameter influences in the connectivity of the Zr-cluster, decreasing from 8-c cubic (orange area) to 6-c hexagonal (blue area) SBUs. The black area represents the exceptional case with smaller linkers that can drive to 12-c icosahedral Zr-SBUs.

Out-of-plane translations were also explored for tetrahedral ligands with pseudo-*para* paracyclophane cores by Farha and coworkers. However, they did not deviate from the most common 4,8-c **flu** net. The Zr-cluster exhibited an 8-c D_{4h} cubic cluster, whereas the linker showed a 4-c D_{2d} tetrahedral shape of a ratio of 0.81 and carboxylate groups rotating 36.49º.[43]

As previously observed in the case of rectangular linkers, the introduction of an atom between the two benzene rings of the biphenyl core produces a bending that desymmetrize the tetrahedral conformation. This effect produced the formation of two structures with very distorted, novel Zr-clusters: the first one directed to the formation of an unprecedented 8-c Zr-cluster with a bicapped trigonal antiprism geometry, reticulating a very distorted **flu** net due to the high level of distortion of the linker (carboxylates rotating 44, 45.38, 60.40 and 66.42º); and the second one directed to another 6-c Zr-cluster with a distorted trigonal antiprism geometry,

reticulating a **cor** net thanks to the higher distortion of the linker that had both bending and torsion of methyl groups in *ortho*-positions that forced the carboxylate groups to rotate to higher degrees (85.23 and 87.69º).[122] Both nets are related by the cluster adopting the same asymmetric, distorted trigonal antiprism conformation, with two extra coordination in the **flu** net.

Lastly, Cui *et al.* investigated the effect of combining this bending with a chiral center introducing an asymmetric central atom in 1,1'-spirobiindane-7,7'-diol (SPINOL)-based linkers, which possess a more rigid and narrow cavity compared to the BINOL. Using this linker unveiled plenty new nets and cluster conformations. The assembly with the enantiomeric SPINOL extended by benzene arms yielded a novel 4^4,12-c net that crystallized in the chiral $C222_1$ space group, with four different crystallographic positions for the linker with very distorted tetrahedral conformations.[155,156] The Zr-SBUs appeared with a 12-c distorted cuboctahedral geometry and D_{4h} symmetry, where two linkers acted as monodentate ligands moving from the ideal positions. Interestingly, expanding the linker arms with naphthalene did not assemble in an isoreticular Zr-MOF. It crystallized in a chiral $I4_122$ system, evolving to a more regular trinodal 4,8-c sqc7929 net, where the Zr-clusters decreased its connectivity featuring an 8-c rare, distorted gyrobifastigium geometry and D_{2d} symmetry, which has never been observed before (Figure 3.17b).[156,157] Here, the linkers adopted more regular conformations in two different crystallographic positions, exhibiting carboxylate groups rotating 4.60 and 51.91º, and 47.84 and 86.74º for each position.

A PO_4-functionalized linker in the chiral pocket modified the bending angle and guided to a completely different and novel 4^2,8^2-c **sjt** net for both benzene and napththalane extended MBBs.[158] The asymmetric linker presents two crystallographic positions with distorted tetrahedral geometries. The Zr-MOFs crystallized in the chiral $P6_222$ and $P3_221$ space groups, respectively. Note that the introduction of the in-plane translation in the arms eliminates the decreased symmetry system by half in some edges. The Zr-clusters are also presented in two

different crystallographic positions with different D_{4h} and D_{2d} symmetries in the first MOF and only D_{2d} symmetric Zr-clusters in the second one. Recently, the same group explored the effect of the asymmetric linker by using a racemic mixture of both PO_4-functionalized enantiomers. The resulting Zr-MOF lost its chirality by crystallizing in the *P6/mmm* space group, comprising both *S*- and *R*-linkers in the same proportion.[159] Surprisingly, a three-fold disorder is present in both MBBs, displaying the 12-c hexagonal prism conformation in the Zr-cluster and a 6-c trigonal prism conformation in the linkers. The underlying net of the MOF is the edge-transitive **alb** topology, and the disordered hampered its conformational study. Another polymorph was achieved by decreasing the temperature to 80 ºC with two different SBUs with an unprecedent geometry. First, the hexanuclear Zr-cluster exhibits an unprecedented 9-c tricapped trigonal antiprism geometry (Figure 3.17c). Then, the nonanuclear Zr-cluster exhibited also an unprecedented defective 6-c trigonal antiprism, where the axial positions of the clusters are occupied by H_2O/OH^- molecules (Figure 3.17d). Both SBUs are joined by a distorted tetrahedral linker that exhibits rotations of the carboxylate groups of 41.88, 51.11, 52.57 and 54.91º. The Zr-MOF crystallized in the trigonal *P-3c1* space group, and the underlying net can be simplified as a trinodal 4,6,9-c net.

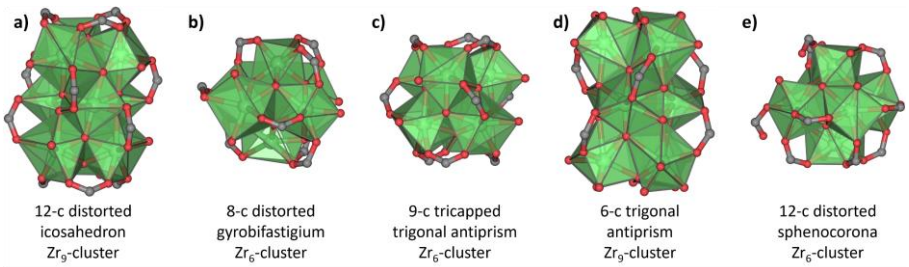


Figure 3.17. Some of the non-conventional Zr-clusters found in Zr-MOFs: a) 4,12-c **ith** net, b) 4,8-c sqc7929 net, c) and d) 4,6,9-c net, and e) 4^4,10-c net; when assembled with tetrahedral linkers with some desymmetrization.

Finally, the same effect on the chirality control with another functionalization of the chiral pocket with an 18-crown-6-ether was observed. The use of an

enantiopure ligand promoted the reticulation of a novel 4^4,10-c net that crystallized in the chiral *C222₁* space group, where the linkers exhibit distorted tetrahedral geometries and the hexanuclear Zr-cluster has a rare 10-c distorted sphenocorona geometry with a D_{2d} symmetry, being two of the linkers coordinating in a monodentate fashion (Figure 3.17e).[155] However, if the linker used is a racemate, the Zr-MOF crystallized in the *Pnma* space group with an underlying **flu** net.[159] In this case, the Zr-cluster has an 8-c cubic geometry, whereas the linker has a distorted tetrahedral conformation. In fact, the former 4^4,10-c net resulted to evolve to a different **flu** net after shrinking its cell and expelling linkers, transforming the Zr hexanuclear cluster into a dimer that connects two clusters through the open metal sites.[155] Alternatively, the structure can also be described as a 4,5-c **tcs** net if the clusters are simplified as different entities and interconnected. This phase transformation is triggered by the topological strain of the net and the low symmetry of the building blocks as well as the flexible 18-crown-6-ether moieties that dramatically vibrate and remove the solvent to initiate the topological transformation. All these polymorph structures shed light on the complexity of linker design and control of synthetic conditions that may direct to different nets, complicating the rational design when deviating from ideal and more regular MBBs.

3.2.1.4. RE-clusters combined with 4-c tetrahedral organic MBBs

As in the previous Section, comparing the assembly of tetrahedral linkers with similar Zr- or RE-clusters can reflect the different tendency for each one. However, the absence of structures limits performing a deep study. The most regular tetrahedral MBBs assembled with RE-clusters were used by the group of Trikalitis, discovering the formation of unprecedented nonanuclear clusters with a rare 8-c bicapped trigonal prismatic geometry and D_{3h} symmetry driven by the 4,4',4'',4'''-methanetetrayltetrabiphenyl-4-carboxylate (MTBC) with a T_d symmetry.[146]

Surprisingly, the RE-cluster presented defaults of connectivity, which is uncommon in the assembly of square/rectangular linkers. The nonanuclear cluster usually has a 12-c hexagonal prism conformation, so half of the carboxylate groups are missing, and two extra carboxylate groups are coordinating in the axial positions capping the open metal sites. This MOF exhibits a novel 4,8-c **ken** net, with a regular [2233] transitivity. In it, the linker has a very regular shape with a short elongation into a ratio of 0.96 and almost planar carboxylate groups that rotate 3.69 and 4.78º. This is in sharp contrast with assembly of the Zr-cluster that formed **flu**-MOFs or higher connected nets. The linker functionalization with a sulfone group also influenced in the assembly of a new net: the S_4 symmetry produced by the bending in the arms directed to a fully connected nonanuclear cluster with hexagonal prism conformation in a novel 4,12-c **hpt** net.[146] The distorted tetrahedron presents a ratio of 0.82 and carboxylate groups rotating 81.22 and 89.18º in perpendicular. It must be mentioned that MTB has been recently assembled with a RE salt in the presence of 2-FBA to yield an 8-c dinuclear RE-cluster in a **flu** net.[160] However, the similarity of this cluster with those found in RE-MOFs that did not use fluorinated modulators in its synthesis indicate the failure in the formation of the desired high-nuclear RE-clusters.[161]

Some other central cores that adopt tetrahedral conformations have been explored. The archetypical biphenyl unit with methyl groups in *ortho*-positions was reticulated with the RE-hexanuclear cluster forming a **flu**-MOF with four missing positions with an 8-c cubic SBU.[134] Here, the ligand has a D_{2d} symmetry with a dihedral angle of 85.24º, a ratio of 0.93 and carboxylate groups rotating 75.73º. Also, replacement of the benzene arms by napthalenes afforded an isostructural **flu**-MOF, with the linker displaying a similar conformation with a dihedral angle of 79.32º, a ratio of 0.88 and carboxylate groups rotating 73.06º; but this time with the missing positions capped with 2-fluorobenzoates. In this case, the RE-MOFs exhibited the same underlying topology and same cluster formation than in the Zr-MOFs. A similar effect was observed when replacing the core by other units such

as 1,4-phenylene-diamine, bicarbazole or even tetraphenylpyrazine (TPP), exhibiting the 8-c RE-cluster in **flu** nets capped by formates in the missing positions.[115,160,162]

The asymmetric elongation of the biphenyl unit resulted in the 5'-(4-carboxyphenyl)-[1,1':3',1''-terphen-yl]-3,4'',5-tricarboxylate (CPTTA). When assembling with the Zr-cluster, this linker promoted to formation of a less-symmetric **csq** net. Differently, when it was assembled with the RE-cluster, a novel 4,8-c net exhibiting a very rare 8-c hemi-cuboctahedral geometry of the hexanuclear cluster was formed.[163] As for the coordinated molecules, six equatorial linkers are positioned in the hexagonal plane, while other two are located on one side of the plane with a formate. The other side of the plane is fully capped by 2-fluorobenzoates, stabilizing the defective cluster. The linker possesses a dihedral angle of 50.86º adopting a distorted tetrahedral geometry, with planar carboxylate groups in the isophthalate moiety and two different planar (4.07º) and perpendicular (82.80º) carboxylate groups. Recently, Trikalitis *et al.* introduced methyl groups in the benzene arms to increase the steric hindrance with the central aromatic ring, forcing to rotate up to 43.8º.[164] This modification promoted the formation of a novel 4,8-c net, changing the hexanuclear cluster connectivity to an 8-c trans-bicapped octahedral geometry, with the remaining positions occupied by 2-FBA and solvent molecules. Instead, replacing the benzene arm by a naphthalene one lead to the discovery of PCN-507 with a new 4,8-c **lxl** net, which is derived from the disordered 6,12-c **alb** net.[134] As in a previous Zr-MOF, the tetrahedral linker is disordered adopting a 6-c trigonal prismatic geometry, connected to a 12-c hexanuclear RE-cluster with hexagonal prism conformation. If the disorder is removed, the hexanuclear cluster resulted in an 8-c cubic conformation with missing positions, which combined with the 4-c tetrahedral organic MBB, resulted in the **lxl** net. Alternatively, if the replacement is in the central ring by a carbazole, the angle between the arms is modified from 120º to 90º, promoting the formation of a rare 8-c RE-cluster with distorted hexagonal bipyramid shape in a novel 4,8-c

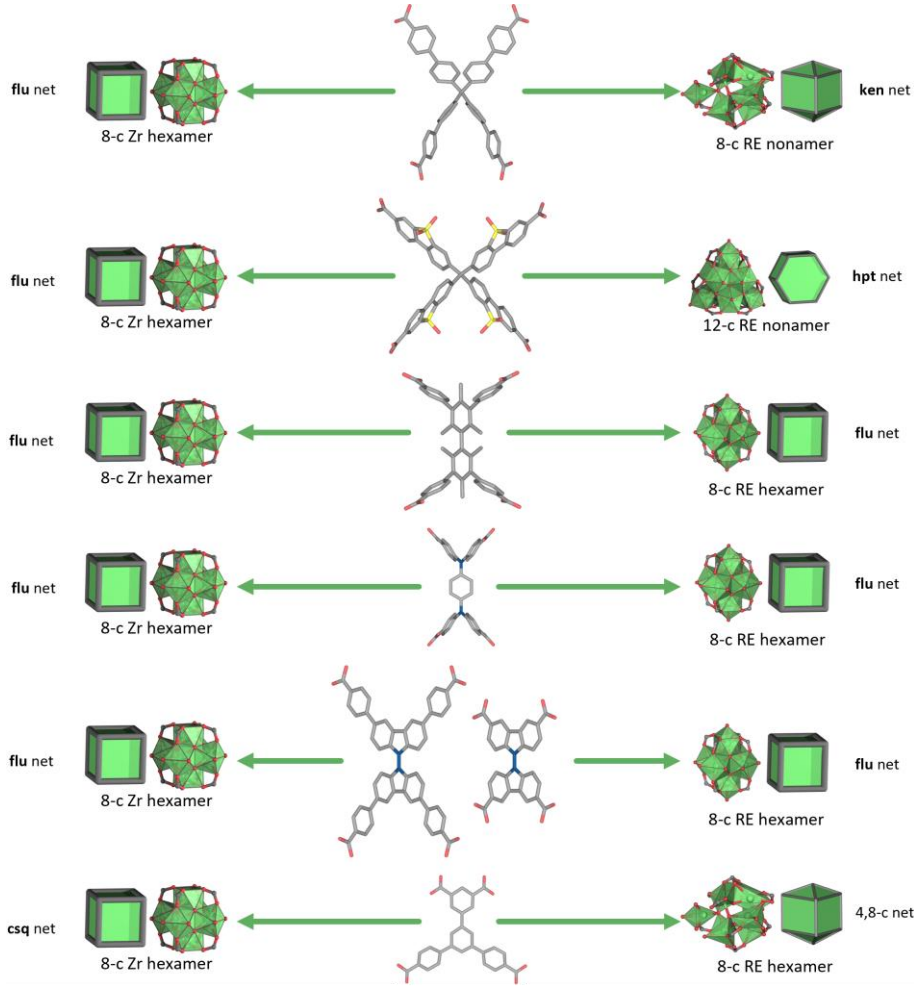


Figure 3.18. Comparison between the assembly of some 4-c tetrahedral linkers with Zr- or RE-clusters. For the Zr-case, the Zr-hexamer always tends to form the 8-c cubic SBU for assembling the **flu** net; while for the RE-case it prefers to evolve and form different clusters.

jun net.[134] Both linkers with benzene and naphthalene arms were crystallized with this underlying topology in PCN-908 and PCN-909, respectively; with a distorted tetrahedral conformation with a dihedral angle of 49.17º and rotations of 15.63 and 21.32º in the isophthalate moiety and 15.48 and 42.96º in the carbazole moiety.

Finally, the most desymmetrized MBBs assembled with RE-clusters were those containing a bent angle in biphenyl units because of a central atom. According to its simulation, the ether-based linker is highly disordered, and the carboxylate groups rotate from 57.69 to 76.69º.[165] These are connected to 12-c nonanuclear clusters with hexagonal prism shape in a new 4,12,12-c **hjz** net, which is close related to the **dfs** net by a shift in a layer of inorganic SBUs due to the linker configuration. This net contrast with the **flu** net when assembling with the Zr-SBU, which exhibited a very distorted 8-c conformation.[122] Combining this bending angle with the torsion produced by methyl groups generate a different **flu** net because of the high rotation of the carboxylate groups of 57.76, 64.99, 71.76 and 73.93º.[165] The linker displays a very distorted tetrahedral geometry, and the RE-hexanuclear cluster an unprecedented 8-c very distorted cubic or hexagonal bipyramid geometry, where two equatorial linkers coordinate as monodentate. This linker also created a very distorted 6-c cluster when assembling with the Zr-SBU, reflecting the power of desymmetrization of organic MBBs in different high-connected nets.

3.2.1.5. Zr-clusters combined with 3-c triangular organic MBBs

Compared to ditopic or tetratopic linkers, there is a very limited number of tritopic organic MBBs combined with high-connected polynuclear clusters. This can be related to the lower number of edge-transitive nets available with 3-c nodes. Even so, some high-connected nets afforded through these linkers include the 3,24-c **rht** or the 3,12-c **ttt** nets, created by combining the tritopic organic MBBs with rhombicuboctahedron or truncated tetrahedron MBBs, respectively. Despite any occurrence of a Zr-MOF assembled with a tritopic linker in an underlying **ttt** net, we believe that, with the proper desymmetrization, this topology can be afforded as the case of a distorted icosahedron with the 12-c cuboctahedral cluster. On the contrary, the assembly of the simplest tritopic BTC with the Zr-cluster assembled into the first Zr-MOF that exhibited an underlying 3,6-c **spn** net and defaults of

connectivity in a 6-c trigonal antiprism conformation of the cluster with D_{3d} symmetry.[141] MOF-808 crystallized in the cubic *Fd-3m* space group, and the remaining positions of the clusters are occupied by formate ligands. In addition, the BTC is not completely planar and bents enlarging the tetrahedral cage and slightly rotating the carboxylate in 4.41º, decreasing the symmetry to C_{3v}. Both bending and twisting were also observed in its isoreticular PCN-777 analogue expanded symmetrically with a triazine core in the TATB, according to its simulation.[166] The carboxylate groups rotate 5.98º, which can be attributed to the bending of the molecules and alter the torsion angle.

If the elongation is performed in the same benzene core, the BTB will rotate the arms because of the steric hindrance of the hydrogen atoms that are absent in the TATB. This was indeed found in the crystal structure of a Zr-MOF assembled with BTB reported by Sun *et al.* This MOF crystallized in the $I4_1/amd$ system with rotations of 47.26 and 48.28º. The Zr-cluster exhibited the opposite coordination of six equatorial linkers in the same plane with a hexagonal geometry and C_{3v} symmetry, reticulating a 2D MOF with an underlying 3,6-c edge-transitive **kgd** net.[167] The 2D layers were found catenated into a 3D structure, in which the linker is in a completely planar conformation but elongated into isosceles triangle of a ratio of 0.98 with a C_{2h} symmetry to afford this net, as two arms rotate in a different direction than the other ones. In contrast to the former structures, the remaining positions were unoccupied by any chelating ligand. A further rotation was favored by functionalizing the available positions of the central core with three methyl groups, forcing the peripheral rings to be perpendicular because of the steric hindrance. When combining with the Zr-cluster, BUT-12/NU-1200 crystallized in the cubic Pm-3m system with an underlying **the** net.[168,169] In this case, the linker shows a highly symmetric D_{3h} conformation in an equilateral triangle with 87.16º rotations of the carboxylate groups and bending towards the cuboctahedral cage. The Zr-cluster exhibited an 8-c cubic cluster with D_{4h} symmetry. An isostructural

BUT-13 was constructed by replacing benzene arms by naphthalenes, but unfortunately it could not be solved by SCXRD.

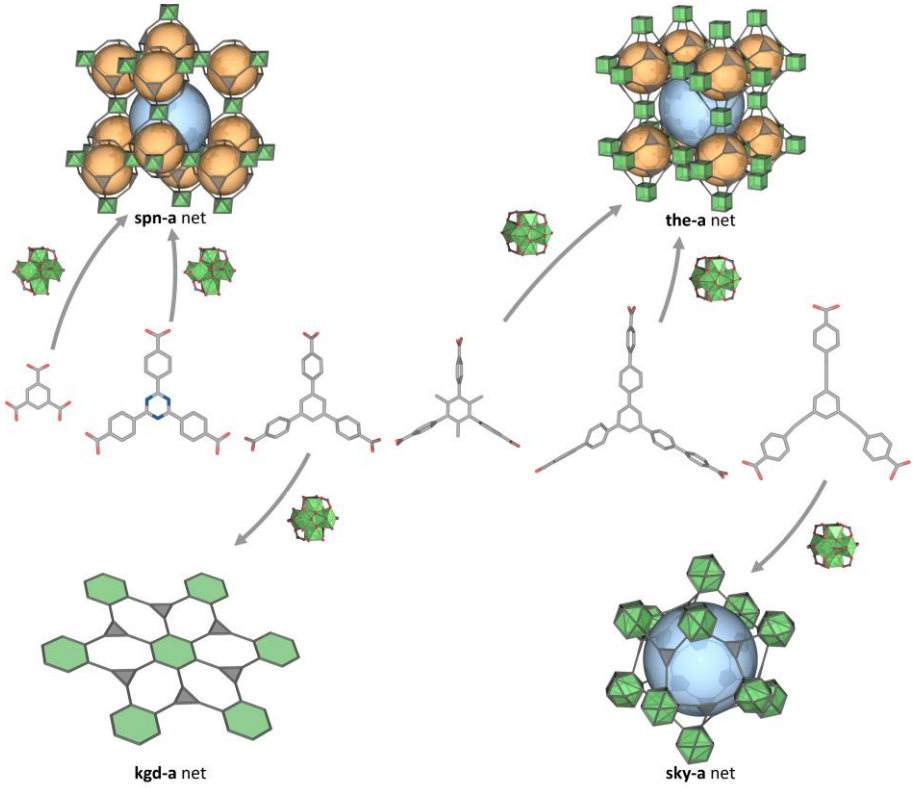


Figure 3.19. Structural evolution of Zr-MOFs when increasing the 3-c triangular linker size from nets based on 6-c Zr_6-SBUs in **spn** or **kgd** nets, to 8-c and 12-c Zr_6-SBUs in **the** or **sky** nets.

Further elongations of the same core with benzene and triple bonds were reported by Yagui and coworkers.[170] An isoreticular **the** net was obtained when elongating the triangular MBB with an extra benzene unit that also hindered the planar conformation and bends towards the cuboctahedral cage, where the linker exhibits the same D_{3h} symmetry and perpendicular carboxylate groups in 86.64º.Due to its larger size a 2-fold interpenetrated structure. Instead, the elongation with a triple bond guided to a MOF with a novel 3,12-c **sky** net that crystallized in the *Pm-3n* space group, composed of the tritopic linker and a 12-c cuboctahedral Zr-SBU.[170]

Remarkably, combining both building blocks were considered incompatible by the group of Eddoaudi.[171] The triple bond favored the planar conjugated conformation, with carboxylate groups rotating 2.28 and 11.26º. This elongated planar conformation deviated from **the** or **kgd** nets, but surprisingly also deviated from the edge-transitive **spn** net to favor a higher connected cluster. To do so, the linker is strongly desymmetrized in a C_{2v} isosceles triangular shape, by elongating it in a ratio of 0.83 and slightly bending towards the icosahedral cage. Despite the **sky** net is not an edge-transitive net, it has a quite regular [2244] transitivity, but needs a higher bending of the molecule compared to the others (Figure 3.19).

The design of ligands with other central cores implies its symmetry decrease, which can be anticipated for the construction of specific nets. For example, the group of Sun reported an imidazole extended with three benzoates that imitated the C_{2v} symmetry in a new isosceles triangular linker with a ratio of 0.80.[172] As expected, the linker promoted the crystallization of a **sky** net and the symmetrically compatible O_h 12-c cuboctahedral Zr-cluster, as the linker is elongated in a similar ratio of 0.80 and the carboxylate groups also rotate 3.76 and 10.32º. The smart design is reflected by the 5-member heteroaromatic ring, that facilitates both the planar conformation due to the absence of hydrogen bonds and the higher angle of 72º of the pentagon, which averts both closer benzenes to rotate in higher degrees. Another isosceles-like linker was designed by the group of Kaskel using a carbazole extended with a benzoate by the nitrogen atom.[36] The reticulation with the Zr_6-cluster also promoted the formation of a 12-c SBU but with distorted cuboctahedral geometry in a novel 3,12-c net, which can be deconstructed as the assembly of chain-like supermolecular structures. The carbazole unit forms the chain by quadruple bridging 8-c Zr-SBUs with carboxylate groups in planar conformations, while the benzoate unit connects to neighboring chains in the remaining four equatorial open metal sites by monodentate carboxylate groups rotating 38.21º.

A simpler design substituting the aromatic central core by a trivalent atom, such as P(III), lead to dramatically decrease the symmetry to C_1, as phosphorus is a

tetrahedral atom considering its electron pair and forms a tripodal shape. This linker was combined with a pre-synthesized Zr_6-dimeric cluster bridged by acetates in the open metal sites under appropriate conditions to perform a site-selective substitution of 6 out of 18 available acetates, obtaining a 2D MOF with the same inorganic SBU and remaining in place the 4 bridging acetate linkers (Figure 3.20a).[173] The structure formed an underlying 3,6-c **kgd** net in an AA packing, with a distorted isosceles linker that has two perpendicular and one planar carboxylate groups. A similar ligand and strategy were reported by Chen, Farha, Cui and coworkers using a metal ion to coordinate the capping pyridines of the INA linkers coordinated to the Zr_3-cluster precursor.[174] However, in this case, the pre-formed zirconocene tripodal metallo-pyridine cluster undergoes a structural rearrangement to evolve to a novel 12-c J_{51} tricapped trigonal prism nonanuclear cluster, which has never been observed in Zr-MOFs or Zr-complexes, and that resembles to that often observed in RE-MOFs (Figure 3.20b). This cluster appeared as a 12-c hexagonal prism when extending with $Pb(NO_3)_2$ in a 2D heterometallic MOF with a new 3,12-c 3,12L4 net in an ABC packing, which can be considered as a daughter net from the parent **kgd** net[140]. Interestingly, this is the first time that the Zr-cluster appeared as a non-disordered hexagonal prism conformation. On the other side, the metalloligand has a more symmetric C_3 tripodal conformation in the octahedral complex. If the metal salt used is PbI_2, a different 2D wavy **kgd** net crystallized in an AB packing, where the Zr_9-clusters have lost half of its connectivity (Figure 3.20c). Curiously, the 6-c cluster has a trigonal antiprism geometry, but occupies the position of hexagons in the net as another example of a mismatch previously mentioned in Section 3.1.1. In this case, there are two C_3 tripodal linkers, being one the metallo-ligand earlier described and the I^- that creates halogen bonds with the pyridines.

The dissymmetric elongation of BTC forms another less-symmetric isosceles-like triangular linker that was already explored for designing Cu(II)-MOFs. Farha *et al.* reported a new Zr-MOF, NU-300, that showed how this linker promotes the

formation of a rare 9-c hexanuclear Zr-cluster with a distorted J_{63} tridiminished icosahedral geometry, where some of the carboxylate groups act as monodentate ligands (Figure 3.20d).[175] However, a closer examination of the structure revealed that there are four different positions of the linker, three of which are tritopic distorted isosceles linkers, but the fourth position is occupied by a ditopic linker with a free uncoordinated carboxylic group. Accordingly, it is better to describe this structure as a novel 3^3,11-c net, where the 11-c cluster has a distorted augmented sphenocorona geometry.

Another design of tritopic linkers can be by truncation of higher connected square or tetrahedral linkers.[176] In fact, the former tripodal linkers can be considered as truncation of tetrahedra. Truncation of squares were reported by the group of Ma by erasing one arm of the porphyrine to obtain a corrole "*T*"-shaped ligand. The assembly with the Zr^{IV} formed a two-fold disordered D_{3d} symmetric 9-c tricapped trigonal antiprism shaped cluster that reticulated in a 3,9-c **gfy** net (Figure 3.20e).[177] The linker displayed two different carboxylate groups in a C_{2v} symmetric conformation with a ratio of 0.75 that rotate 30.88 and 54.07º according to their connections in the equatorial or axial positions, respectively. Another "*T*"-shaped linker was designed by Li and coworkers using a benzimidazole core to fix both 90 and 180º bridging angles between the points of extension. However, the C_{2v} symmetry and ratio of 0.77 of the organic MBB favored the formation of another 9-c Zr-cluster with a different C_3 symmetry and triangular cupola geometry and therefore, to a different 3,9-c **sep** net (Figure 3.20f).[178] This might be related with the steric hindrance in the former corrole linker, which has now disappeared in one direction due to the heteroaromatic ring and have a planar carboxylate group (rotation of 2.86º); while the others rotate 68.13º.

Finally, the lowest connected Zr-cluster ever reported was induced by a tritopic macrocycle, leading to the formation of a 3-c triangular Zr-SBU that assembled in a 2D **hcb-b** net (Figure 3.20g).[179] The linker has a C_3 symmetry and equilateral geometry where the carboxylate groups are almost planar (5.57º), what should

match the assembly into a **spn** net. However, the bulkiness of the aromatic rings in *meta*-positions hampered its formation as cannot fit due to the close proximity with neighboring linkers in the cluster. In addition, the rigidity of the structure prevents its rotation in higher degrees to form **kgd** or **the** nets. Therefore, it evolves to form a low-connected C_3 cluster exhibiting monodentate ligands in the equatorial plane, with the remaining nine positions occupied by benzoates that stabilize the cluster.

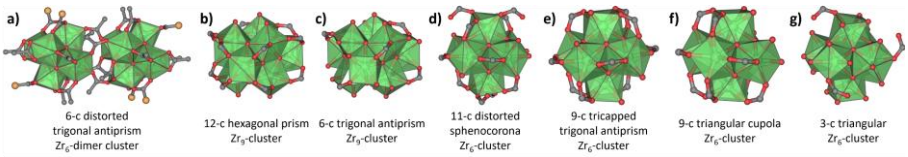


Figure 3.20. Some of the non-conventional Zr-clusters found in crystal structures when assembling Zr^{IV} with triangular linkers with some desymmetrization in MOFs with: a), b) and c) 3,6-c **kgd** net, d) 3^3,11-c net, e) 3,9-c **gfy** net, f) 3,9-c **sep** net, and g) 3^2-c **hcb** net.

3.2.1.6. RE-clusters combined with 3-c triangular organic MBBs

As for RE-MOFs assembled with tritopic linkers, there are only a few examples reported that usually differ from those nets of Zr-MOFs because of the ability of RE metal ions to form highly connected clusters and the difficulty of stabilizing under-connected multinuclear RE-clusters, which tend to evolve into a more thermodynamically stable RE-oxo-chains through a rearrangement. The only example that completely match, is Y-CU-45, which is assembled with BTC forming a **spn** net that exhibits uncommon 6-c trigonal antiprism RE-fluoroclusters.[180] The cluster is stabilized by surrounding fluorinated modulators in the equatorial plane coordinating to the free positions, and the linkers have a perfect equilateral triangular conformations (D_{3h} symmetry) and carboxylate groups that are coplanar with the benzene core. This could be related to the differences of the sphere behavior between Zr and RE metals, as the last ones are more adaptable and prone

to rearrange and form more thermodynamic frameworks compared to the unaltered core Zr-cluster.

Eddaoudi *et al.* reported the symmetric elongation of BTC into BTB, in the quest for the discovery of new structures and/or topologies, as they firstly conceived a mismatch assembly between the 12-c hexanuclear RE-cluster and the tritopic linker. As anticipated, instead of a 3,12-c net, they found that the RE-cluster evolved to a novel 18-c nonanuclear cluster with an elongated triangular orthobicupola (J_{35}).[171] In this net, the RE atoms are arranged in a tricapped trigonal prism conformation, which is the same as the 12-c hexagonal prism shape but with three extra points of extension in each axial position. The MOF has an underlying net with a 3,18-c **gea** topology and minimal [2244] transitivity, which can be alternatively viewed as an AB packing of pillared **hxl** layers. The mismatch between both MBBs is related to the torsion angles produced by the peripheral aromatic rings and the benzene core rotating the carboxylate groups. In fact, the linker in **gea** net is slightly elongated in a 0.99 ratio and exhibits a C_{2v} symmetry, where one carboxylate group is disordered in an almost planar conformation (1.28º) linked to the axial positions, and the other two carboxylate groups rotate 54.77º to bond the equatorial positions. In addition, a polymorph structure was later discovered when using the same linker but modifying the synthetic conditions, where two different RE-SBUs were connected through the BTB in a 3,6,12-c **dnm** net, an **acs**-related net. The structure is a two-fold interpenetrated MOF containing a 12-c nonanuclear RE-fluorocluster with an hexagonal prism shape, and a 6-c trinuclear RE-fluorocluster with a trigonal prism shape.[181,182]

Further expansion with another benzene ring formed the hexanuclear RE-cluster. However, its chemical environment is a bit modified, as two bidentate carboxylates have been substituted by four monodentate carboxylate groups that doubly bridged adjacent RE-clusters, therefore forming a 1D chain of RE_6-clusters.[183] This may be explained by the desymmetrization of the triangular linker into two crystallographically different positions, where one is elongated in a 0.99 ratio and

rotation of 44.16 and 57.97º of the carboxylate groups into a C_2 tritopic linker; while the other one is elongated in a ratio of 0.89 and more planar carboxylate groups (1.31 and 25.38º) into a C_{2v} tetratopic linker, as the later bridge two adjacent clusters. This also affect to the cluster symmetry that decreases to D_{2h}, forming a MOF with a new underlying 3,4,14-c net with rhombic-like channels.

Linker functionalization of BTB with methyl groups modified the angle of connection between both MBBs in the Zr-based MOF and directed to a **the** net. In the case of RE, an isostructural analogue was obtained with unsaturated D_{4h} 8-c cubic RE-clusters and D_{3h} 3-c triangular linkers.[184] Despite their lower capability of defect tolerance, the **the** net is more thermodynamically favored because of the high connectivity of the MBBs. In it, the rigid and symmetric linkers stabilized the RE-hexanuclear clusters with defaults of connectivity. In the MOF, the linker also exhibits a bending of the linker and a rotation of the carboxylate groups in a perpendicular position (84.82º).

To impart control on the linker symmetry, Eddaoudi and coworkers replaced the benzene core with a carbazole extended with a phenyl ring to mimic the C_{2v} symmetry of an isosceles-like triangular MBB. The deliberate choice of the carbazole modified the bending angle into 90º that directed to a RE-MOF constructed with 12-c nonanuclear clusters with the hexagonal prism conformation. The underlying net of the MOF displayed a trinodal 3,12,12-c **aea** topology, where there are two crystallographically different RE-clusters bonded to the two different carboxylate groups of the linker.[185] As expected, the carboxylate groups in the carbazole unit are coplanar (1.12º rotation), the carboxylate group of the phenyl ring rotates 9.86º, and the linker is elongated in a ratio of 0.79. The net has a minimal [3244] transitivity and can be alternatively described as the pillaring of quadruple cross-linked **hcb** layers in the center of the hexagonal pores. Curiously, an additional discrete RE_9-cluster was found in the pores of the **aea**-MOF capped by twelve 2-FBA modulators in a hexagonal prism conformation and connected to the

clusters of the **hcb** layers by axial coordination of a single RE atom bridging both clusters.

Another way of mimicking the isosceles-like shape is by elongating one or two arms of the triangle. Reported by Matzger *et al.*, the elongation of one arm in BTC revealed the *in-situ* formation of two distinct highly connected RE-clusters: an 8-c cubic hexanuclear cluster, where the missing positions are occupied by 2-FBA modulators to stabilize the unsaturated cluster; and a 12-c hexagonal prismatic nonanuclear cluster, with the same coordination environment as the aforementioned structure.[185] Both clusters are joined by the tritopic linkers, where the isophthalate unit join the 8-c RE-clusters and these are connected to the 12-c RE-clusters by the benzoate units, having each cluster different chemical environments. The underlying net has an unprecedented 3,8,12-c **pek** topology, which is also a minimal edge-transitive net with transitivity [3244]. Alternatively, this net can also be described as the pillaring of doubly cross-linked **kgm** layers in the center of the hexagonal pores. The linker has also a C_{2v} symmetry and a ratio of 0.56, where the carboxylate groups in the isophthalate rotates 7.38 and 19.64º, while the carboxylate group in the benzoate rotates 36.00º due to the steric hindrance of both phenyl rings. Further elongation introducing an ether functionalization yielded an isostructural **pek**-MOF. In this case, the C_{2v} symmetric linker has a low ratio of 0.46 and more planar carboxylate group in the benzoate (1.08º rotation) because of the elongation that avoid the steric hindrance, and 18.20º rotation in the carboxylates of the isophthalate unit.

On the other hand, elongation of two arms of BTC promoted the formation of an 18-c nonanuclear RE-cluster with a distorted elongated triangular orthobicupola geometry in a 3^2,18-c novel **ytw** net.[186] The linker adopted two different positions, a more symmetric C_{2v} with an isosceles-like shape with a ratio of 0.70 and two different carboxylate groups that rotate 2.95 and 46.54º; and a more distorted C_1 linker with 4.69, 46.05 and 53.46º rotation of the carboxylate groups. The different coordination environments originated a more distorted SBU, which has a dihedral

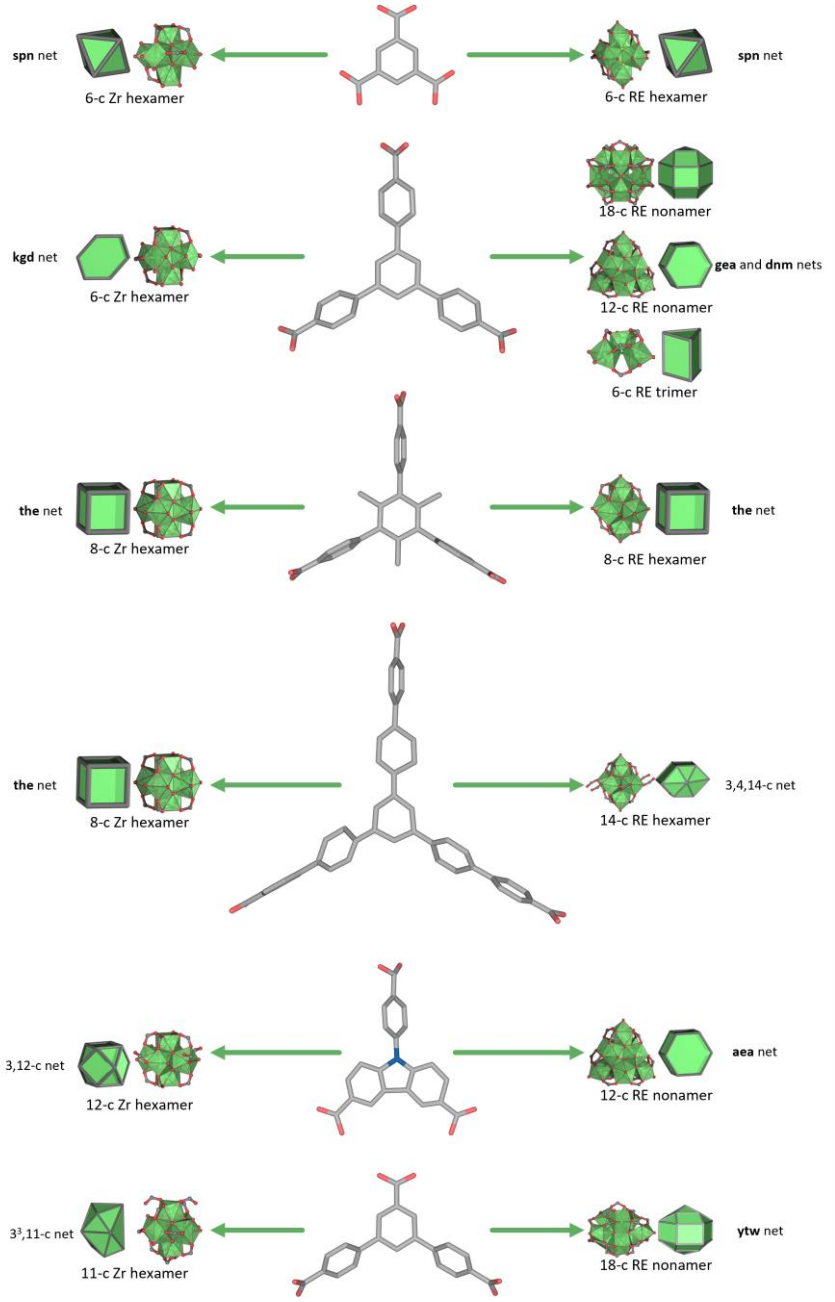


Figure 3.21. Comparison between the assembly of some 3-c triangular linkers with Zr- or RE-clusters. For the Zr-case, it tends to form always the Zr-hexamer SBU; while for the RE-case it prefers to evolve and form different clusters.

angle of 18º between the axial and equatorial positions. Combining the dissymmetric elongation with the torsion angle produced by bulky groups led to complicated networks. If the bulky group is a methyl or chloride, the linker adopted a C_{2v} symmetry. Its ratio decreases down to 0.66, which increases its carboxylate rotation to 75.19º on the benzene arms while the other is coplanar. Surprisingly, the RE_6-cluster is favored and has an unconventional 9-c triangular cupola geometry, which can be regarded as half of the elongated triangular orthobicupola or defective cuboctahedron, as three axial positions in one plane are capped by formates. The planar carboxylate groups connected to the contrary axial positions, while the perpendicular carboxylates connect to the equatorial plane to form a 3,9-c **sep** net.[186] This net is the same as obtained with "*T*"-shaped linkers in Zr-MOFs. If both methyl and hydrogen functionalization are combined, a different 3^2,12-c **flg** net is favored, forming a 12-c RE_9-cluster with hexagonal prism conformation. The two linkers occupy different positions maintaining its C_1 and C_{2v} symmetries, with rotations of 12.42, 36.77 and 58.97º, and 12.51 and 56.84º, respectively.

3.2.1.7. Zr- and RE-clusters combined with 6-c organic MBBs

To date, there are not many examples of their using higher connected organic MBBs in the assembly of MOFs. To the best of our knowledge, there is not a comparable glossary of 8-c or 12-c linkers in Zr- or RE-MOFs, and there are just a few structures made of 6-c organic MBBs. According to the databases, there is not any edge-transitive net composed of a 12-c cuboctahedral node with another 6-c node. However, two 6,12-c nets are based on the assembly of hexagons with truncated tetrahedra and trigonal prisms with hexagonal prisms in the **mgc** and **alb** nets, respectively. As for the 6-c organic MBBs, they can adopt three different geometries: hexagonal, trigonal prismatic, and octahedral shapes.

First, the use of a hexagonal-like favored the formation of a 6-c D_{3d} hexagonal Zr_6-cluster with defaults of connectivity occupied by acetates capping the axial positions.[187] Both MBBs assembled in a 6,6-c **hxg-b** net, where the carboxylate

groups are oriented in 56.94º rotated from the central benzene plane to afford this net with the C_{3v} symmetry and a perfect hexagonal shape (Figure 3.22a). Note that similar rotations were also found in the 6-c hexagonal Zr-hexamer found in the **kgd** net when assembling with BTB;[167] and that the contracted hexatopic linker assembled in a defective **stp** net with two carboxylate groups uncoordinated and deviating to a rectangular/trapezoidal conformation as the rotations were too high due to the steric hindrance of all the benzene arms, which disappear in its extension to adapt a more comfortable angle to be fully connected.[99]

A peripherally extended triptycene (PET) linker with a rigid trigonal prismatic shape was assembled with a three-fold disordered 12-c hexagonal prismatic SBU forming a 6,12-c **alb** net (Figure 3.22a).[39] This net is favored thanks to the D_{3h} symmetry linker, as trigonal prism cannot be assembled in an edge-transitive net with 12-c cuboctahedral or 8-c cubic nodes. To afford this net, the peripheral benzenes and carboxylate groups rotated 75.41, 75.91 and 76.49º.

Finally, a recent addition to the repertoire of Zr-MOFs explored the use of a transition metal center directing to an octahedral geometry upon the coordination of three bipy molecules. As the bipy units resulted to be rigid, extended phenyl rings were added providing the needed torsional flexibility to adapt the rotation of the carboxylate groups into the required net. In this case, the 6-c octahedral ligand reduced the connectivity of the cluster to an 8-c cubic geometry to build a 6,8-c **ocu** net (Figure 3.22a).[188]

To the best of our knowledge, the only reported example of a desymmetrized hexatopic organic MBB is the use of a triphenylene core extended by their six external carbon atoms (Figure 3.22b).[189] This unit modifies the size of the hexagonal shape to a distorted hexagon. Upon combination with the Zr_6-cluster, its connectivity is decreased to 9 and its symmetry to C_3 in a distorted triangular cupola geometry, which was already observed in Zr-MOFs due to the desymmetrization of 3-c organic MBBs. As in previous examples, three formates terminate the

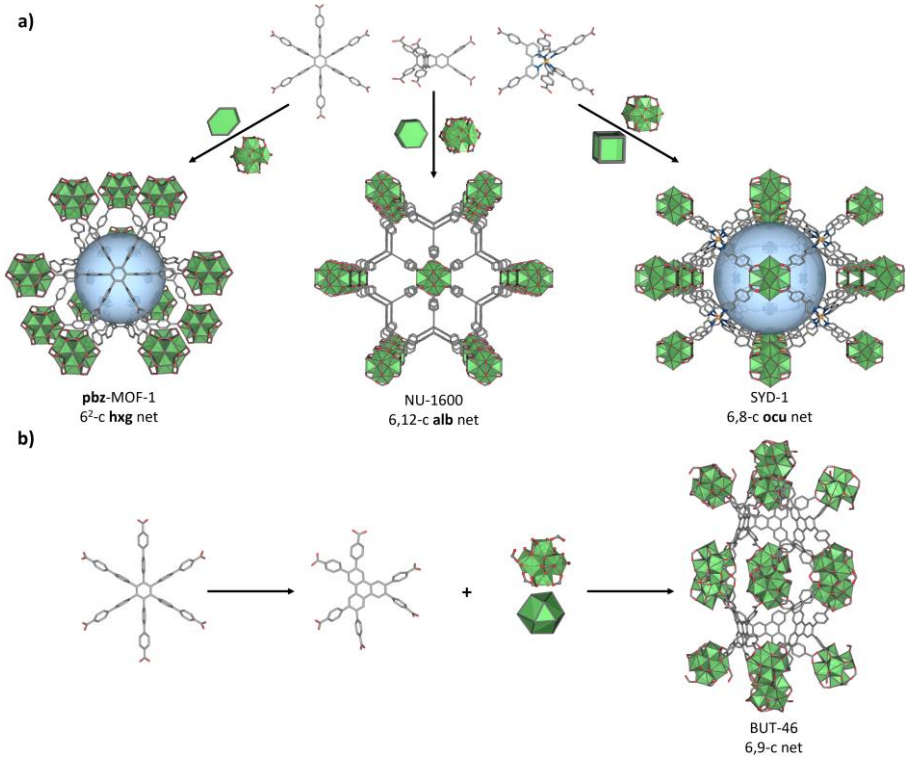


Figure 3.22. a) Comparison between the assembly of the three different shapes in 6-c organic MBBs (hexagonal, trigonal prismatic and octahedral), with Zr-clusters to afford the **hxg**, **alb** and **ocu** nets, respectively. b) Desymmetrization of the 6-c hexagonal linker into a less-symmetric linker that decreases the symmetry and connectivity of the Zr-cluster to 9 with a distorted triangular cupola shape, reticulating a novel 6,9-c net.

remaining axial sites and another three carboxylate groups from the linkers act as monodentates in the equatorial sites distorting from the ideal shape. The overall framework has an unprecedented 6,9-c net, where the linker has a C3v symmetry and three different carboxylate groups that rotate 15.25, 49.88 and 59.88º.

To date, there is only one RE-MOF constructed with a 6-c linker that exhibit a triangular prism geometry for the rotation of *m*-terphenyl arms with neighboring methyl groups. Interestingly, the 6-c linker prompted the formation of a RE_6-cluster with 12-c hexagonal prismatic shape rather than the previous RE_9-cluster, commonly obtained for this geometry.[127] In the cluster, eight linkers act as bidentate

and four act as monodentate, resembling to the cluster exhibited when assembling with the extended BTB. As expected, the MOF has an underlying 6,12-c **alb** net, with a distorted trigonal prism geometry of the linker with different carboxylate orientations; being one planar and monocoordinated and two bidentate rotating 46.34 and 47.78º.

3.2.2. Exploring the desymmetrization effect of 4-c linkers in Zr- and RE-MOFs

Inspired by the exhaustive list of square/rectangular organic MBBs assembled with high-connected Zr- and RE-based clusters, we were motivated to contribute to the study of desymmetrization of these units by designing new linkers. For this, we designed two new linkers exhibiting a decreased h/w ratio combined with an in-plane translation of double bonds: 5',5''''-((1E,1'E)-1,4-phenylenebis(ethene-2,1-diyl))bis(([1,1':3',1''-terphenyl]-4,4''-dicarboxylic acid)) (H_4PDVTTC) and 5'',5''''''-((1*E*,1'*E*)-1,4-phenylenebis(ethene-2,1-diyl))bis(2',2''',5',5'''-tetramethyl-[1,1':4',1'':3'',1''':4''',1''''-quinquephenyl] 4,4''''-dicarboxylic acid) (H_4PDVQTC)

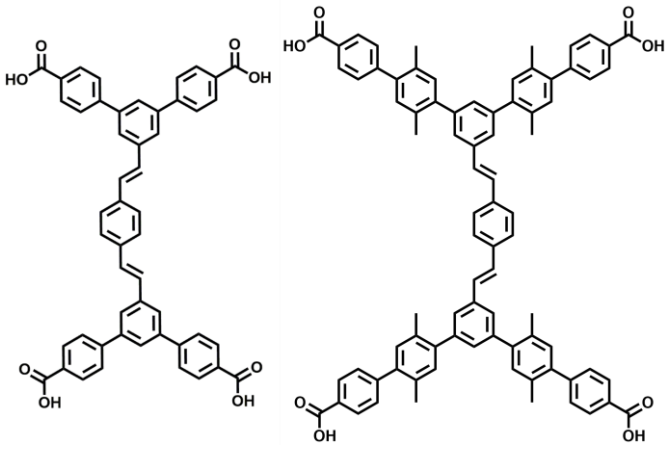


Figure 3.23. Schematic of H_4PDVTTC (left) and H_4PDVQTC (right) linkers.

(Figure 3.23). We decided to introduce methyl groups in PDVQTC to improve its solubility.

Next, we combined them with Zr or RE salts in the presence of modulators and DMF under solvothermal conditions, obtaining a remarkable structural diversity. The first combination of PDVTTC with $ZrOCl_2 \cdot H_2O$ in the presence of TFA as modulator and DMF as solvent yielded yellow cubic crystals after heating 120 ºC for 5 days. SCXRD revealed a new Zr-MOF, here denoted as BCN-38 (BCN stands for Barcelona Material), with an expected underlying **scu/tty** net (Figure 3.24). The Zr-hexamer cluster was present in the structure with an 8-c cubic geometry and D_{4h} symmetry, with formates occupying the four missing positions. This net could be resulted from the desymmetrization of the linker into a ratio of 0.59 and the rotation of peripheral rings and carboxylate groups in 54.52º. Due to the in-plane translation produced by the double bonds, the central phenyl ring is disordered in two different positions and therefore, the linker exhibits a C_{2v} symmetry. BCN-38 crystallized in the *Cmmm* space group, which has been commonly observed for the flexible **scu**-MOFs. In fact, the structure is comparable to the isoreticular Zr-NDI-**scu**-MOF,[114] constructed with a naphthalenediimide (NDI) core that is similar to our central disordered core, which has almost identical cell values. The framework presents rhombic channels (12.34x28.58 Å) along the *c* axis, and the linkers are aligned along this axis. There are three additional channels: two along the *a* axis with hexagonal (13.05x14.56 Å) and rhombic (9.01x15.78 Å) shapes; and an additional hexagonal channel (9.12x13.05 Å) along the *b* axis.

Topologically, if the linker is considered as a single 4-c square node, the underlying net resulted to be the 4,8-c **scu** topology.[190] However, according to the recommendations,[191] if the linker is considered as two 3-c triangular nodes, the underlying net resulted to be the 3,8-c **tty** topology, a **scu**-derived net.

PXRD analysis of the bulk material confirmed the phase purity by comparing it with the PXRD simulated from the SCXRD. It also showed that BCN-38 exhibits certain

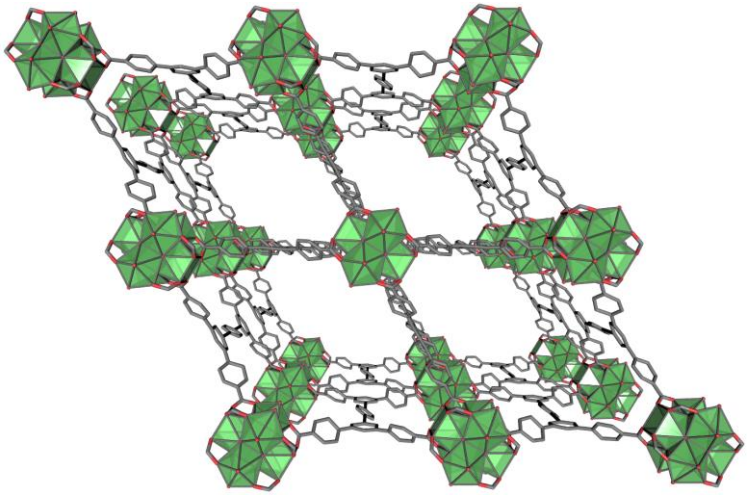


Figure 3.24. Crystal structure of BCN-38, constructed from an 8-c cubic Zr-SBU and showing the underlying **scu**/**tty** net.

structural flexibility after solvent removing or evaporation (Figure 3.25a). This feature was further confirmed by studying its N_2-sorption, obtaining a type-IV isotherm with a lower surface BET area (595 m^2/g) than that expected (Figure 3.25b). This may be attributed to the **scu**/**tty** net, which has been demonstrated to be a flexible net.[114] Analysis of the pore-size distribution and total pore volume further confirmed this theory, as we obtained multiple peaks between 8 and 20 Å and 0.35 cm^3/g at $p/p_0 = 0.95$, respectively, which is not the optimum pore volume (Figure 3.25c). We also studied the thermal stability by running a thermogravimetric analysis (TGA) of the sample, which resisted up to 508 ^oC (Figure 3.25d).

We then combined the same PDVTTC linker with $Y(NO_3)_3{\cdot}6H_2O$ in the presence of 2-FBA as modulator, DMF as solvent and H_2O and HNO_3. From this reaction, we obtained rod-like crystals after 7 days heating at 120 ^oC. SCRXD analysis of the structure disclosed a novel 2D RE-MOF, named as BCN-34, with an *in-situ* formed multinuclear fluorocluster, with a rare **sql**/**bex** net (Figure 3.26). It is not common to form 2-periodic structures with multinuclear clusters. In fact, there are just a few examples reported in literature.[52,101,192,193] Surprisingly, instead of the well-known

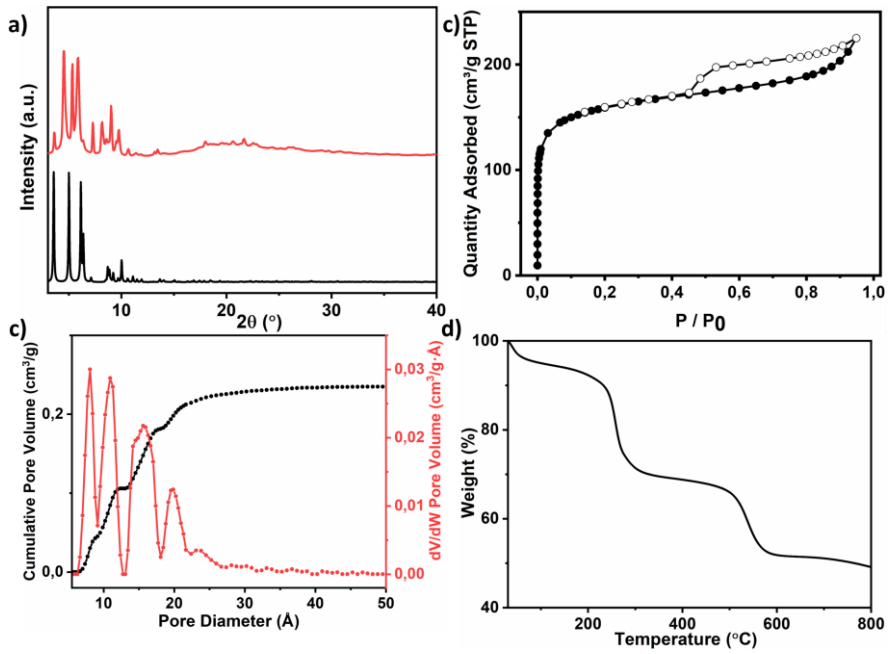


Figure 3.25. a) PXRD pattern of calculated BCN-38 (black) and pristine BCN-38 (red). b) N_2 sorption (filled symbols) and desorption (empty symbols) isotherms at 77 K of BCN-38. c) Pore size distribution estimated by DFT for BCN-38. d) a) TGA analysis of activated BCN-38. The weight loss from ~200 to 450 °C can be attributed to the detachment of partial formates (coming from the degradation of DMF) or trifluoroacetates in the structure, as typically observed in Zr-MOFs.[117,180]

hexanuclear or nonanuclear cluster, BCN-34 exhibited a rare 4-c heptanuclear RE-cluster, coordinated by eight PDVTTC linkers, four 2-FBAs, and multiple open metal sites. To the best of our knowledge, this cluster has never been observed before. However, it was proposed as an intermediate in the evolution of a RE_6-cluster to a RE_9-cluster.[186] This cluster is extended by the PDVTTC linker along the *b* axis to connect four neighboring RE-SBUs, as the linkers are doubly bridging them in a very distorted conformation. There are two different crystallographic linkers, both of them exhibiting a ratio of 0.60 and four different carboxylate groups, being one coplanar to the central core while the others rotate between 42.25 and 61.29°. This net could be resulted from the desymmetrization of the linker, as a similar Zr-MOF has been reported with the same underlying net and double

bridged linkers.[101] BCN-34 crystallized in the $P2_1/a$ space group with an AB packing of the layers. Topological analysis of the structure revealed an underlying 4^2-c **sql-b** net when considering the linker as a single vertex. If, as previously mentioned the linker is divided into 2 3-c nodes, the underlying net has the 3,4-c **bex** topology.

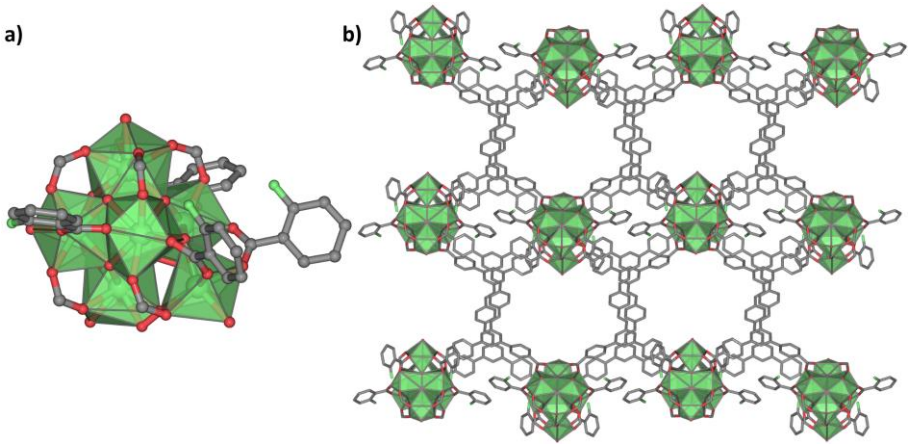


Figure 3.26. Structural illustrations of BCN-34, highlighting: a) the *in-situ* formed 8-c RE_7-fluorocluster; and b) the overall 2D structure of BCN-34 with an underlying **sql-b/bex** net.

According to the PXRD, the bulk sample is pure as both experimental and simulated patterns completely match (Figure 3.27a). We also tested the porosity of the material by running N_2-sorption experiments, obtaining a type-I isotherm with a low surface BET area of 245 m^2/g (Figure 3.27b). We then switched to CO_2 as adsorbed gas to study if the small channels of the structure were not able to let pass N_2, obtaining a CO_2 uptake of 97.8 cm^3/g at 200K and 1 atm (Figure 3.27c).

Further elongation of the linker into PDVQTC directed to the assembly of two completely different structures. Using the same $ZrOCl_2 \cdot H_2O$ salt but this time with formic acid as modulator, yellow drop-like crystals were synthesized by solvothermal synthesis in the presence of DMF after 7 days heating at 120 ºC. The SCXRD data revealed a new Zr-MOF, called as BCN-143, with an unprecedented net with the underlying 3,4T143 topology (Figure 3.28). The Zr_6-cluster formed exhibited an unprecedented 4-c distorted tetrahedral conformation, "*Z-shape*"

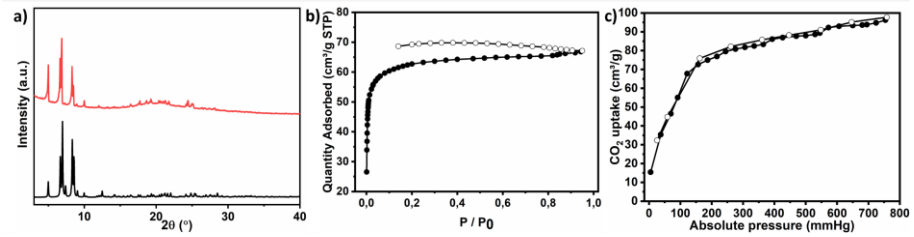


Figure 3.27. a) PXRD pattern of calculated BCN-34 (black) and pristine BCN-34 (red). b) N_2 sorption (filled symbols) and desorption (empty symbols) isotherms at 77 K of BCN-34. c) CO_2 adsorption (filled symbols) and desorption (empty symbols) isotherm at 200 K of BCN-34.

coordination, where four additional formates chelate in the remaining positions of the cubic conformation, and 4 additional monocoordinated formates are located in the open metal sites of the equatorial plane. These later formates are doubly bridging neighboring Zr-clusters in two different directions with 90º difference, forming a zigzag chain of Zr-SBUs along the *a* axis. Moreover, the central core of the linker rotates and crystallized in a tetrahedral conformation, with a dihedral angle of 84.16º between the external phenyl rings in the core, and slightly bending to one side. This feature added up to the elongation of the arms provoke the distortion into a ratio of 0.71. To afford this net, the carboxylate groups need to rotate 45.27 and 60.17º. We believe that the formation of this net is induced by the strong desymmetrization of the PDVQTC linker that dramatically decrease the connectivity of the Zr-cluster in this unconventional form. The structure consists in a very dense 2-fold interpenetrated framework, with two different channels: a hexagonal one (4.10x5.93 Å) along the *c* axis, and a square one (3.88x7.58 Å) along the *a* axis.

Regarding the topological analysis, if we considered the linker as two 3-c nodes, the structure shows an underlying 3,4T143 net, which has never been observed in MOFs constructed with carboxylate or inorganic clusters. Instead, if the linker is considered as a 4-c tetrahedral node, the resulting net is based on a new topology. The same case occurred when considering the connections of the formates for both simplifications, in 3,6-c and 4,6-c new nets, respectively.

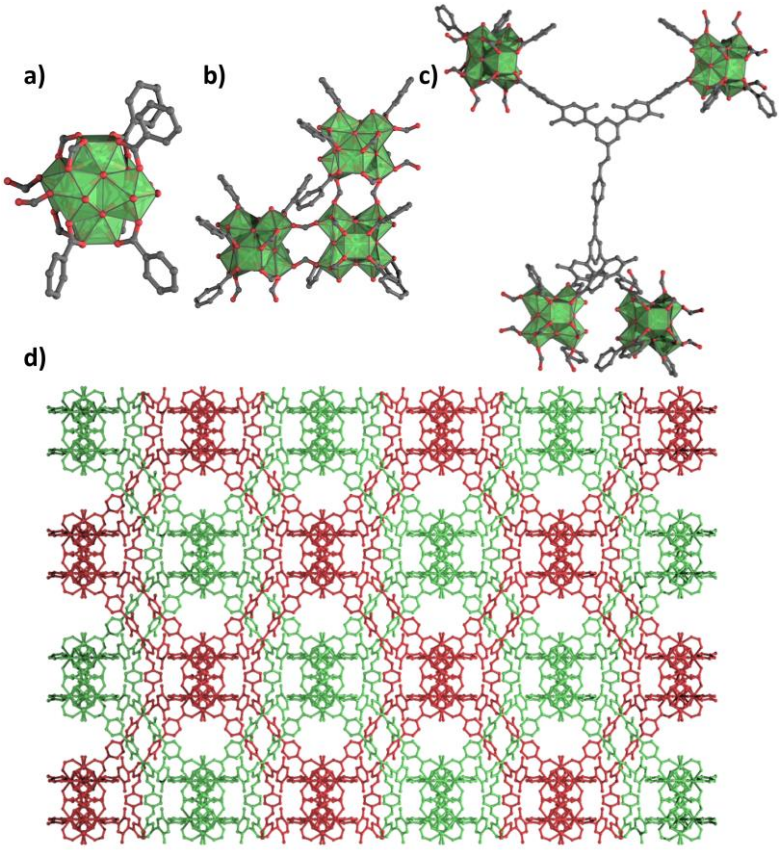


Figure 3.28. Structural illustrations of BCN-143, highlighting: a) the *in-situ* formed 4-c Zr-hexamer SBU; b) the zigzag chain of Zr-clusters connected through double bridging formates in the open metal sites; c) tetrahedral conformation of the linker in the crystal structure; and d) overall twofold interpenetrated structure of BCN-143 with an underlying 3,4T143 net.

The comparison of the experimental PXRD of the bulk sample and the simulated from the obtained SCXRD confirmed the phase purity of BCN-143 (Figure 3.29a). Then, we performed N_2-sorption studies, observing a type-IV isotherm with a surface BET area of 529 m^2/g, in agreement to the high density (ρ = 1.94 g/cm^3) of the material, which is uncommonly observed in MOFs (Figure 3.29b). Accordingly, the total pore volume was found to be 0.27 cm^3/g. Despite its lower cluster connectivity, the Zr-MOF resulted to be a very robust material. According to the

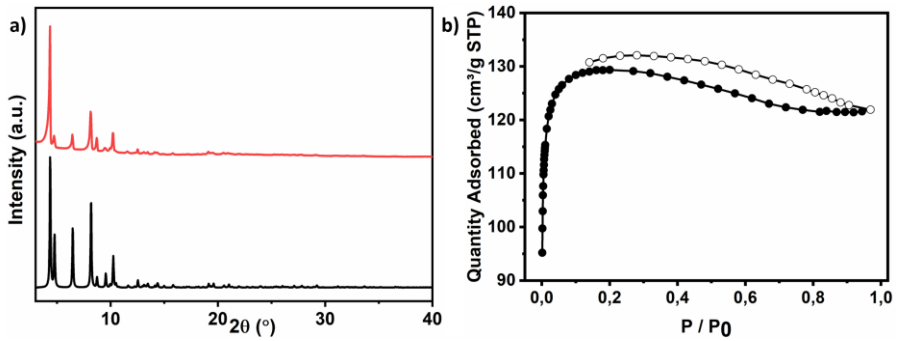


Figure 3.29. a) PXRD pattern of calculated BCN-143 (black) and pristine BCN-143 (red). b) N_2 sorption (filled symbols) and desorption (empty symbols) isotherms at 77 K of BCN-38.

TGA, BCN-143 show high thermal stability resisting up to 495 ºC (Figure 3.30a). Moreover, BCN-143 also demonstrated a great stability in water, retaining completely the crystallinity after incubating the sample in water for 1 h, 12 h and 24 h (Figure 3.30b). In light of these results, we tested the water adsorption of BCN-143, obtaining a 15.4% of its weight adsorbed (Figure 3.30c). The low capacity of the material may be related to its low accessible surface area and complicated access of the water molecules through the channels.

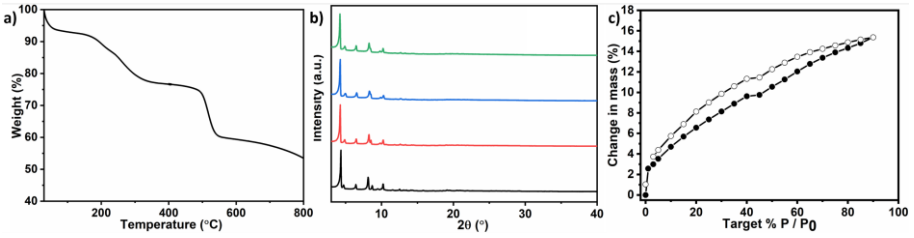


Figure 3.30. a) TGA analysis of activated BCN-143. The weight loss from ~200 to 450 ºC can be attributed to the detachment of partial formates (coming from the degradation of DMF) or trifluoroacetates in the structure, as typically observed in Zr-MOFs.[117,180] b) PXRD patterns of pristine BCN-143 (black) and after its incubation in water for 1 h (red), 12 h (blue) and 24 h (green). c) DSV isotherm plot of the H_2O adsorption (filled symbols) and desorption (empty symbols) at 298 K of BCN-143.

Finally, we explored the last combination of MBBs by replacing the Zr-SBU by its RE analogue. We mixed H_4PDVQTC, $Tb(NO_3)_3{\cdot}5H_2O$, and 2,6-DFBA in DMF at

120 ºC and crystallized big cubic crystals after 7 days of reaction. Unfortunately, the crystals diffracted but with not enough resolution for solving its crystal structure by SCXRD. This was confirmed by PXRD of the bulk material, exhibiting sharp peaks at low degrees and broader ones at higher degrees, indicating the crystallinity of the material with a decreased long-range order (Figure 3.31a). In order to disclose the atomic arrangement of our structure, we modelled a simulated structure with Materials Studio 2021 Program based on a polynuclear RE-cluster. Upon exploration of the possible net to be formed (Section 3.2.1), we considered its rectangular and planar conformation for the construction of a **ftw**-MOF. Comparing the experimental and simulated patterns from the modelled framework, we observed a complete match of the peaks, and a satisfactory Pawley refinement was reached (Rp = 4.94%, Rwp = 8.27%) corresponding to a disordered structure in the *Im-3* space group (Figure 3.31b). Concretely, the simulated net was based on the underlying 3,12-c **kle** topology, a **ftw**-derived net. Accordingly, we named our material as BCN-312.

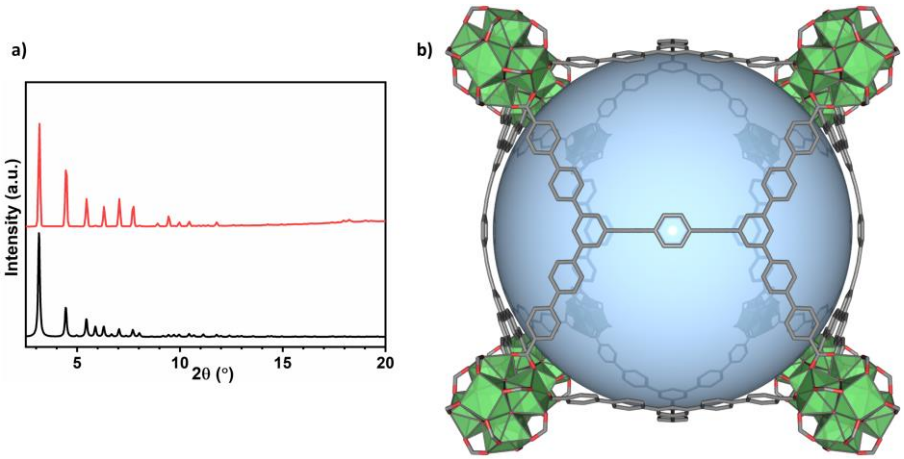


Figure 3.31. a) PXRD patter of simulated BCN-312 (black) and pristine BCN-312 (red). Structural illustrations of simulated BCN-312 with an underlying **kle**/**ftw** net.

According to our simulation, the density of BCN-312 is very low (ρ = 0.28 g/cm^3), indicating potential high porosity of the material. However, upon solvent exchange,

the structure collapse, presumable due to the low long-range order, and therefore preventing the successful N_2-adsorption experiments.

3.2.3. Exploring the desymmetrization effect of 8-c ligand in Zr-MOFs

According to our previous literature survey (Section 3.2.1), high-connected MOFs based on doubly high-connected inorganic and organic MBBs are scarce. We referred to high-connected MOFs to those when at least one of the building blocks that comprises the structure has a connectivity ≥ 8, as their possible nets to form are more constrained and facilitates its prediction.[194] In addition, these reticular materials clearly show a tendency to exhibit higher structural, thermal and chemical stability, as well as a higher tolerance to the structural collapse produce by the defects when growing the structure.

Some of the most common strategies to access high-connected MOFs are based on: (i) using dendritic ligands to connect low-connected clusters;[195–198] (ii) using high-connected inorganic clusters or cages linked by simple linkers;[44,199,200] and (iii) using simultaneously both high-connected inorganic and organic MBBs. However, according to the CCDC database (ConQuest V. 2.0.0, CCDC, Cambridge, UK),[201] only three examples were found corresponding to the last strategy. One structure corresponded to the assembly of an octatopic ligand with octogonal conformation with a trinuclear and linear Ni(II) cluster with a cubic conformation, reticulating an **eps** net;[202] and (ii) two different structures based on the assembly of a nonanuclear RE-based cluster with a 12-c hexagonal prism conformation with an 8-c octagonal-like and a 12-c hexagonal prismatic shape linker, reticulating **kce** and **kex** nets, respectively (Figure 3.32).[203] However, research in this cluster indicates the general tendency to be fully coordinated and evolving to different kind of clusters (such as tetranuclear,[136,137] hexanuclear[199] or nonanuclear[171,185,186]) due to the difficulty of stabilizing defective RE-clusters in the absence of high concentrations of fluorinated-modulators or less-symmetric linkers, complicating the net-prediction

when mixing with new symmetric linkers. In contrast, the strong Zr-O bond always favors the formation of the Zr-oxocluster, enabling defaults of its connectivity according to the symmetry induced by the linker, directing to a target net (Figure 3.32).[4,180,181,204]

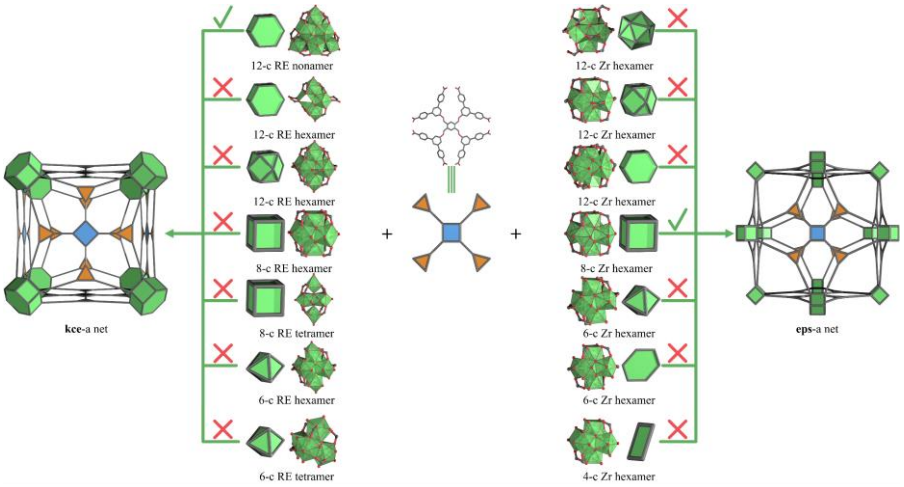


Figure 3.32. Comparison between the effect of the octatopic linker symmetry guiding to different reticular materials when using a RE hydroxo/fluorinated cluster (left) and a Zr oxo/hydroxo-cluster (right). Among the different clusters found in terms of connectivity and nuclearity in minimal edge-transitive nets, the RE-cluster tends to evolve to a high nuclearity to be fully connected and form the **kce** net, whereas the Zr-cluster tends to decrease its connectivity rather than be disordered in 12-c hexagonal prism shape, forming the **eps** net.

To date, the maximum connectivity of the organic linkers reticulated in Zr-MOFs have been limited to 6 in hexagonal-like, trigonal prismatic-like, and octahedral-like linkers.[39,187,188] This fact motivated us to endeavor the assembly of the Zr_6-cluster with high-connected linkers. Based on the two different publications of octagonal shaped linkers, we observed that both linkers present desymmetrizations from the ideal D_{8h} symmetry and geometry, which perfectly match with our study of desymmetrized organic MBBs. So, we synthesized the octatopic 1,2,4,5-tetrakis[3,5-bis(4-carboxyphenyl)phenoxymethyl]benzene (H_8TBCPB) linker according to the

previous reported procedure by Chen *et al.* in order to compare the linker as net-directing agent for the assembly of Zr- and RE-cluster, as we previously observed.[203]

Once synthesized, we combined it with $ZrOCl_2 \cdot H_2O$ in the presence of TFA as modulator and DMF as solvent under solvothermal conditions, heating at 120°C for 5 days. This process yielded colorless cubic crystals that were analyzed by SCRXD revealing a new Zr-MOF, which we called BCN-348, with an underlying **eps** net (Figure 3.33). In this structure, the *in-situ* formed Zr-oxocluster revealed a hexanuclear core with an 8-c cubic geometry with four missing positions induced by the symmetry of the linker. BCN-348 was solved in the cubic *Fm-3* space group with a unit cell parameter of 59.677 Å and resulting in a large cell volume of 212530 $Å^3$, one of the biggest reported for Zr-MOFs. This framework presents two kinds of cavities: a bigger, cuboctahedral cage with a diameter of 38.6 Å containing hexagonal (17.6 Å) and rhombic (12.1 Å) windows; and a smaller, octahedral cage with a diameter of 26.3 Å containing the same hexagonal (17.6 Å) windows (Figure 3.33). The octagonal linker occupies the square face of the cuboctahedral cages

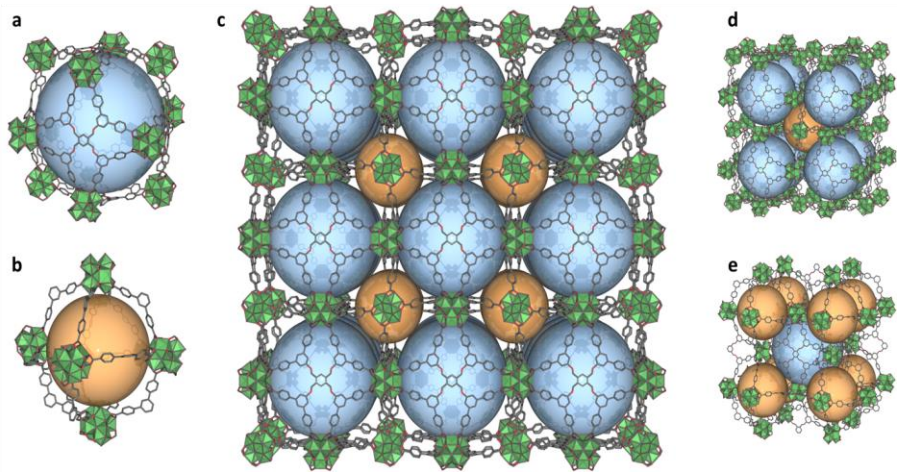


Figure 3.33. Structural illustrations of BCN-348, highlighting a) the cuboctahedral cage assembled with six organic moieties located in the square faces; b) the octahedral cage assembled with twelve partial organic moieties located at the edges; c) the overall structure of BCN-348 across the c-axis; d) the assembly of face-sharing cuboctahedron stacking; and e) the spatial distribution of octahedral cages around the cuboctahedral cavity.

connecting four different clusters, whereas its branches occupy the edges of the octahedral cage connecting two clusters. Curiously, this framework can also be considered as an example of the stacking of face-sharing cuboctahedra, which are Archimedean solids that are interesting for the design of high-symmetrical nets (Figure 3.33d).[205]

The topological analysis of the structure was performed considering the recommendations for the deconstruction of dendritic ligands into more-regular shapes (triangular and square) instead of the less-symmetric octagonal.[191] In this way, the analysis revealed the formation of a 3,4,8-c **eps** net, which has never been observed for Zr- or RE-based MOFs. In fact, there is just one example of a Ni-based MOF exhibiting this net.[202] Also, when we performed a topological analysis without splitting the linker but instead, treating as an octagonal node, the connectivities of this node and of the Zr-oxocluster were halved, resulting in a 4,4-c **nbo-b** net. This finding proves that the **eps** net a **nbo-b**-related net and therefore, corroborates that BCN-348 is the first Zr-MOF based on this related net.[203,206]

Seeking to understand the formation of the aforementioned **eps** net, we did a reticular survey.[207] According to the RCSR database, combining an octagonal-shape linker with a Zr-cluster, which could be 12-c, 8-c, 6-c or 4-c (in the case of the most-regular ones), would lead to the formation of **kce** (3,4,12-c), **eps** (3,4,8-c), **cye** (6,8-c), **cze** (3,4,6-c), or **cyt** (4,8-c) nets, respectively. Among these, we initially excluded the **cye** and **cyt** nets, due to the mismatch between the proximity of two neighbouring Zr-clusters in these nets as well as to the length of the TBCPB linker that we had used. Regarding the **kce** net, this topology had already been reported as resulting from the combination of the TBCPB linker with a 12-c nonanuclear RE-cluster that exhibits a hexagonal prism conformation (Figure 3.32). However, the strong Zr-O bonds always favour the formation of the hexanuclear Zr-oxocluster, enabling defaults in its connectivity,[48,51,53,55,56,58,67,99,117,121,141,154,167–169,187,208–210] rather than being disordered in its 12-c hexagonal prism conformation.[39,59] We hypothesize that together, these features favoured the formation of the **eps** net

rather than either the **kce** net, which would have involved the formation of a disordered 12-c hexagonal prismatic Zr-cluster, or the **cze** net, which is less connected than the **eps** (Figure 3.32).

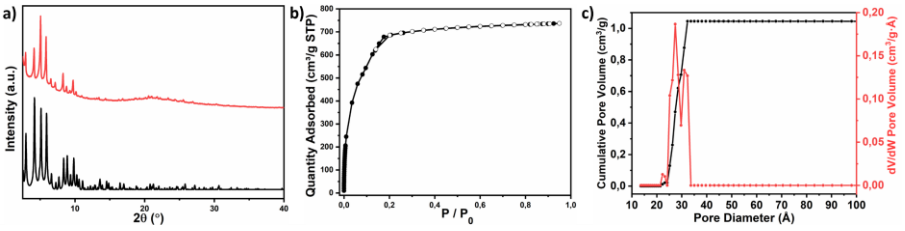


Figure 3.34. a) PXRD pattern of calculated BCN-348 (black) and pristine BCN-348 (red). b) N_2 sorption (filled symbols) and desorption (empty symbols) isotherms at 77 K of BCN-348. c) Pore size distribution estimated by DFT for BCN-348.

Next, we confirmed the phase purity of the bulk BCN-348 sample by PXRD: the experimental results matched the simulated ones that we had obtained by SCXRD (Figure 3.34a). We then studied the porosity of BCN-348 by running the N_2-sorption experiments at 77 K. BCN-348 exhibits an apparent surface BET area of 2564 m^2/g in an isotherm between type-Ib and type-IV (Figure 3.34b).[211] This feature has been commonly observed for the most famous mesoporous MOFs such as MIL-100, MIL-101, PCN-61, PCN-66, NU-111 or DUT-51 (Zr and Hf), where these cavities are connected through the microporosity.[212–216] The total pore volume was found to be 1.14 cm^3/g at $p/p_0 = 0.95$. The pore-size distribution, based on the DFT models, revealed the presence of mesopores of 27.3 Å and 31.7 Å (Figure 3.34c). Moreover, BCN-348 was thermally stable up to 508 °C (Figure 3.35a), and it maintained its phase crystallinity when incubated in water for 1 h, 12 h and 24 h (Figure 3.35b). The fact that BCN-348 combines mesoporosity with thermal and hydrolytic stability illustrates the feasibility of using high-connected clusters and linkers to assemble robust porous MOFs.

Among the most promising recent applications for Zr-MOFs is their use as hydrolytic catalysts for the detoxification of highly toxic organophosphate compounds—namely pesticides, and nerve agents and their simulants.[217–222] These

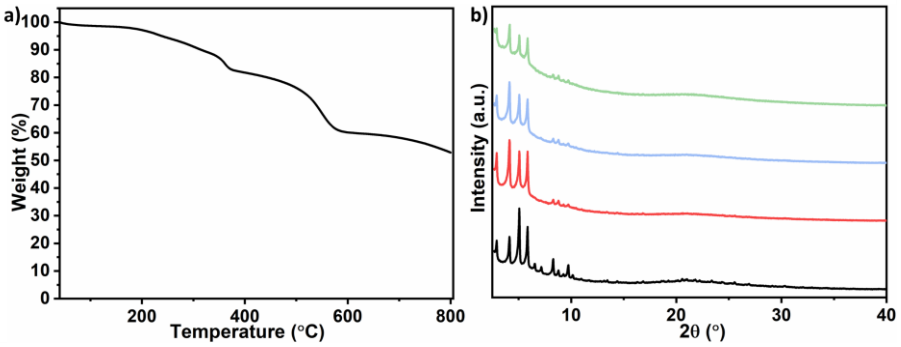


Figure 3.35. a) TGA analysis of activated BCN-348. The weight loss from ~200 to 450 °C can be attributed to the detachment of partial formates (coming from the degradation of DMF) or trifluoroacetates in the structure, as typically observed in Zr-MOFs.[117,180] b) PXRD patterns of pristine BCN-348 (black) and after its incubation in water for 1 h (red), 12 h (blue) and 24 h (green).

detoxification processes imply the activation of the P–X (X = O, S, F) bond by zirconium Lewis acidic and hydroxide basic sites at the oxo-hydroxide Zr-cluster. Consequently, pore size and polarity, framework connectivity, and stability together define the access of water molecules and toxic substrate molecules to the catalytically active metal cluster. To date, most of these Zr-MOF-assisted catalytic processes have been done using simulants with ester P–O bonds, together with corrosive and toxic basic buffers (*N*-ethylmorpholine). Importantly, the toxicity of common nerve agents such as Soman (GD), Sarin (GB) and Cyclosarin (GF) is determined by labile P–F bonds. Consequently, there is pronounced interest in the development of new detoxification materials that could hydrolyze the P–F bonds of hazardous chemicals in unbuffered aqueous solutions.

Table 3.1. Distribution of unreacted and hydrolyzed DIFP in the supernatant and adsorbate phase after 24 h of incubation with BCN-348 determined by ^{1}H NMR in D_2O (0.6 mL) and after extraction with $CDCl_3$ (0.6 mL), respectively.

Hydrolyzed DIFP (DIP) (%)		**Non-hydrolyzed DIFP (%)**	
Supernatant	**Adsorbed[a]**	**Supernatant**	**Adsorbed**
12.8	60	2.2	25

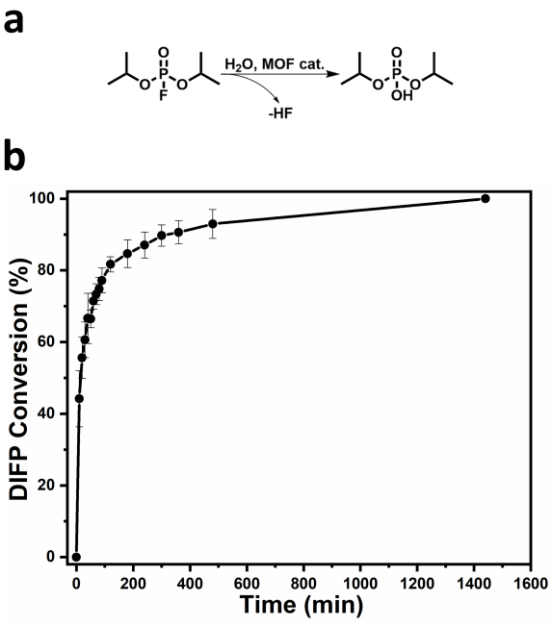


Figure 3.36. a) Hydrolysis of DIFP catalyzed by BCN-348 (denoted as "MOF cat."). b) DIFP removal plotted against time.

Seeking to exploit the accessible pore structure and hydrolytic stability of BCN-348, we tested its catalytic activity in the removal of the simulant diisopropylfluorophosphate (DIFP), which contains a P–F bond. We ran the hydrolysis in an aqueous unbuffered dispersion of BCN-348 using a DIFP/MOF ratio of 1.5 : 1. The removal of DIFP from the solution was first followed by GC. The half-life of detoxification is 72.2 min with quantitative removal of the toxic simulant after 24 h (Figure 3.36b). To have a deep insight into the detoxication mechanism, we performed additional ^{31}P NMR and ^{1}H NMR analysis in D_2O. The results confirmed that DIFP is removed from the supernatant solution after 24 h, with diisopropylphosphate (DIP) appearing as the main hydrolytic product (72.8%). However, there was still a fraction of 27.2% of unreacted DIFP molecules, which were mostly adsorbed by BCN-348 (Table 3.1 and Figure 3.37). These results

confirm the highly accessible porous structure and exposed nature of the Zr metal sites in the metal clusters.

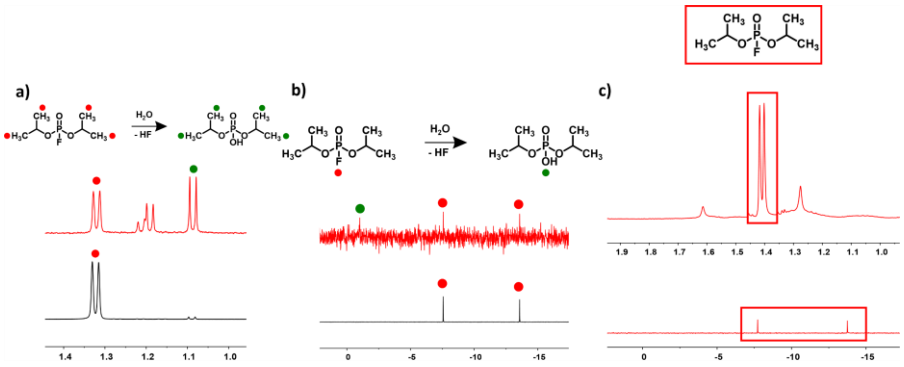


Figure 3.37. a) ^{1}H NMR spectra of supernatant before (black) and after 24 h (red) of suspending BCN-348 with DIFP in unbuffered solution. b) ^{31}P NMR spectra of supernatant before (black) and after 24 h (red) of suspending BCN-348 with DIFP in unbuffered solution. c) ^{1}H NMR (top) and ^{31}P NMR (bottom) spectra of the extracted solution with $CDCl_3$ from BCN-348 after suspension during 24 h with DIFP in unbuffered solution.

3.3. Experimental section

3.3.1. Materials, methods and characterization

3.3.1.1. Materials

Zirconium oxychloride octahydrate ($ZrOCl_2{\cdot}8H_2O$), yttrium(III) nitrate hexahydrate, terbium(III) nitrate pentahydrate, formic acid, potassium carbonate (K_2CO_3), potassium iodide (KI), sodium hydroxide (NaOH), 2,6-difluorobenxoid acid (2,6-DFBA) and bis(triphenylphosphine)palladium(II) dichloride ($PdCl_2[P(Ph)_3]_2$) were purchased from Sigma-Aldrich Co. *N,N*-dimethylformamide (DMF), acetonitrile (MeCN), tetrahydrofuran (THF), hexane, ethylacetate (AcOEt), methanol (MeOH), hydrochloric acid (HCl), nitric acid (HNO_3) and sulfuric acid (H_2SO_4) were obtained from Fisher Chemical. Trifluoroacetic acid

(TFA) and 2-fluorobenzoic acid (2-FBA) were obtained from TCI. 3,5-dibromophenol, 4-carboxyphenylboronic acid and 1,2,4,5-tetrakis(bromomethyl)benzene were purchased from BLDpharm. All the reagents and solvents were used without further purification unless otherwise specified. Deionized water was obtained with a Milli-Q® system (18.2 MΩ·cm).

3.3.1.2. Methods

GC studies

The removal of DIFP was performed using 12 mg of BCN-348 (2.5 μmol) suspended in 0.6 mL of H_2O. Afterwards, 1.5 μL of *N,N*-dimethylacetamide (DMA), used as internal reference, and 1.5 μL of DIFP (3.8 μmol) were added to the suspension (DIFP/MOF ratio of 1.5:1). The evolution of the concentration of DIFP in the supernatant solution was followed at room temperature by means of GC.

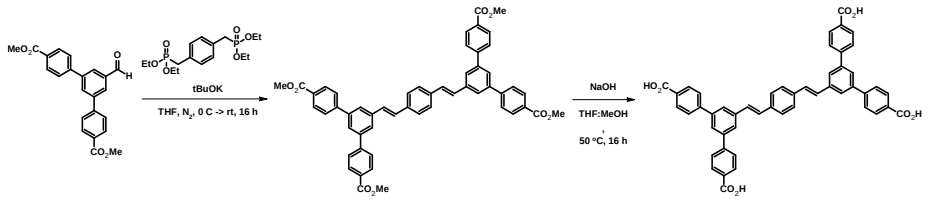
^{1}H and ^{31}P NMR studies

The degradation of DIFP simulant into DIP by BCN-348 was followed by ^{1}H and ^{31}P NMR. Specifically, 12 mg of BCN-348 were suspended in a mixture containing 0.6 mL of D_2O, 0.7 μL of DMP (used as internal reference) and 1.5 μL of DIFP (DIFP/MOF ratio of 1.5:1). The suspension was stirred during 24 h at room temperature and the concentration of DIPF and DIP in the supernatant solution and in the adsorbate phase were quantified by NMR.

After 24 h, the solid was separated from the supernatant by centrifugation (10000 rpm, 5 min). Afterwards, the solid was suspended in $CDCl_3$ for 5 h at room temperature to extract DIFP molecules adsorbed inside the cavities of BCN-348 and the concentration of DIFP and its degradation product DIP were determined by ^{1}H-NMR.

3.3.1.3. Synthesis

Synthesis of 5',5''''-((1E,1'E)-1,4-phenylenebis(ethene-2,1-diyl))bis(([1,1':3',1''-terphenyl]-4,4''-dicarboxylic acid)) (H_4PDVTTC)



Scheme 3.1. Synthetic procedure for H_4PDVTTC linker.

Synthesis of 3,5-bis[(4-methoxycarbonyl)phenyl]benzaldehyde

3,5-bis[(4-methoxycarbonyl)phenyl]benzaldehyde was synthesized according to a previous reported procedure.[223]

Synthesis of tetramethyl 5',5''''-((1E,1'E)-1,4-phenylenebis(ethene-2,1-diyl))bis([1,1':3',1''-terphenyl]-4,4''-dicarboxylate)

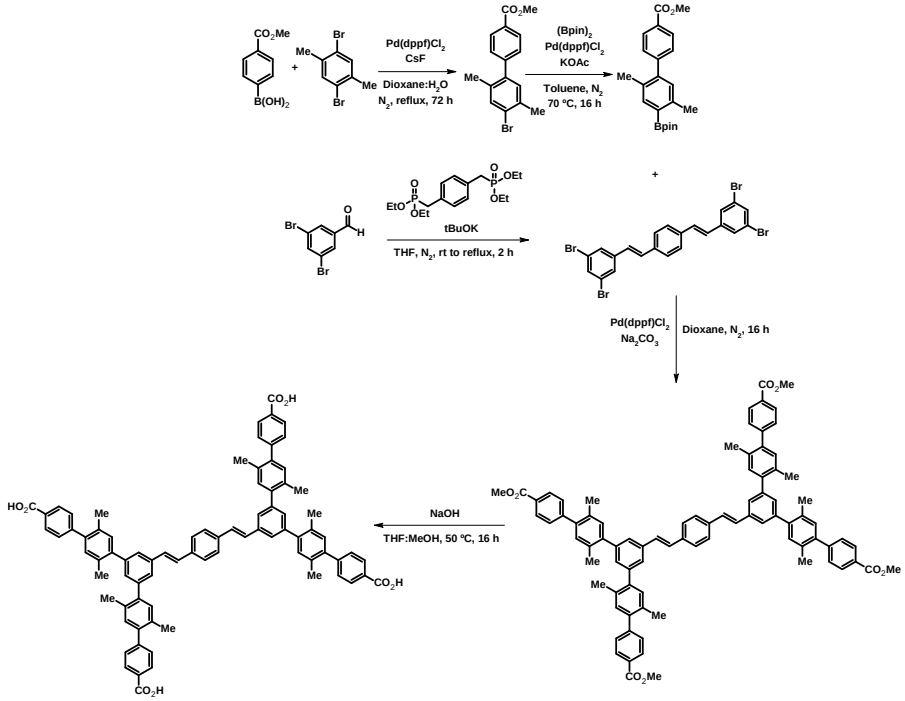
3,5-bis[(4-methoxycarbonyl)phenyl]benzaldehyde (1.1 g, 3 mmol, 2.2 equiv.) and tetraethyl (1,4-phenylenebis(methylene))bis(phosphonate) (0.51 g, 1.36 mmol, 1 equiv.) were placed in a 100 mL round bottomed flask. The flask was purged with N_2. Thereafter, dry THF (40 mL) were added, and the resulting suspension was heated with a heat gun until a clear solution was observed. Afterwards, the solution was cooled down to 0 °C and it was stirred for 10 min at that temperature. After this period, tBuOK (0.34 g, 3 mmol, 2.2 equiv.) was added in one portion, and the resulting suspension was stirred at 0 °C for 10 min. Then, it was allowed to reach room temperature overnight. Thereafter, the suspension was cooled down again to 0 °C and H_2O (10 mL) was added. Most of the THF was removed by rotary evaporation, until an abundant solid appear. The suspension was vacuum filtered to yield the tetraester as a pale white solid (1.04 g, 1.27 mmol, 93% yield). **^{1}H NMR**

(300 MHz, $CDCl_3$) δ 8.18 (d, *J* = 8.6 Hz, 8H), 7.85 – 7.70 (m, 14H), 7.61 (s, 4H), 7.30 (s, 4H), 3.99 (s, 12H); **^{13}C NMR (75 MHz, $CDCl_3$) δ** 166.9 (C), 145.2 (C), 141.3 (C), 138.7 (C), 136.7 (C), 130.2 (CH), 127.2 (CH), 127.1 (CH), 125.1 (CH), 52.2 (CH_3). Given the chemical similarity of various carbon atoms, there are fewer signals than expected. Moreover, most of them appear as broad signals.

Synthesis of 5',5''''-((1E,1'E)-1,4-phenylenebis(ethene-2,1-diyl))bis(([1,1':3',1''-terphenyl]-4,4''-dicarboxylic acid)) (H_4PDVTTC)

5',5''''-((1E,1'E)-1,4-phenylenebis(ethene-2,1-diyl))bis([1,1':3',1''-terphenyl]-4,4''-dicarboxylate) (1.04 g, 1.27 mmol, 1 equiv.) was suspended in MeOH (10 mL) and THF (10 mL). Then, a 10% aqueous solution of NaOH (4 mL) was added. The resulting suspension was stirred at 50 °C for 16 h. After this time, the solvents were carefully removed under reduced pressure. Thereafter, the resulting solid is suspended in H_2O (10 mL) and cooled down to 0 °C. Then, 12 M HCl was added dropwise until pH was 1-2. The resulting solid was filtered under vacuum and dried in a desiccator overnight to obtain the tetraacid as a pale white solid (775 mg, 1.02 mmol, 80% yield). **^{1}H NMR (300 MHz, $CDCl_3$) δ** 8.08 (d, *J* = 8.6 Hz, 8H), 8.05 (d, *J* = 1.4 Hz, 4H), 8.00 (d, *J* = 8.6 Hz, 8H), 7.96 (t, *J* = 1.4 Hz, 2H), 7.72 (s, 4H), 7.58 (s, 2H), 7.53 (s, 2H); **^{13}C NMR (75 MHz, DMSO-d_6) δ** 167.2 (C), 144.0 (C), 140.4 (C), 138.8 (C), 136.6 (C), 129.9 (CH), 127.2 (CH), 127.1 (CH), 124.9 (CH). Given the chemical similarity of various carbon atoms, there are fewer signals than expected. Moreover, most of them appear as broad signals.

Synthesis of 5'',5''''''-((1*E*,1'*E*)-1,4-phenylenebis(ethene-2,1-diyl))bis(2',2''',5',5'''-tetramethyl-[1,1':4',1'':3'',1''':4''',1''''-quinquephenyl]-4,4''''-dicarboxylic acid) (H_4PDVQTC)



Scheme 3.2. Synthetic procedure for H_4PDVQTC linker.

Synthesis of 1,4-Bis((*E*)-3,5-dibromostyryl)benzene

3,5-dibromobenzaldehyde (1.1 g, 4.2 mmol, 2.1 equiv.) and tetraethyl (1,4-phenylenebis(methylene))bis(phosphonate) (0.76 g, 2 mmol, 1 equiv.) were placed in a 50 mL round bottom flask. The flask was purged with N_2. Thereafter, dry THF (20 mL) were added, and the resulting suspension was stirred for 5 min. Then, tBuOK (0.56 g, 5 mmol, 2.5 equiv.) was added in one portion, and the resulting suspension was refluxed for 2 h. Next, it was allowed to reach room temperature and H_2O (10 mL) was added. A bright yellow solid appeared, which was vacuum

filtered and dried in a desiccator to obtain the tetrabromide product as a bright yellow solid (447 mg, 0.75 mmol, 37% yield). 1,4-Bis((*E*)-3,5-dibromostyryl)benzene is insoluble in all available deuterated solvents and therefore it could not be characterized by NMR.

Synthesis of methyl 4'-bromo-2',5'-dimethyl-[1,1'-biphenyl]-4-carboxylate

In a 500 mL three-necked round bottom flask, 1,4-dioxane (100 mL) and H_2O (50 mL) were added and bubbled with N_2 for 30 min. Then, 1,4-dibromo-2,5-dimethylbenzene (13.2 g, 50 mmol, 5 equiv.), (4-(methoxycarbonyl)phenyl)boronic acid (1.8 g, 10 mmol, 1 equiv.) and CsF (4.6 g, 30 mmol, 3 equiv.) were added and the resulting suspension was further bubbled with N_2 for 10 min. Thereafter, $Pd(dppf)Cl_2$ (0.37 g, 0.5 mmol, 5 mol %) was added in one portion and the resulting mixture was refluxed for 72 h. Then, the solution was transferred to a separatory funnel, and the organic layer was extracted with DCM (x3), dried over $MgSO_4$, and concentrated under reduced pressure. The dark residue was purified by column chromatography using hexane:DCM mixtures as eluent to obtain the bromide product as a white solid (2.3 g, 7.21 mmol, 72% yield). **^{1}H NMR (300 MHz, $CDCl_3$) δ** 8.08 (d, *J* = 8.5 Hz, 2H), 7.46 (s, 1H), 7.36 (d, *J* = 8.5 Hz, 2H), 7.08 (s, 1H), 3.95 (s, 3H), 2.39 (s, 3H), 2.20 (s, 3H). The spectroscopic data match with those reported in the bibliography.[224]

Synthesis of methyl-2',5'-dimethyl-4'-(4,4,5,5-tetramethyl-1,3,2-dioxaborolan-2-yl)-[1,1'-biphenyl]-4-carboxylate

Dry toluene (50 mL), methyl 4'-bromo-2',5'-dimethyl-[1,1'-biphenyl]-4-carboxylate (2.3 g, 7.21 mmol, 1 equiv.) and KOAc (1.6 g, 15.9 mmol, 2.2 equiv.) were added in an oven-dried 250 mL three-necked round-bottomed flask, and the resulting suspension was bubbled with N_2 for 30 min. Then, B_2pin_2 (2.2 g, 8.7 mmol, 1.2

equiv.) and $Pd(dppf)Cl_2$ (0.26 g, 0.36 mmol, 5 mol %) were added, and the solution was heated to 70 °C and stirred at this temperature for 16 h. Afterwards, the solvent was removed under reduced pressure and the residue was partitioned with DCM and water in a separatory funnel. The layers were separated, and the aqueous phase was extracted with DCM (x2). The combined organic layers were dried over $MgSO_4$, filtered, and concentrated under reduced pressure. The residue was purified by column chromatography using hexane:AcOEt mixtures as eluent to afford the pinacol borane ester product as a white solid (1.52 g, 4.15 mmol, 58% yield). **^{1}H NMR (300 MHz, $CDCl_3$) δ** 8.09 (d, *J* = 8.6 Hz, 2H), 7.70 (s, 1H), 7.40 (d, *J* = 8.6 Hz, 2H), 7.06 (s, 1H), 3.96 (s, 3H), 2.55 (s, 3H), 2.24 (s, 3H), 1.38 (s, 12H). The spectroscopic data match with those reported in the bibliography.[224]

Synthesis of tetramethyl 5'',5''''''-((1*E*,1'*E*)-1,4-phenylenebis(ethene-2,1-diyl))bis(2',2''',5',5'''-tetramethyl-[1,1':4',1'':3'',1''':4''',1''''-quinquephenyl]-4,4''''-dicarboxylate)

Methyl-2',5'-dimethyl-4'-(4,4,5,5-tetramethyl-1,3,2-dioxaborolan-2-yl)-[1,1'-biphenyl]-4-carboxylate (2.0 g, 5.5 mmol, 6 equiv.), 1,4-Bis((*E*)-3,5-dibromostyryl)benzene (0.54 g, 0.91 mmol, 1 equiv.) and 1,4-dioxane (20 mL) were placed in a 100 mL two-necked round bottom flask. The suspension was bubbled with N_2 for 30 min. Then, aqueous 2 M Na_2CO_3 (4 mL) were added, and the suspension was further bubbled with N_2 for 5 min. Finally, $Pd(dppf)Cl_2$ (0.1 g, 0.14 mmol, 15 mol %) was added and the mixture was refluxed under N_2 for 16 h. Thereafter, the solution was extracted with DCM (x4), dried over $MgSO_4$, filtered, and evaporated under reduced pressure. The residue was purified by column chromatography using hexane:AcOEt (from 95:5 to 80:20) as eluent to yield the tetraester product as a white solid (585.3 mg, 0.47 mmol, 52% yield). **^{1}H NMR (300 MHz, $CDCl_3$) δ** 8.12 (d, *J* = 8.4 Hz, 8H), 7.55 (s, 4H), 7.53 (d, *J* = 1.5 Hz, 4H), 7.48 (d, *J* = 8.5 Hz, 8H), 7.30 (t, *J* = 1.5 Hz, 2H), 7.28 (s, 4H), 7.24 (d, *J* = 3.2 Hz, 4H), 7.20 (s,

4H), 3.96 (s, 12H), 2.39 (s, 12H), 2.31 (s, 12H); **^{13}C NMR (75 MHz, $CDCl_3$) δ** 167.1 (C), 146.4 (C), 141.8 (C), 141.1 (C), 140.0 (C), 137.2 (C), 136.7 (C), 132.9 (C), 132.6 (C), 132.0 (CH), 131.6 (CH), 129.4 (CH), 129.3 (CH), 128.8 (CH), 128.6 (C), 128.4 (CH), 126.9 (CH), 125.9 (CH), 52.1 (CH_3), 20.0 (CH_3), 19.9 (CH_3).

Synthesis of 5'',5''''''-((1*E*,1'*E*)-1,4-phenylenebis(ethene-2,1-diyl))bis(2',2''',5',5'''-tetramethyl-[1,1':4',1'':3'',1''':4''',1''''-quinquephenyl]-4,4''''-dicarboxylic acid) (H_4PDVQTC)

Tetramethyl 5'',5''''''-((1*E*,1'*E*)-1,4-phenylenebis(ethene-2,1-diyl))bis(2',2''',5',5'''-tetramethyl-[1,1':4',1'':3'',1''':4''',1''''-quinquephenyl]-4,4''''-dicarboxylate) (585.3 mg, 0.47 mmol, 1 equiv.) was suspended in MeOH (10 mL) and THF (10 mL). Then, a 10% aqueous solution of NaOH (4 mL) was added. The resulting suspension was stirred at 50 °C for 16 h. After this time, the solvents were carefully removed under reduced pressure. Thereafter, the resulting solid was suspended in H_2O (10 mL) and cooled down to 0 °C. Then, 12 M HCl was added dropwise until pH 1-2. The resulting solid was filtered under vacuum and dried in a desiccator overnight to obtain the tetraacid product as a white solid (490.4 mg, 0.42 mmol, 89% yield). **^{1}H NMR (500 MHz, DMSO-d_6) δ** 12.95 (s, 4H), 8.03 (d, *J* = 8.3 Hz, 8H), 7.66 (d, *J* = 7.4 Hz, 8H), 7.54 (d, *J* = 8.2 Hz, 8H), 7.46 (s, 4H), 7.31 (s, 4H), 7.28 (s, 2H), 7.22 (s, 4H), 2.35 (s, 3H), 2.27 (s, 3H).

Synthesis of 1,2,4,5-tetrakis[3,5-bis(4-carboxyphenyl)phenoxymethyl]benzene (H_8TBCPB)

1,2,4,5-tetrakis[3,5-bis(4-carboxyphenyl)phenoxymethyl]benzene was synthesized according to a previous reported procedure.[203]

Synthesis of BCN-38

A solution of $ZrOCl_2 \cdot 8H_2O$ (27 mg, 0.084 mmol) and $H_4PDVTTC$ (38 mg, 0.05 mmol) in DMF (2 mL) and trifluoroacetic acid (0.6 mL) was prepared in a 23 mL scintillation vial. Then, the sealed vial was placed into a preheated oven at 120 °C for 5 days. After this period, yellow cubic crystals suitable for SCXRD were collected by filtration and washed three times by incubating them with 20 mL of fresh DMF for 12 h. Afterwards, solvent exchange with THF was performed by incubating the crystals three times with 20 mL of THF for 12 h, and the resulting BCN-38 crystals were dried at room temperature.

Synthesis of BCN-34

A solution of $Y(NO_3)_3 \cdot 6H_2O$ (19.7 mg, 0.05 mmol) and $H_4PDVTTC$ (8.4 mg, 0.01 mmol) in DMF (3 mL), HNO_3 (0.7 mL, 3.5 M in H_2O) and 2-FBA (0.28 g, 2 mmol) was prepared in a 23 mL scintillation vial. Then, the sealed vial was placed into a preheated oven at 120 °C for 7 days. After this period, colourless rod-like crystals suitable for SCXRD were collected by filtration and washed three times by incubating them with 20 mL of fresh DMF for 12 h. Afterwards, solvent exchange with THF was performed by incubating the crystals three times with 20 mL of THF for 12 h, and the resulting BCN-34 crystals were dried at room temperature.

Synthesis of BCN-143

A solution of $ZrOCl_2 \cdot 8H_2O$ (19 mg, 0.06 mmol) and $H_4PDVQTC$ (23.6 mg, 0.02 mmol) in DMF (4 mL) and formic acid (8 mL) was prepared in a 23 mL scintillation vial. Then, the sealed vial was placed into a preheated oven at 120 °C for 7 days. After this period, yellow drop-like crystals suitable for SCXRD were collected by filtration and washed three times by incubating them with 20 mL of fresh DMF for 12 h. Afterwards, solvent exchange with THF was performed by incubating the crystals three times with 20 mL of THF for 12 h, and the resulting BCN-143 crystals were dried at room temperature.

Synthesis of BCN-312

A solution of $Tb(NO)_3 \cdot 5H_2O$ (14.8 mg, 0.034 mmol) and H_4PDVQTC (13 mg, 0.011 mmol) in DMF (2 mL) and 2,6-DFBA (79 mg, 0.5 mmol) was prepared in a 23 mL scintillation vial. Then, the sealed vial was placed into a preheated oven at 120 ºC for 7 days. After this period, colourless rod-like crystals suitable for SCXRD were collected by filtration and washed three times by incubating them with 20 mL of fresh DMF for 12 h.

Synthesis of BCN-348

A solution of $ZrOCl_2 \cdot 8H_2O$ (26 mg, 0.08 mmol) and H_8TBCPB (58 mg, 0.04 mmol) in DMF (2 mL) and trifluoroacetic acid (0.6 mL) was prepared in a 23 mL scintillation vial. Then, the sealed vial was placed into a preheated oven at 120 ºC for 5 days. After this period, colourless cubic crystals suitable for SCXRD were collected by filtration and washed three times by incubating them with 20 mL of fresh DMF for 12 h. Afterwards, solvent exchange with acetone was performed by incubating the crystals three times with 20 mL of acetone for 12 h, and the resulting BCN-348 crystals were dried at room temperature.

3.3.1.4. Characterization

Single-Crystal X-Ray Diffraction (SCXRD) data for all the materials were collected at 100 K at XALOC beamline at ALBA synchrotron (0.82656 Å).[225] Data were indexed, integrated and scaled using the XDS program.[226] Absorption correction was not applied. The structures were solved by direct methods and subsequently refined by correction of F2 against all reflections, using SHELXT2018 within Olex2 package.[227–229] All non-hydrogen atoms were refined with anisotropic thermal parameters by full-matrix least-squares calculations on F2 using the program SHELXL2018.[227] We treated the presence of solvent molecules in the cavities of all structures running solvent mask using Olex2 solvent mask.[229] The BCN-348 structure was solved using two space groups: *Fm-3m* and *Fm-3*. Although

the correct symmetry corresponding to the structure is *Fm-3m*, we could not model the disorder of the central benzene ring of the linker (which could not be clearly defined using the maps) using this space group. For this reason, we decided to solve the crystal structure using *F-3m* group, which allowed us to model this benzene ring applying some restraints, such as DFIX, DELU and SIMU. The hydrogen atoms were calculated in their expected positions with the HFIX instruction of SHELXL2018, and refined as riding atoms with Uiso(H) = 1.5 Ueq(C).

Powder X-Ray Diffraction (PXRD) diagrams were collected on a Panalytical X'pert mpd diffractometer with monochromatic Cu-Kα radiation (λ_{Cu} = 1.5406 Å).

Proton Nuclear Magnetic Resonance (^{1}H NMR) spectra were acquired in Bruker Avance DPX of 250 MHz, 360 MHz NMR spectrometers and in Bruker Avance NEO of 300 MHz NMR spectrometer at "Servei de Ressonància Magnètica Nuclear" from Autonomous University of Barcelona (UAB), and in Bruker Avance NEO of 300 MHz, 500 MHz NMR spectrometers at "Servei Central de Suport a la Investigació Experimental (SCIE)" from University of València (UV).

Carbon Nuclear Magnetic Resonance (^{13}C NMR) spectra were acquired in Bruker Avance NEO of 300 MHz, 500 MHz NMR spectrometers at "Servei Central de Suport a la Investigació Experimental (SCIE)" from University of València (UV).

Proton and Phosphorus Nuclear Magnetic Resonance (^{1}H NMR/^{31}P NMR) spectra (for the catalytic experiments) were obtained in a BRUKER Nanobay Avance III HD High Definition 400 MHz (2-channel) NMR spectrometer.

Thermogravimetric analyses (TGA) were performed in a Pyris TGA8000, heating the sample from 25 ºC to 800 ºC at 1 ºC/min under N_2 atmosphere.

N_2 sorption isotherms were collected at 77K (N_2) using an ASAP 2460 HD (Micromeritics). Temperature was controlled by using a liquid nitrogen bath. Prior to the measurements, the samples were activated by solvent exchange with acetone, 3 times per day during 3 days. The specific surface area was obtained using the Brunauer-Emmett-Teller (BET) adsorption method in the range of 0.001 – 0.02 P/P_0 (BETSI software).[7] Total pore volume (V_t) was calculated at $P/P_0 = 0.95$. Pore size distribution was estimated using a density functional theory (DFT) model (HS-2D-NLDFT Carbon Cylindrical Mesopores @ N_2 77K) implemented in the Microactive 4.06 software with a regularization factor of 0.03160.

Gas Chromatography analyses (GC) were carried out in an Agilent 8860 GC chromatograph with a FID dectector and a 16 port autosampler. A HP-5 column of 50 m length, 0.320 mm diameter and 1.05 μm thickness was used, which allowed working from -60 ºC to 325 ºC.

3.3.2. ^{1}H and ^{13}C Nuclear Magnetic Resonance

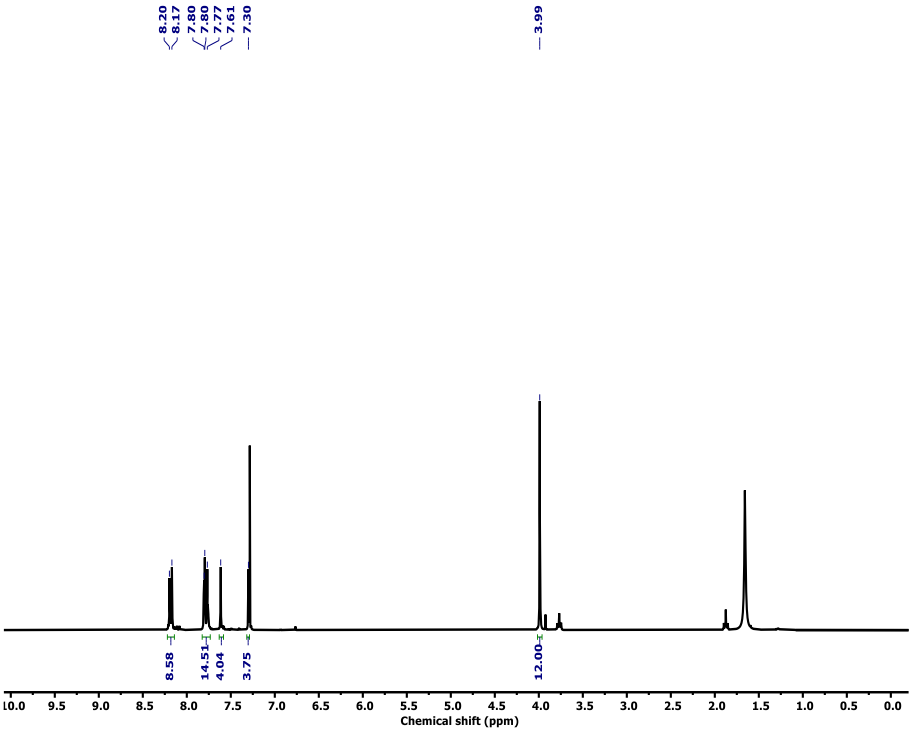


Figure 3.38 ^{1}H NMR spectrum (300 MHz, $CDCl_3$) of 5',5''''-((1E,1'E)-1,4-phenylenebis(ethene-2,1-diyl))bis([1,1':3',1''-terphenyl]-4,4''-dicarboxylate).

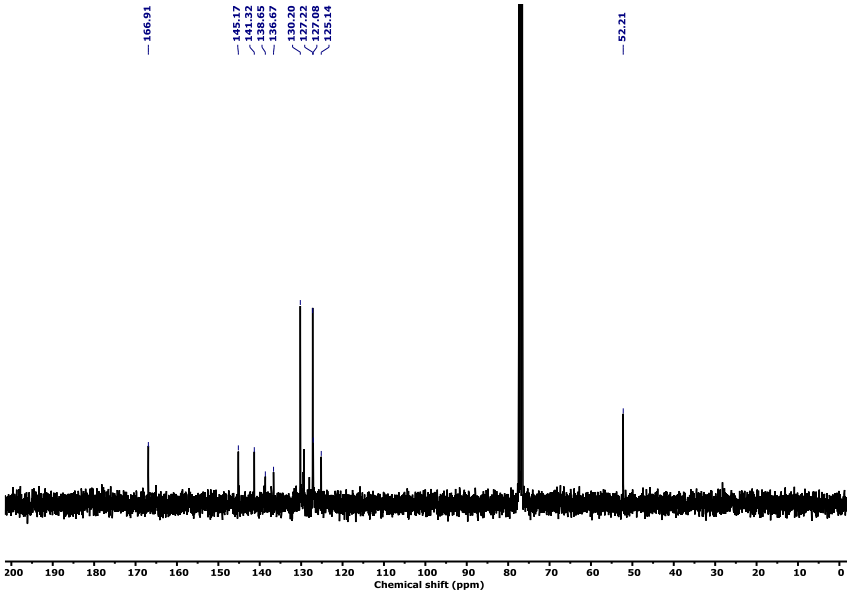


Figure 3.39. ^{13}C NMR spectrum (75 MHz, $CDCl_3$) of 5',5''''-((1E,1'E)-1,4-phenylenebis(ethene-2,1-diyl))bis([1,1':3',1''-terphenyl]-4,4''-dicarboxylate).

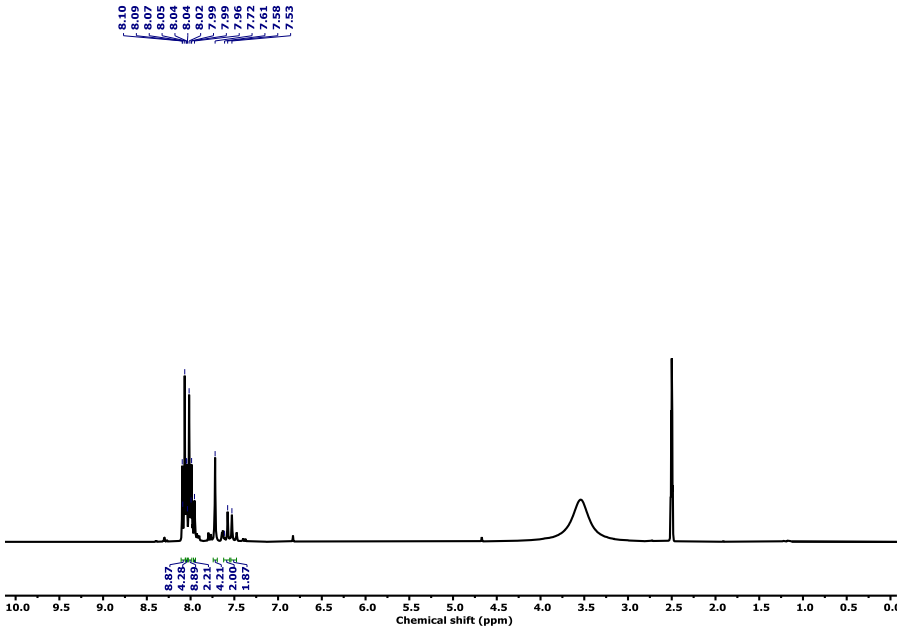


Figure 3.40. ^{1}H NMR spectrum (300 MHz, $CDCl_3$) of H_4PDVTTC.

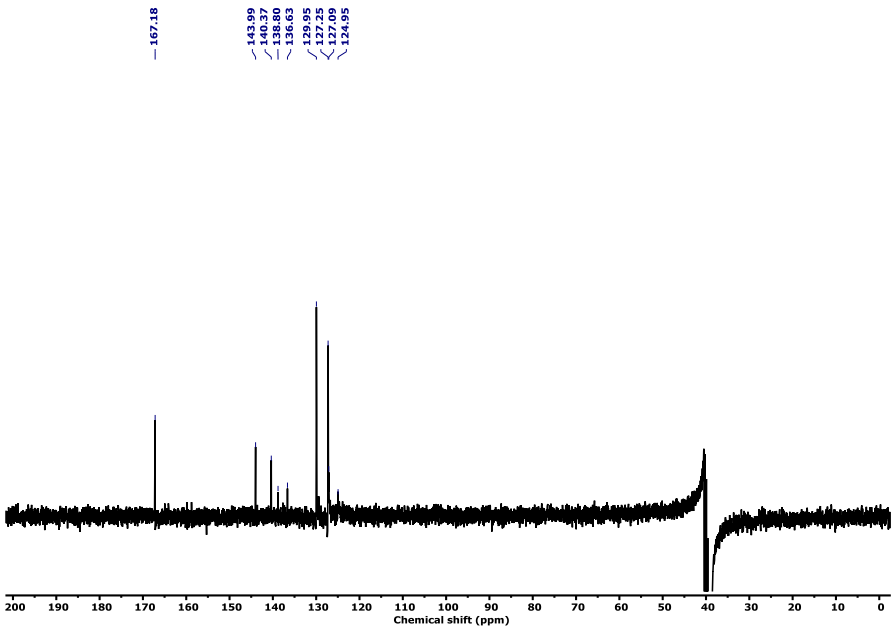


Figure 3.41. ^{13}C NMR spectrum (75 MHz, DMSO-d_6) of H_4PDVTTC.

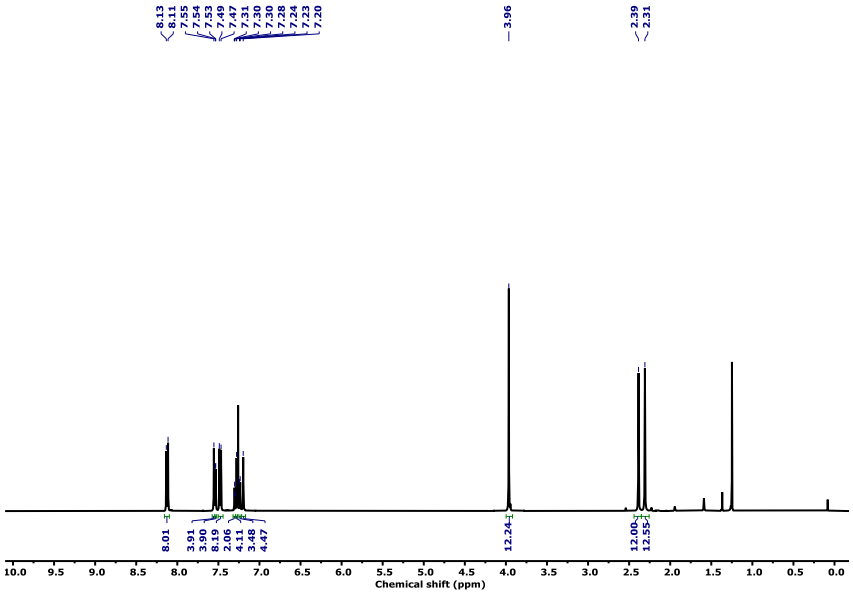


Figure 3.42. ^1H NMR spectrum (400 MHz, $CDCl_3$) of 5'',5'''''''-((1*E*,1'*E*)-1,4-phenylenebis(ethene-2,1-diyl))bis(2',2''',5',5'''-tetramethyl-[1,1':4',1'':3'',1''':4''',1''''-quinquephenyl]-4,4''''-dicarboxylate).

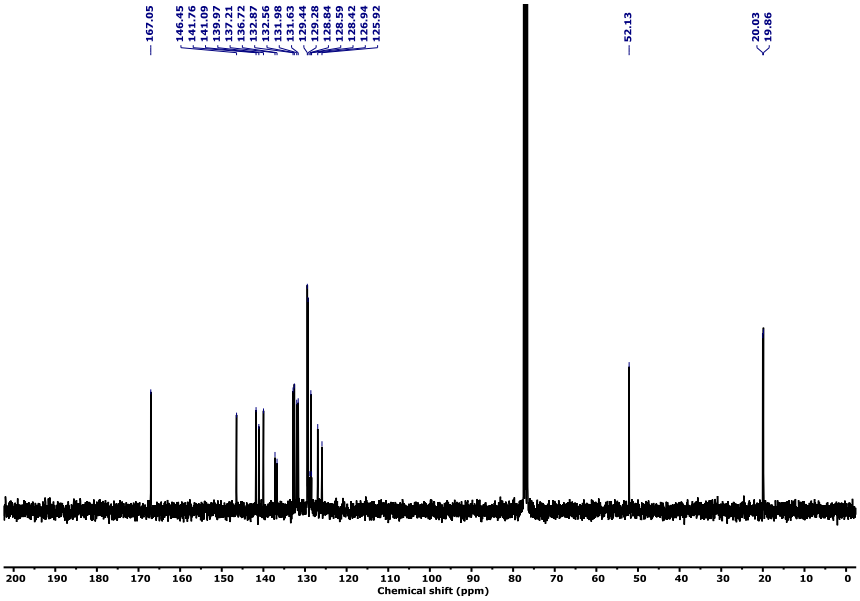


Figure 3.43. ^{13}C NMR spectrum (75 MHz, $CDCl_3$) of 5",5""""-((1*E*,1'*E*)-1,4-phenylenebis(ethene-2,1-diyl))bis(2',2''',5',5'''-tetramethyl-[1,1':4',1":3",1''':4''',1"":quinquephenyl]-4,4""-dicarboxylate).

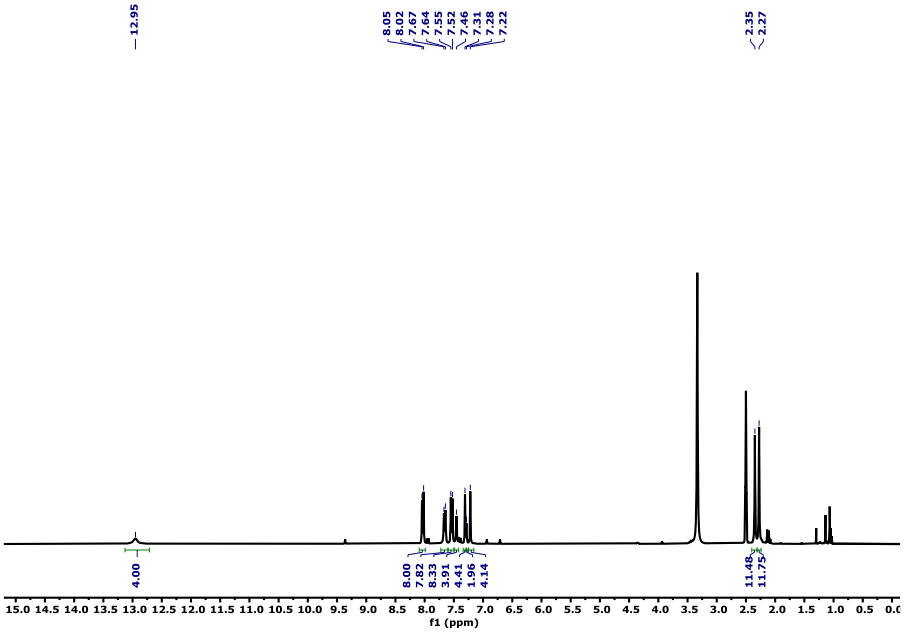


Figure 3.44. ^{1}H NMR spectrum (300 MHz, DMSO-d_6) of H_4PDVQTC.

3.3.3. Single-Crystal X-Ray Diffraction

Table 3.2. Crystal data and structure refinement for BCN-38

Empirical formula	$C_{50}H_{22}O_{16}Zr_3$
Formula weight	1152.33
Temperature/K	100
Crystal system	Orthorhombic
Space group	*Cmmm*
a/Å	20.7750(10)
b/Å	33.3980(10)
c/Å	24.8430(10)
α/°	90
β/°	90
γ/°	90
Volume/Å^3	17237.2(12)
Z	4
ρ_{calc}g/cm^3	0.444
μ/mm^{-1}	0.297
F(000)	2280.0
Crystal size/mm^3	0.08 × 0.08 × 0.05
Radiation	synchrotron (λ = 0.82656)
2Θ range for data collection/°	2.836 to 53.54
Index ranges	0 ≤ h ≤ 22, 0 ≤ k ≤ 36, 0 ≤ l ≤ 26
Reflections collected	68000
Independent reflections	6184 [R_{int} = 0.2035, R_{sigma} = 0.1081]
Data/restraints/parameters	6184/3/163
Goodness-of-fit on F^2	1.083
Final R indexes [I>=2σ (I)]	R_1 = 0.1162, wR_2 = 0.3144
Final R indexes [all data]	R_1 = 0.1456, wR_2 = 0.3412
Largest diff. peak/hole / e Å^{-3}	2.06/-0.74

Table 3.3. Crystal data and structure refinement for BCN-34

Empirical formula	$C_{132}H_{74}O_{36}F_{0.25}Y_7$
Formula weight	2863.03
Temperature/K	100
Crystal system	Monoclinic
Space group	$P2_1/a$
a/Å	14.462(3)
b/Å	26.498(3)
c/Å	35.446(3)
α/°	90
β/°	90.01(2)
γ/°	90
Volume/Å^3	13583(3)
Z	4
ρ_{calc}g/cm^3	1.400
μ/mm^{-1}	0.817
F(000)	5717.0
Crystal size/mm^3	0.07 × 0.06 × 0.06
Radiation	synchrotron (λ = 0.82656)
2Θ range for data collection/°	3.216 to 67.866
Index ranges	-19 ≤ h ≤ 19, 0 ≤ k ≤ 34, 0 ≤ l ≤ 46
Reflections collected	173231
Independent reflections	30194 [R_{int} = 0.0460, R_{sigma} = 0.0332]
Data/restraints/parameters	30194/51/1498
Goodness-of-fit on F^2	1.093
Final R indexes [I>=2σ (I)]	R_1 = 0.0643, wR_2 = 0.2069
Final R indexes [all data]	R_1 = 0.0700, wR_2 = 0.2129
Largest diff. peak/hole / e Å^{-3}	2.36/-1.49

Table 3.4. Crystal data and structure refinement for BCN-143

Empirical formula	$C_{56}H_{44}N_6O_{28}Zr_6$
Formula weight	1796.29
Temperature/K	293(2)
Crystal system	Orthorhombic
Space group	*Pcca*
a/Å	14.116
b/Å	18.852
c/Å	40.354
α/°	90
β/°	90
γ/°	90
Volume/Å^3	10738.9
Z	7
ρ_{calc}g/cm^3	1.944
μ/mm^{-1}	1.077
F(000)	6202.0
Crystal size/mm^3	0.07 × 0.07 × 0.07
Radiation	synchrotron (λ = 0.82656)
2Θ range for data collection/°	3.522 to 46.519
Index ranges	0 ≤ h ≤ 15, 0 ≤ k ≤ 20, 0 ≤ l ≤ 44
Reflections collected	92005
Independent reflections	7726 [R_{int} = 0.0510, R_{sigma} = 0.0278]
Data/restraints/parameters	7726/0/539
Goodness-of-fit on F^2	1.120
Final R indexes [I>=2σ (I)]	R_1 = 0.0850, wR_2 = 0.2788
Final R indexes [all data]	R_1 = 0.10467, wR_2 = 0.3049
Largest diff. peak/hole / e Å^{-3}	1.28/-0.80

Table 3.5. Crystal data and structure refinement for BCN-348

Identification code	CCDC-2255518
Empirical formula	$C_{85}H_{49}O_{36}Zr_6$
Formula weight	2193.56
Temperature/K	100
Crystal system	Cubic
Space group	*Fm-3*
a/Å	59.677(2)
b/Å	59.677(2)
c/Å	59.677(2)
α/°	90
β/°	90
γ/°	90
Volume/Å^3	212530(21)
Z	24
ρ_{calc}g/cm^3	0.411
μ/mm^{-1}	0.288
F(000)	26088.0
Crystal size/mm^3	0.07 × 0.07 × 0.07
Radiation	synchrotron (λ = 0.82656)
2Θ range for data collection/°	1.374 to 49.596
Index ranges	-60 ≤ h ≤ 60, -60 ≤ k ≤ 60, -60 ≤ l ≤ 60
Reflections collected	297617
Independent reflections	10069 [R_{int} = 0.1572, R_{sigma} = 0.0390]
Data/restraints/parameters	10069/121/292
Goodness-of-fit on F^2	1.160
Final R indexes [I>=2σ (I)]	R_1 = 0.1132, wR_2 = 0.2944
Final R indexes [all data]	R_1 = 0.1417, wR_2 = 0.3152
Largest diff. peak/hole / e Å^{-3}	0.38/-2.12

3.3.4. BETSI analysis

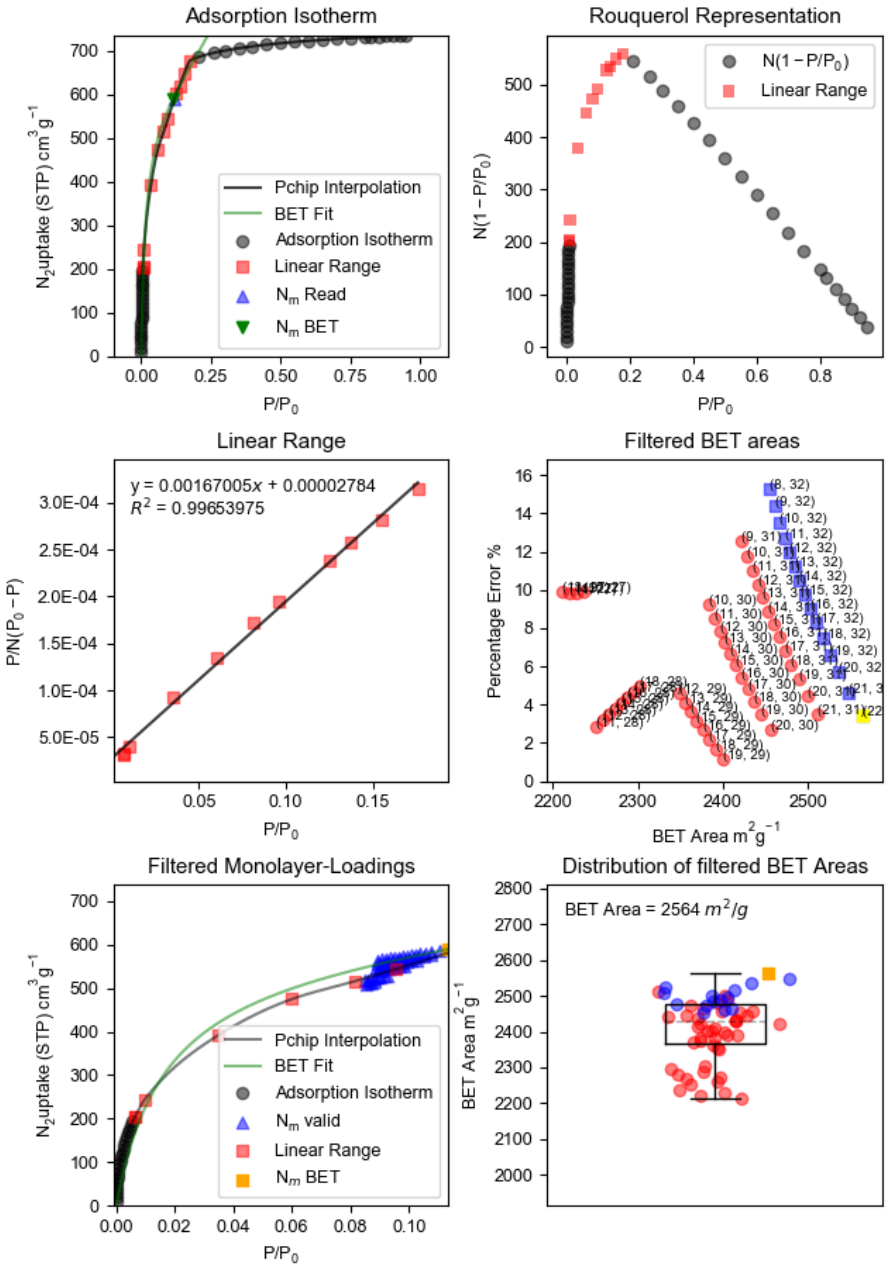


Figure 3.45. BETSI analysis for BCN-348.

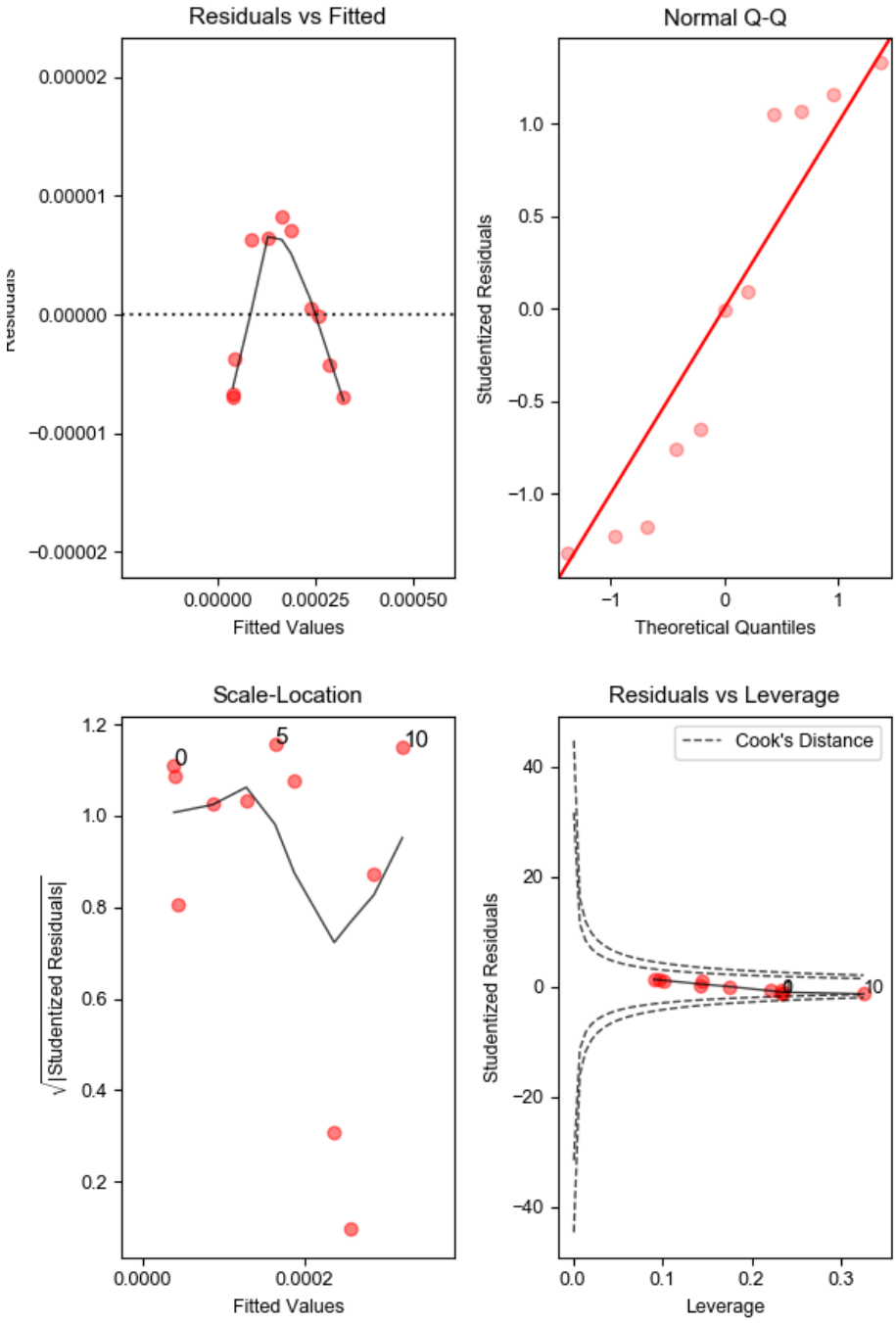


Figure 3.46. BETSI regression diagnostics for BCN-348.

3.4. Conclusions

In this Chapter, we investigated the effect of desymmetrization of organic MBBs in high-connected MOFs constructed with Zr- and RE-based clusters. After a literature exploration, we determined the crucial role of the torsion angles and aspect ratio in 4-c square/rectangular ligands, 4-c tetrahedral linkers and 3-c triangular linkers. We could observe a tendency in the linker metrics expansion, elongation and rotation affecting to the Zr-cluster connectivity and geometry, and therefore, the net formation. In addition, we compared the assembly between Zr- and RE-clusters when using the same linkers, which has never been reported before, highlighting the different tendencies for both SBUs which have traditionally been related to behaving in a similar way.

Then, we contributed with two additional 4-c linkers with expanded metrics and in-plane translation for comparing the behaviour of Zr- and RE-MOFs assembly. We reported the synthesis of four novel MOFs, BCN-38, BCN-34, BCN-143 and BCN-312, based on the underlying **tty/scu**, **bex/sql-b**, 3,4T143 and **kle/ftw** nets, respectively. Our findings suggested that the desymmetrization of these molecules can direct to unconventional structures based on new 4-c Zr_6-clusters or 8-c RE_7-clusters, which have never been observed.

Finally, we expanded our study to higher 8-c organic linkers reporting the design, synthesis and functional validation of BCN-348, a new mesoporous high-connected Zr-MOF. Topologically, BCN-348 exhibits a minimal edge-transitive **eps** net, unlike its RE analogue, which exhibits the minimal edge-transitive **kce** net. Moreover, BCN-348 combines mesoporosity with the presence of Lewis-acid open metal sites and hydrolytic stability, permitting its use as a catalyst for the hydrolytic degradation of toxic chemicals without any assistance from a buffer, which we confirmed on DIFP, a nerve-agent simulant. Our study augments the collection of reticular Zr-MOFs and highlights the endless possibilities of assembling less-

symmetric, high-connected MBBs in novel reticular materials, thus further paving the way to new high-connected frameworks.

3.5. References

(1) Furukawa, H.; Kim, J.; Ockwig, N. W.; O'Keeffe, M.; Yaghi, O. M. Control of Vertex Geometry, Structure Dimensionality, Functionality, and Pore Metrics in the Reticular Synthesis of Crystalline Metal-Organic Frameworks and Polyhedra. *J. Am. Chem. Soc.* **2008**, *130*, 11650–11661.

(2) Eddaoudi, M.; Kim, J.; Vodak, D.; Sudik, A.; Wachter, J.; O'Keeffe, M.; Yaghi, O. M. Geometric Requirements and Examples of Important Structures in the Assembly of Square Building Blocks. *Proc. Nat. Acad. Sci. U. S. A.* **2002**, *99*, 4900–4904.

(3) Furukawa, H.; Go, Y. B.; Ko, N.; Park, Y. K.; Uribe-Romo, F. J.; Kim, J.; O'Keeffe, M.; Yaghi, O. M. Isoreticular Expansion of Metal-Organic Frameworks with Triangular and Square Building Units and the Lowest Calculated Density for Porous Crystals. *Inorg. Chem.* **2011**, *50*, 9147–9152.

(4) Chen, Z.; Hanna, S. L.; Redfern, L. R.; Alezi, D.; Islamoglu, T.; Farha, O. K. Reticular Chemistry in the Rational Synthesis of Functional Zirconium Cluster-Based MOFs. *Coord. Chem. Rev.* **2019**, *386*, 32–49.

(5) Wang, X. Sen; Shengqian, M.; Rauch, K.; Simmons, J. M.; Yuan, D.; Wang, X.; Yildirim, T.; Cole, W. C.; López, J. J.; De Meijere, A.; Zhou, H. C. Metal-Organic Frameworks Based on Double-Bond-Coupled Di-Isophthalate Linkers with High Hydrogen and Methane Uptakes. *Chem. Mater.* **2008**, *20*, 3145–3152.

(6) Cairns, A. J.; Perman, J. A.; Wojtas, L.; Kravtsov, V. C.; Alkordi, M. H.; Eddaoudi, M.; Zaworotko, M. J. Supermolecular Building Blocks (SBBs) and Crystal

Design: 12-Connected Open Frameworks Based on a Molecular Cubohemioctahedron. *J. Am. Chem. Soc.* **2008**, *130*, 1560–1561.

(7) Xue, D. X.; Cadiau, A.; Weseliński, Ł. J.; Jiang, H.; Bhatt, P. M.; Shkurenko, A.; Wojtas, L.; Zhijie, C.; Belmabkhout, Y.; Adil, K.; Eddaoudi, M. Topology Meets MOF Chemistry for Pore-Aperture Fine Tuning: ftw -MOF Platform for Energy-Efficient Separations: Via Adsorption Kinetics or Molecular Sieving. *Chem. Commun.* **2018**, *54*, 6404–6407.

(8) Barthelet, K.; Riou, D.; Férey, G. $[V^{III}(H_2O)]_3O(O_2CC_6H_4CO_2)_3\cdot$(Cl, $9H_2O$) (MIL-59): A Rare Example of Vanadocarboxylate with a Magnetically Frustrated Three-Dimensional Hybrid Framework. *Chem. Commun.* **2002**, *2*, 1492–1493.

(9) Liu, Y.; Eubank, J. F.; Cairns, A. J.; Eckert, J.; Kravtsov, V. Ch.; Luebke, R.; Eddaoudi, M. Assembly of Metal–Organic Frameworks (MOFs) Based on Indium-Trimer Building Blocks: A Porous MOF with soc Topology and High Hydrogen Storage. *Angew. Chem. Int. Ed.* **2007**, *46*, 3278–3283.

(10) Serre, C.; Millange, F.; Surblé, S.; Férey, G. A Route to the Synthesis of Trivalent Transition-Metal Porous Carboxylates with Trimeric Secondary Building Units. *Angew. Chem. Int. Ed* .**2004**, *43*, 6285–6289.

(11) Wang, K.; Feng, D.; Liu, T. F.; Su, J.; Yuan, S.; Chen, Y. P.; Bosch, M.; Zou, X.; Zhou, H. C. A Series of Highly Stable Mesoporous Metalloporphyrin Fe-MOFs. *J. Am. Chem. Soc.* **2014**, *136*, 13983–13986.

(12) Chun, H.; Jung, H. Targeted Synthesis of a Prototype MOF Based on $Zn_4(O)(O_2C)_6$ Units and a Nonlinear Dicarboxylate Ligand. *Inorg. Chem.* **2009**, *48*, 417–419.

(13) Guillerm, V.; Maspoch, D. Geometry Mismatch and Reticular Chemistry: Strategies to Assemble Metal-Organic Frameworks with Non-Default Topologies. *J. Am. Chem. Soc.* **2019**, *141*, 16517–16538.

(14) Jiang, H.; Alezi, D.; Eddaoudi, M. A Reticular Chemistry Guide for the Design of Periodic Solids. *Nat. Rev. Mater.* **2021**, *6*, 466–487.

(15) Eddaoudi, M.; Kim, J.; Rosi, N.; Vodak, D.; Wachter, J.; O'Keeffe, M.; Yaghi, O. M. Systematic Design of Pore Size and Functionality in Isoreticular MOFs and Their Application in Methane Storage. *Science* **2002**, *295*, 469–472.

(16) Li, H.; Eddaoudi, M.; Groy, T. L.; Yaghi, O. M. Establishing Microporosity in Open Metal-Organic Frameworks: Gas Sorption Isotherms for Zn(BDC) (BDC = 1,4-Benzenedicarboxylate) [28]. *J. Am. Chem. Soc.* **1998**, *120*, 8571–8572.

(17) Liu, J.; Lukose, B.; Shekhah, O.; Arslan, H. K.; Weidler, P.; Gliemann, H.; Bräse, S.; Grosjean, S.; Godt, A.; Feng, X.; Müllen, K.; Magdau, I. B.; Heine, T.; Wöll, C. A Novel Series of Isoreticular Metal Organic Frameworks: Realizing Metastable Structures by Liquid Phase Epitaxy. *Sci. Rep.* **2012**, *2*, 1–5.

(18) Bonneau, C.; Delgado-Friedrichs, O.; O'Keeffe, M.; Yaghi, O. M. Three-Periodic Nets and Tilings: Minimal Nets. *Acta Cryst. A* **2004**, *60*, 517–520.

(19) Chui, S. S. Y.; Lo, S. M. F.; Charmant, J. P. H.; Orpen, A. G.; Williams, I. D. A Chemically Functionalizable Nanoporous Material $[Cu_3(TMA)_2(H_2O)_3]_n$. *Science* **1999**, *283*, 1148–1150.

(20) Chen, B.; Eddaoudi, M.; Hyde, S. T.; O'Keeffe, M.; Yaghi, O. M. Interwoven Metal-Organic Framework on a Periodic Minimal Surface with Extra-Large Pores. *Science* **2001**, *291*, 1021–1023.

(21) Ma, S.; Sun, D.; Ambrogio, M.; Fillinger, J. A.; Parkin, S.; Zhou, H. C. Framework-Catenation Isomerism in Metal-Organic Frameworks and Its Impact on Hydrogen Uptake. *J. Am. Chem. Soc.* **2007**, *129*, 1858–1859.

(22) Klein, N.; Senkovska, I.; Baburin, I. A.; Grünker, R.; Stoeck, U.; Schlichtenmayer, M.; Streppel, B.; Mueller, U.; Leoni, S.; Hirscher, M.; Kaskel, S.

Route to a Family of Robust, Non-Interpenetrated Metal-Organic Frameworks with pto-like Topology. *Chem. Eur. J.* **2011**, *17*, 13007–13016.

(23) Müller, P.; Grünker, R.; Bon, V.; Pfeffermann, M.; Senkovska, I.; Weiss, M. S.; Feng, X.; Kaskel, S. Topological Control of 3,4-Connected Frameworks Based on the Cu2-Paddle-Wheel Node: Tbo or Pto, and Why? *CrystEngComm* **2016**, *18* (42), 8164–8171.

(24) Wong-Foy, A. G.; Lebel, O.; Matzger, A. J. Porous Crystal Derived from a Tricarboxylate Linker with Two Distinct Binding Motifs. *J. Am. Chem. Soc.* **2007**, *129*, 15740–15741.

(25) Cage, B.; Cotton, F. A.; Dalal, N. S.; Hillard, E. A.; Rakvin, B.; Ramsey, C. M. Observation of Symmetry Lowering and Electron Localization in the Doublet-States of a Spin-Frustrated Equilateral Triangular Lattice: $Cu_3(O_2C_{16}H_{23})\cdot 1.2C_6H_{12}$. *J. Am. Chem. Soc.* **2003**, *125*, 5270–5271.

(26) Lim, C. S.; Schnobrich, J. K.; Wong-Foy, A. G.; Matzger, A. J. Metal-Dependent Phase Selection in Coordination Polymers Derived from a C_{2v}-Symmetric Tricarboxylate. *Inorg. Chem.* **2010**, *49*, 5271–5275.

(27) Guo, Z.; Li, G.; Zhou, L.; Su, S.; Lel, Y.; Dang, S.; Zhang, H. Magnesium-Based 3D Metal-Organic Framework Exhibiting Hydrogen-Sorption Hysteresis. *Inorg. Chem.* **2009**, *48*, 8069–8071.

(28) Catterick, J.; Hursthouse, M. B.; New, D. B.; Thornton, P. Preparation, X-Ray Crystal Structure, and Magnetic Properties of a Trinuclear Cobalt(II) Carboxylate. *J. Chem. Soc. Chem. Commun.* **1974**, *20*, 843–844.

(29) Coker, E. N.; Boyle, T. J.; Rodriguez, M. A.; Alam, T. M. Structurally Characterized Magnesium Carboxylates with Tuned Melting Points. *Polyhedron* **2004**, *23*, 1739–1747.

(30) Yang, K. C.; Chang, C. C.; Yeh, C. S.; Lee, G. H.; Wang, Y. Synthesis and Structural Studies on $[Mg_3(O_2CC{\equiv}CSiMe_3)_6(HMPA)_4]$: Mechanistic Implications for the Formation of the M_4-H_4 Bonding Type in Carbamato-Bridged Mg6 Cage Compounds. *Organometallics* **2002**, *21*, 1296–1299.

(31) Senkovska, I.; Kaskel, S. Solvent-Induced Pore-Size Adjustment in the Metal-Organic Framework $[Mg_3(ndc)_3(dmf)_4]$ (ndc = Naphthalenedicarboxylate). *Eur. J. Inorg. Chem.* **2006**, *2006*, 4564–4569.

(32) Dincă, M.; Long, J. R. Strong H_2 Binding and Selective Gas Adsorption within the Microporous Coordination Solid $Mg_3(O_2C\text{-}C_{10}H_6\text{-}CO_2)_3$. *J. Am. Chem. Soc.* **2005**, *127*, 9376–9377.

(33) Schnobrich, J. K.; Lebel, O.; Cychosz, K. A.; Dailly, A.; Wong-Foy, A. G.; Matzger, A. J. Linker-Directed Vertex Desymmetrization for the Production of Coordination Polymers with High Porosity. *J. Am. Chem. Soc.* **2010**, *132*, 13941–13948.

(34) Feng, L.; Chen, Z.; Liao, T.; Li, P.; Jia, Y.; Liu, X.; Yang, Y.; Zhou, Y. Supramolecular Isomerism of Metal–Organic Frameworks Derived from a Bicarboxylate Linker with Two Distinct Binding Motifs. *Cryst. Growth Des.* **2009**, *9*, 1505–1510.

(35) Haase, F.; Craig, G. A.; Bonneau, M.; Sugimoto, K.; Furukawa, S. Pseudo-5-Fold-Symmetrical Ligand Drives Geometric Frustration in Porous Metal-Organic and Hydrogen-Bonded Frameworks. *J. Am. Chem. Soc.* **2020**, *142*, 13839–13845.

(36) Krause, S.; Bon, V.; Stoeck, U.; Senkovska, I.; Többens, D. M.; Wallacher, D.; Kaskel, S. A Stimuli-Responsive Zirconium Metal–Organic Framework Based on Supermolecular Design. *Angew. Chem. Int. Ed.* **2017**, *56*, 10676–10680.

(37) Alsadun, N.; Mouchaham, G.; Guillerm, V.; Czaban-Jóźwiak, J.; Shkurenko, A.; Jiang, H.; Bhatt, P. M.; Parvatkar, P.; Eddaoudi, M. Introducing a Cantellation Strategy for the Design of Mesoporous Zeolite-like Metal-Organic Frameworks: Zr-sod-ZMOFs as a Case Study. *J. Am. Chem. Soc.* **2020**, *142*, 20547–20553.

(38) Chen, Z.; Li, P.; Zhang, X.; Li, P.; Wasson, M. C.; Islamoglu, T.; Stoddart, J. F.; Farha, O. K. Reticular Access to Highly Porous acs-MOFs with Rigid Trigonal Prismatic Linkers for Water Sorption. *J. Am. Chem. Soc.* **2019**, *141*, 2900–2905.

(39) Chen, Z.; Li, P.; Wang, X.; Otake, K. I.; Zhang, X.; Robison, L.; Atilgan, A.; Islamoglu, T.; Hall, M. G.; Peterson, G. W.; Stoddart, J. F.; Farha, O. K. Ligand-Directed Reticular Synthesis of Catalytically Active Missing Zirconium-Based Metal-Organic Frameworks. *J. Am. Chem. Soc.* **2019**, *141*, 12229–12235.

(40) Guillerm, V.; Grancha, T.; Imaz, I.; Juanhuix, J.; Maspoch, D. Zigzag Ligands for Transversal Design in Reticular Chemistry: Unveiling New Structural Opportunities for Metal-Organic Frameworks. *J. Am. Chem. Soc.* **2018**, *140*, 10153–10157.

(41) Xue, X.; Wang, J.; Zhu, Q.; Xue, Y.; Liu, H. A Two-Year Water-Stable 2D MOF with Aqueous NIR Photothermal Conversion Ability. *Dalton Trans.* **2021**, *50*, 1374–1383.

(42) Benecke, J.; Grape, E. S.; Fuß, A.; Wöhlbrandt, S.; Engesser, T. A.; Inge, A. K.; Stock, N.; Reinsch, H. Polymorphous Indium Metal-Organic Frameworks Based on a Ferrocene Linker: Redox Activity, Porosity, and Structural Diversity. *Inorg. Chem.* **2020**, *59*, 9969–9978.

(43) Gong, W.; Xie, H.; Idrees, K. B.; Son, F. A.; Chen, Z.; Sha, F.; Liu, Y.; Cui, Y.; Farha, O. K. Water Sorption Evolution Enabled by Reticular Construction of Zirconium Metal-Organic Frameworks Based on a Unique [2.2]Paracyclophane Scaffold. *J. Am. Chem. Soc.* **2022**, *144*, 1826–1834.

(44) Cavka, J. H.; Jakobsen, S.; Olsbye, U.; Guillou, N.; Lamberti, C.; Bordiga, S.; Lillerud, K. P. A New Zirconium Inorganic Building Brick Forming Metal Organic Frameworks with Exceptional Stability. *J. Am. Chem. Soc.* **2008**, *130*, 13850–13851.

(45) Yuan, S.; Lu, W.; Chen, Y.-P.; Zhang, Q.; Liu, T.-F.; Feng, D.; Wang, X.; Qin, J.; Zhou, H.-C. Sequential Linker Installation: Precise Placement of Functional

Groups in Multivariate Metal–Organic Frameworks. *J. Am. Chem. Soc.* **2015**, *137*, 3177–3180.

(46) Bon, V.; Senkovska, I.; Weiss, M. S.; Kaskel, S. Tailoring of Network Dimensionality and Porosity Adjustment in Zr- and Hf-Based MOFs. *CrystEngComm* **2013**, *15*, 9572–9577.

(47) Nguyen, H. T. T.; Tu, T. N.; Nguyen, M. V.; Lo, T. H. N.; Furukawa, H.; Nguyen, N. N.; Nguyen, M. D. Combining Linker Design and Linker-Exchange Strategies for the Synthesis of a Stable Large-Pore Zr-Based Metal–Organic Framework. *ACS Appl. Mater. Interfaces* **2018**, *10*, 35462–35468.

(48) Bon, V.; Senkovskyy, V.; Senkovska, I.; Kaskel, S. Zr(IV) and Hf(IV) Based Metal–Organic Frameworks with Reo-Topology. *Chem. Commun.* **2012**, *48*, 8407–8409.

(49) Pauling, L. The Principles Determining the Structure of Complex Ionic Crystals. *J. Am. Chem. Soc.* **1929**, *51*, 1010–1026.

(50) Lü, B.; Chen, Y.; Li, P.; Wang, B.; Müllen, K.; Yin, M. Stable Radical Anions Generated from a Porous Perylenediimide Metal-Organic Framework for Boosting near-Infrared Photothermal Conversion. *Nat. Commun.* **2019**, *10*, 1–8.

(51) Xie, L. H.; Liu, X. M.; He, T.; Li, J. R. Metal-Organic Frameworks for the Capture of Trace Aromatic Volatile Organic Compounds. *Chem* **2018**, *4*, 1911–1927.

(52) Du, P. Y.; Lustig, W. P.; Teat, S. J.; Gu, W.; Liu, X.; Li, J. A Robust Two-Dimensional Zirconium-Based Luminescent Coordination Polymer Built on a V-Shaped Dicarboxylate Ligand for Vapor Phase Sensing of Volatile Organic Compounds. *Chem. Commun.* **2018**, *54*, 8088–8091.

(53) Morris, W.; Volosskiy, B.; Demir, S.; Gándara, F.; McGrier, P. L.; Furukawa, H.; Cascio, D.; Stoddart, J. F.; Yaghi, O. M. Synthesis, Structure, and Metalation of

Two New Highly Porous Zirconium Metal–Organic Frameworks. *Inorg. Chem.* **2012**, *51*, 6443–6445.

(54) Ma, J.; Tran, L. D.; Matzger, A. J. Toward Topology Prediction in Zr-Based Microporous Coordination Polymers: The Role of Linker Geometry and Flexibility. *Cryst. Growth Des.* **2016**, *16*, 4148–4153.

(55) Wang, H.; Dong, X.; Lin, J.; Teat, S. J.; Jensen, S.; Cure, J.; Alexandrov, E. V.; Xia, Q.; Tan, K.; Wang, Q.; Olson, D. H.; Proserpio, D. M.; Chabal, Y. J.; Thonhauser, T.; Sun, J.; Han, Y.; Li, J. Topologically Guided Tuning of Zr-MOF Pore Structures for Highly Selective Separation of C6 Alkane Isomers. *Nat. Commun.* **2018**, *9*, 1–11.

(56) Jiang, H. L.; Feng, D.; Wang, K.; Gu, Z. Y.; Wei, Z.; Chen, Y. P.; Zhou, H. C. An Exceptionally Stable, Porphyrinic Zr Metal-Organic Framework Exhibiting PH-Dependent Fluorescence. *J. Am. Chem. Soc.* **2013**, *135*, 13934–13938.

(57) Deria, P.; Gómez-Gualdrón, D. A.; Hod, I.; Snurr, R. Q.; Hupp, J. T.; Farha, O. K. Framework-Topology-Dependent Catalytic Activity of Zirconium-Based (Porphinato)Zinc(II) MOFs. *J. Am. Chem. Soc.* **2016**, *138*, 14449–14457.

(58) Feng, D.; Chung, W. C.; Wei, Z.; Gu, Z. Y.; Jiang, H. L.; Chen, Y. P.; Darensbourg, D. J.; Zhou, H. C. Construction of Ultrastable Porphyrin Zr Metal-Organic Frameworks through Linker Elimination. *J. Am. Chem. Soc.* **2013**, *135*, 17105–17110.

(59) Feng, D.; Gu, Z. Y.; Chen, Y. P.; Park, J.; Wei, Z.; Sun, Y.; Bosch, M.; Yuan, S.; Zhou, H. C. A Highly Stable Porphyrinic Zirconium Metal-Organic Framework with shp-a Topology. *J. Am. Chem. Soc.* **2014**, *136*, 17714–17717.

(60) Lyu, J.; Zhang, X.; Otake, K. I.; Wang, X.; Li, P.; Li, Z.; Chen, Z.; Zhang, Y.; Wasson, M. C.; Yang, Y.; Bai, P.; Guo, X.; Islamoglu, T.; Farha, O. K. Topology and Porosity Control of Metal-Organic Frameworks through Linker Functionalization. *Chem. Sci.* **2019**, *10*, 1186–1192.

(61) Feng, D.; Jiang, H. L.; Chen, Y. P.; Gu, Z. Y.; Wei, Z.; Zhou, H. C. Metal-Organic Frameworks Based on Previously Unknown Zr_8/Hf_8 Cubic Clusters. *Inorg. Chem.* **2013**, *52*, 12661–12667.

(62) Koschnick, C.; Stäglich, R.; Scholz, T.; Terban, M. W.; von Mankowski, A.; Savasci, G.; Binder, F.; Schökel, A.; Etter, M.; Nuss, J.; Siegel, R.; Germann, L. S.; Ochsenfeld, C.; Dinnebier, R. E.; Senker, J.; Lotsch, B. V. Understanding Disorder and Linker Deficiency in Porphyrinic Zirconium-Based Metal–Organic Frameworks by Resolving the Zr_8O_6 Cluster Conundrum in PCN-221. *Nat. Commun.* **2021**, *12*, 1–9.

(63) Liu, T. F.; Feng, D.; Chen, Y. P.; Zou, L.; Bosch, M.; Yuan, S.; Wei, Z.; Fordham, S.; Wang, K.; Zhou, H. C. Topology-Guided Design and Syntheses of Highly Stable Mesoporous Porphyrinic Zirconium Metal-Organic Frameworks with High Surface Area. *J. Am. Chem. Soc.* **2015**, *137*, 413–419.

(64) He, T.; Ni, B.; Zhang, S.; Gong, Y.; Wang, H.; Gu, L.; Zhuang, J.; Hu, W.; Wang, X.; He, T.; Ni, B.; Zhang, S.; Wang, H.; Zhuang, J.; Wang, X.; Hu, W.; Gong, Y.; Gu, L. Ultrathin 2D Zirconium Metal–Organic Framework Nanosheets: Preparation and Application in Photocatalysis. *Small* **2018**, *14*, 1703929.

(65) Hu, H.; Wang, Z.; Cao, L.; Zeng, L.; Zhang, C.; Lin, W.; Wang, C. Metal–Organic Frameworks Embedded in a Liposome Facilitate Overall Photocatalytic Water Splitting. *Nat. Chem.* **2021**, *13*, 358–366.

(66) Mondloch, J. E.; Bury, W.; Fairen-Jimenez, D.; Kwon, S.; Demarco, E. J.; Weston, M. H.; Sarjeant, A. A.; Nguyen, S. T.; Stair, P. C.; Snurr, R. Q.; Farha, O. K.; Hupp, J. T. Vapor-Phase Metalation by Atomic Layer Deposition in a Metal-Organic Framework. *J. Am. Chem. Soc.* **2013**, *135*, 10294–10297.

(67) Kung, C. W.; Wang, T. C.; Mondloch, J. E.; Fairen-Jimenez, D.; Gardner, D. M.; Bury, W.; Klingsporn, J. M.; Barnes, J. C.; Van Duyne, R.; Stoddart, J. F.; Wasielewski, M. R.; Farha, O. K.; Hupp, J. T. Metal-Organic Framework Thin

Films Composed of Free-Standing Acicular Nanorods Exhibiting Reversible Electrochromism. *Chem. Mater.* **2013**, *25*, 5012–5017.

(68) Garibay, S. J.; Iordanov, I.; Islamoglu, T.; DeCoste, J. B.; Farha, O. K. Synthesis and Functionalization of Phase-Pure NU-901 for Enhanced CO_2 Adsorption: The Influence of a Zirconium Salt and Modulator on the Topology and Phase Purity. *CrystEngComm* **2018**, *20*, 7066–7070.

(69) Pang, J.; Yuan, S.; Qin, J.; Liu, C.; Lollar, C.; Wu, M.; Yuan, D.; Zhou, H. C.; Hong, M. Control the Structure of Zr-Tetracarboxylate Frameworks through Steric Tuning. *J. Am. Chem. Soc.* **2017**, *139*, 16939–16945.

(70) Yang, S. L.; Li, G.; Guo, M. Y.; Liu, W. S.; Bu, R.; Gao, E. Q. Positive Cooperative Protonation of a Metal-Organic Framework: pH-Responsive Fluorescence and Proton Conduction. *J. Am. Chem. Soc.* **2021**, *143*, 8838–8848.

(71) Kalidindi, S. B.; Nayak, S.; Briggs, M. E.; Jansat, S.; Katsoulidis, A. P.; Miller, G. J.; Warren, J. E.; Antypov, D.; Corà, F.; Slater, B.; Prestly, M. R.; Mart-Gastaldo, C.; Rosseinsky, M. J. Chemical and Structural Stability of Zirconium-Based Metal–Organic Frameworks with Large Three-Dimensional Pores by Linker Engineering. *Angew. Chem. Int. Ed.* **2015**, *54*, 221–226.

(72) Gutov, O. V; Bury, W.; Gomez-Gualdron, D. A.; Krungleviciute, V.; Fairen-Jimenez, D.; Mondloch, J. E.; Sarjeant, A. A.; Al-Juaid, S. S.; Snurr, R. Q.; Hupp, J. T.; Yildirim, T.; Farha, O. K. Water-Stable Zirconium-Based Metal–Organic Framework Material with High-Surface Area and Gas-Storage Capacities. *Chem Eur. J.* **2014**, *20*, 12389–12393.

(73) Wang, T. C.; Bury, W.; Gómez-Gualdrón, D. A.; Vermeulen, N. A.; Mondloch, J. E.; Deria, P.; Zhang, K.; Moghadam, P. Z.; Sarjeant, A. A.; Snurr, R. Q.; Stoddart, J. F.; Hupp, J. T.; Farha, O. K. Ultrahigh Surface Area Zirconium MOFs and Insights into the Applicability of the BET Theory. *J. Am. Chem. Soc.* **2015**, *137*, 3585–3591.

(74) Deria, P.; Gómez-Gualdrón, D. A.; Bury, W.; Schaef, H. T.; Wang, T. C.; Thallapally, P. K.; Sarjeant, A. A.; Snurr, R. Q.; Hupp, J. T.; Farha, O. K. Ultraporous, Water Stable, and Breathing Zirconium-Based Metal-Organic Frameworks with ftw Topology. *J. Am. Chem. Soc.* **2015**, *137*, 13183–13190.

(75) Zou, R.; Ren, X.; Huang, F.; Zhao, Y.; Liu, J.; Jing, X.; Liao, F.; Wang, Y.; Lin, J.; Zou, R.; Sun, J. A Luminescent Zr-Based Metal–Organic Framework for Sensing/Capture of Nitrobenzene and High-Pressure Separation of CH_4/C_2H_6. *J. Mater. Chem. A* **2015**, *3* (46), 23493–23500.

(76) Li, P.; Moon, S. Y.; Guelta, M. A.; Lin, L.; Gómez-Gualdrón, D. A.; Snurr, R. Q.; Harvey, S. P.; Hupp, J. T.; Farha, O. K. Nanosizing a Metal-Organic Framework Enzyme Carrier for Accelerating Nerve Agent Hydrolysis. *ACS Nano* **2016**, *10*, 9174–9182.

(77) Lv, X. L.; Yuan, S.; Xie, L. H.; Darke, H. F.; Chen, Y.; He, T.; Dong, C.; Wang, B.; Zhang, Y. Z.; Li, J. R.; Zhou, H. C. Ligand Rigidification for Enhancing the Stability of Metal-Organic Frameworks. *J. Am. Chem. Soc.* **2019**, *141*, 10283–10293.

(78) Li, P.; Chen, Q.; Wang, T. C.; Vermeulen, N. A.; Mehdi, B. L.; Dohnalkova, A.; Browning, N. D.; Shen, D.; Anderson, R.; Gómez-Gualdrón, D. A.; Cetin, F. M.; Jagiello, J.; Asiri, A. M.; Stoddart, J. F.; Farha, O. K. Hierarchically Engineered Mesoporous Metal-Organic Frameworks toward Cell-Free Immobilized Enzyme Systems. *Chem* **2018**, *4*, 1022–1034.

(79) Xu, L.; Luo, Y. P.; Sun, L.; Xu, Y.; Cai, Z. S.; Fang, M.; Yuan, R. X.; Du, H. Bin. Highly Stable Mesoporous Zirconium Porphyrinic Frameworks with Distinct Flexibility. *Chem. Eur. J.* **2016**, *22*, 6268–6276.

(80) Dong, C.; Bai, J.; Lv, X. L.; Wu, W.; Lv, J.; Li, J. R. Fixing Flexible Arms of Core-Shared Ligands to Enhance the Stability of Metal-Organic Frameworks. *Inorg. Chem.* **2019**, *58*, 15909–15916.

(81) Pang, J.; Yuan, S.; Qin, J.; Wu, M.; Lollar, C. T.; Li, J.; Huang, N.; Li, B.; Zhang, P.; Zhou, H. C. Enhancing Pore-Environment Complexity Using a Trapezoidal Linker: Toward Stepwise Assembly of Multivariate Quinary Metal-Organic Frameworks. *J. Am. Chem. Soc.* **2018**, *140*, 12328–12332.

(82) Lv, X. L.; Xie, L. H.; Wang, B.; Zhao, M.; Cui, Y.; Li, J. R. Flexible Metal–Organic Frameworks for the Wavelength-Based Luminescence Sensing of Aqueous pH. *J. Mater. Chem. C* **2018**, *6*, 10628–10639.

(83) Maldonado, R. R.; Zhang, X.; Hanna, S.; Gong, X.; Gianneschi, N. C.; Hupp, J. T.; Farha, O. K. Squeezing the Box: Isoreticular Contraction of Pyrene-Based Linker in a Zr-Based Metal–Organic Framework for Xe/Kr Separation. *Dalton Trans.* **2020**, *49*, 6553–6556.

(84) Yang, L.; Cai, P.; Zhang, L.; Xu, X.; Yakovenko, A. A.; Wang, Q.; Pang, J.; Yuan, S.; Zou, X.; Huang, N.; Huang, Z.; Zhou, H. C. Ligand-Directed Conformational Control over Porphyrinic Zirconium Metal-Organic Frameworks for Size-Selective Catalysis. *J. Am. Chem. Soc.* **2021**, *143*, 12129–12137.

(85) Lu, Z.; Wang, R.; Liao, Y.; Farha, O. K.; Bi, W.; Sheridan, T. R.; Zhang, K.; Duan, J.; Liu, J.; Hupp, J. T. Isomer of Linker for NU-1000 Yields a New she-Type, Catalytic, and Hierarchically Porous, Zr-Based Metal–Organic Framework. *Chem. Commun.* **2021**, *57*, 3571–3574.

(86) Zhang, Y.; Pang, J.; Li, J.; Yang, X.; Feng, M.; Cai, P.; Zhou, H. C. Visible-Light Harvesting Pyrene-Based MOFs as Efficient ROS Generators. *Chem. Sci.* **2019**, *10*, 8455–8460.

(87) Li, Z. J.; Wang, X.; Zhu, L.; Ju, Y.; Wang, Z.; Zhao, Q.; Zhang, Z. H.; Duan, T.; Qian, Y.; Wang, J. Q.; Lin, J. Hydrolytically Stable Zr-Based Metal-Organic Framework as a Highly Sensitive and Selective Luminescent Sensor of Radionuclides. *Inorg. Chem.* **2022**, *61*, 7467-7476.

(88) Wei, Z.; Gu, Z. Y.; Arvapally, R. K.; Chen, Y. P.; McDougald, R. N.; Ivy, J. F.; Yakovenko, A. A.; Feng, D.; Omary, M. A.; Zhou, H. C. Rigidifying Fluorescent Linkers by Metal-Organic Framework Formation for Fluorescence Blue Shift and Quantum Yield Enhancement. *J. Am. Chem. Soc.* **2014**, *136*, 8269–8276.

(89) Zhang, Q.; Su, J.; Feng, D.; Wei, Z.; Zou, X.; Zhou, H. C. Piezofluorochromic Metal-Organic Framework: A Microscissor Lift. *J. Am. Chem. Soc.* **2015**, *137*, 10064–10067.

(90) Hurlock, M. J.; Hao, L.; Kriegsman, K. W.; Guo, X.; O'Keeffe, M.; Zhang, Q. Evolution of 14-Connected Zr_6 Secondary Building Units through Postsynthetic Linker Incorporation. *ACS Appl. Mater. Interfaces* **2021**, *13*, 51945–51953.

(91) Yu, L.; Wang, H.; Liu, W.; Teat, S. J.; Li, J. Blue-Light-Excitable, Quantum Yield Enhanced, Yellow-Emitting, Zirconium-Based Metal-Organic Framework Phosphors Formed by Immobilizing Organic Chromophores. *Cryst. Growth Des.* **2019**, *19*, 6850–6854.

(92) Lammert, M.; Reinsch, H.; Murray, C. A.; Wharmby, M. T.; Terraschke, H.; Stock, N. Synthesis and Structure of Zr(IV)- and Ce(IV)-Based CAU-24 with 1,2,4,5-Tetrakis(4-Carboxyphenyl)Benzene. *Dalton Trans.* **2016**, *45*, 18822–18826.

(93) Lyu, J.; Zhang, X.; Otake, K. I.; Wang, X.; Li, P.; Li, Z.; Chen, Z.; Zhang, Y.; Wasson, M. C.; Yang, Y.; Bai, P.; Guo, X.; Islamoglu, T.; Farha, O. K. Topology and Porosity Control of Metal–Organic Frameworks through Linker Functionalization. *Chem. Sci.* **2019**, *10*, 1186–1192.

(94) Chen, Y.; Zhang, X.; Mian, M. R.; Son, F. A.; Zhang, K.; Cao, R.; Chen, Z.; Lee, S. J.; Idrees, K. B.; Goetjen, T. A.; Lyu, J.; Li, P.; Xia, Q.; Li, Z.; Hupp, J. T.; Islamoglu, T.; Napolitano, A.; Peterson, G. W.; Farha, O. K. Structural Diversity of Zirconium Metal-Organic Frameworks and Effect on Adsorption of Toxic Chemicals. *J. Am. Chem. Soc.* **2020**, *142*, 21428–21438.

(95) Gong, X.; Noh, H.; Gianneschi, N. C.; Farha, O. K. Interrogating Kinetic versus Thermodynamic Topologies of Metal-Organic Frameworks via Combined Transmission Electron Microscopy and X-Ray Diffraction Analysis. *J. Am. Chem. Soc.* **2019**, *141*, 6146–6151.

(96) Shaikh, S. M.; Usov, P. M.; Zhu, J.; Cai, M.; Alatis, J.; Morris, A. J. Synthesis and Defect Characterization of Phase-Pure Zr-MOFs Based on Meso-Tetracarboxyphenylporphyrin. *Inorg. Chem.* **2019**, *58*, 5145–5153.

(97) Karadeniz, B.; Žilić, D.; Huskić, I.; Germann, L. S.; Fidelli, A. M.; Muratović, S.; Lončarić, I.; Etter, M.; Dinnebier, R. E.; Barišić, D.; Cindro, N.; Islamoglu, T.; Farha, O. K.; Friščić, T.; Užarević, K. Controlling the Polymorphism and Topology Transformation in Porphyrinic Zirconium Metal-Organic Frameworks via Mechanochemistry. *J. Am. Chem. Soc.* **2019**, *141*, 19214–19220.

(98) Lyu, J.; Gong, X.; Lee, S. J.; Gnanasekaran, K.; Zhang, X.; Wasson, M. C.; Wang, X.; Bai, P.; Guo, X.; Gianneschi, N. C.; Farha, O. K. Phase Transitions in Metal-Organic Frameworks Directly Monitored through in Situ Variable Temperature Liquid-Cell Transmission Electron Microscopy and in Situ X-Ray Diffraction. *J. Am. Chem. Soc.* **2020**, *142*, 4609–4615.

(99) Nguyen, P. T. K.; Nguyen, H. T. D.; Nguyen, H. N.; Trickett, C. A.; Ton, Q. T.; Gutiérrez-Puebla, E.; Monge, M. A.; Cordova, K. E.; Gándara, F. New Metal-Organic Frameworks for Chemical Fixation of CO_2. *ACS Appl. Mater. Interfaces* **2018**, *10*, 733–744.

(100) Su, J.; Yuan, S.; Wang, T.; Lollar, C. T.; Zuo, J. L.; Zhang, J.; Zhou, H. C. Zirconium Metal–Organic Frameworks Incorporating Tetrathiafulvalene Linkers: Robust and Redox-Active Matrices for in Situ Confinement of Metal Nanoparticles. *Chem. Sci.* **2020**, *11*, 1918–1925.

(101) Cadiau, A.; Xie, L. S.; Kolobov, N.; Shkurenko, A.; Qureshi, M.; Tchalala, M. R.; Park, S. S.; Bavykina, A.; Eddaoudi, M.; Dincă, M.; Hendon, C. H.; Gascon,

J. Toward New 2D Zirconium-Based Metal-Organic Frameworks: Synthesis, Structures, and Electronic Properties. *Chem. Mater.* **2020**, *32* (1), 97–104.

(102) Wang, Y.; Hao, C.; Fan, W.; Fu, M.; Wang, X.; Wang, Z.; Zhu, L.; Li, Y.; Lu, X.; Dai, F.; Kang, Z.; Wang, R.; Guo, W.; Hu, S.; Sun, D. One-Step Ethylene Purification from an Acetylene/Ethylene/Ethane Ternary Mixture by Cyclopentadiene Cobalt-Functionalized Metal–Organic Frameworks. *Angew. Chem. Int. Ed.* **2021**, *60*, 11350–11358.

(103) Duan, Z.; Li, Y.; Xiao, X.; Huang, X.; Li, X.; Li, Y.; Zhang, C.; Zhang, H.; Li, L.; Lin, Z.; Zhao, Y.; Huang, W. Interpenetrated Metal-Organic Frameworks with ftw Topology and Versatile Functions. *ACS Appl. Mater. Interfaces* **2020**, *12*, 18715–18722.

(104) Gong, W.; Xie, Y.; Wang, X.; Kirlikovali, K. O.; Idrees, K. B.; Sha, F.; Xie, H.; Liu, Y.; Chen, B.; Cui, Y.; Farha, O. K. Programmed Polarizability Engineering in a Cyclen-Based Cubic Zr(IV) Metal-Organic Framework to Boost Xe/Kr Separation. *J. Am. Chem. Soc.* **2023**, *145*, 2679–2689.

(105) Burgess, S. A.; Kassie, A.; Baranowski, S. A.; Fritzsching, K. J.; Schmidt-Rohr, K.; Brown, C. M.; Wade, C. R. Improved Catalytic Activity and Stability of a Palladium Pincer Complex by Incorporation into a Metal-Organic Framework. *J. Am. Chem. Soc.* **2016**, *138*, 1780–1783.

(106) Wang, B.; Yang, Q.; Guo, C.; Sun, Y.; Xie, L. H.; Li, J. R. Stable Zr(IV)-Based Metal-Organic Frameworks with Predesigned Functionalized Ligands for Highly Selective Detection of Fe(III) Ions in Water. *ACS Appl Mater Interfaces* **2017**, *9* (11), 10286–10295.

(107) Ren, D.; Xia, H. L.; Zhou, K.; Wu, S.; Liu, X. Y.; Wang, X.; Li, J. Tuning and Directing Energy Transfer in the Whole Visible Spectrum through Linker Installation in Metal–Organic Frameworks. *Angew. Chem. Int. Ed.* **2021**, *60*, 25048–25054.

(108) Xia, H. L.; Zhou, K.; Yu, L.; Wang, H.; Liu, X. Y.; Proserpio, D. M.; Li, J. Customized Synthesis: Solvent- and Acid-Assisted Topology Evolution in Zirconium-Tetracarboxylate Frameworks. *Inorg. Chem.* **2022**, *61*, 7980-7988.

(109) Xia, H. L.; Zhang, J.; Si, J.; Wang, H.; Zhou, K.; Wang, L.; Li, J.; Sun, W.; Qu, L.; Li, J.; Liu, X. Y. Size- and Emission-Controlled Synthesis of Full-Color Luminescent Metal-Organic Frameworks for Tryptophan Detection. *Angew. Chem. Int. Ed.* **2023**, *62*, e202308506.

(110) Carter, J. H.; Han, X.; Moreau, F. Y.; Da Silva, I.; Nevin, A.; Godfrey, H. G. W.; Tang, C. C.; Yang, S.; Schröder, M. Exceptional Adsorption and Binding of Sulfur Dioxide in a Robust Zirconium-Based Metal-Organic Framework. *J Am Chem Soc* **2018**, *140*, 15564–15567.

(111) Zhang, X.; Frey, B. L.; Chen, Y. S.; Zhang, J. Topology-Guided Stepwise Insertion of Three Secondary Linkers in Zirconium Metal-Organic Frameworks. *J. Am. Chem. Soc.* **2018**, *140*, 7710–7715.

(112) Yu, J.; Anderson, R.; Li, X.; Xu, W.; Goswami, S.; Rajasree, S. S.; Maindan, K.; Gómez-Gualdrón, D. A.; Deria, P. Improving Energy Transfer within Metal-Organic Frameworks by Aligning Linker Transition Dipoles along the Framework Axis. *J. Am. Chem. Soc.* **2020**, *142*, 11192–11202.

(113) Rajasree, S. S.; Yu, J.; Fajardo-Rojas, F.; Fry, H. C.; Anderson, R.; Li, X.; Xu, W.; Duan, J.; Goswami, S.; Maindan, K.; Gómez-Gualdrón, D. A.; Deria, P. Framework-Topology-Controlled Singlet Fission in Metal-Organic Frameworks. *J. Am. Chem. Soc.* **2023**, *145*, 17678-17688.

(114) Mallick, A.; Liang, H.; Shekhah, O.; Jia, J.; Mouchaham, G.; Shkurenko, A.; Belmabkhout, Y.; Alshareef, H. N.; Eddaoudi, M. Made-to-Order Porous Electrodes for Supercapacitors: MOFs Embedded with Redox-Active Centers as a Case Study. *Chem. Commun.* **2020**, *56*, 1883–1886.

(115) Li, X.; Liu, J.; Zhou, K.; Ullah, S.; Wang, H.; Zou, J.; Thonhauser, T.; Li, J. Tuning Metal-Organic Framework (MOF) Topology by Regulating Ligand and Secondary Building Unit (SBU) Geometry: Structures Built on 8-Connected M_6(M = Zr, Y) Clusters and a Flexible Tetracarboxylate for Propane-Selective Propane/Propylene Separation. *J. Am. Chem. Soc.* **2022**, *144*, 21702–21709.

(116) Chen, X.; Xie, H.; Lorenzo, E. R.; Zeman, C. J.; Qi, Y.; Syed, Z. H.; Stone, A. E. B. S.; Wang, Y.; Goswami, S.; Li, P.; Islamoglu, T.; Weiss, E. A.; Hupp, J. T.; Schatz, G. C.; Wasielewski, M. R.; Farha, O. K. Direct Observation of Modulated Radical Spin States in Metal-Organic Frameworks by Controlled Flexibility. *J. Am. Chem. Soc.* **2022**, *144*, 2685–2693.

(117) Zhang, Y.; Zhang, X.; Lyu, J.; Otake, K. I.; Wang, X.; Redfern, L. R.; Malliakas, C. D.; Li, Z.; Islamoglu, T.; Wang, B.; Farha, O. K. A Flexible Metal-Organic Framework with 4-Connected Zr_6 Nodes. *J. Am. Chem. Soc.* **2018**, *140*, 11179–11183.

(118) Zhang, Y.; Zhang, X.; Chen, Z.; Otake, K. ichi; Peterson, G. W.; Chen, Y.; Wang, X.; Redfern, L. R.; Goswami, S.; Li, P.; Islamoglu, T.; Wang, B.; Farha, O. K. A Flexible Interpenetrated Zirconium-Based Metal–Organic Framework with High Affinity toward Ammonia. *ChemSusChem* **2020**, *13*, 1710–1714.

(119) Wang, B.; Wang, P.; Xie, L. H.; Lin, R. B.; Lv, J.; Li, J. R.; Chen, B. A Stable Zirconium Based Metal-Organic Framework for Specific Recognition of Representative Polychlorinated Dibenzo-p-Dioxin Molecules. *Nat. Commun.* **2019**, *10*, 1–8.

(120) Si, J.; Xia, H. L.; Zhou, K.; Li, J.; Xing, K.; Miao, J.; Zhang, J.; Wang, H.; Qu, L. L.; Liu, X. Y.; Li, J. Reticular Chemistry with Art: A Case Study of Olympic Rings-Inspired Metal-Organic Frameworks. *J. Am. Chem. Soc.* **2022**, *144*, 22170–22177.

(121) Wang, S.; Ly, H. G. T.; Wahiduzzaman, M.; Simms, C.; Dovgaliuk, I.; Tissot, A.; Maurin, G.; Parac-Vogt, T. N.; Serre, C. A Zirconium Metal-Organic

Framework with SOC Topological Net for Catalytic Peptide Bond Hydrolysis. *Nat. Commun.* **2022**, *13*, 1–8.

(122) Wang, Y.; Feng, L.; Zhang, K.; Wang, K. Y.; Fan, W.; Wang, X.; Guo, B.; Dai, F.; Zhang, L.; Sun, D.; Zhou, H. C. Uncovering Structural Opportunities for Zirconium Metal–Organic Frameworks via Linker Desymmetrization. *Adv. Sci.* **2019**, *6* (23), 1901855.

(123) Kong, X. J.; He, T.; Zhang, Y. Z.; Wu, X. Q.; Wang, S. N.; Xu, M. M.; Si, G. R.; Li, J. R. Constructing New Metal–Organic Frameworks with Complicated Ligands from "One-Pot" in Situ Reactions. *Chem. Sci.* **2019**, *10*, 3949–3955.

(124) Jiang, H.; Zhang, W.; Hou, B.; Liu, Y.; Cui, Y. Planar Chiral [2.2]Paracyclophane-Based Zr(IV) Metal–Organic Frameworks. *CCS Chem.* **2023**, *5*, 1635–1643.

(125) Luebke, R.; Belmabkhout, Y.; Weseliński, Ł. J.; Cairns, A. J.; Alkordi, M.; Norton, G.; Wojtas, Ł.; Adil, K.; Eddaoudi, M. Versatile Rare Earth Hexanuclear Clusters for the Design and Synthesis of Highly-Connected ftw -MOFs. *Chem. Sci.* **2015**, *6*, 4095–4102.

(126) Wang, H.; Dong, X.; Colombo, V.; Wang, Q.; Liu, Y.; Liu, W.; Wang, X. L.; Huang, X. Y.; Proserpio, D. M.; Sironi, A.; Han, Y.; Li, J. Tailor-Made Microporous Metal–Organic Frameworks for the Full Separation of Propane from Propylene Through Selective Size Exclusion. *Adv. Mat.* **2018**, *30*, 1805088.

(127) Chen, Z.; Weseliński, Ł. J.; Adil, K.; Belmabkhout, Y.; Shkurenko, A.; Jiang, H.; Bhatt, P. M.; Guillerm, V.; Dauzon, E.; Xue, D. X.; O'Keeffe, M.; Eddaoudi, M. Applying the Power of Reticular Chemistry to Finding the Missing alb-MOF Platform Based on the (6,12)-Coordinated Edge-Transitive Net. *J. Am. Chem. Soc.* **2017**, *139*, 3265–3274.

(128) Xu, L.; Zhai, M. K.; Wang, F.; Sun, L.; Du, H. Bin. A Series of Robust Metal–Porphyrinic Frameworks Based on Rare Earth Clusters and Their Application in N–H Carbene Insertion. *Dalton Trans.* **2016**, *45*, 17108–17112.

(129) Zhang, L.; Yuan, S.; Feng, L.; Guo, B.; Qin, J. S.; Xu, B.; Lollar, C.; Sun, D.; Zhou, H. C. Pore-Environment Engineering with Multiple Metal Sites in Rare-Earth Porphyrinic Metal–Organic Frameworks. *Angew. Chem. Int. Ed.* **2018**, *57*, 5095–5099.

(130) Hu, F.; Di, Z.; Wu, M.; Hong, M.; Li, J. A Robust Multifunctional Eu_6-Cluster Based Framework for Gas Separation and Recognition of Small Molecules and Heavy Metal Ions. *Cryst. Growth Des.* **2019**, *19*, 6381–6387.

(131) Abdulhalim, R. G.; Bhatt, P. M.; Belmabkhout, Y.; Shkurenko, A.; Adil, K.; Barbour, L. J.; Eddaoudi, M. A Fine-Tuned Metal-Organic Framework for Autonomous Indoor Moisture Control. *J. Am. Chem. Soc.* **2017**, *139*, 10715–10722.

(132) Quezada-Novoa, V.; Titi, H. M.; Sarjeant, A. A.; Howarth, A. J. Building a shp: A Rare-Earth Metal-Organic Framework and Its Application in a Catalytic Photooxidation Reaction. *Chem. Mater.* **2021**, *33*, 4163–4169.

(133) Su, J.; Yuan, S.; Li, J.; Wang, H. Y.; Ge, J. Y.; Drake, H. F.; Leong, C. F.; Yu, F.; D'Alessandro, D. M.; Kurmoo, M.; Zuo, J. L.; Zhou, H. C. Rare-Earth Metal Tetrathiafulvalene Carboxylate Frameworks as Redox-Switchable Single-Molecule Magnets. *Chem. Eur. J.* **2021**, *27*, 622–627.

(134) Lv, X. L.; Feng, L.; Xie, L. H.; He, T.; Wu, W.; Wang, K. Y.; Si, G.; Wang, B.; Li, J. R.; Zhou, H. C. Linker Desymmetrization: Access to a Series of Rare-Earth Tetracarboxylate Frameworks with Eight-Connected Hexanuclear Nodes. *J. Am. Chem. Soc.* **2021**, *143*, 2784–2791.

(135) Quezada-Novoa, V.; Titi, H. M.; Villanueva, F. Y.; Wilson, M. W. B.; Howarth, A. J.; Quezada-Novoa, V.; Howarth, A. J.; Titi, H. M.; Villanueva, F. Y.; Wilson, M. W. B. The Effect of Linker-to-Metal Energy Transfer on the

Photooxidation Performance of an Isostructural Series of Pyrene-Based Rare-Earth Metal–Organic Frameworks. *Small* **2023**, *19*, 2302173.

(136) Angeli, G. K.; Sartsidou, C.; Vlachaki, S.; Spanopoulos, I.; Tsangarakis, C.; Kourtellaris, A.; Klontzas, E.; Froudakis, G. E.; Tasiopoulos, A.; Trikalitis, P. N. Reticular Chemistry and the Discovery of a New Family of Rare Earth (4,8)-Connected Metal-Organic Frameworks with csq Topology Based on $RE_4(M_3\text{-}O)_2(COO)_8$ Clusters. *ACS Appl. Mater. Interfaces* **2017**, *9*, 44560–44566.

(137) Luo, T. Y.; Liu, C.; Eliseeva, S. V.; Muldoon, P. F.; Petoud, S.; Rosi, N. L. Rare Earth pcu Metal-Organic Framework Platform Based on $RE_4(M_3\text{-}OH)_4(COO)_6^{2+}$ Clusters: Rational Design, Directed Synthesis, and Deliberate Tuning of Excitation Wavelengths. *J. Am. Chem. Soc.* **2017**, *139*, 9333–9340.

(138) Xia, H. L.; Zhou, K.; Guo, J.; Zhang, J.; Huang, X.; Luo, D.; Liu, X. Y.; Li, J. Amino Group Induced Structural Diversity and Near-Infrared Emission of Yttrium-Tetracarboxylate Frameworks. *Chem. Sci.* **2022**, *13*, 9321–9328.

(139) Lv, X. L.; Feng, L.; Wang, K. Y.; Xie, L. H.; He, T.; Wu, W.; Li, J. R.; Zhou, H. C. A Series of Mesoporous Rare-Earth Metal–Organic Frameworks Constructed from Organic Secondary Building Units. *Angew. Chem. Int. Ed.* **2021**, *60*, 2053–2057.

(140) Li, M.; O'Keeffe, M.; Proserpio, D. M.; Proserpio, D. M.; Zhang, H. F. A New Group of Edge-Transitive 3-Periodic Nets and Their Derived Nets for Reticular Chemistry. *Cryst. Growth Des.* **2020**, *20*, 4062–4068.

(141) Furukawa, H.; Gándara, F.; Zhang, Y.-B.; Jiang, J.; Queen, W. L.; Hudson, M. R.; Yaghi, O. M. Water Adsorption in Porous Metal–Organic Frameworks and Related Materials. *J. Am. Chem. Soc.* **2014**, *136*, 4369–4381.

(142) Zhang, M.; Chen, Y. P.; Bosch, M.; Gentle, T.; Wang, K.; Feng, D.; Wang, Z. U.; Zhou, H. C. Symmetry-Guided Synthesis of Highly Porous Metal-Organic Frameworks with Fluorite Topology. *Angew. Chem. Int. Ed.* **2014**, *53*, 815–818.

(143) Ji, P.; Manna, K.; Lin, Z.; Urban, A.; Greene, F. X.; Lan, G.; Lin, W. Single-Site Cobalt Catalysts at New $Zr_8(M_2\text{-}O)_8(M_2\text{-}OH)_4$ Metal-Organic Framework Nodes for Highly Active Hydrogenation of Alkenes, Imines, Carbonyls, and Heterocycles. *J. Am. Chem. Soc.* **2016**, *138*, 12234–12242.

(144) Koschnick, C.; Terban, M. W.; Frison, R.; Etter, M.; Böhm, F. A.; Proserpio, D. M.; Krause, S.; Dinnebier, R. E.; Canossa, S.; Lotsch, B. V. Unlocking New Topologies in Zr-Based Metal-Organic Frameworks by Combining Linker Flexibility and Building Block Disorder. *J. Am. Chem. Soc.* **2023**, *145*, 10051–10060.

(145) Zhang, X.; Zhang, X.; Johnson, J. A.; Chen, Y. S.; Zhang, J. Highly Porous Zirconium Metal-Organic Frameworks with β-UH_3-like Topology Based on Elongated Tetrahedral Linkers. *J. Am. Chem. Soc.* **2016**, *138*, 8380–8383.

(146) Angeli, G. K.; Batzavali, D.; Mavronasou, K.; Tsangarakis, C.; Stuerzer, T.; Ott, H.; Trikalitis, P. N. Remarkable Structural Diversity between Zr/Hf and Rare-Earth MOFs via Ligand Functionalization and the Discovery of Unique (4,8)-c and (4,12)-Connected Frameworks. *J. Am. Chem. Soc.* **2020**, *142*, 15986–15994.

(147) Nateghi, B.; Domasevitch, K. V.; Bulánek, R.; Janiak, C.; Boldog, I. Ligand Excess "Inverse-Defected" Zr_6 Tetrahedral Tetracarboxylate Framework and Its Thermal Transformation. *Inorg. Chem.* **2019**, *58*, 12786–12797.

(148) Yan, Y.; O'Connor, A. E.; Kanthasamy, G.; Atkinson, G.; Allan, D. R.; Blake, A. J.; Schröder, M. Unusual and Tunable Negative Linear Compressibility in the Metal-Organic Framework MFM-133(M) (M = Zr, Hf). *J. Am. Chem. Soc.* **2018**, *140*, 3952–3958.

(149) Jiang, H.; Zhang, W.; Kang, X.; Cao, Z.; Chen, X.; Liu, Y.; Cui, Y. Topology-Based Functionalization of Robust Chiral Zr-Based Metal-Organic Frameworks for Catalytic Enantioselective Hydrogenation. *J. Am. Chem. Soc.* **2020**, *142*, 9642–9652.

(150) Jiang, H.; Yang, K.; Zhao, X.; Zhang, W.; Liu, Y.; Jiang, J.; Cui, Y. Highly Stable Zr(IV)-Based Metal-Organic Frameworks for Chiral Separation in Reversed-Phase Liquid Chromatography. *J. Am. Chem. Soc.* **2021**, *143*, 390–398.

(151) Fiankor, C.; Nyakuchena, J.; Khoo, R. S. H.; Zhang, X.; Hu, Y.; Yang, S.; Huang, J.; Zhang, J. Symmetry-Guided Synthesis of *N,N*-Bicarbazole and Porphyrin-Based Mixed-Ligand Metal-Organic Frameworks: Light Harvesting and Energy Transfer. *J. Am. Chem. Soc.* **2021**, *143*, 20411–20418.

(152) Shu, R.; Khoo, H.; Fiankor, C.; Yang, S.; Hu, W.; Yang, C.; Lu, J.; Morton, M. D.; Zhang, X.; Liu, Y.; Huang, J.; Zhang, J. Postsynthetic Modification of the Nonanuclear Node in a Zirconium Metal–Organic Framework for Photocatalytic Oxidation of Hydrocarbons. *J. Am. Chem. Soc.* **2023**, *145*, 24052-24060.

(153) Xia, H. L.; Zhou, K.; Yu, L.; Wang, H.; Liu, X. Y.; Li, J. A Zirconium-Organic Framework Constructed from Saddle-Shaped Tetratopic Carboxylate for High-Rate and -Efficiency Iodine Capture. *Inorg. Chem.* **2022**, *61*, 17109–17114.

(154) Schulz, M.; Gehl, A.; Schlenkrich, J.; Schulze, H. A.; Zimmermann, S.; Schaate, A. A Calixarene-Based Metal–Organic Framework for Highly Selective NO_2 Detection. *Angew. Chem. Int. Ed.* **2018**, *57*, 12961–12965.

(155) Gong, W.; Zhang, W.; Son, F. A.; Yang, K.; Chen, Z.; Chen, X.; Jiang, J.; Liu, Y.; Farha, O. K.; Cui, Y. Topological Strain-Induced Regioselective Linker Elimination in a Chiral Zr(IV)-Based Metal-Organic Framework. *Chem* **2021**, *7*, 190–201.

(156) Gong, W.; Chen, X.; Zhang, W.; Kirlikovali, K. O.; Nan, B.; Chen, Z.; Si, R.; Liu, Y.; Farha, O. K.; Cui, Y. Leveraging Chiral Zr(IV)-Based Metal-Organic Frameworks To Elucidate Catalytically Active Rh Species in Asymmetric Hydrogenation Reactions. *J. Am. Chem. Soc.* **2022**, *144*, 3117–3126.

(157) Gong, W.; Liu, Y.; Cui, Y. Chiral and Robust Zr(IV)-Based Metal–Organic Frameworks Built from Spiro Skeletons. *Faraday Discuss.* **2021**, *231*, 168–180.

(158) Gong, W.; Chen, X.; Jiang, H.; Chu, D.; Cui, Y.; Liu, Y. Highly Stable Zr(IV)-Based Metal-Organic Frameworks with Chiral Phosphoric Acids for Catalytic Asymmetric Tandem Reactions. *J. Am. Chem. Soc.* **2019**, *141*, 7498–7508.

(159) Gong, W.; Chen, X.; Fahy, K. M.; Dong, J.; Liu, Y.; Farha, O. K.; Cui, Y. Reticular Chemistry in Its Chiral Form: Axially Chiral Zr(IV)-Spiro Metal-Organic Framework as a Case Study. *J. Am. Chem. Soc.* **2023**, *145*, 13869–13878.

(160) Zheng, H.-Q.; Zhang, L.; Lu, M.; Xiao, X.; Yang, Y.; Cui, Y.; Qian, G. Precise Design and Deliberate Tuning of Turn-On Fluorescence in Tetraphenylpyrazine-Based Metal–Organic Frameworks. *Research* **2022**, *2022*, 1-11.

(161) Liu, Y.; Liu, L.; Chen, X.; Liu, Y.; Han, Y.; Cui, Y. Single-Crystalline Ultrathin 2D Porous Nanosheets of Chiral Metal-Organic Frameworks. *J. Am. Chem. Soc.* **2021**, *143*, 3509–3518.

(162) Song, X.; Huang, Q.; Liu, J.; Xie, H.; Idrees, K. B.; Hou, S.; Yu, L.; Wang, X.; Liu, F.; Qiao, Z.; Wang, H.; Chen, Y.; Li, Z.; Farha, O. K. Reticular Chemistry in Pore Engineering of a Y-Based Metal-Organic Framework for Xenon/Krypton Separation. *ACS Appl. Mater. Interfaces* **2023**, *15*, 18229–18235.

(163) Angeli, G. K.; Loukopoulos, E.; Kouvidis, K.; Bosveli, A.; Tsangarakis, C.; Tylianakis, E.; Froudakis, G.; Trikalitis, P. N. Continuous Breathing Rare-Earth MOFs Based on Hexanuclear Clusters with Gas Trapping Properties. *J. Am. Chem. Soc.* **2021**, *143*, 10250–10260.

(164) Loukopoulos, E.; Angeli, G. K.; Tsangarakis, C.; Traka, E.; Froudas, K. G.; Trikalitis, P. N. Reticular Synthesis of Flexible Rare-Earth Metal-Organic Frameworks: Control of Structural Dynamics and Sorption Properties Through Ligand Functionalization. *Chem. Eur. J.* **2023**, e202302709.

(165) Feng, L.; Wang, Y.; Zhang, K.; Wang, K.; Fan, W.; Wang, X.; Powell, J. A.; Guo, B.; Dai, F.; Zhang, L.; Wang, R.; Sun, D.; Zhou, H. Molecular Pivot-Hinge

Installation to Evolve Topology in Rare-Earth Metal–Organic Frameworks. *Angew. Chem. Int. Ed.* **2019**, *131*, 16835–16843.

(166) Feng, D.; Wang, K.; Su, J.; Liu, T.-F.; Park, J.; Wei, Z.; Bosch, M.; Yakovenko, A.; Zou, X.; Zhou, H.-C. A Highly Stable Zeotype Mesoporous Zirconium Metal–Organic Framework with Ultralarge Pores. *Angew. Chem. Int. Ed.* **2015**, *54*, 149–154.

(167) Wang, R.; Wang, Z.; Xu, Y.; Dai, F.; Zhang, L.; Sun, D. Porous Zirconium Metal-Organic Framework Constructed from 2D → 3D Interpenetration Based on a 3,6-Connected kgd Net. *Inorg. Chem.* **2014**, *53*, 7086–7088.

(168) Wang, B.; Lv, X. L.; Feng, D.; Xie, L. H.; Zhang, J.; Li, M.; Xie, Y.; Li, J. R.; Zhou, H. C. Highly Stable Zr(IV)-Based Metal-Organic Frameworks for the Detection and Removal of Antibiotics and Organic Explosives in Water. *J. Am. Chem. Soc.* **2016**, *138*, 6204–6216.

(169) Liu, T. F.; Vermeulen, N. A.; Howarth, A. J.; Li, P.; Sarjeant, A. A.; Hupp, J. T.; Farha, O. K. Adding to the Arsenal of Zirconium-Based Metal–Organic Frameworks: the Topology as a Platform for Solvent-Assisted Metal Incorporation. *Eur. J. Inorg. Chem.* **2016**, *2016*, 4349–4352.

(170) Lee, S.; Bürgi, H. B.; Alshmimri, S. A.; Yaghi, O. M. Impact of Disordered Guest-Framework Interactions on the Crystallography of Metal-Organic Frameworks. *J. Am. Chem. Soc.* **2018**, *140*, 8958–8964.

(171) Guillerm, V.; Weseliński, Ł. J.; Belmabkhout, Y.; Cairns, A. J.; D'Elia, V.; Wojtas, Ł.; Adil, K.; Eddaoudi, M. Discovery and Introduction of a (3,18)-Connected Net as an Ideal Blueprint for the Design of Metal–Organic Frameworks. *Nat. Chem.* **2014**, *6*, 673–680.

(172) Guo, B.; Li, F.; Wang, C.; Zhang, L.; Sun, D. A Rare (3,12)-Connected Zirconium Metal–Organic Framework with Efficient Iodine Adsorption Capacity and pH Sensing. *J. Mater. Chem. A* **2019**, *7*, 13173–13179.

(173) Bezrukov, A. A.; Törnroos, K. W.; Le Roux, E.; Dietzel, P. D. C. Incorporation of an Intact Dimeric Zr_{12} Oxo Cluster from a Molecular Precursor in a New Zirconium Metal–Organic Framework. *Chem. Commun.* **2018**, *54*, 2735–2738.

(174) Gong, W.; Arman, H.; Chen, Z.; Xie, Y.; Son, F. A.; Cui, H.; Chen, X.; Shi, Y.; Liu, Y.; Chen, B.; Farha, O. K.; Cui, Y. Highly Specific Coordination-Driven Self-Assembly of 2D Heterometallic Metal-Organic Frameworks with Unprecedented Johnson-Type (J_{51}) Nonanuclear Zr-Oxocarboxylate Clusters. *J. Am. Chem. Soc.* **2021**, *143*, 657–663.

(175) Chen, Y.; Zhang, X.; Ma, K.; Chen, Z.; Wang, X.; Knapp, J.; Alayoglu, S.; Wang, F.; Xia, Q.; Li, Z.; Islamoglu, T.; Farha, O. K. Zirconium-Based Metal-Organic Framework with 9-Connected Nodes for Ammonia Capture. *ACS Appl. Nano Mater.* **2019**, *2*, 6098–6102.

(176) Zhao, T.; Heering, C.; Boldog, I.; Domasevitch, K. V.; Janiak, C. A View on Systematic Truncation of Tetrahedral Ligands for Coordination Polymers. *CrystEngComm* **2017**, *19*, 776–780.

(177) Zhao, Y.; Qi, S.; Niu, Z.; Peng, Y.; Shan, C.; Verma, G.; Wojtas, L.; Zhang, Z.; Zhang, B.; Feng, Y.; Chen, Y. S.; Ma, S. Robust Corrole-Based Metal-Organic Frameworks with Rare 9-Connected Zr/Hf-Oxo Clusters. *J. Am. Chem. Soc.* **2019**, *141*, 14443–14450.

(178) He, T.; Zhang, Y. Z.; Kong, X. J.; Yu, J.; Lv, X. L.; Wu, Y.; Guo, Z. J.; Li, J. R. Zr(IV)-Based Metal-Organic Framework with T-Shaped Ligand: Unique Structure, High Stability, Selective Detection, and Rapid Adsorption of $Cr_2O_7^{2-}$ in Water. *ACS Appl. Mater. Interfaces* **2018**, *10*, 16650–16659.

(179) Chen, T. H.; Popov, I.; Miljanić, O. A Zirconium Macrocyclic Metal–Organic Framework with Predesigned Shape-Persistent Apertures. *Chem. Eur. J.* **2017**, *23*, 286–290.

(180) Bicalho, H. A.; Saraci, F.; Velazquez-Garcia, J. de J.; Titi, H. M.; Howarth, A. J. Unravelling the Synthesis of a Rare-Earth Cluster-Based Metal–Organic Framework with spn Topology. *Chem. Commun.* **2022**, *58*, 10925–10928.

(181) Sheybani, S.; Abbas, M.; Firouzi, H. R.; Xiao, Z.; Zhou, H. C.; Balkus, K. J. Synthesis of Fluoro-Bridged Ho^{3+} and Gd^{3+} 1,3,5-Tris(4-Carboxyphenyl)Benzene Metal-Organic Frameworks from Perfluoroalkyl Substances. *Inorg. Chem.* **2023**, *62*, 4314–4321.

(182) Li, Y. J.; Wang, Y. L.; Liu, Q. Y. The Highly Connected MOFs Constructed from Nonanuclear and Trinuclear Lanthanide-Carboxylate Clusters: Selective Gas Adsorption and Luminescent pH Sensing. *Inorg. Chem.* **2017**, *56*, 2159–2164.

(183) Loukopoulos, E.; Angeli, G. K.; Kouvidis, K.; Tsangarakis, C.; Trikalitis, P. N. Accessing 14-Connected Nets: Continuous Breathing, Hydrophobic Rare-Earth Metal Organic Frameworks Based on 14-c Hexanuclear Clusters with High Affinity for Non-Polar Vapors. *ACS Appl. Mater. Interfaces* **2022**, *14*, 22242-22251.

(184) Feng, Y.; Xin, X.; Zhang, Y.; Guo, B.; Li, F.; Kong, X.; Wang, Y.; Wang, X.; Wang, Y.; Zhang, L.; Sun, D. Rational Design and Synthesis of Hexanuclear Rare Earth the-a Metal-Organic Frameworks Platform Based on $RE_6O_4(OH)_4(COO)_8$ Clusters. *Cryst. Growth Des.* **2019**, *19*, 1509–1513.

(185) Alezi, D.; Peedikakkal, A. M. P.; Weseliński, Ł. J.; Guillerm, V.; Belmabkhout, Y.; Cairns, A. J.; Chen, Z.; Wojtas, Ł.; Eddaoudi, M. Quest for Highly Connected Metal-Organic Framework Platforms: Rare-Earth Polynuclear Clusters Versatility Meets Net Topology Needs. *J. Am. Chem. Soc.* **2015**, *137*, 5421–5430.

(186) Wang, Y.; Feng, L.; Fan, W.; Wang, K. Y.; Wang, X.; Wang, X.; Zhang, K.; Zhang, X.; Dai, F.; Sun, D.; Zhou, H. C. Topology Exploration in Highly Connected Rare-Earth Metal-Organic Frameworks via Continuous Hindrance Control. *J. Am. Chem. Soc.* **2019**, *141*, 6967–6975.

(187) Alezi, D.; Spanopoulos, I.; Tsangarakis, C.; Shkurenko, A.; Adil, K.; Belmabkhout, Y.; O'Keeffe, M.; Eddaoudi, M.; Trikalitis, P. N. Reticular Chemistry at Its Best: Directed Assembly of Hexagonal Building Units into the Awaited Metal-Organic Framework with the Intricate Polybenzene Topology, pbz-MOF. *J. Am. Chem. Soc.* **2016**, *138*, 12767–12770.

(188) Liang, W.; Noor, M. Z. M.; Lewis, W.; Macmillan, A.; Zhang, X.; Tang, R.; Kochubei, A.; Wiley, D.; Haynes, B. S.; Huang, J. Design of an ocu-Metal-Organic Framework for a Photocatalysis Reaction. *ChemPhotoChem* **2023**, *7*, e202300031.

(189) Zhang, Y. Z.; He, T.; Kong, X. J.; Lv, X. L.; Wu, X. Q.; Li, J. R. Tuning Water Sorption in Highly Stable Zr(IV)-Metal-Organic Frameworks through Local Functionalization of Metal Clusters. *ACS Appl. Mater. Interfaces* **2018**, *10*, 27868–27874.

(190) Blatov, V. A.; Shevchenko, A. P.; Proserpio, D. M. Applied Topological Analysis of Crystal Structures with the Program Package Topospro. *Cryst. Growth Des.* **2014**, *14*, 3576–3586.

(191) O'Keeffe, M.; Yaghi, O. M. Deconstructing the Crystal Structures of Metal-Organic Frameworks and Related Materials into Their Underlying Nets. *Chem. Rev.* **2012**, 112, 675–702.

(192) Panagiotou, N.; Liatsou, I.; Pournara, A.; Angeli, G. K.; Giappa, R. M.; Tylianakis, E.; Manos, M. J.; Froudakis, G. E.; Trikalitis, P. N.; Pashalidis, I.; Tasiopoulos, A. J. Water-Stable 2-D Zr MOFs with Exceptional UO_2^{2+} Sorption Capability. *J. Mater. Chem. A* **2020**, *8*, 1849–1857.

(193) Panagiotou, N.; Moscoso, F. G.; Lopes-Costa, T.; Pedrosa, J. M.; Tasiopoulos, A. J. 2-Dimensional Rare Earth Metal–Organic Frameworks Based on a Hexanuclear Secondary Building Unit as Efficient Detectors for Vapours of Nitroaromatics and Volatile Organic Compounds. *Inorg. Chem. Front.* **2022**, *9*, 4850–4863.

(194) Guillerm, V.; Eddaoudi, M. The Importance of Highly Connected Building Units in Reticular Chemistry: Thoughtful Design of Metal-Organic Frameworks. *Acc. Chem. Res.* **2021**, *54*, 3298–3312.

(195) Eubank, J. F.; Mouttaki, H.; Cairns, A. J.; Belmabkhout, Y.; Wojtas, L.; Luebke, R.; Alkordi, M.; Eddaoudi, M. The Quest for Modular Nanocages: tbo-MOF as an Archetype for Mutual Substitution, Functionalization, and Expansion of Quadrangular Pillar Building Blocks. *J. Am. Chem. Soc.* **2011**, *133*, 14204–14207.

(196) Moreau, F.; Kolokolov, D. I.; Stepanov, A. G.; Easun, T. L.; Dailly, A.; Lewis, W.; Blake, A. J.; Nowell, H.; Lennox, M. J.; Besley, E.; Yang, S.; Schröder, M. Tailoring Porosity and Rotational Dynamics in a Series of Octacarboxylate Metal-Organic Frameworks. *Proc. Nat. Acad. Sci. U. S. A.* **2017**, *114*, 3056–3061.

(197) Eubank, J. F.; Nouar, F.; Luebke, R.; Cairns, A. J.; Wojtas, L.; Alkordi, M.; Bousquet, T.; Hight, M. R.; Eckert, J.; Embs, J. P.; Georgiev, P. A.; Eddaoudi, M.; Luebke, R.; Cairns, A. J.; Alkordi, M.; Eddaoudi, M.; Eubank, J. F.; Nouar, F.; Wojtas, L.; Bousquet, T.; Hight, M. R.; Eckert, J.; Embs, J. P.; Georgiev, P. A. On Demand: The Singular rht Net, an Ideal Blueprint for the Construction of a Metal–Organic Framework (MOF) Platform. *Angew. Chem. Int. Ed.* **2012**, *51*, 10099–10103.

(198) Farha, O. K.; Eryazici, I.; Jeong, N. C.; Hauser, B. G.; Wilmer, C. E.; Sarjeant, A. A.; Snurr, R. Q.; Nguyen, S. T.; Yazaydin, A. Ö.; Hupp, J. T. Metal-Organic Framework Materials with Ultrahigh Surface Areas: Is the Sky the Limit? *J. Am. Chem. Soc.* **2012**, *134*, 15016–15021.

(199) Xue, D. X.; Cairns, A. J.; Belmabkhout, Y.; Wojtas, L.; Liu, Y.; Alkordi, M. H.; Eddaoudi, M. Tunable Rare-Earth fcu-MOFs: A Platform for Systematic Enhancement of CO_2 Adsorption Energetics and Uptake. *J. Am. Chem. Soc.* **2013**, *135*, 7660–7667.

(200) Nouar, F.; Eubank, J. F.; Bousquet, T.; Wojtas, L.; Zaworotko, M. J.; Eddaoudi, M. Supermolecular Building Blocks (SBBs) for the Design and Synthesis of Highly Porous Metal-Organic Frameworks. *J. Am. Chem. Soc.* **2008**, *130*, 1833–1835.

(201) Bruno, I. J.; Cole, J. C.; Edgington, P. R.; Kessler, M.; Macrae, C. F.; McCabe, P.; Pearson, J.; Taylor, R. New Software for Searching the Cambridge Structural Database and Visualizing Crystal Structures. *Acta Crystallogr., Sect. B: Struct. Sci.* **2002**, *58*, 389–397.

(202) Xue, Y. S.; Lu, J. L.; Cheng, W. W.; Wei, J.; Chen, N. N.; Dai, J.; Tao, J. Q. Synthesis, Crystal Structures, Adsorption and Fluorescence Properties of Coordination Polymers Based on a Semirigid Octadentate Ligand. *Transition Met. Chem.* **2018**, *43*, 9–19.

(203) Chen, Z.; Thiam, Z.; Shkurenko, A.; Weselinski, L. J.; Adil, K.; Jiang, H.; Alezi, D.; Assen, A. H.; O'Keeffe, M.; Eddaoudi, M. Enriching the Reticular Chemistry Repertoire with Minimal Edge-Transitive Related Nets: Access to Highly Coordinated Metal-Organic Frameworks Based on Double Six-Membered Rings as Net-Coded Building Units. *J. Am. Chem. Soc.* **2019**, *141*, 20480–20489.

(204) Saraci, F.; Quezada-Novoa, V.; Donnarumma, P. R.; Howarth, A. J. Rare-Earth Metal–Organic Frameworks: From Structure to Applications. *Chem. Soc. Rev.* **2020**, *49*, 7949–7977.

(205) Qiu, Y. C.; Yuan, S.; Li, X. X.; Du, D. Y.; Wang, C.; Qin, J. S.; Drake, H. F.; Lan, Y. Q.; Jiang, L.; Zhou, H. C. Face-Sharing Archimedean Solids Stacking for the Construction of Mixed-Ligand Metal-Organic Frameworks. *J. Am. Chem. Soc.* **2019**, *141*, 13841–13848.

(206) Chen, Z.; Jiang, H.; Li, M.; O'Keeffe, M.; Eddaoudi, M. Reticular Chemistry 3.2: Typical Minimal Edge-Transitive Derived and Related Nets for the Design and Synthesis of Metal-Organic Frameworks. *Chem. Rev.* **2020**, *120*, 8039–8065.

(207) O'Keeffe, M.; Peskov, M. A.; Ramsden, S. J.; Yaghi, O. M. The Reticular Chemistry Structure Resource (RCSR) Database of, and Symbols for, Crystal Nets. *Acc. Chem. Res.* **2008**, *41*, 1782–1789.

(208) Yuan, S.; Lu, W.; Chen, Y. P.; Zhang, Q.; Liu, T. F.; Feng, D.; Wang, X.; Qin, J.; Zhou, H. C. Sequential Linker Installation: Precise Placement of Functional Groups in Multivariate Metal-Organic Frameworks. *J. Am. Chem. Soc.* **2015**, *137*, 3177–3180.

(209) Perfecto-Irigaray, M.; Beobide, G.; Castillo, O.; Da Silva, I.; García-Lojo, D.; Luque, A.; Mendia, A.; Pérez-Yáñez, S. $[Zr_6O_4(OH)_4(\text{Benzene-1,4-Dicarboxylato})_6]_n$: A Hexagonal Polymorph of UiO-66. *Chem. Commun.* **2019**, *55*, 5954–5957.

(210) Feng, D.; Gu, Z. Y.; Li, J. R.; Jiang, H. L.; Wei, Z.; Zhou, H. C. Zirconium-Metalloporphyrin PCN-222: Mesoporous Metal–Organic Frameworks with Ultrahigh Stability as Biomimetic Catalysts. *Angew. Chem. Int. Ed.* **2012**, *51*, 10307–10310.

(211) Osterrieth, J. W. M.; Rampersad, J.; Madden, D.; Rampal, N.; Skoric, L.; Connolly, B.; Allendorf, M. D.; Stavila, V.; Snider, J. L.; Ameloot, R.; Marreiros, J.; Ania, C.; Azevedo, D.; Vilarrasa-Garcia, E.; Santos, B. F.; Bu, X. H.; Chang, Z.; Bunzen, H.; Champness, N. R.; Griffin, S. L.; Chen, B.; Lin, R. B.; Coasne, B.; Cohen, S.; Moreton, J. C.; Colón, Y. J.; Chen, L.; Clowes, R.; Coudert, F. X.; Cui, Y.; Hou, B.; D'Alessandro, D. M.; Doheny, P. W.; Dincă, M.; Sun, C.; Doonan, C.; Huxley, M. T.; Evans, J. D.; Falcaro, P.; Ricco, R.; Farha, O.; Idrees, K. B.; Islamoglu, T.; Feng, P.; Yang, H.; Forgan, R. S.; Bara, D.; Furukawa, S.; Sanchez, E.; Gascon, J.; Telalović, S.; Ghosh, S. K.; Mukherjee, S.; Hill, M. R.; Sadiq, M. M.; Horcajada, P.; Salcedo-Abraira, P.; Kaneko, K.; Kukobat, R.; Kenvin, J.; Keskin, S.; Kitagawa, S.; Otake, K. ichi; Lively, R. P.; DeWitt, S. J. A.; Llewellyn, P.; Lotsch, B. V.; Emmerling, S. T.; Pütz, A. M.; Martí-Gastaldo, C.; Padial, N. M.; García-Martínez, J.; Linares, N.; Maspoch, D.; Suárez del Pino, J. A.; Moghadam, P.; Oktavian, R.;

Morris, R. E.; Wheatley, P. S.; Navarro, J.; Petit, C.; Danaci, D.; Rosseinsky, M. J.; Katsoulidis, A. P.; Schröder, M.; Han, X.; Yang, S.; Serre, C.; Mouchaham, G.; Sholl, D. S.; Thyagarajan, R.; Siderius, D.; Snurr, R. Q.; Goncalves, R. B.; Telfer, S.; Lee, S. J.; Ting, V. P.; Rowlandson, J. L.; Uemura, T.; Iiyuka, T.; van der Veen, M. A.; Rega, D.; Van Speybroeck, V.; Rogge, S. M. J.; Lamaire, A.; Walton, K. S.; Bingel, L. W.; Wuttke, S.; Andreo, J.; Yaghi, O.; Zhang, B.; Yavuz, C. T.; Nguyen, T. S.; Zamora, F.; Montoro, C.; Zhou, H.; Kirchon, A.; Fairen-Jimenez, D. How Reproducible Are Surface Areas Calculated from the BET Equation? *Adv. Mat.* **2022**, *34*, 2201502.

(212) Férey, G.; Serre, C.; Mellot-Draznieks, C.; Millange, F.; Surblé, S.; Dutour, J.; Margiolaki, I. A Hybrid Solid with Giant Pores Prepared by a Combination of Targeted Chemistry, Simulation, and Powder Diffraction. *Angew. Chem. Int. Ed.* **2004**, *43*, 6296–6301.

(213) Férey, C.; Mellot-Draznieks, C.; Serre, C.; Millange, F.; Dutour, J.; Surblé, S.; Margiolaki, I. A Chromium Terephthalate-Based Solid with Unusually Large Pore Volumes and Surface Area. *Science* **2005**, *309*, 2040–2042.

(214) Bon, V.; Senkovskyy, V.; Senkovska, I.; Kaskel, S. Zr(IV) and Hf(IV) Based Metal–Organic Frameworks with reo-Topology. *Chem. Commun.* **2012**, *48*, 8407–8409.

(215) Farha, O. K.; Wilmer, C. E.; Eryazici, I.; Hauser, B. G.; Parilla, P. A.; ONeill, K.; Sarjeant, A. A.; Nguyen, S. T.; Snurr, R. Q.; Hupp, J. T. Designing Higher Surface Area Metal-Organic Frameworks: Are Triple Bonds Better than Phenyls? *J. Am. Chem. Soc.* **2012**, *134*, 9860–9863.

(216) Zhao, D.; Yuan, D.; Sun, D.; Zhou, H. C. Stabilization of Metal-Organic Frameworks with High Surface Areas by the Incorporation of Mesocavities with Microwindows. *J. Am. Chem. Soc.* **2009**, *131*, 9186–9188.

(217) Katz, M. J.; Mondloch, J. E.; Totten, R. K.; Park, J. K.; Nguyen, S. T.; Farha, O. K.; Hupp, J. T.; Katz, M. J.; Mondloch, J. E.; Totten, R. K.; Park, J. K.; Nguyen,

S. T.; Farha, O. K.; Hupp, J. T. Simple and Compelling Biomimetic Metal–Organic Framework Catalyst for the Degradation of Nerve Agent Simulants. *Angew. Chem. Int. Ed.* **2014**, *53*, 497–501.

(218) López-Maya, E.; Montoro, C.; Rodríguez-Albelo, L. M.; Aznar Cervantes, S. D.; Lozano-Pérez, A. A.; Cenís, J. L.; Barea, E.; Navarro, J. A. R. Textile/Metal–Organic-Framework Composites as Self-Detoxifying Filters for Chemical-Warfare Agents. *Angew. Chem. Int. Ed.* **2015**, *54*, 6790–6794.

(219) Mondloch, J. E.; Katz, M. J.; Isley, W. C.; Ghosh, P.; Liao, P.; Bury, W.; Wagner, G. W.; Hall, M. G.; Decoste, J. B.; Peterson, G. W.; Snurr, R. Q.; Cramer, C. J.; Hupp, J. T.; Farha, O. K. Destruction of Chemical Warfare Agents Using Metal–Organic Frameworks. *Nat. Mater.* **2015**, *14*, 512–516.

(220) Islamoglu, T.; Chen, Z.; Wasson, M. C.; Buru, C. T.; Kirlikovali, K. O.; Afrin, U.; Mian, M. R.; Farha, O. K. Metal-Organic Frameworks against Toxic Chemicals. *Chem. Rev.* **2020**, *120*, 8130–8160.

(221) González, L.; Gil-San-Millán, R.; Navarro, J. A. R.; Maldonado, C. R.; Barea, E.; Carmona, F. J. Green Synthesis of Zirconium MOF-808 for Simultaneous Phosphate Recovery and Organophosphorus Pesticide Detoxification in Wastewater. *J. Mater. Chem. A* **2022**, *10*, 19606–19611.

(222) Gil-San-Millan, R.; López-Maya, E.; Platero-Prats, A. E.; Torres-Pérez, V.; Delgado, P.; Augustyniak, A. W.; Kim, M. K.; Lee, H. W.; Ryu, S. G.; Navarro, J. A. R. Magnesium Exchanged Zirconium Metal-Organic Frameworks with Improved Detoxification Properties of Nerve Agents. *J. Am. Chem. Soc.* **2019**, *141*, 11801–11805.

(223) Johnson, J. A.; Lin, Q.; Wu, L. C.; Obaidi, N.; Olson, Z. L.; Reeson, T. C.; Chen, Y. S.; Zhang, J. A "Pillar-Free", Highly Porous Metalloporphyrinic Framework Exhibiting Eclipsed Porphyrin Arrays. *Chem. Commun.* **2013**, *49*, 2828–2830.

(224) Xu, X.; Li, S.; Liu, Q.; Liu, Z.; Yan, W.; Zhao, L.; Zhang, W.; Zhang, L.; Deng, F.; Cong, H.; Deng, H. Isolated π-Interaction Sites in Mesoporous MOF Backbone for Repetitive and Reversible Dynamics in Water. *ACS Appl. Mater. Interfaces* **2019**, *11*, 973–981.

(225) Juanhuix, J.; Gil-Ortiz, F.; Cuní, G.; Colldelram, C.; Nicolás, J.; Lidón, J.; Boter, E.; Ruget, C.; Ferrer, S.; Benach, J. Developments in Optics and Performance at BL13-XALOC, the Macromolecular Crystallography Beamline at the Alba Synchrotron. *J. Synchrotron Radiat.* **2014**, *21*, 679–689.

(226) Kabsch, W. Integration, Scaling, Space-Group Assignment and Post-Refinement. *Acta Cryst. D* **2010**, *66*, 133–144.

(227) Sheldrick, G. M.; IUCr. Crystal Structure Refinement with SHELXL. *Acta Cryst. C* **2015**, *71*, 3–8.

(228) Sheldrick, G. M.; IUCr. SHELXT – Integrated Space-Group and Crystal-Structure Determination. *Acta Cryst. A* **2015**, *71*, 3–8.

(229) Dolomanov, O. V.; Bourhis, L. J.; Gildea, R. J.; Howard, J. A. K.; Puschmann, H. OLEX2: A Complete Structure Solution, Refinement and Analysis Program. *J. Appl. Cryst.* **2009**, *42*, 339–341.

Chapter 4

Net-clipping: Theoretical de-reticulation of nets

This Chapter is based on the following publications:

- Ortín-Rubio, B.; Ghasempour, H.; Guillerm, V.; Morsali, A.; Juanhuix, J.; Imaz, I.; Maspoch, D. Net-Clipping: An Approach to Deduce the Topology of Metal-Organic Frameworks Built with Zigzag Ligands *J. Am. Chem. Soc.* **2020**, *142*, 9135-9140.

- Ortín-Rubio, B.; Rostoll-Berenguer, J.; Vila, C.; Proserpio, D. M.; Guillerm, V.; Juanhuix, J.; Imaz, I.; Maspoch, D. Net-Clipping as a Top-Down Approach for the Prediction of Topologies of MOFs Built from Reduced-Symmetry Linkers *Chem. Sci.* **2023**, *14*, 12984-12994.

4.1. Introduction

4.1.1. Limits of the "bottom-up" approaches

As illustrated in Chapter 3, the principles of reticular chemistry cannot cover certain limits of prediction in the assembly of MOFs related to the polymorphism in nets that require the same building units. This is the case for the most symmetric MBBs. In addition, for the ones that the symmetry is reduced, there is not any design approach that explains when deviating from the default net or observing a mismatch between the geometry of the theoretical node and the MBB used. The main reason lies in that most of the design strategies are based on bottom-up approaches that seek to obtain certain nets by analyzing the most basic geometric information (geometry, connectivity and directionality) of their components.[1–4] Thus, over the past two decades, this simplification of each MBB has allowed the rational classification of MOFs and COFs into underlying nets with various topologies. And probably more importantly, it has allowed the prediction of their structural features, offering various design opportunities for distinct programmed pores and channels.[4–7]

Complementary, the growing interest in the field has pushed researchers to devise more approaches for the rational design of materials with ever-greater complexity. Examples of these approaches include supermolecular building blocks (SBBs),[8,9] chains (SBCs)[10] and layers (SBLs),[11–13] which relate nets with polyhedral (MOPs), chains (1D MOFs) ad layers (2D MOFs), respectively; or the merged-nets approach, which relates different nets of compatible symmetry for the rational design of mixed-linker MOFs.[14] Indeed, over the past few years, structural complexity has been introduced by the desymmetrization of simple organic linkers with the eight fundamental operations (Section 3.1.3.1), by changing the direction of the binding carboxylic groups through geometric design, as in 2-c less-symmetric bent,[15] twisted[16] or zigzag fashion,[17] or through combinations thereof, yielding structures that differ from the default or expected nets.

However, current methods for structural prediction in reticular chemistry are insufficient for desymmetrized MBBs. Indeed, there are no currently general approaches for non-standard parameters such as angles, torsions, width, etc.[18–21] As we previously observed (Section 3.2.1), even though one can use robust, well-defined clusters as SBUs, their combination with organic linkers with reduced symmetry can prohibit, deviate, or direct to different nets due to the defaults of connectivity that can show the cluster or to the evolution to a different SBU. The use of bottom-up strategies cannot consider the effect of desymmetrized MBBs in the cluster or in a net, as this effect is observed when comparing the assembly of crystal structures with similar metrics. In addition, the various possibilities of the orientation of linkers around an inorganic MBB can lead to a high number of theoretical possibilities for polymorphism and therefore, a low structural predictability.[22,23] For example, considering an 8-c cubic MBB surrounded by non-linear ligands with a zigzag shape, the transversal effect can lead to two different possible orientations in the spatial distribution, obtaining 14 possible stereoisomers (Figure 4.1).

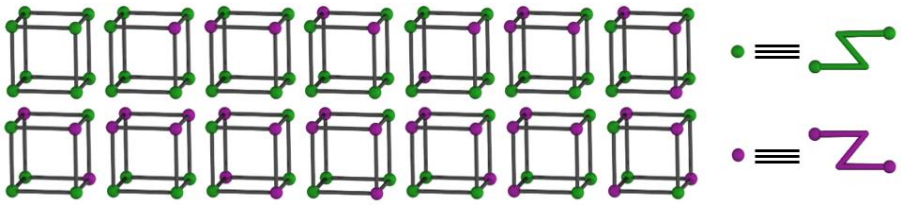


Figure 4.1. Schematic representation of 14 directional stereoisomers of a cubic MBB depending on the orientation of a zigzag linker.

4.1.2. A top-down approach for the prediction of topologies in the assembly of less-symmetric MBBs

The aforementioned drawbacks inspired us to develop a new design approach that, unlike the rational, bottom-up construction of edge-transitive nets, is based on the

top-down de-reticulation of edge-transitive nets. As high symmetry would likely be mostly favored, we reasoned that less-symmetric MBBs could be derived from more-symmetric MBBs of higher connectivity by simply reducing the connectivity of the latter. Considering the difficulty on controlling the connectivity and formation of pre-synthesized clusters, we have focused our approach on the organic MBBs. For example, a zigzag ligand can be formed by removing the two diagonally connecting groups of the two 3-c nodes derived from a rectangular 4-c MBB (Figure 4.2a). Accordingly, we reasoned that MOF structures made of less-symmetric ligands could be anticipated *via* rational clipping of the connecting groups of more symmetric MBBs in edge-transitive nets. This new strategy, which we have called *net-clipping*, is the first top-down structural approach that rationalizes and anticipates MOFs that could be built up with linkers that are less-symmetric than

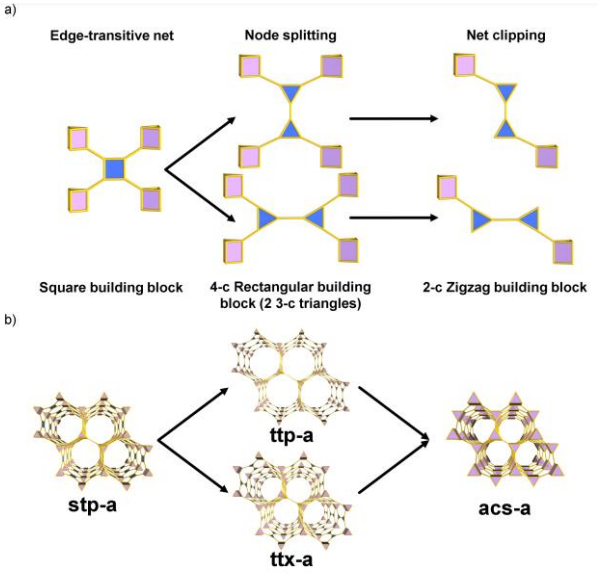


Figure 4.2. a) Schematic of the deconstruction of a 4-c square/rectangular MBB in a zigzag building block by splitting the node into two 3-c triangles in different axes (node splitting), and then removing two diagonally connections (net-clipping). b) Schematic showing an example of our approach (node splitting + net clipping) applied to an edge-transitive net built from 4-c and 6-c triangular prism MBBs.

the original MBBs. Theoretically, its fundamentals are reversed from the obtained merged nets, and permits the prediction of MOF structures that break the basic principles of reticulation, thereby elucidating mismatch topologies and their construction. In this way, we provide further insights to our recent works on transversal reticular chemistry[17] and geometry mismatch,[19] for facilitating the rational design of MOFs built up from less-symmetric MBBs.

Herein, we propose to use the net-clipping strategy to deconstruct MOFs assembled from higher-connected MBBs to deduce the topology of the underlying nets of the MOFs based on less-connected and symmetric MBBs. Accordingly, we applied our method to MOFs based on nets assembled from 4-c square, 4-c tetrahedral, 6-c hexagonal, 8-c cubic and 12-c hexagonal prismatic organic MBBs. Through our analysis, we generated 141 derived and 56 clipped nets, of which 33 derived nets (named *icn*7–*icn*39) and 6 clipped nets (named *icn*1–*icn*6) have never, to the best of our knowledge, previously been reported. Moreover, we reinforced our strategy by literature examples and our experimental findings, synthesizing six novel MOFs constructed with less-symmetric linkers, which match with the topologies predicted by net-clipping.

4.2. Results and discussion

4.2.1. Theoretical deduction: design strategy for net-clipping

4.2.1.1. Identification of the target MBBs

We propose the use of net-clipping to rationalize/anticipate the MOFs that could be built from less-symmetric ligands. To this end, among the most extensively used organic MBBs to reticulate materials, we first selected those in which our clipping process could be applied. We restricted our approach to nodes that may be clipped symmetrically, reducing the connectivity by half into the new node with respect to the original one. Precisely, the clipping should be performed in a manner that the

original node/MBB could be rebuilt upon applying a C_2 operation. Considering the most representative organic MBBs with their geometry matching with nodes from edge-transitive nets, we found that linkers with square, tetrahedral, hexagonal, cubic, or hexagonal prismatic shapes matched this condition (Figure 4.3).

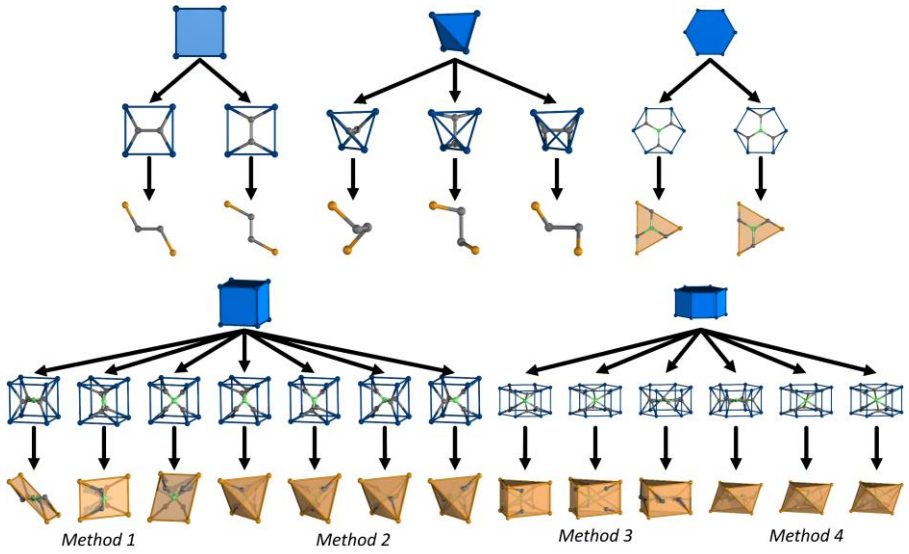


Figure 4.3. Schematic of the deconstruction of (from left to right): a 4-c square MBB into a zigzag MBB; a 4-c tetrahedral MBB into a turned-twisted MBB; a 6-c hexagonal MBB into a 3-c twisted triangular MBB; an 8-c cubic MBB into a 4-c square-like or a 4-c tetrahedral MBB; and a 12-c hexagonal prismatic MBB into a 6-c octahedral or a 6-c trigonal prismatic MBB. This approach comprises two steps: firstly, the splitting of each node into a set of less-symmetric nodes and edges; and secondly, the symmetric clipping of half of the original node's connectivity.

This process is based on two steps: the desymmetrization of the MBB into different directions substituting the original node by a set of less-symmetric nodes and edges; and the subsequently symmetrical clipping of half of the connecting groups maintaining the previous requirement, transforming the new 3-c node into a new edge, and therefore, resulting in less-symmetric MBBs. From these operations, the most basic 4-c square/rectangular MBBs can be clipped into zigzag MBBs; the 4-c tetrahedral MBBs can be clipped into a new 2-c turned-twisted shape MBBs; the 6-c hexagonal MBBs can be clipped into 3-c twisted triangular MBBs; the 8-c cubic

MBBs can be clipped into less-symmetric 4-c square-like or tetrahedral MBBs; and the 12-c hexagonal prismatic MBBs can be clipped into less-symmetric 6-c triangular prismatic or octahedral MBBs. Note that highly connected nodes with cubic or hexagonal prismatic directionality can be clipped into two different modes (as we denote Methods 1 and 2 for the two clipping modes in the cubic MBBs to form square or tetrahedral MBBs, respectively; and Methods 3 and 4 for the clipping modes in the hexagonal prismatic MBBs to form triangular prismatic or octahedral MBBs, respectively).

In contrast, nodes with octahedral, trigonal prismatic, cuboctahedra, or icosahedral directionality cannot be clipped this way, given the absence of a C_2-symmetry axis. Interestingly, we found that these latter nodes present two triangular faces in the same direction, which frustrate the node-clipping and the absence of the C_2 operation (Figure 4.4).

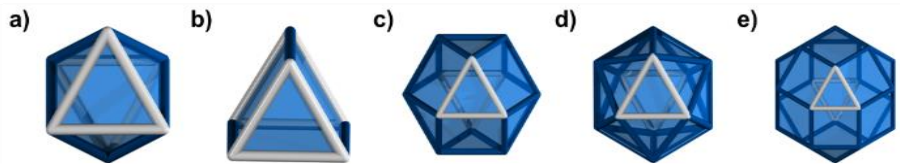


Figure 4.4. Schematic of the different MBBs that frustrate net-clipping in a symmetrical fashion due to the presence of two triangular faces in the same direction highlighted in a) octahedron, b) triangular prism, c) cuboctahedron, d) icosahedron and e) rhombicuboctahedron.

4.2.1.2. Generation of clipped nets from less-symmetric derived nets

Once selected the target MBBs, we analyzed the 54 edge-transitive nets (with D-symbol size ≤ 32, and excluding those with collisions)[24] and selected those comprising nodes matching the vertex figures of 4-c squares, 4-c tetrahedra, 6-c hexagons, 8-c cubes or 12-c hexagonal prisms.[25] We then derived these nets by splitting their nodes to reduce the symmetry of the MBB in all the possible directions (Figure 4.3).[26] This work generated 141 derived nets, discovering 33 of

them for the first time, proving this approach as a facile tool to study and understand the derived nets (Table 4.1).[27] Note that, as the nodes can be splitted in different directions according to its dimensionality (i.e. two directions in the square, three directions in the tetrahedron), multiple derived nets can be generated from the same parent net. Then, we originated the less-symmetric MBBs in the derived nets by clipping half of their connecting groups, forming 56 possible clipped nets. Among them, six nets were reported as new, unravelling new opportunities for the discovery of MOFs and unprecedented assemblies (Table 4.1 and Figure 4.5). These 39 new nets, which we named as *icn*x (*icn* stands for Institut Català de Nanociència i Nanotecnologia), were deposited in the personal.ttd database included in the TopCryst system,[28] with the connectivity according to the latest Topocif dictionary.[29] All the 141 derived and 56 clipped nets are summarized in Tables 4.2-4.6 and will be further discussed for each case according to the MBB clipped.

During the net-clipping step, we identified different scenarios according to the circuits of connections for each net: some of the nets were clipped into new nets with the same periodicity/dimensionality; some of the nets were clipped reducing

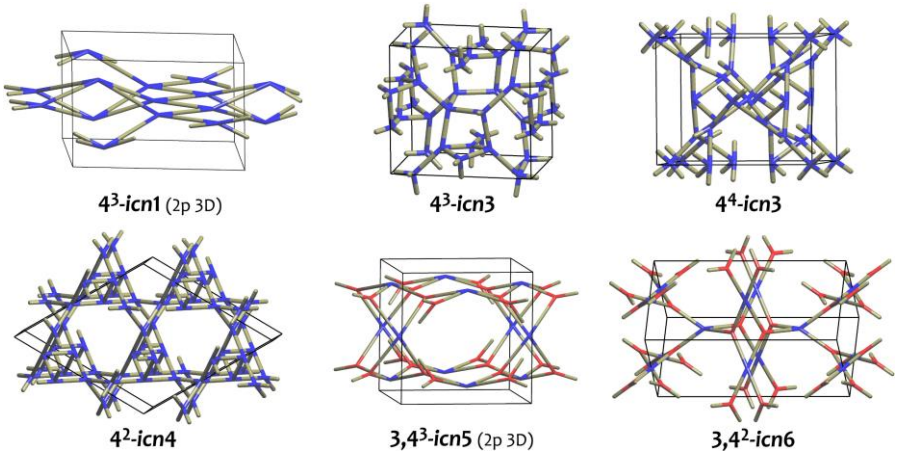


Figure 4.5. Representation of the 6 new clipped nets accessible for MOFs constructed with turned-twisted MBBs (*icn*1, *icn*2, *icn*3, *and icn*4), 3-c twisted triangular MBBs (*icn*5) and 4-c square-like MBBs (*icn*6). For clarity, here and in the tables, we report the coordination of the independent nodes before the *icn* symbol. The two nets *icn*1 and *icn*5 are 2-periodic 3D (thick layers).

Table 4.1. Space Group (S.G.), Connectivity (C.), Point Symbol, Transitivity (Trans.), Tiling and D-symbol size (D) for the new derived and clipped *icn*x nets.

Name	S.G.	C.	Point Symbol	Trans.	Tiling	D
*icn*1	*Pmmm*	4^3	$\{4^2.6^2.8^2\}\{4^4.6^2\}_5$	[34]	2-periodic 3D	-
*icn*2	*C222$_1$*	4^3	$\{4.5^2.6.7.8\}$ $\{4.5^3.7.8\}\{5.6.8^4\}$	[3884]	$[4.5^2]+[8^3]+[5^2.6.8^3]$	156
*icn*3	*C222$_1$*	4^4	$\{3.4.5.6.7^2\}_2\{3.6.7^2.8^2\}_2$ $\{3^2.4.5^2.6\}\{4.6^2.7.8^2\}$	[4651]	$[3^4.4^2.6^2.7^4.10^2]$	80
*icn*4	*R32*	4^2	$\{4.6^3.8^2\}\{4^3.6^2.8\}$	[2352]	$[4^3.12^2]+[6^3.12^2]$	52
*icn*5	*Pmmm*	3, 4^3	$\{4.8^2\}_4\{4^2.8^4\}_2\{8^6\}$	[43]	2-periodic 3D	-
*icn*6	*P4$_2$/mcm*	3, 4^2	$\{4.8^2\}_4\{4^2.8^2.10^2\}_2\{8^6\}$	[3243]	$[4^2.8^2]+[4^2.8^2.12^2]+[8^4.12^2]$	32
*icn*7	*I2$_1$3*	3^3	$\{10^3\}$	[3334]	$5[10^3]+3[10.12^2]+2[12^3]$	108
*icn*8	*P6$_2$22*	3,4	$\{6^2.10^2.11^2\}\{6^2.10\}_2$	[2232]	$[6.11^2]+[10.11^2]$	60
*icn*9/**lcr**	*I43d*	3,4	$\{8^3\}_2\{8^6\}$	[2221]	$[8^3.9^2]$	28
*icn*10	*R3c*	3^2,4	$\{7^2.8\}\{7^3\}\{7^5.9\}$	[3531]	$[7^{12}.9^2]$	68
*icn*11	*P6$_4$22*	3,4	$\{9^2.10\}_2\{9^4.10^2\}$	[2221]	$[9^4.10^2]$	28
*icn*12	*I4$_1$32*	3^2,4	$\{6^2.10\}_2\{6^2.9^2.10^2\}$	[3344]	$3[6^2.10^2]+2[9^2.10^3]$	64
*icn*13	*Pn$\bar{3}$*	3,6	$\{5^3\}_3\{5^6.8^6.10^3\}$	[2222]	$[9^4]+2[5^6.9^2]$	22
*icn*14	*P4$_2$/nnm*	3^2,6	$\{4.6^2\}_2\{4^2.6^4.8^6.10^3\}\{6^2.8\}$	[3443]	$2[4^2.8^2]+4[6^2.8^2]+[8^4]$	48
*icn*15	*P4$_2$/nnm*	3^2,6	$\{5.6^2\}_2\{5^2.6\}\{5^4.6^4.8^4.10^2.11\}$	[3432]	$[8^4]+2[5^4.6^2.8^2]$	32
*icn*16	*Ia$\bar{3}$*	3,6^2	$\{5^3\}_6\{5^6.8^6.10^3\}\{5^6.8^6.11^3\}$	[3332]	$[10^3]+3[5^2.10^2]$	80
*icn*17	*Ia3$\bar{d}$*	3,6	$\{4.9^2\}_3\{4^6.9^6.11^3\}$	[2223]	$2[4^3]+6[4.9^2]+3[9^4]$	44
*icn*18	*I4$_1$32*	3^2,6	$\{6^2.7\}_3\{6^6.7^3.8^6\}$	[3445]	$2[6^3]+3[6.7^2]$ $+3[6.8^2]+3[7^2.8^2]$	84
*icn*19	*I4$_1$32*	3^2,6	$\{4.8^2\}_3\{4^3.6^3.8^3.9^3.10^3\}_2$ $\{6^2.8\}_3$	[3445]	$[4^3]+[6^3]+3[4.9^2]$ $+3[6.8^2]+3[8^2.9^2]$	88
*icn*20	*Ia$\bar{3}$*	3,6	$\{6^2.8\}_3\{6^3.8^{12}\}$	[2322]	$[8^6]+[6^6.8^6]$	44
*icn*21	*I4$_1$32*	3,6^2	$\{6^2.7\}_6\{6^3.7^3.8^3.9^6\}$ $\{6^3.7^9.8^3\}$	[33]	self-catenated Hopf link 8-ring	-
*icn*22	*I2$_1$3*	3^3,6^2	$\{5.7^2\}_3\{5^2.7\}_3\{5^3.7^3.8^3.9^6\}$ $\{5^3.7^6.8^3.9^3\}$	[5653]	$[8^3]+3[5.7.8^2]$ $+[5^3.7^3.8^3]$	112
*icn*23	*I422*	3,8	$\{5^3\}_4\{5^8.6^4.7^4.8^{12}\}$	[2221]	$[5^8.6^4]$	16
*icn*24	*Pm3$\bar{n}$*	3,12	$\{4.6^2\}_6\{4^6.6^{24}.8^{30}.10^6\}$	[2222]	$4[6^3]+3[4^2.6^4]$	14
*icn*25	*P4$_2$32*	3,12	$\{4.6^2\}_6\{4^{12}.6^{18}.8^{30}.10^6\}$	[2233]	$2[4^3]+2[6^3]+3[4^2.6^4]$	26
*icn*26	*Im3$\bar{m}$*	3,24	$\{4.6^2\}_{12}\{4^{36}.6^{84}.8^{144}.10^{12}\}$	[2223]	$12[4.6^2]+3[4^4]+4[6^6]$	16
*icn*27	*F4$_1$32*	3^2,12	$\{4.6^2\}_6\{4^{12}.6^{30}.8^{24}\}\{6^3\}_2$	[3223]	$2[4^3]+6[4.6^2]+[6^{12}]$	16
*icn*28	*P432*	3^2,4	$\{8^2.12\}_{12}\{8^3\}_8\{8^4.12^2\}_3$	[32]	self-catenated Multiple link 12-ring	-
*icn*29	*P6$_2$22*	3^2,4^2	$\{6.8^2\}_2\{6.8^4.10\}\{$ $6^2.8^2.10^2\}_2\{6^2.8\}_2$	[44]	self-catenated Hopf link 6-ring	-
*icn*30	*P6/mmm*	3, 4^2	$\{4.8^2\}_4\{4^2.6^4\}_2\{8^4.12^2\}$	[3255]	$3[4^2.8^2]+2[4^3.6^2]$ $+2[6^2.8^3]+2[8^6.24^2]$	32
*icn*31	*P6/mmm*	3, 4^2	$\{4.8^2\}_4\{4^2.8^2.10^2\}_2$ $\{8^4.12^2\}$	[3255]	$3[4^2.8^2]+4[8^3.12^2]$ $+[4^6.12^2]+[8^6.12^2]$	32
*icn*32	*P62m*	3^2,4^2	$\{4.6^2.8^3\}_2\{4.6^2\}_2$ $\{6.8^2\}_2\{6.8^5\}$	[4465]	$3[4.8^3]+2[6^3.12^2]+2[8^3.12^2]$ $+[4^3.8^3.18^2]+[6^6.18^2]$	68
*icn*33	*P6/m*	3^2,4^2	$\{4.6^2.8^3\}_2\{4.6^2\}_2$ $\{6.8^2\}_2\{6.8^5\}$	[44]	self-catenated Hopf link 8-ring	-

Table 4.1. ***(continued)***

Name	S.G.	C.	Point Symbol	Trans.	Tiling	D
*icn*34	*I422*	3, 4^2	$\{8^3\}_4\{8^4.10^2\}\{8^6\}_2$	[32]	self-catenated Hopf link 8-ring	-
*icn*35	*P4/nnc*	3, 4^2	$\{8^2.10\}_4\{8^4.10^2\}\{8^6\}_2$	[32]	self-catenated Hopf link 10-ring	-
*icn*36	*I4/mmm*	$3^2,4^2,6$	$\{4.8^2\}_{12}\{4^6.8^6.10^3\}_4$ $\{8^4.12^2\}\{8^6\}_2$	[5455]	$4[4^3]+8[8^3]+4[4^2.8^2]$ $+2[8^4]+[4^4.8^8]$	60
*icn*37	*Pn3̄n*	3,4,6	$\{6^2.8^4\}_3\{6^3\}_{12}\{6^6.8^6.10^3\}_4$	[32]	self-catenated Hopf link 6-ring	-
*icn*38	*I432*	3,4,6	$\{4.8^2\}_{12}\{4^3.8^9.10^3\}_4\{8^6\}_3$	[3233]	$12[4.8^2]+12[8^3]+[8^{12}]$	52
*icn*39	*P422*	3,4,8	$\{6^2.8^4\}\{6^3\}_4\{6^8.8^{20}\}$	[32]	self-catenated Hopf link 6-ring	-

their dimensionality (from a 3D net to a 2D layer or 1D chain, or a 2D layer into a 1D chain); and some of the nets could not be clipped into any net (Figure 4.6). *A priori* analysis of the nets revealed that the nets with odd cycles or with the presence of 6-cycles that comprises just 3-c nodes (derived from three clippable nodes) frustrates net-clipping.[30]

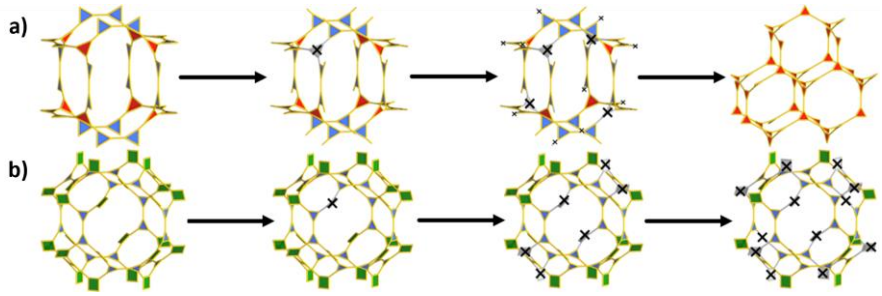


Figure 4.6. Schematic representation of the net-clipping approach, removing half of the nodes and their connections diagonally in the a) **ptd** net to result in a **srs** net; and b) in the **rhr** net that cannot result in any net.

4.2.2. Experimental validation: Synthesis of MOFs based on less-symmetric linkers

4.2.2.1. Net-clipping of 4-c squares

As a first proof-of-concept, we used net-clipping for the de-reticulation of edge-transitive nets assembled from 4-c square-like MBBs to deduce the topology of MOFs based on less-symmetric zigzag ligands. We began by selecting the 17 edge-transitive nets assembled from 4-c square-like MBBs combined with other polygonal and polyhedral MBBs. Three of these nets are uninodal (**nbo**, **rhr** and **lvt**), which were considered in their binary form (**net-b**) to allow the selective splitting of one of their nodes. Then, we derived these nets by splitting the 4-c nodes into two 3-c nodes (Figure 4.2a and 4.3), reducing the symmetry of the square node to a rectangular-like MBB. Note that, when embedded in a net, this split can be performed in two distinct orientations (Figure 4.2b). Notably, this process led to 39 derived nets (Table 4.2). As mentioned above, the use of a bipartite graph and reducing the symmetry of some of other edge-transitive nets (**nbo-b**, **ssb**, **pts**, **scu** and **ftw**) leads to two symmetrically different 4-c rectangular nodes, and therefore, more than two derived nets can be formed as these two nodes can be splitted distinctly. Applying net-clipping to the derived nets by erasing the two diagonally connecting groups originated a new edge that, when transposed into a MOF, generated a zigzag-like MBB. This step led to 10 resultant clipped nets (Table 4.2). According to our results, most of the 3D nets (**pto**, **ssb**, **pts**, **pth**, **she**, **soc**, **stp**, **scu**, and **ftw**) are clipped into other 3D nets (**srs**, **lvt**, **dia**, **qtz**, **hxg**, **crs**, **acs**, **bcu**, and **fcu**, respectively); some 3D nets (**nbo-b**, **lvt-b**, and **ssb**) are clipped into the 2D **sql** net; and the rest of the nets (**tbo**, **rhr-b**, **ssa**, **sqc**, **csq**, and **shp**) cannot be clipped into any other net. Interestingly, we found that all these edge-transitive nets present the aforementioned 6-cycle comprising three 3-c nodes (derived from three 4-c nodes) and three other MBBs, which frustrate the net-clipping in a fully zigzag fashion (Figure 4.7).

Table 4.2. Net-clipping of all the derived nets from 4-c square nodes in the 17 selected edge-transitive nets.

MBB	Main Topology	Derived Net	Clipped Net
	tbo	tbd xaa	-
	pto	ptd	srs
	nbo	fof fog tfb	sql
	rhr	ucp sqc12288[a]	-
	lvt	lil lim	sql
	ssa	sty bbp/Initial structure; Bond sets:1,3:bbp[b]	-
	ssb	stu stw	sql
		stj stx	lvt
	pts	dmd dmg dmh tfi	dia
	pth	hst 3,4T45[c]	qtz
	she	sqc12215[a]	hxg
	soc	cdj edq	crs
	stp	ttp ttx	acs
	scu	tty cut 3,3,8T132[c]	bcu
	sqc	sqc3520[a] sqc3782[a]	-
	csq	xly xlz	-
	ftw	kle kxe ttv	fcu
	shp	ced cec	-

For the derived nets, letters indicate the following: [a]Systre nets in the Epinet database; [b]ToposPro binodal nets;[31] [c]ToposPro symbol for 3-periodic nets.

Net-clipping: Theoretical de-reticulation of nets

Once we had theoretically predicted the underlying nets of MOF structures that could be formed using zigzag ligands, we experimentally validated our strategy with a combination of reported and novel reticular frameworks. To this end, we chose four MOFs assembled from: combining a 4-c square-like MBB or an 8-c cubic MBB with the same 4-c rectangular linker; and combining a 4-c tetrahedral MBB or a 12-c cuboctahedral MBB assembled with the same 4-c rectangular linker. Then, the combination of the zigzag linker analogs (derived from the 4-c MBBs) with the same inorganic clusters resulted in four MOFs whose topologies were predicted by net-clipping. Note that two of these four MOFs were reported in literature, whereas the other two MOFs were synthesized to further support our approach.

We started with PCN-10, a MOF with the underlying **nbo/fof** net, constructed

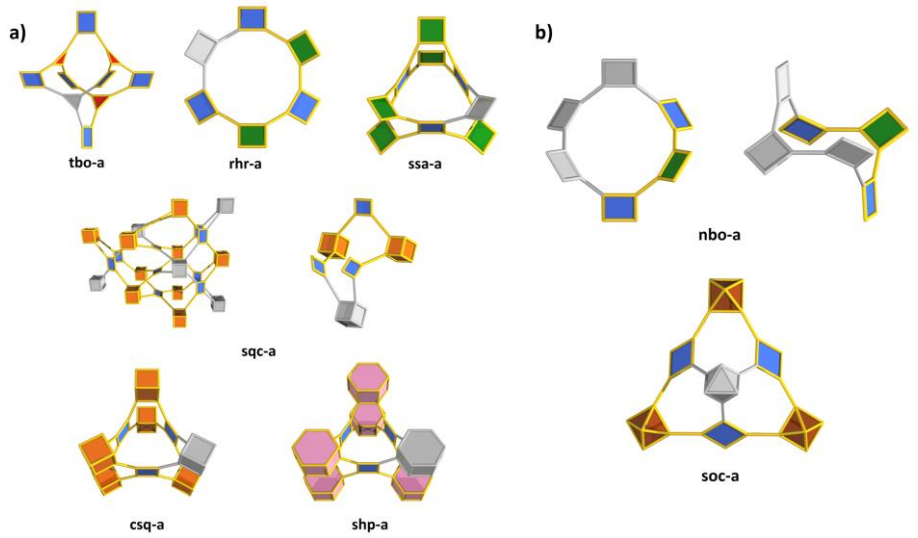


Figure 4.7. a) Fragments of **tbo-a**, **rhr-a**, **sqc-a**, **csq-a** and **shp-a** topologies, where it can be appreciated the 6-cycles that frustrate net clipping in a fully zigzag fashion. b) Fragments of **nbo-a** and **soc-a** topologies, where it can be appreciated a 6-cycle (that is a ring) that does not frustrate net clipping. In **nbo-a**, because of the angle between the 4-c nodes (90 º), the removal of two of these nodes of the 6-cycle enables to clip the structure keeping a 2- or 3-periodic net. In **soc-a**, because of the diagonally connection of the 6-c nodes through the 4-c nodes and an additional node in the middle of the cycle, the removal of two of these nodes diagonally enable to clip the structure keeping a 2- or 3-periodic net.

with the well-known 4-c square-like Cu(II) paddlewheel MBB connected through 4-c 3,3',5,5'-azobenzene-tetracarboxylate (3,3',5,5'-ABTC) linkers.[31] According to net-clipping, the related clipped-MOF should be based on the underlying **sql** net (Table 4.2). Remarkably, replacing the rectangular 3,3',5,5'-ABTC by the related zigzag 3,3'-azobenzene-dicarboxylate (3,3'-ABDC) ligand afforded the expected 2D **sql**-MOF (Figure 4.8a, top). Green needle-shaped crystals of Cu-**sql**-3,3'-ABDC were afforded by mixing copper(II) nitrate salt and $H_2$3,3'-ABDC in DMF under solvothermal conditions. SCXRD revealed the formation of an ABCD packing of a 2D network that crystallizes in the *C2/m* space group. The *in-situ* formed Cu(II) paddlewheel were reticulated by four zigzag 3,3'-ABDC linkers, adopting the 4-c **sql** underlying topology(Figure 4.8a, top). In addition, PXRD analysis of the bulk material confirmed the phase purity by comparing it with the simulated from the SCXRD (Figure 4.9a). Interestingly, an isoreticular structure based on Zn(II) paddlewheels further corroborated our net-clipping approach.[32]

Curiously, the same 4-c rectangular 3,3',5,5'-ABTC linker was used combined with a higher-connected MBB, the 8-c cubic $Zr_6O_4(OH)_4(OOC\text{-}R)_8(H2O)_4(OH)_4$ hexanuclear cluster.[21] This MOF exhibited a **scu** net, in which we reasoned that replacing 3,3',5,5'-ABTC by 3,3'-ABDC would generate a clipped **bcu**-MOF (Table 4.2). Interestingly, our group reported that combination of this 8-c inorganic MBB with a series of zigzag linkers, including 3,3'-ABDC, leads to formation of MOFs with the underlying **bcu** net (Figure 4.8a, bottom), which further supports our prediction.[17]

Next, we shifted to another 4-c rectangular ligand, 3,3',5,5'-biphenyl-tetracarboxylate (3,3',5,5'-BPTC), that upon assembly with the 4-c tetrahedral In(III)-based MBB yielded NOTT-204, a **pts/tfi**-MOF.[33] Precisely, the same inorganic MBB was used for the construction of InOF-4, a **dia**-MOF made by the extension of 3,3'-biphenyl-dicarboxylate (3,3'-BPDC) ligands.[34] Interestingly, both of these MOFs are related by net-clipping, which induced formation of a **dia** net from a **pts** net (Table 4.2 and Figure 4.8b, top).

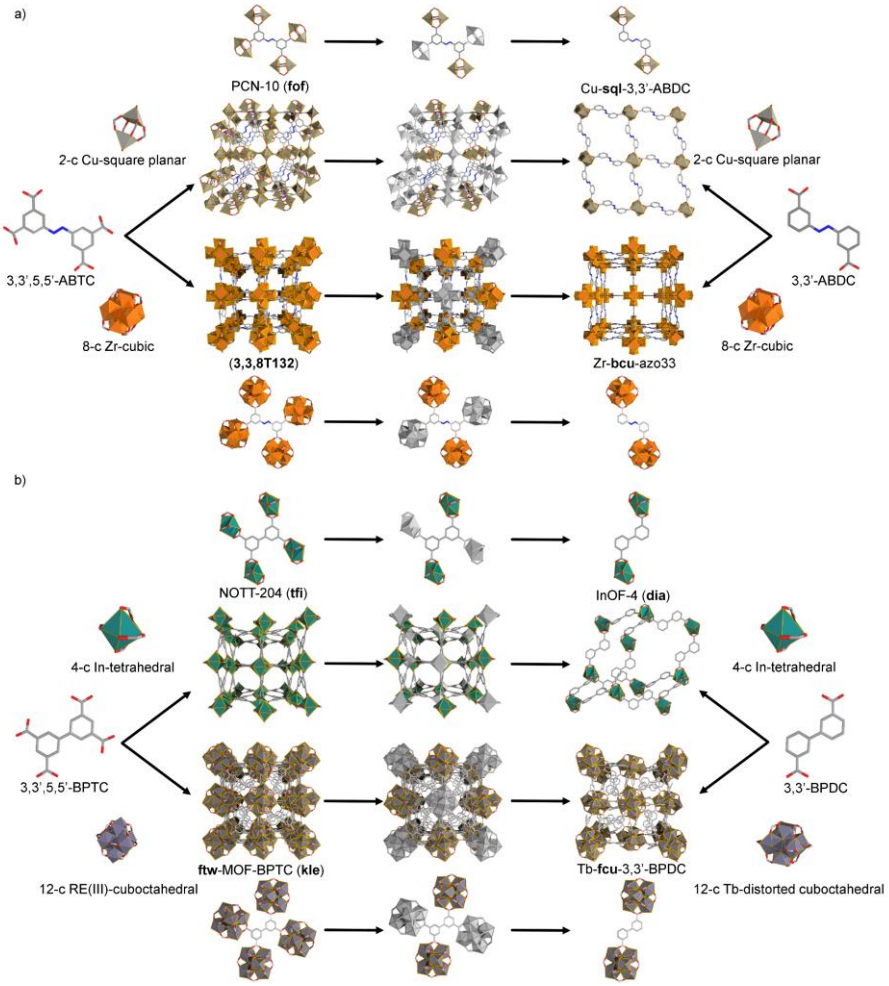


Figure 4.8. Schematic of the net-clipping approach applied to formation of MOFs from a) 3,3',5,5'-ABTC ligand to zigzag 3,3'-ABDC combined with (top) 4-c paddle-wheel Cu(II) MBBs and (bottom) 8-c cubic Zr(IV)-based MBBs; and from b) 3,3',5,5'-BPTC to 3,3'-BPDC ligand combined with (top) 4-c tetrahedral In(III)-based MBBs and (bottom) 12-c cuboctahedral Tb(III)-based MBBs.

Once again, Eddaoudi *et al.* reported that combining 4-c linkers (i.e. 3,3',5,5'-ABTC or 3,3',5,5'-BPTC) with the 12-c cuboctahedral RE-MBBs affords nets with the underlying **ftw/kle** topology.[35] From this topology, net-clipping predicts the formation of a MOF with the underlying **fcu** net. To investigate this, we used the

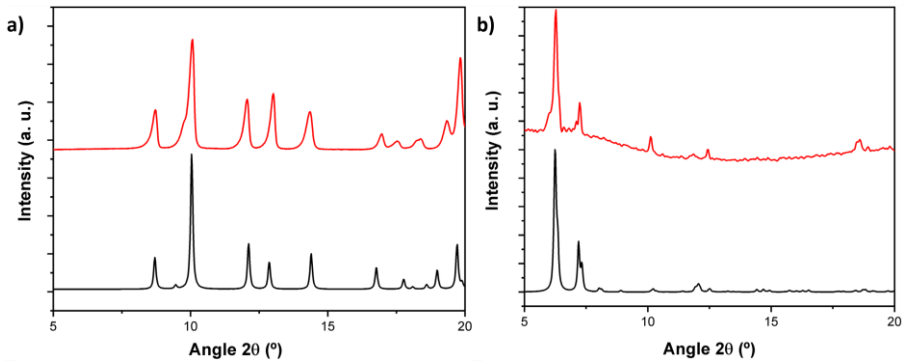


Figure 4.9. a) PXRD pattern of the calculated Cu-**sql**-3,3'-ABDC (black) and pristine Cu-**sql**-3,3'-ABDC (red). b) PXRD pattern of the calculated Tb-**fcu**-3,3'-BPDC (black) and pristine Tb-**fcu**-3,3'-BPDC (red).

zigzag 3,3'-BPDC ligand as a substitute for the 4-c 3,3',5,5'-BPTC linker. Reaction of terbium (III) nitrate salt and $H_2$3,3'-BPDC in the presence of 2-FBA in DMF under solvothermal conditions yielded transparent octahedral crystals of Tb-**fcu**-3,3'-BPDC. SCXRD revealed formation of a 3D **fcu** net which crystallizes in the $P2_1/n$ space group. As we had expected, the presence of 2-FBA as modulator[36]

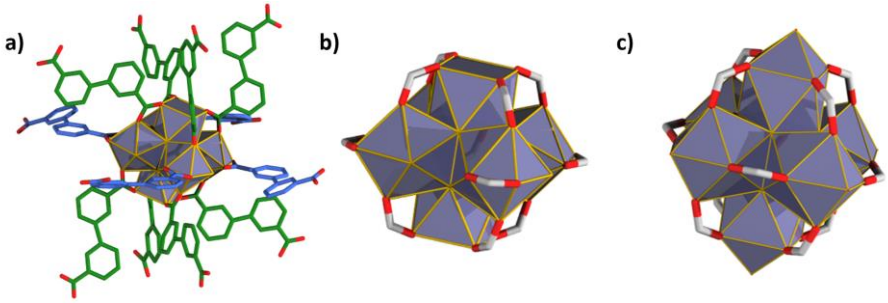


Figure 4.10. a) Cluster representation of Tb-**fcu**-3,3-BPDC with the different coordination modes of the ligand. Green ligands show bridging coordination of metals while blue ligands show chelating coordination to a single metal. Comparison between the coordination of b) the hexanuclear cluster in Tb-**fcu**-3,3-BPDC and c) the hexanuclear RE-cluster in **ftw**-MOF-BPTC structure.[35] Note that the coordination environment of 4 carboxylate groups in the horizontal plane of the cluster in Tb-**fcu**-3,3-BPDC is chelating one single atom, whereas in **ftw**-MOF-BPTC, is bridging two metal atoms. In both cases, the rest of the eight carboxylate groups are bridging the adjacent metals.

enabled the formation of the hexanuclear RE-MBB in Tb-**fcu**-3,3'-BPDC (Figure 4.8b, bottom). According to the PXRD, the bulk sample was pure as both experimental and simulated patterns from the SCXRD completely match (Figure 4.9b). Note that, compared to the archetypical 12-c Zr-**fcu**-4,4'-BPDC (UiO-67),[37] Tb-**fcu**-3,3'-BPDC shows a less-symmetric, distorted structure. We attributed this feature to the transversal parameter of the zigzag linker as well as to the different coordination environment in the inorganic SBU (Figure 4.10).

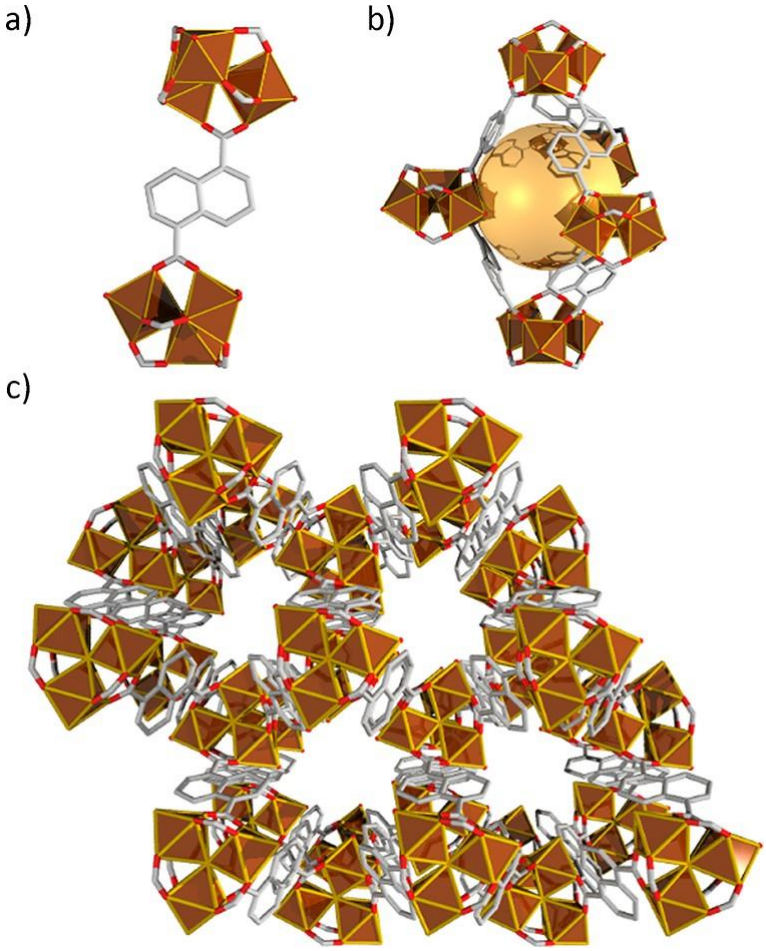


Figure 4.11. Crystal structure of Fe-**acs**-1,5-NDC, showing a) the zigzag connection between the Fe-trimers; b) the trigonal bipyramid cage; and c) the channels formed through the *c* axis.

Finally, we further supported our net-clipping approach designing a rigid, zigzag 1,5-naphthalenedicarboxylate (1,5-NDC) linker that, to the best of our knowledge, its related 4-c rectangular 1,4,5,8-naphthalenetetracarboxylate linker has never been used for the assembly of any MOF. As for the inorganic MBB, we selected the well-known $[Fe(III)]_3O$ trimeric unit as a 6-c trigonal prism MBB. Thus, the corresponding **stp** MOF has never previously been reported. From it, net-clipping induced the formation of an **acs** net. To do so, we firstly synthesized the $H_2$1,5-NDC ligand from the corresponding diamine derivative via several functional group interconversion. Then, the Fe(III)-trimer cluster was synthesized in an acetic acid solution, according to a literature protocol. Lastly, the pre-formed cluster was reacted with $H_2$1,5-NDC in the presence of acetic acid and DMF under solvothermal conditions for 48 h, yielding orange hexagonal crystals. SCXRD revealed the formation of a 3D net with the underlying **acs** topology, which crystallized in the *P-6$_3$m* space group. Fe-**acs**-1,5-NDC exhibited the trimer-cluster connected through 6 zigzag 1,5-NDC linkers (Figure 4.11). Comparison of the experimental PXRD of the bulk sample and the simulated from the SCXRD we confirmed the phase purity of this new MOF (Figure 4.12). Note that the structure of Fe-**acs**-1,5-NDC, although

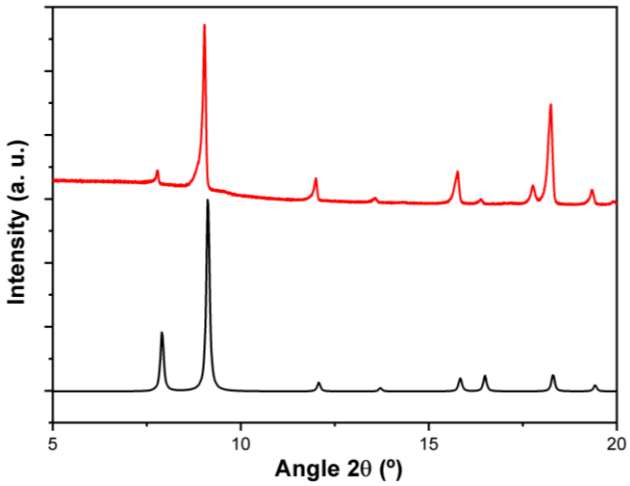


Figure 4.12. PXRD pattern of calculated Fe-**acs**-1,5-NDC (black) and pristine Fe-**acs**-1,5-NDC (red).

slightly distorted, is similar to that of MOF-235/MIL-88B,[38,39] which also exhibits an underlying **acs** topology.

4.2.2.2. Net-clipping of 4-c tetrahedra

Once we had confirmed the feasibility of our net-clipping strategy, we propose to extend it to MOFs made of MBBs of higher symmetry and/or connectivity than 4-c square-like MBBs (Figure 4.3). We first moved to the 4-c tetrahedral MBBs, and we selected the 17 edge-transitive uninodal and binodal nets containing 4-c tetrahedral nodes. Among the six unimodal nets, five of them (**dia**, **sod**, **lcs**, **qtz** and **ana**) were considered in their binary form as explained above. However, we excluded the **lcv** net due to the impossibility of generating a binodal net according to its circuits of connection (Figure 4.13). The binary form of a net is a bipartite graph, and bipartite graphs contain only even cycles, so nets with odd cycles cannot be transformed in a binary form.

We then derived these nets by splitting the 4-c nodes into two 3-c nodes with a 90° connection between them.[26] For tetrahedral nodes embedded in a net, this split can be performed in three distinct orientations (Figure 4.3). Table 4.3 summarizes the 49 resultant derived nets, of which we describe here, for the first time ever, 20

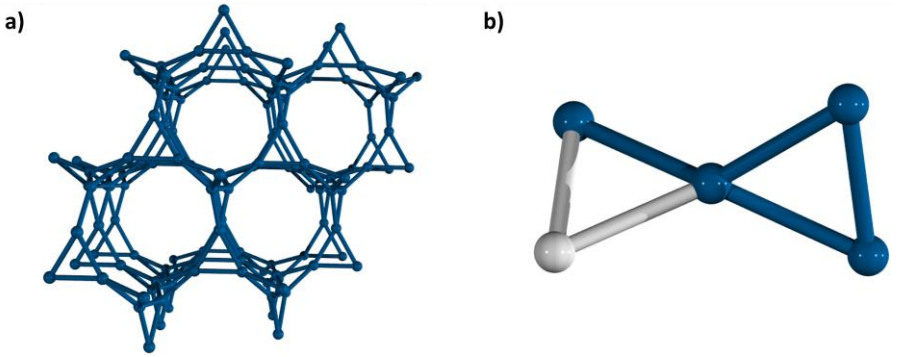


Figure 4.13. a) **lcv** net and b) highlight of 3-cycles present in this net, which illustrates the frustration of generating a binodal net and therefore, net-clipping.

Table 4.3. Net-clipping of all the derived nets from 4-c tetrahedral nodes in the 16 selected edge-transitive nets.

MBB	Main topology	Derived net	Clipped net
	3,4-**bor**	3^2-**bod**	-
		3^2-**boe**	3^2T8[c]/3-**hcb**
	3,4-**ctn**	3^2-**ctn-d**	3-**srs**
		3^3-*icn*7[d]	
	4^2-**pts**	3,4-**tfk**	4^2-**pts**/4-**dia**/4-**sql**/4-**qbd**
		3,4-**sur**	4-**sql**/3-**hcb**/3,4-**bex**/2C1[c]
		3,4T224[c]	4-**dia**/2C1[c]
	4^2-**pth**	3,4-**phx**	4^2-sqc971[a]/4^2T215[c]/4^3-*icn*1[d]
		3,4-**phw**	2C1
		3,4-*icn*8[d]	
	4^2-**dia-b**	3,4-**tfa**	4^2-**pts**/4-**dia**/4-**sql**
		3,4-**tfv**	4-**dia**/4-**sql**
	4^2-**sod-b**	3,4-**xbl**	4-**afw**/4-**lcv**/4^3T4658-HZ[c]
		3,4T60[c]	4-**afw**
		3,4-sqc7390[a]	-
		3^2,4T182[c]	
	4^2-**lcs-b**	3,4-**lcr** = 3,4-*icn*9[e]	4-**afw**
		3,4-sqc7389[a]	-
		3^2,4-*icn*10[d]	
	4^2-**qtz-b**	3,4-**tfq**	4-**uog**/4-**qbd**
		3,4-**qza**	**4-sql**
		3,4-*icn*11[d]	
	4^2-**ana-b**	3,4-sqc12287[a]	4^2-**kea**/4-**unp**/4^3-*icn*2[d]/4^4-*icn*3[d]/4^2-*icn*4[d]
		3,4-sqc12294[a]	-
		3^2,4-*icn*12[d]	4-**lcv**
	4,6-**toc**	3,6-**xab**	-
		3,6-*icn*13[d]	6-**crs**
		3^2,6-*icn*14[d]	4^2-**pts**/4-**dia**/4-**sql**
		3^2,6-*icn*15[d]	-
	4,6-**gar**	**pto-d**-3,6-Ia-3d-1[b]	3-**srs**
		3,6-sqc12213[a]	6-**pcu**/3-**srs**
		3,6^2-*icn*16[d]	6-**pcu**
	4,6-**iac**	3,6-**act**	6-**pcu**
		pto-d-3,6-Ia-3d-2[b]	
		3,6-*icn*17[d]	6-**pcu**/6-**crs**/6^2T26[c]
		3^2,6-*icn*18[d]	6-**pcu**/4-**dia**
		3^2,6-*icn*19[d]	4-**dia**
	4,6-**ibd**	3,6-**ibe**	6-**pcu**
		3,6-*icn*20[d]	6-**pcu**/3-**srs**
		3,6^2-*icn*21[d]	3-**srs**
		3^3,6^2-*icn*22[d]	6-**pcu**
	4,8-**flu**	3,8-**flt**	4^2-**pts**/4-**dia**/4-**sql**
		3,8-**jhw**	4-**sql**
		3,8-*icn*23[d]	

Table 4.3. ***(continued)***

MBB	Main topology	Derived net	Clipped net
	4,12-**ith**	3,12-*icn*24[d]	4-**dia**
		3,12-*icn*25[d]	6-**pcu**/4-**dia**
	4,12-**twf**	3,24-**dni-d**	6-**pcu**
		3,24-*icn*26[d]	4-**dia**

For the derived nets, letters indicate the following: [a]Systre nets in the Epinet database; [b]ToposPro binodal nets;[31] [c]ToposPro symbol for 3-periodic nets; and [d]new nets found using net-clipping approach. [e]*icn*9 is the same as **lcr**, a recent addition to RCSR not recognized by Systre.

(named *icn*7–*icn*26, Table 4.1).[40] Applying net-clipping to the various derived nets generated from the selected edge-transitive nets revealed the exhaustive list of possible combinations of this new set of nodes in different topologies, which can further be translated to organic linkers in reticular chemistry. When transposed into a MOF, this symmetry reduction process erasing two opposite connecting groups generated a new linker shape, which we named turned-twisted, where the connecting groups are twisted in one axis and turned 90° in another axis. We identified 24 possible clipped nets that can be built with a turned-twisted linker, from which four are new nets (named as *icn*1–*icn*4) (Figure 4.5).[40] As in the clipping of 4-c square/rectangular nodes, we found that clipping nets made of tetrahedral nodes can produce 3D nets, 2D layers or 1D chains from the same parent net, due to the different splitting modes/orientation of the tetrahedra. For example, in the case of the **pts** net, the possible clipped nets are the 3D **pts** and **dia** topologies, the 2D **sql**, **hcb** and **bex** topologies, and the 1D **qbd** and the double-bridged linear topologies. For the results of this study and the following, we will not explain Tables 4.3-4.6 in detail as in the previous Section.

To corroborate our net-clipping approach, we identified in literature some examples that match with our predictions. MOF-11, a **pts**-MOF constructed by linking 4-c square-like Cu-based paddlewheels and 4-c tetrahedral-like 1,3,5,7-adamantanetetracarboxylate (1,3,5,7-ATC) linkers (Figure 4.14),[41] can be related to two other reticular materials that net-clipping anticipated among the seven possible nets to form. When clipped, the tetrahedral 1,3,5,7-ATC linker is converted into the

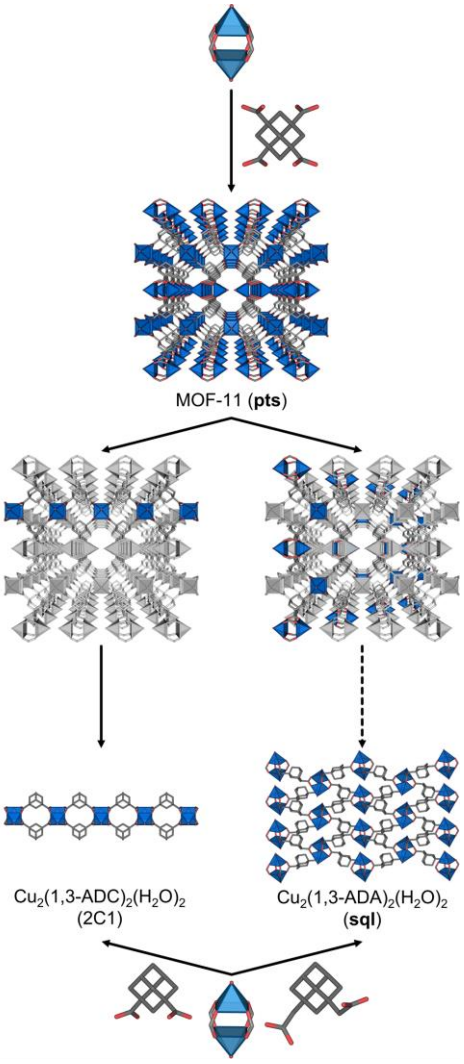


Figure 4.14. Schematic of the net-clipping approach applied to the formation of MOMs from tetrahedral 1,3,5,7-ATC linker to turned-twisted 1,3-ADC (left) or 1,3-ADA (right) linkers combined with 4-c paddlewheel Cu(II) MBBs.

turned-twisted 1,3-adamantanedicarboxylate (1,3-ADC), which had already been combined with 4-c square-like Cu(II) paddlewheels by Zheng *et al.* to obtain the anticipated one-dimensional chain (here as double bridged). In a second example, the same authors similarly combined a closely related linker, 1,3-adamantane-

diacetate (1,3-ADA), which incorporates a methylene group in each of the two carboxylic acid arms of 1,3-ADC (Figure 4.14).[42] Significantly, with this linker, they observed the formation of a **sql**-MOF, also corresponding to a net that we predicted by net-clipping a MOF made of 4-c square-like and tetrahedral MBBs.

4.2.2.3. Net-clipping of 6-c hexagons

The number of edge-transitive nets comprising 6-c hexagonal nodes is much smaller compared to the previous one: there are just five, two among them are 2-periodic nets (**kgd** and **hxl**), and the rest are 3D nets (**she**, **hxg-b** and **mgc**). Among them, we excluded the **hxl** net due to the same unfeasibility to generate a binodal net due to the presence of odd cycles, as for the aforementioned tetrahedral **lcs** net (Figure 4.15).

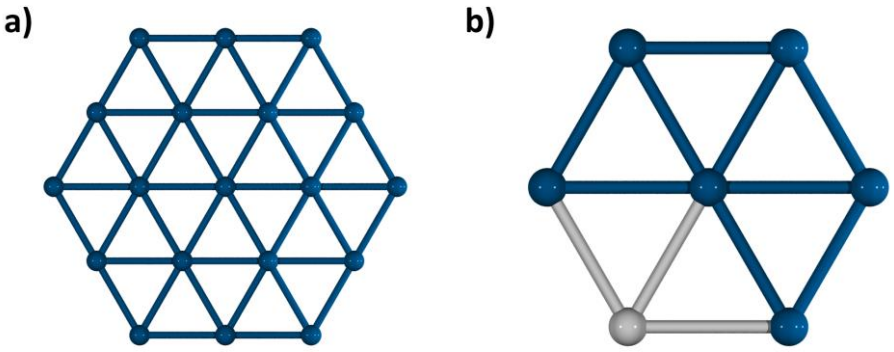


Figure 4.15. a) **hxl** net and b) highlight of 3-cycles present in this net, which illustrates the frustration of generating a binodal net and therefore, net-clipping.

In the remaining four nets (**kgd**, **she**, **hxg-b**, and **mgc**), we derived the hexagon into a central triangle bound to three triangles (Table 4.4). This process led to five derived nets, being one new, *icn*27 (Table 4.1),[40] derived from the **mgc** net. Then, we erased half of their connections to generate a less-symmetric triangular polygon (Figure 4.3). Four clipped nets were obtained when applying net-clipping to these

Table 4.4. Net-clipping of all the derived nets from 6-c hexagonal nodes in the 4 selected edge-transitive nets.

MBB	Main topology	Derived net	Clipped net
	3,6-**kgd**	3^3-**hcb-b3**	3^2-**hcb-b**
	4,6-**she**	3^2,4-**epn**	3,4-**pto**/3,4^3-*icn*5[a]
		3^2,4-**het**	3,4-**pto**
	6^2-**hxg-b**	3^2,6-**dne**	-
	6,12-**mgc**	3^2,12-*icn*27[a]	3,12-**ttt**

For the derived nets, letters indicate the following: [a]new nets found using the net-clipping approach.

five derived nets, being one of them new, *icn*5 (Table 4.1 and Figure 4.5),[40] clipped from the parent **she** net. Note that, for these types of nets, there is only a dimensional reduction from the predicted 3D derived **epn** net to the 2D (more precisely a 2-periodic 3D thick layer) clipped *icn*5 net. Interestingly, the **hxg-b** net is the only one that cannot be clipped into another net without affecting the connectivity of the two 6-c nodes simultaneously.

Application of our net-clipping approach to 6-c hexagonal MBBs is strongly corroborated in the literature with several examples. One of them, **kgd** Zn-MOF-

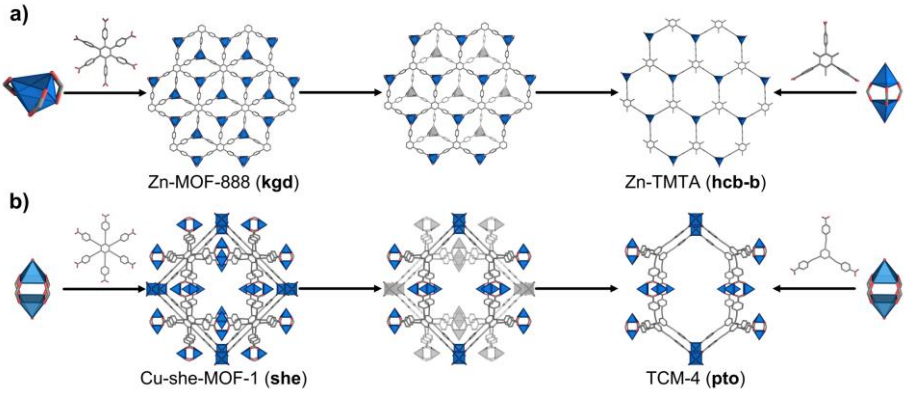


Figure 4.16. Schematic of the net-clipping approach applied to formation of reticular materials from a) hexagonal CPB linker to a trigonal TMTA linker combined with 3-c Zn(II) MBBs; and b) from a hexagonal BHEB linker to a trigonal BTEB combined with 4-c paddlewheel Cu(II) MBBs.

888, is based on the combination of a 3-c Zn(II) metal ion and the 6-c hexagonal 1,2,3,4,5,6-hexakis(4-carboxyphenyl) benzene (CPB).[43] If we clipped this CPB linker into the corresponding trigonal 4,4',4''-(2,4,6-trimethylbenzene-1,3,5-triyl) tribenzoate (TMTA) linker, when assembling with the 3-c Zn(II) cluster, forms the expected **hcb-b** layer,[44] as predicted by our net-clipping approach (Figure 4.16).

The other example is **she**-MOF-1, which is constructed by linking 4-c Cu(II) paddlewheels by the extended 6-c hexagonal 1,2,3,4,5,6-benzene-hexaethynylbenzoate (BHEB) linker (Figure 4.16b).[45] According to net-clipping, combination of the 4-c Cu(II) paddlewheels with the corresponding clipped 1,3,5-benzene-trisethynylbenzoate (BTEB) linker should lead to the formation of a 3D **pto** MOF (Table 4.3). Remarkably, this prediction was confirmed upon the formation of a **pto** MOF, TCM-4.[46] Moreover, the same correlation was observed for a similar pair of MOFs: **she**-MOF-2,[45] built upon the assembly of the 6-c hexagonal 1,2,3,4,5,6-hexakis(4-carboxybiphenyl) benzene (CBPB) with the 4-c square-like Cu(II) paddle-wheel; and for MOF-388, constructed with the triazine functionalized 4,4',4''-(triazine-2,4,6-triyl-tris(benzene-4,1-diyl))tribenzoate (TAPB), which exhibits the anticipated underlying **pto** topology (Figure 4.17).[47]

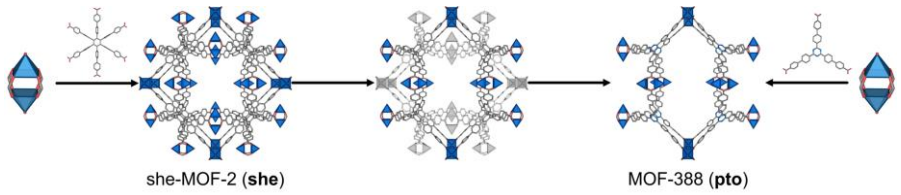


Figure 4.17. Schematic of the net-clipping approach applied to the formation of reticular materials from hexagonal CBPB linker to trigonal TAPB combined with 4-c paddle-wheel Cu(II) MBBs.

4.2.2.4. Net-clipping of 8-c cubes

To expand our net-clipping approach to more highly-connected MBBs (connectivity ≥ 8), we analyzed the seven binodal edge-transitive nets containing 8-

c cubic-like nodes. We noticed that the cube presents two accessible clipping modes: one into a square, and one into a tetrahedron (Figure 4.3). According to Chen *et al.*,[48] a cubic node can be splitted into a tetrahedron surrounded by four triangles (Method 1), or into a square connected to four triangles (Method 2), among other derived modes. As shown in Table 4.5, the use of these methods afforded 34 derived nets, twelve of which were unprecedented (*icn*28–*icn*39, Table 4.1).[40] Applying net-clipping to these derived nets generated 16 clipped nets, of which we discovered a new net topology, which we named *icn*6 (Table 4.1 and Figure 4.5).[40]

In comparison to MOFs built up from organic MBBs of lower connectivity, there are not many examples of MOFs that contain 8-c cubic organic MBBs in the literature. However, we could find an example that corroborated our approach. Gao *et al.* synthesized a **scu** MOF, ZJNU-10, that is based on the assembly of 4-c square-like Cu(II) paddlewheels and 8-c cubic 3,6-dimethyl-tetra(5'-isophthalate)benzene (DMTIB) linker (Figure 4.18a).[49] The net-clipping of **scu** yields a 2D **sql-b** net, a 3D **ssb** net, or a 3D **lvt-b** net when the cube is clipped into a square; or a 3D **pts** net when the cube is clipped into a tetrahedron (Table 4.5). Significantly, the same group reported a **pts** MOF by connecting 4-c Cu(II) paddlewheels with the 4-c tetrahedral 1,2,4,5-tetrakis(3-carboxyphenyl)-benzene (3-TCPB) linker.[50]

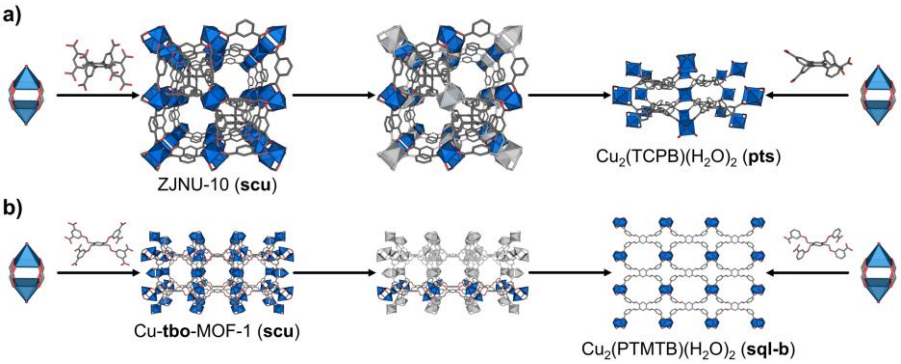


Figure 4.18. Schematic of the net-clipping approach applied to formation of MOMs from a) a cubic DMTIB linker to a tetrahedral 3-TCPB linker, combined with 4-c paddlewheel Cu(II) MBBs; and b) from a cubic PTMTI linker to a square PTMTB linker, combined with 4-c paddlewheel Cu(II) MBBs.

Table 4.5. Net-clipping of all the derived nets from 8-c cubic nodes in the 7 selected edge-transitive nets.

MBB	Main topology	Derived net	Clipped net (Method)
	3,8-**the**	3^2,4-**ffj**	3,4-**bor (M1)** **- (M2)**
		3^2,4-**tfe**	3,4-**bor**/3,4^2-*icn6*[c] **(M1)** 3,4^2-*icn6*[c] **(M2)**
		3^2,4-**tfy**	3,4-**bor**/3^2,4^2T116[b]/3,4^2-**mmm (M1)** 3,4-**tbo**/3^2,4^2T116[b]/3,4^2-**mmm (M2)**
		3^2,4-*icn28*[c]	**- (M1)** 3,4-**tbo (M2)**
	4,8-**scu**	3,4^2-**ffc**	4^2-**pts (M1)** 4^2-**ssb**/4^2-**lvt-b (M2)**
		3,4^2-**eed** 3,4^2-**mmm** 3,4^2-**tbo-b** 3,4^2-**bor-b** 3,4^2-**epz**	4^2-**pts (M1)** 4^2-**sql-b (M2)**
	4,8-**sqc**	3,4^2-**iab** 3,4^2-**epf**	**- (M1 & M2)**
		3,4^2-**tfm**	4^2-**pts (M1)** **- (M2)**
	4,8-**csq**	3^2,4^2-**ffd** 3^2,4^2-*icn29*[c]	**- (M1 & M2)**
		3,4^2-*icn30*[c]	**- (M1)** 4^2-**sql-b (M2)**
		3,4^2-*icn31*[c] 3^2,4^2-*icn32*[c] 3^2,4^2-*icn33*[c] 3,4^2-**dnr**	**- (M1)** 4^2-**ssa (M2)**
	4,8-**flu**	3,4^2-**jaj** 3,4^2-**ofp** 3,4^2-**tfj**	4^2-**dia-b (M1)** 4^2-**pts (M2)**
		3,4^2-*icn34*[c] 3,4^2-*icn35*[c]	**- (M1)** 4^2-**pts (M2)**
	6,8-**ocu**	3,4,6-**pdp** 3,4,6-**twf-d**	4,6-**toc (M1)** **- (M2)**
		3^2,4^2,6-*icn36*[c]	4,6-**toc (M1)** 4^2,6T1[b] **(M2)**
		3,4,6-*icn37*[c] 3,4,6-*icn38*[c]	**- (M1)** 4^2,6T138[b] **(M2)**
	8^2-**bcu-b**	3,4,8-**dnq** 3,4,8-**eft** 3,4,8-*icn39*[c]	4,8-**flu (M1)** 4,8-**scu (M2)**
		3,4,8-sqc886[a]	**- (M1)** 4-**sql (M2)**

For the derived nets, letters indicate the following: [a]Systre nets in the Epinet database; [b]ToposPro symbol for 3-periodic nets; [c]new nets found using the net-clipping approach; M1: Method 1; and M2: Method 2.

Interestingly, this latter 4-c linker can be seen as the clipped tetrahedron version of the 8-c cubic linker (Figures 4.18a and 4.19). Thus, the topology of the underlying net of the synthesized **pts** MOF perfectly matches with the prediction of our net-clipping approach.

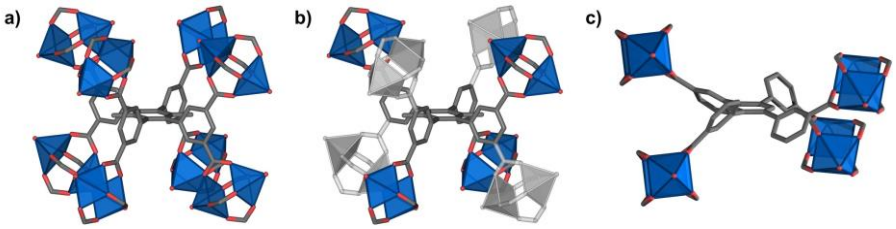


Figure 4.19. Illustration of a) the conformation of the DMTIB linker in the crystal structure of ZJNU-10; b) the predicted conformation of the clipped linker in a square conformation; and c) the conformation of 3-TCPB in the single-crystal structure reticulated with Cu(II)-paddlewheels matching with the prediction made by net-clipping. Note that the approach not only successfully predicted the topology of the MOF assembled with a new low-symmetry linker but also accurately anticipated the conformation adopted by the linker within the structure.

In order to support our net-clipping strategy with all the clipped modes, we were motivated to experimentally contribute with our own structures due to the paucity of literature examples of MOFs made of 8-c cubic organic MBBs. To do so, we synthesized a new 4-c less-symmetric linker, representing the clipped square-like version of an 8-c cubic linker used for the construction of another **scu** MOF. Cu-**tbo**-MOF-1 is built by linking 4-c square-like Cu(II) paddlewheels to 8-c cubic 5,5',5'',5'''-[1,2,4,5-phenyltetramethoxy]tetraisophthalate (PTMTI) linkers.[11] If the linker is considered as a single 8-c node, this structure exhibits the aforementioned **scu** underlying topology; but if it is simplified into more regular 3-c and 4-c nodes, the underlying topology of the net is the **tbo-b** (more precisely **tbo-b3**). Net-clipping of this derived net in the 4-c square-like MBB mode uniquely generated the 2D **sql-b** net (Table 4.5), which contrasts sharply to the 3D **pts** net that we had expected to see from having used the clipped tetrahedral linker. The desymmetrization of the 8-c PTMI linkers into a 4-c linker generated 3,3',3'',3'''-[1,2,4,5-phenyltetramethoxy]tetrabenzoate (PTMTB). After synthesizing the

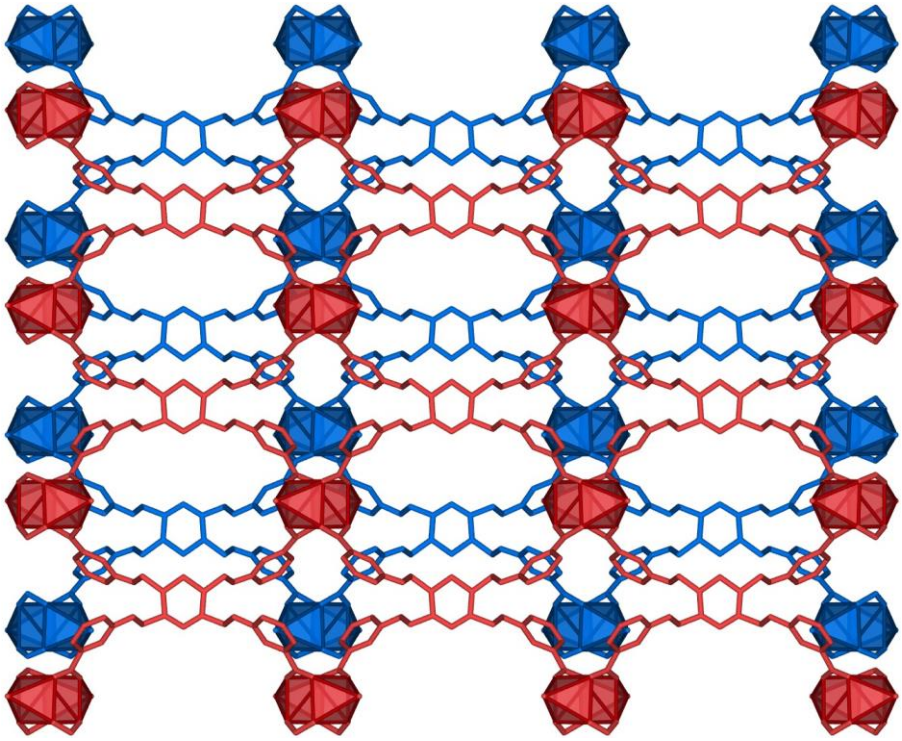


Figure 4.20. AB packing of the 2D $Cu_2(PTMTB)(H_2O)_2$ structure.

H_4PTMTB linker, it was reacted with copper(II) nitrate salt in the presence of HBF_4 and DMF under solvothermal conditions during 24 h, yielding blue square-shaped crystals. Importantly, SCXRD analysis of the crystal structure confirmed the formation of a MOF layer with the expected **sql-b** topology, and therefore, with the corresponding less-symmetric 4-c square-like MBB (Figure 4.18b).[40] This structure, with formula $Cu_2(PTMTB)(H_2O)_2$, crystallizes in the orthorhombic *Cmca* space group with an AB packing (Figure 4.20).

Thus, net-clipping not only predicted the topology of the MOF assembled with a new, less-symmetric linker, but also predicted the conformation adopted of the linker in the structure (Figure 4.21). Notably, the **tbo**-MOF platform already highlighted the disassembly of the **scu** net into pillared **sql** SBLs; however, in another direction of the structure, made of isophthalates bridging 4-c

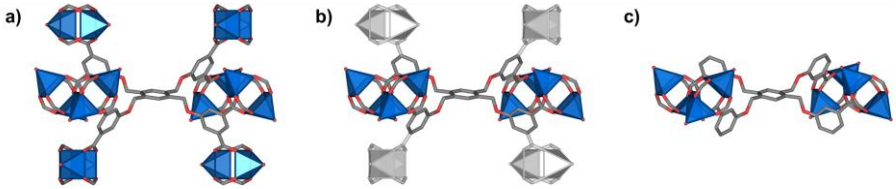


Figure 4.21. Highlight of a) the conformation of the PTMTI linker in the crystal structure of Cu-**tbo**-MOF-**1**; b) the predicted conformation of the clipped linker in a square conformation; and c) the conformation of PTMTB in $Cu_2(PTMTB)(H_2O)_2$ matching with the predicted by net-clipping. Note that the approach not only successfully predicted the topology of the MOF assembled with a new low-symmetry linker but also accurately anticipated the conformation adopted by the linker within the structure.

paddlewheels.[11] Compared to the previous 3-TCPB linker which combination with Cu(II) paddlewheels produced a MOF with the **pts** net, the PTMTB favored the formation of the 2D **sql** net, probably due to the longer distance between the central benzene core and the carboxylic groups, preferring the square conformation of the linker rather than the previous tetrahedral conformation. However, it is not possible to rule out the possibility to isolate synthetic conditions that would

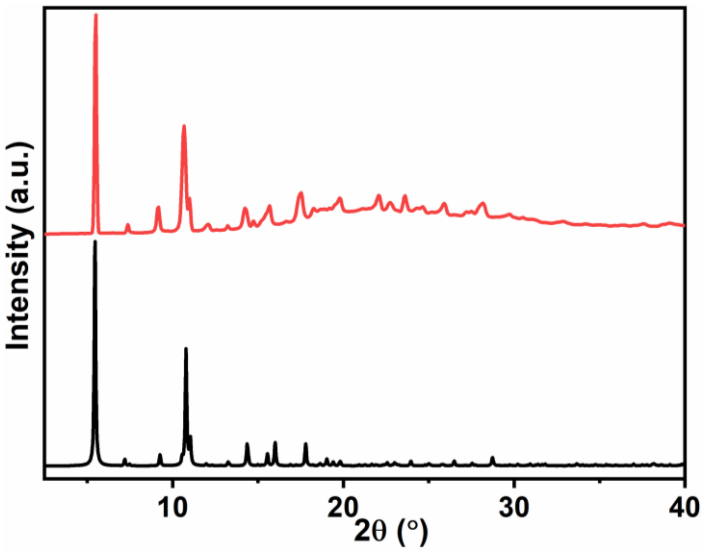


Figure 4.22. PXRD pattern of the calculated $Cu_2(PTMTB)(H_2O)_2$ (black) and pristine $Cu_2(PTMTB)(H_2O)_2$ (red).

promote formation of **sql**-MOF and **pts**-MOF using H_4PTMB, respectively. Thus, we confirmed the phase purity of this material without any evidence of the possible **pts**-MOF by comparing the experimental PXRD of the bulk sample and the simulated from the SCXRD, perfectly matching all the peaks (Figure 4.22).

4.2.2.5. Net-clipping of 12-c hexagonal prisms

Finally, we considered the highest connectivity from the selected MBBs, the 12-c hexagonal prism, which nodes are only found in two edge-transitive nets: the **shp** and **alb** topologies. As in the previous case, hexagonal prismatic MBBs also allow for two clipping modes: one into a 6-c trigonal prism (Method 3); and one into a 6-c octahedron (Method 4) (Figure 4.3). Following both methods produced 14 derived nets, and subsequent net-clipping of the 12-c hexagonal prismatic nodes generated three clipped nets (Table 4.6). Thus, in the **alb** net, clipping the 12-c hexagonal prism to a 6- c trigonal prism (Method 3) affords the binodal **acs-b** topology, whereas clipping it into an octahedron (Method 4) yields a **nia** net. On the other

Table 4.6. Net-clipping of all the derived nets (methods 3 and 4) from 12-c hexagonal prism nodes in the seven selected edge-transitive nets.

MBB	Main topology	Derived net	Clipped net
	4,12-**shp**	3,4,6-**cee**	- **(M3 & M4)**
		3,4,6-**agw**	4,6-**stp (M3)** - **(M4)**
		3,4,6-**cef**	
		3,4,6-**ceg**	
		3,4,6-**ceh**	
		3,4,6-**cej**	
		3,4,6-**cez**	
	6,12-**alb**	3,6^2-**kew**	- **(M3)** 6^2-**nia (M4)**
		3,6^2-**cep**	6^2-**acs-b(M3)** 6^2-**nia (M4)**
		3,6^2-**ceq**	
		3,6^2-**cer**	
		3,6^2-**cet**	
		3,6^2-**key**	6^2-**acs-b(M3)** - **(M4)**
		3,6^2-**kez**	

M1: Method 1; and M2: Method 2.

hand, the 12-c hexagonal prism of the **shp** net can only be clipped into a trigonal prism, which affords the **stp** net.

Our prediction of these three nets via net-clipping is reinforced by several MOFs reported in the literature. Concerning to MOFs based on the **alb** net, In-**alb**-MOF-1 is a 3D structure built up from the connection of 6-c In-trimer clusters through 12-c 1,2,3,4,5,6-hexakis[3,5-bis(4-carboxyl-phenyl)phenoxymethyl]benzene (BCPB) linkers (Figure 4.23a).[51] As we had anticipated, net-clipping of **alb** topology induced the formation of two possible nets exhibiting the **acs-b** (Method 3) or **nia** (Method 4) topologies. Despite the lack of a reported MOF built by combining these clusters and the clipped version of H_{12}BCPB, we did find a closely related MOF, Al-**nia**-MOF-1, made of analogous 6-c trigonal prismatic Al-trimer clusters and the 6-c octahedral 5',5'''',5''''''-((1,3,5-triazine-2,4,6-triyl)tris(azanediyl))tris-(([1,1':3,1''-terphenyl]-4,4''dicarboxylate)) (TTATTDC) linker. This TTATTDC linker shows an octahedral shape similar to that which the clipped 6-c linker from H_{12}BCPB (Method 4) would exhibit. Importantly, Al-**nia**-MOF-1 showed the anticipated underlying **nia** topology (Figure 23a, top).[52] Respect to the other clipping modes, we found Co-THA, which is formed by linking analogous 6-c Co-trimer clusters with the 6-c trigonal prismatic triptycene-hexaacetate (THA) linker, which could be seen as the clipped trigonal prismatic version of a 12-c hexagonal prismatic MBB. In this case, the anticipated **acs-b** net (more precisely, the derived **tsg** net) had also been formed (Figure 23a, bottom).[53]

Regarding MOFs based on the **shp** net, we found Cu-**shp**-MOF-1, a reported framework constructed by the connection of 4-c Cu(II) paddlewheels through the former 12-c BCPB linkers (Figure 23b).[51] Despite the lack of reports on a MOF made by combining Cu(II) paddlewheels with the clipped version of H_{12}BCPB, an analogous linker was found in literature: the 6-c trigonal prismatic 3,3',3'',5,5',5''-benzene-1,3,5-triyl-hexabenzoate (BHB) linker was used in combination with 4-c square-like Cu(II) paddlewheels to form UTSA-20, which is a clipped trigonal prismatic version of a 12-c hexagonal prismatic MBB.[54] This MOF exhibits an

underlying **stp** topology (more precisely, the derived **zyg** net), thus matching with the anticipated topology of the clipped net from the main **shp** topology.

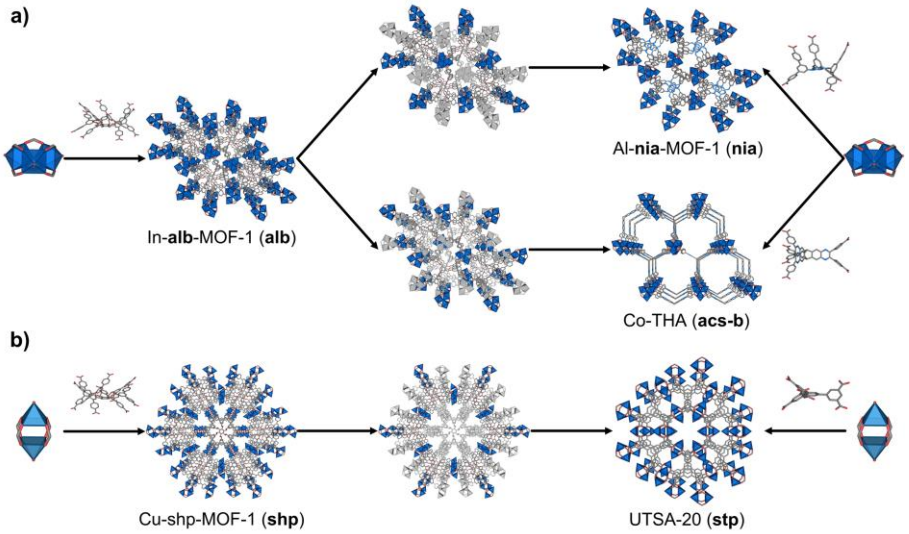


Figure 4.23. Schematic of the net-clipping approach applied to formation of MOMs from a) a hexagonal prism BCPB linker clipped to an octahedral TTATTDC, and trigonal prism THA linkers combined with a 6-c trimer M(III) MBBs; and b) a hexagonal prism BCPB linker clipped to a distorted trigonal prism BHB linker, combined with 4-c paddlewheel Cu(II) MBBs.

4.2.2.6. Net-clipping out of edge-transitive nets

In our attempts to assemble a MOF made of a 4-c tetrahedral organic MBB exhibiting an underlying edge-transitive net, we accidentally deviated from the most regular and symmetric nets. According to literature, three main organic skeletons have been used for the design of tetrahedral linkers: an sp^3 carbon atom,[55] an adamantane unit,[41] and a central biphenyl unit with 90º rotation of the σ-bond at the core, often promoted by the steric hindrance of bulky groups in closeness substituted positions.[56] We selected the last one, which can allow us to precisely modify the geometrical parameters of the linker. We synthesized a new 4-c

tetrahedral 2,2',6,6'-tetramethoxy-[1,1'-biphenyl]-3,3',5,5'-tetracarboxylate (TMBPTC) linker that, as expected, methoxy groups decorated in *ortho* positions of the core lock the linker's conformation in 90º affording a rigid, tetrahedral MBB (Figure 4.24).

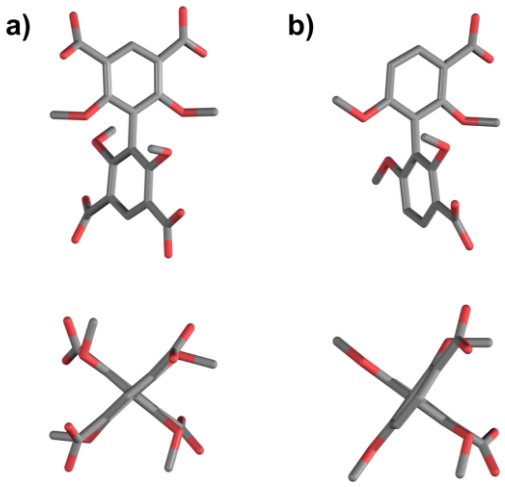


Figure 4.24. a) TMBPTC and b) TMBPDC linkers showing the steric hindrance of the methoxy groups in the *ortho* positions of the biphenyl MBB that produces the deviation of the carboxylates in 90º with respect the others.

Reaction of copper(II) nitrate salt and H_4TMBPTC in DMF under solvothermal conditions yielded green needle-shaped crystals. Analysis of the crystal structure by SCXRD revealed the formation of a new MOF with formula of Cu_2(TMBPTC)(H_2O)$_2$ and an underlying 3D 4^3T2 net,[40] crystallizing in the *C2/c* space group (Figure 4.25). As expected, the 4-c square-like Cu(II) paddlewheels were *in-situ* formed during the reaction conditions. This 4^3T2 topology, which does not belong to an edge-transitive net, is based on two squared nodes joined by a tetrahedral node in a [34] transitivity. In it, the tetrahedral nodes are distributed in a primitive cubic conformation that exhibits a slight shift between two pairs of cubic units (Figure 4.26). This shift results in a desymmetrization of the square MBBs in two different positions produced by the desymmetrization of the elongated tetrahedral MBB,[18,56–59] altering the circuits of connection and frustrating

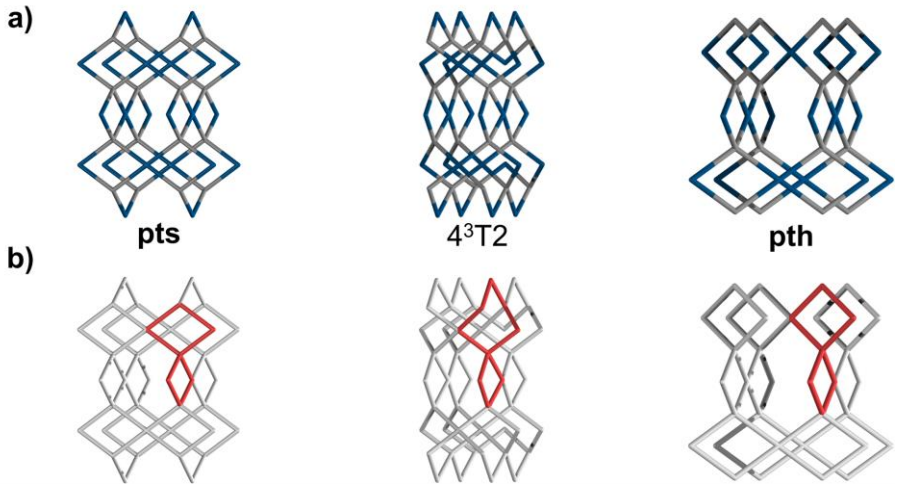


Figure 4.25. a) Net representation of the **pts** (left), 4^3T2 (centre) and **pth** (right) topologies, in blue the square node and gray tetrahedral node. b) Highlight of some characteristic circuits of connections in **pts** (left), 4^3T2 (centre) and **pth** (right) topologies, comparing two adjacent 4-cycles that are in 90º or 45º with respect each other in **pts** or **pth**, respectively; while in the new 4^3T2 net, there is a 6-cycle adjacent to the 4-cycle due to the desymmetrization of the square nodes in two positions, inducing a shift in the position of the tetrahedral nodes.

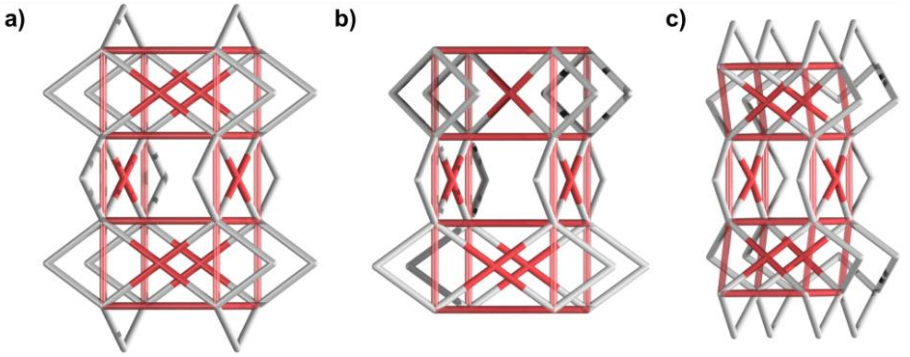


Figure 4.26. Highlight of the tetrahedral MBBs arrangement in a primitive cubic conformation in the a) **pts** net, b) **pth** net and c) 4^3T2 net. Note here that the tetrahedral nodes are in the same positions in **pts** and **pth** topologies, whereas there is a shift between two contiguous cubes in the 4^3T2 net. The square nodes, highlighted in red, are a) alternated in the faces of the cubes in different axis in the **pts** net; b) alternated in the same way as in **pts** net, with an additional square connecting tetrahedral nodes in the diagonal of the cube in the **pth** net; and c) alternated in the faces of the cubes in different axis with a slight inclination in the 4^3T2 net in comparison to the **pts** net.

the formation of two 4-cycles seen in both **pts** and **pth** nets. Instead, a 4-cycle and a diamond-like 6-cycle are formed. In addition, PXRD analysis of the bulk sample comparing the experimental one with the simulated from the obtained SCXRD confirmed the phase purity (Figure 4.27).

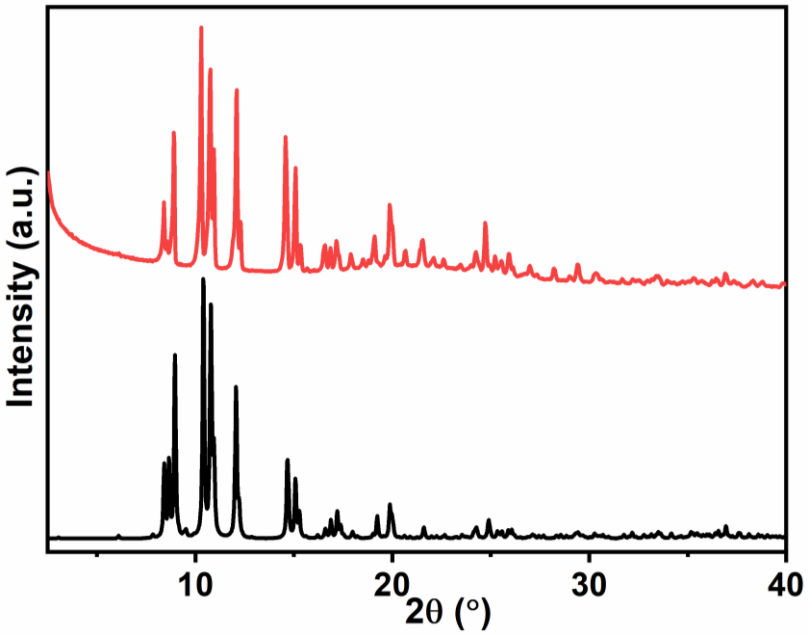


Figure 4.27. PXRD pattern of the calculated $Cu_2(TMBPTC)(H_2O)_2$ (black) and pristine $Cu_2(TMBPTC)(H_2O)_2$ (red).

Inspired by the formation of the aforementioned 4^3T2 MOF, we decided to use this net to challenge our net-clipping approach to ascertain whether MOFs made of less-symmetric linkers could be anticipated from less regular nets. To this end, we applied the net-clipping strategy to the 4^3T2 net resulting in the prediction of two different clipped nets: the 2D **sql** and the 1D 2C1 topologies (Figure 4.28).

Next, we designed and synthesized the rigid 2,2',6,6'-tetramethoxy-[1,1'-biphenyl]-3,3'-dicarboxylate (TMBPDC) linker, which is the clipped, turned-twisted version of the 4-c tetrahedral TMBPTC linker (Figure 4.24). In TMBPDC, the steric

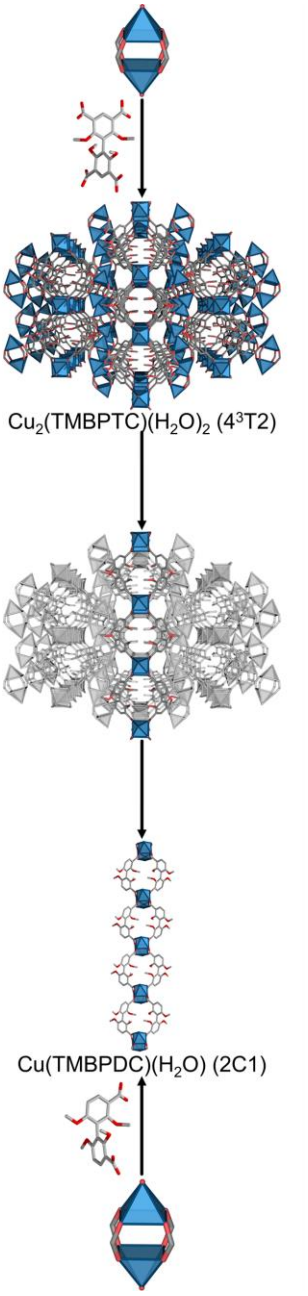


Figure 4.28. Schematic of the net-clipping approach applied to formation of MOMs from a tetrahedral TMBPTC linker to a turned-twisted TMBPDC (left) combined with 4-c paddlewheel Cu(II) MBBs.

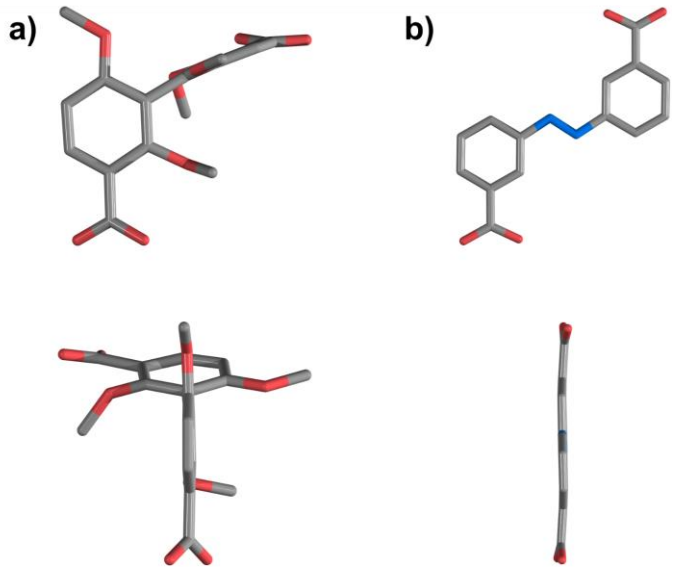


Figure 4.29. a) TMBPDC and b) ABDC linkers showing the difference on the directionality of the carboxylates in the T-T and zigzag conformations, producing the reticulation of different structures when combining with Cu(II)-paddlewheels in a 1D metal-organic chain or in a 2D metal-organic layer, respectively.

hindrance induced by the methoxy groups locks the linker conformation into a turned-twisted shape,[56] which is twisted 90° relative to its reported homologous zigzag linker (Figure 4.29). As we predicted, replacing the tetratopic TMBPTC linker with the ditopic H_2TMBPDC let to the formation of the predicted metal–organic 1D 2C1 chain. Thus, reaction of copper(II) nitrate salt and H_2TMBPDC in the presence of DMF and H_2O under solvothermal conditions for 24 h yielded green polyhedral crystals. SCXRD revealed the formation of a CP with formula Cu(TMBPDC)(H_2O), which crystallizes in the $P2_1/c$ space group (Figure 4.28). In this structure, two pairs of linkers connect to the same 4-c Cu paddlewheel by double bridging. Certainly, just a few structures where the paddlewheel clusters are extended in one dimension have been reported so far,[60] in addition to the recent triple and quadruple bridging of Zr-hexanuclear clusters.[10,61] Compared to the homologous zigzag linker, which combination with Cu(II) paddlewheel produce the 2D MOF Cu-**sql**-3,3'-ABDC, the desymmetrization into a turned-twisted shape

reduced its dimensionality to a 1D CP. According to the PXRD, the bulk sample is pure as both experimental and simulated patterns completely match, without any evidence of the possible **sql**-MOF (Figure 4.30).

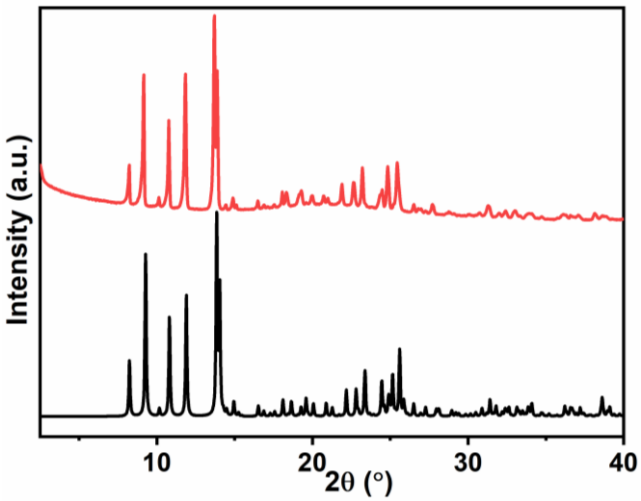


Figure 4.30. PXRD pattern of the calculated Cu(TMBPDC)(H_2O) (black) and pristine Cu(TMBPDC)(H_2O) (red).

4.3. Experimental section

4.3.1. Materials, methods and characterization

4.3.1.1. Materials

Copper(II) nitrate hemi(pentahydrate) ($Cu(NO_3)_2{\cdot}2.5H_2O$), terbium(III) nitrate pentahydrate ($Tb(NO_3)_3{\cdot}5H_2O$), iron(III) nitrate nonahydrate ($Fe(NO_3)_3{\cdot}9H_2O$), hydrated ferric chloride ($FeCl_3{\cdot}6H_2O$), sodium acetate trihydrate ($NaOAc{\cdot}3H_2O$), potassium carbonate (K_2CO_3), potassium iodide (KI), sodium hydroxide (NaOH), sodium nitrite ($NaNO_2$), urea, *n*-butyllithium solution (*n*-BuLi), 2-fluorobenzoic acid (2-FBA), 1,5-diaminonaphthalene, *N,N,N',N'*-tetramethylethylenediamine (TMEDA), paraformaldehyde, *tert*-butanol (*t*-BuOH), sulfuric acid (H_2SO_4), acetic

acid (AcOH), Celite® 512 medium, 2,4-dimethoxybenzene and magnesium sulfate (Mg_2SO_4) were purchased from Sigma-Aldrich Co. Azobenzene-3,3'-dicarboxylic acid and copper(I) cyanide (CuCN) were purchased from TCI. *N,N*-dimethylformamide (DMF), acetone, tetrahydrofuran (THF), hexane, ethylacetate (AcOEt), methanol (MeOH), hydrochloric acid (HCl), dichloromethane (DCM) and diethyl ether (Et_2O) were obtained from Fisher Chemical. Ethanol (EtOH) was obtained from Scharlab. Potassium permanganate ($KMnO_4$) and anhydrous sodium sulfate were obtained from Panreac AppliChem. Anhydrous iron chloride ($FeCl_3$) was purchased from Acros Organics. Sodium borohydride ($NaBH_4$) was obtained from Thermo Scientific Chemicals. Biphenyl-3,3'-dicarboxylic acid was purchased from Combi-Blocks. 2,4-Dimethoxy-1-methylbenzene, methyl 3-hydroxybenzoate and 1,2,4,5-tetrakis(bromomethyl)benzene were purchased from BLDpharm. All the reagents and solvents were used without further purification unless otherwise specified. Deionized water was obtained with a Milli-Q® system (18.2 MΩ·cm).

4.3.1.2. Methods

Generation and discovery of derived nets

For the generation of the derived nets, we used Materials Studio 2021 Program and the following procedure:

(i) We first imposed a less-symmetric group related to the one of the main topology by translation-equivalent and class-equivalent subgroup according to the International Tables of Crystallography.[62]

(ii) We created mass centroids in the middle point between the atom splitted and two neighbouring atoms.

(iii) We substituted the clippable node by a set of less-symmetric nodes and edges by inserting atoms in the coordinates of the mass centroids.

(iv) And we repeated this process with a different set of atoms, splitting the node in the different possible directions.

Net-clipping: Theoretical de-reticulation of nets

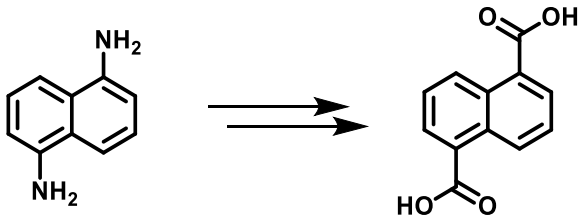
The resulting 102 underlying nets were analysed with the ToposPro 5. 5. 1. 0 program and the TopCryst website (https://topcryst.com/).

Net-clipping

Net-clipping approach was performed by using Materials Studio 2021 Program. The removal of symmetrically half of the nodes (and their connections) was carried out by different methods depending on the space group related to each net. Generally, the adjacent nodes to the clippable node are related by symmetry in the derived nets. Accordingly, it was necessary to break this symmetry by (i) imposing *P1* symmetry, or (ii) creating a supercell of different dimensions (depending on the net) to find the smallest repeating unit, in which these nodes can be removed independently. Then, we removed half of the selected nodes to generate less-symmetric nodes (Figure 1). Each of the 102 derived nets were clipped using these two methods. The resulting 46 underlying nets were analysed with the ToposPro 5. 5. 1. 0 program and the TopCryst website (https://topcryst.com/).

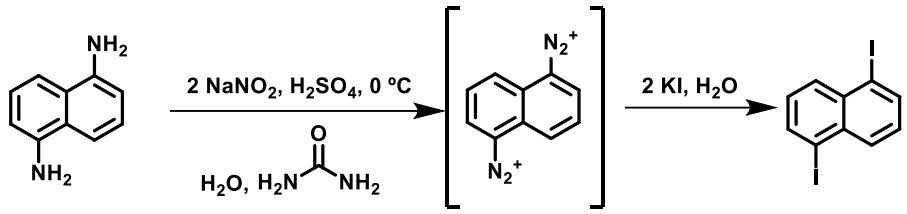
4.3.1.3. Synthesis

Synthesis of 1,5-naphthalenedicarboxylic acid ($H_2$1,5-NDC)



Scheme S1. Scheme of the transformation from the diamine reagent to the dicarboxylic linker by several functional group interconversion (FGI).

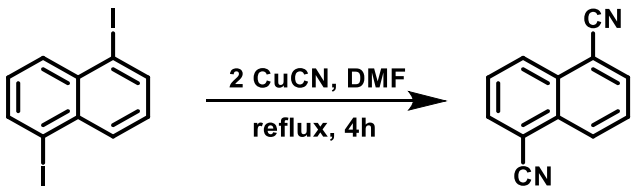
Synthesis of 1,5-diiodonaphthalene



Scheme S2. Scheme of the tetrazotization reaction of the diamine and the subsequent nucleophilic aromatic substitution by iodide.

1,5-diiodonaphthalene was synthesized according to a literature procedure.[63] A partial suspension of 1,5-diaminonaphtalene (12.014 g, 76 mmol) in H_2SO_4 (20 mL) and H_2O (300 mL) was treated at 0 ºC. Then, a solution of sodium nitrite (12.2345 g, 177 mmol) in H_2O (100 mL) was added. After 20 min, when the tetrazotization was completed, urea (2 g, 33.3 mmol) was added in order to remove the nitrous acid excess. The solution was filtered and then a solution of potassium iodide (20.2205 g, 122 mmol) in H_2O (200 mL) was added. The final product was extracted with AcOEt and evaporated at low pressure (18.9385 g, 66%). **^{1}H NMR (250 MHz, DMSO-d_6) δ** 8.25 (d, *J* = 7.3 Hz, 2H), 8.10 (d, *J* = 8.5 Hz, 2H), 7.42 (dd, *J* = 8.5, 7.3 Hz, 2H).

Synthesis of 1,5-dicyanonaphthalene

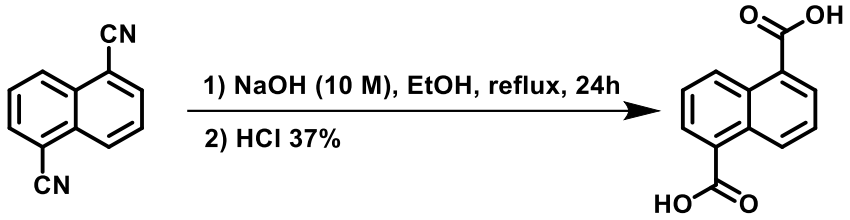


Scheme S3. Scheme of the nucleophilic aromatic substitution by cyanide.

1,5-dicyanonaphthalene was synthesized according to a similar literature procedure.[64] 1,5-diiodonaphthalene (5.0234 g, 13 mmol) and CuCN (2.5320 g, 28

mmol) were dissolved in 25 mL of DMF in a 100 mL round-bottom flask. The reaction was refluxed for 4 h. The resulting mixture was poured into a solution of hydrated ferric chloride (8.1902 g, 30.3 mmol) and conc. HCl (2 mL) of H_2O (12 mL). Then, the reaction was heated at 70 °C for 20 min to decompose the complex. Then, the product was extracted with toluene, washed with 10 mL of a 1:1 mixture solution ($HCl_{conc.}$:H_2O) and a 10% NaOH aqueous solution (1 g) in H_2O (9 mL). Finally, the product was filtered (1.7849g, 76%). **^{1}H NMR (250 MHz, DMSO-d_6) δ** 8.48 (d, *J* = 8.5 Hz, 2H), 8.40 (d, *J* = 7.3 Hz, 2H), 7.97 (dd, *J* = 8.5, 7.3 Hz, 2H).

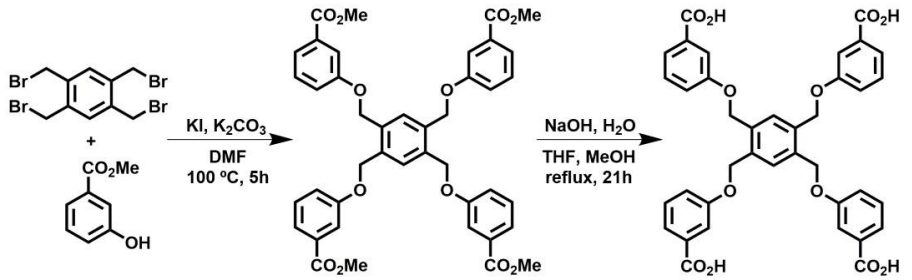
Synthesis of 1,5-naphthalenedicarboxylic acid ($H_2$1,5-NDC)



Scheme S4. Scheme of the hydrolysis on the dicyanide in basic conditions.

H_2(1,5-NDC) was synthesized according to a similar literature procedure.[65] 1,5-dicyanonaphthalene (1.0208 g, 5.73 mmol), 10 M NaOH aqueous solution (20.0345 g, 50 mL) and EtOH (75 mL) were added to a 250 mL round-bottom flask and refluxed for 24 h. After cooling to room temperature, $HCl_{conc.}$ was added until pH = 1. Then, the product was filtered and washed with H_2O and EtOH (0.7508 g, 61%). **^{1}H NMR (250 MHz, DMSO-d_6) δ** 9.04 (d, *J* = 8.7 Hz, 2H), 8.17 (d, *J* = 7.3 Hz, 2H), 7.71 (dd, *J* = 8.7, 7.3 Hz, 2H).

Synthesis of 3,3',3'',3'''-[1,2,4,5-phenyltetramethoxy]tetrabenzoic acid (H_4PTMTB)



Scheme S5. Synthetic procedure for H_4PTMTB linker.

Synthesis of tetramethyl 3,3',3'',3'''-[1,2,4,5-phenyltetramethoxy]tetrabenzoate

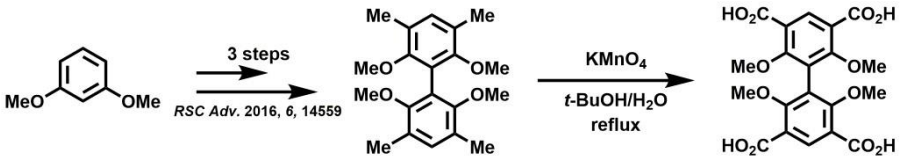
This compound was synthesized according to a similar literature procedure.[66] Methyl 3-hydroxybenzoate (1.15 g, 7.55 mmol) was dissolved in DMF (40 mL) under Ar atmosphere. KI (38.7 mg, 0.23 mmol) and K_2CO_3 (2.19 g, 15.88 mmol) were added to the solution. The solution was heated to 100 °C for 1 h. Then, a solution of 1,2,4,5-tetrakis(bromomethyl)benzene (0.66 g, 1.47 mmol) in DMF (15 mL) was added dropwise. The reaction was heated at 100 °C during 5 h, and then cooled to room temperature. After the addition of H_2O (350 mL) to the solution, a precipitate was formed, which was filtered, washed with H_2O and dried at 65 °C. The solid was heated to reflux overnight in MeOH (150 mL). Finally, it was filtered in hot, washed with MeOH and dried at 65 °C to afford a white solid (0.86 g, 79 %). **^{1}H NMR (300 MHz, $CDCl_3$) δ** 7.72 (s, 2H), 7.67 (d, *J* = 7.6 Hz, 8H), 7.35 (t, *J* = 7.9 Hz, 4H), 7.16 (m, 4H), 5.26 (s, 8H), 3.92 (s, 12H); **^{13}C NMR (75 MHz, $CDCl_3$) δ** 166.8 (C), 158.4 (C), 135.2 (C), 131.6 (CH), 129.9 (CH),129.6 (CH), 122.6 (C), 120.0 (CH), 115.1 (CH), 67.8 (CH_2), 52.2 (CH_3).

Synthesis of 3,3',3'',3'''-[1,2,4,5-phenyltetramethoxy]tetrabenzoic acid (H_4PTMTB)

Tetramethyl 3,3',3'',3'''-[1,2,4,5-phenyltetramethoxy]tetrabenzoate was suspended in a THF (200 mL) and MeOH (20 mL) mixture. An aqueous solution of NaOH (1.6

g, 40 mmol; 100 mL) was added and the reaction was heated at 90 °C for 21 h. It was then concentrated under reduced pressure, diluted with H_2O (100 mL) and washed with AcOEt (70 mL, discarded). Then, a 2N HCl solution was added dropwise to pH = 1, producing a white solid precipitate. The solid was filtered, washed with H_2O and dried at 65 °C to afford a white solid (0.61 g, 60 %). **^{1}H NMR (300 MHz, DMSO-d_6) δ** 12.97 (s, 4H), 7.75 (s, 2H), 7.54 (d, *J* = 8.3 Hz, 8H), 7.40 (t, *J* = 7.8 Hz, 4H), 7.27 (d, *J* = 6.9 Hz, 4H), 5.33 (s, 8H); **^{13}C NMR (75 MHz, $CDCl_3$) δ** 167.5 (C), 158.7 (C), 139.3 (C), 135.3 (CH), 132.7 (CH),130.2 (CH), 122.4 (C), 120.1 (CH), 115.5 (CH), 67.4 (CH_2).

Synthesis of 2,2',6,6'-tetramethoxy-[1,1'-biphenyl]-3,3',5,5'-tetracarboxylic acid (H_4TMBPTC)



Scheme S6. Synthetic procedure for H_4TMBPTC linker.

Synthesis of 2,2',6,6'-tetramethoxy-3,3',5,5'-tetramethyl-1,1'-biphenyl

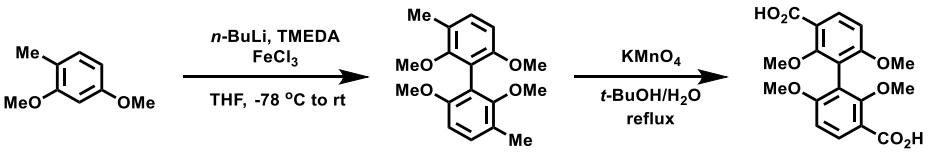
2,2',6,6'-tetramethoxy-3,3'-dimethyl-1,1'-biphenyl was synthesized according to a previous reported procedure.[67]

Synthesis of 2,2',6,6'-tetramethoxy-[1,1'-biphenyl]-3,3',5,5'-tetracarboxylic acid (H_4TMBPTC)

In a 50 mL round bottomed flask, 2,2',6,6'-tetramethoxy-3,3',5,5'-tetramethyl-1,1'-biphenyl (451.7 mg, 1.37 mmol, 1 equiv.) was placed and dissolved in a mixture of *t*-

BuOH:H_2O 1:1 (10+10 mL). Then, $KMnO_4$ (4.6 g, 29 mmol, 10 equiv.) was added and the solution was heated to reflux until the characteristic purple colour of $KMnO_4$ faded (approximately 7 h). The suspension was thereafter filtered over Celite, rinsed with the minimum amount of water, and concentrated under reduced pressure to dryness. HCl 2 M was added until acidic pH (<3) and it was concentrated again to dryness. Then, the white solid was dispersed in acetone, also adding anhydrous Na_2SO_4 to remove traces of water. The solution was filtered and concentrated under reduced pressure. Finally, the residue was purified by flash column chromatography using DCM:acetone mixtures (from 90:10 to 50:50) to afford 2,2',6,6'-tetramethoxy-[1,1'-biphenyl]-3,3',5,5'-tetracarboxylic acid (620.7 mg, 1.71 mmol, 59% yield). **^{1}H NMR (300 MHz, DMSO-d_6) δ** 8.24 (s, 2H), 3.59 (s, 12H); **^{13}C NMR (75 MHz, DMSO-d_6) δ** 166.1 (C), 161.3 (C), 134.8 (CH), 123.5 (C), 119.7 (C), 61.7 (CH_3).

Synthesis of 2,2',6,6'-tetramethoxy-[1,1'-biphenyl]-3,3'-dicarboxylic acid (H_2TMBPDC)



Scheme S7. Synthetic procedure for H_2TMBPDC linker.

Synthesis of 2,2',6,6'-tetramethoxy-3,3'-dimethyl-1,1'-biphenyl

2,4-Dimethoxy-1-methylbenzene (913 mg, 6 mmol, 1 equiv.) was weighted in an oven-dried Schlenk flask and it was subjected to vacuum/N_2 cycles (x3). Then, freshly distilled THF (10 mL) and dry TMEDA (1.08 mL, 7.2 mmol, 1.2 equiv.) were successively introduced via syringe. Thereafter, the solution was cooled down to -

78 °C and it was stirred at that temperature for 5 min. After this period, *n*-BuLi (4.2 mL, 1.6 M in THF, 6.6 mmol, 1.1 equiv.) was slowly added using a programmable pump (8.4 mL/h). Once the addition was completed, the resulting mixture was stirred 10 min at -78 °C and then, the bath was removed, allowing the solution to reach room temperature. After stirring the solution for 3 h at room temperature, a solution of anhydrous $FeCl_3$ (1.17 g, 7.2 mmol, 1.2 equiv.) in dry THF (10 mL) under N_2 was added via cannula, causing the solution to change from light yellow to dark red. This solution was further stirred for 16 h and then, quenched by the dropwise addition of HCl 10% (10 mL). Et_2O (30 mL) was also added, and the phases were separated. The aqueous phase was further extracted with Et_2O (2x20 mL) and the combined organic phases were dried over anhydrous $MgSO_4$, filtered and concentrated under reduced pressure. The oily residue was purified by flash column chromatography using hexane:EtOAc mixtures (from 95:5 to 90:10) as eluent, obtaining 2,2',6,6'-tetramethoxy-3,3'-dimethyl-1,1'-biphenyl (453.6 mg, 1.5 mmol, 50% yield). **^{1}H NMR (300 MHz, $CDCl_3$) δ** 7.15 (dq, *J* = 8.4, 0.7 Hz, 2H), 6.69 (d, *J* = 8.4 Hz, 2H), 3.72 (s, 6H), 3.41 (s, 6H), 2.28 (d, *J* = 0.7 Hz, 6H); **^{13}C NMR (75 MHz, $CDCl_3$) δ** 157.2 (C), 156.6 (C), 130.2 (CH), 123.2 (C), 117.8 (C), 106.4 (CH), 59.7 (CH_3), 56.0 (CH_3), 15.8 (CH_3).

Synthesis of 2,2',6,6'-tetramethoxy-[1,1'-biphenyl]-3,3'-dicarboxylic acid (H_2TMBPDC)

In a 50 mL round bottomed flask, 2,2',6,6'-tetramethoxy-3,3'-dimethyl-1,1'-biphenyl (876.7 mg, 2.9 mmol, 1 equiv.) was placed and dissolved in a mixture of *t*-BuOH:H_2O 1:1 (10+10 mL). Then, $KMnO_4$ (2.3 g, 14.5 mmol, 5 equiv.) was added and the solution was heated to reflux until the characteristic purple colour of $KMnO_4$ faded (approximately 5 h). The suspension was thereafter filtered over Celite, rinsed with the minimum amount of water, and concentrated under reduced pressure to dryness. HCl 2 M was added until acidic pH (<3) and it was concentrated

again to dryness. Then, the white solid was dispersed in acetone, also adding anhydrous Na_2SO_4 to remove traces of water. The solution was filtered and concentrated under reduced pressure. Finally, the residue was purified by flash column chromatography using DCM:acetone mixtures (from 90:10 to 50:50) to afford 2,2',6,6'-tetramethoxy-[1,1'-biphenyl]-3,3'-dicarboxylic acid (620.7 mg, 1.71 mmol, 59% yield). **^{1}H NMR (500 MHz, DMSO-d_6) δ** 7.83 (d, J = 8.7 Hz, 2H), 6.92 (d, J = 8.8 Hz, 2H), 3.71 (s, 6H), 3.44 (s, 6H); **^{13}C NMR (125 MHz, DMSO-d_6) δ** 166.7 (C), 160.9 (C), 159.1 (C), 132.5 (CH), 117.8 (C), 117.4 (C), 106.4 (CH), 61.1 (CH_3), 55.8 (CH_3).

Synthesis of $Fe_3(\mu_3\text{-}O)(AcO)_6$

$Fe_3(\mu_3\text{-}O)$ $(CH_3COO)_6$ was prepared according to reported procedure.[68] A solution of sodium acetate trihydrate (42.0 g, 0.31 mol) in water (70 mL) was added to a filtered stirred solution of iron(III) nitrate nonahydrate (48.5 g, 0.12 mol) in 70 mL of deionized water. The solution was concentrated using a rotary evaporator to allow the precipitation of a brown solid that was filtered off, washed with water and with EtOH and dried in air.

Synthesis of Cu-sql-3,3'-ABDC

$Cu(NO_3)_2{\cdot}2H_2O$ (0.5 mL of a 0.2 M DMF solution, 0.1 mmol, 23.2 mg) and H_2(3,3'-ABDC) (0.5 mL of a 0.2 M DMF solution, 0.1 mmol, 27 mg) were added in a 23 mL scintillation vial. After heating at 85 ^{o}C for 24 h, green needle-like crystals suitable for SCXRD were formed.

Synthesis of Tb-fcu-3,3'-BPDC

$Tb(NO_3)_3{\cdot}5H_2O$ (0.22 mL of a 0.1 M DMF solution, 0.022 mmol, 9.5 mg), H_2(3,3'-BPDC) (0.11 mL of a 0.1 M DMF solution, 0.011 mmol, 2.7 mg) and 2-FBA (0.04

mL of a 10 M DMF solution, 0.4 mmol, 56 mg) were added in a 23 mL scintillation vial. Then, DMF (1.7 mL) and H_2O (0.5 mL) were added to the vial. After heating at 120 °C for 48 h, transparent octahedral crystals suitable for SCXRD were formed.

Synthesis of Fe-acs-1,5-NDC

$Fe_3(\mu\text{-}O)(AcO)_6$ (0.2 mL of a 0.2 M DMF solution, 0.04 mmol, 18.6 mg) and H_2(1,5-NDC) (1.2 mL of a 0.1 M DMF solution, 0.12 mmol, 26 mg) were added in a 23 mL scintillation vial. Then, DMF (0.6 mL) and AcOH (0.4 mL) were added to the vial. After heating at 120 °C for 48 h, orange hexagonal crystals suitable for SCXRD were formed.

Synthesis of $Cu_2(PTMTB)(H_2O)_2$

$Cu(NO_3)_2{\cdot}2.5H_2O$ (12 mg, 0.05 mmol) and H_4PTMTB (27 mg, 0.04 mmol) in DMF (1 mL) and HBF_4 (0.1 mL) was prepared in a 23 mL scintillation vial. Then, the sealed vial was placed into a preheated oven at 85 °C for 24 h. After this period, blue square-shaped crystals suitable for SCXRD were collected by filtration and washed three times by incubating them with 20 mL of fresh DMF for 12 h.

Synthesis of $Cu_2(TMBPTC)(H_2O)_2$

$Cu(NO_3)_2{\cdot}2.5H_2O$ (24 mg, 0.1 mmol) and H_4TMBPTC (45 mg, 0.1 mmol) in DMF (1 mL) was prepared in a 23 mL scintillation vial. Then, the sealed vial was placed into a preheated oven at 85 °C for 24 h. After this period, green needle-shaped crystals suitable for SCXRD were collected by filtration and washed three times by incubating them with 20 mL of fresh DMF for 12 h.

Synthesis of $Cu(TMBPDC)(H_2O)$

$Cu(NO_3)_2{\cdot}2.5H_2O$ (24 mg, 0.1 mmol) and H_2TMBPDC (37 mg, 0.1 mmol) in DMF (1 mL) and H_2O (1 mL) was prepared in a 23 mL scintillation vial. Then, the sealed

vial was placed into a preheated oven at 85 ºC for 24 h. After this period, green needle-shaped crystals suitable for SCXRD were collected by filtration and washed three times by incubating them with 20 mL of fresh DMF for 12 h.

4.3.1.4. Characterization

Single-Crystal X-Ray Diffraction (SCXRD) data for Cu-**sql**-3,3'-ABDC, Tb-**fcu**-3,3'-BPDC, Fe-**acs**-1,5-NDC, $Cu_2(PTMTB)(H_2O)_2$, $Cu_2(TMBPTC)(H_2O)_2$, and $Cu_2(TMBPDC)_2(H_2O)_2$ were collected at 100 K at XALOC beamline at ALBA synchrotron (0.82656 Å).[69] Data were indexed, integrated and scaled using the XDS program.[70] Absorption correction was not applied. The structures were solved by direct methods and subsequently refined by correction of F2 against all reflections, using SHELXT2018 within Olex2 package.[71–73] All non-hydrogen atoms were refined with anisotropic thermal parameters by full-matrix least-squares calculations on F2 using the program SHELXL2018.[71] We treated the presence of solvent molecules in the cavities of all structures running solvent mask using Olex2 solvent mask.[73] The hydrogen atoms were calculated in their expected positions with the HFIX instruction of SHELXL2018, and refined as riding atoms with Uiso(H) = 1.5 Ueq(C).

Powder X-Ray Diffraction (PXRD) diagrams were collected on a Panalytical X'pert mpd diffractometer with monochromatic Cu-Kα radiation (λ_{Cu} = 1.5406 Å).

Proton Nuclear Magnetic Resonance (^{1}H NMR) spectra were acquired in Bruker Avance NEO of 300 MHz NMR spectrometer at "Servei de Ressonància Magnètica Nuclear" from Autonomous University of Barcelona (UAB), and in Bruker Avance NEO of 300 MHz, 500 MHz NMR spectrometers at "Servei Central de Suport a la Investigació Experimental (SCIE)" from University of València (UV).

Carbon Nuclear Magnetic Resonance (^{13}C NMR) spectra were acquired in Bruker Avance NEO of 300 MHz, 500 MHz NMR spectrometers at "Servei Central de Suport a la Investigació Experimental (SCIE)" from University of València (UV).

4.3.2. ^{1}H and ^{13}C Nuclear Magnetic Resonance

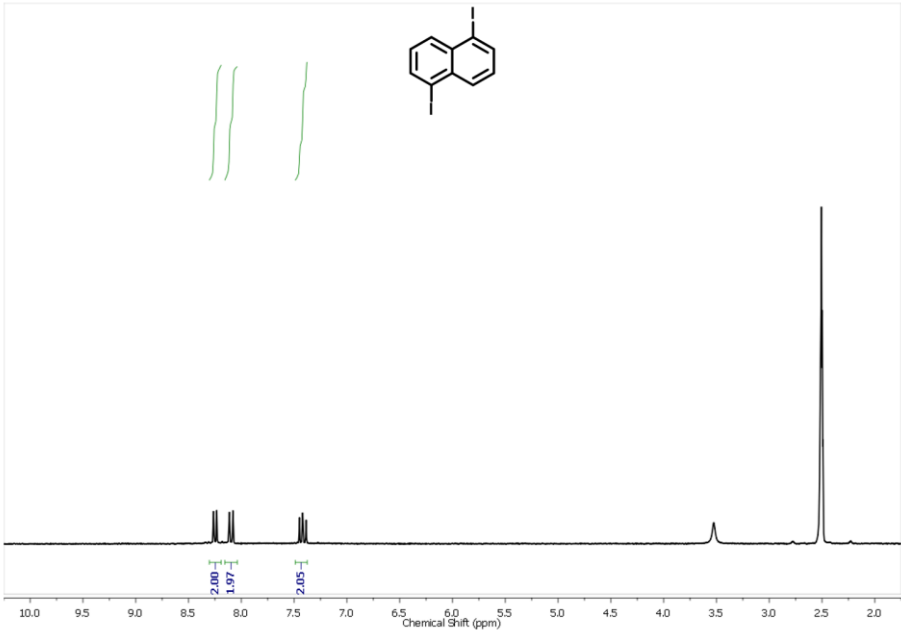


Figure 4.31. ^{1}H NMR spectrum (250 MHz, DMSO-d_6) of 1,5-diiodonaphthalene.

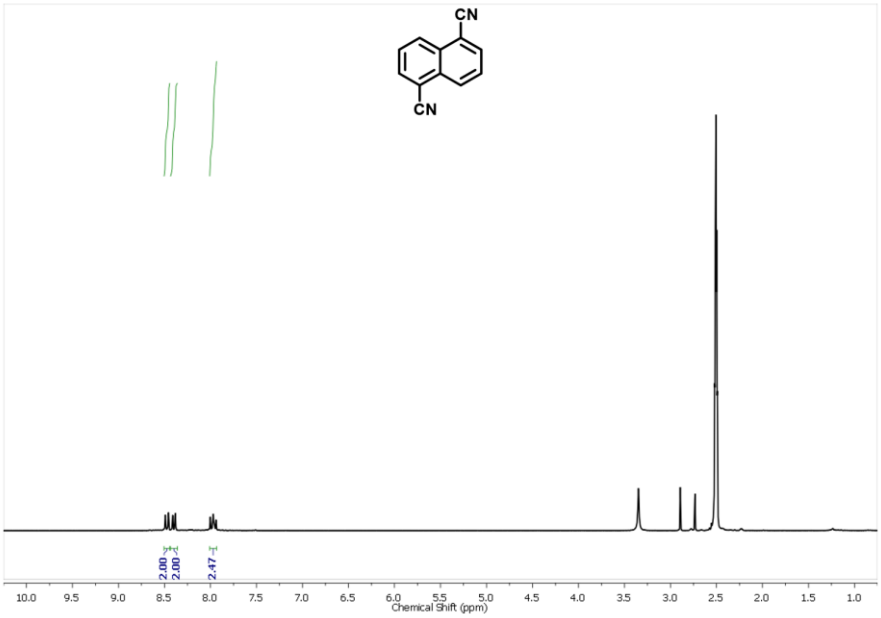


Figure 4.32. ^{1}H NMR spectrum (250 MHz, DMSO-d_6) of 1,5-dicyanonaphthalene.

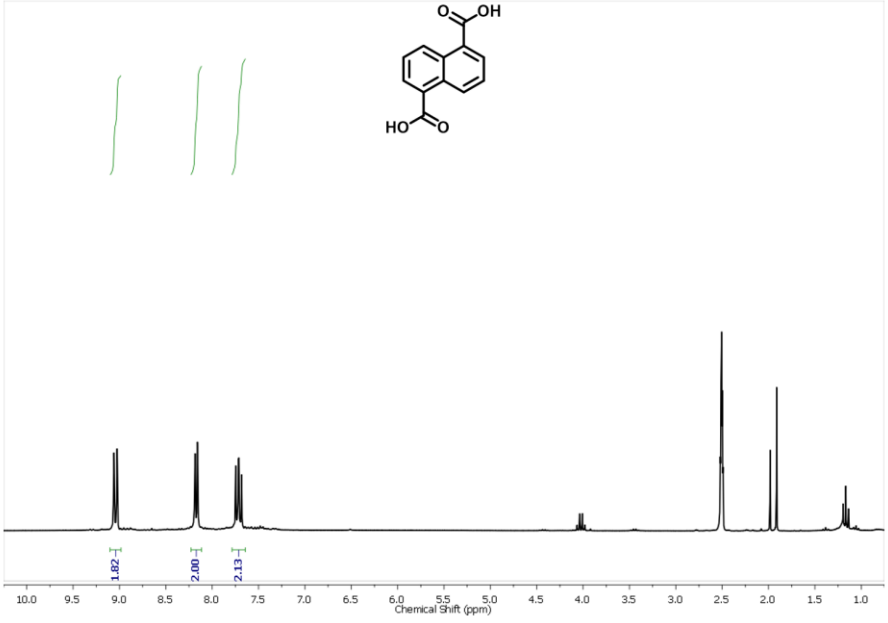


Figure 4.33. ^{1}H NMR spectrum (250 MHz, DMSO-d_6) of $H_2$1,5-NDC.

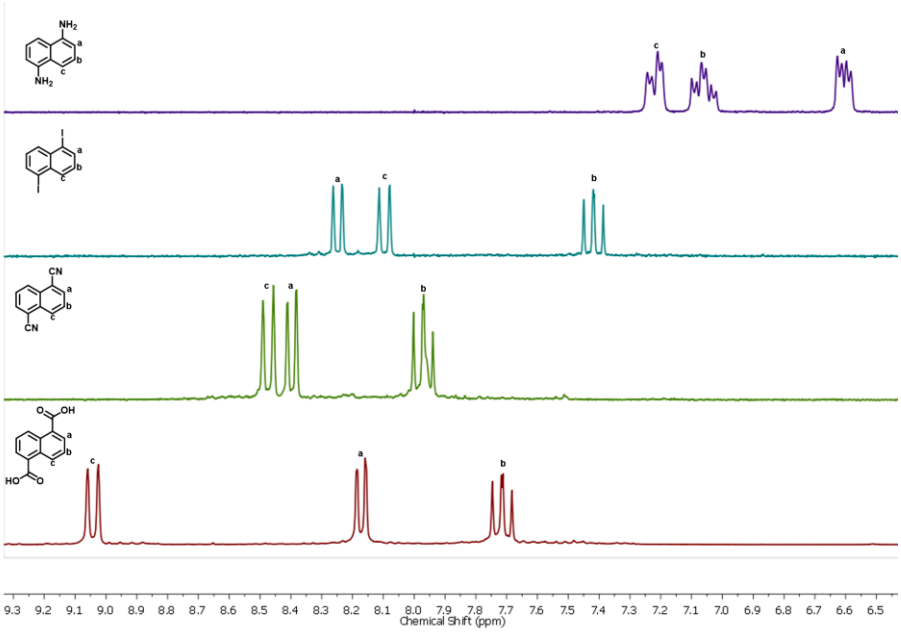


Figure 4.34. Stacked ^{1}H NMR spectra of the evolution of the signals during the synthetic procedure of $H_2$1,5-NDC in DMSO-d_6. Note that through the functional group interconversion to more electro-withdrawing groups the NMR signals shift to higher values, specially the H_c in a *peri* position showing the *peri* effect due to a bigger steric hindrance.

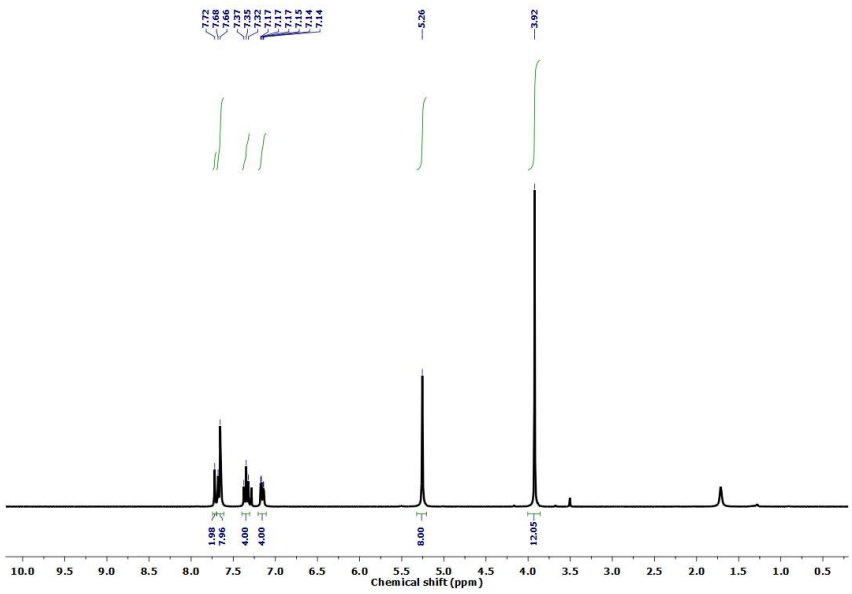


Figure 4.35. ^{1}H NMR spectrum (300 MHz, $CDCl_3$) of tetramethyl 3,3',3'',3'''-[1,2,4,5-phenyltetramethoxy]tetrabenzoate.

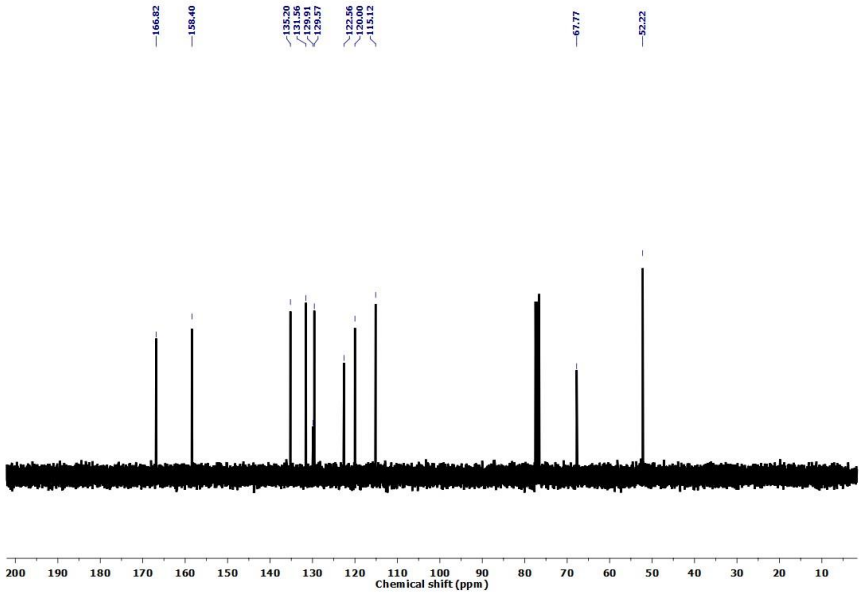


Figure 4.36. ^{13}C NMR spectrum (75 MHz, $CDCl_3$) of tetramethyl 3,3',3'',3'''-[1,2,4,5-phenyltetramethoxy]tetrabenzoate.

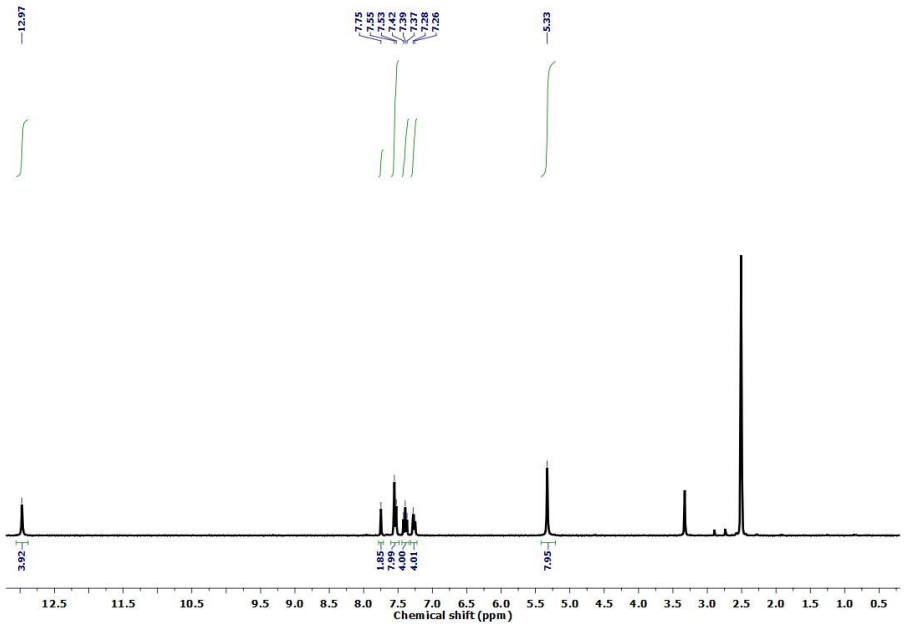


Figure 4.37. ^{1}H NMR spectrum (300 MHz, DMSO-d_6) of H_4PTMTB.

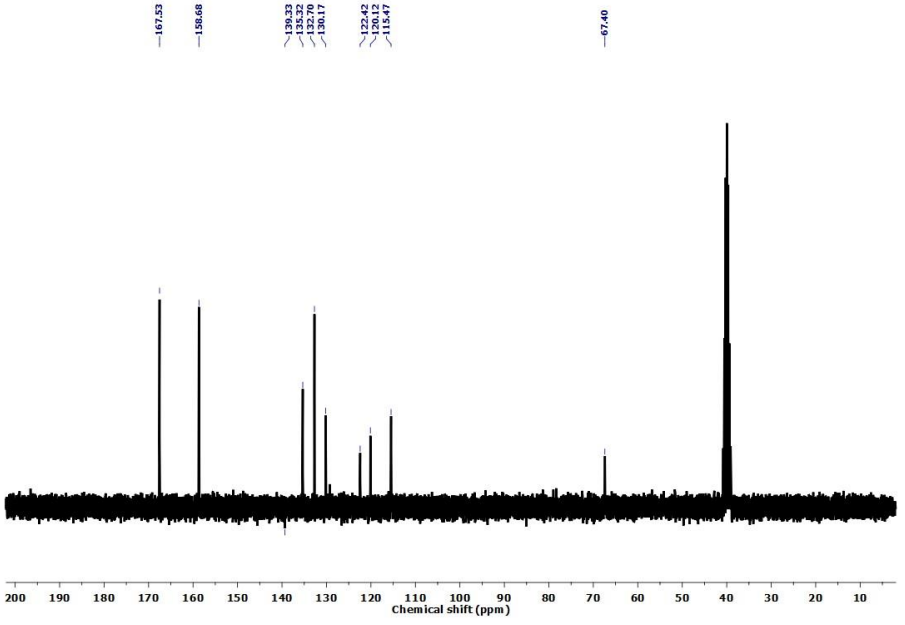


Figure 4.38. ^{13}C NMR spectrum (75 MHz, $CDCl_3$) of H_4PTMTB.

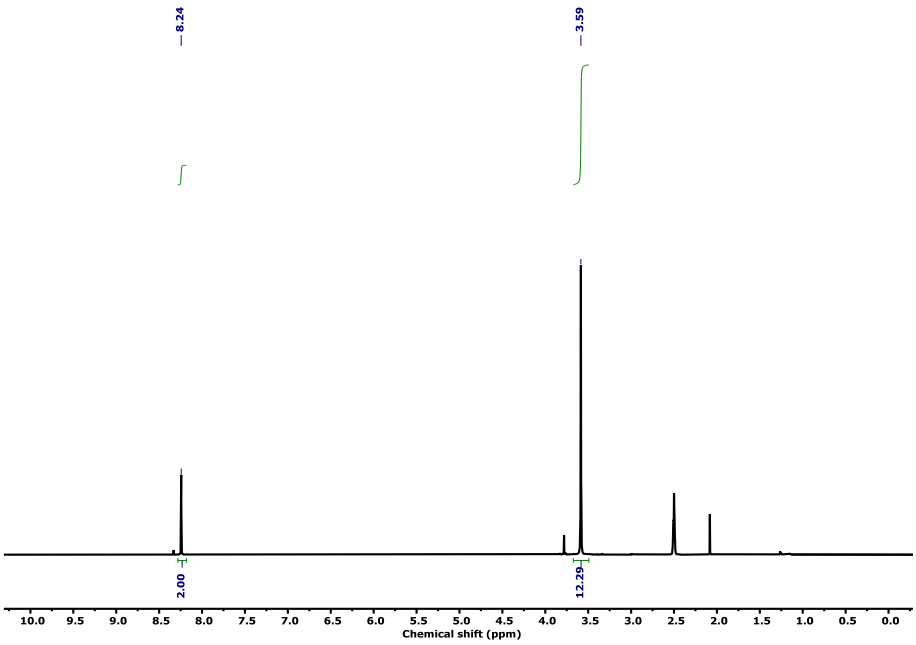


Figure 4.39. ^{1}H NMR spectrum (300 MHz, DMSO-d_6) of H_4TMBPTC.

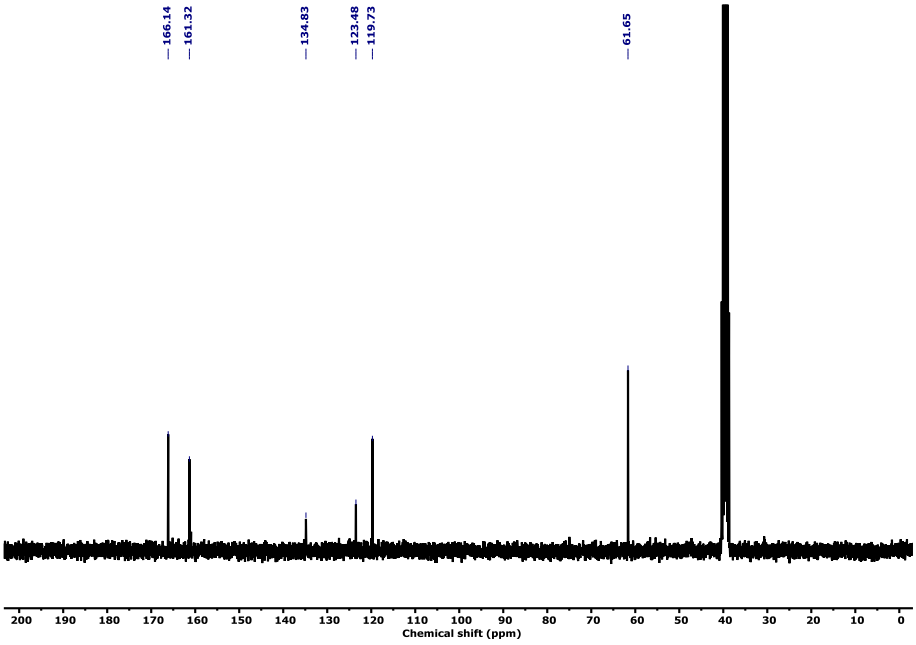


Figure 4.40. ^{13}C NMR spectrum (75 MHz, DMSO-d_6) of H_4TMBPTC.

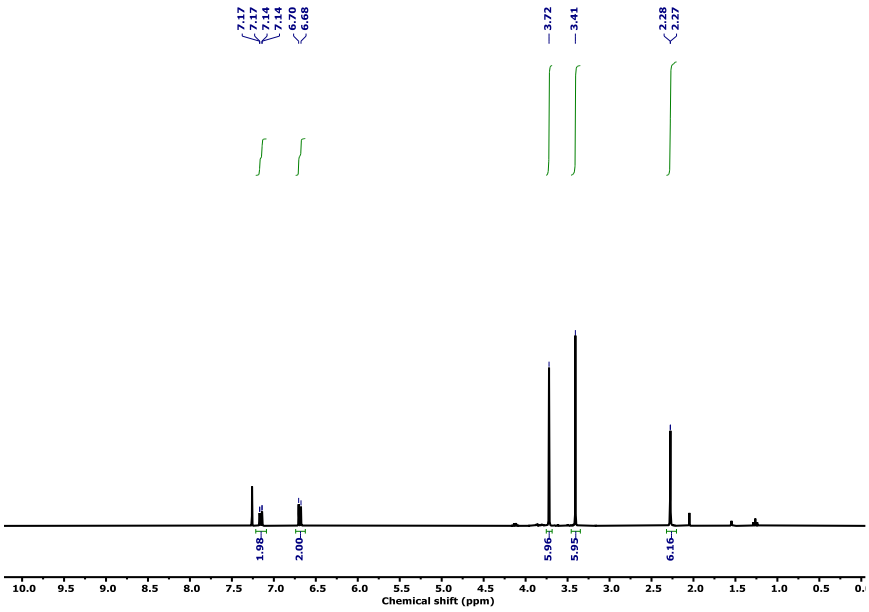


Figure 4.41. ^{1}H NMR spectrum (300 MHz, $CDCl_3$) of 2,2',6,6'-tetramethoxy-3,3'-dimethyl-1,1'-biphenyl.

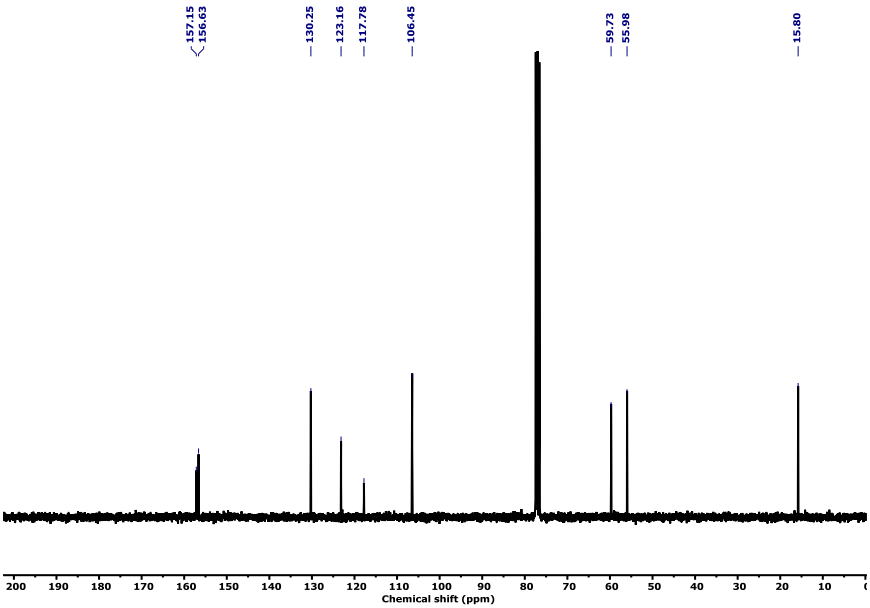


Figure 4.42. ^{13}C NMR spectrum (75 MHz, $CDCl_3$) of 2,2',6,6'-tetramethoxy-3,3'-dimethyl-1,1'-biphenyl.

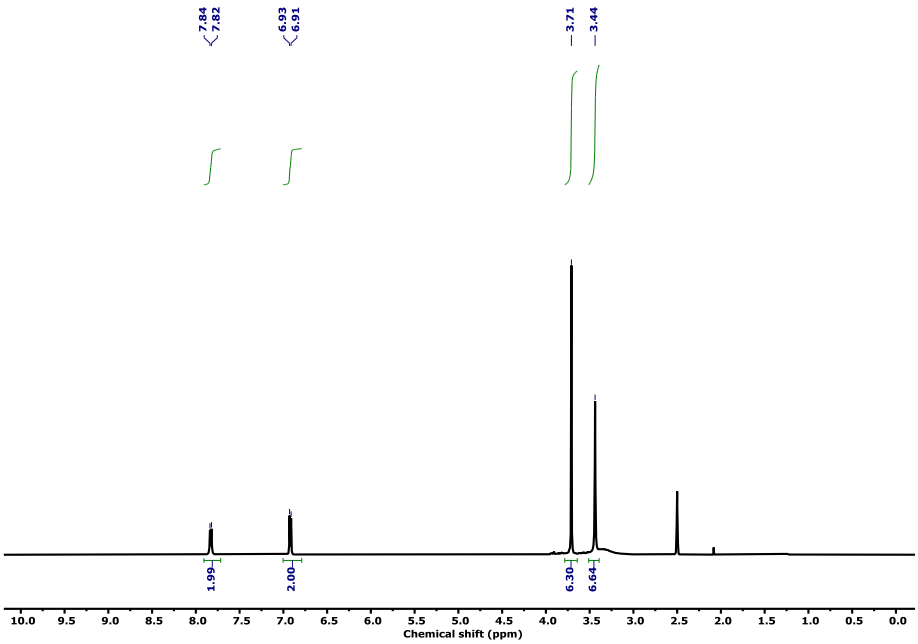


Figure 4.43. ^{1}H NMR spectrum (500 MHz, DMSO-d_6) of H_2TMBPDC.

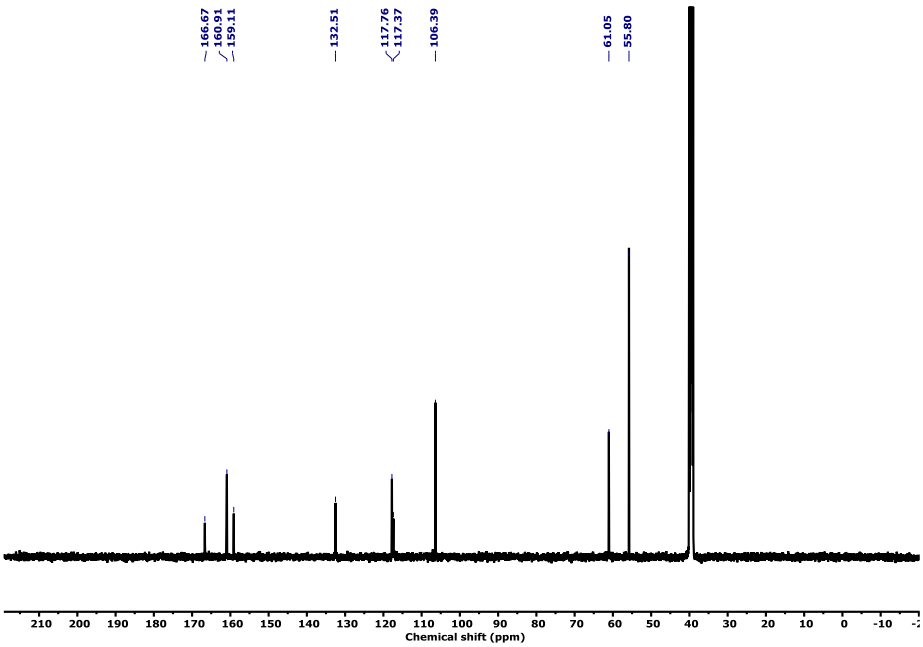


Figure 4.44. ^{13}C NMR spectrum (125 MHz, DMSO-d_6) of H_2TMBPDC.

4.3.3. Single-Crystal X-Ray Diffraction

Table 4.7. Crystal data and structure refinement for Cu-sql-3,3'-ABDC

Identification code	CCDC-1990888
Empirical formula	$C_{17}H_{15}CuN_3O_5$
Formula weight	1928.7
Temperature/K	100
Crystal system	Monoclinic
Space group	*C2/m*
a/Å	10.170(5)
b/Å	18.680(5)
c/Å	10.350(5)
α/°	90
β/°	101.22(5)
γ/°	90
Volume/Å^3	404.87
Z	4
ρ_{calc}g/cm^3	1.384
F(000)	828
Crystal size/mm^3	0.36 × 0.33 × 0.31
Radiation	synchrotron (λ = 0.82653)
2Θ range for data collection/°	2.333 to 33.863
Index ranges	-12 ≤ h ≤ 12, -24 ≤ k ≤ 24, -12 ≤ l ≤ 12
Tot., uniq. data, R(int)	13038, 2211, 0.0622
Observed data [I > 4.0 sigma(I)]	2057
Nref, Npar	2211, 144

Table 4.8. Crystal data and structure refinement for Tb-fcu-3,3'-BPDC

Identification code	CCDC-1990889
Empirical formula	$C_{42}H_{24}O_{18}Tb_3$
Formula weight	1293.4
Temperature/K	100
Crystal system	Monoclinic
Space group	$P2_1/n$
a/Å	17.290(5)
b/Å	17.430(5)
c/Å	24.110(5)
α/°	90
β/°	91.22(5)
γ/°	90
Volume/Å^3	1293.4
Z	4
ρ_{calc}g/cm^3	1.384
F(000)	828
Crystal size/mm^3	0.15 × 0.14 × 0.13
Radiation	synchrotron (λ = 0.82653)
2Θ range for data collection/°	1.669 to 34.035
Index ranges	-23 ≤ h ≤ 23, -21 ≤ k ≤ 21, -30 ≤ l ≤ 30
Tot., uniq. data, R(int)	92.168, 14980, 0.0540
Observed data [I > 4.0 sigma(I)]	13778
Nref, Npar	2211, 532
R, wR2, S	0.0440, 0.1244, 1.098

Table 4.9. Crystal data and structure refinement for Fe-acs-1,5-NDC

Identification code	CCDC-1990887
Empirical formula	$C_{48}H_{45}ClFe_3KN_3O_{18}$
Formula weight	1193.4
Temperature/K	100
Crystal system	Hexagonal
Space group	$P6_3/m$
a/Å	12.790(5)
b/Å	12.790(5)
c/Å	19.510(5)
α/°	90
β/°	90
γ/°	120
Volume/Å^3	1293.4
Z	2
ρ_{calc}g/cm^3	1.435
F(000)	1224
Crystal size/mm^3	0.25 × 0.22 × 0.21
Radiation	synchrotron (λ = 0.82653)
2Θ range for data collection/°	2.183 to 33.872
Index ranges	-17 ≤ h ≤ 17, -17 ≤ k ≤ 17, -26 ≤ l ≤ 26
Tot., uniq. data, R(int)	33698, 2229, 0.0619
Observed data [I > 4.0 sigma(I)]	13778
Nref, Npar	2229, 132
R, wR2, S	0.06651, 0.2093, 1.135

Table 4.10. Crystal data and structure refinement for $Cu_2(PTMTB)(H_2O)_2$

Identification code	CCDC-2270219
Empirical formula	$C_{23.38}H_{16}Cu_{1.23}O_{7.38}$
Formula weight	493.33
Temperature/K	100
Crystal system	Orthorhombic
Space group	*Cmce*
a/Å	32.415(3)
b/Å	23.5559(3)
c/Å	16.0326(2)
α/°	90
β/°	90
γ/°	90
Volume/Å^3	12241.8(13)
Z	13
ρ_{calc}g/cm^3	0.870
μ/mm^{-1}	1.101
F(000)	3264.0
Crystal size/mm^3	0.11 × 0.1 × 0.08
Radiation	synchrotron (λ = 0.82653)
2Θ range for data collection/°	3.86 to 67.616
Index ranges	$0 \le h \le 43$, $0 \le k \le 29$, $-20 \le l \le 0$
Reflections collected	73235
Independent reflections	7164 [R_{int} = 0.1582, R_{sigma} = 0.1028]
Data/restraints/parameters	7164/10/226
Goodness-of-fit on F^2	1.065
Final R indexes [I>=2σ (I)]	R_1 = 0.1077, wR_2 = 0.2922
Final R indexes [all data]	R_1 = 0.1156, wR_2 = 0.2957
Largest diff. peak/hole / e Å^{-3}	1.73/-0.97

Table 4.11. Crystal data and structure refinement for $Cu_2(TMBPTC)(H_2O)_2$

Identification code	CCDC-2270218
Empirical formula	$C_{26}H_{28}Cu_2N_2O_{14}$
Formula weight	719.58
Temperature/K	100
Crystal system	Monoclinic
Space group	*C2/c*
a/Å	34.7885(7)
b/Å	11.2616(2)
c/Å	20.4116(4)
α/°	90
β/°	123.683(2)
γ/°	90
Volume/$Å^3$	6654.2(3)
Z	8
$\rho_{calc}g/cm^3$	1.437
μ/mm^{-1}	2.020
F(000)	2944.0
Crystal size/mm^3	0.08 × 0.08 × 0.07
Radiation	synchrotron (λ = 0.82656)
2Θ range for data collection/°	3.272 to 52.778
Index ranges	-35 ≤ h ≤ 31, 0 ≤ k ≤ 12, 0 ≤ l ≤ 21
Reflections collected	25884
Independent reflections	4166 [R_{int} = 0.2282, R_{sigma} = 0.1471]
Data/restraints/parameters	4166/134/381
Goodness-of-fit on F^2	1.083
Final R indexes [I>=2σ (I)]	R_1 = 0.0797, wR_2 = 0.2317
Final R indexes [all data]	R_1 = 0.1005, wR_2 = 0.2420
Largest diff. peak/hole / e $Å^{-3}$	2.11/-0.73

Table 4.12. Crystal data and structure refinement for Cu(TMBPDC)(H_2O)

Identification code	CCDC-2270220
Empirical formula	$C_{21}H_{23}CuNO_9$
Formula weight	496.94
Temperature/K	100
Crystal system	Monoclinic
Space group	$P2_1/c$
a/Å	11.306(4)
b/Å	14.8702(3)
c/Å	13.0779(4)
α/°	90
β/°	108.499(2)
γ/°	90
Volume/Å^3	2085.1(7)
Z	1
ρ_{calc}g/cm^3	1.583
μ/mm^{-1}	1.655
F(000)	1028.0
Crystal size/mm^3	0.09 × 0.08 × 0.06
Radiation	synchrotron (λ = 0.82656)
2Θ range for data collection/°	4.418 to 67.888
Index ranges	-12 ≤ h ≤ 11, -18 ≤ k ≤ 0, -17 ≤ l ≤ 16
Reflections collected	26209
Independent reflections	4377 [R_{int} = 0.1020, R_{sigma} = 0.0947]
Data/restraints/parameters	4377/0/295
Goodness-of-fit on F^2	1.094
Final R indexes [I>=2σ (I)]	R_1 = 0.0484, wR_2 = 0.1433
Final R indexes [all data]	R_1 = 0.0555, wR_2 = 0.1484
Largest diff. peak/hole / e Å^{-3}	0.64/-1.44

4.4. Conclusions

In this Chapter, we have proposed and validated a new top-down approach, net-clipping, to unveil the different nets that should be accessible for the rational design of MOFs assembled from less-symmetric, organic MBBs. Our approach is based on the de-reticulation of MOFs and edge-transitive nets by clipping MBBs or nodes of higher connectivity and symmetry by half. We applied net-clipping to edge-transitive nets made of 4-c square/rectangular, 4-c tetrahedral, 6-c hexagonal, 8-c cubic, and 12-c hexagonal prismatic linkers, anticipating the formation of 141 derived nets and 56 clipped nets. Among them, 33 new derived nets (*icn*7–*icn*39) and 6 new clipped nets (*icn*1–*icn*6) were not previously described. The discovery of all these nets underscores the potential of net-clipping for the discovery and rational design of MOFs exhibiting new underlying topologies.

First, we applied net-clipping to 4-c square/rectangular MBBs, demonstrating the relationship between these linkers and their clipped zigzag linkers. We studied the edge-transitive nets with 4-c nodes with an associated square vertex figure, and their derived nets, to identify the possible outcomes, predicting the different nets that should be accessible upon assembly of zigzag linkers with different polyhedral MBBs. We demonstrated the feasibility of net-clipping for the obtention of MOFs based of zigzag linkers combined with five different inorganic MBBs through literature examples and the successful design and assembly of three novel MOFs: Cu-**sql**-3,3′-ABDC (4-c, paddle-wheel), Fe-**acs**-1,5-NDC(6-c, trimer), and Tb-**fcu**-3,3′-BPDC (12-c, hexamer), being one of them predicted without any evidence of the corresponding MOF constructed with higher connected MBBs.

Then, we generalized and extended our approach to higher connected/symmetric MBBs. We corroborated through literature examples and our experimental findings that this study could be translated from zigzag MBBs to six additional less-symmetric MBBs, supporting with several examples all the clipping modes exposed for the different MBBs with pairs of MOFs related by net-clipping. Moreover, we

first demonstrated that the use of net-clipping can also be extended to less regular, non-edge transitive nets, a fact that will surely increase the discovery of available topologies in a near future. However, this process will require the study of thousands of complex topologies, representing an exciting challenge for simulation tools.

Finally, we postulated that net-clipping could also be applied to other kind of reticular materials such as covalent–organic frameworks (COFs), which we corroborated through a brief literature survey. The 2D **kgd** COF-360 is an imine-linked COF created by linking the 6-c hexagonal hexaformylphenyl benzene (HFPB) linker and the 3-c triangular 1,3,5-tris(*p*-aminophenyl)benzene (TAPB) linker.[74] From our study, we expected the clipped net to exhibit an **hcb-b** topology, which is precisely what had been observed for TFPB-TAPB-COF, a COF synthesized by imine-based linkage of TAPB and the 3-c triangular 1,3,5-tris(4-formylphenyl)benzene (TFPB), the latter linker being the clipped version of HFPB (Figure 4.45).[75]

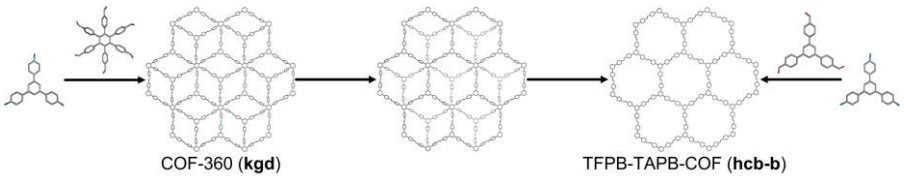


Figure 4.45. Schematic of the net-clipping approach applied to the formation of reticular materials hexagonal HFPB ligand to trigonal TFPB combined with 3-c triaminephenilbenzene MBBs.

Thus, we are confident that net-clipping will continue to inform the design of future porous materials such as MOFs and COFs, by enabling the assembly of new, otherwise inaccessible topologies. Our approach enriches the repertoire for topological predictions, providing new tools for the rational design of more complex reticular materials. In fact, the design of materials with less-symmetric linkers and their relation with higher connected structures has been recently pointed in TRUMOF-1,[76] relating a bent linker with the corresponding 3-c

triangular linker, which can be considered as another example of net-clipping, proving why some MBBs are not targeted for the net-clipping approach, obtaining an aperiodic crystalline MOF. Moreover, the study of the orientation of linkers has been another key point for getting deeper insights in understanding the structure-property relationship in periodic materials. We believe that our findings will be essential for the development of made-to-order materials, and we anticipate the expansion of our approach to even more sophisticated systems.

4.5. References

(1) Yaghi, O. M.; O'Keeffe, M.; Ockwig, N. W.; Chae, H. K.; Eddaoudi, M.; Kim, J. Reticular Synthesis and the Design of New Materials. *Nature* **2003**, *423*, 705–714.

(2) Stein, A.; Keller, S. W.; Mallouk, T. E. Turning down the Heat: Design and Mechanism in Solid-State Synthesis. *Science* **1993**, *259*, 1558–1564.

(3) Eddaoudi, M.; Moler, D. B.; Li, H.; Chen, B.; Reineke, T. M.; O'Keeffe, M.; Yaghi, O. M. Modular Chemistry: Secondary Building Units as a Basis for the Design of Highly Porous and Robust Metal-Organic Carboxylate Frameworks. *Acc. Chem. Res.* **2001**, *34*, 319–330.

(4) O'Keeffe, M.; Yaghi, O. M. Deconstructing the Crystal Structures of Metal-Organic Frameworks and Related Materials into Their Underlying Nets. *Chem. Rev.* **2012**, 112, 675–702.

(5) O'Keeffe, M.; Peskov, M. A.; Ramsden, S. J.; Yaghi, O. M. The Reticular Chemistry Structure Resource (RCSR) Database of, and Symbols for, Crystal Nets. *Acc. Chem. Res.* **2008**, *41*, 1782–1789.

(6) Delgado-Friedrichs, O.; O'Keeffe, M.; Yaghi, O. M. Taxonomy of Periodic Nets and the Design of Materials. *Phys. Chem. Chem. Phys.* **2007**, *9*, 1035–1043.

(7) Wells, A. F. Three-Dimensional Nets and Polyhedral, Wiley, Hoboke, **19**77.

(8) Nouar, F.; Eubank, J. F.; Bousquet, T.; Wojtas, L.; Zaworotko, M. J.; Eddaoudi, M. Supermolecular Building Blocks (SBBs) for the Design and Synthesis of Highly Porous Metal-Organic Frameworks. *J. Am. Chem. Soc.* **2008**, *130*, 1833–1835.

(9) Perry IV, J. J.; Perman, J. A.; Zaworotko, M. J. Design and Synthesis of Metal–Organic Frameworks Using Metal–Organic Polyhedra as Supermolecular Building Blocks. *Chem. Soc. Rev.* **2009**, *38*, 1400–1417.

(10) Krause, S.; Bon, V.; Stoeck, U.; Senkovska, I.; Többens, D. M.; Wallacher, D.; Kaskel, S. A Stimuli-Responsive Zirconium Metal–Organic Framework Based on Supermolecular Design. *Angew. Chem. Int. Ed.* **2017**, *56*, 10676–10680.

(11) Eubank, J. F.; Mouttaki, H.; Cairns, A. J.; Belmabkhout, Y.; Wojtas, L.; Luebke, R.; Alkordi, M.; Eddaoudi, M. The Quest for Modular Nanocages: Tbo -MOF as an Archetype for Mutual Substitution, Functionalization, and Expansion of Quadrangular Pillar Building Blocks. *J. Am. Chem. Soc.* **2011**, *133*, 14204–14207.

(12) Eubank, J. F.; Wojtas, L.; Hight, M. R.; Bousquet, T.; Kravtsov, V. C.; Eddaoudi, M. The next Chapter in MOF Pillaring Strategies: Trigonal Heterofunctional Ligands to Access Targeted High-Connected Three Dimensional Nets, Isoreticular Platforms. *J. Am. Chem. Soc.* **2011**, *133*, 17532–17535.

(13) Ma, B. Q.; Mulfort, K. L.; Hupp, J. T. Microporous Pillared Paddle-Wheel Frameworks Based on Mixed-Ligand Coordination of Zinc Ions. *Inorg. Chem.* **2005**, *44*, 4912–4914.

(14) Jiang, H.; Jia, J.; Shkurenko, A.; Chen, Z.; Adil, K.; Belmabkhout, Y.; Weselinski, L. J.; Assen, A. H.; Xue, D. X.; O'Keeffe, M.; Eddaoudi, M. Enriching the Reticular Chemistry Repertoire: Merged Nets Approach for the Rational Design of Intricate Mixed-Linker Metal-Organic Framework Platforms. *J. Am. Chem. Soc.* **2018**, *140*, 8858–8867.

(15) Eddaoudi, M.; Kim, J.; Vodak, D.; Sudik, A.; Wachter, J.; O'Keeffe, M.; Yaghi, O. M. Geometric Requirements and Examples of Important Structures in the Assembly of Square Building Blocks. *Proc. Nat. Acad. Sci. U. S. A.* **2002**, *99*, 4900–4904.

(16) Eddaoudi, M.; Kim, J.; O'Keeffe, M.; Yaghi, O. M. $Cu_2[o\text{-}BrC_6H_3(CO_2)_2]_2(H_2O)_2{\cdot}(DMF)_8(H_2O)_2$: A Framework Deliberately Designed to Have the NbO Structure Type. *J. Am. Chem. Soc.* **2002**, *124*, 376–377.

(17) Guillerm, V.; Grancha, T.; Imaz, I.; Juanhuix, J.; Maspoch, D. Zigzag Ligands for Transversal Design in Reticular Chemistry: Unveiling New Structural Opportunities for Metal-Organic Frameworks. *J. Am. Chem. Soc.* **2018**, *140*, 10153–10157.

(18) Schnobrich, J. K.; Lebel, O.; Cychosz, K. A.; Dailly, A.; Wong-Foy, A. G.; Matzger, A. J. Linker-Directed Vertex Desymmetrization for the Production of Coordination Polymers with High Porosity. *J. Am. Chem. Soc.* **2010**, *132*, 13941–13948.

(19) Guillerm, V.; Maspoch, D. Geometry Mismatch and Reticular Chemistry: Strategies to Assemble Metal-Organic Frameworks with Non-Default Topologies. *J. Am. Chem. Soc.* **2019**, *141*, 16517–16538.

(20) Haase, F.; Craig, G. A.; Bonneau, M.; Sugimoto, K.; Furukawa, S. Pseudo-5-Fold-Symmetrical Ligand Drives Geometric Frustration in Porous Metal-Organic and Hydrogen-Bonded Frameworks. *J. Am. Chem. Soc.* **2020**, *142*, 13839–13845.

(21) Wang, H.; Dong, X.; Lin, J.; Teat, S. J.; Jensen, S.; Cure, J.; Alexandrov, E. V.; Xia, Q.; Tan, K.; Wang, Q.; Olson, D. H.; Proserpio, D. M.; Chabal, Y. J.; Thonhauser, T.; Sun, J.; Han, Y.; Li, J. Topologically Guided Tuning of Zr-MOF Pore Structures for Highly Selective Separation of C6 Alkane Isomers. *Nat. Commun.* **2018**, *9*, 1–11.

(22) Bon, V.; Senkovska, I.; Baburin, I. A.; Kaskel, S. Zr- and Hf-Based Metal-Organic Frameworks: Tracking down the Polymorphism. *Cryst. Growth Des.* **2013**, *13*, 1231–1237.

(23) Drache, F.; Bon, V.; Senkovska, I.; Getzschmann, J.; Kaskel, S. The Modulator Driven Polymorphism of Zr(IV) Based Metal-Organic Frameworks. *Philos. Trans. R. Soc., A* **2017**, *375*, 20160027.

(24) Li, M.; O'Keeffe, M.; Proserpio, D. M.; Proserpio, D. M.; Zhang, H. F. A New Group of Edge-Transitive 3-Periodic Nets and Their Derived Nets for Reticular Chemistry. *Cryst. Growth Des.* **2020**, *20*, 4062–4068.

(25) Delgado-Friedrichs, O.; O'Keeffe, M. Three-Periodic Tilings and Nets: Face-Transitive Tilings and Edge-Transitive Nets Revisited. *Acta. Crystallogr., Section A: Found. Crystallogr.* **2007**, *63*, 344–347.

(26) Eubank, J. F.; Walsh, R. D.; Poddar, P.; Srikanth, H.; Larsen, R. W.; Eddaoudi, M. Metal-Organic Framework Diversity via Heterocoordination of a Multifunctional Ligand: $SrAl_2$ and a Novel (3,4)-Connected Network. Cryst. Growth Des. **2006**, *6*, 1453-1457.

(27) Li, M.; Li, D.; O'Keeffe, M.; Yaghi, O. M. Topological Analysis of Metal-Organic Frameworks with Polytopic Linkers and/or Multiple Building Units and the Minimal Transitivity Principle. *Chem. Rev.* **2014**, *114*, 1343–1370.

(28) Shevchenko, A. P.; Shabalin, A. A.; Karpukhin, I. Yu.; Blatov, V. A. Topological Representations of Crystal Structures: Generation, Analysis and Implementation in the TopCryst System. *Sci. Technol. Adv. Mater.: Methods* **2022**, *2*, 250–265. https://topcryst.com/.

(29) www.iucr.org/resources/cif/dictionaries/cif_topology.

(30) Blatov, V. A.; O'Keeffe, M.; Proserpio, D. M. Vertex-, Face-, Point-, Schläfli-, and Delaney-Symbols in Nets, Polyhedra and Tilings: Recommended Terminology. *CrystEngComm* **2009**, *12*, 44–48.

(31) Wang, X. Sen; Shengqian, M.; Rauch, K.; Simmons, J. M.; Yuan, D.; Wang, X.; Yildirim, T.; Cole, W. C.; López, J. J.; De Meijere, A.; Zhou, H. C. Metal-Organic Frameworks Based on Double-Bond-Coupled Di-Isophthalate Linkers with High Hydrogen and Methane Uptakes. *Chem. Mater.* **2008**, *20*, 3145–3152.

(32) Chen, Z. F.; Zhang, Z. L.; Tan, Y. H.; Tang, Y. Z.; Fun, H. K.; Zhou, Z. Y.; Abrahams, B. F.; Liang, H. Coordination Polymers Constructed by Linking Metal Ions with Azodibenzoate Anions. *CrystEngComm* **2008**, *10*, 217–231.

(33) Yang, S.; Callear, S. K.; Ramirez-Cuesta, A. J.; David, W. I. F.; Sun, J.; Blake, A. J.; Champness, N. R.; Schröder, M. Pore with Gate: Modulating Hydrogen Storage in Metal-Organic Framework Materials via Cation Exchange. *Faraday Discuss.* **2011**, *151*, 19–36.

(34) Qian, J.; Jiang, F.; Su, K.; Li, Q.; Zhou, K.; Wu, M.; Yuan, D.; Hong, M. Sorption Comparison of Two Indium-Organic Framework Isomers with Syn-Anti Configurations. *CrystEngComm* **2014**, *16*, 7434–7439.

(35) Xue, D. X.; Cadiau, A.; Weseliński, Ł. J.; Jiang, H.; Bhatt, P. M.; Shkurenko, A.; Wojtas, L.; Zhijie, C.; Belmabkhout, Y.; Adil, K.; Eddaoudi, M. Topology Meets MOF Chemistry for Pore-Aperture Fine Tuning: ftw-MOF Platform for Energy-Efficient Separations: Via Adsorption Kinetics or Molecular Sieving. *Chem. Commun.* **2018**, *54*, 6404–6407.

(36) Xue, D. X.; Cairns, A. J.; Belmabkhout, Y.; Wojtas, L.; Liu, Y.; Alkordi, M. H.; Eddaoudi, M. Tunable Rare-Earth fcu-MOFs: A Platform for Systematic Enhancement of CO_2 Adsorption Energetics and Uptake. *J. Am. Chem. Soc.* **2013**, *135*, 7660–7667.

(37) Cavka, J. H.; Jakobsen, S.; Olsbye, U.; Guillou, N.; Lamberti, C.; Bordiga, S.; Lillerud, K. P. A New Zirconium Inorganic Building Brick Forming Metal Organic Frameworks with Exceptional Stability. *J. Am. Chem. Soc.* **2008**, *130*, 13850–13851.

(38) Sudik, A. C.; Côté, A. P.; Yaghi, O. M. Metal-Organic Frameworks Based on Trigonal Prismatic Building Blocks and the New "acs" Topology. *Inorg. Chem.* **2005**, *44*, 2998–3000.

(39) Surblé, S.; Serre, C.; Mellot-Draznieks, C.; Millange, F.; Férey, G. A New Isoreticular Class of Metal-Organic-Frameworks with the MIL-88 Topology. *Chem. Commun.* **2006**, 284–286.

(40) Blatov, V. A.; Shevchenko, A. P.; Proserpio, D. M. Applied Topological Analysis of Crystal Structures with the Program Package Topospro. *Cryst. Growth Des.* **2014**, *14*, 3576–3586.

(41) Chen, B.; Eddaoudi, M.; Reineke, T. M.; Kampf, J. W.; O'Keeffe, M.; Yaghi, O. M. $Cu_2(ATC)\cdot 6H_2O$: Design of Open Metal Sites in Porous Metal-Organic Crystals (ATC: 1,3,5,7-Adamantane Tetracarboxylate). *J. Am. Chem. Soc.* **2000**, *122*, 11559–11560.

(42) Zheng, Y. Z.; Zheng, Z.; Tong, M. L.; Chen, X. M. Structural Evolution and Magnetic Properties of a Series of Coordination Polymers Featuring Dinuclear Secondary-Building Units and Adamantane-Dicarboxylato Ligands. *Polyhedron* **2013**, *52*, 1159–1168.

(43) Amombo Noa, F. M.; Svensson Grape, E.; Brülls, S. M.; Cheung, O.; Malmberg, P.; Inge, A. K.; Mckenzie, C. J.; Mårtensson, J.; Öhrström, L. Metal-Organic Frameworks with Hexakis(4-Carboxyphenyl)Benzene: Extensions to Reticular Chemistry and Introducing Foldable Nets. *J. Am. Chem. Soc.* **2020**, *142*, 9471–9481.

(44) Zhao, X.; He, H.; Dai, F.; Sun, D.; Ke, Y. Supramolecular Isomerism in Honeycomb Metal - Organic Frameworks Driven by CH···α Interactions:

Homochiral Crystallization from an Achiral Ligand through Chiral Inducement. *Inorg. Chem.* **2010**, *49*, 8650–8652.

(45) Gómez-Gualdrón, D. A.; Colón, Y. J.; Zhang, X.; Wang, T. C.; Chen, Y. S.; Hupp, J. T.; Yildirim, T.; Farha, O. K.; Zhang, J.; Snurr, R. Q. Evaluating Topologically Diverse Metal–Organic Frameworks for Cryo-Adsorbed Hydrogen Storage. *Energy Environ. Sci.* **2016**, *9*, 3279–3289.

(46) Zhu, N.; Lennox, M. J.; Tobin, G.; Goodman, L.; Düren, T.; Schmitt, W.; Zhu, N.; Tobin, G.; Goodman, L.; Schmitt, W.; Lennox, M. J.; Düren, T. Hetero-Epitaxial Approach by Using Labile Coordination Sites to Prepare Catenated Metal–Organic Frameworks with High Surface Areas. *Chem. Eur. J.* **2014**, *20*, 3595–3599.

(47) Furukawa, H.; Go, Y. B.; Ko, N.; Park, Y. K.; Uribe-Romo, F. J.; Kim, J.; O'Keeffe, M.; Yaghi, O. M. Isoreticular Expansion of Metal-Organic Frameworks with Triangular and Square Building Units and the Lowest Calculated Density for Porous Crystals. *Inorg. Chem.* **2011**, *50*, 9147–9152.

(48) Chen, Z.; Jiang, H.; Li, M.; O'Keeffe, M.; Eddaoudi, M. Reticular Chemistry 3.2: Typical Minimal Edge-Transitive Derived and Related Nets for the Design and Synthesis of Metal-Organic Frameworks. *Chem. Rev.* **2020**, *120*, 8039–8065.

(49) Gao, X.; Xu, T.; Jiang, Z.; Yu, H.; Wang, Y.; He, Y. Rational Construction and Remarkable Gas Adsorption Properties of a HKUST-1-like tbo-Type MOF Based on a Tetraisophthalate Linker. *Dalton Trans.* **2019**, *48*, 16793–16799.

(50) Yan, D.; Chen, B.; Duan, Q. A Copper-Based Metal–Organic Framework Constructed from a New Tetracarboxylic Acid for Selective Gas Separation. *Inorg. Chem. Commun.* **2014**, *49*, 34–36.

(51) Chen, Z.; Weseliński, Ł. J.; Adil, K.; Belmabkhout, Y.; Shkurenko, A.; Jiang, H.; Bhatt, P. M.; Guillerm, V.; Dauzon, E.; Xue, D. X.; O'Keeffe, M.; Eddaoudi, M. Applying the Power of Reticular Chemistry to Finding the Missing alb-MOF

Platform Based on the (6,12)-Coordinated Edge-Transitive Net. *J. Am. Chem. Soc.* **2017**, *139*, 3265–3274.

(52) Alezi, D.; Jia, J.; Bhatt, P. M.; Shkurenko, A.; Solovyeva, V.; Chen, Z.; Belmabkhout, Y.; Eddaoudi, M. Reticular Chemistry for the Construction of Highly Porous Aluminum-Based nia-Metal-Organic Frameworks. *Inorg. Chem.* **2022**, *61*, 10661–10666.

(53) Chandrasekhar, P.; Savitha, G.; Moorthy, J. N. Robust MOFs of "tsg" Topology Based on Trigonal Prismatic Organic and Metal Cluster SBUs: Single Crystal to Single Crystal Postsynthetic Metal Exchange and Selective CO_2 Capture. *Chem. Eur. J.* **2017**, *23*, 7297–7305.

(54) Guo, Z.; Wu, H.; Srinivas, G.; Zhou, Y.; Xiang, S.; Chen, Z.; Yang, Y.; Zhou, W.; Okeeffe, M.; Chen, B.; Guo, [Z; Xiang, S.; Chen, B.; Wu, H.; Zhou, W.; Srinivas, G.; Zhou, Y.; Chen, Z.; Yang, Y.; O'keeffe, M. A Metal–Organic Framework with Optimized Open Metal Sites and Pore Spaces for High Methane Storage at Room Temperature. *Angew. Chem. Int. Ed.* **2011**, *123*, 3236–3239.

(55) Kim, J.; Chen, B.; Reineke, T. M.; Li, H.; Eddaoudi, M.; Moler, D. B.; O'Keeffe, M.; Yaghi, O. M. Assembly of Metal-Organic Frameworks from Large Organic and Inorganic Secondary Building Units: New Examples and Simplifying Principles for Complex Structures. *J. Am. Chem. Soc.* **2001**, *123*, 8239–8247.

(56) Pang, J.; Yuan, S.; Qin, J.; Liu, C.; Lollar, C.; Wu, M.; Yuan, D.; Zhou, H. C.; Hong, M. Control the Structure of Zr-Tetracarboxylate Frameworks through Steric Tuning. *J. Am. Chem. Soc.* **2017**, *139*, 16939–16945.

(57) Wong-Foy, A. G.; Lebel, O.; Matzger, A. J. Porous Crystal Derived from a Tricarboxylate Linker with Two Distinct Binding Motifs. *J. Am. Chem. Soc.* **2007**, *129*, 15740–15741.

(58) Lv, X. L.; Feng, L.; Xie, L. H.; He, T.; Wu, W.; Wang, K. Y.; Si, G.; Wang, B.; Li, J. R.; Zhou, H. C. Linker Desymmetrization: Access to a Series of Rare-Earth

Tetracarboxylate Frameworks with Eight-Connected Hexanuclear Nodes. *J. Am. Chem. Soc.* **2021**, *143*, 2784–2791.

(59) Ma, J.; Tran, L. D.; Matzger, A. J. Toward Topology Prediction in Zr-Based Microporous Coordination Polymers: The Role of Linker Geometry and Flexibility. *Cryst. Growth Des.* **2016**, *16*, 4148–4153.

(60) Furukawa, H.; Kim, J.; Ockwig, N. W.; O'Keeffe, M.; Yaghi, O. M. Control of Vertex Geometry, Structure Dimensionality, Functionality, and Pore Metrics in the Reticular Synthesis of Crystalline Metal-Organic Frameworks and Polyhedra. *J. Am. Chem. Soc.* **2008**, *130*, 11650–11661.

(61) Alsadun, N.; Mouchaham, G.; Guillerm, V.; Czaban-Jóźwiak, J.; Shkurenko, A.; Jiang, H.; Bhatt, P. M.; Parvatkar, P.; Eddaoudi, M. Introducing a Cantellation Strategy for the Design of Mesoporous Zeolite-like Metal-Organic Frameworks: Zr-sod-ZMOFs as a Case Study. *J. Am. Chem. Soc.* **2020**, *142*, 20547–20553.

(62) Wondratschek, H.; Müller, U. *International Tables for Crystallography, Volume A1: Symmetry relations between space groups*, Springer, Dordrecht, **2004**.

(63) Hodgson, H. H.; Whitehurst, J. S. The Tetrazotisation of 1:5- and 1:8-Naphthylenediamines and the Tetranitration of 1:5- and 1:8-Di-p-Toluenesulphonamidonaphthalenes. *J. Chem. Soc.* **1947**, 80–81.

(64) Friedman, L.; Shechter, H. Dimethylformamide as a Useful Solvent in Preparing Nitriles from Aryl Halides and Cuprous Cyanide; Improved Isolation Techniques. *J. Org. Chem.* **1961**, *26*, 2522–2524.

(65) Huang, Y. L.; Zhong, D. C.; Jiang, L.; Gong, Y. N.; Lu, T. B. Two Li-Zn Cluster-Based Metal-Organic Frameworks: Strong H_2/CO_2 Binding and High Selectivity to CO_2. *Inorg. Chem.* **2017**, *56*, 705–708.

(66) Chen, Z.; Thiam, Z.; Shkurenko, A.; Weselinski, L. J.; Adil, K.; Jiang, H.; Alezi, D.; Assen, A. H.; O'Keeffe, M.; Eddaoudi, M. Enriching the Reticular Chemistry

Repertoire with Minimal Edge-Transitive Related Nets: Access to Highly Coordinated Metal-Organic Frameworks Based on Double Six-Membered Rings as Net-Coded Building Units. *J. Am. Chem. Soc.* **2019**, *141*, 20480–20489.

(67) Zhang, Z.; Chen, C.; Wang, Q.; Han, Z.; Dong, X. Q.; Zhang, X. New Tetraphosphite Ligands for Regioselective Linear Hydroformylation of Terminal and Internal Olefins. *RSC Adv.* **2016**, *6*, 14559–14562.

(68) Feng, D.; Wang, K.; Wei, Z.; Chen, Y. P.; Simon, C. M.; Arvapally, R. K.; Martin, R. L.; Bosch, M.; Liu, T. F.; Fordham, S.; Yuan, D.; Omary, M. A.; Haranczyk, M.; Smit, B.; Zhou, H. C. Kinetically Tuned Dimensional Augmentation as a Versatile Synthetic Route towards Robust Metal–Organic Frameworks. *Nat. Commun.* **2014**, *5*, 1–9.

(69) Juanhuix, J.; Gil-Ortiz, F.; Cuní, G.; Colldelram, C.; Nicolás, J.; Lidón, J.; Boter, E.; Ruget, C.; Ferrer, S.; Benach, J. Developments in Optics and Performance at BL13-XALOC, the Macromolecular Crystallography Beamline at the Alba Synchrotron. *J. Synchrotron Radiat.* **2014**, *21*, 679–689.

(70) Kabsch, W. Integration, Scaling, Space-Group Assignment and Post-Refinement. *Acta Cryst. D* **2010**, *66*, 133–144.

(71) Sheldrick, G. M.; IUCr. Crystal Structure Refinement with SHELXL. *Acta Cryst. C* **2015**, *71*, 3–8.

(72) Sheldrick, G. M.; IUCr. SHELXT – Integrated Space-Group and Crystal-Structure Determination. *Acta Cryst. A* **2015**, *71*, 3–8.

(73) Dolomanov, O. V.; Bourhis, L. J.; Gildea, R. J.; Howard, J. A. K.; Puschmann, H. OLEX2: A Complete Structure Solution, Refinement and Analysis Program. *J. Appl. Cryst.* **2009**, *42*, 339–341.

(74) Zhang, B.; Mao, H.; Matheu, R.; Reimer, J. A.; Alshmimri, S. A.; Alshihri, S.; Yaghi, O. M. Reticular Synthesis of Multinary Covalent Organic Frameworks. *J. Am. Chem. Soc.* **2019**, *141*, 11420–11424.

(75) Zhai, L.; Huang, N.; Xu, H.; Chen, Q.; Jiang, D. A Backbone Design Principle for Covalent Organic Frameworks: The Impact of Weakly Interacting Units on CO_2 Adsorption. *Chem. Commun.* **2017**, *53*, 4242–4245.

(76) Meekel, E. G.; Schmidt, E. M.; Cameron, L. J.; Dharma, A. D.; Windsor, H. J.; Duyker, S. G.; Minelli, A.; Pope, T.; Lepore, G. O.; Slater, B.; Kepert, C. J.; Goodwin, A. L. Truchet-Tile Structure of a Topologically Aperiodic Metal-Organic Framework. *Science* **2023**, *379*, 357–361.

Chapter 5

Clip-off chemistry: Programmed de-reticulation of nets

This Chapter is based on the following publication:

- Yang, Y.; [‡] Broto-Ribas, A.; [‡] Ortín-Rubio, B.; [‡] Imaz, I.; Gándara, F.; Carné-Sánchez, A.; Guillerm, V.; Jurado, S.; Busqué, F.; Juanhuix, J.; Maspoch, D. Clipp-off Chemistry: Synthesis by Programmed Disassembly of Reticular Materials *Angew. Chem. Int. Ed.* **2022**, *61*, e202111228. (‡ = co-first authorship)

5.1. Introduction

5.1.1. Limits of post-synthetic methods

As illustrated in Section 1.8, most of the different post-synthetic strategies reported present several problems that limit the control in the overall structure. Some of the most noticeable limitations are related to the difficulty of achieving the maximum conversion of the reactions in the reticular materials, probably due to diffusion problems attributed to the modification of the chemical environment in the pores/channels, introducing new molecules or functional groups.[1,2] Furthermore, as these reactions cannot be completed, most of these processes dramatically decrease the crystallinity of the materials, generated by the different chemical environment of previous symmetrical units or by the partial framework collapse.

To date, most PSMs use bottom-up strategies that, at the latter stage, mainly entail controlling the formation of new bonds. Generally, bond formation has avoided the former problems when occurs at specific positions (i.e. open metal sites or vacancies generated in the matrix).[3–5] However, the prediction of novel nets and/or structures are limited to just a few cases and cannot access to MOFs constructed with less-

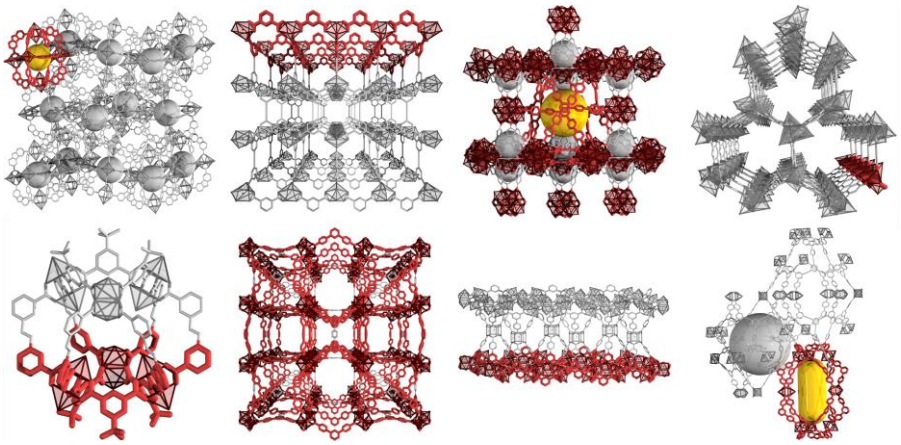


Figure 5.1. Highlight in red of different fragments or frameworks with different circuits of connections and dimensionality that are encoded in reticular materials and could be obtained through a top-down strategy.

symmetric linkers or to the endless variety of fragments and MBBs[6] (*e.g.* metal clusters, cages, cycles, metal layers, metal chains, etc.) that often do not exist in their isolated form (Figure 5.1).

5.1.2. Controlled breaking: Cleavable bonds at specific positions

Continuing with the study in the assembly of less-symmetric MBBs, we envisaged that a new top-down-based strategy could be used for the synthesis of previously inaccessible new molecules and materials. By selectively breaking certain bonds in reticular materials, we could transform them into new frameworks or break them into new molecular fragments or isolated MBBs, as a synthetic strategy towards new materials and molecules. As illustrated in Chapter 4, the strategy would be based on the same principle, but the clipping process will be applied to a precursor reticular material, and not limited to a theoretical design. We hypothesized that we could use a chemical reaction for programmed bond-breaking, such that the de-reticulation process would occur at the molecular level. We reasoned that this would require the presence of cleavable groups at specific positions within the structures of the corresponding reticular materials, and that the placement of these cleavable bonds should be encoded at the organic linkers to ensure the formation of less-symmetric MBBs, otherwise the cleavable bonds would be the coordination bonds and therefore, just obtaining the starting MBBs prior to the synthesis.

Among the different covalent bond cleavage reactions reported (hydrolysis of imines,[7] reduction of disulfide,[8] thermolysis of carbon-carbon or ester bonds,[9,10] and ozonolysis of alkenes[11]), we considered the use of the last reaction as our choice for the cleavage sites/reaction due to: (i) it is an irreversible reaction; (ii) can be performed as a solid-gas reaction; (iii) is quantitative and selective to specific functional groups; (iv) the output can be controlled under different work-up conditions; (v) and the introduction of alkene bonds in the MBBs and therefore, in the precursor reticular materials, would be ideal as its formation has been well-

known studied and are robust, resisting the synthetic conditions of solvothermal methods (Figure 5.2).

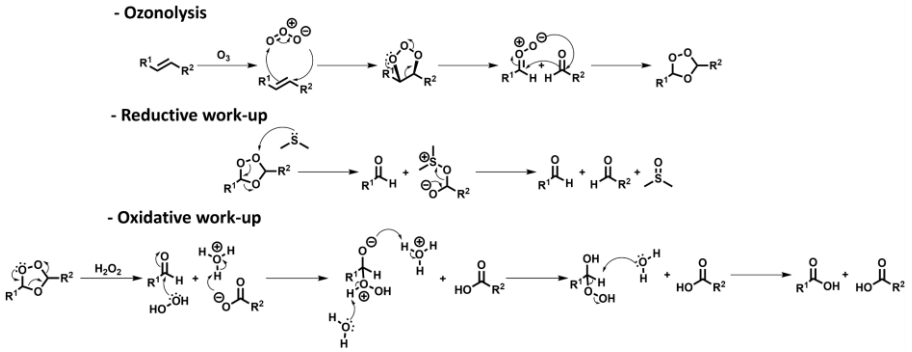


Figure 5.2. Mechanism of the ozonolysis reaction and the reductive and oxidative work-ups.

Thus, reported reticular materials containing linkers featuring olefinic bonds would be ideal starting precursor materials for our strategy. However, we thought that, in the likely event that the targeted structure-precursor did not contain any alkene groups, we could generalize this approach to numerous reticular materials by inserting such groups into the pre-selected linkers without modifying their size or geometry pre- and/or post-synthetically, *via* the isoreticular principle.[12,13] Thus, we extended this concept to the ability to encode the organic linker of an existing MOF by inserting cleavable alkene groups into it, without modifying the linker size or topology, to ultimately enable assembly of the corresponding isoreticular MOF structures containing the desired cleavable group (Figure 5.3).[14]

In this Chapter, we have developed a new top-down synthetic approach, which we called *Clip-off Chemistry*, which is based on the programmed disassembly of reticular materials by controlled breaking of selected bonds. Our strategy was validated by the synthesis of two topologically distinct, three-dimensional (3D) MOFs from two different 3D MOFs. We show that bond-breaking in these structures can be performed at the molecular level, periodically, quantitatively, and selectively; and can occur in a single-crystal-to-single-crystal fashion. Through these two examples, Clip-off Chemistry was demonstrated as a tool to modify reticular materials (more

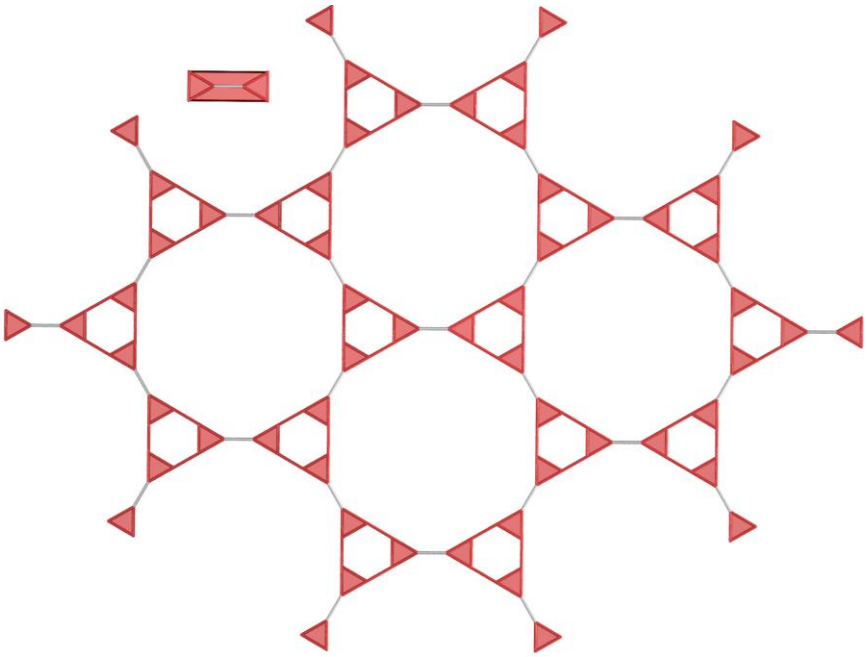


Figure 5.3. Schematic of encoding a 4-c rectangular linker with cleavable sites as an MBB for the assembly into a 2D **kgm** layer that, upon proper disassembly, isolates novel 0D macrocycles.

precisely, MOFs in this case) via cleavage, rather than formation, of bonds in their frameworks, enabling alterations of the circuits of connections in the net and connectivity of their constituent MBBs.

5.2. Results and discussion

5.2.1. Topological analysis of the disassembly: Erasing edges or nodes

Clip-off chemistry is based on using, as starting materials, structures that contain cleavable groups (in this study, alkenes) at specific crystallographic positions, such that cleavage of said groups generates new molecules or materials. Following this principle, we first targeted the clip-off synthesis of a new 3D MOF from a 3D MOF precursor, modifying the topology nut without altering the dimensionality of the

framework. When selecting precursors in Clip-off Chemistry, it is essential to perform a reticular analysis of their underlying nets,[15–17] as bond-breaking in the structure relates the disassembly of certain circuits of connections.[18] The de-reticulation process in reticular materials can be performed mainly by erasing some of the edges or nodes of their underlying nets, which means the cleavage of certain bonds or the extraction of certain MBBs or fragments when translating this analysis to the chemical field, respectively. To do so, two main strategies can be used for the clip-off synthesis of a structure (here, a 3D MOF) from the disassembly of another structure (here, another 3D MOF): (i) a structure built from one type of polytopic linker that contains different circuits of connections between the inorganic clusters, containing a cleavable bond in at least one of the circuits; or (ii) a mixed-linker structure, in which linkers are located at different crystallographic positions, and just one of them contains cleavable bonds (Figure 5.4).

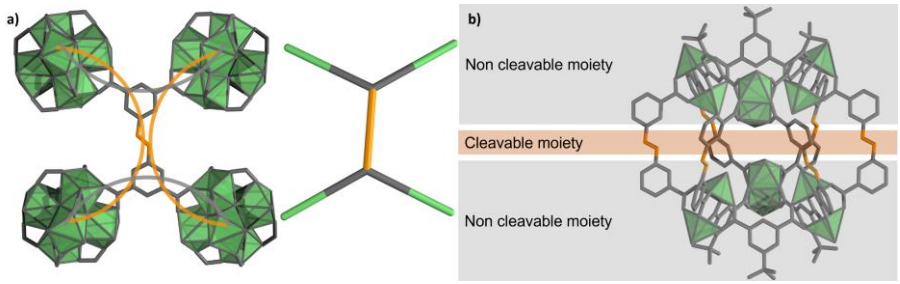


Figure 5.4. a) Representation of a MOF built from one type of polytopic linker with different circuits of connections, where some contains cleavable bonds (orange), and some does not contain them (gray). b) Representation of a mixed-linker MOP containing two different of linkers, the cleavable (containing orange bonds) and non-cleavable.

When using the first strategy (Figure 5.4a), cleavage of the polytopic linker will provoke disassembly of the circuits of connections in which the cleavable bond is involved, thereby forming a structure built up exclusively from those circuits that do not contain the cleavable groups, with a distinct topology of the underlying net. When using the second strategy (Figure 5.4b), cleavage of the linker containing the cleavable bond will provoke disassembly of the circuits of connections in which it

is involved, thereby forming a structure built up exclusively from those circuits that involve the metal-based clusters and the other linkers that do not contain the cleavable bond.

In our choice of precursor for the first 3D MOF synthesis, we followed the first polytopic linker strategy described above. A literature survey revealed us a primising candidate: the Zr-**scu**-MOF,[19] which is constructed upon the assembly of 8-c quadrangular prismatic $Zr_6O_4(OH)_4$ clusters with the 4-c rectangular 3,3',5,5'-ABTC linker, forming a 3D framework with the 4,8-c **scu**/3^2,8T132 underlying net.[20] A closer look to its circuits of connections revealed us the presence of different circuits of connections, which some of them contains cleavable bonds, and the corresponding removal of these edges transforms the 3D net into a new 3D net reducing the connectivity of the nodes (Figure 5.5). Therefore, this net resulted a perfect platform to prove our new top-down approach for the 3D-to-3D topological transformation.

As the reported structure does not contain any cleavable alkene groups (is based on

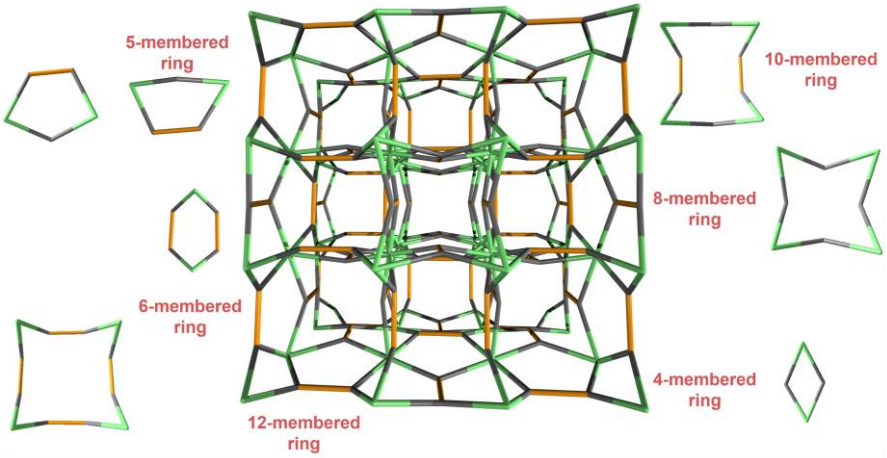


Figure 5.5. Reticular analysis of the circuits of connections of the derived 3^2,8T132 net. In this topology, some circuits of connections contain edges that represent the cleavable bonds (orange) as for the 5-, 6-, 10- and 12-membered rings; and some of them not as for the 4- and 8-membered rings. Erasing the orange edges will transform the topology from the 4,8-c **scu** net into the 6-c **pcu** net, without altering its dimensionality/periodicity.

azo bonds), we had to insert them chemically, using the well-known isoreticular principal.[14] This step of introducing cleavable groups into precursors can be performed before the cleavage step as needed, by replacing at least one of the original linkers with one of similar size and geometry that contains the desired cleavable groups at strategic positions. Once inserted into the isoreticular structure, such linkers generate different circuits of connections, in which at least one circuit contains the cleavable bonds. In our example, we replaced the 3,3',5,5'-ABTC linker with 5-[2-(3,5-dicarboxyphenyl)ethenyl]benzene-1,3-dicarboxylate (3,3',5,5'-EBTC), which contains olefinic bonds for cleavage (Figure 5.6). As anticipated, upon treatment of this framework with ozone,[11,21–24] each 4-c 3,3',5,5'-EBTC linker would be split into two 2-c linkers (doubly deprotonated trimesic acid and/or 5-formylisophthalate). Consequently, only the circuits of connections between the $Zr_6O_4(OH)_4$ clusters and these 2-c linkers would remain, forming a Zr-**pcu**-MOF.

Curiously, we found that the same 4-c 3,3',5,5'-ABTC linker was used for the construction of Sc-**soc**-MOF,[25] a 3D structure which is based on the 6-c triangular prismatic Sc_3O cluster exhibiting the 4,6-c **soc/edq** underlying net. Similarly, reticular analysis of the net revealed us the same case as that exposed above, presenting different circuits of connections with or without the edges representing cleavable groups, and the same possible 3D-to-3D topological transformation from a 4,6-c **soc** net to a 6-c **pcu** net (Figure 5.6). We envisioned that, upon treatment with ozone, the same less-symmetric MBBs (BTC/5-formylisophthalate linkers) would be generated disrupting the circuits of connection containing cleavable bonds forming a 3D Sc-**pcu**-MOF. Furthermore, pure compounds with a single functional group (here, carboxylic acids) could be obtained by treating the samples with a work-up reaction (here, oxidative).

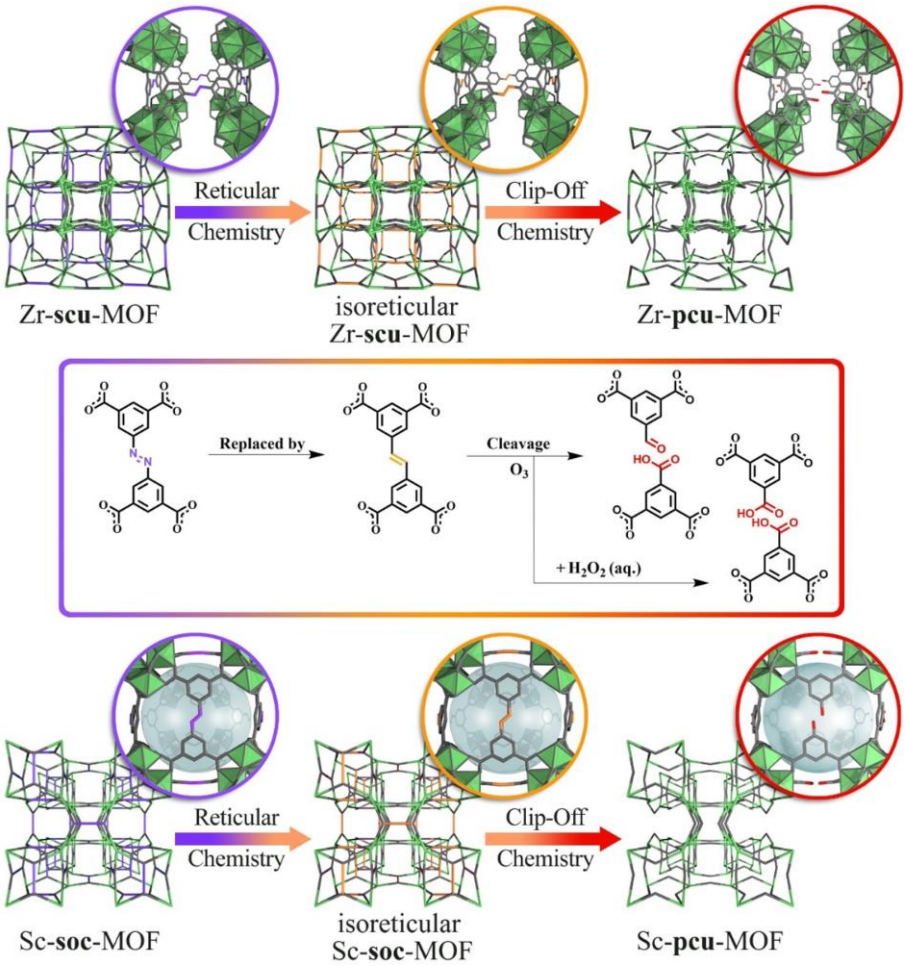


Figure 5.6. Clip-off Chemistry. Representative examples of Clip-off Chemistry, starting with the isoreticular insertion of cleavable (here, alkene) groups into a MOF structure, followed by the quantitative breaking of these cleavable groups by ozonolysis to afford a new structure. Top: clip-off synthesis of Zr-**pcu**-MOF from Zr-**scu**-MOF. Bottom: clip-off synthesis of Sc-**pcu**-MOF from Sc-**soc**-MOF. Middle: chemical reaction for both syntheses. The formation of aldehyde/carboxylic acid groups after ozonolysis is not shown in the lower magnification nets for better illustration of the breaking process. The formation of these groups is shown in the magnified structures, wherein the red groups represent aldehyde or carboxylic acid groups.

5.2.2. Clip-off synthesis of new reticular materials

5.2.2.1. From Zr-scu-MOF to Zr-pcu-MOF

Initially, we synthesized the isoreticular Zr-**scu**-MOF framework built up from different circuits of connections, wherein only some of them contain the cleavable olefinic bonds of 3,3',5,5'-EBTC. Colorless cubic crystals of isoreticular Zr-**scu**-MOF were obtained by solvothermal reaction at 120 ºC of a mixture of $ZrOCl_2 \cdot 8H_2O$ and $H_4$3,3',5,5'-EBTC in DMF and formic acid for 5 days. The crystal structure revealed the expected isoreticular **scu**/3^2,8T132 framework, in which 3,3',5,5'-ABTC had been replaced by 3,3',5,5'-EBTC (Figure 5.7a). Next, we

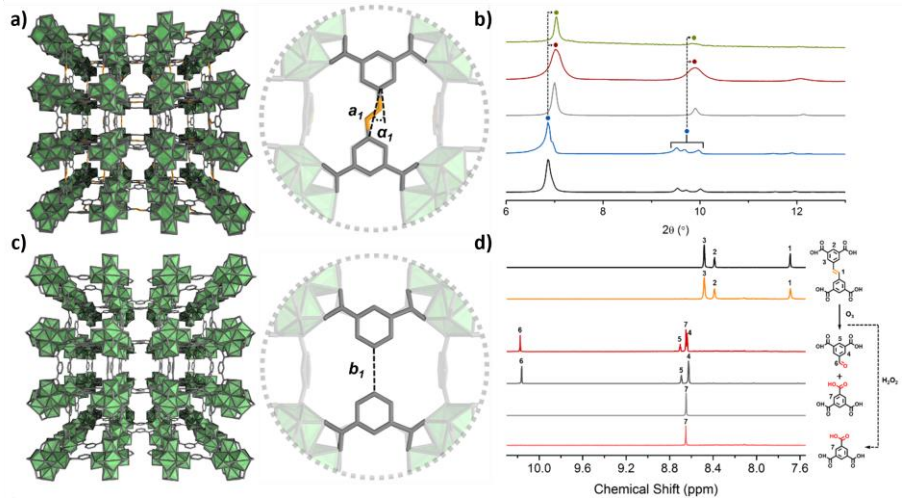


Figure 5.7. Structural and molecular characterization of Zr-**pcu**-MOF. a) and c) Crystal structures of a) isoreticular Zr-**scu**-MOF and c) Zr-**pcu**-MOF. Magnified views highlight the changes observed in the distances and angles of both phenyl rings (from a_1 = 3.77-3.79 Å and α_1 = 14.95-19.71º to b_1 = 3.39-3.65 Å and β_1 = 0º) initially composing 3,3',5,5'-EBTC. b) Magnified view of PXRD spectra for calculated Zr-**scu**-MOF (black), synthesized Zr-**scu**-MOF (blue), calculated Zr-**pcu**-MOF (grey), synthesized Zr-**pcu**-MOF (red) and oxidized Zr-**pcu**-MOF (green). The main structural changes with signal shifts are highlighted. d) ^{1}H NMR spectra (360 MHz, DMSO-d_6) of digested 3,3',5,5'-EBTC (black), Zr-**scu**-MOF (orange), Zr-**pcu**-MOF (red), 5-formylisophthalic acid (dark grey), H_3BTC (light grey) and oxidized Zr-**pcu**-MOF (light red). Assigned proton signals: δ_1 = 7.69 ppm (s, 2H), δ_2 = 8.39 ppm (s, 2H), δ_3 = 8.49 ppm (s, 4H), δ_4 = 8.64 ppm (m, 2H), δ_5 = 8.70 ppm (m, 1H), δ_6 = 10.18 ppm (s, 1H) and δ_7 = 8.65 ppm (s, 3H).

confirmed the phase purity of the bulk sample by PXRD and field-emission scanning electron microscopy (FESEM) (Figures 5.7b and 5.8).

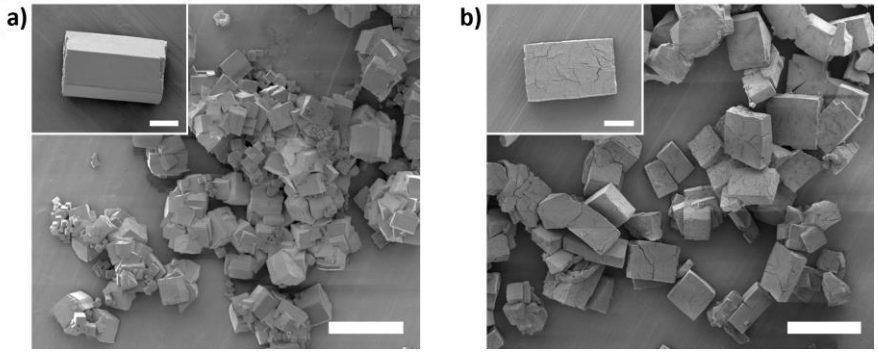


Figure 5.8. FESEM images of a) Zr-**scu**-MOF and b) Zr-**pcu**-MOF. Scale bars: 25 μm (a, b) and 5 μm (insets). In these images, it can be observed that the surface of Zr-**pcu**-MOF crystals shows some degree of cracking. Nevertheless, this cracking does not prevent keeping their single crystal nature.

Then, it was performed the clip-off synthesis of Zr-**pcu**-MOF by packing 20 mg of synthesized Zr-**scu**-MOF crystals into a plastic tube, which was connected on one side to the ozonator (through a $CaCl_2$ humidity trap) and, on the other side, to a vacuum pump (through a KI trap), to ensure a continuous flow of ozone through the column.[11,21] The reaction was run at room temperature for 30 min. Afterwards, the sample was connected to vacuum for another 30 min. This ozonation/vacuum cycle was repeated for nine times to obtain a complete cleavage of all the alkene bonds in Zr-**scu**-MOF, as evidenced by the gradual disappearance of the characteristic olefinic peak at 7.69 ppm in the ^{1}H NMR spectra of the digested Zr-**scu**-MOF crystals (Figure 5.9). After nine cycles, the resulting solid was directly collected from the tube and stored in tetrahydrofuran.

Once the reaction was completed, we characterized the ozonated Zr-**scu**-MOF crystals by SCXRD, which confirmed that they had retained the single-crystal character (Figure 5.7c). For these crystals, synchrotron diffraction data were collected at a maximum resolution of 1.2 Å. Data analyses revealed a variation in the

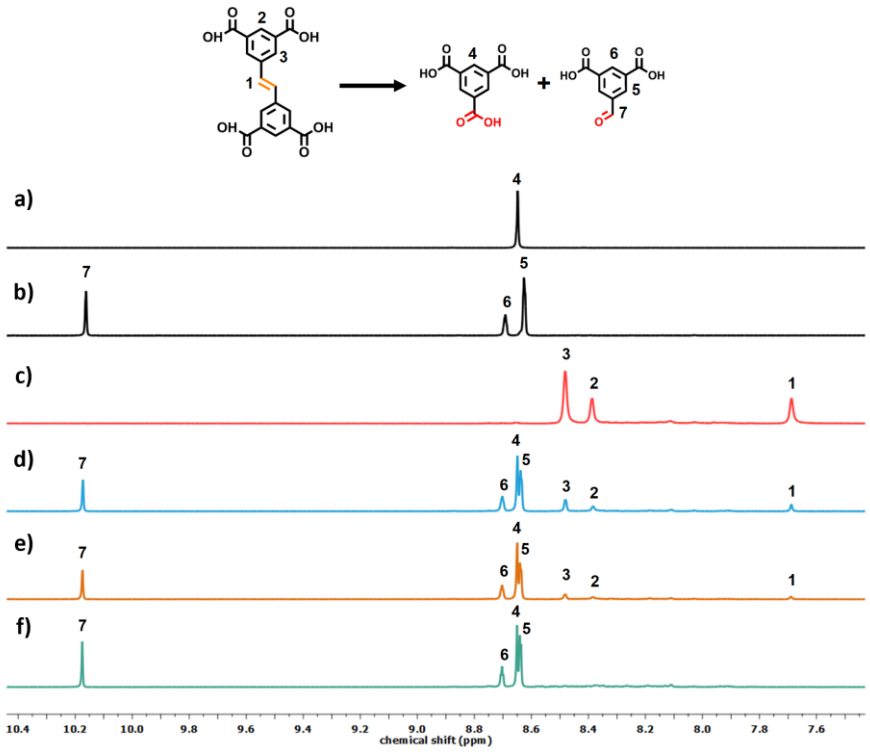


Figure 5.9. ^{1}H NMR spectra (360 MHz, DMSO-d_6) of digested a) H_3BTC, b) 5-formylisophthalic acid, c) Zr-**scu**-MOF, d-f) Zr-**scu**-MOF after d) 3rd, e) 6th and f) 9th cycle of the ozonolysis solid-gas reaction. Note that the spectrum of the 9th cycle corresponds to that of the synthesized Zr-**pcu**-MOF. Assigned proton signals: δ_1 = 7.69 (s, 2H), δ_2 = 8.39 (s, 2H), δ_3 =8.49 (s, 4H), δ_4 =8.65 (s, 3H), δ_5 =8.64 (m, 2H), δ_6 = 8.70 (m, 1H), and δ_7 = 10.18 (s, 1H).

lattice parameters, as compared to the pristine structure. Both pre- and post-ozonolysis crystal structures were solved in the monoclinic *C2/m* space group. However, the cell volume of the ozonated crystal was found to be 16076.00(10) Å^3, whereas that of the pristine Zr-**scu**-MOF was 16957.46(10) Å^3. Analysis of the diffraction data demonstrated the integrity of the inorganic Zr-oxo-hydroxo-clusters after post-synthetic reaction, with no changes in their coordination. Thus, the position of all the atoms in the inorganic SBUs (metals and carboxylate atoms) were assigned and anisotropically refined. As for the rest of the organic linker, carbon atoms belonging to the phenyl ring were located in the difference electron

density maps. However, their high thermal parameter values indicated a possible positional disorder. Moreover, the olefinic carbon atoms could no longer be located, supporting the completeness of the ozonolysis reaction. This is in stark contrast to the pristine MOF, in which the positions of these atoms were clearly visible and refined. The position of the resulting aldehydes or carboxylic groups, newly inserted in the MOF upon cleavage of the carbon-carbon double bond, could not be determined from the analysis of the difference electron density maps. Instead, a large residual electron density was observed in the vicinity of the positions that were initially occupied by the olefinic group. When comparing the two structures, additional differences could be observed in the arrangement of other framework atoms. Most notably, the relative orientation of opposite phenyl rings in a same linker in Zr-**scu**-MOF was different after ozonolysis (Figures 5.7a,c and 5.10a,b), indicating that the olefinic bond was no longer present to fix the angle between these rings. In contrast to the isoreticular Zr-**scu**-MOF precursor, which is based on quadrangular prismatic 8-c Zr-clusters, each $Zr_6O_4(OH)_4$ cluster is still coordinated by 8 linkers in this new Zr-**pcu**-MOF, however its topological connectivity decreases from 8-c to a 6-c because two pairs of the eight 2-c linkers connect the same two clusters (Figure 5.10c,d).[26]

Since the crystal structure of pristine Zr-**scu**-MOF differed markedly to that of ozonated Zr-**scu**-MOF (or Zr-**pcu**-MOF), we also studied these MOFs by PXRD. Remarkably, the PXRD patterns for each sample perfectly matched those calculated from the corresponding structures determined by SCXRD and full-pattern profile refinements further demonstrated phase purity of the samples (Figures 5.7b and 5.11). Altogether, these results corroborate two crucial phenomena for validation of Clip-off Chemistry: firstly, that it is indeed possible to cleave all the periodic olefinic bonds in a 3D structure without destroying it or its single-crystal character; and secondly, that said cleavage, and the resultant formation of a new structure (in this case, Zr-**pcu**-MOF),[17] are homogeneous throughout the bulk crystalline sample.

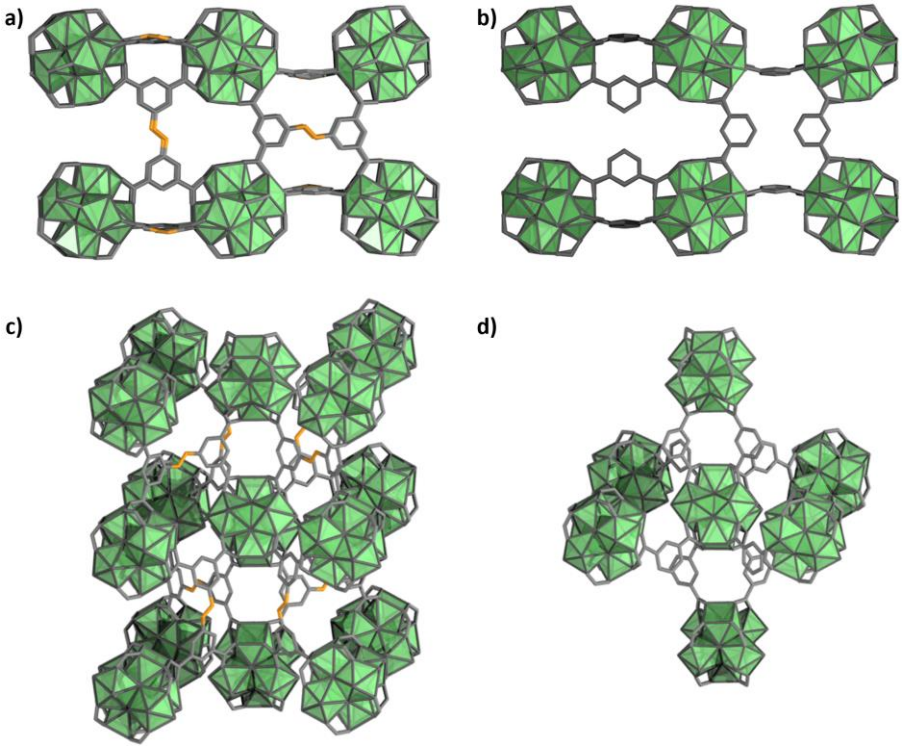


Figure 5.10. Representation of the single-crystal structures of a) Zr-**scu**-MOF and b) Zr-**pcu**-MOF, showing the differences in the orientation of the phenyl rings of the linkers before a) and after b) the cleavage of the olefinic bonds. Comparison of the cluster environment in c) Zr-**scu**-MOF and d) Zr-**pcu**-MOF. In Zr-**scu**-MOF, each Zr-oxo-hydroxo-cluster is connected to 14 neighboring Zr-oxo-hydroxo-clusters by eight 4-c linkers 3,3',5,5'-EBTC. After clip-off treatment, each Zr-oxo-hydroxo-cluster in Zr-**pcu**-MOF is surrounded by 6 neighboring Zr-oxo-hydroxo-clusters, which are interconnected by eight 2-c linkers. In Zr-**scu**-MOF, the connectivity of the Zr-oxo-hydroxo-cluster is in a cubic fashion, matching with the shape of the hexamer cluster. In Zr-**pcu**-MOF, the connectivity of the Zr-oxo-hydroxo-cluster decreases to an octahedral fashion because two pairs of linkers connect to the same clusters; despite the cubic shape of the hexamer cluster.

In order to further evidence the formation of Zr-**pcu**-MOF, ^{1}H NMR spectra of the digested ozonized samples (5% HF/DMSO-d_6) was recorded after each cycle, and then comparing each spectrum to that of the starting Zr-**scu**-MOF (Figures 5.7d and 5.9). Under these digestion conditions, the MOF structures are destroyed due to the protonation and subsequent decoordination of the linkers, which were

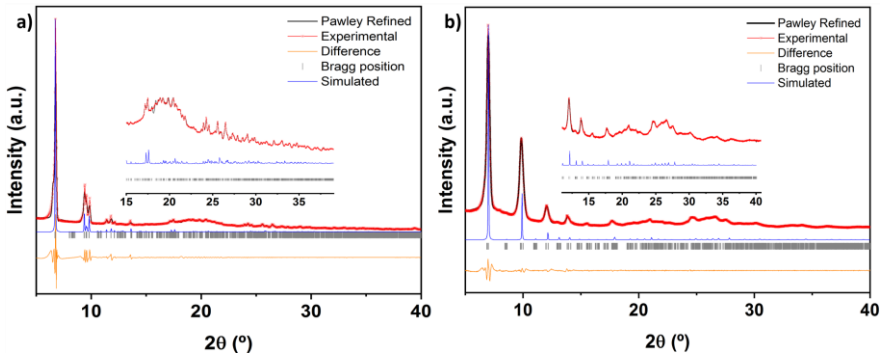


Figure 5.11. PXRD pattern and Pawley refinement of a) Zr-**scu**-MOF and b) Zr-**pcu**-MOF. The experimental pattern (red), the refined Pawley fitting (black), the difference plot (orange), simulated pattern (blue) and the Bragg positions (grey) are provided.

released, thus enabling use of ^{1}H NMR to unveil the composition of the initial MOF structures. The spectrum of the digested Zr-**scu**-MOF showed the characteristic peak of equivalent olefinic protons of $H_4$3,3',5,5'-EBTC at δ = 7.69 ppm. In contrast, the spectra of ozonated crystals after each cycle confirmed a gradual fading of this olefinic signal, which, by the ninth cycle, had fully disappeared. Indeed, ^{1}H NMR of digested ozonated Zr-**scu**-MOF after the ninth cycle confirmed the full conversion of 3,3',5,5'-EBTC into doubly deprotonated trimesic acid and 5-formylisophthalate (Figure 5.9). Beyond the disappearance of the olefinic protons at δ = 7.69 ppm, there was also fading of the phenyl (δ = 8.49 ppm and 8.39 ppm) and the carboxylic acid (δ = 13.32 ppm) protons of $H_4$3,3',5,5'-EBTC, whereas the characteristic signals for the H_3BTC (δ = 13.57 ppm and 8.65 ppm) and 5-formylisophthalic acid (δ = 10.18 ppm, 8.70 ppm and 8.64 ppm) were clearly identifiable. Cleavage of the olefinic bonds was corroborated by negative-mode mass spectrometry and Fourier transform infrared (FT-IR) spectroscopy of both pristine and ozonated Zr-MOFs (Figures 5.12 and 5.13). In the mass spectrum, the molecular ions $[M\text{-H}]^-$ corresponding to H_3BTC (m/z = 209.01) and 5-formylisophthalic acid (m/z = 193.01) were found, in strong contrast to the absence of any molecular ion $[M\text{-H}]^-$ corresponding to $H_4$3,3',5,5'-EBTC (m/z = 355.05). Similarly, in comparison to the spectrum of pristine Zr-**scu**-MOF, the FT-IR spectrum of ozonated Zr-**pcu**-MOF

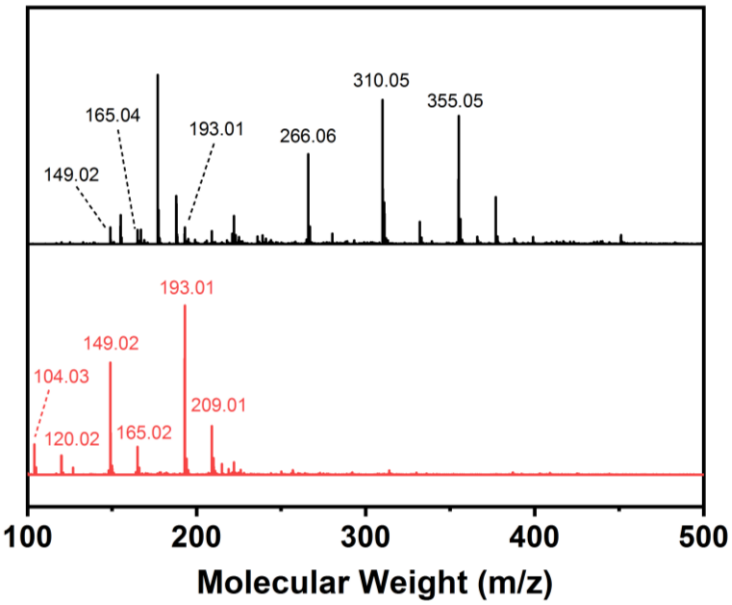


Figure 5.12. ESI-MS spectrometry of digested Zr-**scu**-MOF (black) and Zr-**pcu**-MOF (red). The peak at *m/z* 355.05 is assigned to [3,3',5,5'-EBTC - H]$^-$ in Zr-**scu**-MOF, corresponding to the formula [$C_{18}H_{12}O_8$ - H]$^-$: expected = 355.05, found = 355.05. The peak at *m/z* 193.01 in both samples is assigned to 5-formylisophthalic acid, corresponding to the formula [$C_6H_3(COOH)_2(CHO)$ - H]$^-$: expected = 193.02, found = 193.01. The peak at *m/z* 209.01 in both samples is assigned to H_3BTC, corresponding to the formula [$C_6H_3(COOH)_3$ - H]$^-$: expected = 209.02, found = 209.01.

revealed the appearance of a typical carbonyl (C=O) stretching band at 1700 cm^{-1} and the complete disappearance of an alkene (C=C) stretching band at 1622 cm^{-1}.

Having demonstrated the single-crystal-to-single-crystal synthesis of Zr-**pcu**-MOF by selectively cleaving the olefinic bonds in Zr-**scu**-MOF into a mixture of aldehyde and carboxylic acid groups, it was considered to perform analogous chemistry to synthesize Zr-**pcu**-MOF functionalized exclusively with carboxylic acids to show enhanced control over the final output of the Clip-off Chemistry. To this end, ozonated crystals were soaked in 1 mL of hydrogen peroxide (30 wt. % in H_2O) solution for 3 weeks. During this period, the sample was refreshed with fresh hydrogen peroxide every 24 h. Next, the sample was centrifuged, and then washed twice with water. The transformation to carboxylic acid groups was quantitative,

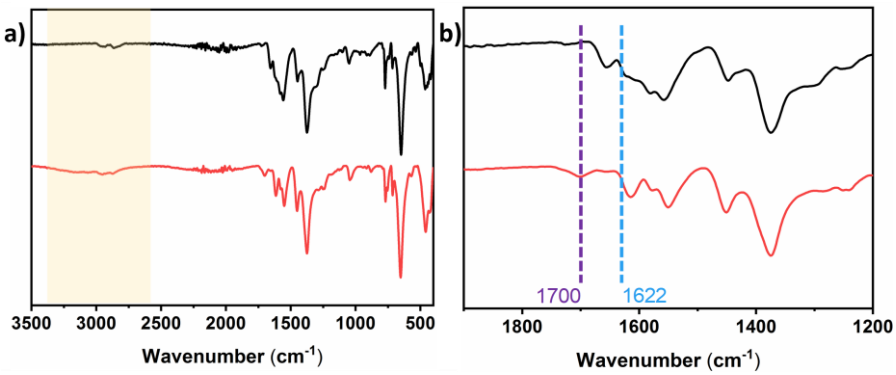


Figure 5.13. a) Full FT-IR spectra of Zr-**scu**-MOF (black), Zr-**pcu**-MOF (red) and b) magnified area. In FT-IR spectra, Zr-**pcu**-MOF displayed a broad band in the region of 3300-2500 cm^{-1}, which was not found in Zr-**scu**-MOF. This could be ascribed to the O-H stretching of the free carboxyl groups. The enhanced vibration signal of the stretching carbonyl (C=O) groups at 1700 cm^{-1} was seen in Zr-**pcu**-MOF. The olefinic bond, which has the characteristic absorbance at 1622 cm^{-1}, disappeared in Zr-**pcu**-MOF, demonstrating the total cleavage of linker 3,3',5,5'-EBTC from Zr-**scu**-MOF.

as confirmed by ^{1}H NMR (Figure 5.7d). Moreover, the crystallinity of the Zr-**pcu**-MOF framework had been preserved, as confirmed by PXRD (Figure 5.7c). The uniqueness of this top-down approach is the obtention of structures that cannot be synthesized by direct synthesis, as has been proven with of the Zr-**pcu**-MOF. Interestingly, the closest literature examples to Zr-**pcu**-MOF are: (i) a 2D MOF made of Zr-oxo-hydroxo-clusters linked by isophthalate, albeit in an **hcb** topology,[27] as our new less-symmetric MBBs could also be seen as exemplifying a connection of Zr-oxo-hydroxo-clusters through BTC linkers, which are coordinated only through two of their three carboxylate groups; and (ii) a 3D MOF-808, made of the same Zr-SBUs combined with BTC linkers in an 3,6-c **spn** net,[28] as the structure could also be considered as the first example of a Zr-structure with a free carboxylic acid using BTC.

5.2.2.2. From Sc-soc-MOF to Sc-pcu-MOF

To show that we could generalize Clip-off Chemistry to other 3D MOF structures, the approach was extended to synthesize a 3-D Sc-**pcu**-MOF from an Sc-**soc**-MOF precursor (Figure 5.6).[29] This structure exhibits a mixture of cubic cavities (size: 11 Å) and 1-D channels (size: 8 Å) along the three axes. As in the previous case, we designed the precursor by replacing 3,3',5,5'-ABTC with 3,3',5,5'-EBTC, thus forming an isoreticular Sc-**soc**-MOF that contains different circuits of connections, some of which contains the cleavable olefins.

In order to start the clip-off synthesis of Sc-**pcu**-MOF via the aforementioned route, the isoreticular Sc-**soc**-MOF precursor was first prepared. Colorless cubic

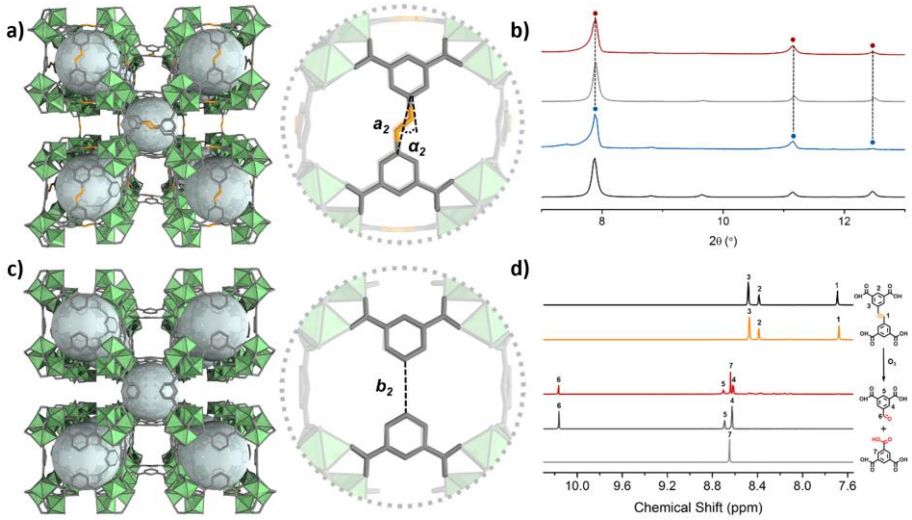


Figure 5.14. Structural and molecular characterization of Sc-**pcu**-MOF. a) and c) Crystal structures of a) isoreticular Sc-**soc**-MOF and c) Sc-**pcu**-MOF. Magnified views highlight the changes observed in the distances and angles of both phenyl rings (from a_2 = 3.82-3.84 Å and α_2 = 15.63-17.34º to b_2 = 3.62-3.63 Å and β_2 = 0º) initially composing 3,3',5,5'-EBTC. b) Magnified view of the PXRD spectra for calculated Sc-**soc**-MOF (black), synthesized Sc-**soc**-MOF (blue), calculated Sc-**pcu**-MOF (grey) and synthesized Sc-**pcu**-MOF (red). d) ^{1}H NMR spectra (360 MHz, DMSO-d_6) of digested 3,3',5,5'-EBTC (black), Sc-**soc**-MOF (orange), Sc-**pcu**-MOF (red), 5-formylisophthalic acid (dark grey) and H_3BTC (light grey). Assigned proton signals: δ_1 = 7.68 ppm (s, 2H), δ_2 = 8.38 ppm (s, 2H), δ_3 = 8.47 ppm (s, 4H), δ_4 = 8.64 ppm (m, 2H), δ_5 = 8.71 ppm (m, 1H), δ_6 = 10.17 ppm (s, 1H) and δ_7 = 8.65 ppm (s, 3H).

crystals of Sc-**soc**-MOF were prepared by heating a solution of $Sc(NO_3)_3{\cdot}xH_2O$ and $H_4$3,3',5,5'-EBTC in DMF, EtOH and formic acid at 120 ºC for 48 h. The crystal structure revealed the expected isoreticular **soc/edq** framework, crystallizing in the *R-3* space group (Figure 5.14a). Then, both PXRD and FESEM confirmed the phase purity of the bulk material (Figures 5.14b and 5.15).

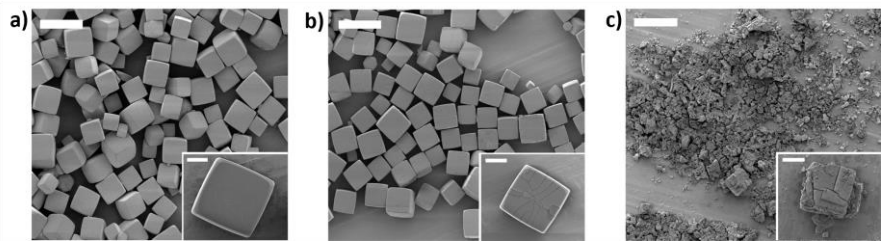


Figure 5.15. FESEM images of a) Sc-**soc**-MOF, b) Sc-**soc**-MOF after the solid-gas ozonolysis for 2 h, and c) Sc-**pcu**-MOF synthesized after solid-gas and suspension-gas ozonolysis. Scale bars: 50 μm (a-c) and 10 μm (insets). The FESEM images revealed that, after the solid-gas ozonolysis reaction for 2 h, the surface of Sc-**soc**-MOF crystals suffered some degree of cracking. Moreover, after the suspension-gas ozonolysis step, the crystals were broken into smaller crystals. These transformations did not change their single-crystals character, which enabled to collect SCXRD data for the fully ozonized sample.

Then, the synthesis of Sc-**pcu**-MOF was performed, however, all attempts at complete ozonolysis were unsuccessful, whether using the same synthetic protocol as for Zr-**scu**-MOF or trying slight modifications (*e.g.* extending the reaction time up to 8 h and/or the number of ozonolysis cycles up to twelve; Figure 5.16). Consequently, cleavage of the olefinic bonds was incomplete, reaching a maximum value of 60% to 70% under certain conditions (*e.g.* exposing the Sc-**soc**-MOF crystals to ozone gas for 2 h). So, a distinct ozonolysis protocol was employed: Sc-**soc**-MOF crystals were immersed in water, and then ozone was bubbled through the suspension under stirring at room temperature for 12 h. These conditions afforded greater cleavage of the olefinic bonds than in the previous strategy, leading to a mixture of H_3BTC, 5-formylisophthalic acid and the intermediate 1,2,4-trioxolane ring (Figure 5.17). Importantly, the presence of this intermediate

indicated that the olefinic bonds had not all been completely cleaved to aldehyde/carboxylic acid groups. Moreover, increasing the reaction time under these solid/liquid conditions did not provide any major improvement in cleavage, although it did lead to a slight decrease in the crystallinity of the ozonated Sc-**pcu**-MOF.

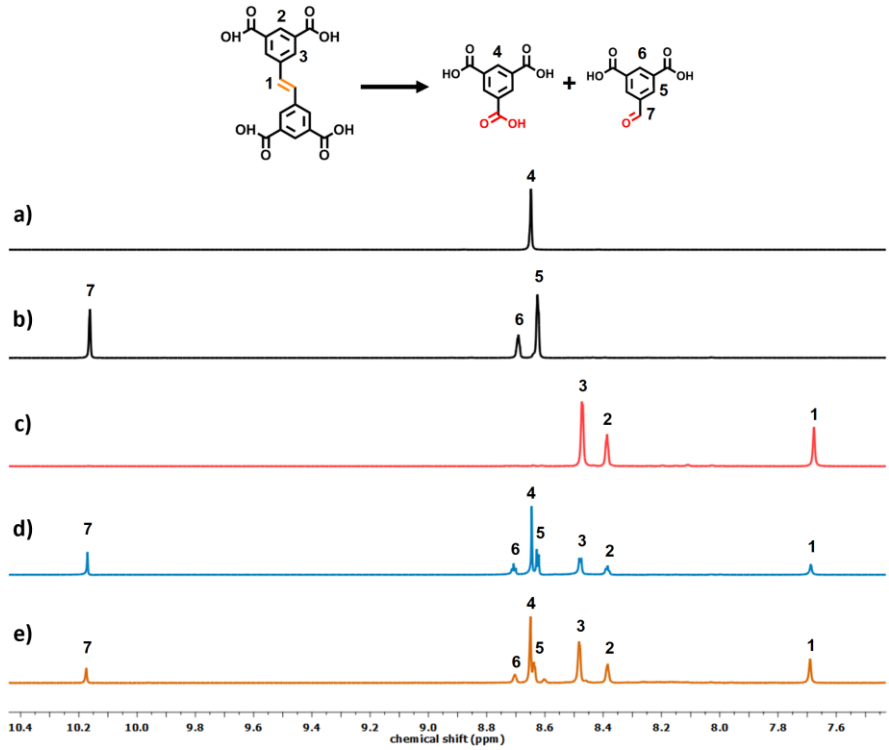


Figure 5.16. ^{1}H NMR spectra (360 MHz, DMSO-d_6) of digested (a) H_3BTC, (b) 5-formylisophthalic acid, (c) Sc-**soc**-MOF, (d) Sc-**soc**-MOF after solid-gas reaction for 8 h, and (e) Sc-**soc**-MOF after solid-gas reaction for 12 cycles. Assigned proton signals: δ_1 = 7.68 (s, 2H), δ_2 = 8.38 (s, 2H), δ_3 =8.47 (s, 4H), δ_4 =8.65 (s, 3H), δ_5 =8.64 (m, 2H), δ_6 = 8.71 (m, 1H), δ_7 = 10.17 (s, 1H). Note that the characteristic protons from the olefinic bond signal at 7.68 ppm of Sc-**soc**-MOF could still be observed after both solid-gas ozonolysis reactions, confirming that the cleavage of olefinic bonds under these synthetic conditions was not quantitative.

To address the above drawbacks, both ozonolysis strategies were combined by first running a solid-gas reaction for 2 h and then, cleaving the remaining alkene bonds

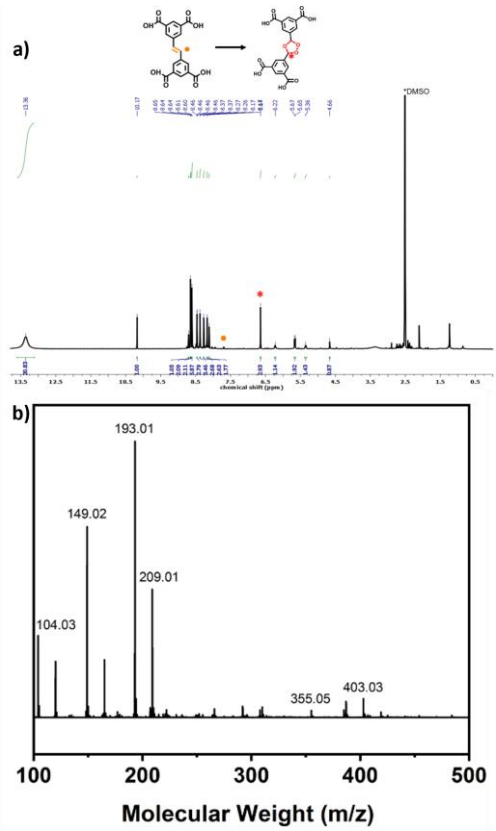


Figure 5.17. Characterization of Sc-**soc**-MOF after ozonolysis only in water suspension for 12 h. a) ^{1}H NMR spectrum (360 MHz, DMSO-d_6) of digested Sc-**soc**-MOF after only in water suspension ozonolysis reaction for 12 h. This sample was digested in 5% HF aqueous solutions at 120 ^{o}C overnight. Note that the peak intensity of protons from the olefinic bond at 7.70 ppm (orange dot) was very weak but it could still be observed, indicating a high degree of cleavage but not quantitative. Moreover, the signal of the proton at 6.64 ppm (red star) was identified as the intermediate trioxolane-metathesis product, which is in accordance with the previous paper published by our group.[11] b) ESI-MS spectrometry of digested Sc-**soc**-MOF after in water suspension ozonolysis reaction for 12 h. The peak at *m/z* 355.05 is assigned to [3,3',5,5'-EBTC - H]$^{-}$ in Sc-**soc**-MOF, corresponding to the formula [$C_{18}H_{12}O_8$ - H]$^{-}$: excepted = 355.05, found = 355.05. The peak at *m/z* 193.01 in both samples is assigned to 5-formylisophthalic acid, corresponding to the formula [$C_6H_3(COOH)_2(CHO)$ - H]$^{-}$: expected = 193.02, found = 193.01. The peak at *m/z* 209.01 is assigned to H_3BTC, corresponding to the formula [$C_6H_3(COOH)_3$ - H]$^{-}$: expected = 209.02, found= 209.01. The peak at *m/z* 403.03 is assigned to the trioxolane intermediate, [$C_{18}H_{12}O_{11}$ - H]$^{-}$: expected = 403.04, found = 403.03. Altogether, these results confirm that, under these suspension-gas conditions, ozonolysis could not fully cleave the olefinic bonds. Moreover, the trioxolane intermediate was also detected.

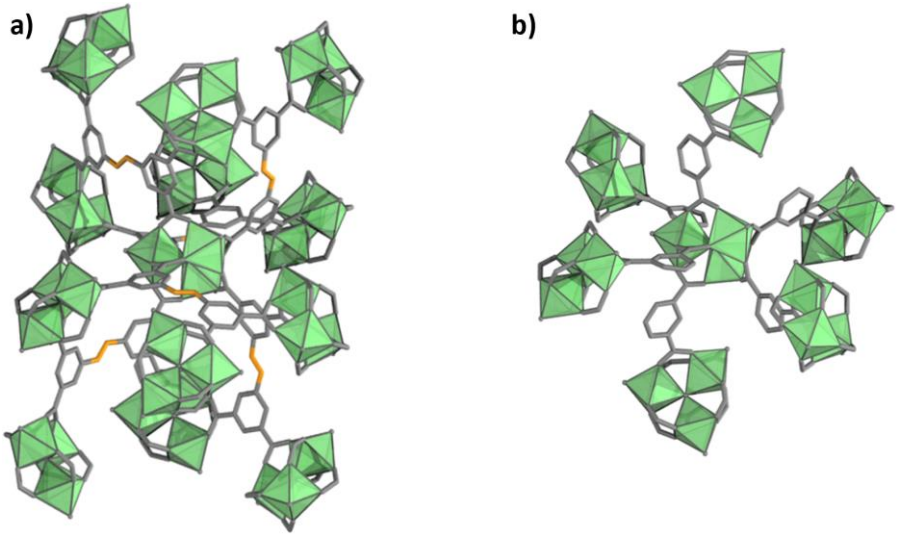


Figure 5.18. Comparison of the cluster environment in a) Sc-**soc**-MOF and b) Sc-**pcu**-MOF. In Sc-**soc**-MOF, each Sc_3O cluster is connected to 12 neighboring clusters by six 4-c linkers 3,3',5,5'-EBTC. After clip-off treatment, each Sc_3O in Sc-**pcu**-MOF is surrounded by only 6 neighboring clusters, which are interconnected by six 2-c linkers. In both cases, the connectivity of Sc_3O clusters is in an octahedral fashion.

via suspension/gas reaction for an additional 6 h. Under these conditions, the double bonds were completely cleaved, as confirmed by all the following characterization techniques. First, SCXRD analysis of the resulting crystals confirmed quantitative single-crystal-to-single-crystal cleavage of the olefinic

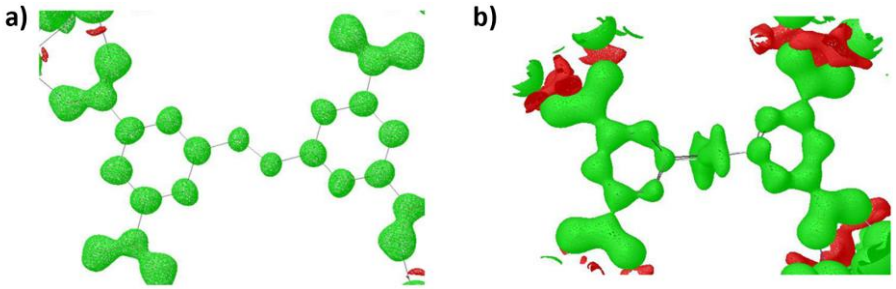


Figure 5.19. 2Fo-Fc maps calculated for both a) Sc-**soc**-MOF and b) Sc-**pcu**-MOF, showing only presence of electron density above and below the plane of the phenyl rings, with no presence of the olefinic carbon atoms.

bonds in Sc-**soc**-MOF to synthesize Sc-**pcu**-MOF (Figure 5.14c).[17] However, in this case, no changes were observed in the volume of the *R-3* rhombohedral unit cell relative to that of the precursor, as also confirmed by PXRD (Figure 5.14b). Nevertheless, SCXRD analysis showed a very similar case to that of ozonated Zr-**scu**-MOF. Thus, the connectivity of the atoms belonging to the inorganic trimeric ScO_3 clusters remained identical to that of the pristine Sc-**soc**-MOF (Figure 5.18).

Refinement of the carbon atoms from the organic linkers evidenced a positional disorder for some of them, and, unlike Sc-**soc**-MOF, the Sc-**pcu**-MOF product did not contain any olefinic atoms. Instead, areas of electron density were observed only between the opposite phenyl rings, with a maximum value at the middle point between the two rings, but at a distance longer than that expected for a C=C bond. This area of higher electron-density points perpendicularly above and below the

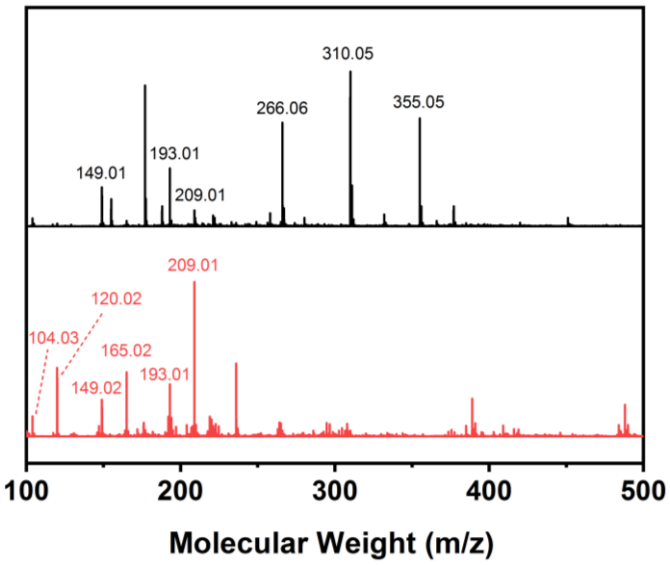


Figure 5.20. ESI-MS spectrometry of digested Sc-**soc**-MOF (black) and Sc-**pcu**-MOF (red). The peak at *m/z* 355.05 is assigned to [3,3',5,5'-EBTC - H]$^-$ in Sc-**soc**-MOF, corresponding to the formula [$C_{18}H_{12}O_8$ - H]$^-$: expected = 355.05, found = 355.05. The peak at *m/z* 193.01 in both samples is assigned to 5-formylisophthalic acid, corresponding to the formula [$C_6H_3(COOH)_2(CHO)$ - H]$^-$: expected = 193.02, found = 193.01. The peak at *m/z* 209.01 in both samples is assigned to H_3BTC, corresponding to the formula [$C_6H_3(COOH)_3$ - H]$^-$: expected = 209.02, found = 209.01.

plane of the phenyl rings. Although the refinement indicates the presence of atoms in this area, these atoms could not be unambiguously assigned to aldehyde or carboxylate groups (Figure 5.19). These findings indicate that the functional groups are not arranged in an orderly fashion within the crystals after ozonolysis but are instead randomly oriented in the pores. This is not surprising, considering that the resulting aldehydes and/or carboxylic groups are randomly distributed and most likely dangle in different orientations into the pores, rather than having a periodically fixed position, such that they would not contribute to the periodic diffraction of the crystal.

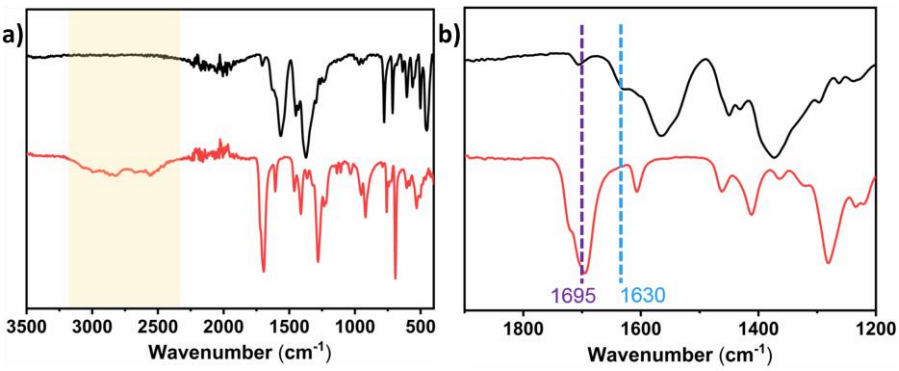


Figure 5.21. a) Full FT-IR spectra of Sc-**soc**-MOF (black), Sc-**pcu**-MOF (red) and b) magnified area. In FT-IR spectra, Sc-**pcu**-MOF displayed a broad band in the region of 3300-2500 cm^{-1}, which was not found in Sc-**soc**-MOF. This could be ascribed to the O-H stretching of the free carboxyl groups. The enhanced vibration signal of the stretching carbonyl (C=O) groups at 1695 cm^{-1} was seen in Sc-**pcu**-MOF. The olefinic bond, which has the characteristic absorbance at 1630 cm^{-1}, disappeared in Sc-**pcu**-MOF, demonstrating the total cleavage of linker 3,3',5,5'-EBTC from Sc-**soc**-MOF.

Consistent with these SCXRD data, cleavage of all olefinic bonds was confirmed by ^{1}H NMR (Figures 5.14d) and negative-mode mass spectrometry of the digested ozonated samples (5% HF/DMSO-d_6) (Figure 5.20), and FT-IR of ozonated Sc-**pcu**-MOF (Figure 5.21), from which the olefinic protons (δ = 7.68 ppm), molecular ion $[M\text{-H}]^-$ of 3,3',5,5'-EBTC and the typical alkene (C=C) stretching band, respectively, were not observed. Conversely, the ^{1}H NMR signals, the molecular ions $[M\text{-H}]^-$ and the carbonyl (C=O) stretching band corresponding to doubly deprotonated trimesic

acid and 5-formylisophthalate were all clearly identifiable, thus further corroborating the clip-off synthesis of Sc-**pcu**-MOF and the overall top-down strategy.

5.3. Experimental section

5.3.1. Materials, methods and characterization

5.3.1.1. Materials

Zirconium oxychloride octahydrate ($ZrOCl_2{\cdot}8H_2O$), formic acid, potassium iodide (KI), scandium(III) nitrate hydrate ($Sc(NO_3)_3{\cdot}xH_2O$), trimesic acid (H_3BTC), anhydrous granular $CaCl_2$ (2-6 mm) and hydrogen peroxide 30 wt. % in H_2O were purchased from Sigma-Aldrich Co. *N,N*-dimethylformamide (DMF), absolute ethanol (EtOH), tetrahydrofuran (THF) and acetone were obtained from Fisher Chemical. 5-[(E)-2-(3,5-dicarboxyphenyl)ethenyl]benzene-1,3-dicarboxylic acid (linker $H_4$3,3',5,5'-EBTC) was obtained from Chemextention Co. All the reagents and solvents were used without further purification unless otherwise specified. Deionized water was obtained with a Milli-Q® system (18.2 MΩ·cm). The ozone generator (model N1668A, 10.4 mmol/h O_3 at room temperature) was purchased from Ozonotec.

5.3.1.2. Methods

Clip-off synthesis of Zr-pcu-MOF via ozonolysis

The synthesis of Zr-**pcu**-MOF was achieved by a solid-gas ozonolysis reaction. This reaction started by packing 20 mg of Zr-**scu**-MOF crystals into a plastic tube, connected on one side to the ozonator (through a $CaCl_2$ humidity trap), and on the other side, to a vacuum pump (through a KI trap), to ensure a continuous flow of ozone through the column. The reaction was run at room temperature for 30 min.

Afterwards, the sample was held in vacuum for another 30 min. This ozonation/vacuum cycle was repeated nine times. Finally, the resulting solid (20 mg) was directly collected from the plastic tube and stored in THF.

Clip-off synthesis of Sc-pcu-MOF via ozonolysis

The clip-off synthesis of Sc-**pcu**-MOF was done in two steps: a first step consisting of a solid-gas ozonolysis reaction, and a second step based on a suspension-gas ozonolysis reaction. In the first step, 20 mg of synthesized Sc-**soc**-MOF crystals were packed into a plastic tube, connected on one side to the ozonator (through a $CaCl_2$ humidity trap), and on the other side, to a vacuum pump (through a KI trap). The reaction was run at room temperature for 2 h. Afterwards, the crystals were collected from the plastic tube and suspended in 4 mL of water. The ozone generator was directly connected to the vial through a syringe. Ozone was bubbled in the suspension for 6 h while magnetically stirring at 880 rpm. The resulting crystals (20 mg) were collected by centrifugation and stored in acetone.

Oxidation of Zr-pcu-MOF to full -COOH pending groups

Dried ozonated crystals were soaked in 1 mL of aqueous H_2O_2 solution (30 wt. % in H_2O) for 3 weeks. During this period, the sample was exchanged with a fresh hydrogen peroxide solution every 24 h. After that, the sample was centrifuged and washed twice with water.

5.3.1.3. Synthesis

Synthesis of Zr-scu-MOF

A solution of $ZrOCl_2{\cdot}8H_2O$ (16 mg, 0.05 mmol) and $H_4$3,3',5,5'-EBTC (7 mg, 0.02 mmol) in DMF (8 mL) and formic acid (8 mL) was prepared in a 23 mL scintillation vial. Then, the sealed vial was placed into a preheated oven at 120 ^oC for 5 days.

After this period, colourless cubic crystals suitable for SCXRD were collected by filtration and washed three times by incubating them with 20 mL of fresh DMF for 12 h. Afterwards, solvent exchange with THF was performed by incubating the crystals three times with 20 mL of THF for 12 h, and the resulting Zr-**scu**-MOF crystals were dried at room temperature (15 mg).

Synthesis of Sc-soc-MOF

A solution of $Sc(NO_3)_3 \cdot xH_2O$ (48 mg, 0.21 mmol) and $H_4$3,3',5,5'-EBTC (16 mg, 0.04 mmol) in DMF (8 mL), EtOH (3.2 mL) and formic acid (1.84 mL) was prepared in a 23 mL scintillation vial. Then, the sealed vial was placed into a preheated oven at 120 ^oC for 48 h. Colourless cubic crystals suitable for SCXRD were collected by filtration and washed three times by incubating them with 20 mL of fresh DMF for 12 h. Afterwards, solvent exchange with acetone was performed by incubating the crystals three times with 20 mL of acetone for 12 h, and the resulting crystals were dried at room temperature (20 mg).

5.3.1.4. Characterization

Single-Crystal X-Ray Diffraction (SCXRD) data of Zr-**scu**-MOF, Zr-**pcu**-MOF, Sc-**soc**-MOF and Sc-**pcu**-MOF were collected at 100 K at BL13-XALOC beamline at ALBA synchrotron (0.82656 Å).[30] Data frames were indexed, integrated and scaled using the XDS program.[31] The structures were solved by direct methods and subsequently refined by correction of F^2 against all reflections, using SHELXST2013 and SHELXL2013 within Olex2 package.[32–34] Non-hydrogen atoms were refined with anisotropic thermal parameters by full-matrix least-squares calculations on F^2 using the program SHELXL2013.[32] Hydrogen atoms were inserted at calculated positions and constrained with isotropic thermal parameters.

Powder X-Ray Diffraction (PXRD) diagrams were collected on a Panalytical X'pert mpd diffractometer with monochromatic Cu-Kα radiation (λ_{Cu} = 1.5406 Å).

Proton Nuclear Magnetic Resonance (^{1}H NMR) spectra were acquired in Bruker Avance DPX of 250 MHz, 360 MHz NMR spectrometers at "Servei de Ressonància Magnètica Nuclear" from Autonomous University of Barcelona (UAB).

Carbon Nuclear Magnetic Resonance (^{13}C NMR) spectra were acquired in Bruker Avance DPX of 250 MHz spectrometer at "Servei de Ressonància Magnètica Nuclear" from Autonomous University of Barcelona (UAB).

Field-emission Scanning Electron Microscopy (FESEM) images were performed in SEM Quanta 650 scanning electron microscopy at an acceleration voltage of 2KV, using aluminium as a support.

Fourier Transform Infrared (FT-IR) spectra were recorded on a Bruker Tensor 27FT-IR spectrometer equipped with a Golden Gate diamond attenuated total reflection (ATR) cell, in transmittance mode at room temperature.

Electrospray Ionization Mass Spectrometry (ESI-MS) spectra were obtained in an Agilent 6210G G1969A LC/MSD TOF mass spectrometer. All the digested MOFs were measured in the negative-ionization mode. The samples for MS analysis were obtained from the ^{1}H NMR digestion samples.

5.3.2. ^{1}H Nuclear Magnetic Resonance

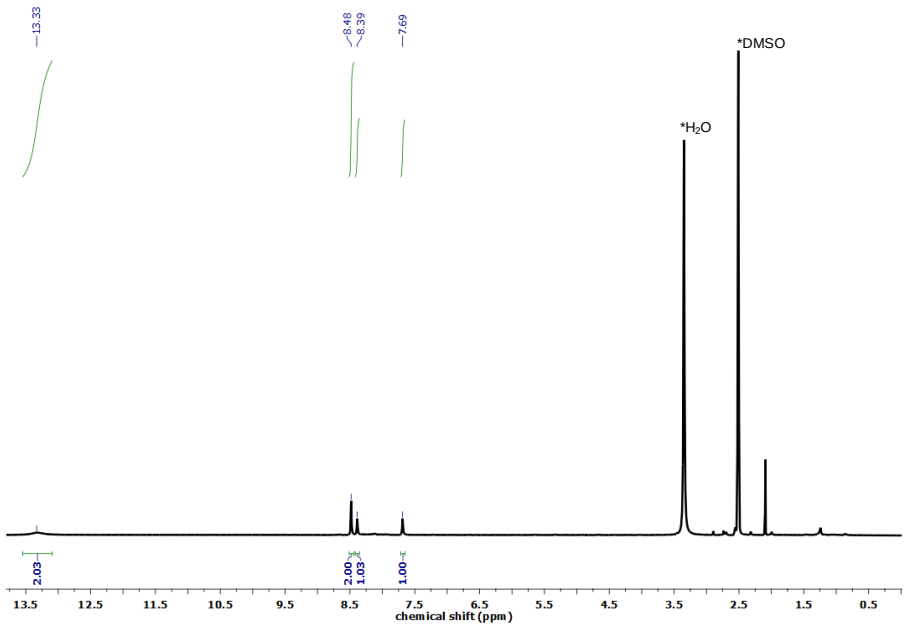


Figure 5.22. ^{1}H NMR spectrum (360 MHz, DMSO-d_6) of the digested Zr-**scu**-MOF. Zr-**scu**-MOF crystals were digested in 5% HF aqueous solutions at 120 °C overnight.

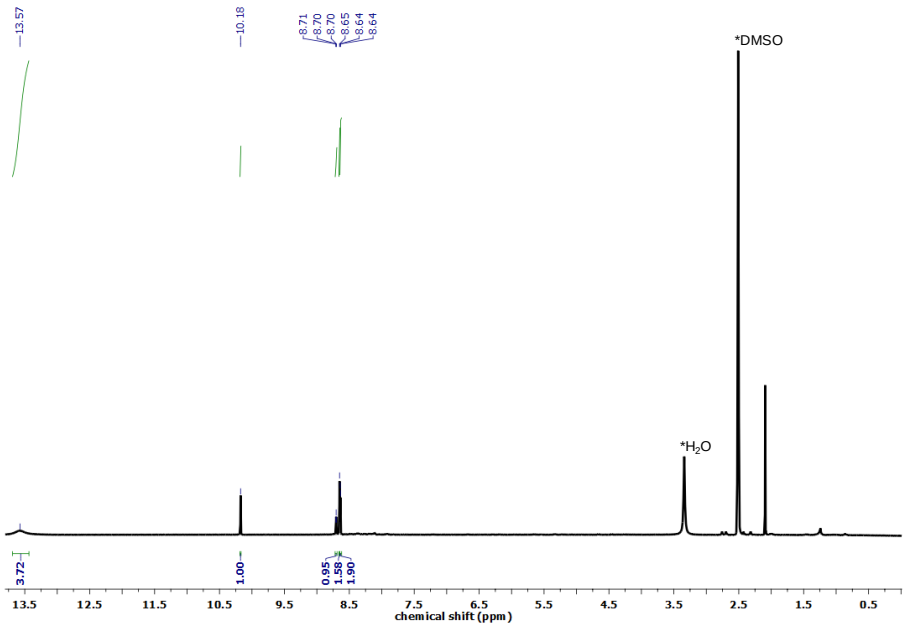


Figure 5.23. ^{1}H NMR spectrum (360 MHz, DMSO-d_6) of the digested Zr-**pcu**-MOF after ozonolysis solid reaction. Zr-**pcu**-MOF crystals were digested in 5% HF aqueous solutions at 120 ^{o}C overnight.

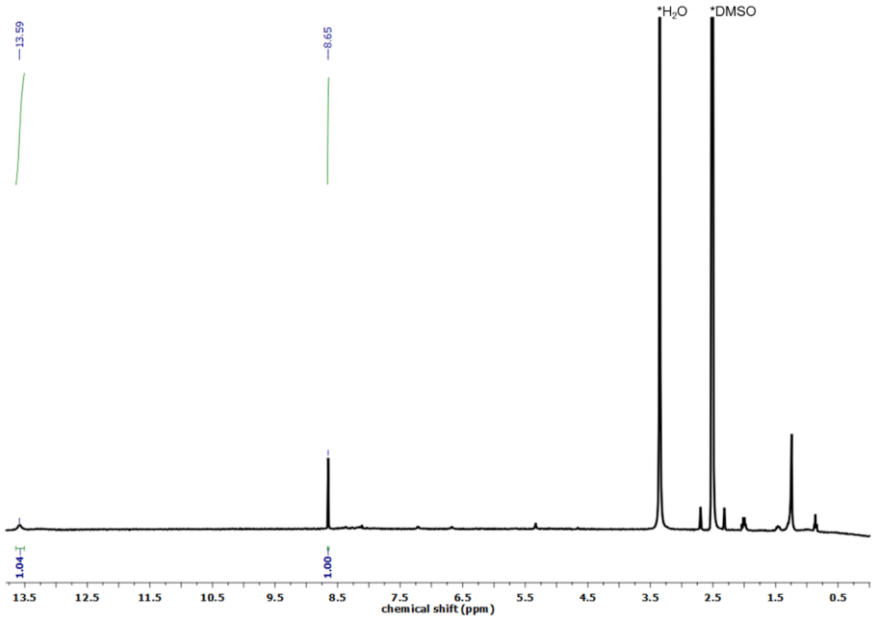


Figure 5.24. ^{1}H NMR spectrum (360 MHz, DMSO-d_6) of the digested oxidized Zr-**pcu**-MOF. Zr-**pcu**-MOF crystals were digested in 5% HF aqueous solutions at 120 °C overnight.

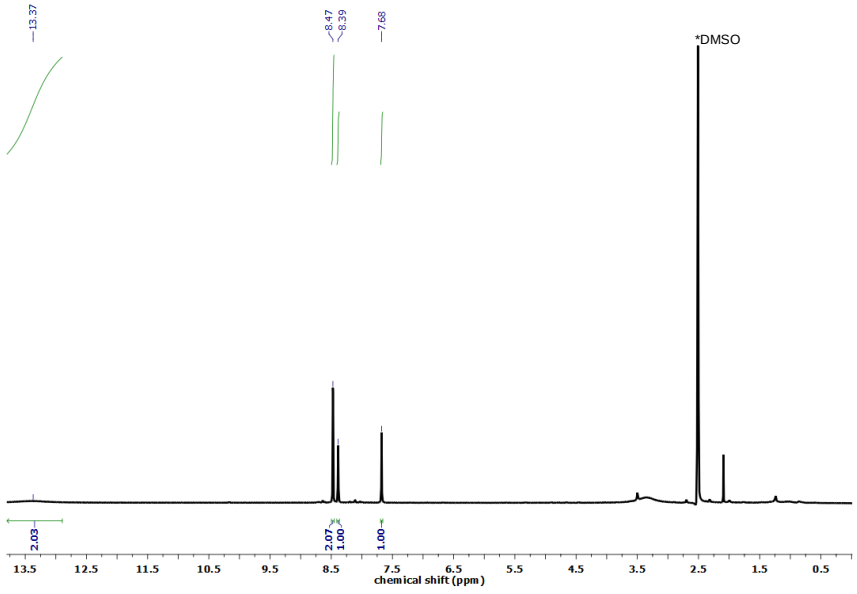


Figure 5.25. ^{1}H NMR spectrum (360 MHz, DMSO-d_6) of the digested Sc-**soc**-MOF. Sc-**soc**-MOF crystals were digested in 5% HF aqueous solutions at 120 °C overnight.

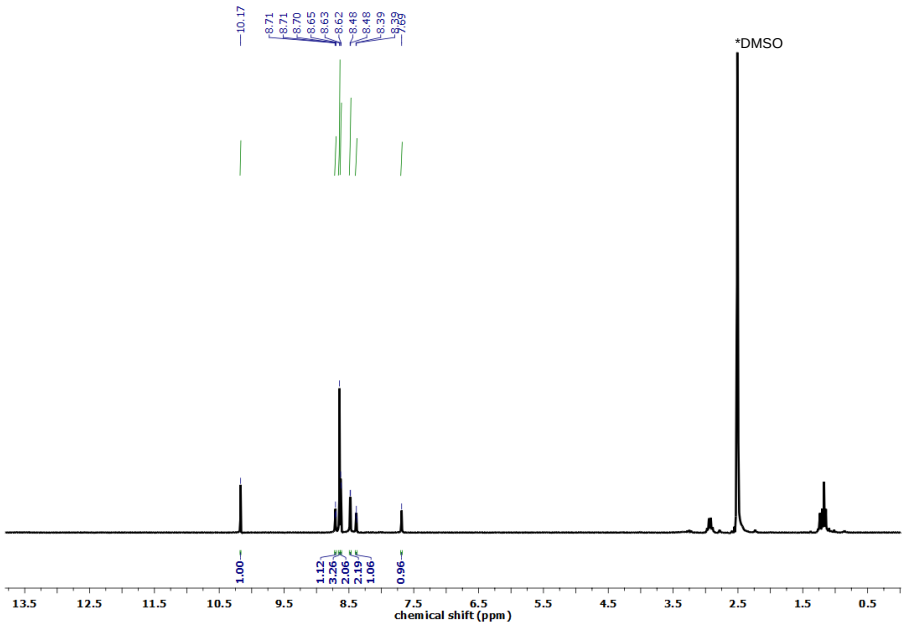


Figure 5.26. ^{1}H NMR spectrum (360 MHz, DMSO-d_6) of the digested Sc-**soc**-MOF after solid-gas ozonolysis reaction for 8 h. The resulting crystals were digested in 5% HF aqueous solutions at 120 °C overnight.

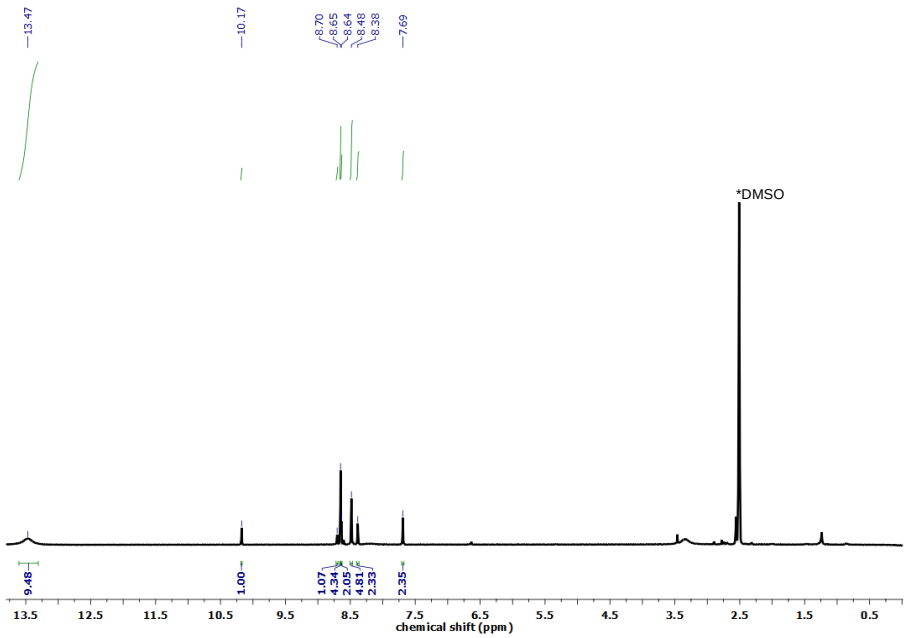


Figure 5.27. ^{1}H NMR spectrum (360 MHz, DMSO-d_6) of the digested Sc-**soc**-MOF after 12 cycles of solid-gas ozonolysis reaction. The resulting crystals were digested in 5% HF aqueous solutions at 120 ^{o}C overnight.

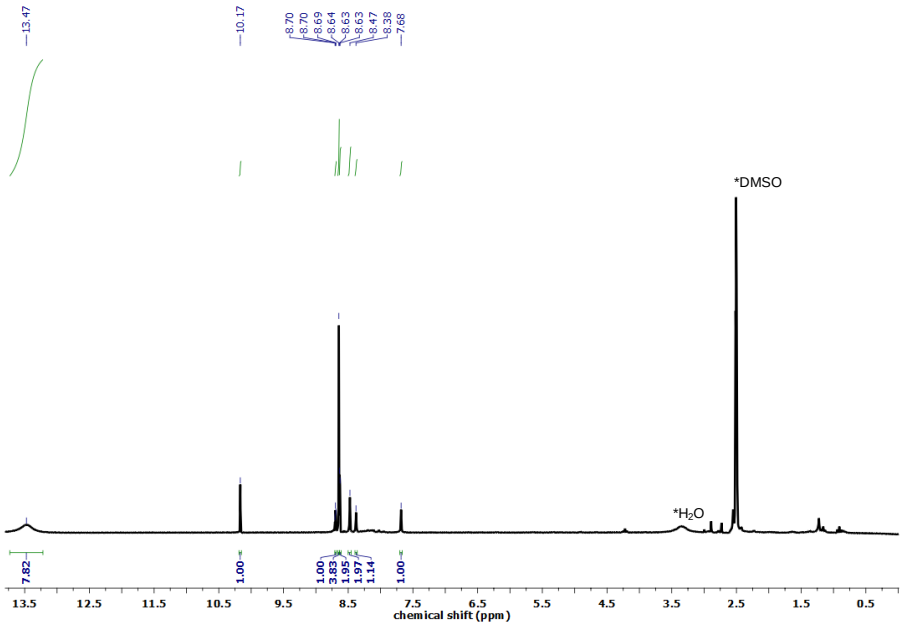


Figure 5.28. ^{1}H NMR spectrum (360 MHz, DMSO-d_6) of the digested Sc-**soc**-MOF after the solid-gas ozonolysis reaction for 2 h. Sc-**soc**-MOF crystals were digested in 5% HF aqueous solutions at 120 °C overnight.

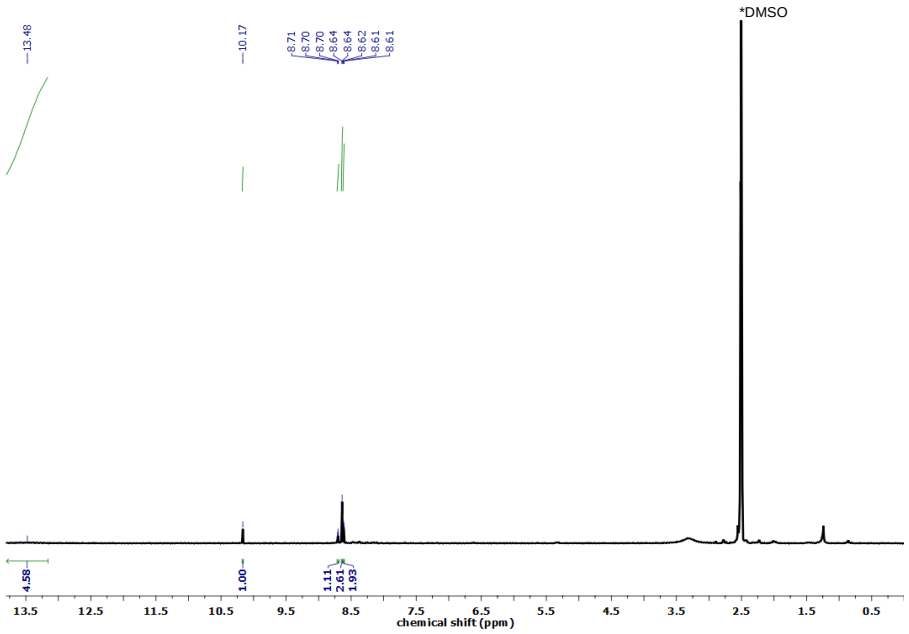


Figure 5.29. ^{1}H NMR spectrum (360 MHz, DMSO-d_6) of the digested Sc-**pcu**-MOF synthesized after the two-step ozonolysis reaction (solid-gas ozonolysis for 2 h and suspension-gas ozonolysis for 6 h). Sc-**pcu**-MOF crystals were digested in 5% HF aqueous solutions at 120 °C overnight.

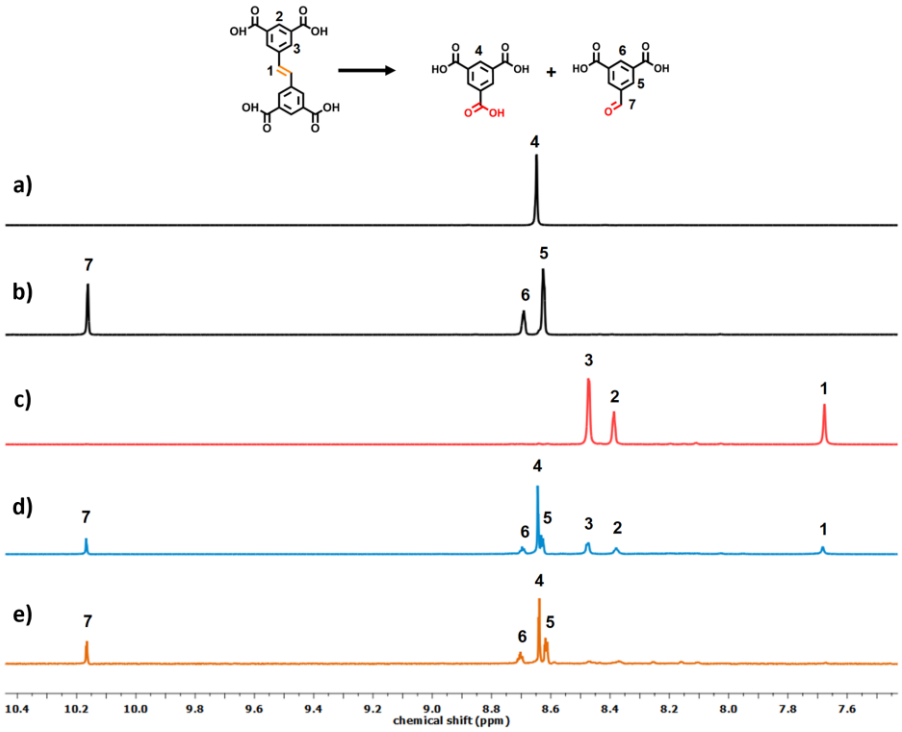


Figure 5.30. ^{1}H NMR spectra (360 MHz, DMSO-d_6) of digested a) H_3BTC, b) 5-formylisophthalic acid, c) Sc-**soc**-MOF, d) Sc-**soc**-MOF after solid-gas reaction (2 h), and e) Sc-**soc**-MOF after solid-gas ozonolysis for 2 h and suspension-gas ozonolysis for 6 h. Note that this latter spectrum corresponds to that of the synthesized Sc-**pcu**-MOF. Assigned proton signals: δ_1 = 7.68 (s, 2H), δ_2 = 8.38 (s, 2H), δ_3 =8.47 (s, 4H), δ_4 =8.65 (s, 3H), δ_5 =8.64 (m, 2H), δ_6 = 8.71 (s, 1H), and δ_7 = 10.17 (s, 1H).

5.3.3. Single-Crystal X-Ray Diffraction

Table 5.1. Crystal data and structure refinement for Zr-scu-MOF

Identification code	CCDC-2080949
Empirical formula	$C_{72}O_{64}Zr_{12}$
Formula weight	2983.36
Temperature/K	100(2)
Crystal system	Monoclinic
Space group	*C2/m*
a/Å	25.637(5)
b/Å	36.223(7)
c/Å	21.661(4)
α/°	90
β/°	122.54(3)
γ/°	90
Volume/Å^3	16958(8)
Z	4
ρ_{calc}g/cm^3	1.169
μ/mm^{-1}	1.157
F(000)	5696.0
Crystal size/mm^3	0.33 × 0.3 × 0.3
Radiation	synchrotron (λ = 0.82653)
2Θ range for data collection/°	2.594 to 58.182
Index ranges	-30 ≤ h ≤ 25, 0 ≤ k ≤ 42, 0 ≤ l ≤ 25
Reflections collected	44506
Independent reflections	14607 [R_{int} = 0.0968, R_{sigma} = 0.1369]
Data/restraints/parameters	14607/114/556
Goodness-of-fit on F^2	1.942
Final R indexes [I>=2σ (I)]	R_1 = 0.1983, wR_2 = 0.4825
Final R indexes [all data]	R_1 = 0.2125, wR_2 = 0.5069
Largest diff. peak/hole / e Å^{-3}	8.61/-6.78

Table 5.2. Crystal data and structure refinement for Zr-pcu-MOF

Identification code	CCDC-2080950
Empirical formula	$C_{71.25}O_{67.5}Zr_{12}$
Formula weight	3030.35
Temperature/K	100(2)
Crystal system	Monoclinic
Space group	*C2/m*
a/Å	35.703(7)
b/Å	25.210(5)
c/Å	25.210(5)
α/°	90
β/°	134.89(3)
γ/°	90
Volume/Å^3	16076(8)
Z	4
ρ_{calc}g/cm^3	1.252
μ/mm^{-1}	0.812
F(000)	5790.0
Crystal size/mm^3	0.38 × 0.32 × 0.32
Radiation	synchrotron (λ = 0.82653)
2Θ range for data collection/°	2.28 to 34.45
Index ranges	-29 ≤ h ≤ 29, -20 ≤ k ≤ 20, -20 ≤ l ≤ 20
Reflections collected	28412
Independent reflections	4867 [R_{int} = 0.13378, R_{sigma} = 0.0877]
Data/restraints/parameters	4867/0/513
Goodness-of-fit on F^2	1.336
Final R indexes [I>=2σ (I)]	R_1 = 0.1277, wR_2 = 0.3291
Final R indexes [all data]	R_1 = 0.1736, wR_2 = 0.3849
Largest diff. peak/hole / e Å^{-3}	1.13/-0.76

Table 5.3. Crystal data and structure refinement for Sc-soc-MOF

Identification code	CCDC-2080951
Empirical formula	$C_{108}O_{64}Sc_{12}$
Formula weight	2860.60
Temperature/K	100
Crystal system	Trigonal
Space group	*R-3*
a/Å	31.750(5)
b/Å	31.750(5)
c/Å	38.800(5)
α/°	90
β/°	90
γ/°	120
Volume/Å^3	33872.7
Z	6
ρ_{calc}g/cm^3	0.842
μ/mm^{-1}	0.594
F(000)	8480
Crystal size/mm^3	0.27 × 0.23 × 0.21
Radiation	synchrotron (λ = 0.82653)
2Θ range for data collection/°	2.584 to 24.409
Index ranges	-31 ≤ h ≤ 31, -31 ≤ k ≤ 31, -38 ≤ l ≤ 38
Reflections collected	78341
Independent reflections	7872 [R_{int} = 0.0448, R_{sigma} = 0.0741]
Data/restraints/parameters	7872/0/548
Goodness-of-fit on F^2	1.161
Final R indexes [I>=2σ (I)]	R_1 = 0.0998, wR_2 = 0.2812
Final R indexes [all data]	R_1 = 0.1047, wR_2 = 0.2870
Largest diff. peak/hole / e Å^{-3}	0.949/-1.316

Table 5.4. Crystal data and structure refinement for Sc-pcu-MOF

Identification code	CCDC-2080952
Empirical formula	$C_{31.75}O_{21.83}Sc_4$
Formula weight	910.49
Temperature/K	293(2)
Crystal system	Trigonal
Space group	*R-3*
a/Å	31.650(5)
b/Å	31.650(5)
c/Å	38.763(8)
α/°	90
β/°	90
γ/°	120
Volume/Å^3	33628(12)
Z	18
ρ_{calc}g/cm^3	0.809
μ/mm^{-1}	0.392
F(000)	8085
Crystal size/mm^3	0.21 × 0.18 × 0.17
Radiation	synchrotron (λ = 0.82653)
2Θ range for data collection/°	0.910 to 20.797
Index ranges	-31 ≤ h ≤ 31, -31 ≤ k ≤ 31, -38 ≤ l ≤ 38
Reflections collected	74052
Independent reflections	7822 [R_{int} = 0.0494, R_{sigma} = 0.0241]
Data/restraints/parameters	7822/0/539
Goodness-of-fit on F^2	2.036
Final R indexes [I>=2σ (I)]	R_1 = 0.1497, wR_2 = 0.4331
Final R indexes [all data]	R_1 = 0.1610, wR_2 = 0.4579
Largest diff. peak/hole / e Å^{-3}	0.559/-0.530

5.4. Conclusions

In this Chapter, we have introduced a new top-down approach, Clip-off Chemistry, to unveil the synthesis of molecules and materials composed of less-symmetric MBBs based selective bond-breaking in reticular precursor materials *via* common organic transformations, permitting the programmed de-reticulation and controlled etching at the molecular level. As proof-of-concept, we transformed two 3D MOFs (Zr-**scu**-MOF and Sc-**soc**-MOF) into two topologically distinct 3D MOFs (Zr-**pcu**-MOF and Sc-**pcu**-MOF, respectively). In the examples that we have reported here, we demonstrated that the cleavage was quantitative and selective; was effective both in solid-phase and solution-phase chemistry; and occurred in a single-crystal-to-single crystal fashion across the entire bulk precursor sample. Moreover, we demonstrated control over the cleavage of each olefinic bond into carboxylic acid groups using oxidative conditions.

Our preliminary results suggest that Clip-off Chemistry is ripe for further exploration. Since it is based on bond cleavage, the dimensionality of the parent reticular material dictates the synthetic feasibility of the target molecules and/or materials (Figure 5.31). Thus, it offers the possibility to modify structures of reticular materials without changing their dimensionality (*e.g.* 3D → 3D, or 2D → 2D). For example, one might employ Clip-off Chemistry for PSM of the topology and/or the porosity of a given material. Moreover, it could be applied to 3D structures to augment the diversity of new 2D materials: for instance, by converting well-known 3D pillared reticular materials into isolated 2D layers, via selective clipping of the pillaring linkers. Similarly, it shows promise for using 3D or 2D structures to isolate 1D materials in the form of metallic chains, or to synthesize 0D systems, including MOPs, macrocycles and clusters, from 3D/2D/1D structures and even from other 0D systems (*e.g.* MOPs). Cleavage of bonds in reticular materials may also be expanded to purely organic structures. Indeed, COFs and organic cages are another endless source of precursors in Clip-off Chemistry for possible

synthesis of organic polymers, cages, macrocycles or other organic compounds. Similarly, other reactions involving the cleavage of bonds (*e.g.* hydrolysis, thermolysis or photolysis) are potential candidates to be applied in reticular materials for their programmable disassembly.[7,9,35–37] In summary, our results prove that the programmed disassembly of reticular materials is feasible, and that Clip-off Chemistry could provide researchers with access to myriad new molecular architectures.

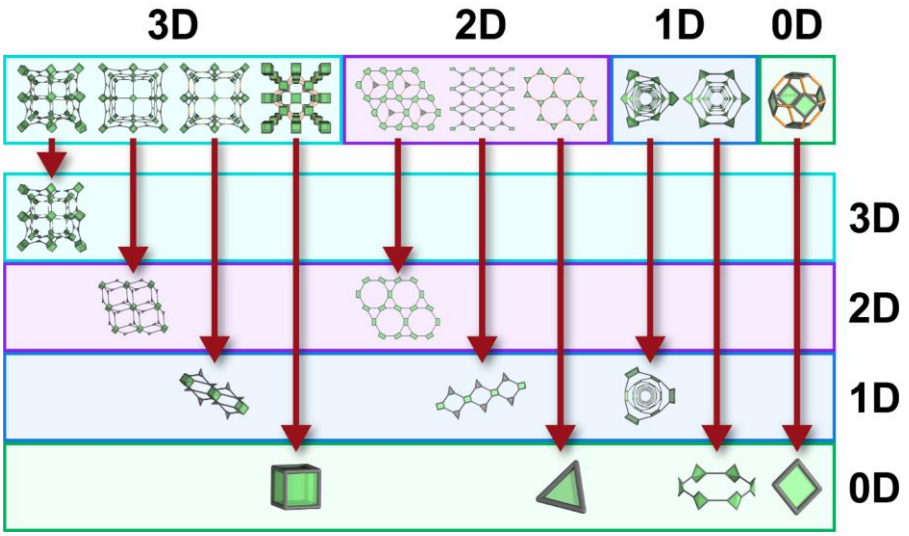


Figure 5.31. Clip-off Chemistry for the synthesis of molecular architectures of different dimensionality. Schematic illustrating the potential outcomes of Clip-off Chemistry, in which the dimensionality of the parent reticular material dictates the dimensionality of the target molecules and structures.

5.5. References

(1) Deria, P.; Mondloch, J. E.; Karagiaridi, O.; Bury, W.; Hupp, J. T.; Farha, O. K. Beyond Post Synthesis Modification: Evolution of Metal–Organic Frameworks via Building Block Replacement. *Chem. Soc Rev.* **2014**, *43*, 5896–5912.

(2) Brozek, C. K.; Dincă, M. Cation Exchange at the Secondary Building Units of Metal–Organic Frameworks. *Chem. Soc. Rev.* **2014**, *43*, 5456–5467.

(3) Tu, B.; Pang, Q.; Wu, D.; Song, Y.; Weng, L.; Li, Q. Ordered Vacancies and Their Chemistry in Metal-Organic Frameworks. *J. Am. Chem. Soc.* **2014**, *136*, 14465–14471.

(4) Yuan, S.; Lu, W.; Chen, Y. P.; Zhang, Q.; Liu, T. F.; Feng, D.; Wang, X.; Qin, J.; Zhou, H. C. Sequential Linker Installation: Precise Placement of Functional Groups in Multivariate Metal-Organic Frameworks. *J. Am. Chem. Soc.* **2015**, *137*, 3177–3180.

(5) Zhai, Q. G.; Bu, X.; Mao, C.; Zhao, X.; Daemen, L.; Cheng, Y.; Ramirez-Cuesta, A. J.; Feng, P. An Ultra-Tunable Platform for Molecular Engineering of High-Performance Crystalline Porous Materials. *Nat. Commun.* **2016**, *7*, 1–9.

(6) Eddaoudi, M.; Moler, D. B.; Li, H.; Chen, B.; Reineke, T. M.; O'Keeffe, M.; Yaghi, O. M. Modular Chemistry: Secondary Building Units as a Basis for the Design of Highly Porous and Robust Metal-Organic Carboxylate Frameworks. *Acc. Chem. Res.* **2001**, *34*, 319–330.

(7) Yuan, S.; Zou, L.; Qin, J. S.; Li, J.; Huang, L.; Feng, L.; Wang, X.; Bosch, M.; Alsalme, A.; Cagin, T.; Zhou, H. C. Construction of Hierarchically Porous Metal–Organic Frameworks through Linker Labilization. *Nat. Commun.* **2017**, *8*, 1–10.

(8) Ding, Y.; Chen, Y. P.; Zhang, X.; Chen, L.; Dong, Z.; Jiang, H. L.; Xu, H.; Zhou, H. C. Controlled Intercalation and Chemical Exfoliation of Layered Metal-Organic Frameworks Using a Chemically Labile Intercalating Agent. *J. Am. Chem. Soc.* **2017**, *139*, 9136–9139.

(9) Feng, L.; Yuan, S.; Zhang, L. L.; Tan, K.; Li, J. L.; Kirchon, A.; Liu, L. M.; Zhang, P.; Han, Y.; Chabal, Y. J.; Zhou, H. C. Creating Hierarchical Pores by Controlled Linker Thermolysis in Multivariate Metal-Organic Frameworks. *J. Am. Chem. Soc.* **2018**, *140*, 2363–2372.

(10) Geary, J.; Wong, A. H.; Xiao, D. J. Thermolabile Cross-Linkers for Templating Precise Multicomponent Metal-Organic Framework Pores. *J. Am. Chem. Soc.* **2021**, *143*, 10317–10323.

(11) Albalad, J.; Xu, H.; Gándara, F.; Haouas, M.; Martineau-Corcos, C.; Mas-Ballesté, R.; Barnett, S. A.; Juanhuix, J.; Imaz, I.; Maspoch, D. Single-Crystal-to-Single-Crystal Postsynthetic Modification of a Metal–Organic Framework via Ozonolysis. *J. Am. Chem. Soc.* **2018**, *140*, 2028–2031.

(12) Eddaoudi, M.; Kim, J.; Rosi, N.; Vodak, D.; Wachter, J.; O'Keeffe, M.; Yaghi, O. M. Systematic Design of Pore Size and Functionality in Isoreticular MOFs and Their Application in Methane Storage. *Science* **2002**, *295*, 469–472.

(13) Cohen, S. M. Postsynthetic Methods for the Functionalization of Metal-Organic Frameworks. *Chem. Rev.* **2012**, *112*, 970–1000.

(14) Yaghi, O. M. Reticular Chemistry: Molecular Precision in Infinite 2D and 3D. *Mol. Front. J.* **2019**, *3*, 66-83.

(15) O'Keeffe, M.; Yaghi, O. M. Deconstructing the Crystal Structures of Metal-Organic Frameworks and Related Materials into Their Underlying Nets. *Chem. Rev.* **2012**, 112, 675–702.

(16) O'Keeffe, M.; Peskov, M. A.; Ramsden, S. J.; Yaghi, O. M. The Reticular Chemistry Structure Resource (RCSR) Database of, and Symbols for, Crystal Nets. *Acc. Chem. Res.* **2008**, *41*, 1782–1789.

(17) Blatov, V. A.; Shevchenko, A. P.; Proserpio, D. M. Applied Topological Analysis of Crystal Structures with the Program Package Topospro. *Cryst. Growth Des.* **2014**, *14*, 3576–3586.

(18) Wells, A. F. Three-Dimensional Nets and Polyhedral, Wiley, Hoboke, **19**77.

(19) Wang, H.; Dong, X.; Lin, J.; Teat, S. J.; Jensen, S.; Cure, J.; Alexandrov, E. V.; Xia, Q.; Tan, K.; Wang, Q.; Olson, D. H.; Proserpio, D. M.; Chabal, Y. J.;

Thonhauser, T.; Sun, J.; Han, Y.; Li, J. Topologically Guided Tuning of Zr-MOF Pore Structures for Highly Selective Separation of C6 Alkane Isomers. *Nat. Commun.* **2018**, *9*, 1–11.

(20) Li, M.; Li, D.; O'Keeffe, M.; Yaghi, O. M. Topological Analysis of Metal-Organic Frameworks with Polytopic Linkers and/or Multiple Building Units and the Minimal Transitivity Principle. *Chem. Rev.* **2014**, *114*, 1343–1370.

(21) Guillerm, V.; Xu, H.; Albalad, J.; Imaz, I.; Maspoch, D. Postsynthetic Selective Ligand Cleavage by Solid–Gas Phase Ozonolysis Fuses Micropores into Mesopores in Metal–Organic Frameworks. *J. Am. Chem. Soc.* **2018**, *140*, 15022–15030.

(22) Criegee, R. Mechanism of Ozonolysis. *Angew. Chem. Int. Ed.* **1975**, *14*, 745–752.

(23) Schiaffo, C. E.; Dussault, P. H. Ozonolysis in Solvent/Water Mixtures: Direct Conversion of Alkenes to Aldehydes and Ketones. *J. Org. Chem.* **2008**, *73*, 4688–4690.

(24) Harding, L. B.; III, W. A. G. Mechanisms of Gas-Phase and Liquid-Phase Ozonolysis. *J. Am. Chem. Soc.* **2002**, *100*, 7180–7188.

(25) Liu, Y.; Eubank, J. F.; Cairns, A. J.; Eckert, J.; Kravtsov, V. Ch.; Luebke, R.; Eddaoudi, M. Assembly of Metal–Organic Frameworks (MOFs) Based on Indium-Trimer Building Blocks: A Porous MOF with Soc Topology and High Hydrogen Storage. *Angew. Chem. Int. Ed.* **2007**, *46*, 3278–3283.

(26) Xie, L. H.; Liu, X. M.; He, T.; Li, J. R. Metal-Organic Frameworks for the Capture of Trace Aromatic Volatile Organic Compounds. *Chem* **2018**, *4*, 1911–1927.

(27) Wang, S.; Chen, L.; Wahiduzzaman, M.; Tissot, A.; Zhou, L.; Ibarra, I. A.; Gutiérrez-Alejandre, A.; Lee, J. S.; Chang, J. S.; Liu, Z.; Marrot, J.; Shepard, W.; Maurin, G.; Xu, Q.; Serre, C. A Mesoporous Zirconium-Isophthalate Multifunctional Platform. *Matter* **2021**, *4*, 182–194.

(28) Furukawa, H.; Gándara, F.; Zhang, Y.-B.; Jiang, J.; Queen, W. L.; Hudson, M. R.; Yaghi, O. M. Water Adsorption in Porous Metal–Organic Frameworks and Related Materials. *J. Am. Chem. Soc.* **2014**, *136*, 4369–4381.

(29) Zhang, J. W.; Qu, P.; Hu, M. C.; Li, S. N.; Jiang, Y. C.; Zhai, Q. G. Topology-Guided Design for Sc-Soc-MOFs and Their Enhanced Storage and Separation for CO2 and C2-Hydrocarbons. *Inorg. Chem.* **2019**, *58*, 16792-16799.

(30) Juanhuix, J.; Gil-Ortiz, F.; Cuní, G.; Colldelram, C.; Nicolás, J.; Lidón, J.; Boter, E.; Ruget, C.; Ferrer, S.; Benach, J. Developments in Optics and Performance at BL13-XALOC, the Macromolecular Crystallography Beamline at the Alba Synchrotron. *J. Synchrotron Radiat.* **2014**, *21*, 679–689.

(31) Kabsch, W. Integration, Scaling, Space-Group Assignment and Post-Refinement. *Acta Cryst. D* **2010**, *66*, 133–144.

(32) Sheldrick, G. M.; IUCr. Crystal Structure Refinement with SHELXL. *Acta Cryst. C* **2015**, *71*, 3–8.

(33) Sheldrick, G. M.; IUCr. SHELXT – Integrated Space-Group and Crystal-Structure Determination. *Acta Cryst. A* **2015**, *71*, 3–8.

(34) Dolomanov, O. V.; Bourhis, L. J.; Gildea, R. J.; Howard, J. A. K.; Puschmann, H. OLEX2: A Complete Structure Solution, Refinement and Analysis Program. *J. Appl. Cryst.* **2009**, *42*, 339–341.

(35) Feng, L.; Wang, K. Y.; Day, G. S.; Ryder, M. R.; Zhou, H. C. Destruction of Metal-Organic Frameworks: Positive and Negative Aspects of Stability and Lability. *Chem. Rev.* **2020**, *120*, 13087–13133.

(36) Wang, K.-Y.; Feng, L.; Yan, T.-H.; Wu, S.; Joseph, E. A.; Zhou, H.-C. Rapid Generation of Hierarchically Porous Metal–Organic Frameworks through Laser Photolysis. *Angew. Chem. Int. Ed.* **2020**, *59*, 11349–11354.

(37) Shieh, P.; Hill, M. R.; Zhang, W.; Kristufek, S. L.; Johnson, J. A. Clip Chemistry: Diverse (Bio)(Macro)Molecular and Material Function through Breaking Covalent Bonds. *Chem. Rev.* **2021**, *121*, 7059-7121.

Chapter 6

General conclusions

This Thesis has been focused on understanding the assembly of less-symmetric organic MBBs in reticular chemistry, developing new top-down approaches, based on the de-reticulation of nets built with higher connected MBBs for the prediction of novel reticular materials.

The first part of this Thesis has studied the different types of desymmetrization of organic MBBs and how this desymmetrization affects in the assembly process when combining the desymmetrized linkers with high-connected inorganic MBBs; more precisely, Zr- and RE-based clusters, deviating from default nets. We determined that the aspect ratio and torsion angles of these linkers have a crucial role for directing to specific nets, observing a tendency in the linker metrics expansion, elongation and rotation. These parameters change the connectivity and geometry of Zr- and RE-cluster, and therefore, the net formation when 3-c triangular, 4-c square/rectangular and 4-c tetrahedral linkers are used. We have contributed to this study with two additional 4-c linkers exhibiting expanded metrics and in-plane translation for comparing the behaviour of the assembly of Zr- and RE-MOFs. From these assemblies, we have synthesized four novel MOFs, suggesting that the desymmetrization of these linkers can direct to unconventional structures based on new 4-c Zr_6-clusters or 8-c RE_7-clusters, which have never been observed. We further expanded our study to 8-c organic linkers, obtaining a mesoporous high-connected Zr-MOF exhibiting a minimal edge-transitive **eps** net, in contrast to the RE analogue that exhibited the edge-transitive **kce** net.

Because of the limitations exposed in the previous Chapter with bottom-up approaches, we have developed and validated a new, theoretical top-down approach, net-clipping, based on the de-reticulation of MOFs and edge-transitive nets by clipping MBBs or nodes of higher connectivity and symmetry by half. After selecting the clippable organic MBBs (square/rectangular, 4-c tetrahedral, 6-c hexagonal, 8-c cubic, and 12-c hexagonal prismatic linkers), we have applied net-clipping to edge-transitive nets based on nodes with this connectivity and shape, anticipating the formation of 141 derived nets and 56 clipped nets. Among them, 33

new derived nets (*icn*7–*icn*39) and 6 new clipped nets (*icn*1–*icn*6) were not previously described. We have predicted the different nets that should be accessible upon assembly of less-symmetric MBBs with different polyhedral MBBs. Our approach was supported by several literature examples and six novel structures, also extending to less regular, non-edge transitive nets, a fact that will surely increase the discovery of available topologies in a near future.

Finally, we have translated our design strategy to the chemical field by developing and validating a novel, synthetic top-down approach, Clip-off Chemistry, based on the programmed disassembly of reticular materials *via* bond breaking. In this Thesis, we have demonstrated the feasibility of clip-off chemistry by synthesizing two new 3D MOFs from two other 3D MOFs via programmed bond breaking. To this end, we have synthesized two 3D MOFs (Zr-**pcu**-MOF and Sc-**pcu**-MOF) from two topologically distinct 3D MOFs (Zr-**scu**-MOF and Sc-**soc**-MOF, respectively). Both MOFs have been constructed with the same linker ($H_4$3,3',5,5'-EBTC), and the subsequent ozonolysis treatment have broken localized edges of the net in a quantitative and selective fashion, demonstrating a precise molecular control with the single-crystal-to-single-crystal transformation of the original MOFs based on the 4,8-c **scu** and 4,6-c **soc** nets into the 6-c **pcu** net.

We are confident that these findings presented in this Thesis enriches the repertoire for topological predictions, providing new tools for the rational design of more complex reticular materials. The use of top-down approaches covered the limitations of the bottom-up design synthetic and post-synthetic strategies, and will continue to inform the design of future porous materials such as MOFs and COFs, by enabling the assembly of new, otherwise inaccessible topologies. We expect that the top-down approaches demonstrated in this Thesis represented a step forward in the prediction of structures in this field, which could inspire and pave the way to novel strategies that we anticipate will arise for the better understanding and control of made-to-order materials.

Annex

List of publications

List of publications

The work described in this PhD Thesis has given rise to the following scientific papers:

1. Ortín-Rubio, B.; Ghasempour, H.; Guillerm, V.; Morsali, A.; Juanhuix, J.; Imaz, I.; Maspoch, D. Net-Clipping: An Approach to Deduce the Topology of Metal-Organic Frameworks Built with Zigzag Ligands *J. Am. Chem. Soc.* **2020**, *142*, 9135-9140.
2. Yang, Y.;[‡] Broto-Ribas, A.;[‡] Ortín-Rubio, B.;[‡] Imaz, I.; Gándara, F.; Carné-Sánchez, A.; Guillerm, V.; Jurado, S.; Busqué, F.; Juanhuix, J.; Maspoch, D. Clipp-off Chemistry: Synthesis by Programmed Disassembly of Reticular Materials *Angew. Chem. Int. Ed.* **2022**, *61*, e202111228. (‡ = co-first authorship)
3. Ortín-Rubio, B.; Perona-Bermejo, C.; Suárez del Pino, J. A.; Carmona, F. J.; Gándara, F.; Navarro, J. A. R.; Juanhuix, J.; Imaz, I.; Maspoch, D. A Mesoporous Zr-Based Metal–Organic Framework Driven by the Assembly of an Octatopic Linker *Chem. Commun.* **2023**, *59*, 7803-7806.
4. Ortín-Rubio, B.; Rostoll-Berenguer, J.; Vila, C.; Proserpio, D. M.; Guillerm, V.; Juanhuix, J.; Imaz, I.; Maspoch, D. Net-Clipping as a Top-Down Approach for the Prediction of Topologies of MOFs Built from Reduced-Symmetry Linkers *Chem. Sci.* **2023**, *14*, 12984-12994.
5. Ortín-Rubio, B.;[‡] Yang, Y.;[‡] Rostoll-Berenguer, J.; Vila, C.; Juanhuix, J.; Imaz, I.; Maspoch, D. Exploring the Effect of Linker Desymmetrization in Zr and Rare Earth Metal-Organic Frameworks Unveils New Topologies with Defective Clusters *In preparation.* (‡ = co-first authorship)
6. Ortín-Rubio, B.; Imaz, I.; Maspoch, D. Desymmetrization of Organic Molecular Building Blocks in Metal-Organic Frameworks Constructed with High-Connected Clusters *In preparation.*

List of publications

The author of this Thesis also contributed to the following publications:

7. Jiménez-Almarza, A.; López-Magano, A.; Cano, R.; Ortín-Rubio, B.; Díaz-García, D.; Gomez-Ruiz, S.; Imaz, I.; Maspoch, D.; Mas-Ballesté, R.; Aleman, J. Engineering Covalent Organic Frameworks in the Modulation of Photocatalytic Degradation of Pollutants Under Visible Light Conditions *Mater. Today Chem.* **2021**, *22*, 100548.
8. López-Magano, A.; Ortín-Rubio, B.; Imaz, I.; Maspoch, D.; Aleman, J.; Mas-Ballesté, R. Photoredox Heterobimetallic Dual Catalysis Using Engineered Covalent Organic Frameworks *ACS Catal.* **2021**, *11*, 12344-12354.
9. Khobotov-Bakishev, A.; von Baeckmann, C.; Ortín-Rubio, B.; Hernández-López, L.; Cortés-Martínez, A.; Martínez-Esaín, J.; Gándara, F.; Juanhuix, J.; Platero-Prats, A. E.; Faraudo, J.; Carné-Sánchez, A.; Maspoch, D. Multicomponent, Functionalized HKUST-1 Analogues Assembled via Reticulation of Prefabricated Metal-Organic Polyhedral Cavities *J. Am. Chem. Soc.* **2022**, *144*, 15745-15753.
10. Yang, Y.; Fernández-Seriñán, P.; Imaz, I.; Gándara, F.; Handke, M.; Ortín-Rubio, B.; Juanhuix, J.; Maspoch, D. Isoreticular Contraction of Metal-Organic Frameworks Induced by Cleavage of Covalent Bonds *J. Am. Chem. Soc.* **2023**, *145*, 17398-17405.
11. Shan, M.; Geng, X.; Imaz, I.; Broto-Ribas, A.; Ortín-Rubio, B.; Maspoch, D.; Ansaloni, L.; Peters, T. A.; Tena, A.; Boerrigter, M. E.; Vermaas, D. A. Metal- and Covalent-Organic Framework Mixed Matrix Membranes for CO_2 Separation: A Perspective on Stability and Scalability *J. Membr. Sci.* **2024**, *691*, 122258.

JACS
JOURNAL OF THE AMERICAN CHEMICAL SOCIETY
pubs.acs.org/JACS
Communication

Net-Clipping: An Approach to Deduce the Topology of Metal–Organic Frameworks Built with Zigzag Ligands

Borja Ortín-Rubio, Hosein Ghasempour, Vincent Guillerm,* Ali Morsali, Judith Juanhuix, Inhar Imaz,* and Daniel Maspoch*

Cite This: J. Am. Chem. Soc. 2020, 142, 9135–9140
Read Online
ACCESS | Metrics & More | Article Recommendations | Supporting Information

ABSTRACT: Herein we propose a new approach for deducing the topology of metal–organic frameworks (MOFs) assembled from organic ligands of low symmetry, which we call *net-clipping*. It is based on the construction of nets by rational deconstruction of edge-transitive nets comprising higher-connected molecular building blocks (MBBs). We have applied net-clipping to predict the topologies of MOFs containing zigzag ligands. To this end, we derived 2-connected (2-c) zigzag ligands from 4-c square-like MBBs by first splitting the 4-c nodes into two 3-c nodes and then clipping their two diagonally connecting groups. We demonstrate that, when this approach is applied to the 17 edge-transitive nets containing square-like 4-c MBBs, net-clipping leads to generation of 10 nets with different underlying topologies. Moreover, we report that literature and experimental research corroborate successful implementation of our approach. As proof-of-concept, we employed net-clipping to form three new MOFs built with zigzag ligands, each of which exhibits the deduced topology.

Reticular chemistry, defined as the "process of assembling judiciously designed rigid molecular building blocks (MBBs) into predetermined ordered structures (networks), which are held together by strong bonding",[1,2] has become essential in the design and synthesis of porous metal–organic frameworks (MOFs). Its success lies in precise analysis of the geometry and connectivity of the MBBs as well as in classification of their assemblies into different topologies.[3] Thus, over the past two decades, application of the mathematics discipline of topology to MBBs[4,5] [or secondary building units (SBUs)][2,6] has enabled synthesis of myriad MOFs based on reticulation of edge-transitive nets or their derived nets. Complementarily to these approaches, researchers have recently devised new design strategies to further expand rational design of MOFs, including supermolecular building blocks (SBBs)[7−9] and supermolecular building layers (SBLs).[9,10] These strategies also include the merged-net approach, which is based on merging two edge-transitive nets into one minimal edge-transitive net, a useful strategy for rational design of mixed-linker MOFs.[11]

Herein we report a new design approach that, unlike the rational, bottom-up construction of edge-transitive nets, is based on the top-down deconstruction of edge-transitive nets. Our group recently reported that the combination of certain building blocks can induce structural irregularity (known as geometry mismatch)[12] that complicates rational design of MOFs, as has been observed with use of less-symmetric, 2-connected (2-c) groups such as bent,[13] twisted,[14] or zigzag ligands/MBBs.[15] In addition, the various possibilities of orientation of nonlinear ligands around inorganic MBBs lead to a high number of theoretical possibilities for polymorphism and, therefore, a low structural predictability (Figure S1).[16,17] However, as high symmetry would likely be mostly favored, we reasoned that less-symmetric ligands could be derived from more-symmetric MBBs of higher connectivity by simply reducing the connectivity of the latter. For example, a zigzag ligand can be formed by removing the two diagonally connecting groups of the two 3-c nodes derived from a 4-c MBB (Figure 1a). Accordingly, we reasoned that MOF structures made of less-symmetric ligands could be anticipated via rational clipping of the connecting groups of more-symmetric MBBs in edge-transitive nets. This new approach, which we have called net-clipping, provides further insights to our recent works on transversal reticular chemistry[15] and geometry mismatch[12] and can facilitate rational design of MOFs built up from less-symmetric MBBs.

We propose the use of net-clipping to rationalize/anticipate the MOFs that could be built from zigzag ligands. To this end, among the 54 edge-transitive nets (with D-symbol size ≤32) reported by O'Keeffe et al.,[18] we first selected the 17 nets assembled from 4-c square-like MBBs. These nets are formed by combining a 4-c MBB with other polygonal and polyhedral MBBs (Table 1). Next, we derived these nets by splitting the 4-c nodes into two 3-c nodes (Figure 1).[19] This node splitting step is important to reduce the symmetry of the 4-c MBBs and convert them into rectangular shapes, from which the two zigzag ligands can be originated by clipping the two diagonally connecting groups (Figure 1).[20] Notably, this process led to 39 derived nets.[21] Importantly, reducing the symmetry of some of the initial edge-transitive nets (**nbo**, **ssb**, **pts**, **scu**, and **ftw**)

Received: March 27, 2020
Published: May 1, 2020



ACS Publications
© 2020 American Chemical Society

https://dx.doi.org/10.1021/jacs.0c03404
J. Am. Chem. Soc. 2020, 142, 9135–9140

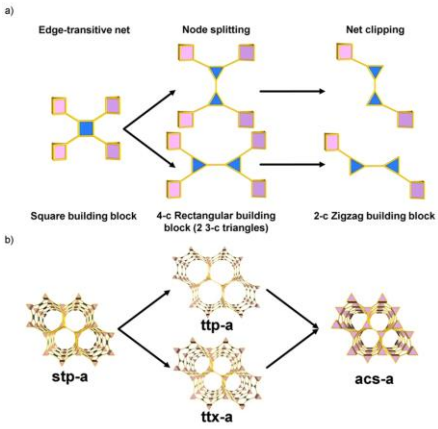


Figure 1. (a) Schematic of the deconstruction of a 4-c square MBB in a zigzag building block by splitting the node into two 3-c triangles in different axes (node splitting) and then removing two diagonally connections (net-clipping). (b) Schematic showing an example of our approach (node splitting + net clipping) applied to an edge-transitive net built from 4-c and 6-c triangular prism MBBs.

leads to two symmetrically different 4-c planar nodes. In these cases, as the two types of nodes can be split distinctly, more than two derived nets can be formed.

We then applied net-clipping to the derived nets by erasing the two diagonally connecting groups to mimic the presence of zigzag-shaped MBBs (Figure 1b; Figures S4–S20). The 10 resultant nets are summarized in Table 1. We concluded that most 3D nets (**pto**, **ssb**, **pts**, **pth**, **she**, **soc**, **stp**, **scu**, and **ftw**) are clipped into other 3D nets (**srs**, **lvt**, **dia**, **qtz**, **hxg**, **crs**, **acs**, **bcu**, and **fcu**, respectively); that some 3D nets (**nbo**, **lvt**, and **ssb**) are clipped into the 2D **sql** net; and that the remaining nets (**tbo**, **rhr**, **ssa**, **sqc**, **csq**, and **shp**) cannot be clipped into other nets. Interestingly, we found a common feature among all these latter edge-transitive nets: the presence of a 6-cycle[22] that comprises three 3-c nodes (derived from three 4-c nodes) and three other MBBs and that frustrates the net clipping in a fully zigzag fashion (Figures S21 and S22).

Once we had theoretically deduced the MOF structures that could be formed using zigzag ligands, we experimentally assessed our net-clipping approach. To this end, we chose two types of MOFs assembled from combining a 4-c MBB with a 4-c square-like MBB or a 12-c cuboctahedral MBB. Then, we combined the zigzag ligand analogs (derived from the 4-c MBB) with the corresponding polyhedral MBBs to synthesize two new MOFs, whose topologies we compared with those that we had deduced by net-clipping. Note that, in two other cases, to further support the net-clipping approach, we used MOF structures already reported in the literature (MOFs made by combining a 4-c MBB with 4-c tetrahedral or 8-c cubic MBBs).

We began with the **nbo** MOF PCN-10 (derived net: **fof**), which is built by connecting 4-c square-like Cu(II) paddle-wheel MBBs through 4-c 3,3′,5,5′-azobenzene-tetracarboxylate (3,3′,5,5′-ABTC) ligands.[23] In this case, net-clipping induced

Table 1. Net-Clipping of All the Derived Nets from 4-c Square Nodes in the 17 Selected Edge-Transitive Nets[a]

MBB	Main Topology	Derived Net	Clipped Net
	tbo	tbd	
		xaa	
	pto	ptd	srs
	nbo	fof	sql
		fog	
		tfb	
	rhr	ucp	
		sqc12288*	
	lvt	lil	sql
		lim	
	ssa	sty	
		Initial structure; Bond sets: 1,3:bbp**	
	ssb	stu	sql
		stw	
		stj	lvt
		stx	
	pts	dmd	dia
		dmg	
		dmh	
		tfi	
	pth	hst	qtz
		3,4T45***	
	she	sqc12215*	hxg
	soc	cdj	crs
		edq	
	stp	ttp	acs
		ttx	
	scu	tty	bcu
		cut	
		3,3,8T132***	
	sqc	sqc3520*	
		sqc3782*	
	csq	xly	
		xlz	
	ftw	kle	fcu
		kxe	
		ttv	
	shp	ced	
		cec	

[a]For the derived nets, asterisks indicate the following: *topologies corresponding to the Systre code in the Epinet database; **topology corresponding to the subnet transformation symbols nomenclature; and ***topologies corresponding to the TOPOS symbols nomenclature.

the formation of a 2D **sql** MOF (Table 1). Remarkably, replacing 3,3′,5,5′-ABTC with the corresponding zigzag 3,3′-azobenzene-dicarboxylate (3,3′-ABDC) ligand afforded the expected 2D **sql** MOF (Figure 2a, top). This entailed reaction of copper(II) nitrate salt and H_2(3,3′-ABDC) in *N*,*N*-dimethylformamide (DMF) under solvothermal conditions,

https://dx.doi.org/10.1021/jacs.0c03404
J. Am. Chem. Soc. 2020, 142, 9135−9140

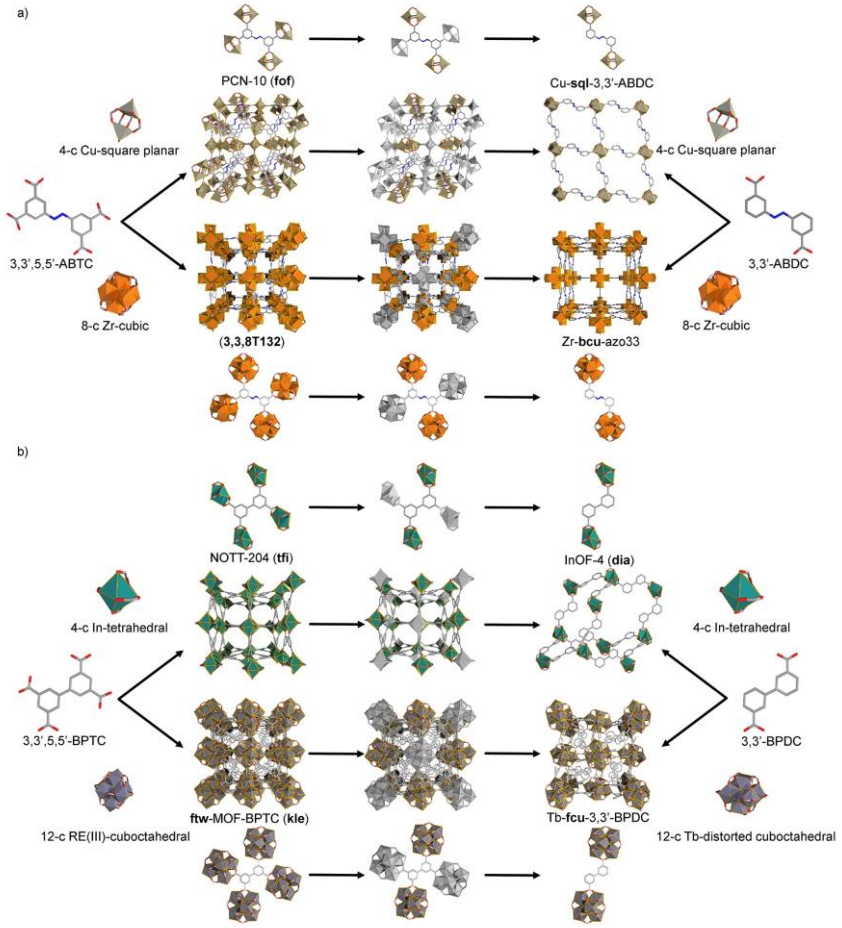


Figure 2. Schematic of the net-clipping approach applied to formation of MOFs from (a) 3,3′,5,5′-ABTC ligand to zigzag 3,3′-ABDC combined with (top) 4-c paddle-wheel Cu(II) MBBs and (bottom) 8-c cubic Zr(IV)-based MBBs, and from (b) 3,3′,5,5′-BPTC to 3,3′-BPDC ligand combined with (top) 4-c tetrahedral In(III)-based MBBs and (bottom) 12-c cuboctahedral Tb(III)-based MBBs.

which yielded green needle-shaped crystals of Cu-**sql**-3,3′-ABDC. Single-crystal X-ray diffraction (SCXRD) revealed formation of an ABCD packing of a 2D network of formula $Cu_2(3,3'\text{-ABDC})_2(H_2O)_2$, which crystallizes in the $C2/m$ space group (Figure 2). As expected, the building unit in Cu-**sql**-3,3′-ABDC is the Cu(II) paddle-wheel unit. In this framework, each of these units is connected to four others through four bridging zigzag 3,3′-ABDC ligands, adopting a 4-c **sql** underlying topology (Figure 2a, top).

Interestingly, our net-clipping approach is further corroborated by the fact that an isostructural **sql** MOF made by linking Zn(II) paddle-wheel units by 3,3′-ABDC ligands had previously been described by Liang et al.[24] Similarly, two other independently, previously reported structures reinforce our approach: NOTT-204,[25] a **pts** MOF (derived net: **tfi**) built by linking the 4-c 3,3′,5,5′-biphenyl-tetracarboxylate (3,3′,5,5′-BPTC) ligand and the 4-c tetrahedral In(III)-based MBB; and InOF-4,[26] a **dia**-MOF made by connecting the same 4-c tetrahedral In(III)-based MBBs through the zigzag 3,3′-biphenyl-dicarboxylate (3,3′-BPDC) ligand. Interestingly, both of these MOF structures are related by net-clipping, which induced formation of a clipped **dia** topology from a **pts** topology (Table 1 and Figure 2b, top).

https://dx.doi.org/10.1021/jacs.0c03404
J. Am. Chem. Soc. 2020, 142, 9135−9140

Next, we shifted our attention to another MOF assembled from the 4-c 3,3′,5,5′-ABTC ligand and a higher-connected MBB, the 8-c cubic $Zr_6O_4(OH)_4(OOC\text{-}R)_8(H_2O)_4(OH)_4$ hexanuclear MBB.[27] This MOF shows the **scu** topology, in which we reasoned that replacement of 3,3′,5,5′-ABTC with 3,3′-ABDC would generate a clipped **bcu** MOF (Table 1). Interestingly, our group recently reported that combination of this 8-c MBB with a series of zigzag ligands, including 3,3′-ABDC, leads to formation of MOFs with the **bcu** topology (Figure 2a, bottom), which further supports net-clipping.[15]

Recently, Eddaoudi et al. reported that combining 4-c ligands (e.g., 3,3′,5,5′-ABTC or 3,3′,5,5′-BPTC) with 12-c cuboctahedral rare earth metal (RE) MBBs affords RE-**ftw**-MOFs (derived net: **kle**).[28] From this topology, net-clipping predicts formation of a MOF with the **fcu** underlying topology. To investigate this, we used the zigzag 3,3′-BPDC ligand as a substitute for the 4-c 3,3′,5,5′-BPTC ligand. Reaction of terbium(III) nitrate salt and H_2(3,3′-BPDC) in the presence of 2-fluorobenzoic acid in DMF under solvothermal conditions yielded transparent octahedral crystals of Tb-**fcu**-3,3′-BPDC. SCXRD revealed formation of a 3D net with formula $[(CH_3)_2NH_2]_2[Tb_6(\mu_3\text{-}OH)_8(3,3'\text{-}BPDC)_6(H_2O)_4]$, which crystallizes in the $P2_1/n$ space group. As we had expected, the presence of 2-fluorobenzoic acid as modulator[29] enabled formation of the hexanuclear RE MBB in Tb-**fcu**-3,3′-BPDC. In this framework, each of these MBBs is connected to 12 others, through 12 bridging zigzag 3,3′-BPDC groups, adopting overall a 12-c **fcu** topology (Figure 2b, bottom). Note that, compared to the archetypical 12-c Zr-**fcu**-4,4′-BPDC (known as UiO-67),[30] Tb-**fcu**-3,3′-BPDC shows a less-symmetric, distorted structure. We attributed this feature to the transversal parameter of the zigzag ligand as well as to the different metal-based MBBs, in which Zr(IV) ions had been replaced with Tb(III) ions, thereby providing a slightly different coordination environment (Figures S30 and S31).

Once we had confirmed the feasibility of our net-clipping approach, we applied it to synthesize a new **acs**-MOF built with a zigzag ligand. To this end, we synthesized a rigid zigzag 1,5-naphthalenedicarboxylate (1,5-NDC) ligand and selected the well-known $[Fe(III)]_3O$ trimeric unit as the trigonal prism MBB.[31] We synthesized this zigzag ligand because, to our knowledge, an **stp** MOF assembled from the corresponding 4-c 1,4,5,8-naphthalenetetracarboxylate ligand and a 6-c trigonal prism MBB—for which net-clipping induced formation of an **acs** topology—has never previously been reported. First, H_2(1,5-NDC) was synthesized from the corresponding diamine derivative via several functional group interconversions (see SI). Then, the Fe(III) trimeric unit was synthesized in an acetic acid solution, according to a literature protocol.[32] Finally, the pre-formed Fe(III) unit was reacted with H_2(1,5-NDC) and acetic acid in DMF under solvothermal conditions for 48 h. After this period, orange hexagonal crystals suitable for SCXRD were collected. SCXRD revealed formation of a 3D structure with formula $Fe_3(\mu_3\text{-}O)(1,5\text{-}NDC)_3(H_2O)_2(OH)$, which crystallizes in the $P\text{-}6_3m$ space group. In Fe-**acs**-1,5-NDC, each trimer is connected to six others through six zigzag 1,5-NDC ligands, adopting the 6-c **acs** underlying topology (Figure 3). Note that the structure of Fe-**acs**-1,5-NDC, although slightly distorted, is similar to that of MOF-235/MIL-88B,[33,34] which also exhibits an underlying **acs** topology.

In summary, we have proposed and validated a new approach, net-clipping, for rational design of MOFs made of zigzag ligands. First, we demonstrated the relationship between these ligands and more symmetric 4-c ligands. Next, we studied the edge-transitive nets with 4-c nodes with an associated square vertex figure, and their derived nets, to identify the possible outcomes. Then, we applied our net-clipping approach to deduce the different topologies that should be accessible upon assembly of zigzag ligands with different polyhedral MBBs. Finally, we demonstrated the feasibility of net-clipping through the successful design and assembly of three novel MOFs based on MBBs with different connectivities: Cu-**sql**-3,3′-ABDC (4-c, paddle-wheel), Fe-**acs**-1,5-NDC (6-c, trimer), and Tb-**fcu**-3,3′-BPDC (12-c, hexamer). Our approach enriches the repertoire for topological predictions, and we anticipate the application of net-clipping to bent ligands, via clipping of 4-c MBBs in other ways, as well as its eventual use with MBBs of other connectivity.

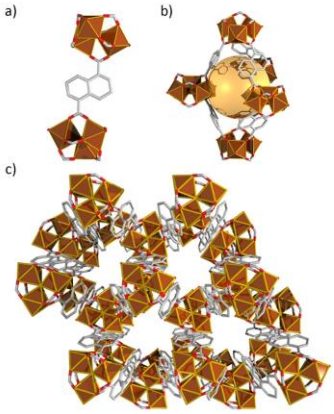


Figure 3. Crystal structure of Fe-**acs**-1,5-NDC, showing (a) the zigzag connection between the Fe trimers, (b) the trigonal bipyramid cage, and (c) the channels formed through the *c* axis.

■ ASSOCIATED CONTENT

Supporting Information

The Supporting Information is available free of charge at https://pubs.acs.org/doi/10.1021/jacs.0c03404.

Chemicals, instrumentation, net-clipping approach and synthetic procedures, schemes of the topologies resulting from the net-clipping, PXRD, crystallographic data, structural details, and ^{1}H NMR spectra, including Figures S1−S31 (PDF)

X-ray crystallographic data for Cu-**sql**-3,3′-ABDC (CIF)

X-ray crystallographic data for Fe-**acs**-1.5-NDC (CIF)

X-ray crystallographic data for Tb-**fcu**-3,3′-BPDC (CIF)

■ AUTHOR INFORMATION

Corresponding Authors

Vincent Guillerm − *Catalan Institute of Nanoscience and Nanotechnology (ICN2), CSIC and Barcelona Institute of Science and Technology, Bellaterra 08193, Barcelona, Spain;* orcid.org/0000-0003-3460-223X; Email: vguillerm@protonmail.com

https://dx.doi.org/10.1021/jacs.0c03404
J. Am. Chem. Soc. 2020, 142, 9135−9140

Inhar Imaz − *Catalan Institute of Nanoscience and Nanotechnology (ICN2), CSIC and Barcelona Institute of Science and Technology, Bellaterra 08193, Barcelona, Spain;* orcid.org/0000-0002-0278-1141; Email: inhar.imaz@icn2.cat

Daniel Maspoch − *Catalan Institute of Nanoscience and Nanotechnology (ICN2), CSIC and Barcelona Institute of Science and Technology, Bellaterra 08193, Barcelona, Spain; ICREA, 08010 Barcelona, Spain;* orcid.org/0000-0003-1325-9161; Email: daniel.maspoch@icn2.cat

Authors

Borja Ortín-Rubio − *Catalan Institute of Nanoscience and Nanotechnology (ICN2), CSIC and Barcelona Institute of Science and Technology, Bellaterra 08193, Barcelona, Spain*

Hosein Ghasempour − *Department of Chemistry, Faculty of Sciences, Tarbiat Modares University, Tehran, Iran*

Ali Morsali − *Department of Chemistry, Faculty of Sciences, Tarbiat Modares University, Tehran, Iran;* orcid.org/0000-0002-1828-7287

Judith Juanhuix − *Alba Synchrotron Light Facility, Cerdanyola del Vallés 08290, Barcelona, Spain;* orcid.org/0000-0003-3728-8215

Complete contact information is available at: https://pubs.acs.org/10.1021/jacs.0c03404

Notes

The authors declare no competing financial interest.

■ ACKNOWLEDGMENTS

This work was supported by the Spanish MINECO (project RTI2018-095622-B-I00), the Catalan AGAUR (project 2017 SGR 238), and the ERC under the EU-FP7 (ERC-Co 615954). It was also funded by the CERCA Program/Generalitat de Catalunya. ICN2 is supported by the Severo Ochoa program from the Spanish MINECO (Grant No. SEV-2017-0706).

■ REFERENCES

(1) Yaghi, O. M.; Kalmutzki, M. J.; Diercks, C. S. *Introduction to Reticular Chemistry*; Wiley, 2019.

(2) Yaghi, O. M.; O'Keeffe, M.; Ockwig, N. W.; Chae, H. K.; Eddaoudi, M.; Kim, J. Reticular Synthesis and the Design of New Materials. *Nature* **2003**, *423*, 705−714.

(3) O'Keeffe, M.; Peskov, M. A.; Ramsden, S. J.; Yaghi, O. M. The Reticular Chemistry Structure Resource (RCSR) Database of, and Symbols for, Crystal Nets. *Acc. Chem. Res.* **2008**, *41*, 1782−1789.

(4) Stein, A.; Keller, S. W.; Mallouk, T. E. Turning down the Heat: Design and Mechanism in Solid-State Synthesis. *Science* **1993**, *259*, 1558−1564.

(5) Eddaoudi, M.; Moler, D. B.; Li, H.; Chen, B.; Reineke, T. M.; O'Keeffe, M.; Yaghi, O. M. Modular Chemistry: Secondary Building Units as a Basis for the Design of Highly Porous and Robust Metal-Organic Carboxylate Frameworks. *Acc. Chem. Res.* **2001**, *34*, 319−330.

(6) O'Keeffe, M.; Yaghi, O. M. Deconstructing the Crystal Structures of Metal-Organic Frameworks and Related Materials into Their Underlying Nets. *Chem. Rev.* **2012**, *112*, 675−702.

(7) Nouar, F.; Eubank, J. F.; Bousquet, T.; Wojtas, L.; Zaworotko, M. J.; Eddaoudi, M. Supermolecular Building Blocks (SBBs) for the Design and Synthesis of Highly Porous Metal-Organic Frameworks. *J. Am. Chem. Soc.* **2008**, *130*, 1833−1835.

(8) Perry VI, J. J.; Perman, J. A.; Zaworotko, M. J. Design and Synthesis of Metal-Organic Frameworks Using Metal-Organic Polyhedra as Supermolecular Building Blocks. *Chem. Soc. Rev.* **2009**, *38*, 1400−1417.

(9) Guillerm, V.; Kim, D.; Eubank, J. F.; Luebke, R.; Liu, X.; Adil, K.; Lah, M. S.; Eddaoudi, M. A Supermolecular Building Approach for the Design and Construction of Metal-Organic Frameworks. *Chem. Soc. Rev.* **2014**, *43*, 6141−6172.

(10) Eubank, J. F.; Mouttaki, H.; Cairns, A. J.; Belmabkhout, Y.; Wojtas, L.; Luebke, R.; Alkordi, M.; Eddaoudi, M. The Quest for Modular Nanocages: tbo-MOF as an Archetype for Mutual Substitution, Functionalization, and Expansion of Quadrangular Pillar Building Blocks. *J. Am. Chem. Soc.* **2011**, *133*, 14204−14207.

(11) Jiang, H.; Jia, J.; Shkurenko, A.; Chen, Z.; Adil, K.; Belmabkhout, Y.; Weselinski, L. J.; Assen, A. H.; Xue, D. X.; O'Keeffe, M.; Eddaoudi, M. Enriching the Reticular Chemistry Repertoire: Merged Nets Approach for the Rational Design of Intricate Mixed-Linker Metal-Organic Framework Platforms. *J. Am. Chem. Soc.* **2018**, *140*, 8858−8867.

(12) Guillerm, V.; Maspoch, D. Geometry Mismatch and Reticular Chemistry: Strategies to Assemble Metal-Organic Frameworks with Non-Default Topologies. *J. Am. Chem. Soc.* **2019**, *141*, 16517−16538.

(13) Eddaoudi, M.; Kim, J.; Vodak, D.; Sudik, A.; Wachter, J.; O'Keeffe, M.; Yaghi, O. M. Geometric Requirements and Examples of Important Structures in the Assembly of Square Building Blocks. *Proc. Natl. Acad. Sci. U. S. A.* **2002**, *99*, 4900−4904.

(14) Eddaoudi, M.; Kim, J.; O'Keeffe, M.; Yaghi, O. M. $Cu_2[o\text{-}Br C_6H_3(CO_2)_2]_2(H_2O)_2\cdot(DMF)_8(H_2O)_2$: A Framework Deliberately Designed to Have the NbO Structure Type. *J. Am. Chem. Soc.* **2002**, *124*, 376−377.

(15) Guillerm, V.; Grancha, T.; Imaz, I.; Juanhuix, J.; Maspoch, D. Zigzag Ligands for Transversal Design in Reticular Chemistry: Unveiling New Structural Opportunities for Metal-Organic Frameworks. *J. Am. Chem. Soc.* **2018**, *140*, 10153−10157.

(16) Bon, V.; Senkovska, I.; Baburin, I. A.; Kaskel, S. Zr- and Hf-Based Metal-Organic Frameworks: Tracking down the Polymorphism. *Cryst. Growth Des.* **2013**, *13*, 1231−1237.

(17) Drache, F.; Bon, V.; Senkovska, I.; Getzschmann, J.; Kaskel, S. The Modulator Driven Polymorphism of Zr(IV) Based Metal-Organic Frameworks. *Philos. Trans. R. Soc., A* **2017**, *375*, 20160027.

(18) Delgado-Friedrichs, O.; O'Keeffe, M. Three-Periodic Tilings and Nets: Face-Transitive Tilings and Edge-Transitive Nets Revisited. *Acta Crystallogr., Sect. A: Found. Crystallogr.* **2007**, *63*, 344−347.

(19) Eubank, J. F.; Walsh, R. D.; Poddar, P.; Srikanth, H.; Larsen, R. W.; Eddaoudi, M. Metal-Organic Framework Diversity via Heterocoordination of a Multifunctional Ligand: $SrAl_2$ and a Novel (3,4)-Connected Network. *Cryst. Growth Des.* **2006**, *6*, 1453−1457.

(20) Luebke, R.; Belmabkhout, Y.; Weseliński, Ł. J.; Cairns, A. J.; Alkordi, M.; Norton, G.; Wojtas, Ł.; Adil, K.; Eddaoudi, M. Versatile Rare Earth Hexanuclear Clusters for the Design and Synthesis of Highly-Connected ftw-MOFs. *Chem. Sci.* **2015**, *6*, 4095−4102.

(21) Li, M.; Li, D.; O'Keeffe, M.; Yaghi, O. M. Topological Analysis of Metal-Organic Frameworks with Polytopic Linkers and/or Multiple Building Units and the Minimal Transitivity Principle. *Chem. Rev.* **2014**, *114*, 1343−1370.

(22) Blatov, V. A.; O'Keeffe, M.; Proserpio, D. M. Vertex-, Face-, Point-, Schläfli-, and Delaney-Symbols in Nets, Polyhedra and Tilings: Recommended Terminology. *CrystEngComm* **2010**, *12*, 44−48.

(23) Wang, X.-S.; Ma, S.; Rauch, K.; Simmons, J. M.; Yuan, D.; Wang, X.; Yildirim, T.; Cole, W. C.; Lopez, J. J.; De Meijere, A.; Zhou, H.-C. Metal-Organic Frameworks Based on Double-Bond-Coupled Di-Isophthalate Linkers with High Hydrogen and Methane Uptakes. *Chem. Mater.* **2008**, *20*, 3145−3152.

(24) Chen, Z. F.; Zhang, Z. L.; Tan, Y. H.; Tang, Y. Z.; Fun, H. K.; Zhou, Z. Y.; Abrahams, B. F.; Liang, H. Coordination Polymers Constructed by Linking Metal Ions with Azodibenzoate Anions. *CrystEngComm* **2008**, *10*, 217−231.

(25) Yang, S.; Callear, S. K.; Ramirez-Cuesta, A. J.; David, W. I. F.; Sun, J.; Blake, A. J.; Champness, N. R.; Schröder, M. Pore with Gate: Modulating Hydrogen Storage in Metal-Organic Framework Materials via Cation Exchange. *Faraday Discuss.* **2011**, *151*, 19−36.

(26) Qian, J.; Jiang, F.; Su, K.; Li, Q.; Zhou, K.; Wu, M.; Yuan, D.; Hong, M. Sorption Comparison of Two Indium-Organic Framework

Isomers with Syn-Anti Configurations. *CrystEngComm* **2014**, *16*, 7434−7439.
(27) Wang, H.; Dong, X.; Lin, J.; Teat, S. J.; Jensen, S.; Cure, J.; Alexandrov, E. V.; Xia, Q.; Tan, K.; Wang, Q.; Olson, D. H.; Proserpio, D. M.; Chabal, Y. J.; Thonhauser, T.; Sun, J.; Han, Y.; Li, J. Topologically Guided Tuning of Zr-MOF Pore Structures for Highly Selective Separation of C6 Alkane Isomers. *Nat. Commun.* **2018**, *9*, 1745.
(28) Xue, D. X.; Cadiau, A.; Weseliński, Ł. J.; Jiang, H.; Bhatt, P. M.; Shkurenko, A.; Wojtas, L.; Zhijie, C.; Belmabkhout, Y.; Adil, K.; Eddaoudi, M. Topology Meets MOF Chemistry for Pore-Aperture Fine Tuning: ftw-MOF Platform for Energy-Efficient Separations: Via Adsorption Kinetics or Molecular Sieving. *Chem. Commun.* **2018**, *54*, 6404−6407.
(29) Xue, D. X.; Cairns, A. J.; Belmabkhout, Y.; Wojtas, L.; Liu, Y.; Alkordi, M. H.; Eddaoudi, M. Tunable Rare-Earth fcu-MOFs: A Platform for Systematic Enhancement of CO_2 Adsorption Energetics and Uptake. *J. Am. Chem. Soc.* **2013**, *135*, 7660−7667.
(30) Cavka, J. H.; Jakobsen, S.; Olsbye, U.; Guillou, N.; Lamberti, C.; Bordiga, S.; Lillerud, K. P. A New Zirconium Inorganic Building Brick Forming Metal Organic Frameworks with Exceptional Stability. *J. Am. Chem. Soc.* **2008**, *130*, 13850−13851.
(31) Schoedel, A.; Zaworotko, M. J. $[M_3(M_3\text{-}O)(O_2CR)_6]$ and Related Trigonal Prisms: Versatile Molecular Building Blocks for Crystal Engineering of Metal-Organic Material Platforms. *Chem. Sci.* **2014**, *5*, 1269−1282.
(32) Feng, D.; Wang, K.; Wei, Z.; Chen, Y. P.; Simon, C. M.; Arvapally, R. K.; Martin, R. L.; Bosch, M.; Liu, T. F.; Fordham, S.; Yuan, D.; Omary, M. A.; Haranczyk, M.; Smit, B.; Zhou, H. C. Kinetically Tuned Dimensional Augmentation as a Versatile Synthetic Route towards Robust Metal-Organic Frameworks. *Nat. Commun.* **2014**, *5*, 5723.
(33) Sudik, A. C.; Côté, A. P.; Yaghi, O. M. Metal-Organic Frameworks Based on Trigonal Prismatic Building Blocks and the New "acs" Topology. *Inorg. Chem.* **2005**, *44*, 2998−3000.
(34) Surblé, S.; Serre, C.; Mellot-Draznieks, C.; Millange, F.; Férey, G. A New Isoreticular Class of Metal-Organic-Frameworks with the MIL-88 Topology. *Chem. Commun.* **2006**, 284−286.

https://dx.doi.org/10.1021/jacs.0c03404
J. Am. Chem. Soc. 2020, 142, 9135−9140

GDCh Research Articles Angewandte International Edition Chemie www.angewandte.org

VIP Metal-Organic Frameworks Very Important Paper

How to cite: *Angew. Chem. Int. Ed.* **2022**, *61*, e202111228
International Edition: doi.org/10.1002/anie.202111228
German Edition: doi.org/10.1002/ange.202111228

Clip-off Chemistry: Synthesis by Programmed Disassembly of Reticular Materials**

Yunhui Yang[+], Anna Broto-Ribas[+], Borja Ortín-Rubio[+], Inhar Imaz, Felipe Gándara, Arnau Carné-Sánchez, Vincent Guillerm, Sergio Jurado, Félix Busqué, Judith Juanhuix, and Daniel Maspoch**

Abstract: *Bond breaking is an essential process in chemical transformations and the ability of researchers to strategically dictate which bonds in a given system will be broken translates to greater synthetic control. Here, we report extending the concept of selective bond breaking to reticular materials in a new synthetic approach that we call Clip-off Chemistry. We show that bond-breaking in these structures can be controlled at the molecular level; is periodic, quantitative, and selective; is effective in reactions performed in either solid or liquid phases; and can occur in a single-crystal-to-single-crystal fashion involving the entire bulk precursor sample. We validate Clip-off Chemistry by synthesizing two topologically distinct 3D metal-organic frameworks (MOFs) from two reported 3D MOFs, and a metal-organic macrocycle from metal-organic polyhedra (MOP). Clip-off Chemistry opens the door to the programmed disassembly of reticular materials and thus to the design and synthesis of new molecules and materials.*

Introduction

Throughout history, innovations in chemical synthesis have yielded previously inaccessible new molecules and materials that have enabled vast improvements in human life, ranging from fine chemicals to complex functional materials. Each new reaction and methodology not only help to expand accessible chemical space, but also inspire researchers to further innovate in the iterative design and preparation of new chemical targets of social, economic or industrial value. To date, most state-of-the-art synthetic approaches use bottom-up strategies that, at the latter stage, mainly entail controlling the formation of new bonds. A relatively recent example of this is reticular chemistry,[1–7] in which judiciously-designed, rigid molecular building blocks (MBBs) are linked by strong bonds to create crystalline open-framework materials[8] such as metal-organic frameworks (MOFs),[1–4] covalent-organic frameworks (COFs)[9] and metal-organic polyhedra (MOPs).[10–12] Reticular materials are a fascinating source of metal-organic and purely organic structures built up from an endless variety of fragments and MBBs[13] (e.g. metal clusters, cages, cycles, metal layers, metal chains, etc.) that often do not exist in their isolated form.

We envisaged that by selectively breaking certain bonds in reticular materials, we could transform them into new frameworks or break them into new molecular fragments or isolated MBBs, as a synthetic strategy towards new materials and molecules. We hypothesized that we could use a chemical reaction for programmed bond-breaking, such that the de-reticulation process would occur at the molecular level. We reasoned that this would require the presence of cleavable groups at specific positions within the structures of the corresponding reticular materials, and that reported reticular materials that contain linkers featuring alkene bonds would be ideal starting materials for this strategy. However, we thought that, in the likely event that the targeted structure-precursor did not contain any alkene groups, we could generalize this approach to numerous reticular materials by inserting such groups into the pre-selected linkers without modifying their size or geometry, via reticular chemistry.

[*] Y. Yang,[+] A. Broto-Ribas,[+] B. Ortín-Rubio,[+] Dr. I. Imaz, Dr. A. Carné-Sánchez, Dr. V. Guillerm, Prof. Dr. D. Maspoch
Catalan Institute of Nanoscience and Nanotechnology (ICN2), CSIC and The Barcelona Institute of Science and Technology
Campus UAB, Bellaterra, 08193 Barcelona (Spain)
E-mail: inhar.imaz@icn2.cat
daniel.maspoch@icn2.cat

Dr. F. Gándara
Department of New Architectures in Materials Chemistry, Materials Science Institute of Madrid—CSIC
Sor Juana Inés de la Cruz 3, 28049 Madrid (Spain)

Dr. S. Jurado, Prof. Dr. F. Busqué
Departament de Química, Universitat Autònoma de Barcelona (UAB)
Cerdanyola del Vallès, 08193 Barcelona (Spain)

Dr. J. Juanhuix
Alba Synchrotron Light Facility
Cerdanyola del Vallès, 08290 Barcelona (Spain)

Prof. Dr. D. Maspoch
ICREA
Pg. Lluís Companys 23, 08010 Barcelona (Spain)

[+] These authors contributed equally to this work.

[**] A previous version of this manuscript has been deposited on a preprint server (10.26434/chemrxiv.14518632.v1).

Supporting information and the ORCID identification number(s) for the author(s) of this article can be found under: https://doi.org/10.1002/anie.202111228.

© 2021 The Authors. Angewandte Chemie International Edition published by Wiley-VCH GmbH. This is an open access article under the terms of the Creative Commons Attribution Non-Commercial NoDerivs License, which permits use and distribution in any medium, provided the original work is properly cited, the use is non-commercial and no modifications or adaptations are made.

© 2021 The Authors. Angewandte Chemie International Edition published by Wiley-VCH GmbH

Indeed, reticular chemistry dictates that for a given framework, the constituents can be chemically functionalized pre- and/or post-synthetically,[14,15] without any loss to framework connectivity. Thus, we extended this concept to the ability to encode the organic linker of an existing MOF by inserting cleavable alkene groups into it, without modifying the linker size or topology, to ultimately enable assembly of the corresponding isoreticular MOF structures containing the desired cleavable group.[16]

Herein we report a new synthetic approach, called Clip-off Chemistry, which is based on the programmed disassembly of reticular materials by controlled breaking of selected bonds. We validated Clip-off Chemistry by synthesizing two topologically distinct, three-dimensional (3D) MOFs from two reported 3D MOFs in single-crystal-to-single-crystal transformations. Through these examples, we demonstrated that reticular materials could be modified via cleavage, rather than formation, of bonds in their frameworks, enabling alterations to the connectivity of their constituent MBBs and therefore, to their topology. Next, we anticipated that Clip-off Chemistry could be generalized by applying it to 0-D molecular systems. To this end, we synthesized a novel metal-organic macrocycle from a MOP precursor. In all the examples we report here, we used ozonolysis as the chemical reaction to cut off constituent organic MBBs or linkers via direct cleavage of their alkene bonds.

Results and Discussion

Clip-off Chemistry is based on using, as starting materials, structures that contain cleavable groups (in this study, alkenes) at specific positions, such that cleavage of said groups generates new molecules or materials. Following this principle, we first targeted the clip-off synthesis of a new 3D MOF from a 3D MOF precursor. When selecting precursors in Clip-off Chemistry, reticular analysis of their underlying nets[17–19] is important, as bond-breaking in the structure relates to disassembly of certain circuits of connections.[20] In reticular materials this disassembly can be performed mainly by erasing some of the edges or nodes. Translating this analysis to the chemical field, the clip-off synthesis of a structure (here, a 3D MOF) from the disassembly of another structure (here, another 3D MOF) can be achieved by selecting either of two potential precursors: i) a structure built from one type of polytopic linker that contains different circuits of connections between the clusters, containing a cleavable bond in at least one of the circuits; or ii) a mixed-linker structure, in which linkers are located at different crystallographic positions, and one of them contains a cleavable bond. Cleavage of the polytopic linker will provoke disassembly of the circuits of connections in which the cleavable bond is involved, thereby forming a structure built up exclusively from those circuits that do not contain the cleavable groups, with a distinct underlying topology. Similarly, in the mixed-linker structure, cleavage of the linker containing the cleavable bond will provoke disassembly of the circuits of connections in which it is involved, thereby forming a structure built up exclusively from those circuits that involve the metal clusters and the other linkers that do not contain the cleavable groups.

In our choice of precursor for the first 3D MOF synthesis, we followed the polytopic linker approach described above (Figure 1). Thus, we selected the Zr-**scu**-MOF,[21] in which the assembly of eight-connected (8-c), quadrangular prismatic $Zr_6O_4(OH)_4$ clusters to 4-c rectangular linkers 5-[(3,5-dicarboxyphenyl)diazenyl]benzene-1,3-dicarboxylate (L_1) forms a 3D framework with a 4,8-c **scu/3,3,8T132** underlying topology[22] and 1D channels (size: ≈7 Å) along one axis. However, as this reported structure does not contain any cleavable alkene groups, we had to insert them chemically, using the well-known isoreticular principle.[16] This step of introducing cleavable groups into precursors can be performed before the cleavage step as needed, by replacing at least one of the original linkers with one of similar size and geometry that contains the desired cleavable groups at strategic positions. Once inserted into the isoreticular structure, such linkers generate different circuits of connections, in which at least one circuit contains the cleavable bonds. In our example, we replaced the linker L_1 with 5-[2-(3,5-dicarboxyphenyl)ethenyl]benzene-1,3-dicarboxylate (L_2), which contains olefinic bonds for cleavage. We thus synthesized an isoreticular Zr-**scu**-MOF framework built up from different circuits of connections, wherein only some of them contain the cleavable olefinic bonds of L_2. We anticipated that, upon treatment of this framework with ozone,[23–27] each 4-c L_2 linker would be split into two 2-c linkers (doubly deprotonated trimesic acid and/or 5-formylisophthalate). Consequently, only the circuits of connections between the $Zr_6O_4(OH)_4$ clusters and these 2-c linkers would remain, forming a Zr-**pcu**-MOF. In contrast to the isoreticular Zr-**scu**-MOF precursor, which is based on quadrangular prismatic 8-c Zr-clusters, each $Zr_6O_4(OH)_4$ cluster is still coordinated by 8 linkers in this new Zr-**pcu**-MOF, however its topological connectivity decreases from 8-c to a 6-c because two pairs of the eight 2-c linkers connect the same two clusters (Figure S2).[28]

We expected that this first clip-off reaction would afford the first-ever example of a 3D MOF made of archetypical Zr-oxo-hydroxo-clusters linked by isophthalate-like linkers in a **pcu** underlying net. Interestingly, the closest literature example of such a structure is that of a 2D MOF made of Zr-oxo-hydroxo-clusters linked by isophthalate, albeit in an **hcb** topology.[29] Our target 3D Zr-**pcu** MOF could also be seen as exemplifying a connection of Zr-oxo-hydroxo-clusters through trimesate linkers, which are coordinated only through two of their three carboxylate groups. Accordingly, it could also be considered as the first example of a Zr-structure with a free carboxylic acid using trimesate, as researchers have previously reported combination of Zr-oxo-hydroxo-clusters with this linker in a **spn** topology of 3,6-connectivity.[30]

We synthesized colorless cubic crystals of isoreticular Zr-**scu**-MOF by solvothermal reaction (120 °C) of a mixture of $ZrOCl_2 \cdot 8H_2O$ and L_2 in *N,N*-dimethylformamide (DMF) and formic acid for 5 days. The crystal structure revealed the expected isoreticular **scu** framework, in which L_1 had been replaced by L_2 (Figure 2a; see Supporting Information (SI), section S2). Next, we confirmed the phase purity of the bulk

© 2021 The Authors. Angewandte Chemie International Edition published by Wiley-VCH GmbH

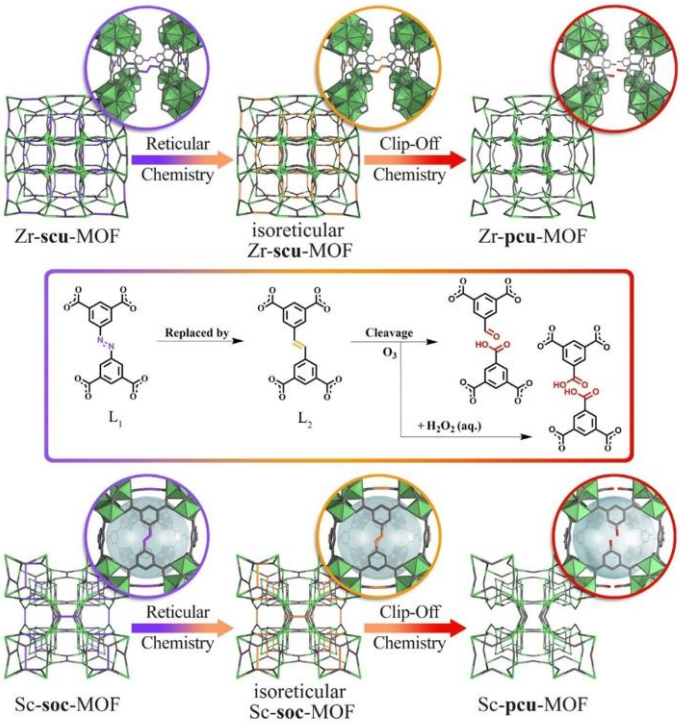


Figure 1. Clip-off Chemistry. Representative examples of Clip-off Chemistry, starting with the isoreticular insertion of cleavable (here, alkene) groups into a MOF structure,[16] followed by the quantitative breaking of these cleavable groups by ozonolysis to afford a new structure. Top: clip-off synthesis of Zr-**pcu**-MOF from Zr-**scu**-MOF. Bottom: clip-off synthesis of Sc-**pcu**-MOF from Sc-**soc**-MOF. Middle: chemical reaction for both syntheses. The formation of aldehyde/carboxylic acid groups after ozonolysis is not shown in the lower magnification nets for better illustration of the breaking process. The formation of these groups is shown in the magnified structures, wherein the red groups represent aldehyde or carboxylic acid groups.

sample by X-ray powder diffraction (XRPD) and scanning electron microscopy (SEM) (Figures 2b, S3, S12).

We began the clip-off synthesis of Zr-**pcu**-MOF by packing 20 mg of synthesized Zr-**scu**-MOF crystals into a plastic tube, connected on one side to the ozonator (through a $CaCl_2$ humidity trap) and, on the other side, to a vacuum pump (through a KI trap), to ensure a continuous flow of ozone through the column.[23,24] The reaction was run at room temperature for 30 min. Afterwards, the sample was connected to vacuum for another 30 min. This ozonation/vacuum cycle was repeated nine times for the complete cleavage of all the alkene bonds in Zr-**scu**-MOF, as evidenced by the gradual disappearance of the characteristic olefinic peak at 7.69 ppm in the ^{1}H NMR spectra of the digested Zr-**scu**-MOF crystals (vide infra; Figure S8). After nine cycles, the resulting solid was directly collected from the tube and stored in tetrahydrofuran.

Next, we characterized the ozonated Zr-**scu**-MOF crystals by single crystal X-ray diffraction (SCXRD), which confirmed that they had retained the single-crystal character (Figures 2c, S1, S2). For these crystals, synchrotron diffraction data were collected at a maximum resolution of 1.2 Å. Data analyses revealed a variation in the lattice parameters, as compared to the pristine structure. Both pre- and post-ozonolysis crystal structures were solved in the monoclinic *C*2/*m* space group. However, the cell volume of the ozonated crystal was found to be 16076.00(10) Å^3, whereas that of the pristine Zr-**scu**-MOF was 16957.46(10) Å^3. Analysis of the diffraction data demonstrated the integrity of the inorganic Zr-oxo-hydroxo-clusters after post-synthetic reaction, with no changes in their coordination. Thus, the position of all the atoms in the inorganic secondary building units (SBUs, metal and carboxylate atoms) were assigned and anisotropically refined. As for the rest of the organic linker, carbon atoms belonging to the phenyl ring were located in the difference electron density maps. However, their high thermal parameter values indicated a possible positional disorder. Moreover, the olefinic carbon atoms could no longer be located, supporting the completeness of the ozonolysis reaction. This is in stark contrast to the pristine MOF, in which the positions of these atoms were clearly visible and refined. The position of the resulting aldehydes or carboxylic groups, newly inserted in the MOF upon cleavage of the carbon-carbon double bond, could not be determined from the analysis of the difference electron density maps. Instead, a large residual electron density was observed in the vicinity of the positions that were initially occupied by the olefinic group. When comparing the two structures, additional differences could be observed in the arrangement of other framework atoms. Most notably, the relative orientation of opposite phenyl rings in a same linker

© 2021 The Authors. Angewandte Chemie International Edition published by Wiley-VCH GmbH

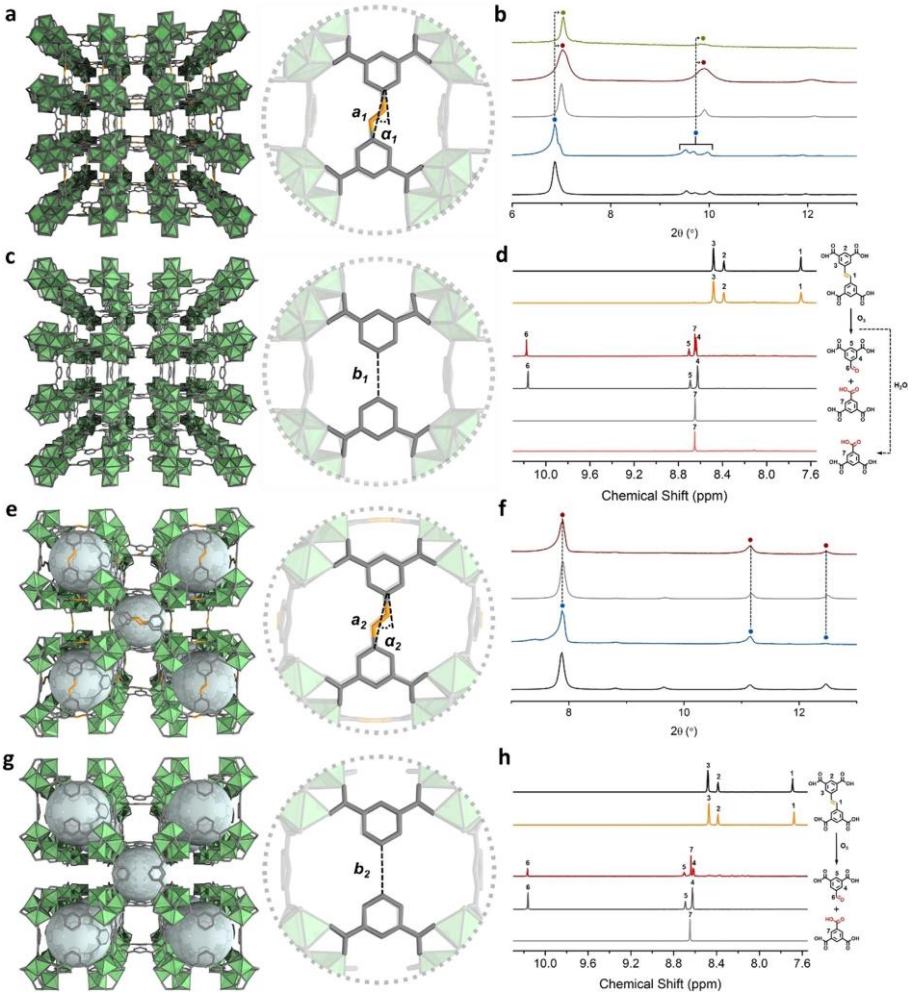


Figure 2. Structural and molecular characterization of Zr-**pcu**-MOF and Sc-**pcu**-MOF. a,c) Crystal structures of isoreticular Zr-**scu**-MOF (a) and Zr-**pcu**-MOF (c). Magnified views highlight the changes observed in the distances and angles of both phenyl rings (from $a_1 = 3.77–3.79$ Å and $\alpha_1 = 14.95–19.71°$ to $b_1 = 3.39–3.65$ Å and $\beta_1 = 0°$) initially composing L_2.[41] b) Magnified view of XRPD spectra for calculated Zr-**scu**-MOF (black), synthesized Zr-**scu**-MOF (blue), calculated Zr-**pcu**-MOF (grey), synthesized Zr-**pcu**-MOF (red) and oxidized Zr-**pcu**-MOF (green). The main structural changes with signal shifts are highlighted. d) ^{1}H NMR spectra (360 MHz, [D$_6$]DMSO) of digested L_2 (black), Zr-**scu**-MOF (orange), Zr-**pcu**-MOF (red), 5-formylisophthalic acid (dark grey), trimesic acid (light grey) and oxidized Zr-**pcu**-MOF (light red). Assigned proton signals: $\delta_1 = 7.69$ ppm (s, 2H), $\delta_2 = 8.39$ ppm (s, 2H), $\delta_3 = 8.49$ ppm (s, 4H), $\delta_4 = 8.64$ ppm (m, 2H), $\delta_5 = 8.70$ ppm (m, 1H), $\delta_6 = 10.18$ ppm (s, 1H) and $\delta_7 = 8.65$ ppm (s, 3H). e,g) Crystal structures of isoreticular Sc-**soc**-MOF (e) and Sc-**pcu**-MOF (g). Magnified views highlight the changes observed in the distances and angles in both phenyl rings (from $a_2 = 3.82–3.84$ Å and $\alpha_2 = 15.63–17.34°$ to $b_2 = 3.62–3.63$ Å and $\beta_2 = 0°$) initially composing L_2.[41] (f) Magnified view of the XRPD spectra for calculated Sc-**soc**-MOF (black), synthesized Sc-**soc**-MOF (blue), calculated Sc-**pcu**-MOF (grey) and synthesized Sc-**pcu**-MOF (red). h) ^{1}H NMR spectra (360 MHz, [D$_6$]DMSO) of digested L_2 (black), Sc-**soc**-MOF (orange), Sc-**pcu**-MOF (red), 5-formylisophthalic acid (dark grey) and trimesic acid (light grey). Assigned proton signals: $\delta_1 = 7.68$ ppm (s, 2H), $\delta_2 = 8.38$ ppm (s, 2H), $\delta_3 = 8.47$ ppm (s, 4H), $\delta_4 = 8.64$ ppm (m, 2H), $\delta_5 = 8.71$ ppm (m, 1H), $\delta_6 = 10.17$ ppm (s, 1H) and $\delta_7 = 8.65$ ppm (s, 3H).

© 2021 The Authors. Angewandte Chemie International Edition published by Wiley-VCH GmbH

in Zr-**scu**-MOF was different after ozonolysis (Figures 2a,c), indicating that the olefin bond was no longer present to fix the angle between these rings.

Since the crystal structure of pristine Zr-**scu**-MOF differed markedly to that of ozonated Zr-**scu**-MOF (or Zr-**pcu**-MOF), we also studied these MOFs by XRPD. Remarkably, the XRPD patterns for each sample perfectly matched those calculated from the corresponding structures determined by SCXRD and full-pattern profile refinements further demonstrated phase purity of the samples (Figures 2b, S3–S5). Altogether, these results corroborate two crucial phenomena for validation of Clip-off Chemistry: firstly, that it is indeed possible to cleave all the periodic olefinic bonds in a 3D structure without destroying it or its single-crystal character; and secondly, that said cleavage, and the resultant formation of a new structure (in this case, Zr-**pcu**-MOF),[19] are homogeneous throughout the bulk crystalline sample.

Next, we gained further evidence of the formation of Zr-**pcu**-MOF by recording the ^{1}H NMR spectra of the digested ozonized samples (5% HF/[D$_6$]DMSO) after each cycle, and then comparing each spectrum to that of the starting Zr-**scu**-MOF (Figures 2d, S6–S8). Under these digestion conditions, the MOF structures are destroyed and the linkers, released, thus enabling use of ^{1}H NMR to unveil the composition of the initial MOF structures. The spectrum of the digested Zr-**scu**-MOF showed the characteristic peak of equivalent olefinic protons of L_2 at $\delta = 7.69$ ppm. In contrast, the spectra of ozonated crystals after each cycle confirmed a gradual fading of this olefinic signal, which, by the ninth cycle, had fully disappeared. Indeed, ^{1}H NMR of digested ozonated Zr-**scu**-MOF after the ninth cycle confirmed the full conversion of L_2 into doubly deprotonated trimesic acid and 5-formylisophthalate. Beyond the disappearance of the olefinic protons at $\delta = 7.69$ ppm, there was also fading of the phenyl ($\delta =$ 8.49 ppm and 8.39 ppm) and the carboxylic acid ($\delta =$ 13.32 ppm) protons of L_2, whereas the characteristic signals for the trimesic acid ($\delta = 13.57$ ppm and 8.65 ppm) and 5-formylisophthalic acid ($\delta = 10.18$ ppm, 8.70 ppm and 8.64 ppm) were clearly identifiable. Cleavage of the olefinic bonds was corroborated by negative-mode mass spectrometry and Fourier transform infrared (FT-IR) spectroscopy of both pristine and ozonated Zr-MOFs (Table S3, Figures S10, S11). In the mass spectrum, the molecular ions $[M-H]^-$ corresponding to trimesic acid ($m/z = 209.01$) and 5-formylisophthalic acid ($m/z = 193.01$) were found, in strong contrast to the absence of any molecular ion $[M-H]^-$ corresponding to L_2 ($m/z = 355.05$). Similarly, in comparison to the spectrum of pristine Zr-**scu**-MOF, the FT-IR spectrum of ozonated Zr-**pcu**-MOF revealed the appearance of a typical carbonyl (C=O) stretching band at 1700 cm^{-1} and the complete disappearance of an alkene (C=C) stretching band at 1622 cm^{-1}.

Having demonstrated the single-crystal-to-single-crystal synthesis of Zr-**pcu**-MOF by selectively cleaving the olefinic bonds in Zr-**scu**-MOF into a mixture of aldehyde and carboxylic acid groups, we next sought to perform analogous chemistry to synthesize Zr-**pcu**-MOF functionalized exclusively with carboxylic acids to show enhanced control over the final output of the Clip-off Chemistry. To this end, ozonated crystals were soaked in 1 mL of hydrogen peroxide (30 wt.% in H_2O) solution for 3 weeks. During this period, the sample was refreshed with fresh hydrogen peroxide every 24 h. Next, the sample was centrifuged, and then washed twice with water. The transformation to carboxylic acid groups was quantitative, as confirmed by ^{1}H NMR (Figures 2d, S9). Moreover, the Zr-**pcu**-MOF framework had been preserved, as confirmed by XRPD (Figures 2b, S3).

To show that we could generalize Clip-off Chemistry to other 3D MOF structures, we next attempted to synthesize a 3D Sc-**pcu**-MOF from an Sc-**soc**-MOF precursor (Figure 1; see SI, section 3),[31] a 3D structure built up from linking 6-c trigonal, prismatic Sc_3O clusters to 4-c L_1 linkers in a 4,6-c **soc**/**edq** topology.[32] This structure exhibits a mixture of cubic cavities (size: 11 Å) and 1D channels (size: 8 Å) along the three axes. As in the previous case, we designed the precursor by replacing L_1 with L_2, thus forming an isoreticular Sc-**soc**-MOF that contains different circuits of connections, some of which contains the cleavable olefins. We envisioned that, upon treatment with ozone, this circuit would be disrupted to form a 3D Sc-**pcu**-MOF whose Sc_3O clusters would be connected through trimesate/5-formylisophthalate linkers.

We began the clip-off synthesis of Sc-**pcu**-MOF via the aforementioned route by first preparing the isoreticular Sc-**soc**-MOF precursor. Colorless cubic crystals of Sc-**soc**-MOF were prepared by heating a solution of $Sc(NO_3)_3{\cdot}xH_2O$ and L_2 in DMF, ethanol and formic acid at 120 °C for 48 h (Figure 2e). However, all attempts at complete ozonolysis were unsuccessful, whether using the same synthetic protocol as for Zr-**scu**-MOF or trying slight modifications (e.g. extending the reaction time up to 8 h and/or the number of ozonolysis cycles up to twelve; Figures S13–S16). Consequently, cleavage of the olefinic bonds was incomplete, reaching a maximum value of 60% to 70% under certain conditions (e.g. exposing the Sc-**soc**-MOF crystals to ozone gas for 2 h). Consequently, a distinct ozonolysis protocol was employed: Sc-**soc**-MOF crystals were immersed in water, and then ozone was bubbled through the suspension under stirring at room temperature for 12 h. These conditions afforded greater cleavage of the olefinic bonds than in the previous strategy, leading to a mixture of trimesic acid, 5-formylisophthalic acid and the intermediate 1,2,4-trioxolane ring (Figure S17). Importantly, the presence of this intermediate indicated that the olefinic bonds had not all been completely cleaved to aldehyde/carboxylic acid groups. Moreover, increasing the reaction time under these solid/liquid conditions did not provide any major improvement in cleavage, although it did lead to a slight decrease in the crystallinity of the ozonated Sc-**pcu**-MOF.

To address the above drawbacks, we decided to combine the two ozonolysis strategies by first running a solid–gas reaction for 2 h and then, cleaving the remaining alkene bonds via suspension/gas reaction for an additional 6 h. Under these conditions, SCXRD of the resulting crystals confirmed quantitative single-crystal-to-single-crystal cleavage of the olefinic bonds of Sc-**soc**-MOF to synthesize Sc-**pcu**-MOF (Figure 2g, S19, S26).[19] However, in this case, no changes were observed in the volume of the *R-3* rhombohedral unit cell relative to that of the precursor, as also confirmed by XRPD (Figures 2f, S20). Nevertheless, SCXRD analysis

© 2021 The Authors. Angewandte Chemie International Edition published by Wiley-VCH GmbH

showed a very similar case to that of ozonated Zr-**scu**-MOF. Thus, the connectivity of the atoms belonging to the inorganic trimeric ScO_3 clusters remained identical to that of the pristine Sc-**soc**-MOF. Refinement of the carbon atoms from the organic linkers evidenced a positional disorder for some of them, and, unlike Sc-**soc**-MOF, the Sc-**pcu**-MOF product did not contain any olefinic atoms. Instead, areas of electron density were observed only between the opposite phenyl rings, with a maximum value at the middle point between the two rings, but at a distance longer than that expected for a C=C bond. This area of higher electron-density points perpendicularly above and below the plane of the phenyl rings. Although the refinement indicates the presence of atoms in this area, these atoms could not be unambiguously assigned to aldehyde or carboxylate groups (Figure S18). These findings indicate that the functional groups are not arranged in an orderly fashion within the crystals after ozonolysis but are instead randomly oriented in the pores. This is not surprising, considering that the resulting aldehydes and/or carboxylic groups are randomly distributed and most likely dangle in different orientations into the pores, rather than having a periodically fixed position, such that they would not contribute to the periodic diffraction of the crystal. Consistent with these SCXRD data, cleavage of all olefinic bonds was confirmed by ^{1}H NMR (Figures 2h, S21–S23) and negative-mode mass spectrometry of the digested ozonated samples (5% HF/[D_6]DMSO) (Figure S24, Table S6), and FT-IR of ozonated Sc-**pcu**-MOF (Figure S25), from which the olefinic protons ($\delta = 7.68$ ppm), molecular ion $[M-H]^-$ of L_2 and the typical alkene (C=C) stretching band, respectively, were not observed. On the contrary, the ^{1}H NMR signals, the molecular ions $[M-H]^-$ and the carbonyl (C=O) stretching band corresponding to doubly deprotonated trimesic acid and 5-

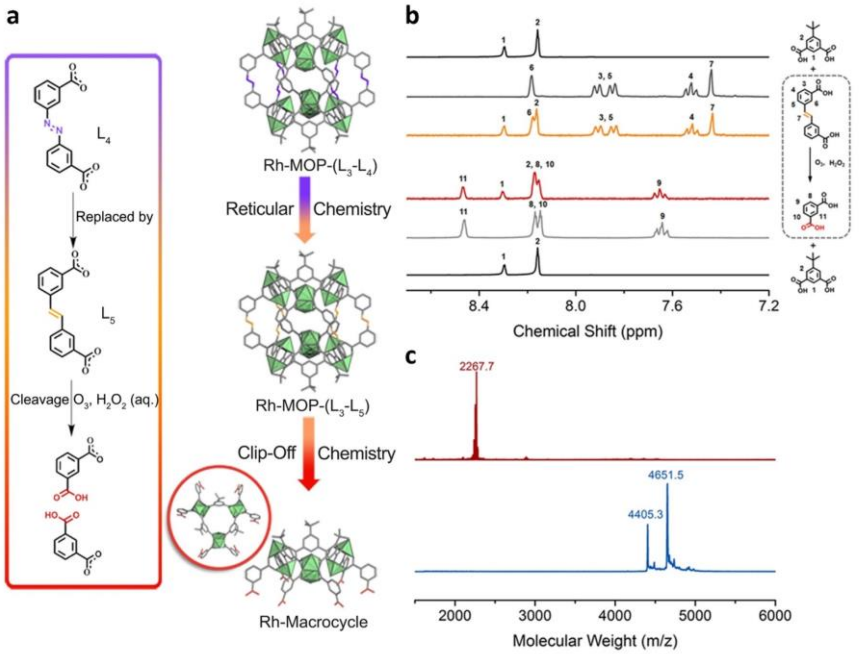


Figure 3. Clip-off synthesis of a triangular Rh-macrocycle. a) Schematic representation of the synthesis of a Rh-macrocycle from a discrete mixed-linker Rh-MOP, in which a linker containing an olefinic bond had been incorporated by reticular chemistry previous to ozonolysis.[41] b) ^{1}H NMR spectra (360 MHz, [D_6]DMSO) of digested L_3 (black), L_5 (dark grey), Rh-MOP (orange), Rh-macrocycle (red), and isophthalic acid (light grey). Assigned proton signals for digested Rh-MOP (orange): $\delta_1 = 8.30$ ppm (s, 1H), $\delta_2 = 8.16$ ppm (s, 2H), $\delta_{3+5} = 7.92$ ppm (d, $J = 7.7$ Hz, 2H), $\delta_{3+5} = 7.85$ ppm (d, $J = 7.7$ Hz, 2H), $\delta_4 = 7.51$ ppm (t, $J = 7.7$ Hz, 2H), $\delta_6 = 8.18$ ppm (s, 2H), and $\delta_7 = 7.43$ ppm (s, 2H). Assigned proton signals for digested Rh-macrocycle (red): $\delta_1 = 8.30$ ppm (s, 1H), $\delta_{2,8,10} = 8.17$–8.15 ppm (m, 6H), $\delta_9 = 7.65$ ppm (t, $J = 7.8$ Hz, 2H), and $\delta_{11} = 8.47$ ppm (s, 2H). c) MALDI-TOF spectra of Rh-MOP (blue) and of Rh-macrocycle fully functionalized with -COOH (red). The mass corresponding to the formula $[Rh_{12}(L_3)_6(L_5)_6(DMA)\ (H_2O)_2(MeOH)_{4+}H]^+$ (expected = 4403.8; found = 4405.3) and $[Rh_{12}(L_3)_6(L_5)_6(H_2O)_2(DMA)_2(CH_3CN)_7+H]^+$ (expected = 4650.0; found = 4651.5) have been highlighted for the Rh-MOP sample. In the case of the Rh-macrocycle, the mass corresponding to the formula $[Rh_6(L_3)_3(C_8H_5O_4)_6+H]^+$ has been highlighted (expected = 2268.8; found = 2267.7).

© 2021 The Authors. Angewandte Chemie International Edition published by Wiley-VCH GmbH

formylisophthalate were all clearly identifiable, thus further corroborating the clip-off synthesis of Sc-**pcu**-MOF.

Finally, we endeavoured to use Clip-off Chemistry to synthesize a metal-organic macrocycle[33–36] from a 0-D MOP system. To this end, we followed the second approach mentioned above, by designing a mixed-linker Rh-MOP that we could transform into a triangular metal-organic macrocycle (Figure 3a, S27–S34). We selected a Rh-MOP[37] built from six 4-c Rh paddle-wheel clusters linked by six 5-*tert*-butylbenzene-1,3-dicarboxylate (L_3) linkers and by six 3-[(3-carboxyphenyl)diazenyl]benzoate (L_4) linkers that together form a cage (diameter: 12 Å). In this cage, three paddle-wheel clusters are linked by three L_3 linkers to form a triangular macrocycle, and two of these units are linked by six L_4 linkers. Following a similar strategy as those explained in the previous examples, we functionalized this MOP with alkene groups by replacing L_4 with 3-[2-(3-carboxyphenyl)ethenyl]benzoate (L_5). We reasoned that the isoreticular Rh-MOP would contain a non-cleavable L_3 linker and a cleavable L_5 linker, which, upon cleavage via ozonolysis, would split the Rh-MOP into two equal fragments. We hypothesized that this splitting would release the metal-organic macrocycle built up from the three 4-c Rh^{II} paddle-wheel units linked to each other by the three L_3 linkers and with six pendant partly deprotonated isophthalic linkers.

We synthesized isoreticular Rh-MOP by heating a suspension of L_3, L_5, Na_2CO_3 and $Rh_2(OAc)_4$ in *N*,*N*-dimethylacetamide (DMA) at 100 °C. After 4 days, the reaction yielded a dark precipitate that was centrifuged to separate out the Na_2CO_3. The resultant solution was precipitated in MeOH to yield a green powder, which was washed several times with MeOH. Finally, diffusion of diethyl ether into a solution of this green powder in DMF afforded green parallelogram-shaped crystals of Rh-MOP. SCXRD confirmed the formation of the expected isoreticular MOP, built up from six L_3 linkers and six cleavable L_5 linkers (Figure 3a). Next, the six linkers were cleaved to synthesize the metal-organic macrocycle by bubbling ozone through a suspension of Rh-MOP in DMA and hydrogen peroxide (50 % wt. in H_2O) at room temperature for 30 min. Note that oxidative conditions were used in this clip-off reaction to obtain a pure Rh-macrocycle functionalized with six carboxylic acid groups. Afterwards, the resulting green suspension was centrifuged, and an aqueous HCl solution was added to the supernatant to precipitate out the Rh-macrocycle as a green solid. This solid was finally separated by centrifugation, washed with water three times, and dried at 85 °C under vacuum.

We confirmed formation of the expected metal-organic Rh-macrocycle by ^{1}H NMR of the digested ozonated Rh-MOP (5 % HF/[D_6]DMSO; Figure 3b), MALDI-TOF mass (Figure 3c) spectrometry and UV/Vis spectroscopy (Figure S33). The ^{1}H NMR spectrum lacked all the characteristic peaks of L_5 (olefinic protons at $\delta = 7.43$ ppm; and phenyl protons at $\delta = 8.18$ ppm, 7.92 ppm, 7.85 ppm and 7.51 ppm), yet it did reveal the characteristic signals of L_3 (phenyl protons at $\delta = 8.30$ ppm and 8.16 ppm; and *tert*-butyl protons at $\delta = 1.33$ ppm) and those of isophthalic acid (phenyl protons at $\delta = 8.47$ ppm, 8.17 ppm and 7.65 ppm; Figure 3b). This integrated spectrum indicated an L_3/isophthalic acid proton ratio of 1:2, consistent with the formula expected for the Rh-macrocycle (Figures S31, S32). Moreover, the absence of any proton signal corresponding to 3-formylbenzoic acid corroborated full cleavage of all the olefinic bonds in the Rh-MOP and their subsequent transformation to carboxylic acid groups.

Finally, we unambiguously confirmed the structure of the targeted macrocycle by positive-mode MALDI-TOF on pristine and ozonated samples of the Rh-MOP. The MALDI-TOF spectrum of the Rh-MOP showed its molecular ion $[M+H]^+$ ($m/z = 4651.5$), whereas that of the ozonated Rh-MOP did not, but did contain a new peak, for the molecular ion $[M+H]^+$ ($m/z = 2267.7$) corresponding to the Rh-macrocycle (Figure 3c). Moreover, UV/Vis analysis of both pristine and ozonated Rh-MOP samples did not reveal any shift in the low-energy absorption band I (λ_{max}) at 592 nm, indicating that the coordination of Rh^{II} ions in the ozonated solid had not changed, thus further corroborating formation of the desired Rh-macrocycle (Figure S33).

Conclusion

We have introduced Clip-off Chemistry, a new approach to synthesizing molecules and materials based on selective bond-breaking in reticular precursors materials via common organic transformations, via programmed de-reticulation and controlled etching at the molecular level. As proof-of-concept, we transformed two 3D MOFs (Zr-**scu**-MOF and Sc-**soc**-MOF) into two topologically distinct 3D MOFs (Zr-**pcu**-MOF and Sc-**pcu**-MOF, respectively). Moreover, we extended Clip-off Chemistry to a 0-D system, by transforming a MOP into a metal-organic macrocycle. In the examples that we have reported here, we demonstrated that the cleavage was quantitative and selective; was effective both in solid-phase and solution-phase chemistry; and occurred in a single-crystal-to-single crystal fashion across the entire bulk precursor sample. Moreover, we demonstrated control over the cleavage of each olefinic bond into carboxylic acid groups using oxidative conditions.

Our preliminary results suggest that Clip-off Chemistry is ripe for further exploration. Since it is based on bond cleavage, the dimensionality of the parent reticular material dictates the synthetic feasibility of the target molecules and/or materials (Figure 4). Thus, it offers the possibility to modify structures of reticular materials without changing their dimensionality (e.g. 3D → 3D, or 2D → 2D). For example, one might employ Clip-off Chemistry for post-synthetic modification of the topology and/or the porosity of a given material. Moreover, it could be applied to 3D structures to augment the diversity of new 2D materials: for instance, by converting well-known 3D pillared reticular materials into isolated 2D layers, via selective clipping of the pillaring linkers. Similarly, it shows promise for using 3D or 2D structures to isolate 1D materials in the form of metallic chains, or to synthesize 0-D systems, including MOPs, macrocycles and clusters, from 3D/2D/1D structures and even from other 0-D systems (e.g. MOPs). Cleavage of bonds in reticular materials may also be expanded to purely organic structures.

© 2021 The Authors. Angewandte Chemie International Edition published by Wiley-VCH GmbH

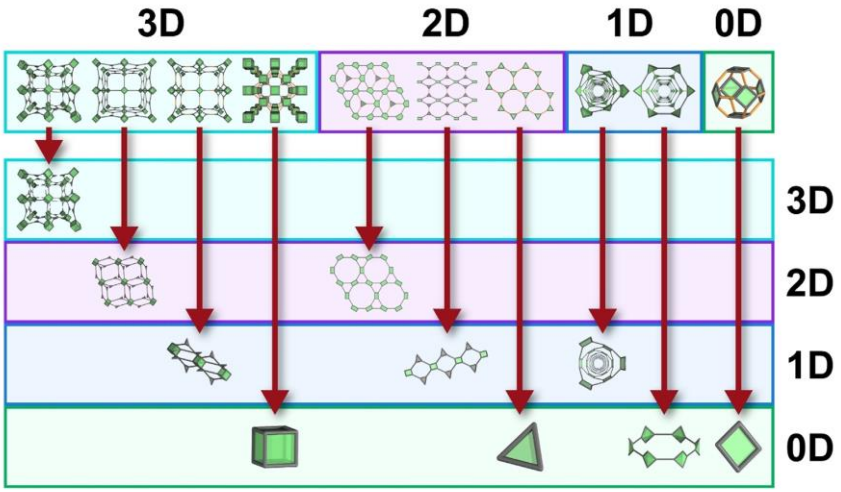


Figure 4. Clip-off Chemistry for the synthesis of molecular architectures of different dimensionality. Schematic illustrating the potential outcomes of Clip-off Chemistry, in which the dimensionality of the parent reticular materials dictates the dimensionality of the target molecules and structures.

Indeed, COFs and organic cages are another endless source of precursors in Clip-off Chemistry for possible synthesis of organic polymers, cages, macrocycles or other organic compounds. Similarly, other reactions involving the cleavage of bonds (e.g. photolysis) are potential candidates to be applied in reticular materials for their programmable disassembly.[38–40] In summary, our results prove that the programmed disassembly of reticular materials is feasible, and that Clip-off Chemistry could provide researchers with access to myriad new molecular architectures.

Acknowledgements

We thank Thais Grancha, Jordi Martínez-Esaín and Teodor Parella for technical assistance. This work has received funding from the European Union's Horizon 2020 research and innovation programme under grant agreement No 101019003, the Spanish MINECO (projects RTI2018-095622-B-I00 and PID2019-106403RB-I00) and the Catalan AGAUR (project 2017 SGR 238). It was also funded by the CERCA Programme/Generalitat de Catalunya. ICN2 is supported by the Severo Ochoa programme from the Spanish MINECO (Grant No. SEV-2017-0706). F.G. acknowledges funding from the Spanish Research Agency (AEI, CTQ2017-87262-R, EUR2019-103824). The project that generated these results received support from a fellowship (LCF/BQ/PR20/11770011) of the "la Caixa" Foundation (ID 100010434). Y.Y. acknowledges the China Scholarship Council for scholarship support.

Conflict of Interest

The authors declare no conflict of interest.

Keywords: bond breaking · disassembly · metal-organic frameworks · metal-organic polyhedra · reticular materials

[1] H. Li, M. Eddaoudi, T. L. Groy, O. M. Yaghi, *J. Am. Chem. Soc.* **1998**, *120*, 8571–8572.
[2] O. M. Yaghi, M. O'Keeffe, N. W. Ockwig, H. K. Chae, M. Eddaoudi, J. Kim, *Nature* **2003**, *423*, 705–714.
[3] H. Li, M. Eddaoudi, M. O'Keeffe, O. M. Yaghi, *Nature* **1999**, *402*, 276–279.
[4] O. M. Yaghi, G. Li, H. Li, *Nature* **1995**, *378*, 703–706.
[5] S. Kitagawa, R. Kitaura, S. I. Noro, *Angew. Chem. Int. Ed.* **2004**, *43*, 2334–2375; *Angew. Chem.* **2004**, *116*, 2388–2430.
[6] B. F. Abrahams, B. F. Hoskins, D. M. Michail, R. Robson, *Nature* **1994**, *369*, 727–729.
[7] B. F. Hoskins, R. Robson, *J. Am. Chem. Soc.* **1989**, *111*, 5962–5964.
[8] O. M. Yaghi, M. J. Kalmutzki, C. S. Diercks, *Introduction to Reticular Chemistry: Metal-Organic Frameworks and Covalent Organic Frameworks*, Wiley-VCH, Weinheim, **2019**.
[9] X. Feng, X. Ding, D. Jiang, *Chem. Soc. Rev.* **2012**, *41*, 6010–6022.
[10] D. J. Tranchemontagne, Z. Ni, M. O'Keeffe, O. M. Yaghi, *Angew. Chem. Int. Ed.* **2008**, *47*, 5136–5147; *Angew. Chem.* **2008**, *120*, 5214–5225.
[11] J. J. Perry IV, J. A. Perman, M. J. Zaworotko, *Chem. Soc. Rev.* **2009**, *38*, 1400–1417.
[12] S. Lee, H. Jeong, D. Nam, M. S. Lah, W. Choe, *Chem. Soc. Rev.* **2021**, *50*, 528–555.

© 2021 The Authors. Angewandte Chemie International Edition published by Wiley-VCH GmbH

[13] M. Eddaoudi, D. B. Moler, H. Li, B. Chen, T. M. Reineke, M. O'Keeffe, O. M. Yaghi, *Acc. Chem. Res.* **2001**, *34*, 319 – 330.
[14] M. Eddaoudi, J. Kim, N. Rosi, D. Vodak, J. Wachter, M. O'Keeffe, O. M. Yaghi, *Science* **2002**, *295*, 469 – 472.
[15] S. M. Cohen, *Chem. Rev.* **2012**, *112*, 970 – 1000.
[16] O. M. Yaghi, *Mol. Front. J.* **2019**, *3*, 66 – 83.
[17] M. O'Keeffe, O. M. Yaghi, *Chem. Rev.* **2012**, *112*, 675 – 702.
[18] M. O'Keeffe, M. A. Peskov, S. J. Ramsden, O. M. Yaghi, *Acc. Chem. Res.* **2008**, *41*, 1782 – 1789.
[19] V. A. Blatov, A. P. Shevchenko, D. M. Proserpio, *Cryst. Growth Des.* **2014**, *14*, 3576 – 3586.
[20] A. F. Wells, *Three-Dimensional Nets and Polyhedral*, Wiley, Hoboke, **1977**.
[21] H. Wang, X. Dong, J. Lin, S. J. Teat, S. Jensen, J. Cure, E. V. Alexandrov, Q. Xia, K. Tan, Q. Wang, D. H. Olson, D. M. Proserpio, Y. J. Chabal, T. Thonhauser, J. Sun, Y. Han, J. Li, *Nat. Commun.* **2018**, *9*, 1745.
[22] M. Li, D. Li, M. O'Keeffe, O. M. Yaghi, *Chem. Rev.* **2014**, *114*, 1343 – 1370.
[23] J. Albalad, H. Xu, F. Gándara, M. Haouas, C. Martineau-Corcos, R. Mas-Ballesté, S. A. Barnett, J. Juanhuix, I. Imaz, D. Maspoch, *J. Am. Chem. Soc.* **2018**, *140*, 2028 – 2031.
[24] V. Guillerm, H. Xu, J. Albalad, I. Imaz, D. Maspoch, *J. Am. Chem. Soc.* **2018**, *140*, 15022 – 15030.
[25] R. Criegee, *Angew. Chem. Int. Ed. Engl.* **1975**, *14*, 745 – 752; *Angew. Chem.* **1975**, *87*, 765 – 771.
[26] C. E. Schiaffo, P. H. Dussault, *J. Org. Chem.* **2008**, *73*, 4688 – 4690.
[27] L. B. Harding, W. A. Goddard III, *J. Am. Chem. Soc.* **1978**, *100*, 7180 – 7188.
[28] L. H. Xie, X. M. Liu, T. He, J. R. Li, *Chem* **2018**, *4*, 1911 – 1927.
[29] S. Wang, L. Chen, M. Wahiduzzaman, A. Tissot, L. Zhou, I. A. Ibarra, A. Gutiérrez-Alejandre, J. S. Lee, J. S. Chang, Z. Liu, J. Marrot, W. Shepard, G. Maurin, Q. Xu, C. Serre, *Matter* **2021**, *4*, 182 – 194.
[30] H. Furukawa, F. Gándara, Y. B. Zhang, J. Jiang, W. L. Queen, M. R. Hudson, O. M. Yaghi, *J. Am. Chem. Soc.* **2014**, *136*, 4369 – 4381.
[31] J. W. Zhang, P. Qu, M. C. Hu, S. N. Li, Y. C. Jiang, Q. G. Zhai, *Inorg. Chem.* **2019**, *58*, 16792 – 16799.
[32] Y. Liu, J. F. Eubank, A. J. Cairns, J. Eckert, V. C. Kravtsov, R. Luebke, M. Eddaoudi, *Angew. Chem. Int. Ed.* **2007**, *46*, 3278 – 3283; *Angew. Chem.* **2007**, *119*, 3342 – 3347.
[33] P. J. Stang, B. Olenyuk, *Acc. Chem. Res.* **1997**, *30*, 502 – 518.
[34] B. Olenyuk, A. Fechtenkötter, P. J. Stang, *J. Chem. Soc. Dalton Trans.* **1998**, 1707 – 1728.
[35] M. Fujita, O. Sasaki, T. Mitsuhashi, T. Fujita, J. Yazaki, K. Yamaguchi, K. Ogura, *Chem. Commun.* **1996**, 1535 – 1536.
[36] F. A. Cotton, L. M. Daniels, C. Lin, C. A. Murillo, *J. Am. Chem. Soc.* **1999**, *121*, 4538 – 4539.
[37] J. R. Li, H. C. Zhou, *Nat. Chem.* **2010**, *2*, 893 – 898.
[38] L. Feng, K. Y. Wang, G. S. Day, M. R. Ryder, H. C. Zhou, *Chem. Rev.* **2020**, *120*, 13087 – 13133.
[39] K. Y. Wang, L. Feng, T. H. Yan, S. Wu, E. A. Joseph, H. C. Zhou, *Angew. Chem. Int. Ed.* **2020**, *59*, 11349 – 11354; *Angew. Chem.* **2020**, *132*, 11445 – 11450.
[40] P. Shieh, M. R. Hill, W. Zhang, S. L. Kristufek, J. A. Johnson, *Chem. Rev.* **2021**, *121*, 7059 – 7121.
[41] Deposition Numbers 2080949 (for Zr-**scu**-MOF), 2080950 (for Zr-**pcu**-MOF), 2080951 (for Sc-**soc**-MOF), 2080952 (for Sc-**pcu**-MOF) and 2080953 (for Rh-MOP) contain the supplementary crystallographic data for this paper. These data are provided free of charge by the joint Cambridge Crystallographic Data Centre and Fachinformationszentrum Karlsruhe Access Structures service www.ccdc.cam.ac.uk/structures.

Manuscript received: August 19, 2021
Accepted manuscript online: November 5, 2021
Version of record online: November 25, 2021

© 2021 The Authors. Angewandte Chemie International Edition published by Wiley-VCH GmbH

ChemComm

COMMUNICATION

View Article Online
View Journal | View Issue

Check for updates

Cite this: *Chem. Commun.*, 2023, **59**, 7803

Received 13th April 2023,
Accepted 22nd May 2023

DOI: 10.1039/d3cc01831h

rsc.li/chemcomm

A mesoporous Zr-based metal–organic framework driven by the assembly of an octatopic linker†

Borja Ortín-Rubio, [ab] Cristina Perona-Bermejo,[c] José A. Suárez del Pino,[ab] Francisco J. Carmona, [c] Felipe Gándara, [d] Jorge A. R. Navarro, [c] Judith Juanhuix, [e] Inhar Imaz*[ab] and Daniel Maspoch *[abf]

Metal–organic frameworks (MOFs) based on high-connected nets are generally very attractive due to their combined robustness and porosity. Here, we describe the synthesis of BCN-348, a new high-connected Zr-MOF built from an 8-connected (8-c) cubic Zr-oxocluster and an 8-c organic linker. BCN-348 contains a minimal edge-transitive 3,4,8-c eps net, and combines mesoporosity with thermal and hydrolytic stability. Encouraging results from preliminary studies on its use as a catalyst for hydrolysis of a nerve-agent simulant suggest its potential as an agent for detoxification of chemical weapons and other pernicious compounds.

Being able to control the connectivity in reticular materials is crucial for researchers to able to design and predict the final structures and hone the properties of these materials.[1] A current goal is the generation of highly connected metal–organic frameworks (MOFs), meaning those with a connectivity ≥ 8.[2] This is mainly due to the tendency of such MOFs to exhibit higher chemical, thermal and compositional stability and interesting topologic profiles: for example, compared to other MOFs, they can incorporate more defects without suffering structural collapse, and their topologies are more constrained and thus, easier to predict. To date, the most common strategies to synthesise high-connected MOFs rely on the use of dendritic organic linkers to connect low-connected clusters;[3] the use of high-connected clusters (*e.g.* 12-connected (12-c) Zr-oxoclusters[4] and their isoreticular rare-earth (RE) analogues)[5] or high-connected cages that are linked by low-connected linkers;[6] and/or the simultaneous use of high-connected linkers and high-connected clusters/cages. However, even though the last of these strategies should lead to high-connected nets, only a few MOFs have actually been assembled that way. Indeed, upon searching the Cambridge Crystallographic Data Centre (CCDC) database (ConQuest v. 2.0.0, CCDC, Cambridge, UK),[7] we were surprised to find only three high-connected MOFs: (i) one assembled by the linkage of rare trinuclear Ni(II) clusters in a cubic conformation by an octatopic linker, giving an **eps** net;[8] and (ii) two assembled by connecting 12-c nonanuclear RE clusters in a hexagonal prism conformation through an octatopic linker, affording a **kce** net (Fig. 1), and through a dodecatopic linker, giving a **kex** net.[9]

Another unexpected observation was the absence of MOFs assembled from (the archetypical) Zr-oxocluster and high-connected linkers.[10] To date, Zr-MOFs have been extensively assembled from ditopic linkers (12-c cuboctahedron **fcu**,[4] 8-c cube **bcu**[11] and **reo**,[12] 8-c hexagonal bipyramid **hex**,[13] 6-c octahedron **pcu**[14]); triangular tritopic linkers (8-c cube **the**,[15] 6-c octahedron **spn**,[16] 6-c hexagonal **kgd**[17]); square tetratopic linkers (12-c cuboctahedron **ftw**,[18] 12-c hexagonal prism **shp**,[19] 8-c cube **csq**,[18,20] **sqc**[21] and **scu**,[22] 6-c octahedron **soc**,[23] 6-c triangular prism **stp**,[24] 6-c hexagonal **she**,[25] 4-c square **lvt**);[26] tetrahedral tetratopic linkers (12-c icosahedral **ith**,[16] 8-c cube **flu**,[16] 6-c hexagonal **gar**);[27] hexagonal hexatopic linkers (6-c hexagonal **hxg**);[28] and trigonal prism hexatopic linkers (12-c hexagonal prism **alb**).[29]

Herein we report the design, synthesis and functional validation of first Zr-MOF (hereafter called BCN-348; BCN stands for Barcelona Material), which was assembled by combining 8-c cubic Zr-oxoclusters with an 8-c octagonal linker, affording the novel 3,4,8-c **eps** net (Fig. 1). In this framework, the octatopic linker promotes the formation of cuboctahedral pores oriented in the six square faces, resulting in a new face-sharing, Archimedean, solid-stacking.[30] BCN-348 is robust and exhibits remarkable porosity, as shown by the apparent Brunauer-Emmett-Teller (BET)

[a] *Catalan Institute of Nanoscience and Nanotechnology (ICN2), CSIC and The Barcelona Institute of Science and Technology, Campus UAB, Bellaterra, Barcelona 08193, Spain. E-mail: inhar.imaz@icn2.cat, daniel.maspoch@icn2.cat*
[b] *Departament de Química, Facultat de Ciències, Universitat Autònoma de Barcelona, Bellaterra 08193, Spain*
[c] *Departamento de Química Inorgánica, Universidad de Granada, Av. Fuentenueva S/N, Granada 18071, Spain*
[d] *Materials Science Institute of Madrid (ICMM), Consejo Superior de Investigaciones Científicas (CSIC), Calle Sor Juana Inés de la Cruz, 3, Madrid 28049, Spain*
[e] *ALBA Synchrotron, Cerdanyola del Vallès, Barcelona 08290, Spain*
[f] *ICREA, Pg. Lluís Companys 23, Barcelona 08010, Spain*

† Electronic supplementary information (ESI) available: Experimental procedures, and PXRD, sorption, TGA and catalysis data. CCDC 2255518. For ESI and crystallographic data in CIF or other electronic format see DOI: **https://doi.org/10.1039/d3cc01831h**

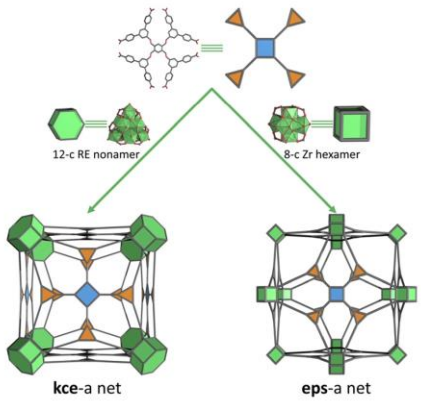


Fig. 1 Schematic of the influence of octatopic TBCPB linker symmetry on the formation of the minimal edge-transitive **kce** net, when a RE hydroxo/fluorinated cluster is used (left),[9] and of the minimal edge-transitive **eps** net, when a Zr oxo/hydroxo-cluster is used (right).

surface area of 2564 $m^2\ g^{-1}$ and the presence of mesopores. We exploited the exposed nature of the metal sites in the Zr-cluster and the stability of this BCN-348 in aqueous media, by testing the catalytic degradation of a nerve agent simulant assisted by the Lewis-acidic Zr sites in the absence of an amine-based buffer.

To prepare BCN-348, we combined $ZrOCl_2{\cdot}8H_2O$ and 1,2,4,5-tetrakis[3,5-bis(4-carboxyphenyl)phenoxymethyl]benzene (H_8TBCPB) in the presence of trifluoroacetic acid (TFA) and *N*,*N*-dimethylformamide (DMF) under solvothermal conditions, which yielded colourless cubic crystals. Single-crystal X-ray diffraction (SCXRD) revealed an **eps** net, where the Zr-oxocluster exhibits an 8-connected cubic shape with four missing positions induced by the symmetry of the linker (Fig. 1). BCN-348 was solved in the cubic $Fm\bar{3}$ space group, with a unit cell parameter of 59.677 Å, resulting in a large cell volume of 212530 $Å^3$. The resulting framework presents two types of cages: a cuboctahedral cage with a diameter of 38.6 Å, which contains hexagonal (17.6 Å) and rhombic (12.1 Å) windows; and a smaller, octahedral cage with a diameter of 26.3 Å, which contains the same hexagonal (17.6 Å) windows (Fig. 2). In this structure, the octatopic ligand occupies the square faces of the cuboctahedral cages, which connect four different clusters, whereas its branches occupy the edges of the octahedral cage, which connects two clusters. Interestingly, this structure can also be described as the stacking of face-sharing Archimedean solids: in this case, cuboctahedra (Fig. 2d).[30]

Next, we performed topological analysis of the structure using ToposPro 5.3.3.5 software[31] and following literature recommendations to deconstruct the linker into more-regular triangular and square shapes, which revealed the formation of a 3,4,8-c **eps** net.[32] To the best of our knowledge, this topology had never previously been observed in Zr- or RE-based MOFs, and there is just one reported example of a structure (a Ni-based MOF) exhibiting this net.[8] Also, when we performed a topological analysis without splitting the linker but instead, treating it as an octagonal node, the connectivities of this node and of the Zr-oxocluster were halved, resulting in a 4,4-c **nbo-b** net. This finding proves that the **eps** net is a **nbo-b**-related net and therefore, corroborates that BCN-348 is the first Zr-MOF based on this related net.[9,33]

Seeking to understand the formation of the aforementioned **eps** net, we did a reticular survey.[1b] According to the RCSR database, combining an octagonal-shape linker with a Zr-cluster, which could be 12-c, 8-c, 6-c or 4-c (in the case of the most-regular ones), would lead to the formation of **kce** (3,4,12-c), **eps** (3,4,8-c), **cye** (6,8-c), **cze** (3,4,6-c), or **cyt** (4,8-c) nets, respectively. Among these, we initially excluded both the **cye** and the **cyt** nets, due to the mismatch between the proximity of two neighbouring Zr-clusters in these nets as well as to the length of the TBCPB linker that we had used. Regarding the **kce** net, this topology had already been reported as resulting from the combination of the TBCPB linker with a 12-c nonanuclear RE-cluster that exhibits a hexagonal prism conformation (Fig. 1). However, the strong Zr–O bonds always favour the formation of the hexanuclear Zr-oxocluster, enabling defaults in its connectivity,[11–18,20–28] rather than being disordered in its 12-c hexagonal prism conformation.[19,29] We hypothesise that together, these features favoured the formation of the **eps** net rather than either the **kce** net, which would have involved the formation of a disordered 12-c hexagonal prismatic Zr-cluster, or the **cze** net, which is less connected than **eps** (Fig. 1).

Next, we confirmed the phase purity of the bulk BCN-348 sample by powder X-ray diffraction (PXRD): the experimental results matched the simulated ones that we had obtained by SCXRD (Fig. S1, ESI†). We then studied the porosity of BCN-348 by running N_2-sorption experiments at 77 K. BCN-348 exhibits an apparent Brunet–Emmett–Teller (BET) area of 2564 $m^2\ g^{-1}$ in an isotherm between type-Ib and type-IV (Fig. S3–S5, ESI†). The total pore volume was found to be 1.14 $cm^3\ g^{-1}$ at P/P_0 = 0.95. The pore-size distribution, based on DFT models, revealed the presence of mesopores of 27.3 Å and 31.7 Å (Fig. S6, ESI†). Moreover, BCN-348 was thermally stable up to 508 °C (Fig. S7, ESI†), and it maintained its phase crystallinity when incubated in water for 1 h, 12 h and 24 h (Fig. S2, ESI†). The fact that BCN-348 combines mesoporosity with thermal and hydrolytic stability illustrates the feasibility of using high-connected clusters and linkers to assemble robust porous MOFs.

Among the most promising recent applications for Zr-MOFs is their use as hydrolytic catalysts for the detoxification of highly toxic organophosphate compounds—namely pesticides, and nerve agents and their simulants.[34] These detoxification processes imply the activation of the P–X (X= O, S, F) bond by zirconium Lewis acidic and hydroxide basic sites at the oxo-hydroxide Zr-cluster. Consequently, pore size and polarity, framework connectivity, and stability together define the access of water molecules and toxic substrate molecules to the catalytically active metal cluster. To date, most of these Zr-MOF-assisted catalytic processes have been done using simulants with ester P–O bonds, together with corrosive and toxic basic buffers (*N*-ethylmorpholine).

 This journal is © The Royal Society of Chemistry 2023

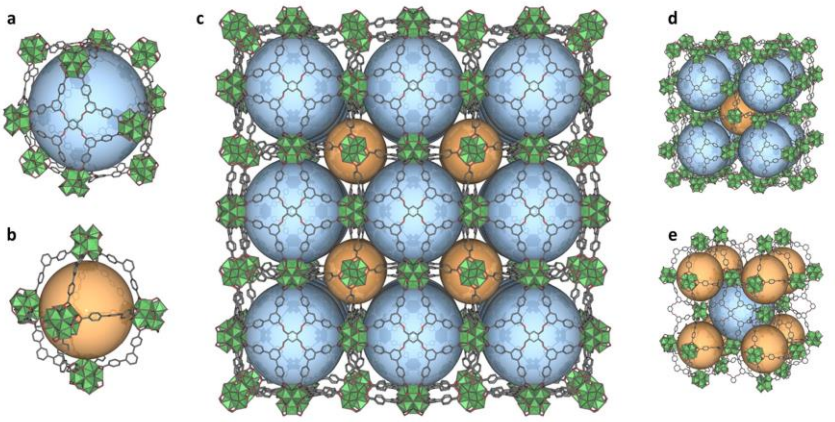


Fig. 2 Structural illustrations of BCN-348, highlighting (a) the cuboctahedral cage assembled with 6 organic moieties located in the square faces; (b) the octahedral cage assembled with 12 partial organic moieties located at the edges; (c) the overall structure of BCN-348 across the *c*-axis; (d) the assembly of face-sharing cuboctahedron stacking; and (e) the spatial distribution of octahedral cages around the cuboctahedral cavity.

Importantly, the toxicity of common nerve agents such as Soman (GD), Sarin (GB) and Cyclosarin (GF) is determined by labile P–F bonds. Consequently, there is pronounced interest in the development of new detoxification materials that could hydrolyse the P–F bonds of hazardous chemicals in unbuffered aqueous solutions.

Seeking to exploit the accessible pore structure and hydrolytic stability of BCN-348, we tested its catalytic activity in the removal of the simulant diisopropylfluorophosphate (DIFP), which contains a P–F bond. We ran the hydrolysis in an aqueous unbuffered dispersion of BCN-348 using a DIFP/MOF ratio of 1.5 : 1. The removal of DIFP from the solution was first followed by GC. The half-life of detoxification is 72.2 min with quantitative removal of the toxic simulant after 24 hours (Fig. 3). To have a deep insight into the detoxication mechanism, we performed additional ^{31}P NMR and ^{1}H NMR analysis in D_2O. The results confirmed that DIFP is removed from the supernatant solution after 24 hours, with diisopropylphosphate (DIP) appearing as the main hydrolytic product (72.8%). However, there was still a fraction of 27.2% of unreacted DIFP molecules, which were mostly adsorbed by BCN-348 (Table S2 and Fig. S8–S10, ESI†). These results confirm the highly accessible porous structure and exposed nature of the Zr metal sites in the metal clusters.

In conclusion, we have reported the design, synthesis and functional validation of BCN-348, a new mesoporous high-connected Zr-MOF, which we assembled by connecting an 8-c cubic Zr-oxocluster through an 8-c organic linker. Topologically, BCN-348 exhibits a minimal edge-transitive **eps** net, unlike its RE analogue, which exhibits the minimal edge-transitive **kce** net. Moreover, BCN-348 combines mesoporosity with the presence of Lewis-acid open metal sites and hydrolytic stability, permitting its use as a catalyst for the hydrolytic degradation of toxic chemicals without any assistance from a buffer, which we confirmed on DIFP, a nerve-agent simulant. Our study augments the collection of reticular Zr-MOFs and highlights the endless possibilities of assembling regular, high-connected, molecular

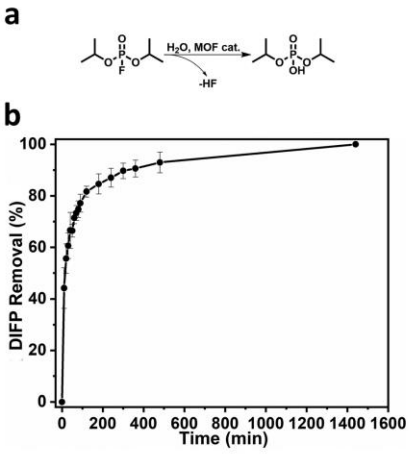


Fig. 3 (a) Hydrolysis of DIFP catalysed by BCN-348 (denoted as "MOF cat."). (b) DIFP removal plotted against time.

building blocks in symmetric reticular materials, thus further paving the way to new high-connected frameworks.

This work has received funding from the European Union's Horizon 2020 research and innovation programme, under grant agreement No 101019003, the Catalan AGAUR (project 2021 SGR 00458), the CERCA Programme/Generalitat de Catalunya, and the Spanish MCIN/AEI/10.13039/501100011033 (Project PID2020-113608RB-I00). ICN2 is supported by the Severo Ochoa Centres of Excellence programme, Grant CEX2021-001214-S, funded by MCIN/AEI/10.13039.501100011033.

Conflicts of interest

There are no conflicts to declare.

Notes and references

1 (*a*) O. M. Yaghi, M. O'Keeffe, N. W. Ockwig, H. K. Chae, M. Eddaoudi and J. Kim, *Nature*, 2003, **423**, 705–714; (*b*) M. O'Keeffe, M. A. Peskov, S. J. Ramsden and O. M. Yaghi, *Acc. Chem. Res.*, 2008, **41**, 1782–1789; (*c*) M. J. Kalmutzki, N. Hanikel and O. M. Yaghi, *Sci. Adv.*, 2018, **4**, eaat9180; (*d*) H. Jiang, D. Alezi and M. Eddaoudi, *Nat. Rev. Mater.*, 2021, **6**, 466–487.
2 V. Guillerm and M. Eddaoudi, *Acc. Chem. Res.*, 2021, **54**, 3298–3312.
3 (*a*) J. F. Eubank, H. Mouttaki, A. J. Cairns, Y. Belmabkhout, L. Wojtas, R. Luebke, M. Alkordi and M. Eddaoudi, *J. Am. Chem. Soc.*, 2011, **133**, 14204–14207; (*b*) F. Moreau, D. I. Kolokolov, A. G. Stepanov, T. L. Easun, A. Dailly, W. Lewis, A. J. Blake, H. Nowell, M. J. Lennox, E. Besley, S. Yang and M. Schröder, *Proc. Natl. Acad. Sci. U. S. A.*, 2017, **114**, 3056–3061; (*c*) J. F. Eubank, F. Nouar, R. Luebke, A. J. Cairns, L. Wojtas, M. Alkordi, T. Bousquet, M. R. Hight, J. Eckert, J. P. Embs, P. A. Georgiev and M. Eddaoudi, *Angew. Chem., Int. Ed.*, 2012, **51**, 10099–10103; (*d*) O. K. Farha, I. Eryazici, N. C. Jeong, B. G. Hauser, C. E. Wilmer, A. A. Sarjeant, R. Q. Snurr, S. T. Nguyen, A. Ö. Yazaydin and J. T. Hupp, *J. Am. Chem. Soc.*, 2012, **134**, 15016–15021.
4 J. H. Cavka, S. Jakobsen, U. Olsbye, N. Guillou, C. Lamberti, S. Bordiga and K. P. Lillerud, *J. Am. Chem. Soc.*, 2008, **130**, 13850–13851.
5 D. X. Xue, A. J. Cairns, Y. Belmabkhout, L. Wojtas, Y. Liu, M. H. Alkordi and M. Eddaoudi, *J. Am. Chem. Soc.*, 2013, **135**, 7660–7667.
6 F. Nouar, J. F. Eubank, T. Bousquet, L. Wojtas, M. J. Zaworotko and M. Eddaoudi, *J. Am. Chem. Soc.*, 2008, **130**, 1833–1835.
7 I. J. Bruno, J. C. Cole, P. R. Edgington, M. Kessler, C. F. Macrae, P. McCabe, J. Pearson and R. Taylor, *Acta Crystallogr., Sect. B: Struct. Sci.*, 2002, **58**, 389–397.
8 Y. S. Xue, J. L. Lu, W. W. Cheng, J. Wei, N. N. Chen, J. Dai and J. Q. Tao, *Transition Met. Chem.*, 2018, **43**, 9–19.
9 Z. Chen, Z. Thiam, A. Shkurenko, L. J. Weselinski, K. Adil, H. Jiang, D. Alezi, A. H. Assen, M. O'Keeffe and M. Eddaoudi, *J. Am. Chem. Soc.*, 2019, **141**, 20480–20489.
10 Z. Chen, S. L. Hanna, L. R. Redfern, D. Alezi, T. Islamoglu and O. K. Farha, *Coord. Chem. Rev.*, 2019, **386**, 32–49.
11 S. Yuan, W. Lu, Y.-P. Chen, Q. Zhang, T.-F. Liu, D. Feng, X. Wang, J. Qin and H.-C. Zhou, *J. Am. Chem. Soc.*, 2015, **137**, 3177–3180.
12 V. Bon, V. Senkovskyy, I. Senkovska and S. Kaskel, *Chem. Commun.*, 2012, **48**, 8407–8409.
13 M. Perfecto-Irigaray, G. Beobide, O. Castillo, I. da Silva, D. García-Lojo, A. Luque, A. Mendia and S. Pérez-Yáñez, *Chem. Commun.*, 2019, **55**, 5954–5957.
14 L. H. Xie, X. M. Liu, T. He and J. R. Li, *Chem*, 2018, **4**, 1911–1927.
15 (*a*) B. Wang, X. L. Lv, D. Feng, L. H. Xie, J. Zhang, M. Li, Y. Xie, J. R. Li and H. C. Zhou, *J. Am. Chem. Soc.*, 2016, **138**, 6204–6216; (*b*) T. F. Liu, N. A. Vermeulen, A. J. Howarth, P. Li, A. A. Sarjeant, J. T. Hupp and O. K. Farha, *Eur. J. Inorg. Chem.*, 2016, 4349–4352.
16 H. Furukawa, F. Gándara, Y.-B. Zhang, J. Jiang, W. L. Queen, M. R. Hudson and O. M. Yaghi, *J. Am. Chem. Soc.*, 2014, **136**, 4369–4381.
17 R. Wang, Z. Wang, Y. Xu, F. Dai, L. Zhang and D. Sun, *Inorg. Chem.*, 2014, **53**, 7086–7088.
18 W. Morris, B. Volosskiy, S. Demir, F. Gándara, P. L. McGrier, H. Furukawa, D. Cascio, J. F. Stoddart and O. M. Yaghi, *Inorg. Chem.*, 2012, **51**, 6443–6445.
19 D. Feng, Z. Y. Gu, Y. P. Chen, J. Park, Z. Wei, Y. Sun, M. Bosch, S. Yuan and H. C. Zhou, *J. Am. Chem. Soc.*, 2014, **136**, 17714–17717.
20 D. Feng, Z. Y. Gu, J. R. Li, H. L. Jiang, Z. Wei and H. C. Zhou, *Angew. Chem., Int. Ed.*, 2012, **51**, 10307–10310.
21 H. L. Jiang, D. Feng, K. Wang, Z. Y. Gu, Z. Wei, Y. P. Chen and H. C. Zhou, *J. Am. Chem. Soc.*, 2013, **135**, 13934–13938.
22 C. W. Kung, T. C. Wang, J. E. Mondloch, D. Fairen-Jimenez, D. M. Gardner, W. Bury, J. M. Klingsporn, J. C. Barnes, R. van Duyne, J. F. Stoddart, M. R. Wasielewski, O. K. Farha and J. T. Hupp, *Chem. Mater.*, 2013, **25**, 5012–5017.
23 S. Wang, H. G. T. Ly, M. Wahiduzzaman, C. Simms, I. Dovgaliuk, A. Tissot, G. Maurin, T. N. Parac-Vogt and C. Serre, *Nat. Commun.*, 2022, **13**, 1–8.
24 P. T. K. Nguyen, H. T. D. Nguyen, H. N. Nguyen, C. A. Trickett, Q. T. Ton, E. Gutiérrez-Puebla, M. A. Monge, K. E. Cordova and F. Gándara, *ACS Appl. Mater. Interfaces*, 2018, **10**, 733–744.
25 D. Feng, W. C. Chung, Z. Wei, Z. Y. Gu, H. L. Jiang, Y. P. Chen, D. J. Darensbourg and H. C. Zhou, *J. Am. Chem. Soc.*, 2013, **135**, 17105–17110.
26 (*a*) H. Wang, X. Dong, J. Lin, S. J. Teat, S. Jensen, J. Cure, E. V. Alexandrov, Q. Xia, K. Tan, Q. Wang, D. H. Olson, D. M. Proserpio, Y. J. Chabal, T. Thonhauser, J. Sun, Y. Han and J. Li, *Nat. Commun.*, 2018, **9**, 1–11; (*b*) Y. Zhang, X. Zhang, J. Lyu, K. I. Otake, X. Wang, L. R. Redfern, C. D. Malliakas, Z. Li, T. Islamoglu, B. Wang and O. K. Farha, *J. Am. Chem. Soc.*, 2018, **140**, 11179–11183.
27 M. Schulz, A. Gehl, J. Schlenkrich, H. A. Schulze, S. Zimmermann and A. Schaate, *Angew. Chem., Int. Ed.*, 2018, **57**, 12961–12965.
28 D. Alezi, I. Spanopoulos, C. Tsangarakis, A. Shkurenko, K. Adil, Y. Belmabkhout, M. O'Keeffe, M. Eddaoudi and P. N. Trikalitis, *J. Am. Chem. Soc.*, 2016, **138**, 12767–12770.
29 Z. Chen, P. Li, X. Wang, K. I. Otake, X. Zhang, L. Robison, A. Atilgan, T. Islamoglu, M. G. Hall, G. W. Peterson, J. F. Stoddart and O. K. Farha, *J. Am. Chem. Soc.*, 2019, **141**, 12229–12235.
30 Y. C. Qiu, S. Yuan, X. X. Li, D. Y. Du, C. Wang, J. S. Qin, H. F. Drake, Y. Q. Lan, L. Jiang and H. C. Zhou, *J. Am. Chem. Soc.*, 2019, **141**, 13841–13848.
31 V. A. Blatov, A. P. Shevchenko and D. M. Proserpio, *Cryst. Growth Des.*, 2014, **14**, 3576–3586.
32 M. O'Keeffe and O. M. Yaghi, *Chem. Rev.*, 2012, **112**, 675–702.
33 Z. Chen, H. Jiang, M. Li, M. O'Keeffe and M. Eddaoudi, *Chem. Rev.*, 2020, **120**, 8039–8065.
34 (*a*) M. J. Katz, J. E. Mondloch, R. K. Totten, J. K. Park, S. T. Nguyen, O. K. Farha and J. T. Hupp, *Angew. Chem., Int. Ed.*, 2014, **53**, 497–501; (*b*) E. Lõpez-Maya, C. Montoro, L. M. Rodríguez-Albelo, S. D. Aznar Cervantes, A. A. Lozano-Pérez, J. L. Cenís, E. Barea and J. A. R. Navarro, *Angew. Chem., Int. Ed.*, 2015, **54**, 6790–6794; (*c*) J. E. Mondloch, M. J. Katz, W. C. Isley, P. Ghosh, P. Liao, W. Bury, G. W. Wagner, M. G. Hall, J. B. Decoste, G. W. Peterson, R. Q. Snurr, C. J. Cramer, J. T. Hupp and O. K. Farha, *Nat. Mat.*, 2015, **14**, 512–516; (*d*) T. Islamoglu, Z. Chen, M. C. Wasson, C. T. Buru, K. O. Kirlikovali, U. Afrin, M. R. Mian and O. K. Farha, *Chem. Rev.*, 2020, **120**, 8130–8160; (*e*) L. González, R. Gil-San-Millán, J. A. R. Navarro, C. R. Maldonado, E. Barea and F. J. Carmona, *J. Mater. Chem. A*, 2022, **10**, 19606–19611; (*f*) R. Gil-San-Millan, E. López-Maya, A. E. Platero-Prats, V. Torres-Pérez, P. Delgado, A. W. Augustyniak, M. K. Kim, H. W. Lee, S. G. Ryu and J. A. R. Navarro, *J. Am. Chem. Soc.*, 2019, **141**, 11801–11805.

 This journal is © The Royal Society of Chemistry 2023

Chemical Science

ROYAL SOCIETY OF CHEMISTRY

EDGE ARTICLE

View Article Online
View Journal | View Issue

Check for updates

Cite this: *Chem. Sci.*, 2023, **14**, 12984

All publication charges for this article have been paid for by the Royal Society of Chemistry

Net-clipping as a top-down approach for the prediction of topologies of MOFs built from reduced-symmetry linkers†

Borja Ortín-Rubio, [ab] Jaume Rostoll-Berenguer,[c] Carlos Vila, [c] Davide M. Proserpio, [d] Vincent Guillerm, [e] Judith Juanhuix, [f] Inhar Imaz*[a] and Daniel Maspoch *[abg]

Received 22nd August 2023
Accepted 25th October 2023

DOI: 10.1039/d3sc04406h

rsc.li/chemical-science

Reticular materials constructed from regular molecular building blocks (MBBs) have been widely explored in the past three decades. Recently, there has been increasing interest in the assembly of novel, intricate materials using less-symmetric ligands; however, current methods for predicting structure are not amenable to this increased complexity. To address this gap, we propose herein a generalised version of the net-clipping approach for anticipating the topology of metal–organic frameworks (MOFs) assembled from organic linkers and different polygonal and polyhedral MBBs. It relies on the generation of less-symmetric nets with less-connected linkers, *via* the rational deconstruction of more-symmetric and more-connected linkers in edge-transitive nets. We applied our top-down strategy to edge-transitive nets containing 4-c tetrahedral, 6-c hexagonal, 8-c cubic or 12-c hexagonal prism linkers, envisaging the formation of 102 derived and 46 clipped nets. Among these, we report 33 new derived nets (*icn7*–*icn39*) and 6 new clipped nets (*icn1*–*icn6*). Importantly, the feasibility of using net-clipping to anticipate clipped nets is supported by literature examples and new experimental additions. Finally, we suggest and illustrate that net-clipping can be extended to less-regular, non-edge transitive nets as well as to covalent–organic frameworks (COFs), thus opening new avenues for the rational design of new reticular materials exhibiting unprecedented topologies.

Introduction

Reticular materials are crystalline, periodic networks assembled by strong bonds, which have been increasingly studied as a promising class of porous solids due to their high level of control, tunability and outstanding performance in many applications pertaining to energy, environment, biomedicine, *etc.*[1–3] The high scope of their properties relies on a wide catalogue of readily available molecular building blocks (MBBs), either organic or inorganic, that can contribute to the framework's features.[4,5] The simplification of each MBB into their basic geometry, connectivity and directionality features has allowed the rational classification of metal–organic frameworks (MOFs) and covalent–organic frameworks (COFs) into underlying nets with various topologies, and probably more importantly, the prediction of their structural features, offering various design opportunities for distinct programmed pores or channels.[6–9]

The growing interest in reticular chemistry demands new approaches for the rational design of materials with ever-greater complexity. Examples of these approaches include supermolecular building blocks (SBBs)[10,11] and layers (SBLs),[12–14] which relate nets with polyhedra (MOPs) or layers (2D MOFs), respectively; or the merged-nets approach, which relates different nets of compatible symmetry for the rational design of mixed-linker MOFs.[15] Indeed, over the past few years, structural complexity has been introduced by the desymmetrisation of simple organic linkers, by changing the direction of the binding carboxylic groups through geometric design in bent,[16] twisted[17] or zigzag fashion,[18,19] or through combinations thereof,[20]

[a]*Catalan Institute of Nanoscience and Nanotechnology (ICN2), CSIC and The Barcelona Institute of Science and Technology, Campus UAB, Bellaterra, 08193 Barcelona, Spain. E-mail: inhar.imaz@icn2.cat; daniel.maspoch@icn2.cat*

[b]*Departament de Química, Facultat de Ciències, Universitat Autònoma de Barcelona, 08193 Bellaterra, Spain*

[c]*Departament de Química Orgànica, Facultat de Química, Universitat de València, 46100 Burjassot, València, Spain*

[d]*Dipartamento di Chimica, Università degli Studi di Milano, Milano, 20133, Italy*

[e]*Division of Physical Sciences and Engineering, Advanced Membranes & Porous Materials Center (AMPM), Functional Materials Design, Discovery & Development Research Group (FMD3), King Abdullah University of Science and Technology (KAUST), Thuwal 23955-6900, Kingdom of Saudi Arabia*

[f]*ALBA Synchrotron, 08290 Cerdanyola del Vallès, Barcelona, Spain*

[g]*ICREA, Pg. Lluís Companys 23, 08010 Barcelona, Spain*

† Electronic supplementary information (ESI) available: The 39 new nets are deposited in the Topcryst database[26] as *icnx* (where ICN stands for "Institut Català de Nanociència i Nanotecnologia, and *x* the number of the net). CCDC 2270218–2270220. For ESI and crystallographic data in CIF or other electronic format see DOI: https://doi.org/10.1039/d3sc04406h

© 2023 The Author(s). Published by the Royal Society of Chemistry

yielding structures that differ from the default or expected nets. However, current methods for structural prediction in reticular chemistry are insufficient for desymmetrised MBBs: presently, there are no general approaches for non-standard parameters such as angles, torsions, width, *etc.*[21–24] Recently, our group reported *net-clipping*, the first top-down structural-prediction approach, which we used for the de-reticulation of edge-transitive nets assembled from 4-c square-like MBBs to deduce the topology of MOFs based on less-symmetric zigzag linkers.[19] This strategy, whose fundamentals are reversed from the design of the obtained merged nets, permits the prediction of MOF structures that break the basic principles of reticulation, thereby elucidating mismatch topologies and their construction.

Herein we propose to extend the net-clipping strategy to MOFs made of MBBs of higher symmetry and/or connectivity than 4-c square-like MBBs, as a method that rationalise and anticipate MOFs that could be built up with linkers that are less-

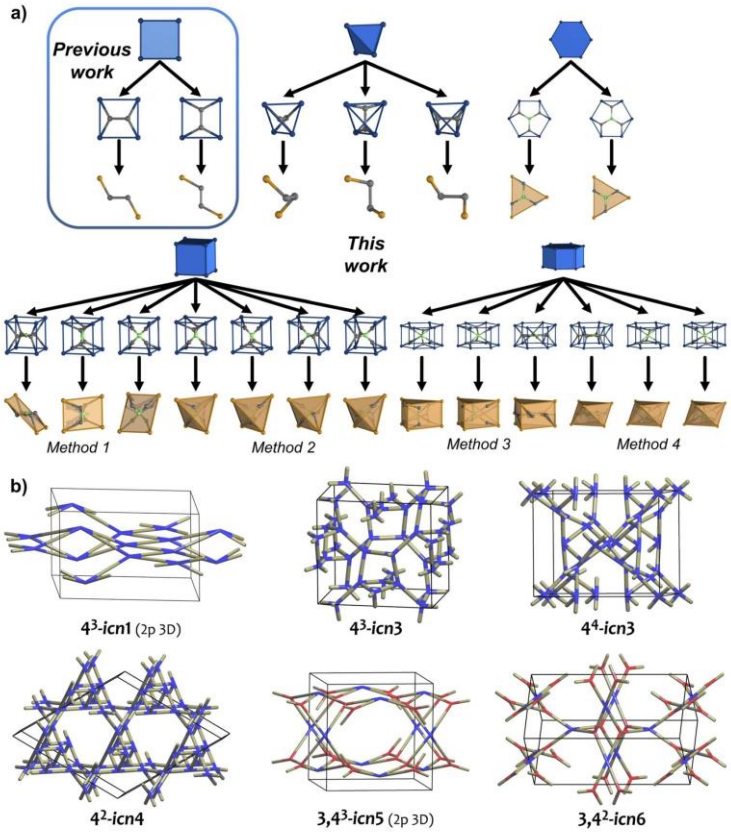


Fig. 1 (a) Schematic of the deconstruction of (from left to right): a 4-c square MBB into a zigzag MBB; a 4-c tetrahedral MBB into a turned-twisted MBB; a 6-c hexagonal MBB into a 3-c twisted triangular MBB; an 8-c cubic MBB into a 4-c square-like or a 4-c tetrahedral MBB; and a 12-c hexagonal prismatic MBB into a 6-c octahedral or a 6-c trigonal prismatic MBB. This approach comprises two steps: firstly, the splitting of each node into a set of less-symmetric nodes and edges; and secondly, the symmetric clipping of half of the original node's connectivity. (b) Representation of the 6 new clipped nets accessible for MOFs constructed with turned-twisted MBBs (*icn*1, *icn*2, *icn*3, *and icn*4), 3-c twisted triangular MBBs (*icn*5) and 4-c square-like MBBs (*icn*6). For clarity, here and in the tables, we report the coordination of the independent nodes before the *icn* symbol. The two nets *icn*1 and *icn*5 are 2-periodic 3D (thick layers).

© 2023 The Author(s). Published by the Royal Society of Chemistry

symmetric than the original MBBs. Accordingly, we have adapted the net-clipping strategy to nets assembled from 4-connected (4-c) tetrahedral, 6-c hexagonal, 8-c cubic and 12-c hexagonal prismatic organic MBBs. Through our analysis we have generated 102 derived and 46 clipped nets, of which 33 derived nets (named *icn*7–*icn*39) and 6 clipped nets (named

Table 1 Net-clipping of all the derived nets from 4-c tetrahedral nodes in the 16 selected edge-transitive nets[a]

MBB	Main topology	Derived net	Clipped net
	3,4-**bor**	3^2-**bod**	-
		3^2-**boe**	3^2T8[c]/3-**hcb**
	3,4-**ctn**	3^2-**ctn-d**	3-**srs**
		3^3-*icn*7[d]	
	4^2-**pts**	3,4-**tfk**	4^2-**pts**/4-**dia**/4-**sql**/ 4-**qbd**
		3,4-**sur**	4-**sql**/3-**hcb**/ 3,4-**bex**/2C1[c]
		3,4T224[c]	4-**dia**/2C1[c]
	4^2-**pth**	3,4-**phx**	4^2-sqc971[a]/4^2T215[c]/ 4^3-*icn*1[d]
		3,4-**phw** 3,4-*icn*8[d]	2C1
	4^2-**dia-b**	3,4-**tfa**	4^2-**pts**/4-**dia**/4-**sql**
		3,4-**tfv**	4-**dia**/4-**sql**
	4^2-**sod-b**	3,4-**xbl**	4-**afw**/4-**lcv**/ 4^3T4658-HZ[c]
		3,4T60[c]	4-**afw**
		3,4-sqc7390[a] 3^2,4T182[c]	-
	4^2-**lcs-b**	3,4-**lcr** = 3,4-*icn*9[e]	4-**afw**
		3,4-sqc7389[a] 3^2,4-*icn*10[d]	-
	4^2-**qtz-b**	3,4-**tfq**	4-**uog**/4-**qbd**
		3,4-**qza** 3,4-*icn*11[d]	4-**sql**
	4^2-**ana-b**	3,4-sqc12287[a]	4^2-**kea**/4-**unp**/ 4^3-*icn*2[d]/4^4-*icn*3[d]/ 4^2-*icn*4[d]
		3,4-sqc12294[a]	-
		3^2,4-*icn*12[d]	4-**lcv**
	4,6-**toc**	3,6-**xab**	-
		3,6-*icn*13[d]	6-**crs**
		3^2,6-*icn*14[d]	4^2-**pts**/4-**dia**/4-**sql**
		3^2,6-*icn*15[d]	-
	4,6-**gar**	**pto-d**-3,6-Ia-3d-1[b]	3-**srs**
		3,6-sqc12213[a]	6-**pcu**/3-**srs**
		$3,6^2$-*icn*16[d]	6-**pcu**
	4,6-**iac**	3,6-**act** **pto-d**-3,6-Ia-3d-2[b]	6-**pcu**
		3,6-*icn*17[d]	6-**pcu**/6-**crs**/6^2T26[c]
		3^2,6-*icn*18[d]	6-**pcu**/4-**dia**
		3^2,6-*icn*19[d]	4-**dia**
	4,6-**ibd**	3,6-**ibe**	6-**pcu**
		3,6-*icn*20[d]	6-**pcu**/3-**srs**
		$3,6^2$-*icn*21[d]	3-**srs**
		$3^3,6^2$-*icn*22[d]	6-**pcu**
	4,8-**flu**	3,8-**flt**	4^2-**pts**/4-**dia**/4-**sql**
		3,8-**jhw** 3,8-*icn*23[d]	4-**sql**
	4,12-**ith**	3,12-*icn*24[d]	4-**dia**
		3,12-*icn*25[d]	6-**pcu**/4-**dia**
	4,12-**twf**	3,24-**dni-d**	6-**pcu**
		3,24-*icn*26[d]	4-**dia**

[a] For the derived nets, letters indicate the following: [a]Systre nets in the Epinet database; [b]ToposPro binodal nets;[21] [c]ToposPro symbol for 3-periodic nets; and [d]new nets found using net-clipping approach. [e]*icn*9 is the same as **lcr**, a recent addition to RCSR not recognized by Systre.

© 2023 The Author(s). Published by the Royal Society of Chemistry

*icn*1–*icn*6) have never, to the best of our knowledge, previously been reported. The coordinates of all 39 nets are given in the ESI† as cif file (with the connectivity according to the latest Topocif dictionary)[25] and have been deposited in the personal.ttd database included in the TopCryst system.[26] Moreover, we experimentally validated our strategy by synthesising three of these less-symmetric linkers, which enabled us to assemble three new MOFs whose topologies match those predicted *via* net-clipping.

Results and discussion

Theoretical deduction: design strategy for net-clipping

Among the most extensively used organic MBBs to reticulate materials, we selected those which could be clipped symmetrically. Ideally, the clipping of a chosen node should produce a new node with half of the original connectivity, which could be rebuilt to the original node upon application of a C_2 operation. We found that linkers with tetrahedral, hexagonal, cubic, or hexagonal prismatic shapes matched this condition (Fig. 1a). Note that highly connected nodes with cubic or hexagonal prismatic directionality can be clipped into two different modes. In contrast, nodes with octahedral, trigonal prismatic, cuboctahedra, or icosahedral directionality cannot be clipped this way, given the absence of a C_2-symmetry axis. Interestingly, we found that these latter nodes present two triangular faces in the same direction, which frustrate the node-clipping and the absence of the C_2 operation (Fig. S1†).

In the present work, we analysed the 54 edge-transitive nets (with D-symbol size ≤ 32, and excluding those with collisions)[27] and selected those comprising nodes with connectivity 4, 6, 8, or 12 matching vertex figures of tetrahedra, hexagons, cubes or hexagonal prisms, respectively.[28] We then derived these nets by splitting their nodes to reduce the symmetry of the MBB (Fig. 1a; for the detailed procedure, see ESI†).[29] The symmetrical clipping of half of the connecting groups resulted in less-symmetric MBBs, transforming the new 3-c node into a new edge. This process led to the formation of 2-c turned-twisted linkers from 4-c tetrahedral MBB; 3-c twisted triangular linkers from 6-c hexagonal MBBs; 4-c square-like or tetrahedral linkers from 8-c cubic MBB; and 6-c triangular prismatic or octahedral linkers from 12-c hexagonal prismatic MBBs. This work enabled the discovery of 39 new topologies, providing a facile approach to study and understand the derived nets.[30]

Net-clipping of 4-c tetrahedra

We began by selecting the 17 edge-transitive nets assembled by the combination of 4-c tetrahedral MBBs with other polygonal and polyhedral MBBs. Among the six uninodal nets, five (**dia**, **sod**, **lcs**, **qtz**, **ana**) were considered to be in their binary form (**net-b**), to allow for selective splitting (Table 1). The sixth tetrahedral net, **lcv**, was excluded, due to the impossibility of generating a binodal net according to its connection circuits (Fig. S2†). The binary form of a net is a bipartite graphs, and bipartite graphs contain only even cycles, so nets with odd cycles (**lcv**, **hxl**) cannot be transformed in a binary form. We then derived these nets by splitting the 4-c nodes into two 3-c nodes with a 90° connection between them.[29] Note that, when embedded in a net, this split can be performed in three distinct orientations (Fig. 1a). When transposed into a MOF, this symmetry reduction process, followed by erasing of two opposite connecting groups, generated a new linker shape, which we

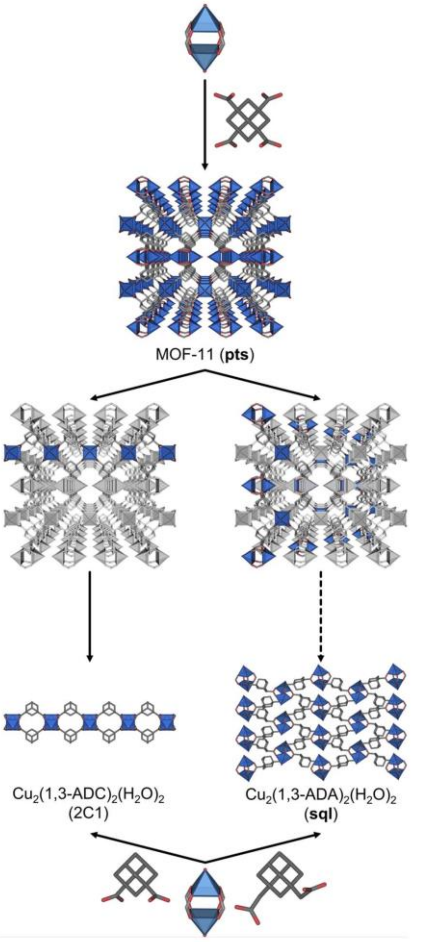


Fig. 2 Schematic of the net-clipping approach applied to the formation of metal–organic materials from tetrahedral 1,3,5,7-ATC linker to turned-twisted 1,3-ADC (left) or 1,3-ADA (right) linkers combined with 4-c paddlewheel Cu(II) MBBs.

© 2023 The Author(s). Published by the Royal Society of Chemistry

Table 2 Net-clipping of all the derived nets from 6-c hexagonal nodes in the 4 selected edge-transitive nets[a]

MBB	Main topology	Derived net	Clipped net
	3,6-**kgd**	3^3-**hcb-b3**	3^2-**hcb-b**
	4,6-**she**	3^2,4-**epn**	3,4-**pto**/3,4^3-*icn*5[a]
		3^2,4-**het**	3,4-**pto**
	6^2-**hxg-b**	3^2,6-**dne**	-
	6,12-**mgc**	3^2,12-*icn*27[a]	3,12-**ttt**

[a] For the derived nets, letters indicate the following: [a]new nets found using the net-clipping approach.

named turned-twisted, where the connecting groups are twisted in one axis and turned 90° in another axis (Fig. S3†).

Applying net-clipping to the various derived nets generated from the selected edge-transitive nets revealed the exhaustive list of possible combinations of this new set of nodes in different topologies, which can further be translated to organic linkers in reticular chemistry. Table 1 summarises the 49 resultant derived nets, of which we describe here, for the first time ever, 20 (named *icn*7–*icn*26).[32] Additionally, we identified 24 possible clipped nets that can be built with a turned-twisted linker, from which 4 are new nets (named as *icn*1–*icn*4) (Fig. 1b).[32] From this study, we found that clipping nets made of tetrahedral MBBs can produce 3D nets, 2D layers or 1D chains from the same parent net, due to the different splitting modes/orientation of the tetrahedra. For example, in the case of the **pts** net, the possible clipped nets are the 3D **pts** and **dia** topologies, the 2D **sql**, **hcb** and **bex** topologies, and the 1D **qbd** and the double-bridged linear topologies.

To corroborate our net-clipping approach, we identified a **pts** MOF, MOF-11, made by linking 4-c square-like Cu-based paddlewheels by tetrahedral 1,3,5,7-adamantane-tetracarboxylate (1,3,5,7-ATC) linkers (Fig. 2).[33] Remarkably, two of these seven anticipated nets have already been found experimentally. When clipped, the tetrahedral 1,3,5,7-ATC linker is converted into the turned-twisted 1,3-adamantane-dicarboxylate (1,3-ADC), which had already been combined with 4-c square-like Cu(II) paddlewheels by Zheng *et al.* to obtain the anticipated one-dimensional chain (here as double bridged). In a second example, the same authors similarly combined a closely related linker, 1,3-adamantane-diacetate (1,3-ADA), which incorporates a methylene group in each of the two carboxylic acid arms of 1,3-ADC.[34] Significantly, with this linker, they observed the formation of a **sql**-MOF, also corresponding to a net that we predicted by net-clipping a MOF made of 4-c square-like and tetrahedral MBBs.

Net-clipping of 6-c hexagons

There are five edge-transitive nets constructed with hexagons: the 2D **kgd** and **hxl** topologies; and the 3D **she**, **hxg-b** and **mgc** nets. Among these, we excluded the **hxl** topology, due to the unfeasibility to generate a binodal net due to the presence of odd cycles, as for the aforementioned tetrahedral **lcs** net (Fig. S4†). In the remaining four nets (**kgd**, **she**, **hxg-b**, and **mgc**), we derived the hexagon into a central triangle bound to three triangles (Table 2). Then, we erased half of their connections to generate a triangular polygon (Fig. 1a). Table 2 shows the 5 derived and 4 clipped nets resulting from applying the net-clipping approach to these nets made of 6-c hexagonal MBBs. Note that, for these types of nets, there is only a dimensional reduction from the predicted 3D derived **epn** net to the 2D (more precisely a 2-periodic 3D thick layer) clipped *icn*5 net. Among these derived/clipped nets, we also identified a new derived net from the parent **mgc** net, the *icn*27 net,[32] as well as a new clipped net from the parent **she** net, the aforementioned *icn*5 net (Fig. 1b).[32] Interestingly, the **hxg-b** net cannot be

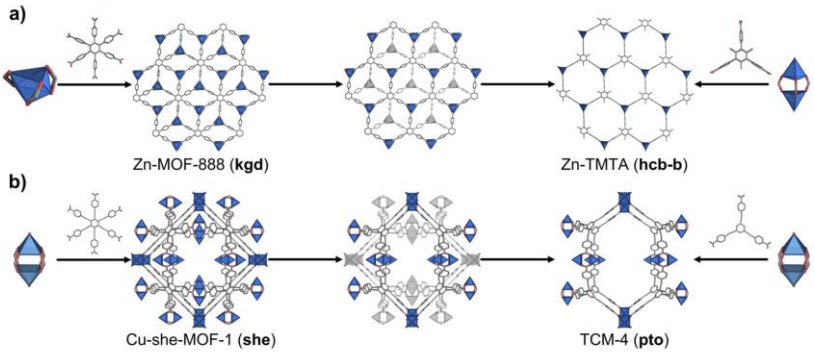


Fig. 3 Schematic of the net-clipping approach applied to formation of reticular materials from (a) hexagonal CPB linker to a trigonal TMTA linker combined with 3-c Zn(II) MBBs; and (b) from a hexagonal BHEB linker to a trigonal BTEB combined with 4-c paddlewheel Cu(II) MBBs.

 © 2023 The Author(s). Published by the Royal Society of Chemistry

clipped into another net without affecting the connectivity of the two 6-c nodes simultaneously.

Application of our net-clipping approach to hexagonal MBBs is strongly corroborated by the literature. For example, **kgd** Zn-MOF-888 (ref. 35) is made by connecting a 3-c Zn(II) metal through the hexagonal 1,2,3,4,5,6-hexakis(4-carboxyphenyl) benzene (CPB). This CPB linker is clipped into the corresponding trigonal 4,4′,4″-(2,4,6-trimethylbenzene-1,3,5-triyl) tribenzoate (TMTA) linker, which, when assembled with the 3-c Zn(II) cluster forms the **hcb-b** layer,[36] as predicted by our net-clipping approach (Fig. 3a). A second example is **she**-MOF-1,[37] which comprises 4-c Cu(II) paddlewheels joined by the extended hexagonal linker 1,2,3,4,5,6-benzene-hexaethynylbenzoate (BHEB) (Fig. 3b). According to net-clipping, combination of the 4-c Cu(II) paddlewheels with the corresponding clipped 1,3,5-benzene-trisethynylbenzoate (BTEB) should lead to the formation of a 3D **pto** MOF (Table 2). Remarkably, this prediction was verified upon the formation of **pto** TCM-4.[38] Moreover, this correlation was also observed for **she**-MOF-2,[37] made of the hexagonal hexatopic 1,2,3,4,5,6-hexakis(4-carboxybiphenyl) benzene (CBPB), and for MOF-388, containing the triazine functionalized 4,4′,4″-(triazine-2,4,6-triyl-tris(benzene-4,1-diyl))

Table 3 Net-clipping of all the derived nets from 8-c cubic nodes in the 7 selected edge-transitive nets[a]

MBB	Main topology	Derived net	Clipped net (Method)
	3,8-**the**	3^2,4-**ffj**	3,4-**bor (M1)** **- (M2)**
		3^2,4-**tfe**	3,4-**bor**/3,4^2-*icn6*[c] **(M1)** 3,4^2-*icn6*[c] **(M2)**
		3^2,4-**tfy**	3,4-**bor**/3^2,4^2T116[b]/ 3,4^2-**mmm (M1)** 3,4-**tbo**/3^2,4^2T116[b]/ 3,4^2-**mmm (M2)**
		3^2,4-*icn28*[c]	**- (M1)** 3,4-**tbo (M2)**
	4,8-**scu**	3,4^2-**ffc**	4^2-**pts (M1)** 4^2-**ssb**/4^2-**lvt-b (M2)**
		3,4^2-**eed** 3,4^2-**mmm** 3,4^2-**tbo-b** 3,4^2-**bor-b** 3,4^2-**epz**	4^2-**pts (M1)** 4^2-**sql-b (M2)**
	4,8-**sqc**	3,4^2-**iab** 3,4^2-**epf**	**- (M1 & M2)**
		3,4^2-**tfm**	4^2-**pts (M1)** **- (M2)**
	4,8-**csq**	3^2,4^2-**ffd** 3^2,4^2-*icn29*[c]	**- (M1 & M2)**
		3,4^2-*icn30*[c]	**- (M1)** 4^2-**sql-b (M2)**
		3,4^2-*icn31*[c] 3^2,4^2-*icn32*[c] 3^2,4^2-*icn33*[c] 3,4^2-**dnr**	**- (M1)** 4^2-**ssa (M2)**
	4,8-**flu**	3,4^2-**jaj** 3,4^2-**ofp** 3,4^2-**tfj**	4^2-**dia-b (M1)** 4^2-**pts (M2)**
		3,4^2-*icn34*[c] 3,4^2-*icn35*[c]	**- (M1)** 4^2-**pts (M2)**
	6,8-**ocu**	3,4,6-**pdp** 3,4,6-**twf-d**	4,6-**toc (M1)** **- (M2)**
		3^2,4^2,6-*icn36*[c]	4,6-**toc (M1)** 4^2,6T1[b] **(M2)**
		3,4,6-*icn37*[c] 3,4,6-*icn38*[c]	**- (M1)** 4^2,6T138[b] **(M2)**
	8^2-**bcu-b**	3,4,8-**dnq** 3,4,8-**eft** 3,4,8-*icn39*[c]	4,8-**flu (M1)** 4,8-**scu (M2)**
		3,4,8-sqc886[a]	**- (M1)** 4-**sql (M2)**

[a] For the derived nets, letters indicate the following: [a]Systre nets in the Epinet database; [b]ToposPro symbol for 3-periodic nets; [c]new nets found using the net-clipping approach; M1: Method 1; and M2: Method 2.

© 2023 The Author(s). Published by the Royal Society of Chemistry

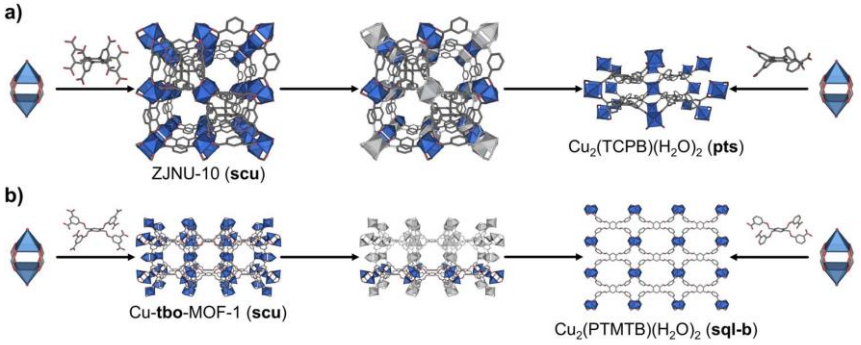


Fig. 4 Schematic of the net-clipping approach applied to formation of metal–organic materials from (a) a cubic DMTIB linker to a tetrahedral TCPB linker, combined with 4-c paddlewheel Cu(II) MBBs; and (b) from a cubic PTMTI linker to a square PTMTB linker, combined with 4-c paddlewheel Cu(II) MBBs.

tribenzoate (TAPB), which exhibits the anticipated underlying **pto** topology (Fig. S5†).[39]

Net-clipping of 8-c cubes

To expand our net-clipping approach to more highly-connected MBBs (connectivity ≥ 8), we began by analysing the 7 binodal edge-transitive nets made of 8-c cubic MBBs. We noticed that the cube presents two accessible clipping modes: one into a square, and one into a tetrahedron (Fig. 1a). According to Chen *et al.*,[40] a cubic node can be split into a tetrahedron surrounded by 4 triangles (Method 1), or into a square connected to 4 triangles (Method 2). As shown in Table 3, our use of these methods afforded 34 derived nets, 12 of which were unprecedented (*icn*28–*icn*39),[32] and 16 clipped nets. Among these latter nets, we discovered a new net topology, which we named *icn*6 (Fig. 1b).[32]

In comparison to MOFs built up from organic MBBs of lower connectivity, there are not many examples of MOFs that contain 8-c cubic organic MBBs in the literature. Gao *et al.* synthesised an **scu** MOF, ZJNU-10, that is constructed by connecting 4-c Cu(II) paddlewheels through the 8-c cubic 3,6-dimethyl-1,2,4,5-tetra(5′-isophthalate)benzene (DMTIB) linker (Fig. 4a).[41] The net-clipping of **scu** yields a 2D **sql-b** net, a 3D **ssb** net, or a 3D **lvt-b** net when the cube is clipped into a square; or a 3D **pts** net when the cube is clipped into a tetrahedron. Significantly, the same group reported a **pts** MOF by connecting 4-c Cu(II) paddlewheels with the 4-c 1,2,4,5-tetrakis(3-carboxyphenyl)-benzene (TCPB) linker. Interestingly, this latter 4-c linker can be seen as the clipped tetrahedron version of the 8-c linker (Fig. 4a and S6†).[42] Thus, the topology of the synthesised **pts** MOF cited matches perfectly with that predicted by our net-clipping approach.

Next, motivated by the paucity of literature examples of MOFs that supported our net-clipping of MOFs made of 8-c cubic MBBs, we synthesised a new 4-c linker, representing the clipped square-like version of an 8-c cubic linker used to make the Cu-**tbo**-MOF-1.[12] Cu-**tbo**-MOF-1 is made by linking 4-c Cu(II) paddlewheels to 8-c 5,5′,5″,5‴-[1,2,4,5-phenyltetramethoxy] tetraisophthalate (PTMTI) linkers. It exhibits the aforementioned **scu** underlying topology when this 8-c linker is considered as a single node, and the **tbo-b** (**tbo-b**3) underlying topology when the linker is simplified into more regular 3-c and 4-c nodes. Importantly, the MOF created with the corresponding clipped 4-c square-like linker generated one of the two expected nets: the **sql** 2D net (Table 3). This topology contrasts sharply to the 3D **pts** net that we had expected to see from having used the clipped tetrahedral linker. The desymmetrisation of these 8-c PTMTI linkers into a 4-c linker generated 3,3′,3′,3‴-[1,2,4,5-phenyltetramethoxy]tetrabenzoate (PTMTB). Once this linker had been prepared, it was reacted with copper(II)

Table 4 Net-clipping of all the derived nets (methods 3 and 4) from 12-c hexagonal prism nodes in the 7 selected edge-transitive nets[a]

MBB	Main topology	Derived net	Clipped net
	4,12-**shp**	3,4,6-**cee**	- **(M3 & M4)**
		3,4,6-**agw**	
		3,4,6-**cef**	
		3,4,6-**ceg**	4,6-**stp (M3)**
		3,4,6-**ceh**	- **(M4)**
		3,4,6-**cej**	
		3,4,6-**cez**	
	6,12-**alb**	3,6^2-**kew**	- **(M3)** 6^2-**nia (M4)**
		3,6^2-**cep**	
		3,6^2-**ceq**	6^2-**acs-b(M3)**
		3,6^2-**cer**	6^2-**nia (M4)**
		3,6^2-**cet**	
		3,6^2-**key**	6^2-**acs-b(M3)**
		3,6^2-**kez**	- **(M4)**

[a] M1: Method 1; and M2: Method 2.

© 2023 The Author(s). Published by the Royal Society of Chemistry

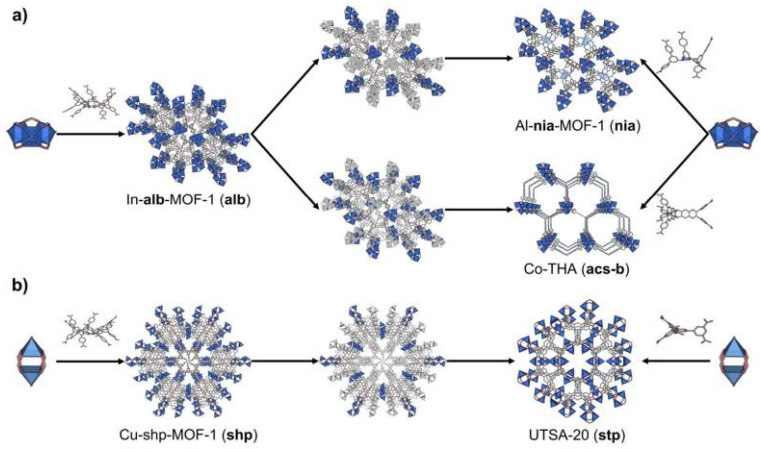


Fig. 5 Schematic of the net-clipping approach applied to formation of metal–organic materials from (a) a hexagonal prism BCPB linker clipped to an octahedral TTATTDC, and trigonal prism THA linkers combined with a 6-c trimer M(III) MBBs; and (b) a hexagonal prism BCPB linker clipped to a distorted trigonal prism BHB linker, combined with 4-c paddlewheel Cu(II) MBBs.

nitrate salt in the presence of DMF and HBF_4 under solvothermal conditions, to yield blue square-shaped crystals. SCXRD analysis of the crystal structure confirmed the formation of a MOF layer with the expected **sql-b** topology (Fig. 4b, right).[32]

Net-clipping of 12-c hexagonal prisms

Finally, we considered the highest connectivity from the selected polyhedra, the hexagonal prism, which is only found in two edge-transitive nets, the **shp** and **alb** topologies. As in the previous case, hexagonal prismatic MBBs also allow for two clipping modes: one into a 6-c trigonal prism (Method 3); and one into a 6-c octahedron (Method 4) (Fig. 1a). Following both methods, net-clipping of MOFs made of 12-c hexagonal prismatic MBBs generated 14 derived nets and 3 clipped nets (Table 4). Thus, in the **alb** net, clipping the 12-c hexagonal prism to a 6-c trigonal prism (Method 3) affords the binodal **acs-b** topology, whereas clipping it into an octahedron (Method 4) yields a **nia** net. On the other hand, the 12-c hexagonal prism of the **shp** net can only be clipped into a trigonal prism, which affords the **stp** net. Our prediction of these nets *via* net-clipping is reinforced by several MOFs reported in the literature. In-**alb**-MOF-1 is a 3D structure built up from the connection of 6-c In-trimer clusters through 12-c 1,2,3,4,5,6-hexakis[3,5-bis(4-carboxyl-phenyl) phenoxymethyl]benzene (BCPB) linkers (Fig. 5a).[43] As we had anticipated, net-clipping of **alb** topology induced the formation of two possible nets exhibiting the **acs-b** (Method 3) or **nia** (Method 4) topologies. Despite the lack of a reported MOF built by combining these clusters and the clipped version of H_{12}BCPB, we did find a closely related MOF, Al-**nia**-MOF-1, made of analogous 6-c Al-trimer clusters and the 6-c 5′,5′′′,5′′′′′-((1,3,5-triazine-2,4,6-triyl)tris(azanediyl))tris-(([1,1′:3,1′′-terphenyl]-4,4′′ dicarboxylate)) (TTATTDC) linker. This TTATTDC linker shows an octahedral shape similar to that which the clipped 6-c linker from H_{12}BCPB (Method 4) would exhibit. Importantly, Al-**nia**-MOF-1 showed the anticipated underlying **nia** topology (Fig. 5a, top).[44] Additionally, we found Co-THA, which is formed by linking analogous Co-trimer clusters with the 6-c triptycene-hexaacetate (THA) linker, which could be seen as the clipped trigonal prismatic version of a 12-c hexagonal prismatic MBB. In this case, the anticipated **acs-b** net had also been formed (Fig. 5a, bottom).[45] Regarding **shp** nets, Cu-**shp**-MOF-1 is a reported framework constructed by the connection of 4-c Cu(II) paddlewheels through 12-c BCPB linkers (Fig. 5b).[43] Despite the lack of reports on this MOF, made by combining Cu(II) paddlewheels with the clipped version of H_{12}BCPB, we again found an analogous one in the literature: in this case, UTSA-20,[46] in which 4-c Cu(II) paddlewheels are connected by 6-c 3,3′,3′′,5,5′,5′′-benzene-1,3,5-triyl-hexabenzoate (BHB) linkers, which is a clipped trigonal prismatic version of a 12-c hexagonal prismatic MBB. This MOF exhibits an underlying **stp** topology, thus matching with the anticipated topology of the clipped net from the main **shp** topology.

Net-clipping out of edge-transitive nets: the first proof of concept

In our attempts to assemble a MOF made of a 4-c tetrahedral MBB exhibiting an edge-transitive net, we created a 4^3T2 MOF with a formula of Cu_2(TMBPTC)$(H_2O)_2$ that is built up from connecting 4-c Cu(II) paddlewheels through 4-c tetrahedral 2,2′,6,6′-tetramethoxy-[1,1′-biphenyl]-3,3′,5,5′-tetracarboxylate

© 2023 The Author(s). Published by the Royal Society of Chemistry

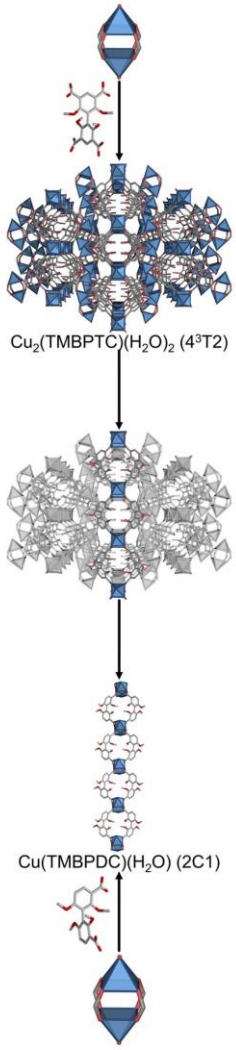


Fig. 6 Schematic of the net-clipping approach applied to formation of metal–organic materials from a tetrahedral TMBPTC linker to a turned-twisted TMBPDC (left) combined with 4-c paddlewheel Cu(II) MBBs.

(TMBPTC) linkers. This 4^3T2 topology,[32] which does not belong to an edge transitive net, is based on two squared nodes joined by a tetrahedral node in a [34] transitivity. In it, the tetrahedral nodes are distributed in a primitive cubic conformation that exhibits a slight shift between two pairs of cubic units (Fig. S17 and S18†). This shift results in a desymmetrisation of the square MBBs in two different positions produced by the desymmetrisation of the elongated tetrahedral MBB,[21,47–50] altering the circuits of connection and frustrating the formation of two 4-cycles seen in both **pts** and **pth** nets. Instead, a 4-cycle and a diamond-like 6-cycle are formed.

Inspired by the formation of the aforementioned 4^3T2 MOF, we decided to use this net to challenge our net-clipping approach to ascertain whether MOFs made of less-symmetric linkers could be anticipated from less regular nets. To this end, we applied the net-clipping strategy to the 4^3T2 net resulting in the prediction of two different clipped nets: the 2D **sql** and the 1D 2C1 topologies.

Next, we designed and synthesised the rigid 2,2′,6,6′-tetramethoxy-[1,1′-biphenyl]-3,3′-dicarboxylate (TMBPDC) linker, which is the clipped, turned-twisted version of the 4-c tetrahedral TMBPTC linker. In TMBPDC, the steric hindrance induced by the methoxy groups locks the linker conformation into a turned-twisted shape[48] that is twisted 90° relative to its reported homologous zigzag linker (Fig. S24†).[19] As we predicted, replacing the tetratopic TMBPTC ligand with the ditopic H_2TMBPDC let to the formation of the predicted metal–organic 1D 2C1 chain. Thus, reaction of copper(II) nitrate salt and H_2TMBPDC in the presence of DMF and H_2O under solvothermal conditions yielded green polyhedral crystals. SCXRD revealed the formation of a coordination polymer with formula Cu(TMBPDC)(H_2O), which crystallises in the $P2_1/c$ space group (Fig. 6). In this structure, two pairs of linkers connect to the same 4-c Cu paddlewheel by double bridging.[51]

Conclusions

In summary, we have generalised the use of net-clipping as a top-down approach to unveil the different topologies that should be accessible for MOFs assembled from organic linkers and different polyhedral MBBs. In our approach, these organic linkers are low-symmetry/connected linkers derived from clipping of higher symmetry/connection linkers in edge-transitive nets. We applied net-clipping to edge-transitive nets made of 4-c tetrahedral, 6-c hexagonal, 8-c cubic, and 12-c hexagonal prismatic linkers, anticipating the formation of 102 derived and 46 clipped nets. Among them, 33 new derived nets (*icn*7–*icn*39) and 6 new clipped nets (*icn*1–*icn*6) were not previously described. The discovery of all these nets underscores the potential of net-clipping for the discovery and rational design of MOFs exhibiting new underlying topologies. Moreover, we first demonstrated that the use of net-clipping can also be extended to less regular, non-edge transitive nets, a fact that will surely increase the discovery of available topologies in a near future. However, this process will require the study of thousands of complex topologies, representing an exciting challenge for

© 2023 The Author(s). Published by the Royal Society of Chemistry

simulation tools. Finally, we postulated that net-clipping could also be applied to covalent–organic frameworks (COFs), which we corroborated through a brief literature survey. The 2D **kgd** COF-360 is an imine-linked COF created by linking the 6-c hexagonal hexaformylphenyl benzene (HFPB) linker and the 3-c 1,3,5-tris(*p*-aminophenyl)benzene (TAPB) linker.[52] From our study, we expected the clipped net to exhibit an **hcb-b** topology, which is precisely what had been observed for TFPB-TAPB-COF,[53] a COF synthesised by imine-based linkage of TAPB and the 3-c 1,3,5-tris(4-formylphenyl)benzene (TFPB), the latter linker being the clipped version of HFPB (Fig. S25†). Thus, we are confident that net-clipping will continue to inform the design of future porous materials such as MOFs and COFs, by enabling the assembly of new, otherwise inaccessible topologies.

Data availability

Data available on request.

Author contributions

B. O.-R., I. I. and D. M. conceived the idea of the project. B. O.-R., J. R.-B. and C. V. designed, synthesized, and characterized the organic linkers. B. O.-R. designed, synthesized, and characterized the metal–organic materials, and performed the theoretical deduction. B. O.-R. and D. M. P. validated the topological analysis of the new nets. I. I. and J. J. performed the SCXRD analysis and solved the structures. B. O.-R., V. G., I. I. and D. M. wrote the manuscript. All authors contributed to the revision of the manuscript.

Conflicts of interest

There are no conflicts to declare.

Acknowledgements

This work has received funding from the European Union's Horizon 2020 research and innovation programme under grant agreement No. 101019003, Grants Ref. PID2021-124804NB-I00 and PID2021-123287OB-I00 funded by MCIN/AEI/10.13039/501100011033/and by "ERDF A way of making Europe", and the Catalan AGAUR (project 2021 SGR 00458). It was also funded by the CERCA program/Generalitat de Catalunya. ICN2 is supported by the Severo Ochoa Centres of Excellence programme, Grant CEX2021-001214-S, funded by MCIN/AEI/10.13039.501100011033. J. R.-B. thanks the Ministerio de Ciencia, Innovación y Universidades for a FPU predoctoral contract (FPU17/00688). C.V. thanks the RyC contract (RYC-2016-20187) funded by MCIN/AEI/10.13039/501100011033 and by "European Union NextGenerationEU/PRTR". D. M. P. thanks the MUR for the grant PRIN2020 "Nature Inspired Crystal Engineering (NICE)" and Prof. Vladislav A. Blatov at the Samara Center for Theoretical Materials Science for providing the free ToposPro software (**https://topospro.com**).[32]

Notes and references

1 M. J. Kalmutzki, N. Hanikel and O. M. Yaghi, *Sci. Adv.*, 2018, **4**, eaat9180.
2 N. W. Ockwig, O. Delgado-Friedrichs, M. O'Keeffe and O. M. Yaghi, *Acc. Chem. Res.*, 2005, **38**, 176–182.
3 O. M. Yaghi, *Mol. Front. J.*, 2019, **3**, 66–83.
4 A. Stein, S. W. Keller and T. E. Mallouk, *Science*, 1993, **259**, 1158–1164.
5 M. Eddaoudi, D. B. Moler, H. Li, B. Chen, T. M. Reineke, M. O'Keeffe and O. M. Yaghi, *Acc. Chem. Res.*, 2001, **34**, 319–330.
6 M. O'Keeffe, M. A. Peskov, S. J. Ramsden and O. M. Yaghi, *Acc. Chem. Res.*, 2008, **41**, 1782–1789.
7 M. O'Keeffe and O. M. Yaghi, *Chem. Rev.*, 2012, **112**, 675–702.
8 O. Delgado-Friedrichs, M. O'Keeffe and O. M. Yaghi, *Phys. Chem. Chem. Phys.*, 2007, **9**, 1035–1043.
9 F. A. Wells, *Three dimensional nets and polyhedra*, Wiley, New York, 1977.
10 F. Nouar, J. F. Eubank, T. Bousquet, L. Wojtas, M. J. Zaworotko and M. Eddaoudi, *J. Am. Chem. Soc.*, 2008, **130**, 1833–1835.
11 J. J. Perry IV, J. A. Perman and M. J. Zaworotko, *Chem. Soc. Rev.*, 2008, **38**, 1400–1417.
12 J. F. Eubank, H. Mouttaki, A. J. Cairns, Y. Belmabkhout, L. Wojtas, R. Luebke, M. Alkordi and M. Eddaoudi, *J. Am. Chem. Soc.*, 2011, **133**, 14204–14207.
13 J. F. Eubank, L. Wojtas, M. R. Hight, T. Bousquet, V. C. Kravtsov and M. Eddaoudi, *J. Am. Chem. Soc.*, 2011, **133**, 17532–17535.
14 B. Q. Ma, K. L. Mulfort and J. T. Hupp, *Inorg. Chem.*, 2005, **44**, 4912–4914.
15 H. Jiang, J. Jia, A. Shkurenko, Z. Chen, K. Adil, Y. Belmabkhout, L. J. Weselinski, A. H. Assen, D. X. Xue, M. O'Keeffe and M. Eddaoudi, *J. Am. Chem. Soc.*, 2018, **140**, 8858–8867.
16 M. Eddaoudi, J. Kim, D. Vodak, A. Sudik, J. Wachter, M. O'Keeffe and O. M. Yaghi, *Proc. Natl. Acad. Sci. U. S. A.*, 2002, **99**, 4900–4904.
17 M. Eddaoudi, J. Kim, M. O'Keeffe and O. M. Yaghi, *J. Am. Chem. Soc.*, 2002, **124**, 376–377.
18 V. Guillerm, T. Grancha, I. Imaz, J. Juanhuix and D. Maspoch, *J. Am. Chem. Soc.*, 2018, **140**, 10153–10157.
19 B. Ortín-Rubio, H. Ghasempour, V. Guillerm, A. Morsali, J. Juanhuix, I. Imaz and D. Maspoch, *J. Am. Chem. Soc.*, 2020, **142**, 9135–9140.
20 N. Alsadun, G. Mouchaham, V. Guillerm, J. Czaban-Jóźwiak, A. Shkurenko, H. Jiang, P. M. Bhatt, P. Parvatkar and M. Eddaoudi, *J. Am. Chem. Soc.*, 2020, **142**, 20547–20553.
21 J. K. Schnobrich, O. Lebel, K. A. Cychosz, A. Dailly, A. G. Wong-Foy and A. J. Matzger, *J. Am. Chem. Soc.*, 2010, **132**, 13941–13948.
22 V. Guillerm and D. Maspoch, *J. Am. Chem. Soc.*, 2019, **141**, 16517–16538.
23 F. Haase, G. A. Craig, M. Bonneau, K. Sugimoto and S. Furukawa, *J. Am. Chem. Soc.*, 2020, **142**, 13839–13845.

© 2023 The Author(s). Published by the Royal Society of Chemistry

24 H. Wang, X. Dong, J. Lin, S. J. Teat, S. Jensen, J. Cure, E. V. Alexandrov, Q. Xia, K. Tan, Q. Wang, D. H. Olson, D. M. Proserpio, Y. J. Chabal, T. Thonhauser, J. Sun, Y. Han and J. Li, *Nat. Commun.*, 2018, **9**, 1745.
25 **www.iucr.org/resources/cif/dictionaries/cif_topology**.
26 A. P. Shevchenko, A. A. Shabalin, I. Y. Karpukhin and V. A. Blatov, *Sci. Technol. Adv. Mater.: Methods*, 2022, **2**, 250–265. **https://topcryst.com/**.
27 M. Li, M. O'Keeffe, D. M. Proserpio and H. F. Zhang, *Cryst. Growth Des.*, 2020, **20**, 4062–4068.
28 O. Delgado-Friedrichs and M. O'Keeffe, *Acta Crystallogr., Sect. A: Found. Crystallogr.*, 2007, **63**, 344–347.
29 J. F. Eubank, R. D. Walsh, P. Poddar, H. Srikanth, R. W. Larsen and M. Eddaoudi, *Cryst. Growth Des.*, 2006, **6**, 1453–1457.
30 M. Li, D. Li, M. O'Keeffe and O. M. Yaghi, *Chem. Rev.*, 2014, **114**, 1343–1370.
31 V. A. Blatov and D. M. Proserpio, *Acta Crystallogr., Sect. A: Found. Crystallogr.*, 2009, **65**, 202–212.
32 V. A. Blatov, A. P. Shevchenko and D. M. Proserpio, *Cryst. Growth Des.*, 2014, **14**, 3576–3586.
33 B. Chen, M. Eddaoudi, T. M. Reineke, J. W. Kampf, M. O'Keeffe and O. M. Yaghi, *J. Am. Chem. Soc.*, 2000, **122**, 11559–11560.
34 Y. Z. Zheng, Z. Zheng, M. L. Tong and X. M. Chen, *Polyhedron*, 2013, **52**, 1159–1168.
35 F. M. Amombo Noa, E. Svensson Grape, S. M. Brülls, O. Cheung, P. Malmberg, A. K. Inge, C. J. Mckenzie, J. Mårtensson and L. Öhrström, *J. Am. Chem. Soc.*, 2020, **142**, 9471–9481.
36 X. Zhao, H. He, F. Dai, D. Sun and Y. Ke, *Inorg. Chem.*, 2010, **49**, 8650–8652.
37 D. A. Gómez-Gualdrón, Y. J. Colón, X. Zhang, T. C. Wang, Y. S. Chen, J. T. Hupp, T. Yildirim, O. K. Farha, J. Zhang and R. Q. Snurr, *Energy Environ. Sci.*, 2016, **9**, 3279–3289.
38 N. Zhu, M. J. Lennox, G. Tobin, L. Goodman, T. Düren and W. Schmitt, *Chem. – Eur. J.*, 2014, **20**, 3595–3599.
39 H. Furukawa, Y. B. Go, N. Ko, Y. K. Park, F. J. Uribe-Romo, J. Kim, M. O'Keeffe and O. M. Yaghi, *Inorg. Chem.*, 2011, **50**, 9147–9152.
40 Z. Chen, H. Jiang, M. Li, M. O'Keeffe and M. Eddaoudi, *Chem. Rev.*, 2020, **120**, 8039–8065.
41 X. Gao, T. Xu, Z. Jiang, H. Yu, Y. Wang and Y. He, *Dalton Trans.*, 2019, **48**, 16793–16799.
42 D. Yan, B. Chen and Q. Duan, *Inorg. Chem. Commun.*, 2014, **49**, 34–36.
43 Z. Chen, Ł. J. Weseliński, K. Adil, Y. Belmabkhout, A. Shkurenko, H. Jiang, P. M. Bhatt, V. Guillerm, E. Dauzon, D. X. Xue, M. O'Keeffe and M. Eddaoudi, *J. Am. Chem. Soc.*, 2017, **139**, 3265–3274.
44 D. Alezi, J. Jia, P. M. Bhatt, A. Shkurenko, V. Solovyeva, Z. Chen, Y. Belmabkhout and M. Eddaoudi, *Inorg. Chem.*, 2022, **61**, 10661–10666.
45 P. Chandrasekhar, G. Savitha and J. N. Moorthy, *Chem. – Eur. J.*, 2017, **23**, 7297–7305.
46 Z. Guo, H. Wu, G. Srinivas, Y. Zhou, S. Xiang, Z. Chen, Y. Yang, W. Zhou, M. O'Keeffe and B. Chen, *Angew. Chem., Int. Ed.*, 2011, **123**, 3236–3239.
47 A. G. Wong-Foy, O. Lebel and A. J. Matzger, *J. Am. Chem. Soc.*, 2007, **129**, 15740–15741.
48 J. Pang, S. Yuan, J. Qin, C. Liu, C. Lollar, M. Wu, D. Yuan, H. C. Zhou and M. Hong, *J. Am. Chem. Soc.*, 2017, **139**, 16939–16945.
49 X. L. Lv, L. Feng, L. H. Xie, T. He, W. Wu, K. Y. Wang, G. Si, B. Wang, J. R. Li and H. C. Zhou, *J. Am. Chem. Soc.*, 2021, **143**, 2784–2791.
50 J. Ma, L. D. Tran and A. J. Matzger, *Cryst. Growth Des.*, 2016, **16**, 4148–4153.
51 H. Furukawa, J. Kim, N. W. Ockwig, M. O'Keeffe and O. M. Yaghi, *J. Am. Chem. Soc.*, 2008, **130**, 11650–11661.
52 B. Zhang, H. Mao, R. Matheu, J. A. Reimer, S. A. Alshmimri, S. Alshihri and O. M. Yaghi, *J. Am. Chem. Soc.*, 2019, **141**, 11420–11424.
53 L. Zhai, N. Huang, H. Xu, Q. Chen and D. Jiang, *Chem. Commun.*, 2017, **53**, 4242–4245.

© 2023 The Author(s). Published by the Royal Society of Chemistry

Materials Today Chemistry 22 (2021) 100548

Contents lists available at ScienceDirect

Materials Today Chemistry

journal homepage: www.journals.elsevier.com/materials-today-chemistry/

Engineering covalent organic frameworks in the modulation of photocatalytic degradation of pollutants under visible light conditions

A. Jiménez-Almarza [a], A. López-Magano [a], R. Cano [a], B. Ortín-Rubio [b], D. Díaz-García [c], S. Gomez-Ruiz [c], I. Imaz [b], D. Maspoch [b, d], R. Mas-Ballesté [a, e, *], J. Alemán [e, f, **]

[a] Department of Inorganic Chemistry (Module 7), Facultad de Ciencias, Universidad Autónoma de Madrid, Madrid, 28049, Spain
[b] Catalan Institute of Nanoscience and Nanotechnology (ICN2), CSIC and The Barcelona Institute of Science and Technology, Barcelona, 08193, Spain
[c] COMET-NANO Group, Departamento de Biología y Geología, Física y Química Inorgánica, E.S.C.E.T., Universidad Rey Juan Carlos, Calle Tulipán s/n, Móstoles, Madrid, E-28933, Spain
[d] Institució Catalana de Recerca i Estudis Avançats (ICREA), Pg. Lluís Companys 23, Barcelona, 08010, Spain
[e] Institute for Advanced Research in Chemical Sciences (IAdChem), Universidad Autónoma de Madrid, Madrid, 28049, Spain
[f] Department of Organic Chemistry (Module 1), Facultad de Ciencias, Universidad Autónoma de Madrid, Madrid, 28049, Spain

ARTICLE INFO

Article history:
Received 20 May 2021
Received in revised form
13 July 2021
Accepted 1 August 2021
Available online 3 September 2021

Keywords:
Organic porous materials
Photocatalysis
Photodegradation
Organic contaminants

ABSTRACT

Mixtures of triphenylamine (TPA) and phenyl phenothiazine (PTH) fragments have been incorporated into a series of extended polyimine structures that have been applied in the photodegradation of pollutants of different nature under visible light irradiation. Results obtained revealed that materials containing PTH as the sole photoactive unit resulted in the most active photocatalytic material in the degradation of polybrominated diphenyl ether-1 and Sudan Red III. In contrast, the covalent organic framework containing only TPA acted as the best photocatalyst for the degradation of Methylene Blue. These different trends are related to the versatility of PTH moiety to trigger both photoredox and energy transfer processes, while TPA is only an effective energy transfer catalyst.

© 2021 Elsevier Ltd. All rights reserved.

1. Introduction

Photocatalysis is a highly promising tool for environmental clean-up and organic synthesis that can result in accelerating photo-activated reactions [1]. Although the photocatalytic scenario is very complex, the two main photocatalytic pathways are energy transfer processes [2] and photoredox reactions [3]. Therefore, to be successful in a photochemical reaction or the photodegradation of a pollutant, the selection of a photocatalyst able to proceed through an energy transfer or a photoredox pathway is very important. For these reasons, there is a panoply of homogeneous systems based on metal complexes [4] and several organic dyes [5,6], which are able to perform a wide range of photocatalytic transformations. This variety offers the tool to point towards specific photocatalytic activities under visible-light irradiation.

The difficult recovery of homogenous catalysts [7,8] makes heterogeneous systems very desirable because they allow easy separation of the catalyst, as well as its recyclability [9]. In addition, the design of materials through a combination of suitable building blocks paves the opportunity to tune and direct photocatalytic activity in a manner that is unprecedented for homogeneous catalysis. One strategy that has been used in the last years is the incorporation of photocatalytic units, normally used in homogeneous catalysis, into porous materials. In particular, reticular materials such as metal-organic frameworks and covalent organic frameworks (COFs) offer many possibilities for their use in photocatalysis [10,11]. As a consequence, photocatalytic applications of reticular materials have been reported in the areas of organic chemical synthesis, degradation of pollutants, CO_2 reduction, and water splitting among others [12,13].

In recent years, COFs have attracted much attention [14,15]. This emerging family of porous materials are stable laminar or 3D reticular polymeric structures, similar to metal-organic frameworks, but only composed of organic linkers connected through

* Corresponding author.
** Corresponding author.
E-mail addresses: ruben.mas@uam.es (R. Mas-Ballesté), jose.aleman@uam.es (J. Alemán).
URL: https://www.uam.es/jose.aleman

https://doi.org/10.1016/j.mtchem.2021.100548
2468-5194/© 2021 Elsevier Ltd. All rights reserved.

covalent bonds. Thus, they are constituted by earth-abundant elements and show low toxicity, low density and adjustable pore size, chemical structure, and functionality. Consequently, applications of COFs have been reported in myriad fields, such as storage and separation of gases [16], energy storage [17], drug delivery [18], proton conduction [19], optoelectronics [17] and catalysis [20,21]. In the field of catalysis, COFs and their amorphous analogs have also been shown to be promising candidates as photocatalysts [22–29], which performances have been enhanced by incorporating predesigned photocatalytic units into the framework, such as benzothiadiazole [30], benzodifuran [31], rose Bengal [32], benzobisthiadiazole [33], thioxanthone [34], platinum complex [35], benzooxadiazole [36], BODIPY [37], and azulene [38].

The versatility of COF materials offers an optimal platform to be applied in the degradation of organic pollutants of different nature [28]. A particular case of persistent organic pollutants are polybrominated diphenyl ethers (PBDEs), generally used as flame retardants. Tetra-, penta-, hexa- and hepta-bromo diphenyl ethers are commonly considered persistent organic pollutants [39] and evolve generating less brominated derivatives, which are even more toxic and bioaccumulative than the original congeners [40,41]. For this reason, mono-brominated PBDE-1 is widely used as a model substrate to study the photoreduction of polybrominated pollutants that results in hydrodebrominated final products [42]. Synthetic dyes are another class of polluting chemical species commonly used in textile, food or cosmetic industries [43]. Among them, azo dyes are one of the most detrimental classes of pollutants because they are highly persistent in the aquatic environment [44]. Sudan dyes, such as Sudan Red III, are common red-colored azo dyes used in cosmetics [45,46]. Furthermore, ionic heterocyclic aromatic dyes, such as Methylene Blue, are a harmful class of pollutants, coming from the manufacture of products related to inkjet printing, photography and xerography, as well as cellulosic and textile industries [47,48].

The use of different materials attending their preferred catalytic pathways is usually required to achieve the degradation of specific pollutants. Therefore, there is a need for strategies to systematically tune, direct, and modulate the photocatalytic activity of predesigned materials. In this work, we targeted this challenge by designing a series of extended polyimine COFs with different combinations of two photoactive units (Fig. 1). We selected triphenylamine (TPA) and phenyl phenothiazine (PTH) as photoactive units because they show distinct optical and redox properties. Therefore, they can act as photocatalysts capable of degrading pollutants *via* different pathways [49,50]. In addition, they work as typical trigonal building blocks to construct COFs *via* the introduction of aldehyde groups at *para* positions of each phenyl ring. After this strategy, a series of five 2D COFs **4a-e** with **hcb** (honeycomb) topology and built-up from different proportions of TPA and PTH was synthesized by reacting triarylaldehydes **TFPA** (containing TPA as a photoactive unit) and/or **3** (containing PTH as a photoactive unit) with 1,3,5-tris(4-aminophenyl)benzene) (Scheme 2). We anticipate that the photocatalytic activity of the resulting COFs, which was essayed for the degradation of three different model pollutants (PBDE-1, Sudan Red III and Methylene Blue) under visible-light conditions, can be modulated by enriching the polyimine structure with one or another photoactive unit (Fig. 1).

2. Experimental

2.1. Synthesis of building block 3

2.1.1. 10-Phenyl-10H-phenothiazine, 1

[51] A solution of the corresponding phenothiazine (1.99 g, 10 mmol) and aryl bromide (1 mL, 11 mmol) in toluene (10 mL) was added to an oven-dried sealed tube equipped with a magnetic stir bar, followed by addition of $Pd_2(dba)_3$ (275 mg, 0.3 mmol), $[(^tBu)_3PH]BF_4$ (145 mg, 0.5 mmol) and NaO^tBu (1.11 g, 11.5 mmol). The reaction was refluxed for 48 h under an inert atmosphere and monitored by thin-layer chromatography (TLC) (phosphomolybdic acid stain solution). Then, the mixture was cooled to room temperature, diluted with DCM (20 mL), and filtered through a plug of celite. The filter cake was washed with DCM (2 × 10 mL), and the filtrate was concentrated under reduced pressure. The resulting crude mixture was purified by flash column chromatography (*c*-Hex) to provide **1** (78% yield). ^{1}H NMR (300 MHz, $CDCl_3$) δ 7.62 (t, J = 7.7 Hz, 2H), 7.52–7.50 (m, 1H), 7.42 (dd, J = 8.3, 1.1 Hz, 2H), 7.05 (dd, J = 6.7, 2.4 Hz, 2H), 6.87–6.83 (m, 4H), 6.23 (dd, J = 7.6, 1.6 Hz, 2H) ppm. ^{13}C NMR (75 MHz, $CDCl_3$) δ 144.4, 141.1, 130.9, 130.8, 128.3, 126.9, 126.8, 122.6, 120.3, 116.2 ppm.

2.1.2. 3,7-Dibromo-10-(4-bromophenyl)-10H-phenothiazine, 2

A solution of *N*-bromo-succinimide (3.11 g, 1.75 mmol) in THF (40 mL) was added dropwise to a round flask equipped with a

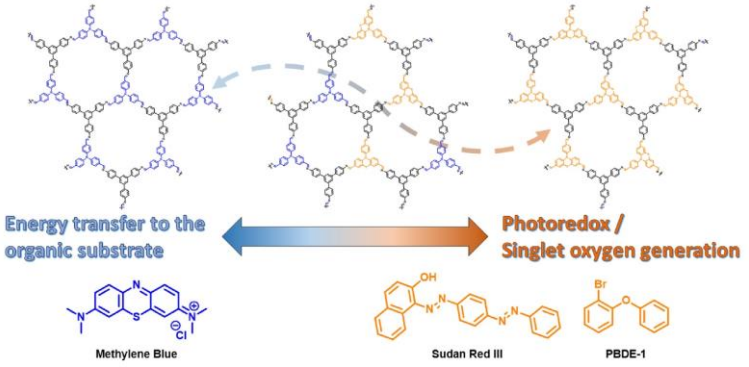


Fig. 1. Conceptual idea of this work, modulating the COF isostructural material in photocatalysis. COF, covalent organic framework.

magnetic stir bar and a solution of **1** (1.38 g, 0.5 mmol) in THF (10 mL). The reaction was stirred in an ice bath for 3 h and monitored by TLC. Then, NaOH 3 M (20 mL) was added to the reaction mixture, and it was extracted with 3 × 20 mL of AcOEt. The organic phase was separated, dried by $MgSO_4$, filtrated, and evaporated under reduced pressure. The resulting crude mixture was purified by flash column chromatography (*c*-Hex/AcOEt = 99:1 vol/vol) to provide **2** (60% yield). ^{1}H NMR (300 MHz, $CDCl_3$) δ 7.74 (d, J = 8.7 Hz, 2H), 7.23 (d, J = 8.7 Hz, 2H) 7.12 (d, J = 2.3 Hz, 2H), 6.94 (dd, J = 8.8, 2.3 Hz, 2H), 6.02 (d, J = 8.8 Hz, 2H) ppm. ^{13}C NMR (75 MHz, $CDCl_3$) δ 142.9, 139.5, 134.6, 132.3, 130.0, 129.2, 122.8, 122.0, 117.4, 115.3 ppm.

2.1.3. 10-(4-Formylphenyl)-10H-phenothiazine-3,7-dicarbaldehyde, building block 3

A solution of **2** (450 mg, 0.90 mmol) in dry THF (12 mL) was stirred in a round flask with a magnetic stir bar under an inert atmosphere. Keeping the inert atmosphere at −78 °C, *n*-BuLi 1.6 M (2.2 mL) was added dropwise to the reaction mixture for 1 h. After that, still, at −78 °C, dry DMF (0.27 mL) was added, and the reaction was stirred for 3 h. Finally, HCl 1.2 M (6 mL) was added to quench the reaction mixture at 0 °C, and it was stirred for 30 min. The reaction mixture was extracted with 5 × 20 mL of DCM. The organic phase was separated, dried by $MgSO_4$, filtrated, and evaporated under reduced pressure. The resulting crude mixture was purified by flash column chromatography (*c*-Hex/AcOEt = 99:1 vol/vol) to provide **3** (96% yield). Orange solid. ^{1}H NMR (300 MHz, $CDCl_3$) δ 10.17 (s, 1H), 9.75 (s, 2H) 8.22 (d, J = 8.1 Hz, 2H), 7.60 (d, J = 7.9 Hz, 2H), 7.51 (s, 2H), 7.33 (dd, J = 8.5, 1.8 Hz, 2H), 6.17 (d, J = 8.5 Hz, 2H) ppm. ^{13}C NMR (75 MHz, $CDCl_3$) δ 190.6, 189.5, 146.8, 144.7, 136.8, 132.7, 132.4, 131.3, 129.9, 127.7, 120.6, 116.1 ppm.

2.1.4. Synthesis of materials 4a-e

A solvothermal reactor was charged with 1,3,5-tris(4-aminophenyl)benzene (50.0 mg, 0.14 mmol), and different proportions of the synthesized building block **3** or/and tris(4-formylphenyl)amine (**TFPA**), 0.6 mL of anhydrous dioxane, 5.4 mL of mesitylene and 0.6 mL of 6 M acetic acid in water. The reactor was heated at 120 °C for 72 h, yielding a solid, which was isolated by filtration and washed with DMF, MeOH, and THF. The resulting powder was immersed in anhydrous THF for 24 h and dried first at room temperature under vacuum for 12 h, and then at 100 °C for 2 h to afford an orange-yellow powder. For the characterization, see Supporting Information.

2.1.5. General procedure for the photodegradation of PBDE-1

An oven-dried 10 mL vial equipped with a magnetic stir bar was charged with photocatalyst COF **4a-e** (1 mg) and PBDE-1 (8.3 mg, 0.033 mmol). Then, acetonitrile (1 mL) and *N,N-diisopropylethylamine* (DIPEA) (14.2 μL, 0.08 mmol) were added. The vial was closed with a rubber septum and the reaction mixture was degassed by three cycles of vacuum/argon of 'freeze-pump-thaw'. The vial was placed on the blue light LED photoreactor (420 nm) and the reaction mixture was stirred at 25 °C. The reaction was checked by ^{1}H NMR after 24 h. The crude was filtered through a membrane filter and purified by flash chromatography.

2.1.6. Leaching test

An oven-dried 10 mL vial equipped with a magnetic stir bar was charged with photocatalyst **4e** (1 mg) and PBDE-1 (8.3 mg, 0.033 mmol). Then, acetonitrile (1 mL) and DIPEA (14.2 μL, 0.08 mmol) were added. The vial was closed with a rubber septum, and the reaction mixture was degassed by three cycles of vacuum/argon of 'freeze-pump-thaw. Then the vial was placed on the blue light LED photoreactor (420 nm), and the reaction mixture was stirred at 25 °C for 24 h. The conversion was determined by an ^{1}H NMR analysis of the crude mixture. Then, the vial was opened, and the crude mixture was filtered through a membrane filter. PBDE-1 (8.3 mg, 0.033 mmol) and DIPEA (14.2 μL, 0.08 mmol) were added again for the next run without photocatalyst COF. The previous conversion was determined by an ^{1}H NMR analysis of the crude mixture. The vial was closed, and the reaction mixture was degassed following the same procedure as before. After 24 h, the conversion of the crude mixture was determined by ^{1}H NMR analysis, and it was shown that there was no photodegradation (see Supporting Information).

2.1.7. Recyclability test

An oven-dried 10 mL vial equipped with a magnetic stir bar was charged with photocatalyst **4e** (1 mg) and PBDE-1 (8.3 mg, 0.033 mmol). Then, acetonitrile (1 mL) and DIPEA (14.2 μL, 0.08 mmol) were added. The vial was closed with a rubber septum, and the reaction mixture was degassed by three cycles of vacuum/argon of 'freeze-pump-thaw'. Then the vial was placed on the blue light LED photoreactor (420 nm) and the reaction mixture was stirred at 25 °C for 24 h. The conversion was determined by an ^{1}H NMR analysis of the crude mixture. Then, the vial was opened and PBDE-1 (8.3 mg, 0.033 mmol) and DIPEA (14.2 μL, 0.08 mmol) were added again for the next run. After that, the vial was closed, and the reaction mixture was degassed following the same procedure as before. Seven consecutive cycles have been carried out.

2.1.8. General procedure for the photodegradation of Sudan Red III

A 30 mL screw vial equipped with a magnetic stir bar was charged with photocatalyst COF **4a-e** (2 mg) and the dye Sudan Red III (1.25×10^{-2} mM) in toluene (10 mL). Then, the mixture was sonicated to disperse the COF. The closed vial was placed under the blue spotlight, and the reaction mixture was stirred at room temperature. The photodegradation was determined by UV−Vis spectrophotometer after 34 h.

2.1.9. General procedure for the photodegradation of Methylene Blue

A 30 mL screw vial equipped with a magnetic stir bar was charged with photocatalyst COF **4a-e** (2 mg) and the dye Methylene Blue (2.25×10^{-2} mM) in acetonitrile (20 mL). Then, the mixture was sonicated to disperse the COF. The closed vial was placed under the blue spotlight, and the reaction mixture was stirred at room temperature. The photodegradation was determined by UV−Vis spectrophotometer after 4 h.

2.1.10. Mechanistic experiments

A 30 mL screw vial equipped with a magnetic stir bar was charged with photocatalyst **4e** (2 mg) and the dye Sudan Red III (1.25×10^{-2} mM) in toluene (10 mL) or with photocatalyst COF **4a** (2 mg) and the dye Methylene Blue (2.25×10^{-2} mM) in acetonitrile (20 mL). DABCO or benzoquinone was added (5 equiv.) to the reaction mixture. Then, the mixture was sonicated to disperse the COF. Another vial was closed with a rubber septum and the reaction mixture was degassed by three cycles of vacuum/argon of 'freeze-pump-thaw'. Then, all closed vials were placed under the blue spotlight. The reaction mixture was stirred at room temperature. The photodegradation was determined by UV−Vis spectrophotometer after 20 h for Sudan Red III and after 3 h in the case of Methylene Blue.

3. Results and discussion

3.1. Synthesis and characterization

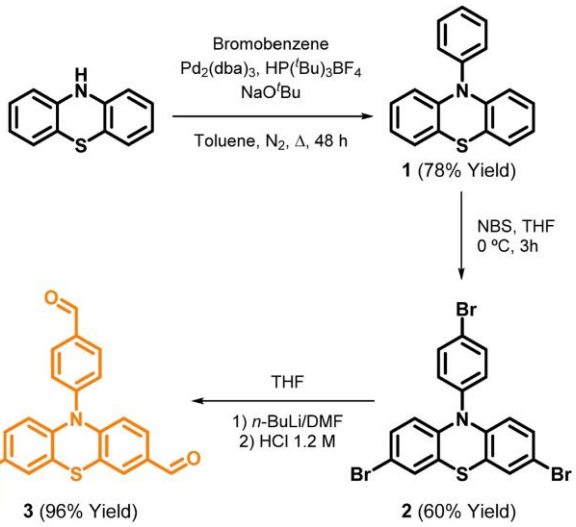
The synthetic strategy followed in this work is presented in Scheme 2. We initially started with the synthesis of a new building block, 10-(4-formylphenyl)-10*H*-phenothiazine-3,7-dicarbaldehyde (**3**), containing the PTH unit. This unit is a known homogeneous photocatalyst with excellent redox properties (oxidation potential at the excited state: −2.1 V *vs* SCE) [52], and it is able to catalyze different photochemical processes, such as hydrodehalogenation [52], halogenation [53], oxidative coupling of primary amines [54] and photopolymerization processes [55]. Building block **3** was synthesized in three steps (Scheme 1), starting from phenothiazine and aryl bromide.

Then, the resulting intermediate was brominated with *N*-bromo-succinimide. Finally, **3** was generated by the reaction of brominated intermediate in the presence of *n*-butyllithium 1.6 M with dry DMF at −78 °C, followed by treatment with HCl 1.2 M at 0 °C. Thus, **3** was obtained as an orange solid after flash-column chromatography purification.

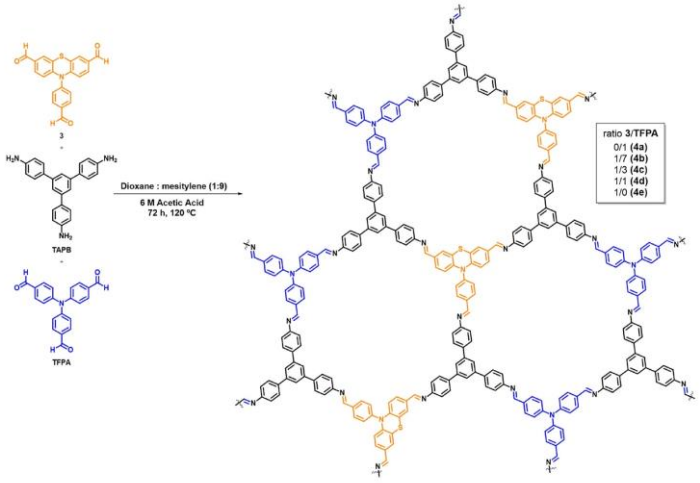
We then synthesized the five materials **4a-e** by solvothermal reaction of mixtures of variable relative amounts of **3** and tris(4-formylphenyl)amine (**TFPA**) with the trianiline precursor **TAPB** (Scheme 2). The feasibility of this design lays in the fact that both building blocks (**3** and **TFPA**) impose very similar geometric constraints, being possible to substitute one by the other without major distortion of the laminar COF structure. In this series, we synthesized COF **4a** using only **TFPA** [56,57] and material **4e** using **3**, to compare the photocatalytic activity of TPA and PTH units embedded into the polyimine frameworks. In addition, we isolated three more mixed-photoactive-linker COFs **4b-d** containing mixtures of **3** and **TFPA** (ratio TPA/PTH: 7, 3 and 1, see Table 1).

The formation and quality of synthesized materials **4a-e** were studied by powder X-ray diffraction (PXRD; Fig. 2) and Brunauer-Emmett-Teller surface area (S_{BET}) measured by N_2 sorption analysis performed at 77 K (Fig. 3). PXRD of COFs **4a-d** showed similar patterns indicating that comparable structures can be proposed for all of them. Using the *Materials Studio 8.0* program, we compared these experimental PXRD data with the pattern simulated from the model structure of **4a** proposed by Jiang *et al.* [56] and Verduzco *et al.* [57]. Based on this structure, we applied a geometrical energy minimization using the universal force field. The unit cell parameters found for the eclipsed structure was $a = 23.47$ Å, $b = 23.47$ Å, and $c = 3.89$ Å in a *P3* (nº 143) symmetry group. However, applying this model structure did not fit well with all our experimental PXRD peaks [56]. The major disagreement consisted of an additional strong peak at 5.5°. To this respect, Lukose *et al.* [58] proposed in different COFs that inclined stacking of the layers can originate this peak. Based on this hypothesis, we applied a geometrical energy minimization in a model that considered this inclined stacking. We found unit cell parameters for the inclined eclipsed structure of $a = 40.84$ Å, $b = 23.96$ Å and $c = 4.63$ Å in a *P1* (nº 1) symmetry group. Consistently, the experimental PXRD for **4b-d** corresponded to the pattern simulated from the inclined COF model (see Supporting Information, Tables S6 and S7). However, we observed a slight gradual decrease of all peaks when the proportion of **3** was increased in the COF formation, indicating the introduction of disorder in these structures. In fact, this evolution was clearly seen for **4e**, in which an amorphous material was obtained.

These changes in the structural order were also consistent with the adsorption properties of the synthesized COFs (Fig. 3). COF **4a** showed a S_{BET} of 522 $m^2 \cdot g^{-1}$ and a pore size distribution (calculated using a density functional theory model (N_2 −cylindrical pores−oxide surface) with a main peak at 1.6 nm (see Supporting Information, Fig. S35), which are in good agreement with the



Scheme 1. Synthesis of the new building block **3** based on PTH. PTH, phenyl phenothiazine.



Scheme 2. Synthesis of the series of materials **4a-e**, which were obtained by variating the **TFPA**/**3** molar ratio.

Table 1
Proportion of **3** and **TFPA** used in the synthesis of COFs **4a-e**.[a]

Material	mol % of 3	mol % of TFPA	Ratio 3/TFPA	Elemental Analysis[b] (S %)[c]
4a	0	100	0/1	0.03 (0.00)
4b	12.5	87.5	1/7	0.42 (0.59)
4c	25	75	1/3	1.21 (1.17)
4d	50	50	1/1	2.20 (2.31)
4e	100	0	1/0	4.67 (4.51)

[a] All materials were prepared in solvothermal reactors charged with **TAPB** (0.14 mmol), the corresponding proportion (0.14 mmol) of the synthesized **3** or/and **TFPA**, 2.7 mL of anhydrous dioxane and 0.6 mL of 3 M acetic acid in water, at 120 °C for 72 h.
[b] Experimental value.
[c] Expected values are included in brackets.

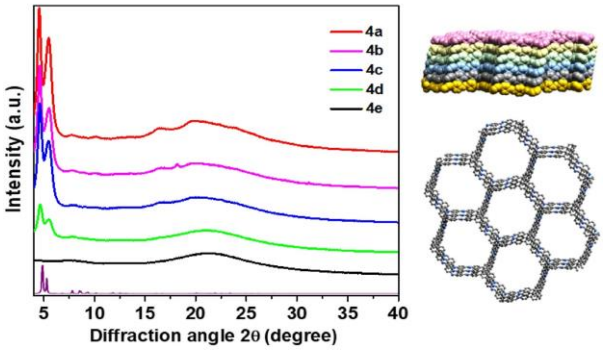


Fig. 2. X-Ray diffractograms of **4a** (**red** data), **4b** (**pink**), **4c** (**blue**), **4d** (**green**) and **4e** (**black**) and the simulated X-Ray diffractogram of the model of **4a** considering an inclined stacking (**purple**).

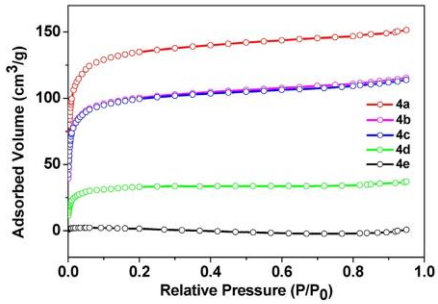


Fig. 3. N_2 adsorption isotherm of **4a** (**red** data), **4b** (**pink**), **4c** (**blue**), **4d** (**green**) and **4e** (**black**).

reported values [56]. However, when the proportion of **3** increased to 12.5% in **4b**, 25% in **4c**, 50% in **4d** and 100% in **4e**, the S_{BET} decreased to 386 $m^2 \cdot g^{-1}$, 382 $m^2 \cdot g^{-1}$, 126 $m^2 \cdot g^{-1}$ and 10 $m^2 \cdot g^{-1}$, respectively.

The relative content of PTH in materials **4a-e** was determined by elemental analysis (Table 1). The sulfur percentage detected was in good agreement with the expected values considering the proportions of **3** and **TFPA** used in each reaction. This result confirmed that there is not a preference for one or another building block, being both completely exchangeable. Analysis of the chemical structure was completed by IR and ^{13}C-CP-MAS-NMR (see Supporting Information, Figs. S10 to S14 and S24 to S28). IR showed the typical vibration bands associated with imine groups, and NMR showed the expected signals in the aromatic region together with the iminic carbons. Therefore, altogether these characterization results were fully consistent with the formation of the predesigned 2D hexagonally-ordered polyimine structures (Scheme 2). In addition, their microstructures were examined by scanning electron microscopy, in which the hexagonal symmetry of the 2D structures was readily observed as hexagonal platelets in all synthesized materials (Fig. 4). Finally, thermogravimetric analysis revealed excellent thermal stability of the 5 materials synthesized. In the case of COF **4a**, a slight decrease in its thermal stability (up to 430 °C) was observed in comparison with materials containing PTH unit **4b-4e** (up to 495 °C) (see Supporting Information, Figs. S51 to S55).

A study of the optical properties of **4a-e** was carried out by means of diffuse reflectance and solid-state luminescence experiments. Fig. 5a shows the absorption spectra normalized with the most intense peak in the region of 400–700 nm. Interestingly, the maximum absorption was dependent on the PTH/TPA content, being at 456 nm for the **TFPA**-based COF **4a** and at 504 nm for the material **4e** that only contains the tritopic aldehyde **3**.

Mixed-photoactive-linker COFs **4b-d** also showed mixed spectroscopic features. In normalized spectra, the absorption value of both signals appeared equally intense. However, in non-normalized data (see inset in Fig. 5a), it is clear that the absorption at 504 nm observed for **4e** is significantly more intense than the signal at 456 nm measured for **4a**. From these data, we have obtained the bandgap values of **4a-e** through Kubelka–Munk theory (2.33–2.25 eV, see Supporting information for details).

Emission experiments were fully consistent with the absorption data (Fig. 5b and c). While the COF **4a** showed a maximum emission at 555 nm, the gradual enrichment of COFs **4b-d** with PTH induced a progressive redshift in the emission peak, which reached 590 nm for the PTH-based material **4e** (Fig. 5c). Although an evident effect on the nature of the photoactive unit was found in the optical properties of the synthesized COFs, it is worth mentioning that the data obtained are not unique because of PTH and TPA units. In fact, molecular PTH and TPA building blocks (**3** and **TFPA**, respectively) absorb at significantly higher energies. Furthermore, the emission is only observed for PTH containing building block **3** (at 530 nm), while **TFPA** does not emit at all (see Supporting Information, page S8). Therefore, the observed photophysical properties are the result of the electronic structure of the overall imine-based material, which is modulated by the distinct nature of TPA and PTH moieties. Taken together, optical data suggest that, by irradiating, TPA-based COF **4a** produces a more energetic excited state than PTH-containing materials **4b-e**. These differences can be crucial to determine what type of photocatalytic process can be mediated by one or another material.

In addition, we have compared the emission of materials **4a**, **4d** and **4e** with an equimolecular mixture of material **4a**+**4e**. As it can

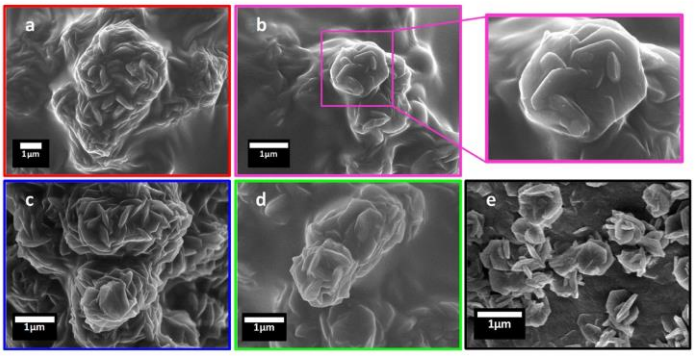


Fig. 4. SEM images of materials **4a** (**red** data), **4b** (**pink**), **4c** (**blue**), **4d** (**green**) and **4e** (**black**). SEM, scanning electron microscopy.

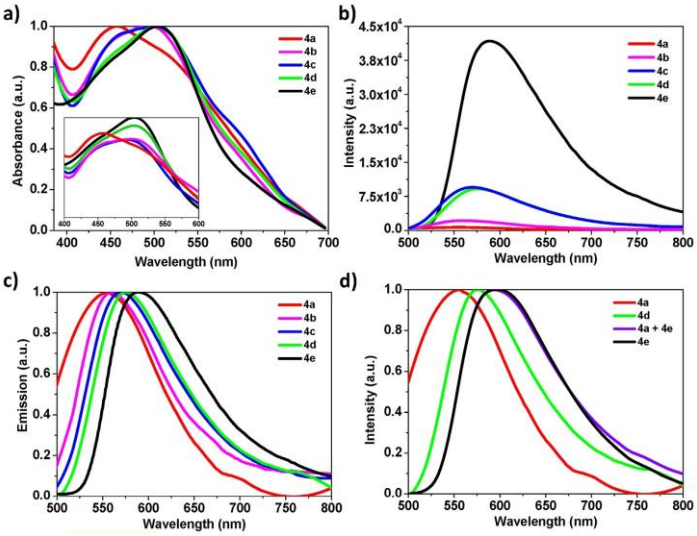


Fig. 5. **a**) Absorption spectra of materials **4a** (**red** data), **4b** (**pink**), **4c** (**blue**), **4d** (**green**) and **4e** (**black**). (**b**) Non-normalized emission spectra. (**c**) Normalized emission spectra. (**d**) Comparison of normalized emission of materials **4a**, **4d** and **4e** with an equimolecular mixture of material **4a**+**4e**.

be seen in Fig. 5d, the mixture of materials **4a**+**4e** shows an identical signal of pure **4e**. This is because the emission of **4a** is much less intense (see non-normalized emission, Fig. 5b), and therefore, only the emission of **4e** was detected. These experiments and the emission of **4d** at a lower wavelength demonstrated that this material (**4d**) is not composed of a mixture from **4a** and **4e**, and it is just a hybrid material containing both building blocks **3** and **TFPA**.

Furthermore, we measured the energy of the valence band of **4a** and **4e** from the first oxidation signal of the cyclic voltammetry (see Supporting Information, Figs. S43 and S44). Thus, we found that the valence band energy level of **4a** is -4.90 eV and for **4e** is -4.54 eV. This indicates the easier tendency of material **4e** for triggering photoredox processes, which is in agreement with the observed catalytic activity (see in the following).

3.2. Determination of specific activity of each COF toward degradation of PBDE-1, Sudan Red III and Methylene Blue

Prompted by the distinctive optical properties of materials **4a-e**, we decided to compare their photocatalytic activity toward three processes of different nature. In particular, we studied the photodegradation of three pollutants, PBDE-1, Sudan Red III and Methylene Blue (Fig. 1). The initial conditions used for the photocatalytic degradation of these pollutants were based on some precedents using other photoactive materials [59–61]. Moreover, we determined the optimal reaction times by an initial assessment of the kinetics of each reaction. For this purpose, we chose **4e** as the initial model photocatalytic material (see Supporting Information).

A first experiment was carried out adding 1 mg of **4e** in 1 mL of acetonitrile containing PBDE-1 (8.3 mg, 0.033 mmol) and DIPEA (14.2 μL, 0.08 mmol), and irradiating the resulting mixture under blue light irradiation (450 nm LED) in an inert atmosphere for 24 h (see Supporting Information). To our delight, we observed that the use of **4e** resulted in the hydrodebrominated product in good yield (85%) after this reaction time. The degradation did not proceed in the absence of the photocatalytic material **4e** or without irradiation. To compare the photocatalytic activity of the remaining

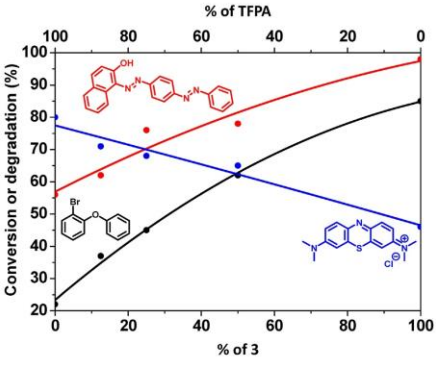
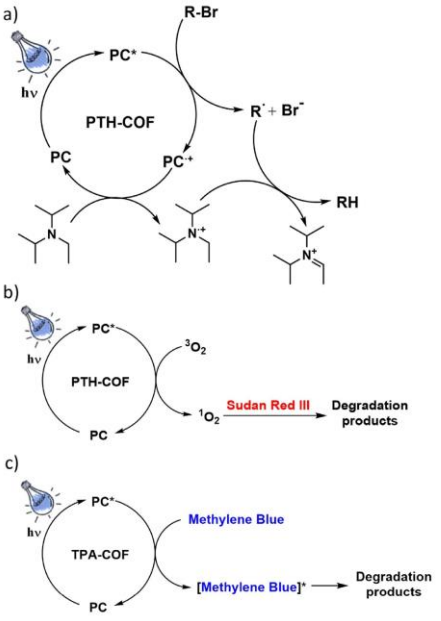


Fig. 6. Conversion (%) of PBDE-1 to the debrominated product (black trace), and degradation (%) of Sudan Red III (red trace) and Methylene Blue (blue trace), using the five materials **4a-e** (see Supporting Information for further details).



Scheme 3. Mechanistic proposals for the degradation of pollutants, (**a**) PBDE-1, (**b**) Sudan Red III, and (**c**) Methylene Blue.

COFs (**4a-d**), they were also tested for 24 h under identical conditions. The results of these experiments are presented in Fig. 6. As can be seen for the black trace in Fig. 6, the best catalytic material for the hydrodebromination of PBDE-1 was **4e**, which only contains PTH as a photoactive unit. We also found that COFs with a lower proportion of PTH showed the worst catalytic activities.

A similar set of experiments was carried out using 2 mg of **4e** under blue light irradiation for 34 h in 10 mL of toluene containing 1.25×10^{-2} mM of Sudan Red III. This substrate was almost completely degraded by **4e** after this reaction time. We also checked that the degradation barely progressed in the absence of the photocatalytic material **4e**, and it did not proceed at all in the absence of visible light. We also performed a comparative study of the different photoactivity depending on the proportion of **3** and **TFPA** used in the synthesis of COFs **4a-d**. Under identical conditions, photodegradation of Sudan Red III using this series of COFs revealed that the catalytic performance is also better when PTH fragment is higher in the COF structure (red trace in Fig. 6).

Finally, Methylene Blue photodegradation was studied using 2 mg of **4e** under blue light irradiation for 4 h in 20 mL of acetonitrile containing 2.25×10^{-2} mM of Methylene Blue (see Supporting Information). This pollutant was partially degraded by **4e** after this time (46% degradation). In the absence of the photocatalytic material, the reaction also proceeded but with much slower kinetics (12% degradation after 4 h). In contrast, it did not progress at all in the absence of visible light (see Supporting Information). When we tested all COFs **4a-e** in the photodegradation of Methylene Blue under identical conditions, we observed the opposite trend than for PBDE-1 and Sudan Red III. In this case, the best result obtained was observed with COF **4a** that only contains TPA as the photoactive unit (80% degradation after 4 h). These results suggest that when the amount of TPA units increases in the structure of COFs, the degradation of Methylene Blue is more effective (blue trace in Fig. 6). The high solubility of Methylene Blue in water allowed us to test the catalytic activity of **4a** and **4e**, founding a very similar behavior to the one observed in the organic solvent (see Supporting Information for kinetics).

Overall, a main observation of this work is that PTH and TPA units showed different preferences as photocatalysts in the studied systems. While activation of PBDE-1 and Sudan Red III are better performed by the PTH-containing material **4e**, photodegradation of Methylene Blue is better achieved by the TPA-based COF **4a**. Mixed-photoactive-linker COFs **4b-d** always showed intermediate catalytic results, indicating that no cooperative/synergistic effects are observed.

3.3. Mechanistic considerations

Photocatalytic hydrodebromination is a well-studied process [35,62] initiated by the electron transfer from the photocatalyst in its excited state to the organo-brominated substrate (Scheme 3a) and under an inert atmosphere. Then, it readily evolves through the C–Br bond cleavage, producing the bromide anion and the corresponding organic radical species. Tertiary amines, such as DIPEA, act as the final reducing agent that ultimately closes the catalytic cycle, regenerating the starting photocatalytic material, and producing the corresponding amine radical cation. Finally, the radical organic intermediate evolves through a hydrogen atom transfer from the oxidized amine radical cation to finally generate the hydrodebrominated product and the iminium cation. In this process, the optimal performance of a photocatalyst is the result of the balance between the ability to perform two key steps, (i) electron transfer from the photocatalyst in its excited state to the organo-brominated substrate; and (ii) the reduction of oxidized photocatalyst by the sacrificial electron donor (DIPEA). While TPA-containing COF **4a** showed almost a negligible activity toward hydrodebromination of PBDE-1, PTH-based material **4e** was very active.

In the case of Sudan Red III degradation, the presence of oxygen was required. Thus, when this process was carried out under argon atmosphere, Sudan Red III did not react (Table 2, entries 1 and 2). Therefore, PTH-based material **4e** in its excited state must be able to activate O_2, resulting in the Sudan Red III oxidative degradation.

Table 2
Photodegradation of Sudan Red III[a] and Methylene Blue[b] under blue light irradiation with different reaction conditions.

Entry	Pollutant	Material	O_2/Ar	Additive[c]	(%) Degradation[d]
1	SR III	4e	O_2	–	48
2	SR III	4e	Ar	–	9
3	SR III	4e	O_2	DABCO	4
4	SR III	4e	O_2	BQ	45
5	MB	4a	O_2	–	60
6	MB	4a	Ar	–	59
7	MB	4a	O_2	DABCO	67
8	MB	4a	O_2	BQ	63

[a] All reactions were carried out using Sudan Red III (SR III) (1.25×10^{-2} mM) and 2 mg of **4e** as photocatalyst in 10 mL of toluene under blue light irradiation for 30 h.
[b] All reactions were carried out using Methylene Blue (MB) (2.25×10^{-2} mM) and 2 mg of COF **4a** as photocatalyst in 20 mL of acetonitrile under blue light irradiation for 3 h.
[c] 5 equivalents of DABCO and benzoquinone (BQ) additives were added.
[d] Determined by UV–Vis spectrophotometry.

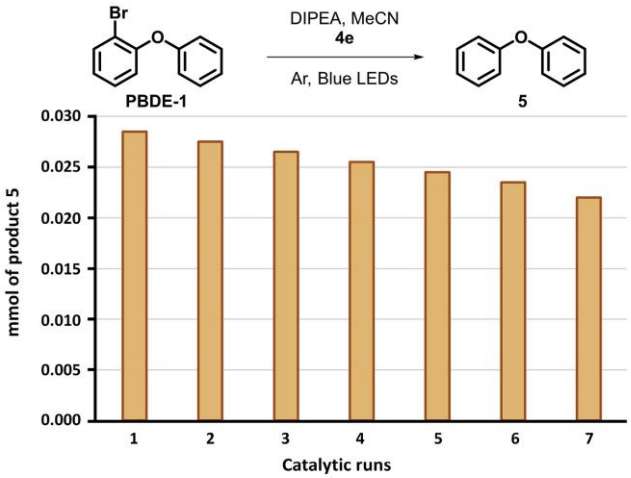


Fig. 7. Photocatalytic runs in the photodegradation of PBDE-1 with **4e**. **PBDE, polybrominated diphenyl ether.**

Two different mechanisms are possible for this reaction, (i) an energy transfer process, where singlet oxygen is the reactive species [63]; or (ii) a photoredox process, where the transformation is mediated by superoxide radical anion [64]. Differentiation between these two mechanisms can be achieved by using additives that can act as selective scavengers, regardless of the nature of the degraded substrate. In particular, quenching by benzoquinone is indicative of a photoredox mechanism [64,65]. DABCO is another scavenger that can be used, which reacts with singlet oxygen, inhibiting the energy transfer pathway [63,66].

Photodegradation of Sudan Red III was uniquely inhibited by addition of DABCO, indicating the involvement of singlet oxygen (Table 2, entries 3 and 4).

The degradation of Methylene Blue proceeds without the need for oxygen (Table 2, entries 5 and 6). Consistently, no specific quenching was found for this process when the reaction was carried out under an open atmosphere in the presence of DABCO or benzoquinone (Table 2, entries 7 and 8). Considering that photodegradation of Methylene Blue works without any final oxidizing agent (such as oxygen) or reducing agent (such as DIPEA), the role of COFs should consist of transferring energy from its excited state to the Methylene Blue molecule. Such a pathway implies that the activated Methylene Blue molecule is able to spontaneously decompose after excitation. Consistently, Methylene Blue showed some level of degradation in the absence of photocatalytic material [67], albeit slower than in the presence of photocatalytic COFs. In fact, Methylene Blue degradation reached a 12% value after 4 h under blue light irradiation in the absence of photocatalyst. Overall, the role of photocatalytic COFs is as photosensitizers acting as mediators in the excitation of Methylene Blue.

In conclusion, the gradual replacement of PTH by TPA in the COFs resulted in progressive inhibition of the photoredox process. According to spectroscopic data shown above (Fig. 5), TPA-based COF **4a** absorbs and emits at higher energies than PTH-based material **4e**, indicating that more energetic excited states are generated. As a consequence, TPA units in this series of COFs enhances the efficiency on transferring energy to Methylene Blue, which has a singlet-triplet gap (1.36 eV) [68] higher than the $^3\Sigma_g$-$^1\Sigma_g$ energy difference for oxygen molecule (0.98 eV approx.) [69], which is effectively activated by **4e**.

4. Recyclability

The durability and recyclability of the photocatalytic materials were analyzed by considering as a model system the photodegradation of PDBE-1 catalyzed by **4e**. To discard the leaching of active molecular fragments into the reaction medium, the crude mixture was filtered through membrane filter after a photocatalytic run of 24 h for the degradation of PBDE-1. Thereafter, PBDE-1 (0.033 mmol) and DIPEA (0.08 mmol) were added again to the filtered solution for a new run in the absence of the photocatalytic material. In this case, NMR analysis showed that degradation did not progress after being irradiated in the absence of **4e** (see ESI).

With the aim of evaluating the recyclability of **4e**, we performed seven consecutive 24 h catalytic runs (total 168 h, Fig. 7). Remarkably, only 1 mg of **4e** was able to degrade 0.178 mmol (44.3 mg) of PBDE-1. After one catalytic run, we analyzed the chemical integrity of **4e** by means of IR spectroscopy, observing that no degradation was found after the catalytic reaction. In addition, SEM images confirmed that no structural erosion was found after one photocatalytic run. Moreover, the emission properties of **4e** were also totally conserved (see Supporting Information, Figs. S4 and S5).

5. Conclusions

Two structurally analogous COFs with different properties were isolated by using two different building blocks **3** and **TFPA** containing PTH and TPA photoactive units, respectively. In addition, a combination of both building blocks results in three additional mixed-photoactive-linker COFs with similar structures and intermediate physical and chemical characteristics. This synthetic

strategy opens new avenues for developing a diverse variety of photoactive COFs showing good performances in different photodegradation processes, depending on the content of one or another photoactive unit. The COFs synthesized work under visible-light conditions without leaching molecular fragments into the reaction media and show a high degree of recyclability and stability under the reaction conditions. In particular, they were able to efficiently perform the photodegradation of three pollutants of distinct nature, PBDE-1, Sudan Red III and Methylene Blue. PTH-based material **4e** was the best catalyst for the photoredox degradation of PBDE-1. However, the efficiency of processes triggered by energy transfer to different chemical species is highly dependent on the PTH/TPA relative content. Thus, energy transfer to Methylene Blue was better achieved by TPA-based COF **4a**, whereas singlet oxygen generation works better using PTH-based material **4e**, resulting in the degradation of Sudan Red III. Overall, this work expands the use of COFs in a wide range of photocatalytic transformations and contributes to the design of innovative strategies to modulate and direct the activity of photocatalytic porous materials.

Credit author statement

Alicia-Jimenez-Almarza: Conceptualization, Investigation, Formal analysis.
Alberto López-Magano: Conceptualization, Investigation, Formal analysis.
Rafael Cano: Investigation, Formal analysis.
Borja Ortín-Rubio: Investigation, Formal analysis.
Inhar Imaz: Conceptualization, Investigation, Formal analysis.
Daniel Maspoch: Conceptualization, Investigation, Formal analysis.
Rubén Mas-Ballesté: Conceptualization, Writing - Review & Editing, Supervision.
Jose Alemán: Conceptualization, Writing - Review & Editing, Supervision.

Declaration of competing interest

The authors declare that they have no known competing financial interests or personal relationships that could have appeared to influence the work reported in this paper.

Acknowledgments

Financial support was provided by the European Research Council (ERC-CoG, contract number: 647550), Spanish Government (PID2019-110637RB-I00, RTI2018-095038-B-I00 and RTI2018-095622-B-I00), "Comunidad de Madrid" and European Structural Funds (S2018/NMT-4367). It was also funded by the CERCA Program/Generalitat de Catalunya. ICN2 is supported by the Severo Ochoa program from the Spanish MINECO (Grant No. SEV-2017-0706). Alberto López-Magano thanks to UAM for FPI-UAM predoctoral fellowship.

Appendix A. Supplementary data

Supplementary data to this article can be found online at https://doi.org/10.1016/j.mtchem.2021.100548.

References

[1] P. Venkata Laxma Reddy, K.H. Kim, Y.H. Kim, A review of photocatalytic treatment for various air pollutants, Asian J. Atmos. Environ. 5 (2011) 181–188, https://doi.org/10.5572/ajae.2011.5.3.181.
[2] N.J. Turro, Energy transfer processes, Pure Appl. Chem. 49 (1977) 405–429.
[3] C.R.J. Stephenson, Y. Tehshik P, D.W.C. MacMillan, Visible Light Photocatalysis in Organic Chemistry, Wiley - VCN Verlag GmbH Co. KGaA, 2018.
[4] J. Twilton, C.C. Le, P. Zhang, M.H. Shaw, R.W. Evans, D.W.C. MacMillan, The merger of transition metal and photocatalysis, Nat. Rev. Chem. 1 (2017) 52, https://doi.org/10.1038/s41570-017-0052.
[5] N.A. Romero, D.A. Nicewicz, Organic photoredox catalysis, Chem. Rev. 116 (2016) 10075–10166, https://doi.org/10.1021/acs.chemrev.6b00057.
[6] S.G.E. Amos, M. Garreau, L. Buzzetti, J. Waser, Photocatalysis with organic dyes: facile access to reactive intermediates for synthesis, Beilstein J. Org. Chem. 16 (2020) 1163–1187, https://doi.org/10.3762/bjoc.16.103.
[7] R. Ameta, S. Benjamin, A. Ameta, S.C. Ameta, Photocatalytic degradation of organic pollutants: a review, Mater. Sci. Forum 734 (2013) 247–272, https://doi.org/10.4028/www.scientific.net/MSF.734.247.
[8] N. Hoffmann, Photochemical reactions as key steps in organic synthesis, Chem. Rev. 108 (2008) 1052–1103, https://doi.org/10.1021/cr0680336.
[9] S. Gisbertz, B. Pieber, Heterogeneous photocatalysis in organic synthesis, ChemPhotoChem 4 (2020) 456–475, https://doi.org/10.1002/cptc.202000014.
[10] J.-D. Xiao, H.-L. Jiang, Metal–organic frameworks for photocatalysis and photothermal catalysis, Acc. Chem. Res. 52 (2019) 356–366, https://doi.org/10.1021/acs.accounts.8b00521.
[11] G.-B. Wang, S. Li, C.-X. Yan, F.-C. Zhu, Q.-Q. Lin, K.-H. Xie, Y. Geng, Y.-B. Dong, Covalent organic frameworks: emerging high-performance platforms for efficient photocatalytic applications, J. Mater. Chem. A. 8 (2020) 6957–6983, https://doi.org/10.1039/D0TA00556H.
[12] J. Wang, S. Zhuang, Covalent organic frameworks (COFs) for environmental applications, Coord. Chem. Rev. 400 (2019) 213046, https://doi.org/10.1016/j.ccr.2019.213046.
[13] A. López-Magano, A. Jiménez-Almarza, J. Alemán, R. Mas-Ballesté, Metal–organic frameworks (MOFs) and covalent organic frameworks (COFs) applied to photocatalytic organic transformations, Catalysts 10 (2020) 720, https://doi.org/10.3390/catal10070720.
[14] A.P. Côté, A.I. Benin, N.W. Ockwig, M. O'Keeffe, A.J. Matzger, O.M. Yaghi, Porous, crystalline, covalent organic frameworks, Science (80-.) 310 (2005), https://doi.org/10.1126/science.1120411, 1166 LP – 1170.
[15] R.K. Sharma, P. Yadav, M. Yadav, R. Gupta, P. Rana, A. Srivastava, R. Zboril, R.S. Varma, M. Antonietti, M.B. Gawande, Recent development of covalent organic frameworks (COFs): synthesis and catalytic (organic-electro-photo) applications, Mater. Horiz. 7 (2020) 411–454, https://doi.org/10.1039/C9MH00856J.
[16] L. Zhu, Y.-B. Zhang, Crystallization of covalent organic frameworks for gas storage applications, Molecules 22 (2017), https://doi.org/10.3390/molecules22071149.
[17] A.K. Mandal, J. Mahmood, J.-B. Baek, Two-dimensional covalent organic frameworks for optoelectronics and energy storage, ChemNanoMat 3 (2017) 373–391, https://doi.org/10.1002/cnma.201700048.
[18] Q. Fang, J. Wang, S. Gu, R.B. Kaspar, Z. Zhuang, J. Zheng, H. Guo, S. Qiu, Y. Yan, 3D porous crystalline polyimide covalent organic frameworks for drug delivery, J. Am. Chem. Soc. 137 (2015) 8352–8355, https://doi.org/10.1021/jacs.5b04147.
[19] H. Ma, B. Liu, B. Li, L. Zhang, Y.-G. Li, H.-Q. Tan, H.-Y. Zang, G. Zhu, Cationic covalent organic frameworks: a simple platform of anionic exchange for porosity tuning and proton conduction, J. Am. Chem. Soc. 138 (2016) 5897–5903, https://doi.org/10.1021/jacs.5b13490.
[20] S.-Y. Ding, J. Gao, Q. Wang, Y. Zhang, W.-G. Song, C.-Y. Su, W. Wang, Construction of covalent organic framework for catalysis: Pd/COF-LZU1 in suzuki–miyaura coupling reaction, J. Am. Chem. Soc. 133 (2011) 19816–19822, https://doi.org/10.1021/ja206846p.
[21] J. Luis-Barrerra, R. Cano, G. Imani-Shakibaei, J. Heras-Domingo, J. Pérez-Carvajal, I. Imaz, D. Maspoch, X. Solans-Monfort, J. Alemán, R. Mas-Ballesté, Switching acidic and basic catalysis through supramolecular functionalization in a porous 3D covalent imine-based material, Catal. Sci. Technol. 9 (2019) 6007–6014, https://doi.org/10.1039/C9CY01527B.
[22] X. Wang, L. Chen, S.Y. Chong, M.A. Little, Y. Wu, W.-H. Zhu, R. Clowes, Y. Yan, M.A. Zwijnenburg, R.S. Sprick, A.I. Cooper, Sulfone-containing covalent organic frameworks for photocatalytic hydrogen evolution from water, Nat. Chem. 10 (2018) 1180–1189, https://doi.org/10.1038/s41557-018-0141-5.
[23] J. Chen, X. Tao, C. Li, Y. Ma, L. Tao, D. Zheng, J. Zhu, H. Li, R. Li, Q. Yang, Synthesis of bipyridine-based covalent organic frameworks for visible-light-driven photocatalytic water oxidation, Appl. Catal. B Environ. 262 (2020) 118271, https://doi.org/10.1016/j.apcatb.2019.118271.
[24] L. Guo, S. Jin, Stable covalent organic frameworks for photochemical applications, ChemPhotoChem 3 (2019) 973–983, https://doi.org/10.1002/cptc.201900089.
[25] X. Kang, X. Wu, X. Han, C. Yuan, Y. Liu, Y. Cui, Rational synthesis of interpenetrated 3D covalent organic frameworks for asymmetric photocatalysis, Chem. Sci. 11 (2020) 1494–1502, https://doi.org/10.1039/C9SC04882K.
[26] J. Yuan, Q. Xia, W. Zhu, C. Wu, B. Wang, B. Liu, X. Yang, Y. Xu, H. Xu, Sunlight-Driven synthesis of 1,2,4-thiadiazoles via oxidative construction of a nitrogen-sulfur bond catalyzed by a reusable covalent organic framework, ChemPhotoChem (2020), https://doi.org/10.1002/cptc.201900263 n/a.
[27] S. Wang, Q. Sun, W. Chen, Y. Tang, B. Aguila, Y. Pan, A. Zheng, Z. Yang, L. Wojtas, S. Ma, F.-S. Xiao, Programming covalent organic frameworks for photocatalysis: investigation of chemical and structural variations, Matter 2 (2020) 416–427, https://doi.org/10.1016/j.matt.2019.10.026.
[28] H. Xue, S. Xiong, K. Mi, Y. Wang, Visible-light degradation of azo dyes by imine-linked covalent organic frameworks, Green Energy Environ. (2021), https://doi.org/10.1016/j.gee.2020.09.010.

[29] A. Jiménez-Almarza, A. López-Magano, L. Marzo, S. Cabrera, R. Mas-Balleste, J. Alemán, Imine-based covalent organic frameworks as photocatalysts for metal free oxidation processes under visible light conditions, ChemCatChem 11 (2019) 4916, https://doi.org/10.1002/cctc.201901061.
[30] S. Ren, R. Dawson, D.J. Adams, A.I. Cooper, Low band-gap benzothiadiazole conjugated microporous polymers, Polym. Chem. 4 (2013) 5585–5590, https://doi.org/10.1039/C3PY00690E.
[31] N. Kang, J.H. Park, K.C. Ko, J. Chun, E. Kim, H.W. Shin, S.M. Lee, H.J. Kim, T.K. Ahn, J.Y. Lee, S.U. Son, Tandem synthesis of photoactive benzodifuran moieties in the formation of microporous organic networks, Angew. Chem. Int. Ed. 52 (2013) 6228–6232, https://doi.org/10.1002/anie.201300655.
[32] J.-X. Jiang, Y. Li, X. Wu, J. Xiao, D.J. Adams, A.I. Cooper, Conjugated microporous polymers with rose bengal dye for highly efficient heterogeneous organo-photocatalysis, Macromolecules 46 (2013) 8779–8783, https://doi.org/10.1021/ma402104h.
[33] Z.J. Wang, S. Ghasimi, K. Landfester, K.A.I. Zhang, A conjugated porous poly-benzobisthiadiazole network for a visible light-driven photoredox reaction, J. Mater. Chem. A. 2 (2014) 18720–18724, https://doi.org/10.1039/C4TA03887H.
[34] S. Dadashi-Silab, H. Bildirir, R. Dawson, A. Thomas, Y. Yagci, Microporous thioxanthone polymers as heterogeneous photoinitiators for visible light induced free radical and cationic polymerizations, Macromolecules 47 (2014) 4607–4614, https://doi.org/10.1021/ma501001m.
[35] A. López-Magano, A.E. Platero-Prats, S. Cabrera, R. Mas-Balleste, J. Alemán, Incorporation of photocatalytic Pt(II) complexes into imine-based layered covalent organic frameworks (COFs) through monomer truncation strategy, Appl. Catal. B Environ. 272 (2020) 119027, https://doi.org/10.1016/j.apcatb.2020.119027.
[36] Z.J. Wang, S. Ghasimi, K. Landfester, K.A.I. Zhang, Molecular structural design of conjugated microporous poly(benzooxadiazole) networks for enhanced photocatalytic activity with visible light, Adv. Mater. 27 (2015) 6265–6270, https://doi.org/10.1002/adma.201502735.
[37] M. Liras, M. Iglesias, F. Sánchez, Conjugated microporous polymers incorporating BODIPY moieties as light-emitting materials and recyclable visible-light photocatalysts, Macromolecules 49 (2016) 1666–1673, https://doi.org/10.1021/acs.macromol.5b02511.
[38] S. Ghasimi, S.A. Bretschneider, W. Huang, K. Landfester, K.A.I. Zhang, A conjugated microporous polymer for palladium-free, visible light-promoted photocatalytic stille-type coupling reactions, Adv. Sci. (Weinheim, Baden-Wurttemberg, Ger. 4 (2017) 1700101, https://doi.org/10.1002/advs.201700101.
[39] All POPs listed in the Stockholm Convention, (n.d.). http://www.pops.int/TheConvention/ThePOPs/AllPOPs/tabid/2509/Default.aspx (accessed August 25, 2021).
[40] U. Gill, I. Chu, J.J. Ryan, M. Feeley, Polybrominated diphenyl ethers: human tissue levels and toxicology, Rev. Environ. Contam. Toxicol. 183 (2004) 55–97, https://doi.org/10.1007/978-1-4419-9100-3_3.
[41] A.O. Souza, M.J. Tasso, A.M.C. Oliveira, L.C. Pereira, F. V Duarte, D.P. Oliveira, C.M. Palmeira, D.J. Dorta, Evaluation of polybrominated diphenyl ether toxicity on HepG2 cells – hexabrominated congener (BDE-154) is less toxic than tetrabrominated congener (BDE-47), Basic Clin. Pharmacol. Toxicol. 119 (2016) 485–497, https://doi.org/10.1111/bcpt.12598.
[42] J.D. Raff, R.A. Hites, Gas-phase reactions of brominated diphenyl ethers with OH radicals, J. Phys. Chem. A. 110 (2006) 10783–10792, https://doi.org/10.1021/jp0630222.
[43] B. Padhi, Pollution due to synthetic dyes toxicity & carcinogenicity studies and remediation, Int. J. Environ. Sci. 3 (2012) 940–955, https://doi.org/10.6088/ijes.2012030133002.
[44] B. de C. Ventura-Camargo, M.A. Marin-Morales, Azo dyes: characterization and toxicity– A review, Text. Light Ind. Sci. Technol. 2 (2015) 85–103.
[45] M. Hou, F. Li, X. Liu, X. Wang, H. Wan, The effect of substituent groups on the reductive degradation of azo dyes by zerovalent iron, J. Hazard Mater. 145 (2007) 305–314, https://doi.org/10.1016/j.jhazmat.2006.11.019.
[46] H. Pan, J. Feng, G.-X. He, C.E. Cerniglia, H. Chen, Evaluation of impact of exposure of Sudan azo dyes and their metabolites on human intestinal bacteria, Anaerobe 18 (2012) 445–453, https://doi.org/10.1016/j.anaerobe.2012.05.002.
[47] J. Ma, D. Huang, J. Zou, L. Li, Y. Kong, S. Komarneni, Adsorption of methylene blue and Orange II pollutants on activated carbon prepared from banana peel, J. Porous Mater. 22 (2015) 301–311, https://doi.org/10.1007/s10934-014-9896-2.
[48] T.M. Albayati, A.A. Sabri, R.A. Alazawi, Separation of methylene blue as pollutant of water by SBA-15 in a fixed-bed column, Arab. J. Sci. Eng. 41 (2016) 2409–2415, https://doi.org/10.1007/s13369-015-1867-7.
[49] L. Lan, F. Liu, Y. Dan, L. Jiang, Facile fabrication of triphenylamine-based conjugated porous polymers and their application in organic degradation under visible light, New J. Chem. 44 (2020) 2986–2995, https://doi.org/10.1039/C9NJ05500B.
[50] X. Kong, A.P. Kulkarni, S.A. Jenekhe, Phenothiazine-based conjugated Polymers: synthesis, electrochemistry, and light-emitting properties, Macromolecules 36 (2003) 8992–8999, https://doi.org/10.1021/ma035087y.
[51] A.F. Garrido-Castro, N. Salaverri, M.C. Maestro, J. Alemán, Intramolecular homolytic substitution enabled by photoredox catalysis: sulfur, phosphorus, and silicon heterocycle synthesis from aryl halides, Org. Lett. 21 (2019) 5295–5300, https://doi.org/10.1021/acs.orglett.9b01911.
[52] E.H. Discekici, N.J. Treat, S.O. Poelma, K.M. Mattson, Z.M. Hudson, Y. Luo, C.J. Hawker, J.R. de Alaniz, A highly reducing metal-free photoredox catalyst: design and application in radical dehalogenations, Chem. Commun. 51 (2015) 11705–11708, https://doi.org/10.1039/C5CC04677C.
[53] B. Ma, F. Lu, H. Yang, X. Gu, Z. Li, R. Li, H. Pei, D. Luo, H. Zhang, A. Lei, Visible light mediated external oxidant free selective C5 bromination of 8-aminoquinoline amides under ambient conditions, Asian J. Org. Chem. 8 (2019) 1136–1140, https://doi.org/10.1002/ajoc.201900293.
[54] J.H. Park, K.C. Ko, E. Kim, N. Park, J.H. Ko, D.H. Ryu, T.K. Ahn, J.Y. Lee, S.U. Son, Photocatalysis by phenothiazine dyes: visible-light-driven oxidative coupling of primary amines at ambient temperature, Org. Lett. 14 (2012) 5502–5505, https://doi.org/10.1021/ol302584y.
[55] S. Dadashi-Silab, X. Pan, K. Matyjaszewski, Phenyl benzo[b]phenothiazine as a visible light photoredox catalyst for metal-free atom transfer radical polymerization, Chem. A Eur. J. 23 (2017) 5972–5977, https://doi.org/10.1002/chem.201605574.
[56] L. Zhai, N. Huang, H. Xu, Q. Chen, D. Jiang, A backbone design principle for covalent organic frameworks: the impact of weakly interacting units on CO2 adsorption, Chem. Commun. 53 (2017) 4242–4245, https://doi.org/10.1039/C7CC01921A.
[57] D. Zhu, L.B. Alemany, W. Guo, R. Verduzco, Enhancement of crystallinity of imine-linked covalent organic frameworks via aldehyde modulators, Polym. Chem. 11 (2020) 4464–4468, https://doi.org/10.1039/D0PY00776E.
[58] B. Lukose, A. Kuc, T. Heine, The structure of layered covalent-organic frameworks, Chem. A Eur. J. 17 (2011) 2388–2392, https://doi.org/10.1002/chem.201001290.
[59] X. Feng, H. Ju, T. Song, T. Fang, W. Liu, W. Huang, Highly efficient photocatalytic degradation performance of CsPb(Br1−xClx)3-Au nanoheterostructures, ACS Sustain. Chem. Eng. 7 (2019) 5152–5156, https://doi.org/10.1021/acssuschemeng.8b06023.
[60] T. Aarthi, P. Narahari, G. Madras, Photocatalytic degradation of Azure and Sudan dyes using nano TiO2, J. Hazard Mater. 149 (2007) 725–734, https://doi.org/10.1016/j.jhazmat.2007.04.038.
[61] K.K. Senapati, C. Borgohain, K.C. Sarma, P. Phukan, Photocatalytic degradation of methylene blue in water using CoFe2O4–Cr2O3–SiO2 fluorescent magnetic nanocomposite, J. Mol. Catal. A Chem. 346 (2011) 111–116, https://doi.org/10.1016/j.molcata.2011.07.001.
[62] D. González-Muñoz, A. Casado-Sánchez, I. del Hierro, S. Gómez-Ruiz, S. Cabrera, J. Alemán, Size-selective mesoporous silica-based Pt(II) complex as efficient and reusable photocatalytic material, J. Catal. 373 (2019) 374–383, https://doi.org/10.1016/j.jcat.2019.04.015.
[63] P.R. Ogilby, Singlet oxygen: there is indeed something new under the sun, Chem. Soc. Rev. 39 (2010) 3181–3209, https://doi.org/10.1039/B926014P.
[64] M. Hayyan, M.A. Hashim, I.M. AlNashef, Superoxide ion: generation and chemical implications, Chem. Rev. 116 (2016) 3029–3085, https://doi.org/10.1021/acs.chemrev.5b00407.
[65] R.I. Samoilova, A.R. Crofts, S.A. Dikanov, Reaction of superoxide radical with quinone molecules, J. Phys. Chem. A. 115 (2011) 11589–11593, https://doi.org/10.1021/jp204891n.
[66] C. Ouannes, T. Wilson, Quenching of singlet oxygen by tertiary aliphatic amines. Effect of DABCO (1,4-diazabicyclo[2.2.2]octane), J. Am. Chem. Soc. 90 (1968) 6527–6528, https://doi.org/10.1021/ja01025a059.
[67] Y. Xu, X. Shi, R. Hua, R. Zhang, Y. Yao, B. Zhao, T. Liu, J. Zheng, G. Lu, Remarkably catalytic activity in reduction of 4-nitrophenol and methylene blue by Fe3O4@COF supported noble metal nanoparticles, Appl. Catal. B Environ. 260 (2020) 118142, https://doi.org/10.1016/j.apcatb.2019.118142.
[68] V.Y. Gak, V.A. Nadtochenko, J. Kiwi, Triplet-excited dye molecules (eosine and methylene blue) quenching by H2O2 in aqueous solutions, J. Photochem. Photobiol. A Chem. 116 (1998) 57–62, https://doi.org/10.1016/S1010-6030(98)00230-5.
[69] G.P. Brasseur, S. Solomon, Aeronomy of the Middle Atmosphere, Springer, Springer Science & Business Media, 2005. https://www.springer.com/gp/book/9781402032844.

ACS Catalysis

pubs.acs.org/acscatalysis

Research Article

Photoredox Heterobimetallic Dual Catalysis Using Engineered Covalent Organic Frameworks

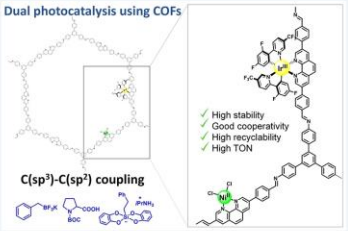
Alberto López-Magano, Borja Ortín-Rubio, Inhar Imaz, Daniel Maspoch, José Alemán,* and Rubén Mas-Ballesté*

Cite This: *ACS Catal.* 2021, 11, 12344–12354

Read Online

ACCESS | Metrics & More | Article Recommendations | Supporting Information

ABSTRACT: The functionalization of an imine-based layered covalent organic framework (COF), containing phenanthroline units as ligands, has allowed the obtention of a heterobimetallated material. Photoactive Ir and Ni fragments were immobilized within the porous structure of the COF, enabling heterogeneous light-mediated Csp^3–Csp^2 cross-couplings. As radical precursors, potassium benzyl- and alkoxy-trifluoroborates, organic silicates, and proline derivatives were employed, which brings out the good versatility of **Ir,Ni@Phen-COF**. Moreover, in all the studied cases, an enhanced activity and stability have been observed in comparison with analogous homogenous systems.



KEYWORDS: *covalent organic frameworks, photocatalysis, dual catalysis, C–C bond formation, heterogeneous catalysis*

1. INTRODUCTION

Carbon–carbon couplings are one of the most useful and important transformations in modern chemistry.[1] They include classical cross-coupling reactions,[2] such as Suzuki, Sonogashira, and olefin metathesis;[3] some of them recognized with the Nobel prize.[4] The importance of these reactions relies on their key role in the synthesis of pharmaceutical drugs, construction of complex molecules, and late stage functionalizations. However, there is still a need of searching new synthetic methodologies with high functional group tolerance, in which are included new Csp^3–Csp^2 bonds. In this sense, photocatalytic reactions have appeared as a new tool in the last decade, solving some of the problems associated with the formation of C–C bonds under mild reaction conditions.[5] Among them, photoredox Ir–Ni dual catalysis has become an outstanding solution (top, Figure 1).[5] In this reaction, two well-distinguished and connected catalytic cycles are combined: first, the Ir photocatalyst generates a radical intermediate under light irradiation; and second, the Ni species mediates in the formation of the new C–C bond.[6,7] Although this is a very powerful methodology, Ir–Ni dual photocatalysis also suffers of some general drawbacks. First, iridium is an expensive metal center and its recyclability in the homogeneous system is difficult,[8] increasing the costs of these processes. Furthermore, Ni sources commonly undergo deactivation in the presence of light, oxygen, or organic reactive species, giving rise to the formation of unreactive agglomerated Ni/NiO nanoparticles. This hampers the furtherance of the reaction, leading to lower yields and turnover numbers (TONs).[9] Therefore, a plausible strategy to overcome the limitations of homogenous Ir–Ni dual catalysis would consist of the design of heterogeneous systems.

The use of catalytic heterogeneous materials allows their easy separation from the reaction medium. In addition, the immobilization and isolation of catalytically active sites may enhance their stability and reactivity, due to the hampering of unproductive encounters or deactivation pathways,[10] such as the formation of inactive agglomerated Ni/NiO nanoparticles.[9] Besides, cooperative phenomena between distinct isolated catalytic centers can be enhanced by the control of proximity in predetermined sites on the material. To this end, it would be a feasible strategy to immobilize molecular metallic catalytic sites into porous materials, such as covalent organic frameworks (COFs).[11,12] This family of materials is in its heyday on their catalytic applications.[13] They constitute a class of crystalline and porous reticular materials formed by the assembly of covalent bonds of different nature.[14] Among them, imine-based COFs have attracted a good deal of attention, due to their stability, availability of the constituting building blocks, and the easy isolation of crystalline and porous structures under mild reaction conditions.[15,16] The accessibility

Received: August 11, 2021
Revised: September 9, 2021
Published: September 21, 2021



ACS Publications

© 2021 American Chemical Society

https://doi.org/10.1021/acscatal.1c03634
ACS Catal. 2021, 11, 12344–12354

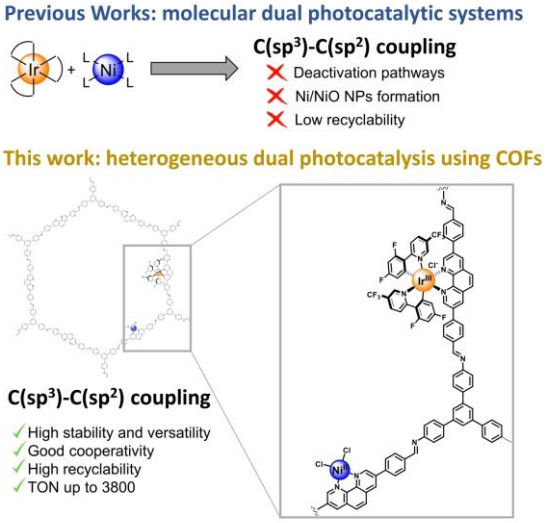
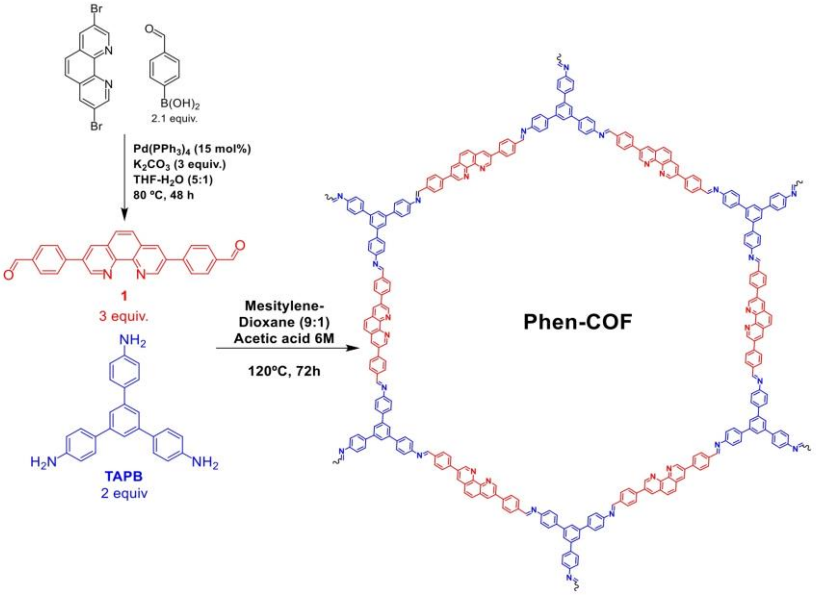


Figure 1. Previous works and the conceptual strategy of this work.

Scheme 1. Synthesis of Phen-COF



https://doi.org/10.1021/acscatal.1c03634
ACS Catal. 2021, 11, 12344−12354

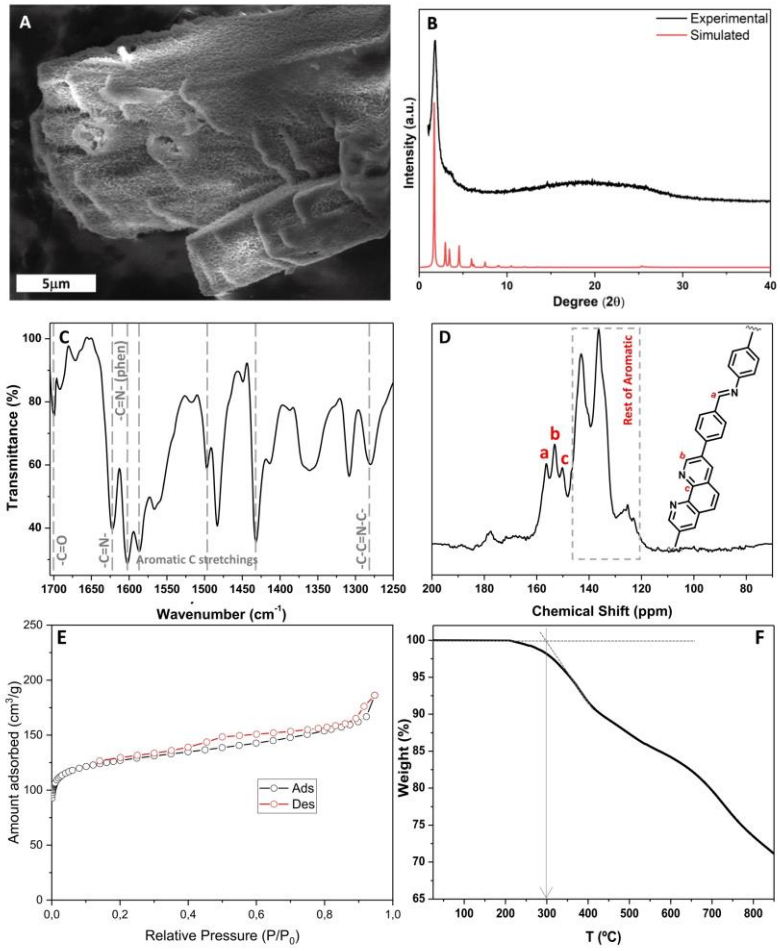


Figure 2. Characterization of **Phen-COF**. (A) SEM image; (B) PXRD simulated and experimental pattern; (C) FT-IR spectra; (D) ^{13}C NMR-CPMAS spectrum; (E) adsorption−desorption N_2 isotherm; and (F) thermogravimetric analysis.

to a variety of building blocks allows the design of COFs containing different functional units in their framework.[17] In particular, some COFs have been isolated containing donor groups (e.g., bipyridine,[18] salen,[19] porphyrin,[20] or catechol,[21] among others)[19,22−24] that can act as ligands toward a variety of metal centers. As a result, different organic transformations have been achieved with a variety of metals.[17,22,23,25] However, dual bimetallic photocatalytic processes are a challenging goal that never have been tackled with this family of materials. In particular, dual catalytic systems require a high level of synchronicity between the two catalytic sites, because the intermediates involved in such processes are very reactive and not isolable. The proximity and cooperativity between the distinct catalytic sites are a key issue in the design of a dual catalytic process, and therefore catalytic sites must work in close proximity.[26]

Regarding this issue, two pioneering works using metal organic frameworks (MOFs) have reported the isolation of Ni and Ir centers through coordination to bipyridine fragments, achieving dual photocatalytic processes.[27,28] In addition, nonporous amorphous linear polymers designed with pending arms containing bipyridine fragments have also been used for

https://doi.org/10.1021/acscatal.1c03634
ACS Catal. 2021, 11, 12344−12354

these purposes.[29] Inspired by these precedents, this work is intended to design a bimetallated COF that requires simple synthetic procedures and to obtain a very stable and active material. In particular, we immobilize Ir and Ni fragments into phenanthroline units in a new imine-based COF (hereafter called **Phen-COF**), allowing the interplay of both catalytic metal centers for the formation of Csp^3-Csp^2 bonds (bottom, Figure 1). This heterogeneous strategy permits the improvement of the catalytic performance compared with the homogeneous version of the coupling reaction.

2. RESULTS AND DISCUSSION

2.1. Synthesis and Characterization. **Phen-COF** was prepared by combining the symmetric building block **1**, which contains a centered phenanthroline unit and two aldehyde groups located at its ends, and the well-known triamine 1,3,5-tris(4-aminophenyl)benzene (TAPB) (see Scheme 1).[12] First, the dialdehyde **1** was made by a double Suzuki–Miyaura cross-coupling between 3,8-dibromo-1,10-phenanthroline and 4-formylphenylboronic acid. Then, a screening of typical conditions for the synthesis of **Phen-COF** was performed. In most of the cases, a yellow amorphous material was obtained (see Table S1 of Supporting Information), probably because of the poor solubility of phenanthroline building block **1**. Interestingly, using a mixture of 9:1 (v/v) of mesitylene-dioxane and 6 M acetic acid on a sealed solvothermal reactor, we were able to isolate a material with moderate crystallinity after 3 days at 120 °C (entry 15, Table S1). Longer reaction times, higher temperatures, or the use of acid catalysts of different nature did not improve the crystallinity of the material, not even post-thermal annealing treatments or activation with supercritical CO_2. Field-emission scanning electron microscopy (FE-SEM) of the resulting yellow powder revealed the formation of a layered-type COF (Figure 2A). The formation of the expected layered polyimine structure of **Phen-COF** (Scheme 1) was first confirmed by powder X-ray diffraction (PXRD) (Figure 2B). Using the Materials Studio 8.0 Program, we compared this experimental PXRD data with the pattern simulated from the analogous layered, eclipsed structure of PI-COF-3 previously reported by Yan et al.[30] Based on this structure, we applied a geometrical energy minimization using the universal force field. The unit cell parameters found for the layered eclipsed structure were a = 3.52 Å, b = 102.59 Å, and c = 59.23 Å in an *Amm*2 (no. 38) symmetry group. Consistently, the most intense peak at 1.73° of our experimental PXRD matched with the peak corresponding to the (100) plane in the eclipsed pattern simulated from the COF model (Figure 2B).

Moreover, Fourier-transform infrared spectroscopy (FT-IR) (Figures 2C and S1 of Supporting Information) showed the most important vibration peaks at 1621 and 1282 cm^{-1} (attributed to the C=N and C–C=N–C stretching of imine moieties), indicating the formation of the polyimine network.[10] In addition, the presence of phenanthroline fragments in this network was corroborated by the vibration found at 1603 cm^{-1}, also observed in **1**, which was attributed to the C=N stretching. The vibration peak at 1697 cm^{-1} was assigned to the C=O stretching of unreacted aldehydes, which agrees with the appearance of Fermi resonance peaks at 2919 and 2850 cm^{-1}. Moreover, the two peaks at 3349 and 3418 cm^{-1} are related to the symmetric and asymmetric N–H stretchings of the free amino groups. The corresponding C–C aromatic ring stretchings at 1588, 1497, and 1432 cm^{-1} and $C_{aromatic}$–H stretchings centered at 3027 cm^{-1} are also important in typical polyaromatic networks that contain **TAPB** as the building block.[10,12] In addition, solid-^{13}C NMR experiments using Cross Polarization combined to Magic Angle Spinning (^{13}C-CP-MAS) showed the characteristic iminic carbon peak at 156.4 ppm as well as the peaks centered at 153.2 and 150.1 ppm, which were assigned to the tertiary and quaternary carbons in the alpha position to the phenanthroline-nitrogen atom (Figure 2D. For the comparison with the ^{13}C-CP-MAS spectrum of **1**, see Figure S4 of Supporting Information). The rest of the signals correspond to several aromatic carbons present in the covalent structure. These results match with those observed in comparable pristine layered-COFs.[10] As indicated in Figure 2E, N_2 sorption analysis at 77 K showed that **Phen-COF** is porous with a Brunauer–Emmett–Teller surface area (S_{BET}) of 482 m^2/g. The pore size distribution was calculated, finding pores of 13.4 and 15.6 Å (Figure S7 of Supporting Information). Finally, thermogravimetric analysis (TGA) showed that **Phen-COF** possesses good thermal stability, up to 300 °C even under an oxidant atmosphere (Figure 2F).

In order to study the optical properties of **Phen-COF**, diffuse reflectance spectroscopy (DRS) was performed, revealing a continuous intense absorption of the material up to 450 nm (Figure S8 of Supporting Information). Applying Kubelka–Munk theory, the band gap of **Phen-COF** was found to be around 2.56 eV, which is comparable to that of other pristine layered imine-based COFs.[12] Additionally, fluorescence emission spectroscopy of **Phen-COF** showed broad emission bands with maximums centered at 470 and 537 nm, respectively (Figure S9 of Supporting Information). Electrochemical properties were determined by cyclic voltammetry measurements (Figure S10 of Supporting Information). One reduction and one oxidation process were observed at −0.10 and +0.82 V (vs Ag/AgCl), respectively. Reduction processes are expected due to the presence of phenanthroline, which is known as redox active at negative potentials (Figure S10, Supporting Information). The oxidation signal is attributed to the electron transfer from the valence band (VB) of the material, which leads to an energy value determined as 5.21 eV (see Figure 3 for determination of energy levels).

2.2. Postsynthetic Metalation. Postsynthetic metalation of **Phen-COF** consisted of dispersing it in acetonitrile and 6 M aqueous acetic acid in the presence of $[(dF(CF_3)ppy)_2\text{-Ir-}\mu\text{-Cl}]_2$ and $NiCl_2$·glyme (see Supporting Information for further details). For this metalation, $[(dF(CF_3)ppy)_2\text{-Ir-}\mu\text{-Cl}]_2$ was

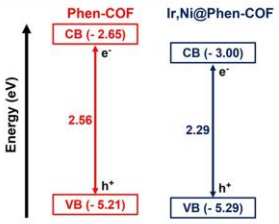


Figure 3. Energy levels of **Phen-COF** and **Ir.Ni@Phen-COF**. The values of the VB were calculated from the first oxidation signal of the cyclic voltammetry curve. Band gap values were obtained from the DRS spectra and subsequent application of Kubelka–Munk theory.

https://doi.org/10.1021/acscatal.1c03634
ACS Catal. 2021, 11, 12344–12354

chosen as the iridium source[31] because it would enable the incorporation of a powerful photoredox complex through coordination with the phenanthroline ligands contained in **Phen-COF**.[6] $NiCl_2$·glyme was selected as the Ni source due to the ability of glyme ligands to undergo exchange with phenanthroline moieties. Note that acetic acid was used in the metalation process because it was essential to preserve the crystallinity of **Phen-COF**,[32] as its absence always led to amorphization of the structure.

The content of Ir and Ni incorporated into the metallated **Phen-COF** (hereafter called **Ir,Ni@Phen-COF**) was analyzed by total X-ray fluorescence (TXRF, see Supporting Information, Figure S17).[33] We found that the Ir and Ni contents in **Ir,Ni@Phen-COF** are 4.0 and 2.8% in weight, respectively. These values mean that 45% of the phenanthroline ligands present in **Phen-COF** coordinates to metals: 15% to Ir and 30% to Ni. Interestingly, the metal uptake from the solution is quite efficient. In fact, the 71% of the Ir species in solution is incorporated into the material, while the 82% of the Ni precursor is bound to the framework. Thus, the Ir/Ni ratio in the precursor's solution is kept in the postfunctionalized material. Moreover, FT-IR, ^{13}C NMR-CPMAS, PXRD, TGA, and FE-SEM performed on **Ir,Ni@Phen-COF** did not show any significant differences between the pristine and metallated **Phen-COF** (see Supporting Information).

The energy-dispersive X-ray (SEM−EDX) mapping images showed the presence of homogeneously distributed C, N, Ir, Ni, Cl, and F atoms in the framework (see Figure S16 in Supporting Information). This result is in accordance with the X-ray photoelectron spectroscopy (XPS) analysis results of the bimetallated material (Figures S24 and S25 of Supporting Information). The binding energy of the Ni 2p band at 855.9 eV corresponds to Ni(II) species, which is close to that of the $NiCl_2$(bpy) complex,[26,34] suggesting the coordination of Ni to the phenanthroline ligands present in the framework. The two peaks located at 62.2 (Ir $4f_{7/2}$) and 65.3 (Ir $4f_{5/2}$) eV are indicative of octahedral Ir(III) polypyridyl species coordinated to both C,N and N,N bidentate ligands,[35,36] which is consistent with the proposed expected coordination of Ir complexes to the phenanthroline ligands of the framework, as can be seen in Figure 1. The peak at 688 eV is assigned to fluorine (F 1s) present in the ligands of the Ir complex.[35] Furthermore, the N 1s signal centered at 399.1 eV is similar to the observed features for related materials containing pyridyl and iminic nitrogen atoms reported in the literature.[37] Interestingly, the presence of Ir and Ni centers has a significant impact on the N 1s XPS features. While the signals observed in the pristine material are conserved, also electrons at lower energies are detected (Figure S26 of Supporting Information). According to previous reports,[37] pyridinic N atoms are observed at lower energies than the iminic ones. Therefore, this observation indicates that N-phenanthroline atoms are affected by the presence of metal centers. Thus, these data are consistent with the coordination of phenanthroline units to Ni and Ir fragments.

Transmission electron microscopy (TEM) of **Ir,Ni@Phen-COF** confirmed the absence of inorganic nanoparticles (see Supporting Information, Figure S44, left). **Ir,Ni@Phen-COF** conserved the porosity with a S_{BET} of 432 m^2/g (see Supporting Information, Figure S17). The pore size distribution analysis showed values of 13.4 and 15.6 Å (Figure S18).

With respect to the optical properties of **Ir,Ni@Phen-COF**, DRS unveiled a slight increase of the visible absorption of this material in comparison with the pristine one (Figure S20, Supporting Information). This observation is translated into a decrease in the band gap of the material, which changes from 2.56 eV in the pristine material to 2.29 eV in the metallated one. Moreover, the fluorescence emission spectra showed again a broad emission band at the same wavelengths than that observed for the pristine material. However, also a sharp emission at 442 nm becomes the maximum intensity signal in the spectrum (Figure S21). Furthermore, electrochemical features of the organic material mask the expected signals for the metal centers (Figure S22). As a consequence, no significant differences between pristine and metallated materials are observed by cyclic voltammetry, and the valence band value was determined to be −5.29 eV (see Figure 3).[38] Considering that only the bimetallated material is active in the catalytic process (see below), it is worth noting that properties determined by electrochemical measurements are not relevant for such activity.

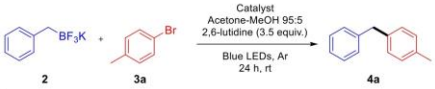
The role of phenanthroline was furtherly proved by comparing the metal uptake of **Phen-COF** with that of a well-known layered imine-based COF without coordinating units. This imine-based COF has been previously studied in the incorporation of metal centers for catalysis, such as Pd(II).[12] These materials (**Phen-COF** and **Crystalline Laminar-COF**) were incubated under the same specific reaction conditions in the presence of Ir and Ni metal precursors. Remarkably, very low quantities of both metal centers were found after TXRF analyses (<0.1%), using the COF without phenanthroline fragments (see Supporting Information, Figure S40). It is worth noting that the procedure used in these essays includes an exhaustive overnight washing by Soxhlet extraction. This treatment can wash out molecular metallic species that could interact weakly with the COF structure as a result of supramolecular interactions[39] or through coordination to the iminic nitrogens.[40] Therefore, strong metal−phenanthroline interactions resulting from the chelating effect stabilizes the metalation of the COF structure, even after exhaustive washing. As a consequence, a robust heterogeneous catalytic system is achieved by using **Phen-COF** as a porous platform, in which the metallic sites will be permanently immobilized over the whole catalytic procedure.

Additionally, this metalation process was repeated forming the mono-metallated **Ni@Phen-COF** and **Ir@Phen-COF** with a Ir and Ni loading of 3.9 and 2.9% in weight, respectively (see Supporting Information, Figures S31 and S37). Remarkably, these values are similar to those found for **Ir,Ni@Phen-COF**, making them good materials to be used as control in catalytic experiments for comparison purposes (*vide infra*).

2.3. Catalytic Activity. The catalytic performance of **Ir,Ni@Phen-COF** was initially evaluated studying as a model reaction the light-mediated cross-coupling between potassium benzyltrifluoroborate and 4-bromotoluene, which was reported using an homogeneous catalytic system by Molander and co-workers.[7] To our delight, bimetallated **Ir,Ni@Phen-COF** effectively catalyzed this reaction, reaching 90% conversion under blue light irradiation (Table 1, entry 1; see optimization in Table S2 of Supporting Information). As control experiments, we evaluated the performance of the pristine **Phen-COF** (Table 1, entry 2). In addition, we also carried out the reaction in the absence of any catalyst or under dark conditions (Table 1, entries 3 and 4). In the three cases, we observed negligible conversion. Moreover, the use of the **Post-Functionalized-Crystalline Laminar-COF** with an extremely

https://doi.org/10.1021/acscatal.1c03634
ACS Catal. 2021, 11, 12344−12354

Table 1. Experiments for the Light-Mediated Cross-Coupling between Potassium Benzyltrifluoroborates and Aryl Bromides[a]



2 3a 4a

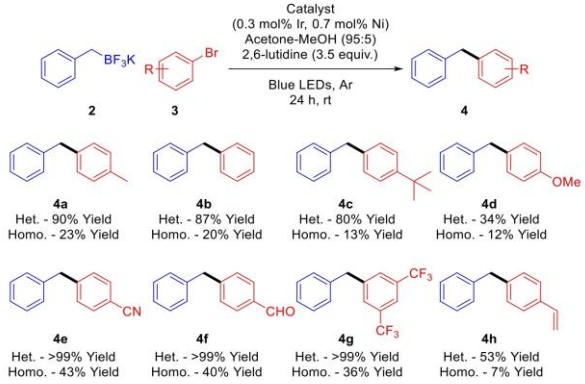
entry	catalyst	yield (%)[b]	TON (Ir/Ni)
1	**Ir,Ni@Phen-COF** (1.2 mg, 4.0% Ir, 2.8% Ni)	90	270/118
2	**Phen-COF** (1.2 mg)	0	
3	No Catalyst	0	
4	**Ir,Ni@Phen-COF** (1.2 mg) (dark)	0	
5	**PF−Crystalline Laminar COF** (1.2 mg)	0	
6	**Ni@Phen-COF** (1.2 mg)	0	
7	**Ir@Phen-COF** (1.2 mg)	0	
8	**Ni@Phen-COF** (0.6 mg) **Ir@Phen-COF** (0.6 mg)	0	
9	$[Ir(dF(CF_3)ppy)_2(bpy)]PF_6$ (0.3 mol %) $[NiCl_2(phen)]$ (0.7 mol %)	23	69/30
10	**Ir,Ni@Phen-COF** (1.2 mg, 7.0% Ir, 4.2% Ni)	87	149/76
11	**Ir,Ni@Phen-COF** (1.2 mg, 2.0% Ir, 1.4% Ni)	25	150/66
12	**Ir,Ni@Phen-COF** (1.2 mg, 2.2% Ir, 2.8% Ni)	42	229/55
13	**Ir,Ni@Phen-COF** (1.2 mg, 9.0% Ir, 2.8% Ni)	46	61/60

[a]The reaction was carried out using **2a** (0.15 mmol), **3a** (0.075 mmol), 2,6-lutidine (0.26 mmol), the corresponding catalyst, and 1 mL of solvent under an Ar atmosphere and blue light irradiation (blue LEDs, 23 W, 450 nm). [b]The yield was determined by ^{1}H NMR using nitromethane as the internal standard.

low content of Ni showed no conversion (Table 1, entry 5). In order to disclose the effect of having a heterogeneous system that included both Ni and Ir centers in the same material, we tried the reaction using the mono-metallated **Ni@Phen-COF** or **Ir@Phen-COF**, observing zero conversion in both cases (Table 1, entries 6 and 7). In the case of **Ni@Phen-COF**, it is worth mentioning that no product formation was observed, due to the lack of the photocatalytic unit. Therefore, the Ir center is required to generate the desired product. Nevertheless, when **Ni@Phen-COF** and **Ir@Phen-COF** were mixed in the same reaction medium, the photocatalytic process did not result in any product either (Table 1, entry 8). These observations are indicative of the requirements for the appropriate cooperativity in dual heterogeneous photocatalysis. In fact, these results account for a mechanism implying very reactive radical intermediates, which is characteristic of dual catalysis. Otherwise, in the reported molecular Ir/Ni dual catalysis in solution, their interplay depends on concentration and diffusion of active intermediates and catalysts. Thus, despite interesting activities have been reported in homogenous systems, the variable proximity in solution of catalytic sites can limits their efficiency. Design of heterobimetallic materials fixes the proximity between Ir and Ni centers, optimizing their cooperativity, which represents an advantage of the heterogeneous system with respect to the homogeneous one.

To assess the advantage of the bimetallated COF *versus* a mixture of comparable homogeneous catalysts, we tested the performance of the molecular version of our catalytic system. To this end, we studied the reaction using as catalysts $[Ir(dF(CF_3)ppy)_2(bpy)]PF_6$ and $[NiCl_2(phen)]$ in the catalytic loadings analogous to the Ni and Ir contents in **Ir,Ni@Phen-COF** (0.7 and 0.3 mol %, respectively). Remarkably, when the homogeneously catalyzed reaction was performed, the reaction reached 23% conversion (Table 1, entry 9), while almost full conversion was achieved using the bimetallated material under comparable conditions. This observation points out the limitation of the homogeneous system, which is probably due to the formation of unreactive aggregated Ni/NiO particles.[9] Accordingly, after one catalytic run, it was observed that a dark solid is formed. Finally, we also studied the influence of metal-loading on the catalytic outcome. For this purpose, maintaining the 2:1 molar ratio between Ni and

Scheme 2. Scope of Light-Mediated Cross-Coupling between Potassium Benzyltrifluoroborates and Aryl Bromides[a]



[a]The heterogeneously catalyzed reaction (Het.) was performed using **Ir,Ni@Phen-COF** as the catalyst. The homogeneously catalyzed reaction (Homo.) was performed using $[Ir(dF(CF3)ppy)_2(bpy)]PF_6$ and $[NiCl_2(phen)]$ as catalysts. The yields were determined by ^{1}H NMR using nitromethane as the internal standard

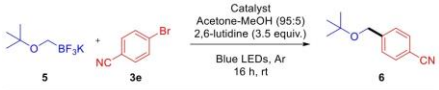
https://doi.org/10.1021/acscatal.1c03634
ACS Catal. 2021, 11, 12344−12354

Ir centers, we obtained two other different materials: one by doubling and the other by halving the amount of metal precursors employed in the postfunctionalization stage. Under the same conditions, both materials did not improve the yields observed for the initial **Ir,Ni@Phen-COF** (see Table 1, entries 10 and 11, and Table S3 of Supporting Information). The optimal Ni/Ir ratio found was 2:1 because other proportions (such as 4:1 and 1:1) gave worse yields and TONs (see Table 1, entries 12 and 13, and Table S3 of Supporting Information).

The applicability of our heterogeneous system has been also evaluated for a variety of aryl bromides, allowing not only the introduction of several electron withdrawing or electron donating groups, but also more hindered or even with olefinic substituents. Thus, eight different unsymmetrical diarylmethanes were isolated from moderate to good yields applying this heterogeneous system. In all the studied cases, the observed catalytic activity for **Ir,Ni@Phen-COF** was, at least, double that the observed for the homogenously catalyzed version (Scheme 2).

In order to further evaluate the scope of this dual heterogeneous catalytic system, we explored the use of other radical precursors of different nature. Therefore, we decided to substitute potassium benzyltrifluoroborate by *tert*-butoxytrifluoroborate, from which radical formation is thermodynamically slightly less favored.[41] Under the same reaction conditions, the photocatalytic cross-coupling between this substrate and 4-bromobenzonitrile was effectively performed, obtaining 76% of yield of product 6 (Table 2, entry 1).

Table 2. Experiments for the Light-Mediated Cross-Coupling between Potassium *tert*-Butyltrifluoroborate and Aryl Bromides[a]



5 3e 6

entry	catalyst	NMR yield (%)[b]
1	**Ir,Ni@Phen-COF** (1.2 mg)	76
2	**Phen-COF** (1.2 mg)	0
3	No Catalyst	0
4	**Ir,Ni@Phen-COF** (1.2 mg) (dark)	0
5	**Ni@Phen-COF** (1.2 mg)	0
6	**Ir@Phen-COF** (1.2 mg)	0
7	**Ni@Phen-COF** (0.6 mg) + **Ir@Phen-COF** (0.6 mg)	0
8	$[Ir(dF(CF_3)ppy)_2(bpy)]PF_6$ (0.3 mol %) + $[NiCl_2(phen)]$ (0.7 mol %)	12

[a]The reaction was carried out using **5** (0.15 mmol), **3e** (0.075 mmol), 2,6-lutidine (0.26 mmol), the corresponding catalyst, and 1 mL of solvent under an Ar atmosphere and blue light irradiation (blue LEDs, 450 nm). [b]The yield was determined by ^{1}H NMR using nitromethane as the internal standard.

However, the homogeneously catalyzed reaction only achieved 12% of yield under the same reaction conditions (Table 2, entry 8). For this reaction, it was impossible to reach any conversion when the reaction was carried out in absence of a catalyst, or by the monometallic functionalized COFs, or when both monometallic materials were mixed in the same reaction medium (Table 2, entries 3 to 7).

Another interesting type of reagents that can trigger photomediated cross-couplings are organic silicates. These substrates can offer some advantages in comparison with organic potassium trifluoroborates, such as avoiding byproducts, better solubility, and easier generation of unstabilized primary radicals because their redox potential is lower.[42] Therefore, we performed the light-mediated cross-coupling between organic silicate **7** and 4-bromobenzonitrile under typical reaction conditions and using **Ir,Ni@Phen-COF** as a heterogeneous photocatalyst. As a result, the reaction reached 92% of yield after 14 h of irradiation at room temperature (Table 3, entry 1). Control experiments showed again that

Table 3. Control Experiments for the Light-Mediated Cross-Coupling between Organic Silicates and Aryl Bromides[a]



7 3e 8

entry	catalyst	NMR yield (%)[b]
1	**Ir,Ni@Phen-COF** (1.2 mg)	92
2	**Phen-COF** (1.2 mg)	0
3	No Catalyst	0
4	**Ir,Ni@Phen-COF** (1.2 mg) (dark)	0
5	**Ni@Phen-COF** (1.2 mg)	0
6	**Ir@Phen-COF** (1.2 mg)	0
7	**Ni@Phen-COF** (0.6 mg) + **Ir@Phen-COF** (0.6 mg)	0
8	$[Ir(dF(CF_3)ppy)_2(bpy)]PF_6$ (0.3 mol %) + $[NiCl_2(phen)]$ (0.7 mol %)	26

[a]The reaction was carried out using **7** (0.225 mmol), **3e** (0.15 mmol), the corresponding catalyst, and 3 mL of solvent under an Ar atmosphere and blue light irradiation (blue LEDs, 450 nm). [b]The yield was determined by ^{1}H NMR using nitromethane as the internal standard.

proximity and cooperativity between immobilized Ir and Ni complexes into **Phen-COF** were indispensable for triggering this organic transformation (Table 3, entries 2 to 7). In addition, the homogeneously catalyzed reaction only gave 26% under analogous conditions (Table 3, entry 8).

Alternatively, proline derivatives can also be used as radical precursors. The photocatalytic decarboxylative arylation of alkyl carboxylic acids is interesting from the chemical point of view, because of the easy accessibility to these radical precursors and the potential interest of heterocyclic chemistry.[43] Thus, we performed the photocatalytic cross-coupling between *N*-protected proline **9** and 4-bromobenzonitrile under reaction conditions previously reported for a homogeneous system (see Supporting Information for further details).[43] In this case, acetonitrile was employed as a solvent and cesium carbonate as a base to trigger the deprotonation of the corresponding α-amino acid derivative. In this case, the reaction catalyzed by **Ir,Ni@Phen-COF** reached 86% of isolated yield of the corresponding cross-coupled product **10** (Table 4, entry 1), while the homogeneous version was stalled at 58% (Table 4, entry 8). No background (Table 4, entries 2 and 3) or monometallic-catalyzed reactions (Table 4, entries 5 and 6) gave rise to the desired product, neither when both

https://doi.org/10.1021/acscatal.1c03634
ACS Catal. 2021, 11, 12344−12354

Table 4. Control Experiments for the Light-Mediated Decarboxylative Arylation of Alkyl Carboxylic Acids.[a]



entry	catalyst	NMR yield (%)[b]
1	**Ir,Ni@Phen-COF** (1.2 mg)	86
2	**Phen-COF** (1.2 mg)	0
3	No Catalyst	0
4	**Ir,Ni@Phen-COF** (1.2 mg) (dark)	0
5	**Ni@Phen-COF** (1.2 mg)	0
6	**Ir@Phen-COF** (1.2 mg)	0
7	**Ni@Phen-COF** (0.6 mg) **Ir@Phen-COF** (0.6 mg)	0
8	$[Ir(dF(CF_3)ppy)_2(bpy)]PF_6$ (0.3 mol %) $[NiCl_2(phen)]$ (0.7 mol %)	58

[a]The reaction was carried out using **6** (0.225 mmol), **3e** (0.15 mmol), caesium carbonate (0.225 mmol), the corresponding catalyst, and 4 mL of solvent under an Ar atmosphere and blue light irradiation (blue LEDs, 450 nm). [b]The yield was determined by ^{1}H NMR using nitromethane as the internal standard.

monometallic-functionalized COFs were reunited in the same reaction container (Table 4, entry 7).

The main observation of this work is that a heterogeneous system has a significantly higher catalytic performance than the analogous homogeneous counterparts. From the data found in the literature,[7,41−43] it can be concluded that the homogeneous system used in this work shows comparable activities to the previously published systems (see Table S3, Supporting Information). Furthermore, our heterogeneous **Ir,Ni@Phen-COF** catalyst allowed achieving significantly higher TONs than any of the homogeneous catalytic versions.

2.4. Leaching Tests and Recyclability. An important requirement of heterogeneous functionalized materials consists of avoiding the leaching processes of molecular active fragments into the reaction solution.[44] This is important because one of the most interesting advantages of heterogeneous catalysis is the easy separation of the catalyst (by a simple filtration) preventing the release of any spurious species into the pure fractions of products. In our case, under the experimental conditions of the four studied reactions, we discarded leaching processes through filtration of the catalyst after one catalytic run and analysis of the supernatant by ICP measurements. Analytical data revealed that no metal species were found in the solution after simple filtration of the catalyst. In addition, when the filtered solution was used in the presence of additional amounts of the different starting materials, we found no reactivity at all, indicating that no catalytic species were leached into the reaction media.

Moreover, to prove the recyclability of our catalyst, **Ir,Ni@Phen-COF** was recovered by centrifugation, confirming the preservation of its chemical identity by FT-IR (Figure 4). Crystallinity was retrieved after simple solvothermal treatment of the material (Figure 4). In addition, TEM reveals that

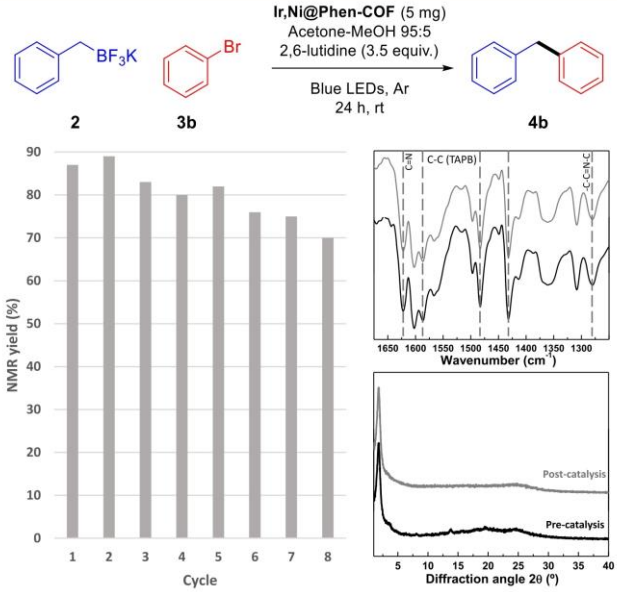


Figure 4. Recycling of **Ir,Ni@Phen-COF** as a heterogeneous photocatalyst for light-mediated cross-coupling of potassium benzyltrifluoroborates and bromobenzene.

https://doi.org/10.1021/acscatal.1c03634
ACS Catal. 2021, 11, 12344−12354

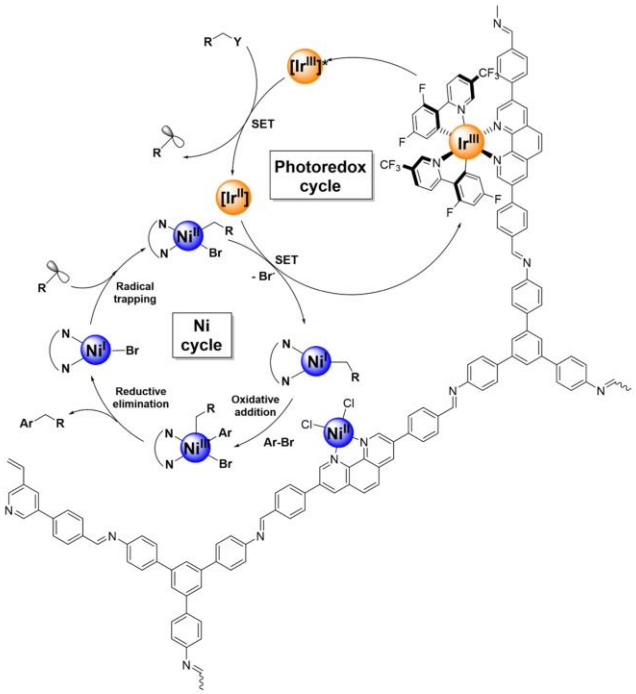


Figure 5. Mechanism of the transformations carried out in this work using **Ir,Ni@Phen-COF** as a heterogeneous dual catalytic system.

nanoparticles were not formed during the catalytic process (see Supporting Information, Figure S42). Moreover, this material can be used for eight consecutive catalytic cycles with minor loss of activity, generating 1 mmol (168 mg) of diphenylmethane **4b** using 5 mg of **Ir,Ni@Phen-COF** overall (Figure 4). In terms of TON, this catalyst showed after the eight runs 925 TON for Ir and 424 TON for Ni, confirming its sturdiness and recyclability. Finally, as a proof for the scalability of this system, we performed this reaction at 5 mmol scale, maintaining the catalyst loading at 5 mg. A yield of 79% was reached after 96 h of irradiation, which implies 3800 TON for Ir and 1650 TON for Ni.

2.5. Mechanistic Considerations. The mechanism for dual catalytic systems closely related to this work has been previously considered using homogeneous species[7] and MOFs with similar coordinating units (Figure 5).[27] According to the available data, it is well established that Ir(III) species in the excited state is able to oxidize the radical precursor, which generates paramagnetic species that binds to a Ni(I) center through radical trapping. The corresponding Ni(II) center is reduced by the transient Ir(II) intermediate, regenerating the Ir photocatalyst and producing a Ni(I) species that can furtherly evolve through an oxidative addition by reaction with an aryl bromide. The final product is generated by a reductive elimination process. Combination of emission and cyclic voltammetry measurements performed for $[Ir(dF(CF_3)ppy)_2(bpy)]PF_6$ indicates that this species has a reduction potential at an excited state of +1.32 V versus SCE (see Supporting Information, Figure S1). This potential demonstrates that oxidation of the radical precursors employed in this work (E_{ox} from −0.87 to −1.11 V vs SCE)[7,41−43,45] is plausible. Furthermore, comparison of measured reduction potential of the $[NiCl_2(phen)]$ complex with the data obtained using $[Ir(dF(CF_3)ppy)_2(bpy)]PF_6$ indicates that Ir(II) + Ni(II) → Ir(III) + Ni(I) is thermodynamically feasible (see Supporting Information, Figure S1). Therefore, our data are fully consistent with the mechanistic scenario previously proposed for Ir/Ni dual catalytic systems.

3. CONCLUSIONS

The predesign, synthesis, and characterization of a new phenanthroline-containing imine-based layered COF have been performed in this work. This new material was postfunctionalized with Ir and Ni metal complexes in order to obtain a heterogeneous photoredox nickel dual catalytic system. In this unprecedented COF, the phenanthroline group plays a key role in stabilizing the coordination of the metal centers. The obtained **Ir,Ni@Phen-COF** presents high catalytic activity toward photocatalytic cross-couplings between aryl bromides and four different radical precursors (*N*-

https://doi.org/10.1021/acscatal.1c03634
ACS Catal. 2021, 11, 12344−12354

protected proline, organic alkyl silicates, and potassium benzyl- and alkoxy-trifluoroborates). The comparison between our heterogeneous system and its homogeneous analogues and those reported in the literature makes clear the superiority of the newly obtained catalytic material in terms of activity and stability for a variety of substrates. The different nature of the catalytic systems essayed brings out the good versatility of the new material synthesized. In addition, the sturdiness and the stability of the COF was studied by discarding leaching processes. Recyclability experiments showed that approximatively 1000 TONs for the Ir and more than 400 TONs for the Ni can be reached.

■ ASSOCIATED CONTENT

Supporting Information

. The Supporting Information is available free of charge at https://pubs.acs.org/doi/10.1021/acscatal.1c03634.

Materials and methods information; characterization of the materials and compounds; and additional experimental data (PDF)

■ AUTHOR INFORMATION

Corresponding Authors

José Alemán − *Institute for Advanced Research in Chemical Sciences (IAdChem) and Organic Chemistry Department, Módulo 1, Universidad Autónoma de Madrid, 28049 Madrid, Spain;* orcid.org/0000-0003-0164-1777; Email: ruben.mas@uam.es

Rubén Mas-Ballesté − *Inorganic Chemistry Department, Módulo 7 and Organic Chemistry Department, Módulo 1, Universidad Autónoma de Madrid, 28049 Madrid, Spain;* orcid.org/0000-0003-1988-8700; Email: jose.aleman@uam.es

Authors

Alberto López-Magano − *Inorganic Chemistry Department, Módulo 7, Universidad Autónoma de Madrid, 28049 Madrid, Spain*

Borja Ortín-Rubio − *Catalan Institute of Nanoscience and Nanotechnology (ICN2), CSIC and The Barcelona Institute of Science and Technology, 08193 Barcelona, Spain;* orcid.org/0000-0002-0533-3635

Inhar Imaz − *Catalan Institute of Nanoscience and Nanotechnology (ICN2), CSIC and The Barcelona Institute of Science and Technology, 08193 Barcelona, Spain;* orcid.org/0000-0002-0278-1141

Daniel Maspoch − *Catalan Institute of Nanoscience and Nanotechnology (ICN2), CSIC and The Barcelona Institute of Science and Technology, 08193 Barcelona, Spain; Institució Catalana de Recerca y Estudis Avançats (ICREA), 08010 Barcelona, Spain;* orcid.org/0000-0003-1325-9161

Complete contact information is available at: https://pubs.acs.org/10.1021/acscatal.1c03634

Author Contributions

This manuscript was written through contributions of all authors. All authors have given approval to the final version of the manuscript.

Notes

The authors declare no competing financial interest.

■ ACKNOWLEDGMENTS

Financial support was provided by the European Research Council (ERC-CoG, contract no. 647550), the Spanish Government (RTI2018-095038-B-I00, PID2019-110637RB-I00), "Comunidad de Madrid", and European Structural Funds (S2018/NMT-4367). A.L.M. thanks to UAM for FPI-UAM predoctoral fellowship. ICN2 is supported by the Severo Ochoa programme from the Spanish MINECO (Grant No. SEV-2017-0706).

■ REFERENCES

(1) Johansson Seechurn, C. C. C.; Kitching, M. O.; Colacot, T. J.; Snieckus, V. Palladium-Catalyzed Cross-Coupling: A Historical Contextual Perspective to the 2010 Nobel Prize. *Angew. Chem., Int. Ed.* **2012**, *51*, 5062−5085.

(2) Campeau, L.-C.; Hazari, N. Cross-Coupling and Related Reactions: Connecting Past Success to the Development of New Reactions for the Future. *Organometallics* **2019**, *38*, 3−35.

(3) Ogba, O. M.; Warner, N. C.; O'Leary, D. J.; Grubbs, R. H. Recent Advances in Ruthenium-Based Olefin Metathesis. *Chem. Soc. Rev.* **2018**, *47*, 4510−4544.

(4) Casey, C. P. 2005 Nobel Prize in Chemistry. Development of the Olefin Metathesis Method in Organic Synthesis. *J. Chem. Educ.* **2006**, *83*, 192.

(5) Milligan, J. A.; Phelan, J. P.; Badir, S. O.; Molander, G. A. Alkyl Carbon−Carbon Bond Formation by Nickel/Photoredox Cross-Coupling. *Angew. Chem., Int. Ed.* **2019**, *58*, 6152−6163.

(6) Twilton, J.; Le, C.; Zhang, P.; Shaw, M. H.; Evans, R. W.; MacMillan, D. W. C. The Merger of Transition Metal and Photocatalysis. *Nat. Rev. Chem.* **2017**, *1*, 52.

(7) Tellis, J. C.; Primer, D. N.; Molander, G. A. Single-Electron Transmetalation in Organoboron Cross-Coupling by Photoredox/Nickel Dual Catalysis. *Science* **2014**, *345*, 433−436.

(8) Price Pressures on Metals. *Nat. Catal.* **2019**, *2* (), 735. DOI: 10.1038/s41929-019-0359-7.

(9) Gisbertz, S.; Reischauer, S.; Pieber, B. Overcoming Limitations in Dual Photoredox/Nickel-Catalysed C−N Cross-Couplings Due to Catalyst Deactivation. *Nat. Catal.* **2020**, *3*, 611−620.

(10) López-Magano, A.; Platero-Prats, A. E.; Cabrera, S.; Mas-Ballesté, R.; Alemán, J. Incorporation of Photocatalytic Pt(II) Complexes into Imine-Based Layered Covalent Organic Frameworks (COFs) through Monomer Truncation Strategy. *Appl. Catal., B* **2020**, *272*, 119027.

(11) Dumeignil, F.; Paul, J.-F.; Paul, S. Heterogeneous Catalysis with Renewed Attention: Principles, Theories, and Concepts. *J. Chem. Educ.* **2017**, *94*, 675−689.

(12) Jiménez-Almarza, A.; López-Magano, A.; Marzo, L.; Cabrera, S.; Mas-Ballesté, R.; Alemán, J. Imine-Based Covalent Organic Frameworks as Photocatalysts for Metal Free Oxidation Processes under Visible Light Conditions. *ChemCatChem* **2019**, *11*, 4916−4922.

(13) Sharma, R. K.; Yadav, P.; Yadav, M.; Gupta, R.; Rana, P.; Srivastava, A.; Zbořil, R.; Varma, R. S.; Antonietti, M.; Gawande, M. B. Recent Development of Covalent Organic Frameworks (COFs): Synthesis and Catalytic (Organic-Electro-Photo) Applications. *Mater. Horiz.* **2020**, *7*, 411−454.

(14) Côté, A. P.; Benin, A. I.; Ockwig, N. W.; O'Keeffe, M.; Matzger, A. J.; Yaghi, O. M. Porous, Crystalline, Covalent Organic Frameworks. *Science* **2005**, *310*, 1166−1170.

(15) Uribe-Romo, F. J.; Hunt, J. R.; Furukawa, H.; Klöck, C.; O'Keeffe, M.; Yaghi, O. M. A Crystalline Imine-Linked 3-D Porous Covalent Organic Framework. *J. Am. Chem. Soc.* **2009**, *131*, 4570−4571.

(16) Segura, J. L.; Mancheño, M. J.; Zamora, F. Covalent Organic Frameworks Based on Schiff-Base Chemistry: Synthesis, Properties and Potential Applications. *Chem. Soc. Rev.* **2016**, *45*, 5635−5671.

(17) Segura, J. L.; Royuela, S.; Mar Ramos, M. Post-Synthetic Modification of Covalent Organic Frameworks. *Chem. Soc. Rev.* **2019**, *48*, 3903−3945.
(18) Johnson, E. M.; Haiges, R.; Marinescu, S. C. Covalent-Organic Frameworks Composed of Rhenium Bipyridine and Metal Porphyrins: Designing Heterobimetallic Frameworks with Two Distinct Metal Sites. *ACS Appl. Mater. Interfaces* **2018**, *10*, 37919−37927.
(19) Li, L.-H.; Feng, X.-L.; Cui, X.-H.; Ma, Y.-X.; Ding, S.-Y.; Wang, W. Salen-Based Covalent Organic Framework. *J. Am. Chem. Soc.* **2017**, *139*, 6042−6045.
(20) Lin, G.; Ding, H.; Chen, R.; Peng, Z.; Wang, B.; Wang, C. 3D Porphyrin-Based Covalent Organic Frameworks. *J. Am. Chem. Soc.* **2017**, *139*, 8705−8709.
(21) Shi, Y.; Zhang, X.; Liu, H.; Han, J.; Yang, Z.; Gu, L.; Tang, Z. Metalation of Catechol-Functionalized Defective Covalent Organic Frameworks for Lewis Acid Catalysis. *Small* **2020**, *16*, 2001998.
(22) Leng, W.; Peng, Y.; Zhang, J.; Lu, H.; Feng, X.; Ge, R.; Dong, B.; Wang, B.; Hu, X.; Gao, Y. Sophisticated Design of Covalent Organic Frameworks with Controllable Bimetallic Docking for a Cascade Reaction. *Chem.—Eur. J.* **2016**, *22*, 9087−9091.
(23) Leng, W.; Ge, R.; Dong, B.; Wang, C.; Gao, Y. Bimetallic Docked Covalent Organic Frameworks with High Catalytic Performance towards Tandem Reactions. *RSC Adv.* **2016**, *6*, 37403−37406.
(24) Romero-Muñiz, I.; Mavrandonakis, A.; Albacete, P.; Vega, A.; Briois, V.; Zamora, F.; Platero-Prats, A. E. Unveiling the Local Structure of Palladium Loaded into Imine-Linked Layered Covalent Organic Frameworks for Cross-Coupling Catalysis. *Angew. Chem., Int. Ed.* **2020**, *59*, 13013−13020.
(25) Dong, J.; Han, X.; Liu, Y.; Li, H.; Cui, Y. Metal−Covalent Organic Frameworks (MCOFs): A Bridge Between Metal−Organic Frameworks and Covalent Organic Frameworks. *Angew. Chem., Int. Ed.* **2020**, *59*, 13722−13733.
(26) Chen, H.; Liu, W.; Laemont, A.; Krishnaraj, C.; Feng, X.; Rohman, F.; Meledina, M.; zhang, Q.; Van Deun, R.; Leus, K.; Van Der Voort, P. A Visible-Light-Harvesting Covalent Organic Framework Bearing Single Nickel Sites as a Highly Efficient Sulfur-Carbon Cross-Coupling Dual Catalyst. *Angew. Chem., Int. Ed.* **2021**, *60*, 10820−10827.
(27) Zhu, Y. Y.; Lan, G.; Fan, Y.; Veroneau, S. S.; Song, Y.; Micheroni, D.; Lin, W. Merging Photoredox and Organometallic Catalysts in a Metal−Organic Framework Significantly Boosts Photocatalytic Activities. *Angew. Chem., Int. Ed.* **2018**, *57*, 14090−14094.
(28) Lan, G.; Quan, Y.; Wang, M.; Nash, G. T.; You, E.; Song, Y.; Veroneau, S. S.; Jiang, X.; Lin, W. Metal−Organic Layers as Multifunctional Two-Dimensional Nanomaterials for Enhanced Photoredox Catalysis. *J. Am. Chem. Soc.* **2019**, *141*, 15767−15772.
(29) Pan, Y.; Zhang, N.; Liu, C.-H.; Fan, S.; Guo, S.; Zhang, Z.-M.; Zhu, Y.-Y. Boosting Photocatalytic Activities for Organic Transformations through Merging Photocatalyst and Transition-Metal Catalyst in Flexible Polymers. *ACS Catal.* **2020**, *10*, 11758−11767.
(30) Fang, Q.; Zhuang, Z.; Gu, S.; Kaspar, R. B.; Zheng, J.; Wang, J.; Qiu, S.; Yan, Y. Designed Synthesis of Large-Pore Crystalline Polyimide Covalent Organic Frameworks. *Nat. Commun.* **2014**, *5*, 4503.
(31) Oderinde, M. S.; Johannes, J. W. Practical Syntheses of [2,2′-Bipyridine]Bis[3,5-Difluoro-2-[5-(Trifluoromethyl)-2-Pyridinyl]-Phenyl]Iridium(III) Hexafluorophosphate, [Ir{dF(CF3)Ppy}2-(Bpy)]PF6 and [4,4′-Bis(Tert-Butyl)-2,2′-Bipyridine]Bis[3,5-Difluoro-2-[5-(Trifluoromethyl)-2-Pyridinyl]Ph. *Org. Synth.* **2018**, *94*, 77−92.
(32) Rodríguez-San-Miguel, D.; Abrishamkar, A.; Navarro, J. A. R.; Rodriguez-Trujillo, R.; Amabilino, D. B.; Mas-Ballesté, R.; Zamora, F.; Puigmartí-Luis, J. Crystalline Fibres of a Covalent Organic Framework through Bottom-up Microfluidic Synthesis. *Chem. Commun.* **2016**, *52*, 9212−9215.
(33) Fernández-Ruiz, R.; von Bohlen, A.; Friedrich K, E. J.; Redrejo, M. J. Analysis of Coke Beverages by Total-Reflection X-Ray Fluorescence. *Spectrochim. Acta, Part B* **2018**, *145*, 99−106.
(34) Zhong, W.; Sa, R.; Li, L.; He, Y.; Li, L.; Bi, J.; Zhuang, Z.; Yu, Y.; Zou, Z. A Covalent Organic Framework Bearing Single Ni Sites as a Synergistic Photocatalyst for Selective Photoreduction of CO2 to CO. *J. Am. Chem. Soc.* **2019**, *141*, 7615−7621.
(35) Xu, Z.-Y.; Luo, Y.; Zhang, D.-W.; Wang, H.; Sun, X.-W.; Li, Z.-T. Iridium Complex-Linked Porous Organic Polymers for Recyclable, Broad-Scope Photocatalysis of Organic Transformations. *Green Chem.* **2020**, *22*, 136−143.
(36) Liang, H.-P.; Chen, Q.; Han, B.-H. Cationic Polycarbazole Networks as Visible-Light Heterogeneous Photocatalysts for Oxidative Organic Transformations. *ACS Catal.* **2018**, *8*, 5313−5322.
(37) Lu, H.; Ning, F.; Jin, R.; Teng, C.; Wang, Y.; Xi, K.; Zhou, D.; Xue, G. Two-Dimensional Covalent Organic Frameworks with Enhanced Aluminum Storage Properties. *ChemSusChem* **2020**, *13*, 3447−3454.
(38) Pommerehne, J.; Vestweber, H.; Guss, W.; Mahrt, R. F.; Bässler, H.; Porsch, M.; Daub, J. Efficient Two Layer Leds on a Polymer Blend Basis. *Adv. Mater.* **1995**, *7*, 551−554.
(39) López-Magano, A.; Jiménez-Almarza, A.; Alemán, J.; Mas-Ballesté, R. Metal−Organic Frameworks (MOFs) and Covalent Organic Frameworks (COFs) Applied to Photocatalytic Organic Transformations. *Catalysts* **2020**, *10*, 720.
(40) Ding, S.-Y.; Gao, J.; Wang, Q.; Zhang, Y.; Song, W.-G.; Su, C.-Y.; Wang, W. Construction of Covalent Organic Framework for Catalysis: Pd/COF-LZU1 in Suzuki−Miyaura Coupling Reaction. *J. Am. Chem. Soc.* **2011**, *133*, 19816−19822.
(41) Karakaya, I.; Primer, D. N.; Molander, G. A. Photoredox Cross-Coupling: Ir/Ni Dual Catalysis for the Synthesis of Benzylic Ethers. *Org. Lett.* **2015**, *17*, 3294−3297.
(42) Lévêque, C.; Chenneberg, L.; Corcé, V.; Goddard, J.-P.; Ollivier, C.; Fensterbank, L. Primary Alkyl Bis-Catecholato Silicates in Dual Photoredox/Nickel Catalysis: Aryl- and Heteroaryl-Alkyl Cross Coupling Reactions. *Org. Chem. Front.* **2016**, *3*, 462−465.
(43) Zuo, Z.; Ahneman, D. T.; Chu, L.; Terrett, J. A.; Doyle, A. G.; MacMillan, D. W. C. Merging Photoredox with Nickel Catalysis: Coupling of α-Carboxyl sp3-Carbons with Aryl Halides. *Science* **2014**, *345*, 437−440.
(44) Yang, W.; Vogler, B.; Lei, Y.; Wu, T. Metallic Ion Leaching from Heterogeneous Catalysts: An Overlooked Effect in the Study of Catalytic Ozonation Processes. *Environ. Sci.: Water Res. Technol.* **2017**, *3*, 1143−1151.
(45) Nicewicz, D.; Roth, H.; Romero, N. Experimental and Calculated Electrochemical Potentials of Common Organic Molecules for Applications to Single-Electron Redox Chemistry. *Synlett* **2016**, *27*, 714−723.

https://doi.org/10.1021/acscatal.1c03634
ACS Catal. 2021, 11, 12344−12354

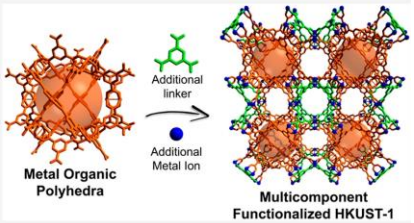
JACS
JOURNAL OF THE AMERICAN CHEMICAL SOCIETY
pubs.acs.org/JACS
Article

Multicomponent, Functionalized HKUST-1 Analogues Assembled via Reticulation of Prefabricated Metal−Organic Polyhedral Cavities

Akim Khobotov-Bakishev, Cornelia von Baeckmann, Borja Ortín-Rubio, Laura Hernández-López, Alba Cortés-Martínez, Jordi Martínez-Esaín, Felipe Gándara, Judith Juanhuix, Ana E. Platero-Prats, Jordi Faraudo, Arnau Carné-Sánchez,* and Daniel Maspoch*

Cite This: J. Am. Chem. Soc. 2022, 144, 15745−15753
Read Online
ACCESS | Metrics & More | Article Recommendations | Supporting Information

ABSTRACT: Metal−organic frameworks (MOFs) assembled from multiple building blocks exhibit greater chemical complexity and superior functionality in practical applications. Herein, we report a new approach based on using prefabricated cavities to design isoreticular multicomponent MOFs from a known parent MOF. We demonstrate this concept with the formation of multicomponent HKUST-1 analogues, using a prefabricated cavity that comprises a cuboctahedral Rh(II) metal−organic polyhedron functionalized with 24 carboxylic acid groups. The cavities are reticulated in three dimensions via Cu(II)-paddlewheel clusters and (functionalized) 1,3,5-benzenetricarboxylate linkers to form three- and four-component HKUST-1 analogues.



INTRODUCTION

The combination of multiple organic linkers and metal ions into multicomponent or multivariate metal−organic frameworks (MOFs) is a fruitful strategy to achieve greater chemical complexity in MOFs, expand the catalogue of MOFs accessible by synthesis, and optimize the use of MOFs for applications such as gas storage,[1] water harvesting,[2] and catalysis.[3] In these MOFs, complexity derives from the random or periodic arrangement of multiple organic and metallic functionalities into the same structure.[4] To date, strategies to design multicomponent or multivariate MOFs include bottom-up synthesis by using any of the following: distinct linkers that have identical backbones but differ in their respective side groups or isostructural clusters comprising different metal ions, to produce multivariate MOFs;[5,6] or structurally different linkers or metal clusters, to generate ordered multicomponent MOFs.[7−10] Alternatively, the complexity of parent MOF structures can be augmented through post-synthetic modification via covalent and coordination chemistry,[11,12] ligand installation,[13] and linker- or metal-exchange.[14]

Herein we propose a new approach to isoreticular, multicomponent MOFs by starting with a known MOF. Reticular chemistry enables the rational synthesis of MOFs through the connection of basic molecular building blocks (MBBs).[15,16] For example, the archetypical HKUST-1 is typically described as a 3,4-connected (3,4-c) network with an underlying **tbo** topology that is assembled from two MBBs: the 4-c Cu(II)-paddlewheel cluster and the 3-c 1,3,5-benzenetricarboxylate (btc) linker.[17] However, on a conceptual level, MOFs can also be seen as the product of connecting higher order structures[18,19] such as different cavities or metal−organic polyhedral (MOP)[20] units, whether directly or through additional, small MBBs.[21,22] Herein, we propose using MOPs as prefabricated cavities from which a parent MOF structure can be replicated, whereby its composition is changed.

Our strategy begins with a de-reticulation exercise in which a repetitive cavity of the parent MOF is identified. Following the example of HKUST-1, this enabled us to identify a repetitive cavity that defines a 24-c cuboctahedral MOP. Thus, we reasoned that the formation of the HKUST-1 structure would require the connection of these MOPs through the original 4-c Cu(II)-paddlewheel cluster and the 3-c btc. This leads to a change in the structural description of HKUST-1, from a binary 3,4-c structure that comprises one inorganic (Cu(II)-paddlewheel cluster) and one organic (btc) MBB to a tertiary 3,4,24-c structure that comprises these two MBBs and the 24-c MOP. We anticipated that this would enable use of three components in the synthesis of HKUST-1 that, if distinct, would occupy specific positions in the replicated structure, thereby generating ordered multicomponent MOFs isoreticular to HKUST-1. The basis of our approach is also supported

Received: June 12, 2022
Published: August 16, 2022



ACS Publications
© 2022 The Authors. Published by American Chemical Society

https://doi.org/10.1021/jacs.2c06131
J. Am. Chem. Soc. 2022, 144, 15745−15753

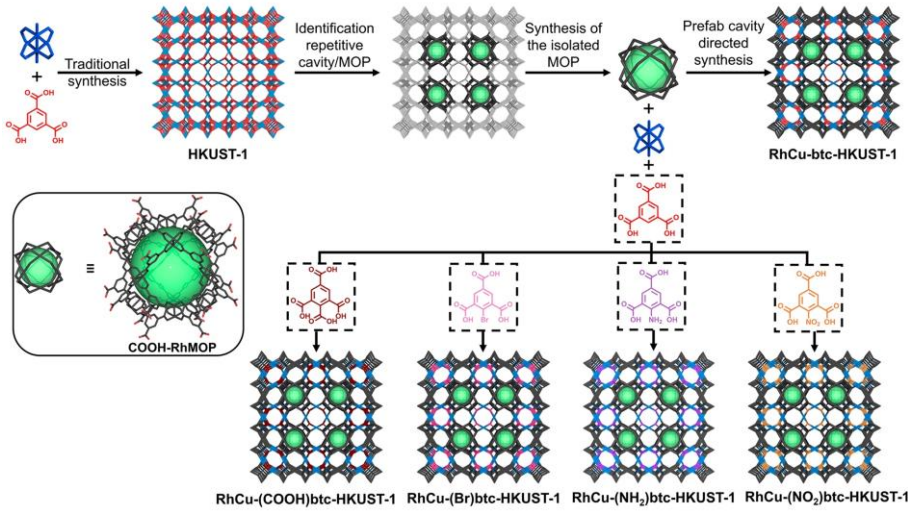


Figure 1. Schematic of the synthesis of three- and four-component HKUST-1 analogues using our design approach to multicomponent MOFs, based on the identification and exploitation of prefabricated cavities in the corresponding parent MOF.

by the supermolecular building block approach described by Eddaoudi et al., in which an *in situ*-synthesized[23,24] or pre-assembled[25] MOP is used as a highly connected node encoded with specific geometric and connectivity information to reduce the degrees of freedom of the network's constituents and direct their assembly toward a target highly connected structure. However, herein, we use MOPs in a different way. In the prefabricated directed synthesis, the MOP does not behave as an *in situ*-formed node in a network, but rather as a preformed tiling of the targeted network, one which dictates the arrangement of the metallic and organic MBBs around it to ultimately generate a structure that is not necessarily described as highly connected (in this case, HKUST-1). Thus, the work that we present here expands the utility of MOPs in MOF chemistry, thereby providing a new route to complex multicomponent networks.

■ RESULTS AND DISCUSSION

Prefabricated Cavity-Directed Synthesis of Multimetallic HKUST-1. We first applied our prefabricated cavity approach to HKUST-1 (Figure 1), choosing our previously reported Rh(II) cuboctahedral MOP functionalized with 24 carboxylic acid groups (hereafter named COOH-RhMOP) as the prefabricated cavity.[25,26] We selected COOH-RhMOP because of its high chemical stability[27] and its structural difference relative to its Cu(II) analogue, which would lead to pure HKUST-1. Using this MOP as a prefabricated cavity enabled us to replicate the structure of HKUST-1, thereby forming the isoreticular three-component RhCu-btc-HKUST-1 comprising COOH-RhMOPs, Cu(II)-paddlewheel clusters, and btc.

Using COOH-RhMOP as a prefabricated cavity in the synthesis of RhCu-btc-HKUST-1 requires the stoichiometric addition of the three MBBs: COOH-RhMOP, the Cu(II)-paddlewheel cluster, and btc. To determine this stoichiometry, we studied the connectivity of the three MBBs in the targeted structure (Figure 2). To mimic this structure, each COOH-RhMOP must be connected to six neighboring COOH-RhMOPs through 24 Cu(II)-paddlewheel clusters. In this connectivity, each COOH-RhMOP is bridged to a neighboring COOH-RhMOP via four Cu(II)-paddlewheel clusters (Figure 2, yellow inset). Each Cu(II)-paddlewheel cluster must then be connected to four other Cu(II) clusters, via coordination of two btc linkers to their two remaining adjacent positions (Figure 2, violet inset). Overall, this connectivity defines a Cu(II)-cluster/btc/COOH-RhMOP ratio of 12:8:1. This connectivity also defines the relative position of each metal ion within the HKUST-1 network. Thus, RhCu-btc-HKUST-1 would present two types of cuboctahedral cavities in its structure: the Rh(II)-based cavity that derives from the prefabricated cavity, and a mixed-metal cavity containing Cu(II) and Rh(II) ions generated upon the self-assembly reaction. These cavities alternate throughout the structure (Figure S1). This degree of control over the relative position of cavities that contain different functionalities within porous frameworks has only been demonstrated for mixed-cage porous solids, in which different MOPs are co-precipitated.[28−30]

We began the synthesis of RhCu-btc-HKUST-1, whose formula is $[COOH\text{-}RhMOP(Cu)_{24}(btc)_8]$, by heating a mixture of COOH-RhMOP with 24 mol equiv of $Cu(NO_3)_2{\cdot}3H_2O$ and 8 mol equiv of btc in *N*,*N*-dimethylformamide (DMF) at 85 °C for 1 day. The solvothermal reaction yielded a colloidal green dispersion. A green crystalline solid (yield: 78%; Figure 3a) was then isolated through centrifugation, washed with DMF, methanol, water, and acetone, and then dried at room temperature. Field emission scanning electron microscopy (FESEM) analysis of the green

https://doi.org/10.1021/jacs.2c06131
J. Am. Chem. Soc. 2022, 144, 15745−15753

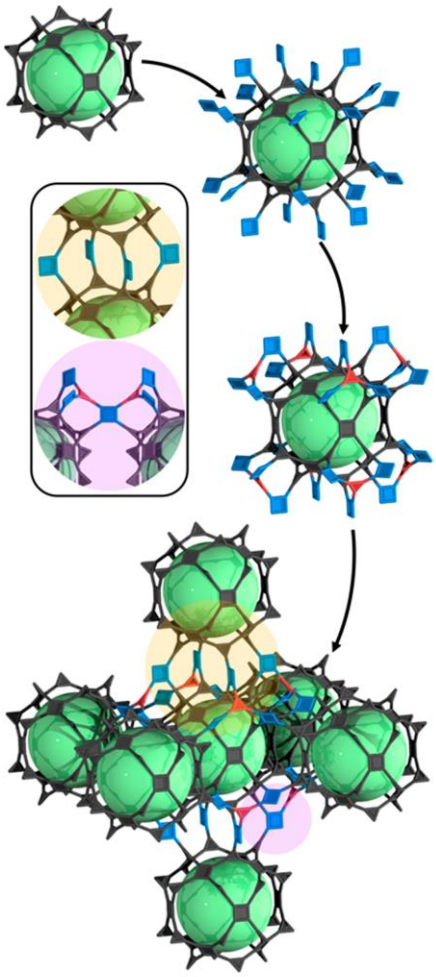


Figure 2. Schematic of the connectivity of COOH-RhMOPs (dark gray cages), Cu(II)-paddlewheel clusters (blue squares), and btc linkers (red triangles) to form RhCu-btc-HKUST-1. The inset details the connectivity between two COOH-RhMOPs.

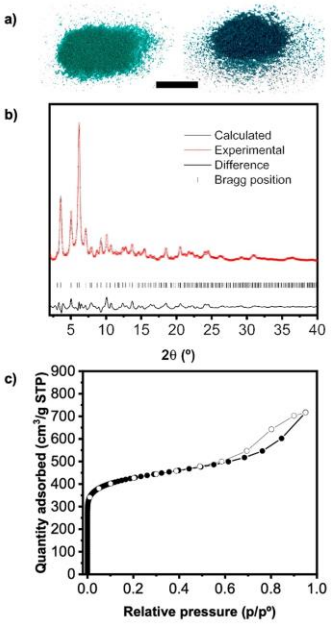


Figure 3. (a) Photographs of as-made (left) and activated (right) RhCu-btc-HKUST-1 powder. Scale bar: 1 cm. (b) Rietveld analysis of RhCu-btc-HKUST-1. (c) N_2-sorption isotherms for RhCu-btc-HKUST-1.

solid revealed the formation of a uniform sample comprising particles having an average size of 22 ± 3 nm (Figure S2). Energy-dispersive X-ray spectroscopy performed on these single particles using high-resolution transmission electron microscopy corroborated the presence of both Rh and Cu in each tested particle (Figure S3). Moreover, the oxidation states of both Rh and Cu were found to be +2 through X-ray photoelectron spectroscopy (Figure S4). Inductively coupled plasma-mass spectrometry (ICP-MS) measurements performed in acid-digested samples revealed that the Cu/Rh ratio was 1.02 ± 0.02, in agreement with the expected ratio in RhCu-btc-HKUST-1.

Synchrotron powder X-ray diffraction (PXRD) data collected on RhCu-btc-HKUST-1 revealed a pattern nearly coincidental with that of the parent Cu(II)-based HKUST-1 (Figure S5), with only slight shifts in the position of the peaks attributable to small differences in lattice parameters. Starting with the reported HKUST-1 atomic positions in the cubic $Fmm\bar{3}m$ space group, a satisfactory Rietveld refinement was reached (Rp = 3.32%, Rwp = 4.68%), corresponding to a structure in which Rh(II) and Cu(II) atoms each occupy 50% of the crystallographic metal site in the paddlewheel clusters (Figure 3b and Table S1). This refinement demonstrated that RhCu-btc-HKUST-1 is isoreticular to HKUST-1, having the same network type. While the metal atoms in RhCu-btc-HKUST-1 are located at topologically and symmetrically equivalent positions, their framework distribution in the MBBs is directed by using COOH-RhMOP. In addition, pair distribution function analyses of synchrotron X-ray scattering data showed the uniquely occurrence of Cu···Cu and Rh···Rh distances, thereby demonstrating the lack of hetero-bimetallic paddlewheel clusters in RhCu-btc-HKUST-1 (Figures S6 and S7).

https://doi.org/10.1021/jacs.2c06131
J. Am. Chem. Soc. 2022, 144, 15745−15753

To further confirm the MOP-guided assembly of RhCu-btc-HKUST-1, we ran a series of control experiments (see the Supporting Information (SI)). Initially, we corroborated the stability of COOH-RhMOP under the reaction conditions (DMF, 85 °C, 1 day) by ^{1}H NMR, UV−vis, and mass spectrometry (Figures S9−S11). Then, we ran three blank reactions under the above conditions but lacking one of the three MBBs. As expected, we did not observe the formation of RhCu-btc-HKUST-1 in any of those reactions. Specifically, the reaction of Cu(II) and btc yielded microcrystals of the expected parent, Cu(II)-HKUST-1. The reaction of COOH-RhMOP with btc produced a clear green solution without any precipitate. This result further confirms that there is no leaching of Rh(II) ions from COOH-RhMOP; as these eventual leached Rh(II) ions would react with btc to yield an extended coordination polymer.[26] Finally, the reaction of COOH-RhMOP with Cu(II) yielded an amorphous coordination polymer. Additionally, we reacted preformed Cu(II)-HKUST-1 crystals with COOH-RhMOP in a mixture containing the same molar ratio of Cu(II)-cluster/btc/COOH-RhMOP as that (12:8:1) used for the synthesis of RhCu-btc-HKUST-1. Under these conditions, we did not observe the formation of RhCu-btc-HKUST-1 crystals (Figure S12). This experiment demonstrates that the reaction mechanism cannot proceed through an initial formation of Cu(II)-HKUST-1 crystals that evolve through solubilization−recrystallization toward the formation of RhCu-btc-HKUST-1. We reasoned that, conversely, the most plausible scenario is that the presence of the COOH-RhMOP rapidly nucleates the formation of RhCu-btc-HKUST-1, thereby suppressing the formation of Cu(II)-HKUST-1.

We confirmed the presence of COOH-RhMOP cavities and btc linkers within the structure of RhCu-btc-HKUST-1 through solid-state cross-polarized/magic angle spinning (CP/MAS) ^{13}C NMR (Figure S13). To quantify the molar ratio between the prefab cavities and the added btc linkers, we developed a methodology to revert the assembly process into its initial components, which we identified and then quantified (Figures S14−S17). This was based on the high chemical stability of COOH-RhMOP. Upon exposing a DMF dispersion of RhCu-btc-HKUST-1 crystals to acidic conditions (see SI), we found that they become fully redissolved. ^{1}H NMR (DMF-d_7) of the resulting solution revealed a btc/COOH-RhMOP ratio of 8:1, in agreement with the ratio expected in RhCu-btc-HKUST-1 (Figure S16). We were able to quantify the amount of liberated COOH-RhMOP by UV−vis spectroscopy. From this experiment, we calculated a concentration of 93.3 μmol COOH-RhMOP/g of RhCu-btc-HKUST-1, which is very close to the theoretical value (94.2) (Figure S17 and Table S2). Altogether, our results confirmed the formation of RhCu-btc-HKUST-1 without significant defects and that COOH-RhMOP remains intact during its synthesis.

Next, we performed N_2-sorption measurements on activated RhCu-btc-HKUST-1 at 77 K, finding that it is microporous to N_2, with a BET surface area (S_{BET}) of 1606 m^2/g (Figure 3c, Figure S18). Furthermore, pore-size distribution analysis revealed the presence of the three characteristic cavities of the HKUST-1 structure together with some mesoporosity, which we ascribed to the interparticle voids (Figure S20). This extrinsic porosity is also responsible for the increased uptake at high pressure ($P/P_0 \approx 0.6$) and the observed hysteresis loop, as previously observed for other nanoscopic MOFs.[31] PXRD diffractogram recorded after these sorption studies confirmed that the RhCu-btc-HKUST-1 had retained its crystallinity (Figure S21).

Hydrolytic Stability of RhCu-btc-HKUST-1. We reasoned that the presence of the water-stable COOH-RhMOP cavity within RhCu-btc-HKUST-1 could confer the overall structure with greater hydrolytic stability relative to the parent Cu(II)-HKUST-1. To test this hypothesis, we incubated RhCu-btc-HKUST-1 and the parent Cu(II)-HKUST-1 in liquid water at room temperature from 1 to 31 days. The water-incubated samples were then characterized through FESEM, PXRD, and N_2 sorption. To our surprise, RhCu-btc-HKUST-1 had retained its morphology, crystallinity, composition, and porosity, even after 1 month of incubation in liquid water (Figure 4a,b, Figures S23 and S30−S35). Conversely, upon exposure to water, the parent Cu(II)-HKUST-1 had undergone the well-reported phase change, with a corresponding loss of porosity from 1888 to 502 m^2/g within the first day (Figures S24−S29).[32]

The hydrolytic stability that we observed for RhCu-btc-HKUST-1 implies that not only the COOH-RhMOP cavities,

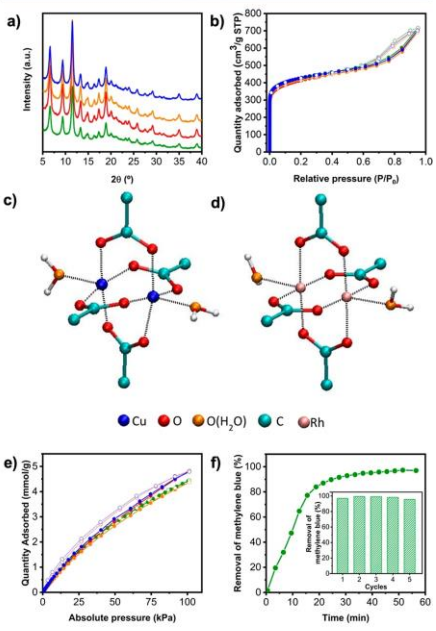


Figure 4. (a) PXRD diffractogram and (b) N_2-sorption isotherms for RhCu-btc-HKUST-1 initially (green) and after incubation in water for 3 (red), 14 (orange), and 31 days (blue). Snapshots (orthographic views) of the optimized DFT structures of (c) Cu(II)- and (d) Rh(II)-paddlewheel clusters in water. (e) CO_2-sorption isotherms at 298 K for RhCu-btc-HKUST-1 initially (green) and after incubation in water for 3 days (red), 14 days (orange), and 31 days (blue). (f) Removal of MB in water by RhCu-btc-HKUST-1 as a function of time. Inset: five consecutive MB-removal/regeneration cycles using RhCu-btc-HKUST-1.

https://doi.org/10.1021/jacs.2c06131
J. Am. Chem. Soc. 2022, 144, 15745−15753

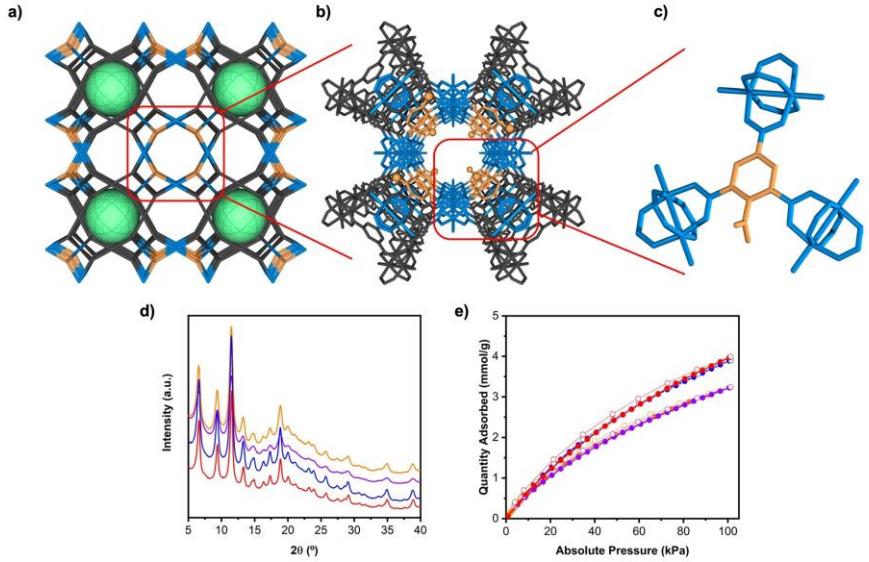


Figure 5. (a) Schematic of the four-component HKUST-1 analogues, showing the three types of channels that are generated when the COOH-RhMOP (structure depicted in gray and cavity depicted in green) is co-assembled with Cu(II) paddlewheels (blue) and (functionalized) btc linkers (orange). (b) Highlight of the chemical structure of the 1D channel decorated exclusively with functionalized btc linkers. (c) Highlight of the coordination environment of the (COOH)btc linker within the channels of RhCu-(COOH)btc-HKUST-1. (d) PXRD diffractogram of RhCu-(NH_2)btc-HKUST-1 (blue), RhCu-(NO_2)btc-HKUST-1 (orange), RhCu-(Br)btc-HKUST-1 (purple), and RhCu-(COOH)btc-HKUST-1 (red). (e) CO_2-adsorption isotherms at 298 K for RhCu-(NH_2)btc-HKUST-1 (blue), RhCu-(NO_2)btc-HKUST-1 (orange), RhCu-(Br)btc-HKUST-1 (purple), and RhCu-(COOH)btc-HKUST-1 (red).

but also the Cu(II)-carboxylate bonds that link them, withstand the incubation in water. Thus, in an effort to rationalize the higher hydrolytic stability of RhCu-btc-HKUST-1, we performed electronic structure calculations in water of both Cu(II)- and Rh(II)-paddlewheel clusters (Figure 4c,d). For this, we employed Gaussian 16[33] at the M06-L/SDD level of theory[34] in the presence of implicit water solvent modeled with the IEFPCM formalism, as described in the SI.[35] Our implicit solvent calculations showed that the Cu(II)-paddlewheel undergoes a significant torsion when exposed to water, whereas the Rh(II)-paddlewheel remains stable (Figures S36−S38). This torsion is enhanced after coordination of a water molecule to the axial position of Cu(II) (Figure 4c, Figures S39−S41), disrupting the original symmetrical bidentate binding with carboxylate ligands (Figure S42). We propose that Cu(II)-paddlewheels are hydrolyzed through this mechanical distortion as pivotal step, provoking the instability of the parent Cu(II)-HKUST-1. In the case of RhCu-btc-HKUST-1, each Cu(II)-paddlewheel is connected to two Rh(II)-paddlewheel clusters, which are not altered by water. The inertness of the Rh(II)-paddlewheel blocks the mechanical instability of the neighboring Cu(II)-paddlewheel, thereby inhibiting the hydrolysis process.

We envisioned that the stability of RhCu-btc-HKUST-1 could enable its use as an adsorbent in aqueous environments or after aqueous exposure. As a proof of concept, we evaluated the CO_2 adsorption capacity of RhCu-btc-HKUST-1 after being incubated in water for up to 31 days. As observed in Figure 4e, CO_2 uptake capacity did not decrease after the incubation. Additionally, we tested the adsorption capabilities of RhCu-btc-HKUST-1 in liquid water. To this end, we incubated RhCu-btc-HKUST-1 in an aqueous solution of methylene blue (MB) at 20 ppm (pH = 7) and then monitored the decrease of MB over 1 h. We found that, after 51 min, 97% of the MB had been removed by the RhCu-btc-HKUST-1 (Figure 4f). Moreover, after the MB-adsorption, the RhCu-btc-HKUST-1 fully retained its crystallinity (Figure S44). This contrasts sharply to the case of its parent, Cu(II)-HKUST-1, which, in the same amount of time, could adsorb 62% of the MB, due to its degradation and amorphization in water (Figures S43 and S45). To explore the MB-removal performance of each analogue after reutilization, we tested them over five consecutive removal/regeneration cycles. The removal step was identical to the one followed above. The regeneration step entailed the recovery of the adsorbent through centrifugation, followed by successive washings with water and acetone. Finally, the adsorbent was activated at 85 °C under vacuum for 1 h. The results showed that uptakes of RhCu-btc-HKUST-1 were similar among the five cycles (Figure 4f, inset), meaning that it had remained stable and that the regeneration was sufficient to maintain its removal capacity. Contrariwise, under these conditions, the MB-

https://doi.org/10.1021/jacs.2c06131
J. Am. Chem. Soc. 2022, 144, 15745−15753

removal capacity of Cu(II)-HKUST-1 dropped from 62% to ~10% (from the second to third cycles), and then to ~3−4% (for the fourth and fifth cycles) (Figure S43). Thus, the difference in MB-removal performance between RhCu-btc-HKUST-1 and Cu(II)-HKUST-1 only widened after reutilization, suggesting a new mechanism for stabilization of Cu(II) paddlewheel clusters based on the mechanical interlock between Rh(II) and Cu(II) paddlewheels, which results in water-resistant adsorbents.

Reticulation of Varied Linkers into the HKUST-1 Structure via Prefabricated Cavity-Directed Synthesis. We envisaged that our prefabricated cavity strategy would provide access to four-component HKUST-1 analogues, given the possibility to differentiate the btc linkers that form the COOH-RhMOP from those that bridge the Cu(II)-paddlewheel clusters, during the synthesis. However, we reasoned that such four-component analogues would require a functionalized btc linker, rather than the previously used btc linker. In this new configuration, the connectivity of the prefabricated COOH-RhMOP cavity dictates that the added functionalized btc linkers will be located on top of the triangular windows that connect three Cu(II) paddlewheels. These positions align into 1D channels, thus generating four-component HKUST-1 analogues in which alternating functionalized and non-functionalized 1D channels coexist (Figure 5a). This scenario differs from the outcome obtained when linkers with the same connectivity but different side functionalities are combined to generate isoreticular frameworks. In this latter case, one generally obtains structures in which the different linkers are randomly distributed or are organized into a non-atomically precise pattern.[36]

Based on the prefab cavity-induced desymmetrization of the organic linkers within the HKUST-1 network, we attempted the synthesis of four-component HKUST-1 analogues, using btc linkers having a pendant functional group [(Br)btc, (NO_2)btc and (NH_2)btc] at the second position of the phenylic ring as one of the reagents. Thus, we followed a synthetic strategy identical to the one that we had used for RhCu-btc-HKUST-1, except that we substituted the non-functionalized btc linker with either (Br)btc, (NO_2)btc or (NH_2)btc to generate RhCu-(Br)btc-HKUST-1, RhCu-(NO_2)btc-HKUST-1, and RhCu-(NH_2)btc-HKUST-1, respectively. The three reactions afforded green crystalline samples composed of particles with an average size of 24 ± 2 nm, for RhCu-(Br)btc-HKUST-1 (yield: 82%); 23 ± 2 nm, for RhCu-(NO_2)btc-HKUST-1 (yield: 78%); and 21 ± 3 nm, for RhCu-(NH_2)btc-HKUST-1 (yield: 74%) (Figures S46, S53, and S60).

Next, we characterized RhCu-(Br)btc-HKUST-1, RhCu-(NO_2)btc-HKUST-1, and RhCu-(NH_2)btc-HKUST-1 by PXRD, finding that their patterns matched the one that we had previously obtained for RhCu-btc-HKUST-1 (Figure 5d). ICP-MS on fully digested RhCu-(Br)btc-HKUST-1, RhCu-(NO_2)btc-HKUST-1, and RhCu-(NH_2)btc-HKUST-1 gave Cu/Rh molar ratios of 1.16 ± 0.01, 1.10 ± 0.01, and 1.09 ± 0.02, respectively. These values are in good agreement with the value (1) expected for their molecular formula. Moreover, ^{1}H NMR signals of the digested materials showed btc/(Br)btc, btc/(NO_2)btc, and btc/(NH_2)btc ratios of 8:1, also in perfect agreement with the expected ratio according to their formula (Figures S48, S55, and S62).

We measured the porosity of RhCu-(Br)btc-HKUST-1, RhCu-(NO_2)btc-HKUST-1, and RhCu-(NH_2)btc-HKUST-1 in N_2-sorption experiments, finding S_{BET} values of 1215, 1133, and 1212 m^2/g, respectively (Figures S49, S56, and S63). In all cases, PXRD diagrams collected after the sorption studies also confirmed their stability (Figures S51, S58, and S65). All these S_{BET} values are lower than the S_{BET} value for RhCu-btc-HKUST-1. We ascribed their inferior porosity to steric hindrance of the side groups located within the pores—a feature common to many other MOFs, such as those of the UiO-66 family.[37] Whereas N_2-sorption isotherms at 77 K accounted for the steric hindrance of the functional groups introduced into these four-component HKUST-1 analogues, CO_2-adsorption measured at 298 K highlighted their different affinities toward CO_2. Thus, the presence of free amine groups in RhCu-(NH_2)btc-HKUST-1 made it a better adsorbent for CO_2 than its Br or NO_2 analogues (Figure 5e).

COOH-Functionalized HKUST-1 Analogue. Having observed the structure-directing properties of the COOH-RhMOP prefabricated cavity on the synthesis of multi-component HKUST-1 analogues, we envisaged that it could be employed to reticulate tetracarboxylate linkers to functionalize the HKUST-1 architecture with free carboxylic acid groups. Thus, we employed 1,2,3,5-benzenetetracarboxylic acid (hereafter named (COOH)btc) as the organic MBB in the co-assembly of COOH-RhMOP with Cu(II) paddlewheels to yield RhCu-(COOH)btc-HKUST-1 (Figure 5b,c). The solvothermal reaction between COOH-RhMOP, $Cu(NO_3)_2 \cdot 3H_2O$, and (COOH)btc afforded a green crystalline sample made of particles of an average size of 20 ± 3 nm (yield: 65%) (Figure S67). PXRD analysis of RhCu-(COOH)btc-HKUST-1 revealed a pattern consistent with RhCu-btc-HKUST-1 (Figure 5d). The successful reticulation of (COOH)btc within the HKUST-1 network was confirmed by the ^{1}H NMR spectrum of the acid-digested sample, which showed a btc/(COOH)btc ratio of 8:1 (Figure S69). The thermally activated sample retained its crystallinity (Figure S72), which enabled measurement of its gas sorption, for which an S_{BET} of 1380 m^2/g (Figure S70) and a CO_2 uptake (at 298 K and 1 bar) of 4.0 mmol/g were found (Figure 5e).

To further confirm that RhCu-(COOH)btc-HKUST-1 contained free carboxylic acid groups within its channels, we performed a series of spectroscopic characterizations. First, ICP measurements performed on the acid-digested sample revealed that the Cu:Rh molar ratio was 0.94. The fact that there is no excess of Cu(II) ions in the HKUST-1 structure suggests that only three of the four COOH groups of the (COOH)btc are coordinated to Cu(II) ions. Next, infrared spectroscopy performed on RhCu-(COOH)btc-HKUST-1 showed a clear vibration band at 1702 cm^{-1}, which we ascribed to the stretching band of C═O, which indicates the presence of uncoordinated carboxylic acid groups (Figure S73). Altogether, our results illustrate that our prefabricated-cavity approach can be employed to restrict the connectivity of polycarboxylate linkers to introduce free carboxylic acid groups into multicomponent isoreticular structures. Accordingly, this approach enabled the synthesis of a COOH-functionalized HKUST-1 analogue without generation of any defective structures.[38,39]

Finally, as a proof-of-concept, we aimed to demonstrate that the carboxylic acid groups located within the RhCu-(COOH)-btc-HKUST-1 structure are functional and accessible. To this end, we evaluated the behavior of RhCu-(COOH)btc-HKUST-1 as catalyst in a model acid-catalyzed reaction: the conversion of benzaldehyde dimethyl acetal to benzalde-

https://doi.org/10.1021/jacs.2c06131
J. Am. Chem. Soc. 2022, 144, 15745−15753

hyde.[40,41] We observed that, under identical conditions, RhCu-(COOH)btc-HKUST-1 could convert up to 64% of benzaldehyde dimethyl acetal into benzaldehyde, whereas non-functionalized RhCu-btc-HKUST-1 only afforded 32% conversion (Figure S74). Considering that the acidic groups of RhCu-btc-HKUST-1 can only be located at its surface, we ascribed the superior conversion obtained with RhCu-(COOH)btc-HKUST-1 to the activity of the inner carboxylic acid groups, which would confirm their accessibility. Importantly, both RhCu-btc-HKUST-1 and RhCu-(COOH)-btc-HKUST-1 fully retained their crystallinity after the acid catalysis (Figure S75).

■ CONCLUSIONS

We have presented an alternative methodology to synthesize multicomponent MOFs, which is based on the co-assembly of prefabricated cavities (in the form of carboxylic acid-functionalized MOPs) and small MBBs. The methodology benefits from the structure-directing influence of the MOP to organize varied organic and metallic MBBs through the crystal lattice of the targeted MOF, thus providing a greater degree of control over the synthesis of atomically precise multicomponent MOFs.

■ ASSOCIATED CONTENT

Supporting Information

The Supporting Information is available free of charge at https://pubs.acs.org/doi/10.1021/jacs.2c06131.

Detailed syntheses, FESEM data and images, PXRD diffractogram, XPS, UV−vis, and NMR, as well as porosity measurements, including Figures S1−S75 and Tables S1−S3 (PDF)

■ AUTHOR INFORMATION

Corresponding Authors

Arnau Carné-Sánchez − *Catalan Institute of Nanoscience and Nanotechnology (ICN2), CSIC, Barcelona Institute of Science and Technology, 08193 Bellaterra, Barcelona, Spain; Departament de Química, Facultat de Ciències, Universitat Autònoma de Barcelona, 08193 Bellaterra, Spain;* orcid.org/0000-0002-8569-6208; Email: arnau.carne@icn2.cat

Daniel Maspoch − *Catalan Institute of Nanoscience and Nanotechnology (ICN2), CSIC, Barcelona Institute of Science and Technology, 08193 Bellaterra, Barcelona, Spain; Departament de Química, Facultat de Ciències, Universitat Autònoma de Barcelona, 08193 Bellaterra, Spain; ICREA, 08010 Barcelona, Spain;* orcid.org/0000-0003-1325-9161; Email: daniel.maspoch@icn2.cat

Authors

Akim Khobotov-Bakishev − *Catalan Institute of Nanoscience and Nanotechnology (ICN2), CSIC, Barcelona Institute of Science and Technology, 08193 Bellaterra, Barcelona, Spain; Departament de Química, Facultat de Ciències, Universitat Autònoma de Barcelona, 08193 Bellaterra, Spain*

Cornelia von Baeckmann − *Catalan Institute of Nanoscience and Nanotechnology (ICN2), CSIC, Barcelona Institute of Science and Technology, 08193 Bellaterra, Barcelona, Spain; Departament de Química, Facultat de Ciències, Universitat Autònoma de Barcelona, 08193 Bellaterra, Spain*

Borja Ortín-Rubio − *Catalan Institute of Nanoscience and Nanotechnology (ICN2), CSIC, Barcelona Institute of Science and Technology, 08193 Bellaterra, Barcelona, Spain; Departament de Química, Facultat de Ciències, Universitat Autònoma de Barcelona, 08193 Bellaterra, Spain;* orcid.org/0000-0002-0533-3635

Laura Hernández-López − *Catalan Institute of Nanoscience and Nanotechnology (ICN2), CSIC, Barcelona Institute of Science and Technology, 08193 Bellaterra, Barcelona, Spain; Departament de Química, Facultat de Ciències, Universitat Autònoma de Barcelona, 08193 Bellaterra, Spain*

Alba Cortés-Martínez − *Catalan Institute of Nanoscience and Nanotechnology (ICN2), CSIC, Barcelona Institute of Science and Technology, 08193 Bellaterra, Barcelona, Spain; Departament de Química, Facultat de Ciències, Universitat Autònoma de Barcelona, 08193 Bellaterra, Spain*

Jordi Martínez-Esaín − *Catalan Institute of Nanoscience and Nanotechnology (ICN2), CSIC, Barcelona Institute of Science and Technology, 08193 Bellaterra, Barcelona, Spain;* orcid.org/0000-0002-8420-8559

Felipe Gándara − *Consejo Superior de Investigaciones Científicas (CSIC), Materials Science Institute of Madrid (ICMM), 28049 Madrid, Spain;* orcid.org/0000-0002-1671-6260

Judith Juanhuix − *ALBA Synchrotron, 08290 Cerdanyola del Vallés, Barcelona, Spain;* orcid.org/0000-0003-3728-8215

Ana E. Platero-Prats − *Departamento de Química Inorgánica, Facultad de Ciencias, Universidad Autónoma de Madrid, 28049 Madrid, Spain; Condensed Matter Physics Center (IFIMAC), Universidad Autónoma de Madrid, 28049 Madrid, Spain;* orcid.org/0000-0002-2248-2739

Jordi Faraudo − *Institut de Ciència de Materials de Barcelona (ICMAB-CSIC), 08193 Bellaterra, Spain;* orcid.org/0000-0002-6315-4993

Complete contact information is available at: https://pubs.acs.org/10.1021/jacs.2c06131

Notes

The authors declare no competing financial interest.

■ ACKNOWLEDGMENTS

This work was supported by the Spanish MINECO (project RTI2018-095622-B-I00), the Catalan AGAUR (project 2017 SGR 238), the CERCA Program/Generalitat de Catalunya, and the MCIN/AEI/10.13039/501100011033 and by the European Union "NextGenerationEU"/PRTR (EUR2020-112294). We also thank CESGA Supercomputing center for technical support and computer time at the supercomputer Finisterrae III. ICN2 and ICMAB are supported by the Severo Ochoa program from the Spanish MINECO (grants SEV-2017-0706 and CEX2019-000917-S). The project that gave rise to these results received the support of a fellowship (LCF/BQ/PR20/11770011) from "la Caixa" Foundation (ID 100010434). A.E.P.-P. acknowledges a Ramón y Cajal fellowship (RYC2018-024328-I). We acknowledge the Diamond Light Source, U.K., for the provision of synchrotron access to the beamline I15-1 (CY28079) and thank Dr. Philip Chater for his assistance with data collection.

https://doi.org/10.1021/jacs.2c06131
J. Am. Chem. Soc. 2022, 144, 15745−15753

REFERENCES

(1) Jiang, J.; Furukawa, H.; Zhang, Y.-B.; Yaghi, O. M. High Methane Storage Working Capacity in Metal-Organic Frameworks with Acrylate Links. *J. Am. Chem. Soc.* **2016**, *138*, 10244−10251.

(2) Hanikel, N.; Pei, X.; Chheda, S.; Lyu, H.; Jeong, W.; Sauer, J.; Gagliardi, L.; Yaghi, O. M. Evolution of water structures in metal-organic frameworks for improved atmospheric water harvesting. *Science* **2021**, *374*, 454−459.

(3) Liu, Q.; Cong, H.; Deng, H. Deciphering the Spatial Arrangement of Metals and Correlation to Reactivity in Multivariate Metal-Organic Frameworks. *J. Am. Chem. Soc.* **2016**, *138*, 13822−13825.

(4) Feng, L.; Wang, K.-Y.; Day, G. S.; Zhou, H.-C. The Chemistry of Multi-Component and Hierarchical Framework Compounds. *Chem. Soc. Rev.* **2019**, *48*, 4823−4853.

(5) Deng, H.; Doonan, C. J.; Furukawa, H.; Ferreira, R. B.; Towne, J.; Knobler, C. B.; Wang, B.; Yaghi, O. M. Multiple Functional Groups of Varying Ratios in Metal-Organic Frameworks. *Science* **2010**, *327*, 846−850.

(6) Ji, Z.; Li, T.; Yaghi, O. M. Sequencing of Metals in Multivariate Metal-Organic Frameworks. *Science* **2020**, *369*, 674−680.

(7) Liu, L.; Konstas, K.; Hill, M. R.; Telfer, S. G. Programmed Pore Architectures in Modular Quaternary Metal-Organic Frameworks. *J. Am. Chem. Soc.* **2013**, *135*, 17731−17734.

(8) Muldoon, P. F.; Liu, C.; Miller, C. C.; Koby, S. B.; Gamble Jarvi, A.; Luo, T.-Y.; Saxena, S.; O'Keeffe, M.; Rosi, N. L. Programmable Topology in New Families of Heterobimetallic Metal-Organic Frameworks. *J. Am. Chem. Soc.* **2018**, *140*, 6194−6198.

(9) Matsunaga, S.; Hasada, K.; Sugiura, K.; Kitamura, N.; Kudo, Y.; Endo, N.; Mori, W. Hetero Bi-Paddle-Wheel Coordination Networks: A New Synthetic Route to Rh-Containing Metal-Organic Frameworks. *Bull. Chem. Soc. Jpn.* **2012**, *85*, 433−438.

(10) Gao, W.-Y.; Sur, A.; Wang, C.-H.; Lorzing, G. R.; Antonio, A. M.; Taggart, G. A.; Ezazi, A. A.; Bhuvanesh, N.; Bloch, E. D.; Powers, D. C. Atomically Precise Crystalline Materials Based on Kinetically Inert Metal Ions via Reticular Mechanopolymerization. *Angew. Chem. Int. Ed.* **2020**, *59*, 10878−10883.

(11) Fracaroli, A. M.; Siman, P.; Nagib, D. A.; Suzuki, M.; Furukawa, H.; Toste, F. D.; Yaghi, O. M. Seven Post-Synthetic Covalent Reactions in Tandem Leading to Enzyme-like Complexity within Metal-Organic Framework Crystals. *J. Am. Chem. Soc.* **2016**, *138*, 8352−8355.

(12) Yuan, S.; Qin, J.-S.; Li, J.; Huang, L.; Feng, L.; Fang, Y.; Lollar, C.; Pang, J.; Zhang, L.; Sun, D.; Alsalme, A.; Cagin, T.; Zhou, H.-C. Retrosynthesis of Multi-Component Metal-organic Frameworks. *Nat. Commun.* **2018**, *9*, 808.

(13) Yuan, S.; Lu, W.; Chen, Y.-P.; Zhang, Q.; Liu, T.-F.; Feng, D.; Wang, X.; Qin, J.; Zhou, H.-C. Sequential Linker Installation: Precise Placement of Functional Groups in Multivariate Metal-Organic Frameworks. *J. Am. Chem. Soc.* **2015**, *137*, 3177−3180.

(14) Kim, M.; Cahill, J. F.; Fei, H.; Prather, K. A.; Cohen, S. M. Postsynthetic Ligand and Cation Exchange in Robust Metal-Organic Frameworks. *J. Am. Chem. Soc.* **2012**, *134*, 18082−18088.

(15) Yaghi, O. M.; Kalmutzki, M. J.; Diercks, C. S. *Introduction to Reticular Chemistry: Metal-Organic Frameworks and Covalent Organic Frameworks*; John Wiley and Sons, 2019; pp 1−27.

(16) Eddaoudi, M.; Moler, D. B.; Li, H.; Chen, B.; Reineke, T. M.; O'Keeffe, M.; Yaghi, O. M. Modular Chemistry: Secondary Building Units as a Basis for the Design of Highly Porous and Robust Metal-Organic Carboxylate Frameworks. *Acc. Chem. Res.* **2001**, *34*, 319−330.

(17) Chui, S. S.-Y.; Lo, S. M.-F.; Charmant, J. P. H.; Orpen, A. G.; Williams, I. D. A Chemically Functionalizable Nanoporous Material $[Cu_3(TMA)_2(H_2O)_3]n$. *Science* **1999**, *283*, 1148−1150.

(18) Eubank, J. F.; Mouttaki, H.; Cairns, A. J.; Belmabkhout, Y.; Wojtas, L.; Luebke, R.; Alkordi, M.; Eddaoudi, M. The Quest for Modular Nanocages: Tbo -MOF as an Archetype for Mutual Substitution, Functionalization, and Expansion of Quadrangular Pillar Building Blocks. *J. Am. Chem. Soc.* **2011**, *133*, 14204−14207.

(19) Belmabkhout, Y.; Mouttaki, H.; Eubank, J. F.; Guillerm, V.; Eddaoudi, M. Effect of Pendant Isophthalic Acid Moieties on the Adsorption Properties of Light Hydrocarbons in HKUST-1-like Tbo-MOFs: Application to Methane Purification and Storage. *RSC Adv.* **2014**, *4*, 63855−63859.

(20) Eddaoudi, M.; Kim, J.; Wachter, J. B.; Chae, H. K.; O'Keeffe, M.; Yaghi, O. M. Porous Metal-Organic Polyhedra: 25 Å Cuboctahedron Constructed from 12 $Cu_3(CO_2)_4$ Paddle-Wheel Building Blocks. *J. Am. Chem. Soc.* **2001**, *123*, 4368−4369.

(21) Kim, D.; Liu, X.; Lah, M. S. Topology Analysis of Metal-Organic Frameworks Based on Metal-Organic Polyhedra as Secondary or Tertiary Building Units. *Inorg. Chem. Front.* **2015**, *2*, 336−360.

(22) Perry, J. J., IV; Perman, J. A.; Zaworotko, M. J. Design and Synthesis of Metal-Organic Frameworks Using Metal-Organic Polyhedra as Supermolecular Building Blocks. *Chem. Soc. Rev.* **2009**, *38*, 1400−1417.

(23) Nouar, F.; Eubank, J. F.; Bousquet, T.; Wojtas, L.; Zaworotko, M. J.; Eddaoudi, M. Supermolecular Building Blocks (SBBs) for the Design and Synthesis of Highly Porous Metal-Organic Frameworks. *J. Am. Chem. Soc.* **2008**, *130*, 1833−1835.

(24) Guillerm, V.; Kim, D.; Eubank, J. F.; Luebke, R.; Liu, X.; Adil, K.; Lah, M. S.; Eddaoudi, M. A Supermolecular Building Approach for the Design and Construction of Metal-Organic Frameworks. *Chem. Soc. Rev.* **2014**, *43*, 6141−6172.

(25) Grancha, T.; Carné-Sánchez, A.; Zarekarizi, F.; Hernández-López, L.; Albalad, J.; Khobotov, A.; Guillerm, V.; Morsali, A.; Juanhuix, J.; Gándara, F.; Imaz, I.; Maspoch, D. Synthesis of polycarboxylate rhodium(II) metal-organic polyhedra (MOPs) and their use as building blocks for highly connected Metal-Organic Frameworks (MOFs). *Angew. Chem., Int. Ed.* **2021**, *60*, 5729−5733.

(26) Albalad, J.; Carné-Sánchez, A.; Grancha, T.; Hernández-López, L.; Maspoch, D. Protection Strategies for Directionally-Controlled Synthesis of Previously Inaccessible Metal-Organic Polyhedra (MOPs): The Cases of Carboxylate- and Amino-Functionalised Rh(II)-MOPs. *Chem. Commun.* **2019**, *55*, 12785−12788.

(27) Furukawa, S.; Horike, N.; Kondo, M.; Hijikata, Y.; Carné-Sánchez, A.; Larpent, P.; Louvain, N.; Diring, S.; Sato, H.; Matsuda, R.; Kawano, R.; Kitagawa, S. Rhodium-Organic Cuboctahedra as Porous Solids with Strong Binding Sites. *Inorg. Chem.* **2016**, *55*, 10843−10846.

(28) Gosselin, A. J.; Decker, G. E.; Antonio, A. M.; Lorzing, G. R.; Yap, G. P. A.; Bloch, E. D. A Charged Coordination Cage-Based Porous Salt. *J. Am. Chem. Soc.* **2020**, *142*, 9594−9598.

(29) Markwell-Heys, A. W.; Roemelt, M.; Slattery, A. D.; Linder-Patton, O. M.; Bloch, W. M. Linking metal−organic cages pairwise as a design approach for assembling multivariate crystalline materials. *Chem. Sci.* **2021**, *13*, 68−73.

(30) Nam, D.; Kim, J.; Hwang, E.; Nam, J.; Jeong, H.; Kwon, T.-H.; Choe, W. Multivariate Porous Platform Based on Metal-Organic Polyhedra with Controllable Functionality Assembly. *Matter* **2021**, *4*, 2460−2473.

(31) Liu, X.; Shen, Z.-Q.; Xiong, H.-H.; Chen, Y.; Wang, X.-N.; Li, H.-Q.; Li, Y.-T.; Cui, K.-H.; Tian, Y.-Q. Hierarchical porous materials based on nanoscale metal-organic frameworks dominated with permanent interparticle porosity. *Microporous Mesoporous Mater.* **2015**, *204*, 25−33.

(32) Majano, G.; Martin, O.; Hammes, M.; Smeets, S.; Baerlocher, C.; Pérez-Ramírez, J. Solvent-Mediated Reconstruction of the Metal-Organic Framework HKUST-1 $(Cu_3(BTC)_2)$. *Adv. Funct. Mater.* **2014**, *24*, 3855−3865.

(33) Frisch, M. J.; Trucks, G. W.; Schlegel, H. B.; Scuseria, G. E.; Robb, M. A.; Cheeseman, J. R.; Scalmani, G.; Barone, V.; Petersson, G. A.; Nakatsuji, H.; Li, X.; Caricato, M.; Marenich, A. V.; Bloino, J.; Janesko, B. G.; Gomperts, R.; Mennucci, B.; Hratchian, H. P.; Ortiz, J. V.; Izmaylov, A. F.; Sonnenberg, J. L.; Williams-Young, D.; Ding, F.; Lipparini, F.; Egidi, F.; Goings, J.; Peng, B.; Petrone, A.; Henderson, T.; Ranasinghe, D.; Zakrzewski, V. G.; Gao, J.; Rega, N.; Zheng, G.; Liang, W.; Hada, M.; Ehara, M.; Toyota, K.; Fukuda, R.; Hasegawa, J.;

https://doi.org/10.1021/jacs.2c06131
J. Am. Chem. Soc. 2022, 144, 15745−15753

Ishida, M.; Nakajima, T.; Honda, Y.; Kitao, O.; Nakai, H.; Vreven, T.; Throssell, K.; Montgomery, J. A., Jr.; Peralta, J. E.; Ogliaro, F.; Bearpark, M. J.; Heyd, J. J.; Brothers, E. N.; Kudin, K. N.; Staroverov, V. N.; Keith, T. A.; Kobayashi, R.; Normand, J.; Raghavachari, K.; Rendell, A. P.; Burant, J. C.; Ivengar, S. S.; Tomasi, J.; Cossi, M.; Millam, J. M.; Klene, M.; Adamo, C.; Cammi, R.; Ochterski, J. W.; Martin, R. L.; Morokuma, K.; Farkas, O.; Foresman, J. B.; Fox, D. J. *Gaussian 16*, Revision B.01; Gaussian, Inc., Wallingford, CT, 2016.

(34) Zhao, Y.; Truhlar, D. G. The M06 Suite of Density Functionals for Main Group Thermochemistry, Thermochemical Kinetics, Noncovalent Interactions, Excited States, and Transition Elements: Two New Functionals and Systematic Testing of Four M06-Class Functionals and 12 Other Functionals. *Theor. Chem. Acc.* **2008**, *120*, 215−241.

(35) Tomasi, J.; Mennucci, B.; Cammi, R. Quantum Mechanical Continuum Solvation Models. *Chem. Rev.* **2005**, *105*, 2999−3094.

(36) Kong, X.; Deng, H.; Yan, F.; Kim, J.; Swisher, J. A.; Smit, B.; Yaghi, O. M.; Reimer, J. A. Mapping of Functional Groups in Metal-Organic Frameworks. *Science* **2013**, *341*, 882−885.

(37) Garibay, S. J.; Cohen, S. M. Isoreticular Synthesis and Modification of Frameworks with the UiO-66 Topology. *Chem. Commun.* **2010**, *46*, 7700−7702.

(38) Zhang, W.; Kauer, M.; Guo, P.; Kunze, S.; Cwik, S.; Muhler, M.; Wang, Y.; Epp, K.; Kieslich, G.; Fischer, R. A. Impact of Synthesis Parameters on the Formation of Defects in HKUST-1. *Eur. J. Inorg. Chem.* **2017**, *5*, 925−931.

(39) Steenhaut, T.; Grégoire, N.; Barozzino-Consiglio, G.; Filinchuk, Y.; Hermans, S. Mechanochemical Defect Engineering of HKUST-1 and Impact of the Resulting Defects on Carbon Dioxide Sorption and Catalytic Cyclopropanation. *RSC Adv.* **2020**, *10*, 19822−19831.

(40) Li, J.; Yang, X.; Ma, J.; Yuan, C.; Ren, Y.; Cheng, X.; Deng, Y. Controllable Multicomponent Co-Assembly Approach to Ordered Mesoporous Zirconia Supported with Well-Dispersed Tungsten Oxide Clusters as High-Performance Catalysts. *ChemCatChem* **2021**, *13*, 2863−2872.

(41) Robinson, M. W. C.; Graham, A. E. Mesoporous Aluminosilicate Promoted Protection and Deprotection of Carbonyl Compounds. *Tetrahedron Lett.* **2007**, *48*, 4727−4731.

Recommended by ACS

Reticular Design of Precise Linker Installation into a Zirconium Metal–Organic Framework to Reinforce Hydrolytic Stability

Yongwei Chen, Omar K. Farha, *et al.*
JANUARY 25, 2023
JOURNAL OF THE AMERICAN CHEMICAL SOCIETY READ

Tuning Metal–Organic Framework (MOF) Topology by Regulating Ligand and Secondary Building Unit (SBU) Geometry: Structures Built on 8-Connected M_6 (M = Zr, ...

Xingyu Li, Jing Li, *et al.*
NOVEMBER 01, 2022
JOURNAL OF THE AMERICAN CHEMICAL SOCIETY READ

Combination of Low-Polar and Polar Binding Sites in Aliphatic MOFs for the Efficient C_2H_6/C_2H_4 Separation

Jingyi Zhou, Qiwei Yang, *et al.*
JANUARY 06, 2023
ACS APPLIED MATERIALS & INTERFACES READ

Reversible Discrete-to-Extended Metal–Organic Polyhedra Transformation by Sulfonic Acid Surface Functionalization

Javier Troyano, Shuhei Furukawa, *et al.*
OCTOBER 12, 2022
JOURNAL OF THE AMERICAN CHEMICAL SOCIETY READ

Get More Suggestions >

https://doi.org/10.1021/jacs.2c06131
J. Am. Chem. Soc. 2022, 144, 15745−15753

JACS
JOURNAL OF THE AMERICAN CHEMICAL SOCIETY
pubs.acs.org/JACS
Article

Isoreticular Contraction of Metal–Organic Frameworks Induced by Cleavage of Covalent Bonds

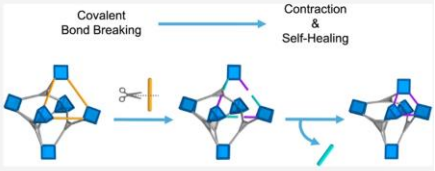
Yunhui Yang, Pilar Fernández-Seriñán, Inhar Imaz,* Felipe Gándara, Marcel Handke, Borja Ortín-Rubio, Judith Juanhuix, and Daniel Maspoch*

Cite This: J. Am. Chem. Soc. 2023, 145, 17398–17405

Read Online

ACCESS | Metrics & More | Article Recommendations | Supporting Information

ABSTRACT: Isoreticular chemistry, in which the organic or inorganic moieties of reticular materials can be replaced without destroying their underlying nets, is a key concept for synthesizing new porous molecular materials and for tuning or functionalization of their pores. Here, we report that the rational cleavage of covalent bonds in a metal–organic framework (MOF) can trigger their isoreticular contraction, without the need for any additional organic linkers. We began by synthesizing two novel MOFs based on the MIL-142 family, (In)BCN-20B and (Sc)BCN-20C, which include cleavable as well as noncleavable organic linkers. Next, we selectively and quantitatively broke their cleavable linkers, demonstrating that various dynamic chemical and structural processes occur within these structures to drive the formation of isoreticular contracted MOFs. Thus, the contraction involves breaking of a covalent bond, subsequent breaking of a coordination bond, and finally, formation of a new coordination bond supported by structural behavior. Remarkably, given that the single-crystal character of the parent MOF is retained throughout the entire transformation, we were able to monitor the contraction by single-crystal X-ray diffraction.



■ INTRODUCTION

Metal–organic frameworks (MOFs), a class of crystalline materials assembled by combining inorganic metal-based nodes with organic linkers, exhibit long-range ordered structures with permanent porosity.[1,2] Given the nearly infinite possible permutations of their building blocks, MOFs are highly versatile: they can be designed to have distinctive features such as an exceptionally large surface area and adjustable pore sizes.

The design and synthesis of MOFs have been expanded by reticular chemistry, which provides high levels of chemical control. This is achieved mainly by either of two strategies: (i) predesign of a novel target net through judicious design of the molecular building blocks or (ii) use of a known net as a blueprint for a novel material, designed by applying the isoreticular principle.[3−6] The primary aim of isoreticular chemistry is to tune or functionalize the organic or inorganic moieties without altering their underlying nets. Thus, it has proven invaluable for modulating the properties of MOFs and for optimizing their performance in myriad applications. Isoreticular MOFs can be synthesized by common direct synthesis[7−9] or by postsynthetic modification (PSM). PSM-based methodologies to synthesize isoreticular MOFs include linker functionalization, transmetalation, sequential linker installation, and solvent-assisted linker exchange (SALE).[10−12] Among these, SALE is based on substitution of a linker that bridges two metal ions/clusters, with an external linker, in the presence of a solvent. This enables generation of new isoreticular MOFs: for example, ones in which interpenetration can be controlled[13,14] or that can exhibit nondefault topologies.[15] In SALE, replacement is performed chiefly by using external linkers whose length is equal to or greater than that of the original linkers, thereby affording a lattice of the same or greater size.[16−18] Alternatively, a few studies have shown that the framework can also be contracted, by using shorter linkers, although this approach has not been widely explored.[14,19,20] The contraction of lattices can also confer the resultant MOFs[21] with unusual properties such as negative and stepwise gas-adsorption, modulation of the radical spin stated in solid state, or stimuli responsiveness and selectivity, which can be utile for applications such as gas storage and separation, catalysis, sensing, and controlled release.[22−28]

Herein, we report a new approach to isoreticular contraction of MOFs that is based on breaking of covalent bonds and does not require addition of any external linkers (Figure 1). Recently, we described clip-off chemistry, a new synthetic

Received: May 25, 2023
Published: July 26, 2023



ACS Publications
© 2023 The Authors. Published by American Chemical Society

https://doi.org/10.1021/jacs.3c05469
J. Am. Chem. Soc. 2023, 145, 17398–17405

Journal of the American Chemical Society pubs.acs.org/JACS Article

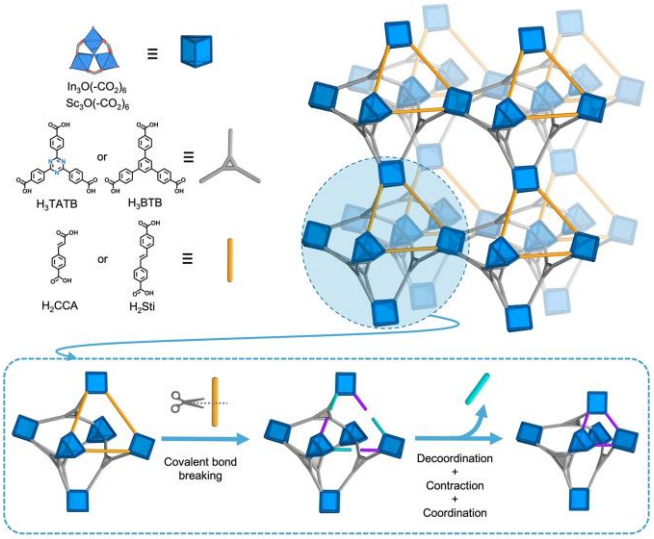


Figure 1. Schematic of the isoreticular contraction of (In)BCN-20B and (Sc)BCN-20C induced by cleavage of covalent bonds.

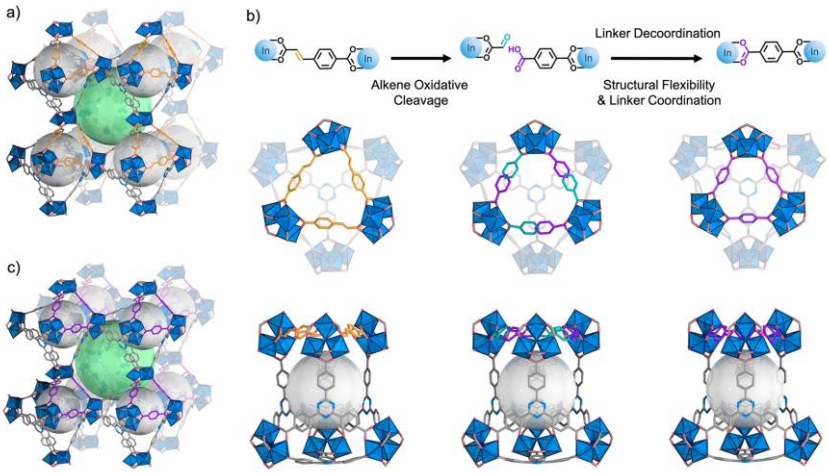


Figure 2. (a) Crystal structure of (In)BCN-20B. (b) Schematic of the stepwise isoreticular contraction from (In)BCN-20B (left) to (In)BCN-20B′ (middle) to (In)BCN-20A (right). Corresponding SCXRD data, revealing the octahedral cages viewed along the crystallographic *c* and *b* axes, highlighting transformation of the CCA linker (orange) to the shorter BDC linker (violet), and contraction of the triangular face. (c) Crystal structure of (In)BCN-20A.

strategy to make new molecules and materials based on the selective, quantitative, and controlled cleavage of bonds in reticular materials.[29] Here, we show that this concept can be applied to control the stepwise synthesis of isoreticular MOFs exhibiting contracted structures relative to their parent MOFs. To this end, we have designed two new mixed-linker parent MOFs that are isoreticular to the **nht**-(Fe)MIL-142 family:[30,31] (In)BCN-20B and (Sc)BCN-20C (BCN stands for Barcelona

https://doi.org/10.1021/jacs.3c05469
J. Am. Chem. Soc. 2023, 145, 17398−17405

Material). This new isoreticular synthetic approach begins with the cleavage of an olefinic bond of one of the bridging linkers, which splits the linker into two monocoordinated ligands. This periodic and quantitative fracture in the MOF is followed by the decoordination of one of the monocoordinated ligands, using solvents. This ligand removal instantaneously induces both contraction of the lattice and a self-healing phenomenon, which involves the migration and coordination of the monocoordinated ligand remaining in the structure to the accessible metal ions. Interestingly, this stepwise isoreticular contraction of MOFs, which involves breaking of a covalent bond, subsequent breaking of a coordination bond, and finally, formation of a new coordination bond supported by dynamic structural behavior, can be followed by single-crystal X-ray diffraction (SCXRD), as these events occur in a single-crystal to single-crystal manner.

■ RESULTS AND DISCUSSION

We began by synthesizing (In)BCN-20B. First, a dispersion of $In(NO_3)_3{\cdot}xH_2O$, 4,4′,4″-(1,3,5-triazine-2,4,6-triyl)tribenzoic acid (H_3TATB) and 4-carboxycinnamic acid (H_2CCA) in *N*,*N*-dimethylformamide (DMF) and HNO_3 (3.5 M in DMF) was heated at 120 °C for 30 h. Next, the resulting hexagonal prismatic crystals were analyzed by SCXRD, which confirmed formation of a 3D framework isoreticular to **nht**-(Fe)MIL-142B. (In)BCN-20B crystallizes in a trigonal lattice with an $R\bar{3}c$ (No. 167) space group, with unit cell parameters of $a = b =$ 30.820 and c = 95.540 Å (Table S1). The 3D structure of (In)BCN-20B is formed by vertex-sharing distorted octahedral cages, with an underlying **nht** topology (Figure 2a). Each cage is formed by six trigonal prismatic $In_3O(-CO_2)_6$ clusters located at vertices, which are connected by four tritopic TATB linkers and three ditopic CCA linkers. Note that these CCA linkers are symmetrically disordered about an inversion center, which results in similarity of spatial occupation between the dislocated aromatic rings of the CCA linker and those of a naphthalene molecule (Figures S1 and S2). The location of the two types of linkers within the cage defines one triangular face, whose edges are occupied by three CCA linkers (Figure 2b, left and Figure S3), and four triangular faces, each of which is occupied by one TATB linker. This means that each of the three remaining faces shares one of the edges occupied by a CCA linker with the first triangular face, whereas the other two edges are unoccupied. The overall framework of (In)BCN-20B shows a 2-fold interpenetrated structure, in which two catenane-like octahedral cages from two different **nht** nets interlocked via one of their pure TATB triangular faces (Figure S4). Further characterization of (In)BCN-20B confirmed its phase purity, as the experimental powder-XRD (PXRD) pattern matched the simulated one (Figure 3a). Furthermore, the ^{1}H-NMR spectrum of the digested sample contained the expected TATB/CCA ratio of 4:3 (Figure S6).

Having synthesized (In)BCN-20B, we then cleaved all its alkene bonds and subsequently converted them into aldehyde/carboxylic acid groups via a solid−gas ozonolysis reaction.[29,32,33] First, 20 mg of single crystals of solvent-free (In)BCN-20B were packed into a plastic tube. Next, dry ozone was flowed (~15 g/Nm^3) continuously through the sample for 35 min. Finally, the resultant crystals were analyzed by SCXRD, showing that ozonized (In)BCN-20B′ crystallized in a trigonal lattice with an $R\bar{3}m$ (No. 166) space group, having unit cell parameters of $a = b =$ 30.830 and c = 47.592 Å (Table S2). Overall, (In)BCN-20B′ exhibited a related 3D structure to

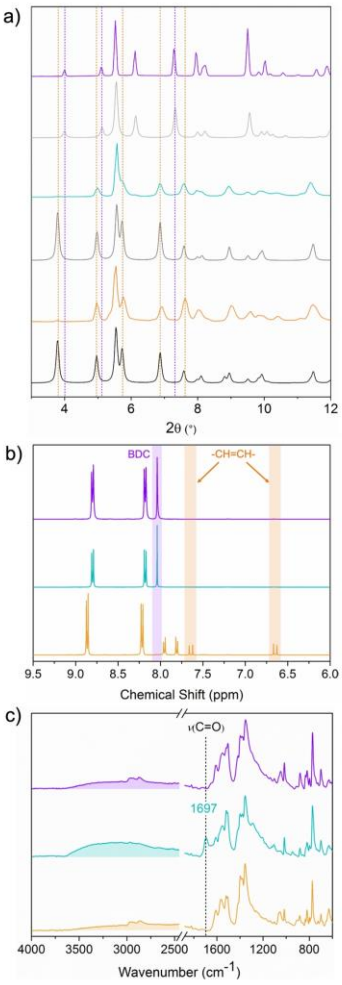


Figure 3. (a) PXRD patterns of simulated (black) and experimental (orange) (In)BCN-20B; simulated (gray) and experimental (cyan) (In)BCN-20B′; and simulated (light gray) and experimental (violet) (In)BCN-20A. (b) ^{1}H-NMR spectra of (In)BCN-20B (orange), (In)BCN-20B′ (cyan), and (In)BCN-20A (violet). The protons from olefinic bonds and terephthalate have been highlighted in orange and violet, respectively. (c) Infrared spectra of (In)BCN-20B (orange), (In)BCN-20B′ (cyan), and (In)BCN-20A (violet).

that of (In)BCN-20B but with evident changes in its connectivity through the CCA linkers. Indeed, SCXRD data confirmed the integrity of the inorganic In-oxo clusters and of the TATB linkers. However, at the positions initially occupied

https://doi.org/10.1021/jacs.3c05469
J. Am. Chem. Soc. 2023, 145, 17398−17405

by the CCA linkers, the similarity in spatial occupation between the dislocated aromatic rings of the CCA linker and the naphthalene molecule was lost (Figure 2b, middle). This observation clearly suggested that the CCA linkers no longer existed.

To confirm the oxidative cleavage of CCA linkers into the expected monocoordinated glyoxylate and single deprotonated terephthalic acid (BDC) ligands (Figure 2b), we analyzed a digested (In)BCN-20B′ sample by ^{1}H NMR and then compared the resulting spectrum to that of the starting (In)BCN-20B (Figures 3b and S6, S8). The spectrum of the digested (In)BCN-20B showed the characteristic peaks of the olefinic protons of CCA at δ = 7.64 and δ = 6.65 ppm. In contrast, the spectrum of the digested (In)BCN-20B′ corroborated the disappearance of this olefinic signal. It also revealed the disappearance of the phenyl (δ = 7.94 and δ = 7.81 ppm) and the carboxylic acid (δ = 13.06 ppm) protons of the CCA but did show the characteristic signals for the terephthalic acid (BDC, δ = 8.04 ppm). Unfortunately, the aldehyde proton of the glyoxylic acid was not detected, presumably due to the fact that its boiling point (111 °C) is lower than the temperature (120 °C) at which the digestion took place overnight. However, the presence of glyoxylic acid was confirmed by electrospray ionization mass spectrometry (ESI-MS) analysis in a negative ion mode using a (In)BCN-20B′ sample digested under milder conditions (HF in DMSO at room temperature). The ESI-MS spectrum showed a peak at m/z = 72.99, which matches the molecular mass of the deprotonated glyoxylate $[C_2HO_3]^-$ (m/z = 73.03; Figure S9). These results clearly indicated that the olefinic bond of the ditopic CCA linkers had been quantitatively cleaved by ozonolysis and subsequently converted into two monocoordinated ligands: a single deprotonated BDC and a glyoxylate. Supporting this oxidative cleavage reaction, the FTIR spectrum of the ozonated (In)BCN-20B′ exhibited a more intense C═O stretch band at 1697 cm^{-1} relative to that in the spectrum of the non-ozonated (In)BCN-20B. Moreover, it showed enhanced, broad absorbance at around 3300 cm^{-1}, indicative of large perturbations caused by H-bonded hydroxyl groups of the free carboxylic acid groups (Figures 3c and S10).[34,35] Next, we performed PXRD on a bulk sample of ozonated (In)BCN-20B′ to confirm its crystallinity and phase purity. The resulting PXRD pattern matched the one calculated from the crystal structure (Figures 3a and S11), confirming that the cleavage of alkene bonds via ozonolysis did not compromise the crystallinity throughout the bulk sample. Together these results confirmed the quantitative cleavage of CCA linkers and the consequent formation of a new structure with less connectivity among its trimeric In^{3+} clusters. Indeed, analysis of the topology of (In)BCN-20B′ using the ToposPro 5.3.3.5 software,[36] and considering TATB linkers as 3-connected points of extension (3-c), and $In_3O(-CO_2)_6$ clusters as nodes that have four coordination points (4-c), revealed formation of a 2-fold interpenetrated MOF with two independent underlying trinodal (3,3,4)-c nets (topological code **3,3,4T22**, Figure S12).

Having demonstrated that ditopic CCA linkers could be cleaved into two monocoordinated ligands, we then explored the possibility of substituting these monocoordinated ligands with solvent molecules. First, crystals of (In)BCN-20B′ were incubated in DMF for 1 week at room temperature. Next, the resultant crystals were analyzed by SCXRD, which revealed that a new 3D structure (In)BCN-20A had been formed (Figure 2c). This new MOF crystallizes in the trigonal lattice with the space group $R\bar{3}m$ (No. 166) and lattice parameters of $a = b$ = 28.783 and c = 47.708 Å (Table S3). (In)BCN-20A, which is isostructural to **nht**-(Fe)MIL-142A,[30] recovers the initial 3D **nht** framework formed by vertex-sharing distorted octahedral cages. However, its cages are instead formed by six $In_3O(-CO_2)_6$ clusters connected by four tritopic TATB linkers and three ditopic BDC linkers, the latter occupying the analogous position of the CCA linkers in (In)BCN-20B (Figure 2b, right).

The phase transition from (In)BCN-20B′ to (In)BCN-20A unambiguously unveiled a self-healing behavior, which we envisaged occurs in three steps within the pores. First, DMF molecules enter the pores and replace the glyoxylate linkers. Here, the release of glyoxylate from the MOF was experimentally confirmed by analyzing the DMF supernatant resulting from the incubation process by ESI-MS, from which the characteristic peak at m/z = 72.99 was detected (Figure S13). Second, the decoordination of glyoxylate causes the framework to act dynamically. In the third and final step, this behavior leads to coordination of the free carboxylic acid group of each BDC linker to the In^{3+} metal sites that were previously occupied by the glyoxylate. Accordingly, the BDC linker would have to migrate a distance of ∼2.4 Å.

To further evaluate the degree of the aforementioned flexibility, we compared the unit cell volumes of the three MOFs: the initial (In)BCN-20B, the ozonated (In)BCN-20B′, and the self-healed (In)BCN-20A (Table S4). From (In)BCN-20B to (In)BCN-20B′, the unit cell volume only shrunk by 0.3%. However, from (In)BCN-20B′ to (In)BCN-20A, the cell volume decreased by 12.6%, an obvious volumetric contraction. We reasoned that the movements involving this dynamic behavior could also be studied by comparing the structural changes in the octahedral cage units (Figures 2b and S14). In the octahedral cage of the initial (In)BCN-20B, the length (note: all lengths were calculated starting from the carbon atoms of the carboxylate groups of the linkers) of the edges of the face constructed with CCA linkers is 8.0 Å, and the average length of the remaining edges is 12.1 Å. As we had expected, cleavage of the CCA linkers barely affected this octahedral cage unit: the length of the edges of the face occupied by the cleaved CCA linkers only increased to 8.2 Å. We attributed this slight increase to the steric hindrance effects of both the BDC and the glyoxylate linkers. In (In)BCN-20A, this length decreases significantly, down to 5.7 Å, because the BDC linker is much smaller than both the initial and the cleaved CCA linkers. Contrariwise, this contraction barely affects the other edges involving the TATB linker, exhibiting an average length of 12.0 Å.

Given that the structure of (In)BCN-20A differs markedly from that of (In)BCN-20B or (In)BCN-20B′, we studied whether this transformation would occur throughout the bulk sample, using PXRD. Supporting a homogeneous transformation, the PXRD pattern of (In)BCN-20A matched the one calculated from the corresponding structure determined by SCXRD (Figures 3a and S15). Comparing the PXRD patterns of (In)BCN-20A and (In)BCN-20B, we found that the diffraction peak of (In)BCN-20B at 2θ = 3.8° which corresponds to the $(10\bar{2})$ crystallographic plane being shifted to a higher angle (2θ = 5.1°) in the same plane of (In)BCN-20A, thus confirming the compression of the framework. Phase homogeneity was also studied by FTIR and ^{1}H NMR (Figures S16 and S17). The FTIR spectrum revealed that the stretching

https://doi.org/10.1021/jacs.3c05469
J. Am. Chem. Soc. 2023, 145, 17398−17405

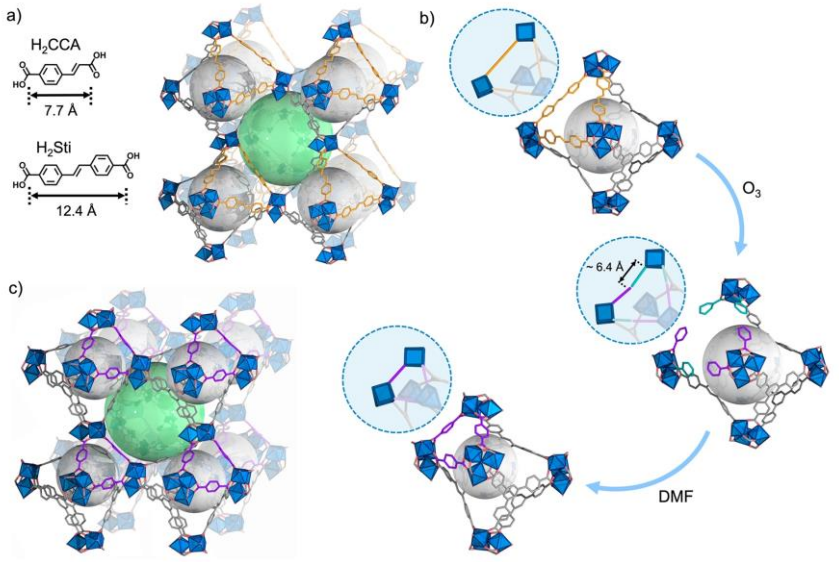


Figure 4. (a) Crystal structure of (Sc)BCN-20C. (b) Schematic and corresponding SCXRD structures of the stepwise isoreticular contraction from (Sc)BCN-20C (top) to (Sc)BCN-20C′ (middle) to (Sc)BCN-20A (down). (c) Crystal structure of (Sc)BCN-20A.

band of characteristic carbonyl groups (1697 cm^{-1}) and the broad absorbance at around 3300 cm^{-1} had been dramatically attenuated, identically to that of the initial (In)BCN-20B (Figure 3c). The ^{1}H NMR spectrum confirmed the expected TATB/BDC ratio of 4:3.

We would like to highlight that all our attempts to transform (In)BCN-20B into (In)BCN-20A by direct linker exchange of CCA by BDC were unsuccessful (see Section 2 of the Supporting Information). This suggests that covalent bond cleavage of the CCA linker highly facilitates the internal restructuration of the framework, involving both flexible and self-healing behavior.

Seeking to investigate whether such behavior could occur in an isoreticular framework with greater distances between metal clusters, we substituted the CCA linker with the 4,4′-stilbenedicarboxylic acid (H_2Sti) linker, which is longer (Figure 4a). However, all our attempts at synthesizing the isostructural MOF using In^{3+} were unsuccessful. Fortunately, we were able to synthesize its Sc^{3+} analogue using the (ditopic) Sti linker and the (tritopic) 1,3,5-tris(4-carboxyphenyl)-benzene (BTB) linker (Figure 4a). (Sc)BCN-20C crystallizes in the monoclinic symmetry with a $C2/c$ space group (No. 15) and lattice parameters of a = 60.279, b = 34.723, and c = 37.136 Å (Table S5). As its analogues, it contains a 2-fold interpenetrated structure with two underlying **nht** nets (Figure S18). Note that the two nets are interconnected by formate linkers that can be formed upon decomposition of DMF aided by HNO_3.[31,37] These nets are built up from vertex-sharing distorted octahedral cages, which are larger than those of (In)BCN-20B or (In)BCN-20A. Their main difference lies in the edges of the triangular face defined by three Sti linkers, whose length is increased to 12.2 Å. The other edges of the octahedra are slightly longer (12.3 Å) than those of (In)BCN-20B. The phase purity of (Sc)BCN-20C was confirmed by PXRD, whose pattern matched the one simulated from SCXRD data (Figures S19 and S20), and by ^{1}H NMR, the spectrum confirmed the expected BTB/Sti ratio of 4:3 (Figure S23).

Next, we performed a cleavage experiment on the Sti linkers similar to the previous experiment on the CCA linkers (Figure 4b). Thus, ozone was flowed (~15 g/Nm^3) continuously through a crystalline sample of solvent-free (Sc)BCN-20C for 5 min. The quantitative cleavage of Sti linkers and conversion of the resultant fragments to the expected monocoordinated HBDC and 4-formylbenzoate (4-FBA) were corroborated by ^{1}H NMR, SCXRD, PXRD, and FTIR (Table S6, Figures S21, S24, S25, and S29). Additionally, SCXRD data revealed that the structure of (Sc)BCN-20C′ is very similar to that of the initial (Sc)BCN-20C, with the corresponding octahedral cage units having similar dimensions. However, we observed one significant difference: benzoate ligands—most likely, 4-FBA linkers with highly disordered aldehyde groups—bridging the two interpenetrated nets and partially substituting the formate ligands. This observation evidenced the mobility of these monocoordinated ligands inside the pores upon cleavage of the ditopic linkers.

Finally, endeavoring to remove the 4-FBA ligands and induce the dynamic and self-healing behavior for the formation of the isoreticular (Sc)-BCN-20A, we immersed (Sc)BCN-20C′ in DMF for a week. Interestingly, SCXRD of the resulting crystals confirmed the formation of this MOF (Table S7, Figures S18, S19, S22, and S26–S29), whose structure is

https://doi.org/10.1021/jacs.3c05469
J. Am. Chem. Soc. 2023, 145, 17398−17405

isostructural to that of (In)BCN-20A (Figure 4b,c). (Sc)-BCN-20A crystallizes in a trigonal system with the space group $R\bar{3}c$ (No. 167) and lattice parameters of $a = b = 28.682$ and $c = 95.606$ Å. Accordingly, through this dynamic, self-healing phenomenon, the cell volume had been dramatically compressed by 30.7% (Table S8 and Figure S31). In this process, all BDC linkers traveled a distance of ~6.4 Å to coordinate to the Sc^{3+} metal sites, shrinking one of the triangular faces of the cages from 12.2 to 6.1 Å.

CONCLUSIONS

In conclusion, we have shown that the cleavage of covalent bonds within bridging organic linkers in an MOF can trigger a series of chemical and structural dynamic processes that drive the formation of an isoreticular contracted MOF. Remarkably, as the single-crystal character of the parent MOF is retained throughout the entire isoreticular transformation, we were able to use SCXRD to obtain invaluable crystallographic snapshots of the stepwise processes. Initially, applying our concept of clip-off chemistry, we were able to cleave each bridging alkene-containing organic linker into two monocoordinated ligands via ozonolysis, thereby disconnecting two metal clusters. Among these monocoordinated ligands, one is terminated with a carboxylic acid group, whereas the other ends in an aldehyde group. As this latter ligand is weaker, we were able to decoordinate it from the metal center by simply treating the MOF with DMF. This removal process conferred the structure with dynamic behavior that involved the migration and subsequent coordination of the other monocoordinated ligand with a free carboxylic acid group to the open metal site. In what we have called "self-healing behavior", the metal clusters that had been disconnected during cleavage of the linker bond reconnected to form a new MOF isoreticular to the initial one, with a contracted structure. Thus, the complete transformation involves breaking of covalent bonds, breaking and formation of coordination bonds, and contraction of the crystal structure, with reductions in the cell volume of up to 30.7%, all occurring in a single-crystal to single-crystal manner. Overall, these stepwise isoreticular transformations exemplify the rich chemistry that can be done inside MOF pores. They also underscore the potential of clip-off chemistry (i.e., breaking of covalent bonds) to discover new phenomena in MOFs and to synthesize new MOFs or other materials.

ASSOCIATED CONTENT

Supporting Information

The Supporting Information is available free of charge at https://pubs.acs.org/doi/10.1021/jacs.3c05469.

Detailed syntheses, optical microscopy images, PXRD diffractogram, FT-IR, ESI-MS, NMR, and crystallographic details (PDF)

Accession Codes

CCDC 2264121−2264126 contain the supplementary crystallographic data for this paper. These data can be obtained free of charge via www.ccdc.cam.ac.uk/data_request/cif, or by emailing data_request@ccdc.cam.ac.uk, or by contacting The Cambridge Crystallographic Data Centre, 12 Union Road, Cambridge CB2 1EZ, UK; fax: +44 1223 336033.

AUTHOR INFORMATION

Corresponding Authors

Inhar Imaz − *CSIC, and Barcelona Institute of Science and Technology, Catalan Institute of Nanoscience and Nanotechnology (ICN2), Bellaterra, Barcelona 08193, Spain; Departament de Química, Facultat de Ciències, Universitat Autònoma de Barcelona, Bellaterra 08193, Spain;* orcid.org/0000-0002-0278-1141; Email: inhar.imaz@icn2.cat

Daniel Maspoch − *CSIC, and Barcelona Institute of Science and Technology, Catalan Institute of Nanoscience and Nanotechnology (ICN2), Bellaterra, Barcelona 08193, Spain; Departament de Química, Facultat de Ciències, Universitat Autònoma de Barcelona, Bellaterra 08193, Spain; ICREA, Barcelona 08010, Spain;* orcid.org/0000-0003-1325-9161; Email: daniel.maspoch@icn2.cat

Authors

Yunhui Yang − *CSIC, and Barcelona Institute of Science and Technology, Catalan Institute of Nanoscience and Nanotechnology (ICN2), Bellaterra, Barcelona 08193, Spain; Departament de Química, Facultat de Ciències, Universitat Autònoma de Barcelona, Bellaterra 08193, Spain*

Pilar Fernández-Seriñán − *CSIC, and Barcelona Institute of Science and Technology, Catalan Institute of Nanoscience and Nanotechnology (ICN2), Bellaterra, Barcelona 08193, Spain; Departament de Química, Facultat de Ciències, Universitat Autònoma de Barcelona, Bellaterra 08193, Spain;* orcid.org/0000-0002-6456-7386

Felipe Gándara − *Consejo Superior de Investigaciones Científicas (CSIC), Materials Science Institute of Madrid (ICMM), Madrid 28049, Spain;* orcid.org/0000-0002-1671-6260

Marcel Handke − *CSIC, and Barcelona Institute of Science and Technology, Catalan Institute of Nanoscience and Nanotechnology (ICN2), Bellaterra, Barcelona 08193, Spain; Departament de Química, Facultat de Ciències, Universitat Autònoma de Barcelona, Bellaterra 08193, Spain*

Borja Ortín-Rubio − *CSIC, and Barcelona Institute of Science and Technology, Catalan Institute of Nanoscience and Nanotechnology (ICN2), Bellaterra, Barcelona 08193, Spain; Departament de Química, Facultat de Ciències, Universitat Autònoma de Barcelona, Bellaterra 08193, Spain;* orcid.org/0000-0002-0533-3635

Judith Juanhuix − *ALBA Synchrotron, Cerdanyola del Vallès, Barcelona 08290, Spain;* orcid.org/0000-0003-3728-8215

Complete contact information is available at: https://pubs.acs.org/10.1021/jacs.3c05469

Notes

The authors declare no competing financial interest.

ACKNOWLEDGMENTS

We thank Dr. Jorge Albalad for converting PXRD patterns and Dr. Dongsik Nam for useful discussions about crystallography. This work has received funding from the European Union's Horizon 2020 research and innovation program under grant agreement no. 101019003, Grants Ref. PID2021-124804NB-I00 and PID2021-123287OB-I00 funded by MCIN/AEI/10.13039/501100011033/ and by "ERDF A way of making Europe", and the Catalan AGAUR (project 2021 SGR 00458).

This work was also funded by the CERCA program/Generalitat de Catalunya. ICN2 is supported by the Severo Ochoa Centres of Excellence program, Grant CEX2021-001214-S, funded by MCIN/AEI/10.13039.501100011033. Y.Y. acknowledges the China Scholarship Council for scholarship support.

■ REFERENCES

(1) Zhou, H.-C.; Long, J. R.; Yaghi, O. M. Introduction to Metal−Organic Frameworks. *Chem. Rev.* **2012**, *112*, 673−674.
(2) Howarth, A. J.; Liu, Y.; Li, P.; Li, Z.; Wang, T. C.; Hupp, J. T.; Farha, O. K. Chemical, thermal and mechanical stabilities of metal−organic frameworks. *Nat. Rev. Mater.* **2016**, *1*, 15018.
(3) Yaghi, O. M.; O'Keeffe, M.; Ockwig, N. W.; Chae, H. K.; Eddaoudi, M.; Kim, J. Reticular synthesis and the design of new materials. *Nature* **2003**, *423*, 705−714.
(4) Chen, Z.; Hanna, S. L.; Redfern, L. R.; Alezi, D.; Islamoglu, T.; Farha, O. K. Reticular chemistry in the rational synthesis of functional zirconium cluster-based MOFs. *Coord. Chem. Rev.* **2019**, *386*, 32−49.
(5) Jiang, H.; Alezi, D.; Eddaoudi, M. A reticular chemistry guide for the design of periodic solids. *Nat. Rev. Mater.* **2021**, *6*, 466−487.
(6) Yaghi, O. M. Reticular Chemistry: Molecular Precision in Infinite 2D and 3D. *Mol. Front. J.* **2019**, *03*, 66−83.
(7) Eddaoudi, M.; Kim, J.; Rosi, N.; Vodak, D.; Wachter, J.; O'Keeffe, M.; Yaghi, O. M. Systematic Design of Pore Size and Functionality in Isoreticular MOFs and Their Application in Methane Storage. *Science* **2002**, *295*, 469−472.
(8) Deng, H.; Grunder, S.; Cordova, K. E.; Valente, C.; Furukawa, H.; Hmadeh, M.; Gándara, F.; Whalley, A. C.; Liu, Z.; Asahina, S.; Kazumori, H.; O'Keeffe, M.; Terasaki, O.; Stoddart, J. F.; Yaghi, O. M. Large-Pore Apertures in a Series of Metal-Organic Frameworks. *Science* **2012**, *336*, 1018−1023.
(9) Li, P.; Chen, Q.; Wang, T. C.; Vermeulen, N. A.; Mehdi, B. L.; Dohnalkova, A.; Browning, N. D.; Shen, D.; Anderson, R.; Gómez-Gualdrón, D. A.; Cetin, F. M.; Jagiello, J.; Asiri, A. M.; Stoddart, J. F.; Farha, O. K. Hierarchically Engineered Mesoporous Metal-Organic Frameworks toward Cell-free Immobilized Enzyme Systems. *Chem* **2018**, *4*, 1022−1034.
(10) Wang, Z.; Cohen, S. M. Postsynthetic modification of metal−organic frameworks. *Chem. Soc. Rev.* **2009**, *38*, 1315−1329.
(11) Deria, P.; Mondloch, J. E.; Karagiaridi, O.; Bury, W.; Hupp, J. T.; Farha, O. K. Beyond post-synthesis modification: evolution of metal−organic frameworks via building block replacement. *Chem. Soc. Rev.* **2014**, *43*, 5896−5912.
(12) Kirchon, A.; Feng, L.; Drake, H. F.; Joseph, E. A.; Zhou, H.-C. From fundamentals to applications: a toolbox for robust and multifunctional MOF materials. *Chem. Soc. Rev.* **2018**, *47*, 8611−8638.
(13) Bury, W.; Fairen-Jimenez, D.; Lalonde, M. B.; Snurr, R. Q.; Farha, O. K.; Hupp, J. T. Control over Catenation in Pillared Paddlewheel Metal−Organic Framework Materials via Solvent-Assisted Linker Exchange. *Chem. Mater.* **2013**, *25*, 739−744.
(14) Feng, L.; Yuan, S.; Qin, J.-S.; Wang, Y.; Kirchon, A.; Qiu, D.; Cheng, L.; Madrahimov, S. T.; Zhou, H.-C. Lattice Expansion and Contraction in Metal-Organic Frameworks by Sequential Linker Reinstallation. *Matter* **2019**, *1*, 156−167.
(15) Li, Y.; Su, J.; Zhao, Y.; Feng, L.; Gao, L.; Xu, X.; Yin, Y.; Liu, Y.; Xiao, P.; Yuan, L.; Qin, J.-S.; Wang, Y.; Yuan, S.; Zheng, H.; Zuo, J.-L. Dynamic Bond-Directed Synthesis of Stable Mesoporous Metal−Organic Frameworks under Room Temperature. *J. Am. Chem. Soc.* **2023**, *145*, 10227−10235.
(16) Li, T.; Kozlowski, M. T.; Doud, E. A.; Blakely, M. N.; Rosi, N. L. Stepwise Ligand Exchange for the Preparation of a Family of Mesoporous MOFs. *J. Am. Chem. Soc.* **2013**, *135*, 11688−11691.
(17) Yuan, S.; Zhang, P.; Zhang, L.; Garcia-Esparza, A. T.; Sokaras, D.; Qin, J.-S.; Feng, L.; Day, G. S.; Chen, W.; Drake, H. F.; Elumalai, P.; Madrahimov, S. T.; Sun, D.; Zhou, H.-C. Exposed Equatorial Positions of Metal Centers via Sequential Ligand Elimination and Installation in MOFs. *J. Am. Chem. Soc.* **2018**, *140*, 10814−10819.
(18) Yuan, S.; Qin, J.-S.; Su, J.; Li, B.; Li, J.; Chen, W.; Drake, H. F.; Zhang, P.; Yuan, D.; Zuo, J.; Zhou, H.-C. Sequential Transformation of Zirconium(IV)-MOFs into Heterobimetallic MOFs Bearing Magnetic Anisotropic Cobalt(II) Centers. *Angew. Chem., Int. Ed.* **2018**, *57*, 12578−12583.
(19) Burnett, B. J.; Barron, P. M.; Hu, C.; Choe, W. Stepwise Synthesis of Metal−Organic Frameworks: Replacement of Structural Organic Linkers. *J. Am. Chem. Soc.* **2011**, *133*, 9984−9987.
(20) Cao, L.-H.; Liu, X.; Tang, X.-H.; Liu, J.; Xu, X.-Q.; Zang, S.-Q.; Ma, Y.-M. A fivefold linker length reduction in an interpenetrated metal−organic framework via sequential solvent-assisted linker exchange. *Chem. Commun.* **2019**, *55*, 12671−12674.
(21) Xiao, Y.; Chen, Y.; Wang, W.; Yang, H.; Hong, A. N.; Bu, X.; Feng, P. Simultaneous Control of Flexibility and Rigidity in Pore-Space-Partitioned Metal−Organic Frameworks. *J. Am. Chem. Soc.* **2023**, *145*, 10980−10986.
(22) Krause, S.; Bon, V.; Senkovska, I.; Stoeck, U.; Wallacher, D.; Többens, D. M.; Zander, S.; Pillai, R. S.; Maurin, G.; Coudert, F.-X.; Kaskel, S. A pressure-amplifying framework material with negative gas adsorption transitions. *Nature* **2016**, *532*, 348−352.
(23) Schneemann, A.; Bon, V.; Schwedler, I.; Senkovska, I.; Kaskel, S.; Fischer, R. A. Flexible metal−organic frameworks. *Chem. Soc. Rev.* **2014**, *43*, 6062−6096.
(24) Douvali, A.; Tsipis, A. C.; Eliseeva, S. V.; Petoud, S.; Papaefstathiou, G. S.; Malliakas, C. D.; Papadas, I.; Armatas, G. S.; Margiolaki, I.; Kanatzidis, M. G.; Lazarides, T.; Manos, M. J. Turn-on luminescence sensing and real-time detection of traces of water in organic solvents by a flexible metal−organic framework. *Angew. Chem., Int. Ed.* **2015**, *54*, 1651−1656.
(25) Chang, Z.; Yang, D.-H.; Xu, J.; Hu, T.-L.; Bu, X.-H. Flexible Metal−Organic Frameworks: Recent Advances and Potential Applications. *Adv. Mater.* **2015**, *27*, 5432−5441.
(26) Zhang, Y.; Zhang, X.; Lyu, J.; Otake, K.-I.; Wang, X.; Redfern, L. R.; Malliakas, C. D.; Li, Z.; Islamoglu, T.; Wang, B.; Farha, O. K. A Flexible Metal−Organic Framework with 4-Connected Zr6 Nodes. *J. Am. Chem. Soc.* **2018**, *140*, 11179−11183.
(27) Chen, X.; Xie, H.; Lorenzo, E. R.; Zeman, C. J. I. V.; Qi, Y.; Syed, Z. H.; Stone, A. E. B. S.; Wang, Y.; Goswami, S.; Li, P.; Islamoglu, T.; Weiss, E. A.; Hupp, J. T.; Schatz, G. C.; Wasielewski, M. R.; Farha, O. K. Direct Observation of Modulated Radical Spin States in Metal−Organic Frameworks by Controlled Flexibility. *J. Am. Chem. Soc.* **2022**, *144*, 2685−2693.
(28) Yang, H.; Chen, Y.; Dang, C.; Hong, A. N.; Feng, P.; Bu, X. Optimization of Pore-Space-Partitioned Metal−Organic Frameworks Using the Bioisosteric Concept. *J. Am. Chem. Soc.* **2022**, *144*, 20221−20226.
(29) Yang, Y.; Broto-Ribas, A.; Ortín-Rubio, B.; Imaz, I.; Gándara, F.; Carné-Sánchez, A.; Guillerm, V.; Jurado, S.; Busqué, F.; Juanhuix, J.; Maspoch, D. Clip-off Chemistry: Synthesis by Programmed Disassembly of Reticular Materials. *Angew. Chem., Int. Ed.* **2022**, *61*, No. e202111228.
(30) Chevreau, H.; Devic, T.; Salles, F.; Maurin, G.; Stock, N.; Serre, C. Mixed-Linker Hybrid Superpolyhedra for the Production of a Series of Large-Pore Iron(III) Carboxylate Metal−Organic Frameworks. *Angew. Chem., Int. Ed.* **2013**, *52*, 5056−5060.
(31) Prasad, R. R. R.; Pleass, C.; Rigg, A. L.; Cordes, D. B.; Lozinska, M. M.; Georgieva, V. M.; Hoffmann, F.; Slawin, A. M. Z.; Wright, P. A. Isoreticular chemistry of scandium analogues of the multi-component metal−organic framework MIL-142. *CrystEngComm* **2021**, *23*, 804−812.
(32) Albalad, J.; Xu, H.; Gándara, F.; Haouas, M.; Martineau-Corcos, C.; Mas-Ballesté, R.; Barnett, S. A.; Juanhuix, J.; Imaz, I.; Maspoch, D. Single-Crystal-to-Single-Crystal Postsynthetic Modification of a Metal−Organic Framework via Ozonolysis. *J. Am. Chem. Soc.* **2018**, *140*, 2028−2031.
(33) Guillerm, V.; Xu, H.; Albalad, J.; Imaz, I.; Maspoch, D. Postsynthetic Selective Ligand Cleavage by Solid−Gas Phase

https://doi.org/10.1021/jacs.3c05469
J. Am. Chem. Soc. 2023, 145, 17398−17405

Ozonolysis Fuses Micropores into Mesopores in Metal−Organic Frameworks. *J. Am. Chem. Soc.* **2018**, *140*, 15022−15030.
(34) Ragon, F.; Campo, B.; Yang, Q.; Martineau, C.; Wiersum, A. D.; Lago, A.; Guillerm, V.; Hemsley, C.; Eubank, J. F.; Vishnuvarthan, M.; Taulelle, F.; Horcajada, P.; Vimont, A.; Llewellyn, P. L.; Daturi, M.; Devautour-Vinot, S.; Maurin, G.; Serre, C.; Devic, T.; Clet, G. Acid-functionalized UiO-66(Zr) MOFs and their evolution after intra-framework cross-linking: structural features and sorption properties. *J. Mater. Chem. A* **2015**, *3*, 3294−3309.
(35) Hadjiivanov, K. I.; Panayotov, D. A.; Mihaylov, M. Y.; Ivanova, E. Z.; Chakarova, K. K.; Andonova, S. M.; Drenchev, N. L. Power of Infrared and Raman Spectroscopies to Characterize Metal-Organic Frameworks and Investigate Their Interaction with Guest Molecules. *Chem. Rev.* **2021**, *121*, 1286−1424.
(36) Blatov, V. A.; Shevchenko, A. P.; Proserpio, D. M. Applied Topological Analysis of Crystal Structures with the Program Package ToposPro. *Cryst. Growth Des.* **2014**, *14*, 3576−3586.
(37) Reinares-Fisac, D.; Aguirre-Díaz, L. M.; Iglesias, M.; Snejko, N.; Gutiérrez-Puebla, E.; Monge, M. Á.; Gándara, F. A Mesoporous Indium Metal−Organic Framework: Remarkable Advances in Catalytic Activity for Strecker Reaction of Ketones. *J. Am. Chem. Soc.* **2016**, *138*, 9089−9092.

https://doi.org/10.1021/jacs.3c05469
J. Am. Chem. Soc. 2023, 145, 17398−17405

Journal of Membrane Science 691 (2024) 122258

Contents lists available at ScienceDirect

Journal of Membrane Science

journal homepage: www.elsevier.com/locate/memsci

Metal- and covalent-organic framework mixed matrix membranes for CO_2 separation: A perspective on stability and scalability

Meixia Shan [a,b,**], Xiumei Geng [a], Inhar Imaz [c], Anna Broto-Ribas [c], Borja Ortín-Rubio [c], Daniel Maspoch [c,d], Luca Ansaloni [e], Thijs A. Peters [e], Alberto Tena [f,g], Marcel E. Boerrigter [h], David A. Vermaas [b,*]

[a] School of Chemical Engineering, Zhengzhou University, Zhengzhou, 450001, PR China
[b] Chemical Engineering Department, Delft University of Technology, van der Maasweg, 9, 2629, HZ Delft, the Netherlands
[c] Catalan Institute of Nanoscience and Nanotechnology (ICN2), CSIC and the Barcelona Institute of Science and Technology, Campus UAB, Bellaterra, 08193, Barcelona, Spain
[d] ICREA, Pg. Lluís Companys 23, 08010, Barcelona, Spain
[e] SINTEF Industry, P.O. Box 124 Blindern, N-0314, Oslo, Norway
[f] Membrane Science and Technology, Faculty of Science and Technology, MESA+ Institute for Nanotechnology, University of Twente, P.O. Box 217, AE Enschede, the Netherlands
[g] Surfaces and Porous Materials (SMAP), Associated Research Unit to CSIC, Institute of Sustainable Processes (ISP), Dr. Mergelina S/n, University of Valladolid, 47071, Valladolid, Spain
[h] LEITAT Technological Center, Carrer de Pallars, 179-185, 08005, Barcelona, Spain

A B S T R A C T

Membrane technology has attracted great industrial interest in carbon capture and separation owing to the merits of energy-efficiency, environmental friendliness and low capital investment. Conventional polymeric membranes for CO_2 separation suffer from the trade-off between permeability and selectivity. Introducing porous fillers in polymers is one approach to enhance membrane separation performance. Metal-organic frameworks (MOFs), with ordered porous structure and diverse chemical functionalities, are promising fillers to prepare mixed matrix membranes (MMMs) for CO_2 separation. However, the main issue of MOF based MMMs in industry is their stability and processability. This review analyses recent work on stable and scalable MOF based MMMs for CO_2 separation. The typical stable MOFs, MOF-based MMMs and the scalable MOF synthesis are summarized. A large number of MOF-based MMM suffer from instability upon exposure to contaminants. For that reason, we also discuss the use of covalent organic frameworks (COFs) as an alternative to prepare MMMs for CO_2 separation, considering their excellent stability and good compatibility with polymers. Finally, a brief conclusion and current challenges on obtaining scalable and stable MMMs are outlined. This review may provide some guidance for designing high performance MMMs for industrial CO_2 capture and separation to help achieving carbon neutrality.

1. Introduction

Global warming due to the enhanced and continuing emission of greenhouse gases has caused great public concern. Different approaches are being considered and adopted by various countries to reduce CO_2 emissions, including the potential key carbon capture and storage (CCS) technology [1]. However, the conventional technologies using amine scrubbing or sorbents are facing covdnstraints like scale-up issues, high cost, large footprint, high energy consumption and are potentially environmental unfriendly [2]. Membranes offer a viable energy-saving alternative approach to capture CO_2 due to their versatility, scalability, ease of operation, small footprint and energy efficiency [3]. Nowadays, polymer membranes dominate the membrane market due to the low cost and good processability. For example, the removal of CO_2 from natural gas, the recovery of H_2 (in cracking processes) and oxygen/nitrogen separation using cellulose acetate or polyimide membranes are commercial applications in industry [4,5]. However, the separation performance of polymeric membranes for gas separation obey an intrinsic trade-off relation between permeability and selectivity [6,7]. Furthermore, plasticization and aging issues also restrict their industrial application [8–11]. To overcome the limit of polymer membranes, one pursued method is the preparation of mixed-matrix membranes (MMMs), where inorganic/organic fillers such as carbon molecular sieves (CMSs) [12], carbon nanotubes [13], zeolites [14,15],

* Corresponding author. Chemical Engineering Department, Delft University of Technology, van der Maasweg, 9, 2629, HZ Delft, the Netherlands.
** Corresponding author. School of Chemical Engineering, Zhengzhou University, Zhengzhou, 450001, PR China.
E-mail addresses: mxshan@zzu.edu.cn (M. Shan), D.A.Vermaas@tudelft.nl (D.A. Vermaas).

https://doi.org/10.1016/j.memsci.2023.122258
Received 25 September 2023; Received in revised form 5 November 2023; Accepted 7 November 2023
Available online 11 November 2023
0376-7388/© 2023 The Authors. Published by Elsevier B.V. This is an open access article under the CC BY license (http://creativecommons.org/licenses/by/4.0/).

covalent organic frameworks (COFs) [16–18] and metal organic frameworks (MOFs) [19–24] are dispersed in a continuous polymer matrix. MMMs could combine the advantages of both fillers and polymer matrixes, for which selectivity and permeability is observed to surpass the limits of conventional polymer membranes [25–28].

Among the different families of fillers, metal-organic frameworks (MOFs), represent an important class of crystalline molecular sieves that are constructed from linking metal-ions clusters and organic linkers through coordination bonds [29,30]. MOFs are known for their extraordinary structural variability, as both metal ion/clusters and organic linkers can be independently chosen to form MOFs with diverse pore structures and functionalities. MOFs display several advantages over other solid materials, such as permanent porosity with high surface area, flexibility and adjustable pore sizes and tuneable pore surface modifications [31], which enable them as good candidates to be used as fillers in developing novel MMMs [32–36]. Although (idealized) lab-scale experiments have convincingly demonstrated increased selectivity and/or permeability for several MOF-polymer combinations, the large-scale deployment of MOF-based MMM's for CO_2 capture is still awaiting. The development of MOF-based MMMs has been largely restricted by their chemical stability; *e.g.,* ambient moisture or variable pH may result in the degradation of the framework for most of the early MOFs [37–40]. In this context, developing stable-MOF membranes are necessary for real industrial gas separation applications where the feed gas stream may contain trace contaminants such as NO_x, SO_2 or NH_3, specially under humid conditions [41,42].

The diversity and number of MOF structures has grown in recent years, including synthesis of thermally and chemically stable MOFs [43–45], enabling the possibility to be processed into stable MMMs. In addition to stability, process scalability is also a critical factor that needs to be taken into account when choosing MOFs to prepare the MMM: scalability may indeed become the main barrier for membrane commercialization. There have been several previous reviews [46–50], focussing on the performance under idealized lab-conditions. While real conditions require long-term stability and large-scale manufacturing, very few papers [51–55] have assessed upscaled real-life conditions. Instead, a substantial amount of individual works has assessed the stability of MOF-based MMM's in lab-environment.

To assess the practical potential of MOF-based MMMs, this review provides an overview on reported stability of MOF-based MMMs and assess their manufacturability. We aim to provide insight in the stability and manufacturability of MOF-based MMM's in non-idealized conditions and proposed methods for upscaled manufacturability. In this review, we highlight the current progress and identify the future opportunities of stable and scalable MOF based mixed-matrix membranes for CO_2 separation. Due to the challenging stability of MOFs under real-life gas conditions, we also analyse the recent use of covalent-organic frameworks (COFs; analogues of MOFs but made exclusively of organic linkers [56,57]) as a promising type of fillers in MMMs.

2. Framework of industrial conditions for CO_2 capture

Industrial gas streams include contaminants that are typically neglected in lab-scale tests, such as water vapor, hydrocarbons, aromatic compounds and corrosive gases. Table 1 listed the typical contaminate gases in CO_2 capture processes.

In the pre-combustion CO_2 capture process, CO_2 needs to be removed from fossil fuels before combustion is completed. For example, the fossil fuels first undergo partially oxidization in steam and oxygen/air at high pressure and temperature to generate synthesis gas. The syngas obtained after combustion reaction is a mixture of H_2, CO, CO_2 and small amounts of CH_4 [58].

For post-combustion CO_2 capture applications related to power generation, the gas streams are mainly composed by CO_2 and N_2 with up to 20 wt% moisture, 200–5000 ppmv SOx before desulphurisation (mainly in the form of SO_2 with a small proportion of SO_3) and 150–300 ppmv NOx with NO as main component and <10 ppmv NO_2 [59]. It is important to note that the levels of impurities are dependent on the fuel type used in the combustion. For example, for an advanced supercritical (ASC) pulverized fuel (PF) bituminous power plant, the flue gas after desulphurisation is expected to contain 30 ppm of SO_2 [60]. The content of SO_2 can be further reduced an additional washing step. In the case of post-combustion capture retrofitted to a cement plant, small amount of NH_3 (15–50 ppm), HCl (0.5–1 ppm) and suspended particulate matter (2–5 mg/Nm^3) can also be present in the gaseous stream fed to the separation module [59]. Also with respect to flue gases from the major CO_2 emission sources in an integrated steel mill, SOx (10–300 mg/Nm^3), NOx (30–280 mg/Nm^3) and dust (<5 mg/Nm^3) represent the major contaminants [61]. H_2S is often present in natural gas upgrading (potentially in the %-level, depending on gas field). For upgrading of biogas, traces of H_2S, NH_3, CO and saturated or halogenated carbohydrates can be present. The H_2S content can vary with the organic being composted, but typical values of 10–10,000 ppmv (0.0001–1 vol%) are reported [62].

Table 1
The content of typical contaminants in different feed gas.

Feed type	Major gas components	Typical contaminants	Ref.
Pre-combustion CO_2 capture	H_2/CO_2 mixture	H_2O, CO, CH_4, H_2S	[58]
Post-combustion CO_2 capture	CO_2/N_2 mixture	20 wt% moisture, 200–5000 ppmv SOx, 150–300 ppmv NOx, <10 ppmv NO_2, NH_3 (15–50 ppm), HCl (0.5–1 ppm), suspended particulate matter (2–5 mg/Nm^3)	[59]
		30 ppm of SO_2	[60]
		SOx (10–300 mg/Nm^3), NOx (30–280 mg/Nm^3), Dust (<5 mg/Nm^3)	[61]
Upgrading of biogas	CO_2/CH_4 mixture	10–10,000 ppmv (0.0001–1 vol%) H_2S, Traces of H_2S, NH_3, CO, Halogenated carbohydrates	[62]

3. Stability of MOFs to industrial gas stream conditions

3.1. Stability to humidity

MOFs could potentially be affected by the presence of water vapor and other gases (NH_3, SO_2 and H_2S) in industrial gas streams. These gaseous contaminants can break the metal-ligand bonds by coordinating to, oxidizing or hydrolyzing the metal centers and/or by protonating the ligands. Thus, MOFs designed for practical CO_2-applications must resist such gases for extended periods of time without suffering any loss in functionality [3]. Unfortunately, there have not yet been any studies evaluating the stability of such MOFs under real conditions of industrial gas streams. The limited number of literature on the stability of MOFs to gases is focused on their hydrolytic stability, although there have been some reports confirming that certain MOFs are stable to pure NH_3, H_2S or SO_2 [63]. These data may help researchers in their design of stable MOFs for industrial-scale CO_2-capture.

Many of the archetypical MOFs used to generate the first MMMs, including HKUST-1, Cr-MIL-101 and MOF-5 (plus some related IRMOFs), are expected not to be stable to water vapor or other industrial gases. For example, these MOFs are not stable to water vapor, which causes their relatively weak metal-oxygen bonds to undergo phase transformation, leading to framework decomposition. This type of decomposition is signalled analytically by degradation or loss of reflection at specific positions in the powder X-ray diffraction (PXRD) pattern; and functionally, by loss in the porosity and gas uptake of the MOF [64–66]. Similarly to water vapor, NH_3 gas reacts with HKUST-1, driving transformations that cause irreversible losses in structure and porosity, as described by Peterson et al. [67] They observed that under

dry conditions, this reaction generates a diamine−copper(II) complex, whereas under humid conditions, it generates $Cu(OH)_2$ and $(NH_4)_3BTC$. Such structural damage has obvious functional consequences: for example, Saha and Deng reported that exposure of MOF-5 or *iso*reticular IRMOFs to NH_3 leads to the formation of hydrogen bonds between the Zn_4O centers and NH_3, triggering a massive decrease in the adsorption capacities of each MOF [68]. Furthermore, acidic gases can induce protonation of the metal-bound ligands in MOFs, causing the bonds to break and consequently, to deteriorated MOF performance. This has been reported for reaction of H_2S with ZIF-8 and with HKUST-1; in the latter case, protonation of the trimesic acid ligand leads to framework collapse [69].

The ZIF-type MOFs have been extensively studied. Yaghi et al. [70] reported the highly stable ZIF-8 and -11, demonstrating remarkable chemical resistance towards refluxing organic solvents, water and aqueous alkaline solution. However, Liu et al. [71] observed a different phenomenon that ZIF-8 and other ZIFs (ZIF-7, ZIF-93) underwent hydrolysis under hydrothermal conditions when employing low crystal concentration (0.060 wt%). The authors concluded that ZIF-8 is stable in water at high crystal concentrations due to the protection of its released ligands, which originates from the residuals on the ZIF-8 and (or) few early decomposed ZIF-8. The bare ZIF-8 itself is not stable at 353 K in water and its stability can be highly improved by a shell-ligand –exchange-reaction.

3.2. Stability to other contaminants

The effects of corrosive gas exposure have been studied in other MOFs proposed for CO_2-adsorption applications, including the MOF-74/CPO-27 series, which is built from metal-oxide chains interconnected through 2,5-dioxido-1,4-benzenedicarboxylate linkers. Liu et al. reviewed literature on the effect of water vapor on the CO_2-adsorption capacity of MOF-74 members and concluded that those with less-reductive metal centers are more stable than those possessing more-reductive metal centers: for example, that Ni^{2+}-MOF-74 is more stable to water vapor than is Mg^{2+}-MOF-74 [72]. Similarly, Tan et al. studied the selective co-adsorption capacities of these MOFs towards CO_2 in competition with water vapor, NH_3, SO_2, NO, NO_2, N_2, O_2 and CH_4 [73]. Although they did not observe any framework degradation during the adsorption, they did report that the presence of water vapor was detrimental to the CO_2-uptake capacity of the MOFs, due to the high affinity of their open metal sites for water molecules. For more intuition, we summarize the impact of several contaminants on MOFs in the industrial gas streams in Table 2.

Interestingly, MOFs that contain high-valence metals (*e.g.* Zr^{4+}, $Ti^{4+}$and Al^{3+}, shown in Fig. 1) and broadly-connected nodes bridged by oxo- and hydroxo-groups tend to exhibit relatively high stability to coordinating vapors and gases [74–77]. Among them, there are several MOF families that are known for their hydrolytic stability. These include UiO-type MOFs, which are *iso*reticular MOFs comprising Zr^{4+}-oxide clusters ($Zr_6O_4(OH)_4$) connected through polycarboxylate linkers; several members of MIL MOFs, such as MIL-125(Ti) and MIL-101(Cr); and some Al^{3+}-MOFs built from highly stable, high-nuclearity, oxo--chains, including CAU-10 [78,79]. Remarkably, several studies have shown that some of these MOFs are also stable to H_2S, NH_3 and/or SO_2. For example, Walton et al. demonstrated that UiO-66, MIL-125(Ti) and MIL-101(Cr) are stable to H_2S exposure [78]. They conducted adsorption experiments using multicomponent gas mixtures, including H_2S/CH_4 (1:99 mol/mol) and $H_2S/CO_2/CH_4$ (1:10:89 mol/mol), confirming that the MOFs retained their adsorption capacities. Likewise, Khabzina and co-workers reported that UiO-66_COOH, a UiO-66 analog that contains free carboxylic groups, showed excellent stability to NH_3 [80]. Moreover, Carter et al. found that $[Zr_6(\mu_3\text{-}O)_4(\mu_3\text{-}OH)_4(OH)_4(H_2O)_4(L)_2]$ (also known as *MFM-601*; where L = 4,4′,4″,4‴-(1,4-phenylenebis(pyridine-4,2,6-triyl))tetrabenzoate), could adsorb 12.3 mmol SO_2/g MOF without any signs of degradation [81]. Finally, highly connected Al^{3+}-MOFs such as CAU-10 and isostructural MIL-160 have been reported to be stable in the presence of H_2O, NH_3 and H_2S [82,83].

Many hydrolytic and gas-stable MOFs contain another critical structural feature: strongly donating ligands such as azolates, which enable stronger metal-ligand bonds. Dinca et al. reported that a series of azolate-based MOFs exhibited excellent stability to different contaminant gases [84,85]. For example, Co_2Cl_2BTDD (where BTDD is bis(1H-1,2,3-triazolato [4,5-b],[4′,5′-i])dibenzo [1,4]dioxin) was highly resistance to both water vapor and NH_3. Similarly, Navarro et al. reported a series of MOFs featuring the linker BDP-X^{2-} (where BDP-X^2 is 1,4-benzene-dipyrazolate-2-X (X = H, OH or NH_2)) for SO_2 adsorption. Breakthrough experiments were conducted using typical complex flue gas mixtures consisting of $N_2/CO_2/SO_2$ (83.5:14:2.5) and $N_2/H_2O/SO_2$ (94.1:3.4:2.5). The presence of water vapor or CO_2 does not significantly affect the SO_2 adsorption in 1@$Ba(OH)_2$ (Fig. 2), indicating that the prepared MOFs fully retained their structural integrity [86].

Table 2
Possible effects of the presence of contaminants in the gas streams on the MOFs.

Contaminant	Possible effect	Ref.
Water vapor	Weakening metal-oxygen interaction	[64–66]
	Bonds undergo to phase transformation leading to a framework decomposition	[73]
	Competitive sorption with CO_2 and other gases	
NH_3	Irreversible losses in the structural porosity	[67]
	Creation of diamine-metal complex	
NH_3+H_2O	Decomposition of the MOF	[68]
	H_2 bonding between metals leading to a massive decrease in adsorption capabilities	
H_2S	Protonation of bond between metals and ligands leading to a break and framework collapsing	[69]

3.3. Mechanisms for stable MOF-structures

Stability of MOFs, especially to water vapor, may derive from structural features other than their constituent metal clusters and ligands, which can be introduced during synthesis or post-synthetically. Fig. 3 shows the factors controlling the stability of MOF in water. MOFs with improved stability either should show tolerance for hydrolysis (thermodynamic stability) or strong steric hindrance for water to cluster or approach MOF (kinetic stability) [87]. For a thermodynamically-stable MOF, its structure should show great tolerance for irreversible hydrolysis, meaning that the metal coordination sites (electron acceptor) are inert enough to resist the attack of oxygen (electron donor) from water. In this line, the metal-ligand bond strength and the lability of the metal cluster towards water controls the MOF's thermodynamic stability. As shown in Fig. 3, the metal-ligand bond strength is governed by the pKa of the coordination atom on the ligand, metal oxidation state and ionic radius. Ligands with high pKa values (such as pyrazolate ligand, pKa = 19.8) have been successfully used in the preparation of highly stable Co-, Ni, Zn- and Cu-based MOFs [88,89]. Also metals with high oxidation state, such as Fe^{3+}, Cr^{3+} and Zr^{4+} have been selected to synthesize water-resistant MOFs, for example, in UiO-type MOFs [44,74,90,91].

In addition to increasing the metal-ligand bond strength, the lability of the metal cluster toward water which are influenced by the reduction potential, Irving-Williams series of the metal and the coordination geometry of the ligand, need also to be considered. Liu et al. [72] investigated the steam conditioning effect on CO_2 adsorption capacity of DOBDC MOF/MOF-74 series and found that MOFs with less reductive metal centers are even more stable than those possessing more reductive metal centers (e. g. stability Ni/DOBDC > Mg/DOBDC). As to the kinetic stability, increasing the activation energy for hydrolysis is the primary goal to maintain the MOF structure stable under humid conditions. Commonly used methods, including the introduction of hydrophobic

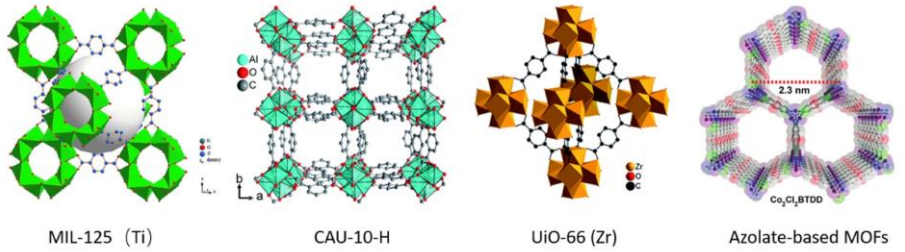


Fig. 1. Some typical stable MOF structures. Reproduced with permission from refs. 77, 79, 84, Copyright Royal Society of Chemistry and American Chemical Society.

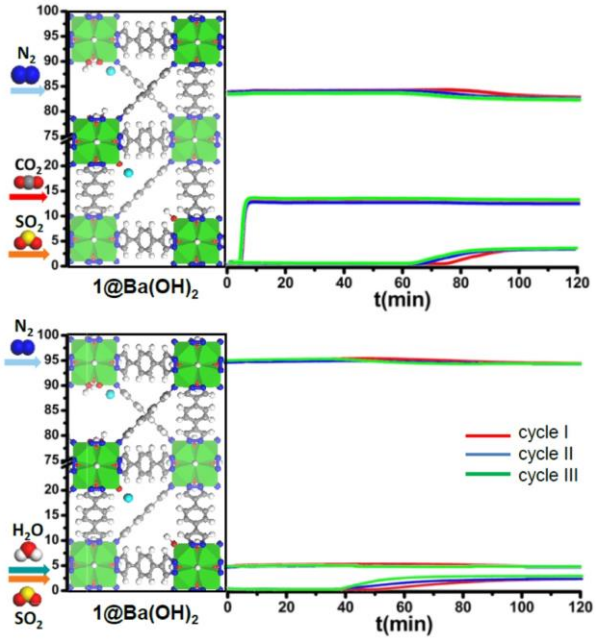


Fig. 2. Flue gas $SO_2/CO_2/N_2$ (82.5:15:2.5) breakthrough curves for 1@Ba(OH)2 at 303K showing the effect of the competitive adsorption of CO_2 on the capture of SO_2 (top). Effect of the presence of 80 % relative humidity on the SO_2 capture properties of $1@Ba(OH)_2$ (down). Time scale normalized to 1g of MOF adsorbent. Reproduced with permission from ref. 86, Copyright 2017, Springer Nature.

groups onto the pore surface [92–94], incorporation of desired functionality at the metal node [95], and coating hydrophobic protective layer on the crystal surface [96,97], have been used to prevent the attack of water molecules to the coordination bonds to improve MOF stability.

4. Stability of MOF-based membranes

MOF membranes can generally be divided in three families. In the first one, an intergrown thin MOF layer supported by a porous support is acting as the selective layer. In the other two families, MOF particles are dispersed in a polymer matrix (MMM) and either used in a self-supported manner, or applied as a thin composite asymmetric MOF MMMs on a support. The first type of MOF membrane was reported in 2008 by growing $Cu_3(BTC)_2$ on alumina support using a seeding approach [98]. After that, Zhu et al. successfully prepared a defect-free $Cu_3(BTC)_2$ with high H_2 selectivity over other gases by means of "twin

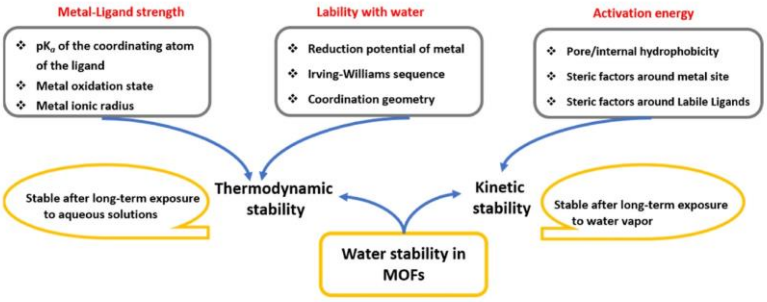


Fig. 3. Factors controlling water stability in MOFs. Reproduced from ref.87, Copyright 2014, American Chemical Society.

copper source" technique [99]. Then, different methods, such as second growth, contra-diffusion, interfacial synthesis, covalent functionalization, layer by layer growth and electrochemical synthesis were developed for preparing thin supported MOF membranes [100–108]. Despite these achievements, the synthesis of large-area, defect-free, long term-stable pure MOF membranes on a porous support remains still very challenging. In this sense, it is more convenient to prepare large-scale MOF-based MMMs without defects since only a small concentration of MOFs is required in processable polymers. Since the first research on free-standing symmetric MOF MMMs in 2004 [109], a large number of MOFs have been incorporated into polymer matrices to develop high-performance membranes [19,110,111]. Symmetric (self-standing) MOF MMMs is by far the most frequently studied class of membranes owing to the simple preparation processes. However, the symmetric MOF-based MMMs normally have a thickness of more than ~50 μm to maintain required mechanical stability, reflecting in significantly lower permeance of the membrane, and are seemingly of prime fundamental and academic interest. Considering practical industrial applications, composite asymmetric MOF-based MMMs with a thin selective MOF-polymer matrix layer on top of porous support are a potentially good trade-off between facile production at large scale and achieving high permeance [112,113]. The MOF particle size should be small enough (less than 1/3 size of the thickness of the selective layer) or use of MOF nanosheets as fillers to obtain a thin selective top layer [33,114,115]. Another important factor is the expensive cost of the synthetic MOFs. However, as only a very tiny amount of MOF is needed for the preparation of thin composite MMMs, the MOF price is in fact negligible. Recently, several reviews have summarized the progress and rational design strategies of obtaining high-performance MOF MMMs for gas separation [47,48,116]. However, only a limited number has discussed the long-term stability of MOF-based MMMs for CO_2 separation. In this sense, Table 3 summarizes most MOF-based MMMs that has undergone long-time measurements or were tested using a feed gas with relevant contaminants.

4.1. Stability of ZIF based MMMs

Table 3 shows that ZIF and UiO series are the most studied MOFs that have been tested for a longer duration in MMMs [26,143–145]. Li et al. [135] synthesized an amino-functionalized ZIF-7 via mixed-linker strategy and embedded them as fillers in cross-linked polyethylene oxide (XLPEO) to prepare MMMs. As shown in Fig. 4a, the CO_2 permeability was greatly improved after the incorporation of ZIF-7-NH_2. More importantly, the incorporation of ZIF-7-NH_2 interacts with the polymer matrix eliminating somehow the rubbery behavior and showing the typical behavior of a glassy polymer due to the chelating effect between the zinc nodes of the filler and the ester group of XLPEO. Only 9 % reduction in CO_2/CH_4 selectivity was observed for the MMMs up to 30 bar feed pressure, while more than 40 % reduction for the pure XLPEO membrane appeared already at 20 bar (Fig. 4a and b). In addition, the MMMs exhibited an excellent stability at 10 bar with satisfied CO_2 permeability and CO_2/CH_4 selectivity for more than 1000 h (Fig. 4c). Yang et al. [122] reported the stability of 27 wt% ZIF-8@P84 MMMs tested for CO_2/CH_4 separation at a feed pressure of 3 bar and room temperature. The membrane performance was evaluated for 720 h with constant CO_2/CH_4 selectivity and CO_2 permeability, indicating its long-term stability.

In addition to the above long-term test under dry feed conditions, Chuang's group [118] investigated the effect of CO and water vapor on the mixed H_2/CO_2 separation performance. The results demonstrated that the presence of CO in the feed stream has almost has no effect on the CO_2 permeability but leads to a slight decrease in H_2 permeability, resulting in an overall decrease of the H_2/CO_2 selectivity for the 30 wt% ZIF-8@PBI membrane. However, for the 60 wt% ZIF-8@PBI membrane, both CO_2 and H_2 permeabilities decreased (more significant for CO_2), resulting in an increased H_2/CO_2 selectivity. This is due to the competitive sorption of gas molecules and the pore blocking effect by CO. CO has the largest kinetic diameters (~3.76 Å) among these three gas mixtures, while ZIF-8 only processes a very small window aperture (~3.4 Å) for gas molecules to pass through. Thus, the presence of CO might affect both the diffusion and sorption for H_2 and CO_2, but the affectation degree varies with ZIF-8 loading in the polymer matrix.

Water vapor in the feed gas did not significantly change the membrane performance at 503 K, indicating the stable separation performance of ZIF-8@PBI membranes. However, the influence of moisture on the separation performance of ZIF-8 based MMMs may differ from each other when using different polymers or different test conditions. For example, Dai et al. [146] reported that water vapor caused a dramatic decrease of CO_2 permeability with limited effect on CO_2/N_2 selectivity of ZIF-8/PTMSP membranes upon the introduction of a small amount of water vapor (Relative humidity ≈ 25) in the feed gas mixtures at room temperature. This is an indication that the behavior of MMMs is highly depending on the type of polymer matrix used. For highly permeable polymers, as poly(1-trimethylsilyl-1-propyne) (PTMSP), the water vapor is "condensed" in the outer part of the MOF. In the other hand, for "low-permeable "or "ultralow-permeable "polymers such as polybenzimidazole (PBI), the water vapor diffuses preferentially through the MOF, which avoids condensation of water at the outer part of the MOF. This may reduce the free volume at the polymer/particle interface, and further hinder the gas transport through the membrane. However, higher operating temperatures could limit the water condensation in the membrane, and thus moisture in the feed has a negligible effect on the

Table 3
MOF- based MMMs that have been tested for longer duration or tested under feed gas with contaminant.

MMMs			Performance							Operation conditions				Testing time/h	$\alpha_{mof}/\alpha_{net}$	Ref.
MOF	Polymer	MOF loading wt %	P_{CO2} (Barrer)	P_{N2}	P_{H2}	P_{CH4}	$\alpha_{CO2/N2}$ –	$\alpha_{CO2/CH4}$	$\alpha_{H2/CO2}$	T (K)	P (Bar)	Contaminants				
ZIF-8	Pebax 2533	30	~750	~14	–	–	~52	–	–			100 % humidified mixed gas		29	~100 %	[117]
	PBI	30	15	–	490	–	–	–	27	503	2	1 mol. % CO		–		[116]
		60	150		2800				12							
		30	19		650				27			1–11 mol. % H_2O		–		
		60	37		2900				14					–		
	Pebax 1657	20	290	9.4	–	–	31	–	–	298	2	–		360	~97 %	[110]
	PVA/PG	5	320	0.94	–	–	340	–	–	308	2.5	–		432	~87 %	[120]
	Polyimide	6.4	253.2		338	–	–	–	14.6	453	3	–		168	~100 %	[121]
	PI84	27	11			0.12		93		298	3	–		720	~100 %	[122]
	Matrimid	20	14	–	–	2.1	–	29	–	308	8.5	humidified		–		[123]
PEI ZIF-8	Pebax 1657	5	136GPU	0.26GPU	–		49	–	–	298	1	–		240	~88 %	[124]
ZIF-8-d-MK	PVAm	3	257GPU	2.49GPU	–	–	95.3	–	–	298	1	–		360	~100	[125]
MWCNT@ZIF-8	Pebax® MH 1657	8	186.3	3			61.3			308	5	–		168	% ~100 %	[126]
UiO-66	Matrimid	20	13			2.6		34		–	–	–				[123]
	6FDA-DAM	14	385			25.3		15.2		308	20	–		20–30		[53]
UiO-66-NH_2	PEBA	10	130	1.8	–	–	72	–	–	293	1	85 % RH		100	~103 %	[127]
	Pebax 1657	2	224	–	–	14.4	–	18.5	–	298	5	Humid		–		[128]
	PVAm	1.5	267			8.6		26								
		28.5	424	4.7	–	–	91	–	–	298	3	149 ppm SO_2, 70 ppm NO_x, 100 ppm CO, 6.5 vol% O_2		80	~84 %	[129]
	PEI	18	394		33	–	–	–	12	298	1	–		100	~100 %	[130]
UiO-66-NH_2-$COCH_3$	6FDA-DAM	16	243	–	–	25.5	–	9.5	–	308	20	5 mol.% H_2S		20–30		[131]
UiO-66@HNT	6FDA-DAM	16	193	–	–	10.6		18.2	–							
	Pebax	20	119.98	1.56	–		76.26			298	5			168	~100 %	[131]
ZIF-300	PEBA	30	83	0.98	–	–	84	–	–	298	4	–		100	~106 %	[132]
ZIF-301	6FDA	20	891			30.4		29.3		298	4			120	~100 %	[133]
	DAM															
ZIF-302	PI84	30	5.5	0.11			50			333	3	30 % RH		33	~100 %	[134]
ZIF-7-NH2(70)	XLPEO	30	200	–	–	4	–	50	–	308	10	–		1000	~98 %	[135]
MOF-801	PEBA	7.5	281	–	–	–	66	–	–	293	1	–		120	~97 %	[136]
	PIM	5	9646 ± 799	362 ± 40			27 ± 1.6							120	~107 %	[137]
Y-fum-fcu-MOF	6FDA-DAM	13	475	–	–	–	–	43.9[a]		308	6.7	20 % H_2S		–		[110]
CuBTC-m	PIM-1	10	1112.5	–	–	17	–	15.6	–	298	1	–		100	~88 %	[114]
Cu-BTC-SC	Pebax® 1657	15	1004.6GPU	20.13GPU		32.91GPU	54.8	32.5		298	1.5	H_2O		100	~80 %	[138]
Gly@CuBTC	Pebax MH 1657	5	175			6.03		29				humidified		100	~88 %	[139]
MFU-4	6FDA-Durene	10	1180 (H2S + CO2)			28		42.0[a]		308	2	20/20/60$H_2S/CO_2/CH_4$				[140]
(001)-ABPHE	6FDA-DAM	59.6	358.6					135.6[a]		308	10	1/9/90$H_2S/CO_2/CH_4$		720	~100	[141]
PVAm Modified MIL-101(Cr)	DAT	44.44	305.5					143.7[a]				5/5/90$H_2S/CO_2/CH_4$			% ~100 %	[142]
	PVAm		823GPU	3.4GPU			242			298	5	14.2 % CO_2, 6.5 % O_2, 220 ppm SO_x, 80 ppm NO_x, 10 ppm CO, and balanced with N_2		150	~100 %	[143]

[a] $\alpha_{CO2 / H2S/CH4}$.

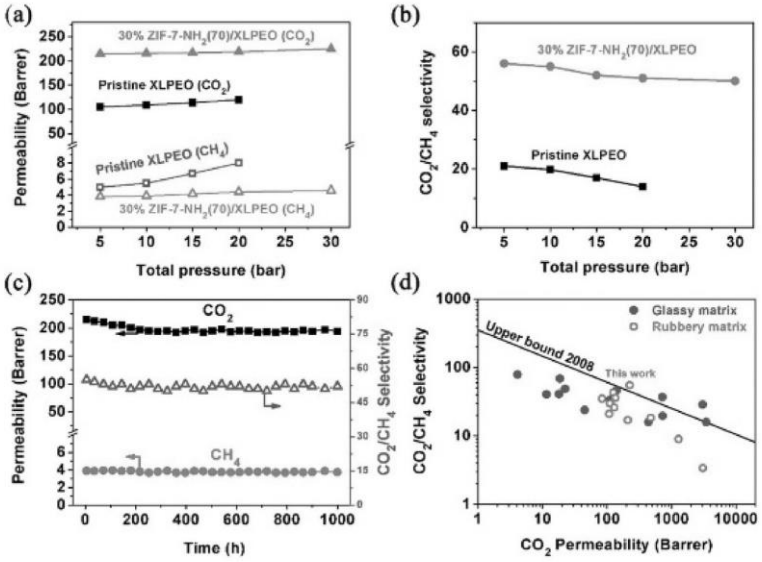


Fig. 4. (a) Permeability and b) separation factor of equimolar CO_2/CH_4 mixed-gas on the pristine XLPEO membrane and 30 % ZIF-7-NH2(70)/XLPEO MMMs, c) long-term stability for CO_2/CH_4 separation on 30 % ZIF-7-NH_2(70)/XLPEO MMMs at 10 bar and 35 °C, d) comparison of CO_2/CH_4 separation performance with previously reported MMMs from both glassy and rubbery matrices. Reproduced with permission from ref. 135, Copyright 2017, Wiley-VCH.

separation performance of some ZIF-8 based MMMs tested at elevated temperatures.

4.2. Stability of UiO- based MMMs

Compared to ZIF-8 based MMMs, UiO-66 based MMMs are more stable under humid conditions. The Jin group [127] reported the effect of humidity on the separation performance of UiO-66-NH_2-PEBA MMMs towards CO_2/N_2. The CO_2 permeability significantly increased with slightly enhanced CO_2/N_2 selectivity after humidifying. This is due to the facilitated CO_2 transport in the membranes triggered by water vapor, arising from the hydrophilic as well as CO_2-philic properties of UiO-66-NH_2. More excitingly, the 10 wt% UiO-66-NH_2-PEBA membrane exhibited high and stable performance with an average CO_2 permeability of 130 Barrer and a CO_2/N_2 selectivity of 72 during 100 h with 85 % relative humidity in the feed gas.

Wang et al. [129] utilized a 'bridging-cross-linking' method to connect poly(vinylamine) (PVAm) and UiO-66-NH_2 nanoparticles via poly (ethylene glycol) diglycidyl ether (PEGDE) (the abbreviation of this mixture is BUPP) and then coated the BUPP solution on modified polysulfone (mPSU) substrates. The prepared composite BUPP/mPSU membrane (28.5 wt% UiO-66-NH_2) achieved a high CO_2 permeance of 531 Barrer together with a CO_2/N_2 selectivity of 91 at 3 bar under dry feed conditions. Importantly, Wang et al. [129] first tested MOF MMMs under practical industrial flue gas mixtures containing SO_2, NOx, CO and O_2 as well as large amount of CO_2 and N_2. As shown in Fig. 5, the BUPP/mPSU membrane (28.5 wt% UiO-66-NH_2) was first treated with CO_2/N_2 (v/v 15/85) for 8 h and then evaluated under a synthetic feed gas mixture (14.5 vol% CO_2, 6.5 vol% O_2, 140 ppm SO_2, 70 ppm NOx, 10 ppm CO and balanced by N_2) for 80 h. The CO_2 permeability and

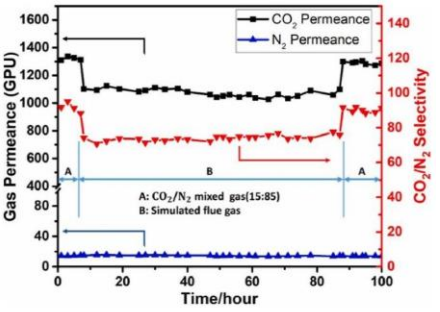


Fig. 5. The stability test of the BUPP/mPSU membrane. Feed gas: CO_2/N_2 (15/85) mixed gas and simulated flue gas (14.5 vol% CO_2, 6.5 vol% O_2, 140 ppm SO_2, 70 ppm NOx, 10 ppm CO and balanced by N_2). Feed gas pressure: 3 bar. Reproduced with permission from ref. 129, Copyright 2019, Elsevier.

CO_2/N_2 selectivity of the BUPP/membrane decreased by 19.5 and 16.5 %, respectively, when the feed gas changed from a CO_2/N_2 (v/v 15/85) mixture to a simulated flue gas. The separation performance remained stable under simulated flue gas and could retrieve the initial performance when switched the feed gas to CO_2/N_2 mixture.

4.3. Stability of other MOF based MMMs

Both CO_2 and H_2S, present as typical impurities in natural gas, must be removed from CH_4. The removal performance can be evaluated by testing the total acid gas permeability [$P(CO_2) + P(H_2S)$] and selectivity [$P(CO_2) + P(H_2S)$]/$P(CH_4)$] [110,140,141]. In 2018, Eddaoudi et al. [110] prepared a 13 wt% Y-fum-fcu-MOF/6FDA-DAM hybrid membrane for the separation of 20/20/60$H_2S/CO_2/CH_4$ mixtures. Likely, the resultant composite membranes exhibited a $(CO_2+H_2S)/CH_4$ selectivity of 43.9 and a high permeability of 475 Barrer for total acid gases. Recently, their research group developed an acid-stable MOF-based MMM composed by in-plane aligned (001)-AlFFIVE-1-Ni nanosheets and 6FDA-DAM-DAT matrix. The prepared MMMs were tested under realistic raw natural gas composition ($H_2S/CO_2/CH_4$: 1/9/90; 5/5/90). As shown in Fig. 6, under each $H_2S/CO_2/CH_4$ mixture, both the mixed gas ($H_2S + CO_2$) permeability and the $(H_2S + CO_2)/CH_4$ selectivity were relatively constant for at least 30 days of continuous testing at 10 bar and 35 °C [141]. Smith et al. [140] synthesized an MMM system made from a 6FDA−Durene polymer and an MFU-4 MOF, for which the mixed $(H_2S + CO_2)/CH_4$ permselectivity could reach to 42 together with high CO_2 and H_2S permeability. The above studies demonstrated that MOF-based MMMs can reach exceptionally performance and long-term stability for carbon dioxide separation from natural gas.

4.4. Perspective for future MOF-based MMM stability studies

In a broader view, the results in Table 3 also demonstrate that stability of MOF-based MMMs is insufficiently studied to warrant success in industrial application. Most studies test the membrane stability for approximately 100 h. Only three studies were found that tested for more than 500 h, and none of the stability studies was prolonging for over 1000 h (which is just over a month). At the same time, industrial deployment requires stability for years. Hence, either longer stability tests or accelerated stress tests are required to prepare MOF-based MMM for practical applications.

Regarding the type of contaminations, humidity is best studied for several MOF types. Also sulphur-based contaminants have been studied for several MOF-based MMMs, with mixed results. However, other acidic and basic contaminants, such as HCl and NH_3, are poorly studied for any of the MOF-based MMMs. At the same time, it is known that acid gases and NH_3 can cause MOF degradation (Table 2). MOF-based MMMs are available for NH_3/N_2 or NH_3/H_2 separation [147], which offers perspective for also making NH_3-stable MOF-based MMMs for CO_2 separation. Introducing functional groups containing Lewis acid site (carboxyl-, sulfonic-, hydroxyl-) into MOFs enable the prepared MMMs absorb ammonia basic gas from CO_2 gas mixture and at the meantime increase the solubility coefficient towards CO_2 through the chemical interaction between these polar groups and CO_2, thus obtaining excellent gas separation performance.

Apart from long-term stability under contaminate gases, it is essential to pay attention to the anti-aging and plasticizing characteristics of MMMs used for gas separation. The physical aging process of membranes can result in a reduction in gas permeability while a slight increase in selectivity especially for high fraction free volume polymers, which is unfavourable for industrial applications [148–150]. Introducing MOFs in polymer matrix can usually improve the anti-aging of polymer membranes through good interface interaction. For example, Qiao et al. [151] incorporated defective UiO-66-FA into the PIM-1 matrix and enhanced the interfacial compatibility by forming a hydrogen bond network. The gas permeability of the MMMs only decreased by 25 % after 160 days of continuous operation. This improvement can be attributed to the incorporation of MOF nanoparticles acted as supports which effectively prevents the pore collapse in PIM-1 membrane, consequently mitigating its aging process. In contrast to aging, membrane plasticization causes the permeable components to swell through the membrane, resulting in reduced selectivity for gas separation. Currently, loading MOFs into polymer membranes is an effective approach to improve their resistance to plasticization [150,152]. For instance, Ahmad et al. [153] added Zr-MOFs nanoparticles into 6FDA--DAM polyimide to fabricate MMMs and investigated their plasticization behavior in the CO_2/CH_4 separation system. The study revealed that as the pressure increased to 20 bar, the CO_2 permeability coefficient and CO_2/CH_4 separation factor exhibited a decrease trend. Overall, MOF fillers can usually effectively inhibit the aging and plasticization of polymer membranes by restricting the polymer chain mobility through good interface interaction [151–153].

5. Scalable synthesis of MOFs and MOF-based MMMs

5.1. Scalable synthesis of MOFs

MOFs are lauded for their potential in diverse industrial applications such CO_2 capture. However, the progress of MOFs into the commercial sphere remains limited by several factors, including the scale-up of laboratory syntheses to pilot production [154]. Among processes explored for production of MOFs, solvothermal batch synthesis was the first to enable production of MOFs above laboratory scale. Solvothermal synthesis involves the use of sealed reactors in which a solvent is heated

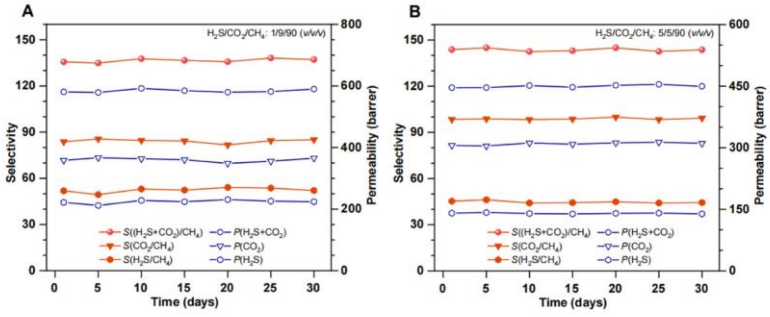


Fig. 6. (A and B) Membrane stability under different H_2S concentration, (A) $H_2S/CO_2/CH_4$: 1/9/90; (B) $H_2S/CO_2/CH_4$:5/5/90. Robust $H_2S/CO_2/CH_4$ separation properties of (001)-AlFFIVE(59.6)/6FDA-DAM-DAT membrane for at least 30 days. Feed pressure at 10 bar and 35 °C. Reproduced with permission from ref. 141, Copyright 2022, Science.

to temperatures above the boiling point of all solvents, to dissolve the reagents (inorganic salts and organic linkers) and favor their reaction to form the target MOF. Using this approach, Wang et al. prepared 80 g of HKUST-1 [155] and Stock and Biswas prepared 50 g of MOF-5 [156]. Similarly, Seo et al. synthesized Mg-MOF, and Czaja, Trukhan and Müller synthesized MIL-100(Fe), both at the kilogram scale, obtaining space-time yields (STY) of 300 kg/m^3·day and 1700 kg/m^3·day, respectively [157,158].

Although the solvothermal batch method is common in industry, it suffers from certain drawbacks. For example, heating of large reaction vessels is energy intensive. Moreover, since crystallization of MOFs occurs preferentially at vessel surfaces, and increasing the size of a reactor vessel decreases its surface-to-volume ratio, increasing the scale of MOF production leads to a diminishing number of nucleation sites. This scaling problem can be mitigated using microwave irradiation. Microwaves acts as high-frequency electric fields, causing any materials that have electric charges (*e.g.* ions or polar molecules) to move and consequently, to heat up. The thermal energy generated inside a microwaved solution can be transformed into chemical energy for endothermic reactions. Thus, while in classical solvothermal reactions, MOFs preferentially crystallize on the vessel wall, in microwave-assisted solvothermal reactions, MOFs begin to crystallize in solution. Accordingly, microwave-assisted solvothermal synthesis tends to be faster and more efficient than the traditional method. It also tends to produce smaller crystals in comparison to standard solvothermal reactions, which is desirable for MMM for which MOF crystals must be incorporated into defect-free films. Using this methodology, Jhunget and coworkers first prepared MIL-100(Cr) [159]. Since then, numerous reports of microwave-assisted MOF syntheses have revealed that MOF particle-size, crystallinity and morphology can all be controlled by modulating the irradiation time, reagent concentration, temperature or substrate composition [160–162]. For example, Férey et al. optimized the crystallinity of MIL-100(Cr) and controlled the particle size (from 40 nm to 200 nm) by increasing the irradiation time. Alternatively, Masel et al. and Ahn et al. each demonstrated that, by increasing the temperature, power level and reagent concentrations, they could accelerate the synthesis of IRMOFs, albeit with a concomitant loss in crystal quality. Recently, Cao et al. reported the gram-scale production of nine microporous lanthanide MOFs *via* microwave synthesis [163], and Taddei and co-workers described an optimized microwave-assisted production of UiO-66 (particle size: 300 nm), with an excellent STY of 2241 kg/m^3·day [164].

For industrial production of MOFs, in parallel to batch synthesis, several methods for continuous production have been developed [165,166]. One example is flow chemistry, whereby reactions occur in a continuously flowing stream characterized by a higher surface-to-volume ratio than in traditional reaction vessels, thus providing superior heat transfer than in batch syntheses of comparable scale. Moreover, compared to batch synthesis, flow chemistry synthesis can be readily scaled-up, as the reaction parameters can be precisely controlled and the reactors, easily scaled-up. Thus, given its lower energy consumption, and its lower demands for solvent volume, flow chemistry tends to be more cost-effective and environmentally friendly than batch synthesis. There are various flow-reaction systems, including microfluidic reactors, plug-flow reactors and stirred-tank reactors. Ameloot et al. pioneered the use of microfluidic reactors to synthesize MOFs. For instance, using a biphasic reaction mixture comprising two immiscible solvents, each of which contained one of the two components of HKUST-1, they induced HKUST-1 crystallization in a liquid–liquid interface, obtaining homogeneous HKUST-1 membranes [167]. Unfortunately, this methodology is limited to lab scale, as scale-up would require large volumetric reactors. An alternative to microfluidic reactors is a plug-flow reactor, in which solutions of the precursors are introduced separately into a tube reactor, flowed through it and then, reacted. This method was first used by Gimeno-Fabre et al. to synthesize HKUST-1 (particle size: 10 μm) and Ni-CPO-27 (particle size: 20 nm) [168]. Using the same system, Mann and co-workers later synthesized ZIF-8 at the kilogram scale, obtaining an STY of 11,625 kg/m^3·day [169]. Remarkably, Rubio-Martínez et al. reported the efficient synthesis of a series of MOFs using a pilot plug-flow reactor (volume: 1394 L), including Al-Fum (particle size: 200 nm) at an STY of 97,159 kg/m^3·day [170]. Finally, in stirred-tank reactors, which marry batch synthesis to continuous flow, the reagents are continuously introduced into a heated, stirred reactor vessel. As the reagents are gradually added, the newly-formed MOFs are continuously recovered from the vessel to regenerate the reaction medium. This method was firstly used by Schoeneker et al. to synthesize 10 g of UiO-66-NH$_2$ in a 2-L flow crystallization reactor [171]. Using a similar approach, McKinstry et al. improved the synthesis of MOF-5, obtaining an STY of 1000 kg/m^3·day.

Using this same strategy of continuous flow reactors, MOF synthesis can be performed in microwave-assisted flow chemistry, which in some cases has provided markedly higher STY values than in the corresponding microwave-assisted batch reactions. For instance, Ranocchiari, Taddei and co-workers reported the continuous-flow, microwave-assisted synthesis of UiO-66, MIL-53(Al) and HKUST-1 with STY values of 7204 kg/m^3·day, 3618 kg/m^3·day and 64,800 kg/m^3·day, respectively [172]. Likewise, Stock et al. produced Zr-fum at an STY of 2733 kg/m^3·day [173]. More recently, the groups of McKinstry and of Laybourn synthesized HKUST-1 (size: 100 nm) at STY values of 632,000 kg/m^3·day, using a continuous-flow oscillatory baffled reactor equipped with a homogeneous, controllable microwave [174]. In 2013, Carné-Sánchez et al. reported [174] a new approach, known as spray-drying, which entails the atomization of a solution of MOF precursors into a spray of microdroplets, using a nozzle. This is accomplished by simultaneously injecting the solution and compressed air or nitrogen gas into a reaction chamber. Next, the atomized microdroplets are heated by the injected gas, causing the solvent to evaporate which induces the formation of MOF nanocrystals. Full evaporation of the solvents leads to formation of MOF nanocrystals, which in turn assemble into spherical compact or hollow MOF beads. Note that the MOF-precursor solution can be injected using a two-fluid nozzle, a three-fluid nozzle or a T-junction. Also, this solution can be pre-heated before injection, using a flow reactor. To date, myriad MOF beads (*e.g.* HKUST-1, MOF-74 family, ZIF-8, UiO-66 and CuBDC) have been synthesized by spray-drying. In some cases, the resultant MOF beads can be mechanically disassembled into MOF nanocrystals, which can then be isolated. This has been reported for isolation of nanoparticulate HKUST-1 (Fig. 7, size: 75 nm), UiO-66 (size: 30 nm), ZIF-8 (size: 50 nm), MOF-74(Ni) (size: 130 nm) and NOTT-100 (size: 60 nm) [175]. Recently, Avci-Camur et al. explored the use of water as solvent in spray-drying synthesis of MOFs such as UiO-66 MOFs and HKUST-1 [176]. For instance, using this technique at a pilot spray-drying plant, they produced 60 kg of HKUST-1.

Finally, another valuable method for large-scale production of MOFs is mechano-synthesis, whereby (typically) solid reagents are mechanically reacted to form diverse molecular or supramolecular compounds. This enables solvent-free chemistry, or at least, use of only minimal volumes of solvent. The mechanical energy that underpins the reactions is typically generated by grinding a physical mixture of two solid reagents in a mortar, ball-mill or extruder. This approach allows for use of MOF precursors with poor solubility (in water or organic solvents), including carbonates, hydroxides and oxides. Accordingly, compared to other methods for industrial MOF production, mechano-synthesis can be considered faster, more environmentally friendly and more efficient, as it often affords MOFs in quantitative yields. Representative mechano-syntheses of crystalline structures include work by James et al., who recently prepared HKUST-1 and Cu(INA)$_2$ this way [177]. Mechano-syntheses have been scaled-up via *extrusion*, a continuous process that involves the movement of material along a set of screws. James et al. reported synthesis of Al-Fum and of HKUST-1 with twin-screw extrusion, and of ZIF-8 in single-screw extrusion, obtaining STY values of 27,000 kg/m^3·day (Al-Fum), 144,000 kg/m^3·day

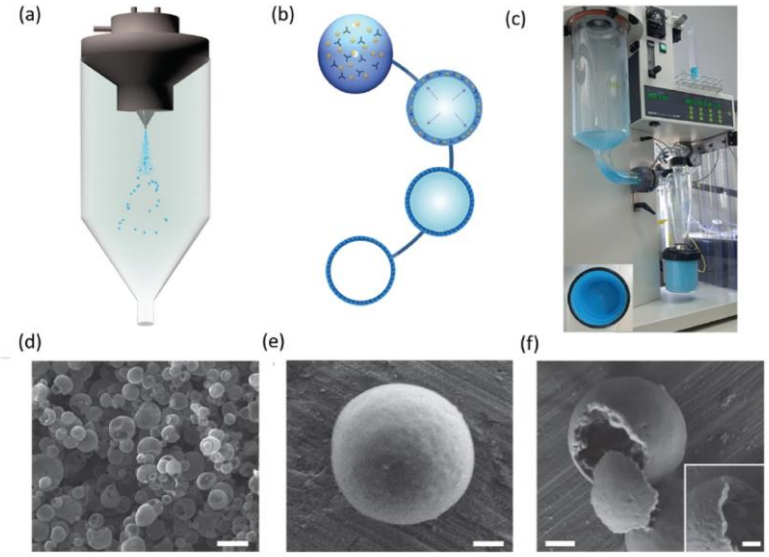


Fig. 7. (a) Schematic showing the spray-drying process used to synthesize HKUST-1 superstructures. Blue dots, sprayed solution; blue spheres, formed spherical superstructures. (b) Proposed spherical superstructure formation process (emphasized by purple arrows), which implies the crystallization of nanoMOF crystals. (c) Photograph of the spray-dryer after its use in synthesizing large amounts of blue HKUST-1 superstructures. d–f, Representative FESEM images showing a general view of the spherical HKUST-1 superstructures (d), the wall of a single HKUST-1 superstructure showing the assembly of nanoHKUST-1 crystals (e), and a mechanically broken hollow superstructure showing the internal cavity and the thickness of its wall (f and inset). Scale bars: 5 μm (d), 500 nm (e, f), and 200 nm (f inset). Reproduced with permission from ref. 175, Copyright 2013, Springer Nature. (For interpretation of the references to colour in this figure legend, the reader is referred to the Web version of this article.)

(HKUST-1) and 144,000 kg/m^3·day (ZIF-8) [178]. Similarly, Karak et al. recently applied twin-screw extrusion to large-scale synthesis of COFs, reaching production rates of several kg/h [179]. Finally, the company MOF Technologies has been exploring mechano-chemical synthesis of various MOFs, having demonstrated rapid syntheses on the multi-kilogram scale. Table 4 summarize the different methods used for scale-up synthesis of different MOFs.

5.2. Scalable synthesis of MOF-based MMMs

A number of MOF-based membranes developed at lab-scale are showing promising performances suitable for industrial applications. Although multiple examples of scalable synthesis of MOF membranes have been reported [190–192], the large scale production of defect-free MOF-based membranes is still a great challenge and commercial MOF membranes are still rarely seen. The main barriers are polymer-filler incompatibility, plasticization, MOF agglomeration or unstable MOF-polymer suspensions, leading to the formation of interfacial defects and irregular distribution of the in inorganic materials along the membrane [193–195]. Also, the required adaptation of the current membrane production processes to be able to incorporate MOF on large scale plays a significant role.

Scaling MOF-based mixed matrix membranes is strongly tied with the membrane structure and membrane module type. Most commercially available gas separation membranes are fabricated via a phase inversion process in a single step forming an asymmetric structure, or via a coating/interfacial polymerization (IP) process in one or multiple steps creating a Thin Film Composite (TFC). The shape of the membrane, and thereby also the manufacturing methods, depends on the membrane module. For gas separation applications commonly two membrane geometries are used: flat sheet and hollow fibers [196–198] (see Fig. 8). For both membrane geometries, MOF-based membranes fabrication is regular reported literature.

Table 5 lists previous work of MOF-based TFC membranes for CO_2 separation. In general, both flat sheet membranes and hollow fiber modules are able to manufacture MOF-based MMM at cm^2-scale with reasonable selectivities. While flat sheet membranes require less advanced equipment to manufacture defect-free layers, hollow fiber modules benefit from their large surface to volume ratio when scaling to larger modules [195]. Nevertheless, very few research data has been reported for MOF-based MMM at substantial scale. From Table 5, the largest scale unit (340 cm^2) that was assessed for CO_2 permeance was a hollow fiber module with ZIF-8 particles deposited by gel-vapor deposition [199]. The ultrathin layer (<100 nm) allowed to achieve an extremely high permeance.

Sasikumar et al. [205] reported a single step fabrication of a polysulfone (PSf) hollow fiber MOF membrane. The ZIF-8, SiO_2/ZIF-8, and amine-modified SiO_2/ZIF-8 were dispersed into the polymer dope solution and subsequently the hollow fiber MMM was synthesized via the phase inversion technique. Their research found, besides improved membrane performance, excellent scalability of the MOF membrane process which can be easily further developed into membrane prototypes and membrane modules for effective CO_2 separation.

Scalable synthesis of hollow fiber MOF TFC membranes was reported

Table 4
Scale-up synthesis of different MOFs using different methods.

MOF	Technique	STY (kg/m3-day)	Reference
HKUST-1	Extrusion mechano-chemical	144,000	[178]
ZIF-8	Extrusion mechano-chemical	144,000	[178]
Al-Fum	Extrusion mechano-chemical	27,000	[178]
ZIF-8	Flow chemistry (MR)	210,000	[180, 181]
Al-Fum	Flow chemistry (PFR)	97,159	[170]
HKUST-1	Flow chemistry (PFR)	64,800	[172]
MOF-5	Flow chemistry (CSTR)	1000	[182]
UiO-66	Spray-drying	19.6	[183]
$MgFe_2O_4$@UiO-66-NH_2	Flow chemistry	300	[184]
CUP-1	Flow chemistry (MR)	550	[185]
CUP-1	Hydrothermal	20	[185]
MOF-801	Flow chemistry (MR)	367.2	[186]
HKUST-1	Flow chemistry (microwave, continuous flow, oscillatory baffled reactor)	632,000	[174]
HKUST-1	Flow chemistry (microwave, continuous flow, oscillatory baffled reactor)	400,000	[187]
MOF-74-Ni	Continuous-flow microwave reactor	720	[188]
UiO-66	Continuous-flow microwave reactor	7204	[172]
MIL-53(Al)	Continuous-flow microwave synthesis	3618	[172]
Al-Fum	Hydrothermal	3600	[189]

Abbreviations: Fum: Fumarate; MR: Microfluidic reactor; PFR: Plugged-flow reactor; CSTR: Continuous-stirred tank reactor; STY: Space-Time Yield.

by Sutrisna et al. [202], incorporating various UiO-66, and ZIF-7 MOF types into a thin PEBAX selective layer on a PVDF support with gutter layer (Fig. 9). Simultaneously improvement of the CO_2 permeance and selectivity was observed. A similar approach was reported by Li et al. [203]. Incorporating amine functionalized UiO-66 nanoparticles into the Pebax® 2533 thin selective layer on a polypropylene (PP) hollow fiber supports via dip coating process. They observed that the surface morphology of the prepared membranes was influenced by the incorporation of UiO-66 nanoparticles. The CO_2 permeance increased along with an increase of UiO-66 nanoparticles content, while the CO_2/N_2 ideal gas selectively firstly increased whereafter a decrease was observed due to the aggregation of UiO-66 nanoparticles.

Literature often indicates that a multistep coating approach is required. An intermediate gutter layer is generally based on a polydimethylsiloxane (PDMS) coating to cover up the surface defect is added to the membrane formation process [206]. Additionally, since, very thin selective layers are needed (30–100 nm) to achieve high permeance, the size of the MOFs particles is crucial in order to obtain defect-free membranes. The dual layer formation has been also tested for MMMs where again [33,117,207,208], depending on the particle content, the presence of defects is often detected. For more details on the hollow fiber MMM manufacturing process, we refer to previous review work [190].

The multiple layer coating process can be merged in a single step approach, denominated dual layer membrane formation [209]. The process has to be optimized for the particular polymeric systems in order to have a better control of the adhesion of the phases [210,211]. Dai et al. [204] reported the production of asymmetric dual layer hollow fiber membranes containing MOF ZIF-8 fillers in a polyetherimide skin layer via the dry jet-wet quench method. Enhanced permselectivity of 20 % over pure polymer was found. Although the performance was limited by the relatively low permeability of the polyetherimide. Additionally, when the solution containing the MOF is only in the outer layer, the cost of the process significantly drops since the amount of the inorganic filler used is very small.

A different approach was reported by Echaide-Górriz et al. [212] synthesizing a bilayered polyamide-MOF membrane on a hollow fiber support for application in nanofiltration. The continuous MOF layer was crystallized by liquid phase crystal growth, whereafter a polyamide layer was added on the top of the MOF via interfacial polymerization.

For scalable flat sheet membranes, Lan et al. [213] recently used an in-situ heat-assisted solvent-evaporation method to massively produce MOF-based MMMs rapidly. Importantly, this method was applicable to different polymers and MOF types. Using this method, they can obtain MMMs at industrial standards with 4 m of membrane roll in a batch

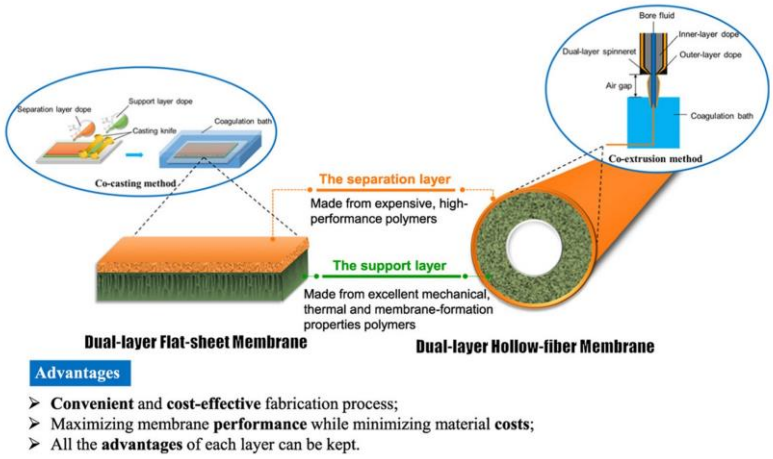


Fig. 8. Conceptual schematic of dual-layer flat-sheet and hollow fiber membranes and fabrication methods. Reprinted with permission from Ref.196, Copyright 2018, Elsevier.

Table 5
MOF-based MMM with reported area and CO_2 permeance. Data was collected for research that operated between 25 and 35 °C Selectivity is either measured from mixed gas or from the ratio in pure gas permeance.

Composition selective layer	Module type	Scale (cm^2)	Type separation	Selectivity	CO_2 Permeance (GPU)	Reference
PVA/PG/ZIF-8	Flat sheet	8.5	CO_2/N_2	370	82	[120]
PEI/ZIF-8	Flat sheet	1.1	CO_2/N_2	49	13	[124]
PVAm/ZIF-8	Flat sheet	12.6	CO_2/N_2	86.7	169	[125]
PVAm/UiO-66	Flat sheet	19.3	CO_2/N_2	91	1295	[129]
PI/MIL-53	Flat sheet	2.2	CO_2/N_2	23	20	[200]
PI/MIL-53	Flat sheet	2.2	CO_2/CH_4	23	20	[200]
PEBAX/CuBTC	Flat sheet	20	CO_2/N_2	54.8	1103	[138]
PEBAX/CuBTC	Flat sheet	20	CO_2/CH_4	32.5	1070	[138]
PI/Cu3(BTC)2	Hollow fiber	1.1	CO_2/N_2	5.9	65	[201]
PI/Cu3(BTC)2	Hollow fiber	1.1	CO_2/CH_4	7.7	65	[201]
PEBAX/ZIF-8	Hollow fiber	17	CO_2/N_2	30	290	[119]
PEBAX/UiO-66-NH_2	Hollow fiber	17	CO_2/N_2	57	338	[202]
PEBAX/UiO-66-NH_2	Hollow fiber	8.2	CO_2/N_2	37	26	[203]
Ultem/ZIF-8	Hollow fiber	10.5	CO_2/N_2	36	26	[204]
PSF/ZIF-8	Hollow fiber	340	CO_2/N_2	7.3	11529	[199]
PSF/ZIF-8	Hollow fiber	340	CO_2/CH_4	8.9	11529	[199]
PSF/ZIF-8	Hollow fiber	340	CO_2/C_3H_8	1030	11529	[199]

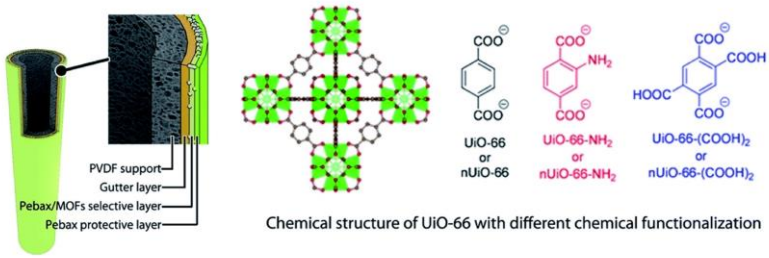


Fig. 9. Schematic diagram of the composite membrane and the chemical structure of UiO-66, for the application in hollow fiber for CO_2 separation. Reprinted with permission from Ref.202, Copyright 2018, RSC.

experiment. These MMMs demonstrated excellent mechanical strength and great performance for dye separation (Fig. 7), and they could also be readily assembled as separator in Li–S battery. Since MOF-based MMMs for CO_2 separation have been widely studied, future studies should be focused on using this powerful method for massively produce other MOF-based MMMs for CO_2 capture. Another impressive method for processing MOFs into polymer is using MOF-loaded porous liquids. Recently, Gascon et al. [214,215] used *N*-heterocyclic carbenes (NHCs) to modify the outer surface of ZIFs to make them solution processable. The NHC-functionalized ZIFs were able to form stable colloidal solutions in nonpolar organic solvents, which could then be easily co-processed with many polymers to yield high loaded MOF-based MMMs. With this method, it is expected to be able to fabricate MOF-based MMMs in large-scale considering its solution-processability.

6. Emerging COF membranes for CO_2 separation

6.1. COF based MMMs

Given the challenges in stability of MOF-based MMMs, alternative materials that can still exhibit the supreme size selectivity of crystalline MOF structures are interesting to study. Because the instability of MOF-based structures is often originating from the metal atom, either by the oxidation state or interaction with the organic structure (see Fig. 3), eliminating the metal site provides potential route for more intrinsically stable structures. This is represented in the concept of covalent organic frameworks (COFs).

COFs are a relatively new class of crystalline porous materials that are analogous to MOFs but made exclusively of organic linkers [216]. Compared to the inorganic-organic hybrid nature of MOFs materials, the pure organic nature of COFs could result in better compatibility with polymers, reducing the possibility of forming defects at the interface between polymer and filler when preparing MMMs. This compatibility was demonstrated by Banerjee et al. [18], who has successfully dispersed two chemical-stable isorecticular COFs (TpPa-1 and TpBD) in PBI-BuI to prepare MMMs with a COF loading as high as 50 %. For comparison, it is very difficult for most MOFs to reach similar loading in a polymer matrix.

The first generation of boronate-linked COFs were found unstable in presence of water, acids and alcohols [217]. This is because the electron-deficient boron sites are susceptible to be attacked by nucleophiles such as water. Therefore, even a slight amount of water vapor present in air could potentially induce the decomposition of boronate-linked COFs. Although a post-synthetic modification of the COF framework by pyridine or alkyl has been evaluated to improve the structural stability [218–220], such boron-containing COFs have still not shown the required stability for real applications. Later, hydrone-, azine-, triazine- and imine-linked COFs were successfully synthesized, demonstrating enhanced stability in neutral water, but still hydrolysis under acid conditions [221,222]. In these COFs, the introduction of special functional groups in their organic components, creating hydrogen bonding in intramolecular or interlayers, has proved helpful to further enhance their stability. For example, a robust and stable azine-linked COF, COF-JLU3, was made by forming intramolecular

O–H···N=C hydrogen bonding in the network through introducing an –OH group adjacent to the Schiff-base centers [223]. Jiang et al. [224] synthesized an imine-linked COF that is stable in water and under strong acids and bases by incorporating methoxy groups (-OCH_3) into the pore walls to reinforce interlayer interactions. The introduction of two electron-donating – OCH_3 groups to each phenyl edge delocalized the two lone pairs from the oxygen atom over to the central phenyl ring. In this way, the interlayer interaction was reinforced, and the COF structure was stabilized. This COF demonstrated a high thermal stability up to 673 K, together with a strong resistance towards boiling water, 12 M HCl, 14 M NaOH and common solvents, such as DMF, DMSO, THF, MeOH and cyclohexanone. Recently, Qiu et al. [225] also reported a polyarylether-based COF with a strong resistance towards boiling water, strong acid and bases, oxidation and reduction conditions. Its ultra-high stability was attributed to the inert nature of polyarylether-based building blocks.

For the fabrication of COF-based MMMs, COFs were initially incorporated into polymers to improve the gas permeability of purely polymeric membrane. In such a context, Zhao et al. [226] reported the fabrication of MMMs by incorporating two water-stable COF nanosheets (NUS-2 and NUS-3) into a poly(ether imide) (Ultem) and polybenzimidazole (PBI). As previously indicated, the COF fillers exhibit an excellent compatibility with the polymer matrix, as indicated by the homogeneous texture of the resulting MMMs. Interestingly, the 20 wt % NUS-2@PBI MMM showed a H_2/CO_2 selectivity of 31.4, a value which exceeds the 2008 Robeson upper bound. Later, Shan et al. [16,17] incorporated a stable azine-linked COF (ACOF-1) into Matrimid™ 5218, 6FDA-DAM or Polyactive™ to construct MMMs for CO_2/CH_4 and CO_2/N_2 separation applications. The best performance was observed for the MMMs made of Matrimid, showing more than higher CO_2 permeability and CO_2/N_2 selectivity at 16 wt% of COF loading. Also, Tan et al. [227] prepared 2D-COF based MMMs from π-conjugated viologen-COF precursors and PEO monomers through an in situ bottom-up growth method. The resulting MMMs exhibited exceptional one-month operational stability with a CO_2 permeability of about 772.7 Barrer.

Recently, Zhao et al. [228] combined a 3D COF (COF-300) with two different polymer matrices, including 6FDA-DAM and Pebax-10, to prepare defect-free MMMs due to the good polymer-filler interfacial compatibility. Notably, both membranes exhibited good anti-moisture (relative humidity: 85 %) performance, accompanied by an impressive stability for CO_2/CH_4 separation after continuous operation up to 100 h. Jiang et al. [229] used an imidazolium-based ionic liquid [bmim][Tf_2N]-modified COF-300 as fillers and blended the composite particles IL@COF-300 in Pebax® MH 1657 matrix to synthesize MMMs for CO_2/CH_4 separation. The resultant 7 wt% IL@COF-300/Pebax MMMs showed an excellent CO_2 permeability of 1601 Barrer, together with good stability over 60 days at 1 bar in humidified state. One year later, they also prepared PEG@COF-3/Pebax MMMs that showed a stable CO_2/CH_4 separation performance during a 144 h operation test [57].

In addition to free-standing symmetric COF-based MMMs, thin composite asymmetric COF MMMs have also been reported for CO_2 separation. Jin et al. [230] successfully obtained a honeycomb-like COF-nanosheet cluster with a high CO_2/N_2 adsorption selectivity through a facile mechanical synthesis method. Furthermore, the as-prepared PEBA based MMMs containing only 1 wt% of these COF nanosheet filler could reach a CO_2/N_2 mixed gas selectivity of 72. More importantly, a decent stability was obtained for 120 h of operation (Fig. 10).

6.2. Continuous COF membranes

Besides MMMs, the direct growth of a continuous COF film layer on an appropriate mechanical support through solvothermal approach or interfacial polymerization to prepare thin composites membranes is an alternative to scale up COF membranes [231–235]. However, most of this research has focused on applications in nanofiltration or water treatment. Few studies on COF membranes targeted gas separation because of the remarkably larger pore size of COFs compared to the kinetic diameter of gas molecules. Ben et al. [236] first came up with the idea to grow a COF layer on top of a MOF membrane to prepare COF-MOF composite membranes with the purpose to increase the H_2/CO_2 selectivity compared to their individual counterparts. However, the improvement (from 6 and 7–9 for individual COF and MOF membrane, respectively, to 12–14 for COF-MOF composite MMMs) was not as high as expected.

The same authors further prepared a COF-based composite membrane through strong chemical bonding of a MOF film to a COF layer in the vertical direction. The hybrid membrane achieved a H_2/CO_2 gas mixture selectivity of 32.9 and an ultrahigh H_2 permeability, significantly superior to the state-of-the-art membranes [237]. Inspired by the staggered stacking mode of 2D COFs, Caro et al. [238] developed a novel COF–COF bilayer membrane by growing COF-LZU1 (LZU stands for Lanzhou University) on top of an azine-linked ACOF-1 membrane. Due to the hexagonal pore structure of both COFs, the COF-LZU1-ACOF-1 bilayer membrane is in an appropriate size range of the kinetic diameters of gas molecules by forming interlaced pores. The COF–COF membrane exhibited an excellent separation performance towards H_2/CH_4, H_2/N_2, H_2/CO_2 with selectivity of 100, 84 and 24, respectively, together with a high thermal and long-term operational stability, indicating the great promise of using COF membranes for H_2 production and purification. Similarly, Zhao et al. [239] reported a multilayer COF membranes prepared by a layer-by-layer interfacial crystallization of two COFs (TpPa-SO_3H and $TpTG_{Cl}$) with distinct apertures atop the COF (COF-LZU1) film gutter layer. These composite membranes showed

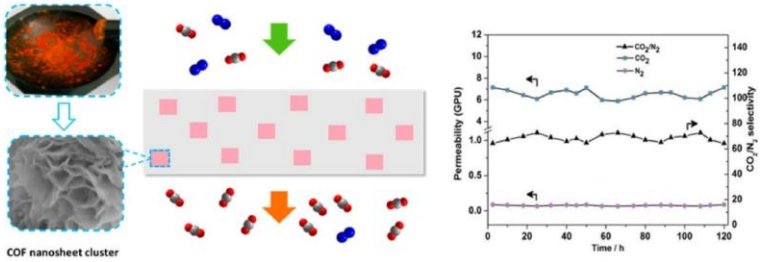


Fig. 10. COF nanosheets cluster based MMMs for CO_2/N_2 separation (equimolar CO_2/N_2 mixture, tested at room temperature and 1 bar). Reproduced with permission from ref. 230, Copyright 2017, Elsevier.

narrowed pores at the COF–COF interfaces, desirable H2/CO2 separation performance and outstanding hydrothermal stability under long continuous testing cycles of dry-humid feed conditions for 96 h.

To better control the stacking modes and maximize the membrane separation performance, Zhao et al. [240] stacked two ionic COF nanosheets (iCONs) with opposite charges to generate strong interlayer interactions through electrostatic attractive interactions between two COF layers. This approach allowed the formation of ultrathin membranes with reduced apertures that showed high H_2 permeance (~2566 GPU) and H_2/CO_2 separation factor (~23), together with an excellent long-term stability under dry or wet conditions at 423 K. Recently, Caro et al. [241] reported another approach that uses the COF interlayer spacing to separate gas mixtures. These authors to successfully grew vertically-aligned COF layers inside vertical CoAl-layered double hydroxide (LDH) nanosheets. The resulting vertical COF membrane exhibited appreciable selectivity towards H_2/CO_2 (31.6) and H_2/CH_4 (29.5), accompanied by an appropriate long-term stability at room temperature (Fig. 11). Although COF membranes used for CO_2 separation have been reported, the long-term stability of COF membrane under realistic conditions are still very limited, more efforts should be devoted to this field.

7. Conclusions

In this review, we have summarized MOFs, MOF-based mixed matrix membranes and methods to improve their stability. In addition, the scalable synthesis of some MOFs and MOF-based membranes was also reviewed. Pioneering work has yet demonstrated stable performance for particular MOF-based MMMs for long duration under dry feed gas steams or water-containing feed. Some pioneering work even reported the CO_2 separation performance of MOF-based MMMs under industrial relevant conditions for which the feed contains water moisture, SO_2, CO, O_2, and NO_X. However, a very limited number of MOF MMMs have been tested under such harsh conditions, and those stability tests only report data up to 100 h. Some MOF-based MMMs could achieve stable performance over 1000 h, though these were only evaluated under dry conditions. Hence, there is still a long way to apply MOF-based MMMs in industry. For example, practical strategies such as coating them with a hydrophobic protective layer need to be implemented to improve their stability. In addition, some studies have demonstrated that the incorporation of MOFs could well improve the stability or plasticization resistance of polymer membranes. Thus, future research should focus more on how to control the interaction between both MOF and polymer chains to improve membranes physical aging and plasticization-resistant properties.

In addition to stability, processability is also an important factor for

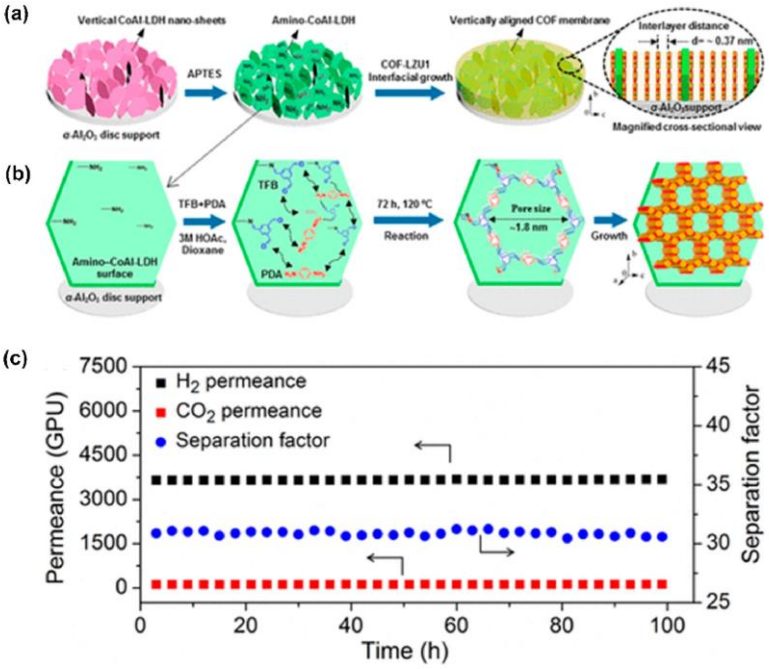


Fig. 11. (a) Schematic representation of the engineering of a vertically aligned COF membrane; (b) Magnified scheme showing the growth of the 2D COF-LZU1 parallel to the surface of a hexagon-shaped amino-CoAl-LDH Nanosheets. (c) Long-term test of the vertically aligned COFLZU1 membrane for equimolar H_2/CO_2 mixture. All measurements at 298 K and 1 bar. Reproduced with permission from ref. 241, Copyright 2020, American Chemical Society.

large-scale manufacturing MOF-based MMMs. Solution processable of MOF fillers is the future direction for preparing MMMs. Finally, as a new emerging filler in MMMs, COFs have already demonstrated better compatibility and stability than MOFs. However, the scale up synthesis of COFs is still at the infancy stage. Effective methods for large scale synthesis of COF fillers are needed; for example, green synthesis conditions, like non-hazardous raw material or solvents, low temperature and pressure should be tried to realize rapid and scalable COF synthesis. With the rapid development of materials synthesis technology, we believe that these problems will be tackled, and MOF- and COF-based MMMs will encounter a blooming development.

Declaration of competing interest

The authors declare the following financial interests/personal relationships which may be considered as potential competing interests: David Vermaas, Inhar Imaz, Thijs Peters, Marcel Boerrigter reports financial support was provided by European Union. Meixia Shan reports financial support was provided by National Natural Science Foundation of China. Meixia Shan, Xiumei Geng reports financial support was provided by China Postdoctoral Science Foundation. Inhar Imaz, Daniel Maspoch, Anna Broto-Ribas, Borja Ortin-Rubio reports financial support was provided by Government of Catalonia.

Data availability

No data was used for the research described in the article.

Acknowledgments

The authors acknowledge financial support from the European Union's Horizon 2020 research and innovation program under grant agreement No 760899, the National Natural Science Foundation of China (Nos. 52003250) and China Postdoctoral Science Foundation (No. 2020M682351). This work was also supported by the Catalan AGAUR (project 2017 SGR 238) and the CERCA Program/Generalitat de Catalunya. ICN2 is supported by the Severo Ochoa program from the Spanish MINECO (grant SEV-2017-0706).

References

[1] R.S. Haszeldine, Carbon capture and storage: how green can black Be? Science 325 (5948) (2009) 1647–1652.
[2] B.P. Spigarelli, S.K. Kawatra, Opportunities and challenges in carbon dioxide capture, J. CO_2 Util. 1 (2013) 69–87.
[3] B. Seoane, J. Coronas, I. Gascon, M.E. Benavides, O. Karvan, J. Caro, F. Kapteijn, J. Gascon, Metal-organic framework based mixed matrix membranes: a solution for highly efficient CO_2 capture? Chem. Soc. Rev. 44 (8) (2015) 2421–2454.
[4] R. M, William J. Koros, Pushing the limits on possibilities for large scale gas separation: which strategies? J. Membr. Sci. 175 (2) (2000) 181–196.
[5] X. He, M.B. Hägg, Membranes for environmentally friendly energy processes, Membranes 2 (4) (2012) 706–726.
[6] L.M. Robeson, The upper bound revisited, J. Membr. Sci. 320 (1–2) (2008) 390–400.
[7] H.B. Park, J. Kamcev, L.M. Robeson, M. Elimelech, B.D. Freeman, Maximizing the right stuff: the trade-off between membrane permeability and selectivity, Science 356 (6343) (2017) 1138–1148.
[8] J.E. Bachman, J.R. Long, Plasticization-resistant Ni_2(dobdc)/polyimide composite membranes for the removal of CO_2 from natural gas, Energy Environ. Sci. 9 (6) (2016) 2031–2036.
[9] J.E. Bachman, Z.P. Smith, T. Li, T. Xu, J.R. Long, Enhanced ethylene separation and plasticization resistance in polymer membranes incorporating metal-organic framework nanocrystals, Nat. Mater. 15 (8) (2016) 845–849.
[10] H. Lin, E.V. Wagner, B.D. Freeman, L.G. Toy, R.P. Gupta, Plasticization-enhanced hydrogen purification using polymeric membranes, Science 311 (5761) (2006) 639–642.
[11] Z.X. Low, P.M. Budd, N.B. McKeown, D.A. Patterson, Gas permeation properties, physical aging, and its mitigation in high free volume glassy polymers, Chem. Rev. 118 (12) (2018) 5871–5911.
[12] D.Q. Vu, W.J. Koros, S.J. Miller, Mixed matrix membranes using carbon molecular sieves: I. Preparation and experimental results, J. Membr. Sci. 211 (2) (2003) 311–334.
[13] M.M. Khan, V. Filiz, G. Bengtson, S. Shishatskiy, M.M. Rahman, J. Lillepaerg, V. Abetz, Enhanced gas permeability by fabricating mixed matrix membranes of functionalized multiwalled carbon nanotubes and polymers of intrinsic microporosity (PIM), J. Membr. Sci. 436 (2013) 109–120.
[14] B. Zornoza, O. Esekhile, W.J. Koros, C. Téllez, J. Coronas, Hollow silicalite-1 sphere-polymer mixed matrix membranes for gas separation, Sep. Purif. Technol. 77 (1) (2011) 137–145.
[15] A.M.W. Hillock, S.J. Miller, W.J. Koros, Crosslinked mixed matrix membranes for the purification of natural gas: effects of sieve surface modification, J. Membr. Sci. 314 (1–2) (2008) 193–199.
[16] M. Shan, B. Seoane, E. Rozhko, A. Dikhtiarenko, G. Clet, F. Kapteijn, J. Gascon, Azine-linked covalent organic framework (COF)-Based mixed-matrix membranes for CO_2/CH_4 separation, Chem. Eur J. 22 (41) (2016) 14467–14470.
[17] M. Shan, B. Seoane, E. Andres-Garcia, F. Kapteijn, J. Gascon, Mixed-matrix membranes containing an azine-linked covalent organic framework: influence of the polymeric matrix on post-combustion CO_2-capture, J. Membr. Sci. 549 (2018) 377–384.
[18] B.P. Biswal, H.D. Chaudhari, R. Banerjee, U.K. Kharul, Chemically stable covalent organic framework (COF)-Polybenzimidazole hybrid membranes: enhanced gas separation through pore modulation, Chem. Eur J. 22 (14) (2016) 4695–4699.
[19] T. Rodenas, I. Luz, G. Prieto, B. Seoane, H. Miro, A. Corma, F. Kapteijn, F. X. Llabrés i Xamena, J. Gascon, Metal–organic framework nanosheets in polymer composite materials for gas separation, Nat. Mater. 14 (1) (2015) 48–55.
[20] B. Zornoza, A. Martinez-Joaristi, P. Serra-Crespo, C. Tellez, J. Coronas, J. Gascon, F. Kapteijn, Functionalized flexible MOFs as fillers in mixed matrix membranes for highly selective separation of CO_2 from CH_4 at elevated pressures, Chem. Commun. 47 (33) (2011) 9522–9524.
[21] X. Liu, Y. Li, G. Zhu, Y. Ban, L. Xu, W. Yang, An organophilic pervaporation membrane derived from metal-organic framework nanoparticles for efficient recovery of bio-alcohols, Angew. Chem. Int. Ed. 50 (45) (2011) 10636–10639.
[22] A. Pustovarenko, M.G. Goesten, S. Sachdeva, M. Shan, Z. Amghouz, Y. Belmabkhout, A. Dikhtiarenko, T. Rodenas, D. Keskin, I.K. Voets, B. M. Weckhuysen, M. Eddaoudi, L. de Smet, E.J.R. Sudhölter, F. Kapteijn, B. Seoane, J. Gascon, Nanosheets of nonlayered aluminum metal-organic frameworks through a surfactant-assisted method, Adv. Mater. 30 (26) (2018), 1707234.
[23] N. Tien-Binh, D. Rodrigue, S. Kaliaguine, In-situ cross interface linking of PIM-1 polymer and UiO-66-NH_2 for outstanding gas separation and physical aging control, J. Membr. Sci. 548 (2018) 429–438.
[24] Z. Wang, D. Wang, S. Zhang, L. Hu, J. Jin, Interfacial design of mixed matrix membranes for improved gas separation performance, Adv. Mater. 28 (17) (2016) 3399–3405.
[25] B. Zornoza, C. Téllez, J. Coronas, O. Esekhile, W.J. Koros, Mixed matrix membranes based on 6FDA polyimide with silica and zeolite microsphere dispersed phases, AIChE J. 61 (12) (2015) 4481–4490.
[26] B. Ghalei, K. Sakurai, Y. Kinoshita, K. Wakimoto, A.P. Isfahani, Q. Song, K. Doitomi, S. Furukawa, H. Hirao, H. Kusuda, S. Kitagawa, E. Sivaniah, Enhanced selectivity in mixed matrix membranes for CO_2 capture through efficient dispersion of amine-functionalized MOF nanoparticles, Nat. Energy 2 (7) (2017), 17086.
[27] Z. Wang, H. Ren, S. Zhang, F. Zhang, J. Jin, Polymers of intrinsic microporosity/metal–organic framework hybrid membranes with improved interfacial interaction for high-performance CO_2 separation, J. Mater. Chem. A 5 (22) (2017) 10968–10977.
[28] G. Chen, C. Chen, Y. Guo, Z. Chu, Y. Pan, G. Liu, G. Liu, Y. Han, W. Jin, N. Xu, Solid-solvent processing of ultrathin, highly loaded mixed-matrix membrane for gas separation, Science 381 (6664) (2023) 1350–1356.
[29] X. Zhao, Y. Wang, D.-S. Li, X. Bu, P. Feng, Metal–organic frameworks for separation, Adv. Mater. 30 (37) (2018), 1705189.
[30] X. Wang, C. Chi, K. Zhang, Y. Qian, K.M. Gupta, Z. Kang, J. Jiang, D. Zhao, Reversed thermo-switchable molecular sieving membranes composed of two-dimensional metal-organic nanosheets for gas separation, Nat. Commun. 8 (2017), 14460.
[31] H. Li, Y. Yin, L. Zhu, Y. Xiong, X. Li, T. Guo, W. Xing, Q. Xue, A hierarchical structured steel mesh decorated with metal organic framework/graphene oxide for high-efficient oil/water separation, J. Hazard Mater. 373 (2019) 725–732.
[32] A. Sabetghadam, X. Liu, M. Benzaqui, E. Gkaniatsou, A. Orsi, M.M. Lozinska, C. Sicard, T. Johnson, N. Steunou, P.A. Wright, C. Serre, J. Gascon, F. Kapteijn, Influence of filler pore structure and polymer on the performance of MOF-based mixed-matrix membranes for CO_2 capture, Chem. Eur J. 24 (31) (2018) 7949–7956.
[33] A. Sabetghadam, X. Liu, S. Gottmer, L. Chu, J. Gascon, F. Kapteijn, Thin mixed matrix and dual layer membranes containing metal-organic framework nanosheets and Polyactive™ for CO_2 capture, J. Membr. Sci. 570–571 (2019) 226–235.
[34] M. Ahmadi, S. Janakiram, Z. Dai, L. Ansaloni, L. Deng, Performance of mixed matrix membranes containing porous two-dimensional (2D) and three-dimensional (3D) fillers for CO_2 separation: a review, Membranes 8 (3) (2018) 50.
[35] A. Knebel, J. Caro, Metal-organic frameworks and covalent organic frameworks as disruptive membrane materials for energy-efficient gas separation, Nat. Nanotechnol. 17 (9) (2022) 911–923.
[36] A. Kertik, L.H. Wee, M. Pfannmöller, S. Bals, J.A. Martens, I.F.J. Vankelecom, Highly selective gas separation membrane using in situ amorphised metal–organic frameworks, Energy Environ. Sci. 10 (11) (2017) 2342–2351.
[37] M.S. Denny Jr., J.C. Moreton, L. Benz, S.M. Cohen, Metal–organic frameworks for membrane-based separations, Nat. Rev. Mater. 1 (2016), 16078.

[38] A.J. Howarth, Y. Liu, P. Li, Z. Li, T.C. Wang, J.T. Hupp, O.K. Farha, Chemical, thermal and mechanical stabilities of metal–organic frameworks, Nat. Rev. Mater. 1 (2016), 15018.

[39] H. Furukawa, K.E. Cordova, M. O'Keeffe, O.M. Yaghi, The chemistry and applications of metal-organic frameworks, Science 341 (6149) (2013), 1230444.

[40] H. Li, M. Eddaoudi, M. O'Keeffe, O.M. Yaghi, Design and synthesis of an exceptionally stable and highly porous metal-organic framework, Nature 402 (1999) 276–279.

[41] S. Kanehashi, A. Aguiar, H.T. Lu, G.Q. Chen, S.E. Kentish, Effects of industrial gas impurities on the performance of mixed matrix membranes, J. Membr. Sci. 549 (2018) 686–692.

[42] Z. Li, F. Liao, F. Jiang, B. Liu, S. Ban, G. Chen, C. Sun, P. Xiao, Y. Sun, Capture of H_2S and SO_2 from trace sulfur containing gas mixture by functionalized UiO-66 (Zr) materials: a molecular simulation study, Fluid Phase Equil. 427 (2016) 259–267.

[43] O. Shekhah, Y. Belmabkhout, Z. Chen, V. Guillerm, A. Cairns, K. Adil, M. Eddaoudi, Made-to-order metal-organic frameworks for trace carbon dioxide removal and air capture, Nat. Commun. 5 (2014) 4228.

[44] M. Kandiah, M.H. Nilsen, S. Usseglio, S. Jakobsen, U. Olsbye, M. Tilset, C. Larabi, E.A. Quadrelli, F. Bonino, K.P. Lillerud, Synthesis and stability of tagged UiO-66 Zr-MOFs, Chem. Mater. 22 (24) (2010) 6632–6640.

[45] S. Yuan, J.S. Qin, C.T. Lollar, H.C. Zhou, Stable metal-organic frameworks with group 4 metals: current status and trends, ACS Cent. Sci. 4 (4) (2018) 440–450.

[46] Z. Zhang, Z.-Z. Yao, S. Xiang, B. Chen, Perspective of microporous metal–organic frameworks for CO_2 capture and separation, Energy Environ. Sci. 7 (9) (2014) 2868–2899.

[47] Z. Kang, L. Fan, D. Sun, Recent advances and challenges of metal–organic framework membranes for gas separation, J. Mater. Chem. A 5 (21) (2017) 10073–10091.

[48] R. Lin, B.V. Hernandez, L. Ge, Z. Zhu, Metal organic framework based mixed matrix membranes: an overview on filler/polymer interfaces, J. Mater. Chem. A 6 (2) (2018) 293–312.

[49] Q. Qian, P.A. Asinger, M.J. Lee, G. Han, K. Mizrahi Rodriguez, S. Lin, F. M. Benedetti, A.X. Wu, W.S. Chi, Z.P. Smith, MOF-based membranes for gas separations, Chem. Rev. 120 (16) (2020) 8161–8266.

[50] Z. Kang, H. Guo, L. Fan, G. Yang, Y. Feng, D. Sun, S. Mintova, Scalable crystalline porous membranes: current state and perspectives, Chem. Soc. Rev. 50 (3) (2021) 1913–1944.

[51] M.Z. Ahmad, T.A. Peters, N.M. Konnertz, T. Visser, C. Téllez, J. Coronas, V. Fila, W.M. de Vos, N.E. Benes, High-pressure CO_2/CH_4 separation of Zr-MOFs based mixed matrix membranes, Sep. Purif. Technol. 230 (2020), 115858.

[52] Z. Lai, Development of ZIF-8 membranes: opportunities and challenges for commercial applications, Curr. Opin. Chem. Eng. 20 (2018) 78–85.

[53] X. Liu, X. Wang, F. Kapteijn, Water and metal–organic frameworks: from interaction toward utilization, Chem. Rev. 120 (16) (2020) 8303–8377.

[54] R. Freund, O. Zaremba, G. Arnauts, R. Ameloot, G. Skorupskii, M. Dincă, A. Bavykina, J. Gascon, A. Ejsmont, J. Gościańska, M. Kalmutzki, U. Lächelt, E. Ploetz, C. Diercks, S. Wuttke, The current status of MOF and COF applications, Angew. Chem. Int. Ed. 60 (45) (2021) 23975–24001.

[55] Y. Cheng, S.J. Datta, S. Zhou, J. Jia, O. Shekhah, M. Eddaoudi, Advances in metal-organic framework-based membranes, Chem. Soc. Rev. 51 (19) (2022) 8300–8350.

[56] L. Hu, K. Clark, T. Alebrahim, H. Lin, Mixed matrix membranes for post-combustion carbon capture: from materials design to membrane engineering, J. Membr. Sci. 644 (2022).

[57] Y. Liu, H. Wu, S. Wu, S. Song, Z. Guo, Y. Ren, R. Zhao, L. Yang, Y. Wu, Z. Jiang, Multifunctional covalent organic framework (COF)-based mixed matrix membranes for enhanced CO_2 separation, J. Membr. Sci. 618 (2021), 118693.

[58] J. Lee, S. Hong, H. Cho, B. Lyu, M. Kim, J. Kim, I. Moon, Machine learning-based energy optimization for on-site SMR hydrogen production, Energy Convers. Manag. 244 (2021), 114438.

[59] H.T. Lu, S. Kanehashi, C.A. Scholes, S.E. Kentish, The potential for use of cellulose triacetate membranes in post combustion capture, Int. J. Greenh. Gas Control 55 (2016) 97–104.

[60] R. Anantharaman, O. Bolland, N. Booth, E.v. Dorst, C. Ekstrom, E.S. Fernandes, F. Franco, E. Macchi, G. Manzolini, D. Nikolic, A. Pfeffer, M. Prins, S. Rezvani, L. Robinson, European Best Practice Guidelines for Assessment of CO_2 Capture Technologies, DECARBit Consortium, 2011.

[61] C. Zhang, R.S. Patil, T. Li, C.L. Barnes, S.J. Teat, J.L. Atwood, Preparation of magnesium-seamed C-Alkylpyrogallol[4]arene nanocapsules with varying chain lengths, Chemistry 23 (35) (2017) 8520–8524.

[62] X.Y. Chen, H. Vinh-Thang, A.A. Ramirez, D. Rodrigue, S. Kaliaguine, Membrane gas separation technologies for biogas upgrading, RSC Adv. 5 (31) (2015) 24399–24448.

[63] T. Islamoglu, Z. Chen, M.C. Wasson, C.T. Buru, K.O. Kirlikovali, U. Afrin, M. R. Mian, O.K. Farha, Metal-organic frameworks against toxic chemicals, Chem. Rev. 120 (16) (2020) 8130–8160.

[64] S.S. Kaye, A. Dailly, O.M. Yaghi, J.R. Long, Impact of preparation and handling on the hydrogen storage properties of $Zn_4O(1,4\text{-benzenedicarboxylate})_3$ (MOF-5), J. Am. Chem. Soc. 129 (46) (2007) 14176–14177.

[65] J.G. Nguyen, S.M. Cohen, Moisture-resistant and superhydrophobic metal-organic frameworks obtained via postsynthetic modification, J. Am. Chem. Soc. 132 (13) (2010) 4560–4561.

[66] K. Xie, Q. Fu, J. Kima, H. Lu, Y. He, Q. Zhao, J. Scofield, P.A. Webley, G.G. Qiao, Increasing both selectivity and permeability of mixed-matrix membranes: sealing the external surface of porous MOF nanoparticles, J. Membr. Sci. 535 (2017) 350–356.

[67] G.W. Peterson, G.W. Wagner, A. Balboa, J. Mahle, T. Sewell, C.J. Karwacki, Ammonia vapor removal by $Cu_3(BTC)_2$ and its characterization by MAS NMR, J. Phys. Chem. C 113 (31) (2009) 13906–13917.

[68] D. Saha, S. Deng, Ammonia adsorption and its effects on framework stability of MOF-5 and MOF-177, J. Colloid Interface Sci. 348 (2) (2010) 615–620.

[69] J. Ethiraj, F. Bonino, C. Lamberti, S. Bordiga, H_2S interaction with HKUST-1 and ZIF-8 MOFs: a multitechnique study, Microporous Mesoporous Mater. 207 (2015) 90–94.

[70] K.S. Park, Z. Ni, A.P. Côté, J.Y. Choi, R. Huang, F.J. Uribe-Romo, H.K. Chae, M. O'Keeffe, O.M. Yaghi, Exceptional chemical and thermal stability of zeolitic imidazolate frameworks, Proc. Natl. Acad. Sci. USA 103 (27) (2006) 10186–10191.

[71] X. Liu, Y. Li, Y. Ban, Y. Peng, H. Jin, H. Bux, L. Xu, J. Caro, W. Yang, Improvement of hydrothermal stability of zeolitic imidazolate frameworks, Chem. Commun. (Camb.) 49 (80) (2013) 9140–9142.

[72] J. Liu, A.I. Benin, A.M. Furtado, P. Jakubczak, R.R. Willis, M.D. LeVan, Stability effects on CO_2 adsorption for the DOBDC series of metal-organic frameworks, Langmuir 27 (18) (2011) 11451–11456.

[73] K. Tan, S. Zuluaga, Q. Gong, Y. Gao, N. Nijem, J. Li, T. Thonhauser, Y.J. Chabal, Competitive co-adsorption of CO_2 with H_2O, NH_3, SO_2, NO, NO_2, N_2, O_2, and CH_4 in M-MOF-74 (M= Mg, Co, Ni): the role of hydrogen bonding, Chem. Mater. 27 (6) (2015) 2203–2217.

[74] J.H. Cavka, S. Jakobsen, U. Olsbye, N. Guillou, C. Lamberti, S. Bordiga, K. P. Lillerud, A new zirconium inorganic building brick forming metal organic frameworks with exceptional stability, J. Am. Chem. Soc. 130 (42) (2008) 13850–13851.

[75] F. Jeremias, A. Khutia, S.K. Henninger, C. Janiak, MIL-100(Al, Fe) as water adsorbents for heat transformation purposes—a promising application, J. Mater. Chem. A 22 (20) (2012) 10148–10151.

[76] H. Kummer, F. Jeremias, A. Warlo, G. Füdner, D. Fröhlich, C. Janiak, R. Gläser, S. K. Henninger, A functional full-scale heat exchanger coated with aluminum fumarate Metal–Organic framework for adsorption heat transformation, Ind. Eng. Chem. Res. 56 (29) (2017) 8393–8398.

[77] F. Ragon, B. Campo, Q. Yang, C. Martineau, A.D. Wiersum, A. Lago, V. Guillerm, C. Hemsley, J.F. Eubank, M. Vishnuvarthan, F. Taulelle, P. Horcajada, A. Vimont, P.L. Llewellyn, M. Daturi, S. Devautour-Vinot, G. Maurin, C. Serre, T. Devic, G. Clet, Acid-functionalized UiO-66(Zr) MOFs and their evolution after intra-framework cross-linking: structural features and sorption properties, J. Mater. Chem. A 3 (7) (2015) 3294–3309.

[78] J.N. Joshi, G. Zhu, J.J. Lee, E.A. Carter, C.W. Jones, R.P. Lively, K.S. Walton, Probing metal–organic framework design for adsorptive natural gas purification, Langmuir 34 (29) (2018) 8443–8450.

[79] D. Fröhlich, E. Pantatosaki, P.D. Kolokathis, K. Markey, H. Reinsch, M. Baumgartner, M.A. van der Veen, D.E. De Vos, N. Stock, G.K. Papadopoulos, S. K. Henninger, C. Janiak, Water adsorption behaviour of CAU-10-H: a thorough investigation of its structure–property relationships, J. Mater. Chem. A 4 (30) (2016) 11859–11869.

[80] Y. Khabzina, J. Dhainaut, M. Ahlhelm, H.-J. Richter, H. Reinsch, N. Stock, D. Farrusseng, Synthesis and shaping scale-up study of functionalized UiO-66 MOF for ammonia air purification filters, Ind. Eng. Chem. Res. 57 (24) (2018) 8200–8208.

[81] J.H. Carter, X. Han, F.Y. Moreau, I. da Silva, A. Nevin, H.G.W. Godfrey, C.C. Tang, S. Yang, M. Schroder, Exceptional adsorption and binding of sulfur dioxide in a robust zirconium-based metal-organic framework, J. Am. Chem. Soc. 140 (46) (2018) 15564–15567.

[82] S. Nandi, H. Reinsch, S. Biswas, A vinyl functionalized mixed linker CAU-10 metal-organic framework acting as a fluorescent sensor for the selective detection of H_2S and palladium(II), Microporous Mesoporous Mater. 293 (2020), 109790.

[83] N. Tannert, C. Jansen, S. Nießing, C. Janiak, Robust synthesis routes and porosity of the Al-based metal–organic frameworks Al-fumarate, CAU-10-H and MIL-160, Dalton Trans. 48 (9) (2019) 2967–2976.

[84] A.J. Rieth, M. Dincă, Controlled gas uptake in metal–organic frameworks with record ammonia sorption, J. Am. Chem. Soc. 140 (9) (2018) 3461–3466.

[85] A.J. Rieth, S. Yang, E.N. Wang, M. Dincă, Record atmospheric fresh water capture and heat transfer with a material operating at the water uptake reversibility limit, ACS Cent. Sci. 3 (6) (2017) 668–672.

[86] L.M. Rodriguez-Albelo, E. Lopez-Maya, S. Hamad, A.R. Ruiz-Salvador, S. Calero, J.A. Navarro, Selective sulfur dioxide adsorption on crystal defect sites on an isoreticular metal organic framework series, Nat. Commun. 8 (2017), 14457.

[87] N.C. Burtch, H. Jasuja, K.S. Walton, Water stability and adsorption in metal-organic frameworks, Chem. Rev. 114 (20) (2014) 10575–10612.

[88] H.J. Choi, M. Dincă, A. Dailly, J.R. Long, Hydrogen storage in water-stable metal–organic frameworks incorporating 1,3- and 1,4-benzenedipyrazolate, Energy Environ. Sci. 3 (1) (2010) 117–123.

[89] V. Colombo, S. Galli, H.J. Choi, G.D. Han, A. Maspero, G. Palmisano, N. Masciocchi, J.R. Long, High thermal and chemical stability in pyrazolate-bridged metal–organic frameworks with exposed metal sites, Chem. Sci. 2 (7) (2011) 1311–1319.

[90] D. Feng, Z.-Y. Gu, J.-R. Li, H.-L. Jiang, Z. Wei, H.-C. Zhou, Zirconium-metalloporphyrin PCN-222: mesoporous metal–organic frameworks with ultrahigh stability as biomimetic catalysts, Angew. Chem. Int. Ed. 51 (41) (2012) 10307–10310.

[91] T.-F. Liu, D. Feng, Y.-P. Chen, L. Zou, M. Bosch, S. Yuan, Z. Wei, S. Fordham, K. Wang, H.-C. Zhou, Topology-guided design and syntheses of highly stable

mesoporous porphyrinic zirconium metal–organic frameworks with high surface area, J. Am. Chem. Soc. 137 (1) (2015) 413–419.
[92] J.M. Taylor, R. Vaidhyanathan, S.S. Iremonger, G.K.H. Shimizu, Enhancing water stability of metal–organic frameworks via phosphonate monoester linkers, J. Am. Chem. Soc. 134 (35) (2012) 14338–14340.
[93] C. Serre, Superhydrophobicity in highly fluorinated porous metal-organic frameworks, Angew. Chem. Int. Ed. 51 (25) (2012) 6048–6050.
[94] T.H. Chen, I. Popov, O. Zenasni, O. Daugulis, O.S. Miljanic, Superhydrophobic perfluorinated metal-organic frameworks, Chem. Commun. 49 (61) (2013) 6846–6848.
[95] T. Li, D.-L. Chen, J.E. Sullivan, M.T. Kozlowski, J.K. Johnson, N.L. Rosi, Systematic modulation and enhancement of CO_2 : N_2 selectivity and water stability in an isoreticular series of bio-MOF-11 analogues, Chem. Sci. 4 (4) (2013) 1746–1755.
[96] S.J. Yang, C.R. Park, Preparation of highly moisture-resistant black-colored metal organic frameworks, Adv. Mater. 24 (29) (2012) 4010–4013.
[97] W. Zhang, Y. Hu, J. Ge, H.L. Jiang, S.H. Yu, A facile and general coating approach to moisture/water-resistant metal–organic frameworks with intact porosity, J. Am. Chem. Soc. 136 (49) (2014) 16978–16981.
[98] J. Gascon, S. Aguado, F. Kapteijn, Manufacture of dense coatings of $Cu_3(BTC)_2$ (HKUST-1) on α-alumina, Microporous Mesoporous Mater. 113 (1–3) (2008) 132–138.
[99] H. Guo, G. Zhu, I.J. Hewitt, S. Qiu, "Twin copper source" growth of metal-organic framework membrane: $Cu_3(BTC)_2$ with high permeability and selectivity for recycling H_2, J. Am. Chem. Soc. 131 (5) (2009) 1646–1647.
[100] S. Zhou, O. Shekhah, A. Ramirez, P. Lyu, E. Abou-Hamad, J. Jia, J. Li, P.M. Bhatt, Z. Huang, H. Jiang, T. Jin, G. Maurin, J. Gascon, M. Eddaoudi, Asymmetric pore windows in MOF membranes for natural gas valorization, Nature 606 (7915) (2022) 706–712.
[101] H.T. Kwon, H.K. Jeong, A.S. Lee, H.S. An, J.S. Lee, Heteroepitaxially grown zeolitic imidazolate framework membranes with unprecedented propylene/propane separation performances, J. Am. Chem. Soc. 137 (38) (2015) 12304–12311.
[102] Y. Liu, Y. Ban, W. Yang, Microstructural engineering and architectural design of metal–organic framework membranes, Adv. Mater. 29 (31) (2017), 1606949.
[103] X. Liu, C. Wang, B. Wang, K. Li, Novel organic-dehydration membranes prepared from zirconium metal-organic frameworks, Adv. Funct. Mater. 27 (3) (2017), 1604311.
[104] H. Bux, A. Feldhoff, J. Cravillon, M. Wiebcke, Y.-S. Li, J. Caro, Oriented zeolitic imidazolate framework-8 membrane with sharp H_2/C_3H_8 molecular sieve separation, Chem. Mater. 23 (8) (2011) 2262–2269.
[105] B.A. Al-Maythalony, O. Shekhah, R. Swaidan, Y. Belmabkhout, I. Pinnau, M. Eddaoudi, Quest for anionic MOF membranes: continuous sod-ZMOF membrane with CO_2 adsorption-driven selectivity, J. Am. Chem. Soc. 137 (5) (2015) 1754–1757.
[106] A. Huang, W. Dou, J. Caro, Steam-stable zeolitic imidazolate framework ZIF-90 membrane with hydrogen, J. Am. Chem. Soc. 132 (44) (2010) 15562–15564.
[107] Y. Hu, X. Dong, J. Nan, W. Jin, X. Ren, N. Xu, Y.M. Lee, Metal-organic framework membranes fabricated via reactive seeding, Chem. Commun. 47 (2) (2011) 737–739.
[108] A.J. Brown, N.A. Brunelli, K. Eum, F. Rashidi, J.R. Johnson, W.J. Koros, C. W. Jones, S. Nair, Interfacial microfluidic processing of metal-organic framework hollow fiber membranes, Science 345 (6192) (2014) 72–75.
[109] T.J.P.H. Yehia, J.P. Ferraris, K.J. Balkus, I.H. Musselman, Methane facilitated transport using copper(II) biphenyl dicarboxylate-triethylenediamine/poly(3-acetoxyethylthiophene) mixed matrix membranes, Polym. Prepr. (Am. Chem. Soc., Div. Polym. Chem.) 45 (2004) 35–36.
[110] G. Liu, V. Chernikova, Y. Liu, K. Zhang, Y. Belmabkhout, O. Shekhah, C. Zhang, S. Yi, M. Eddaoudi, W.J. Koros, Mixed matrix formulations with MOF molecular sieving for key energy-intensive separations, Nat. Mater. 17 (3) (2018) 283–289.
[111] M.W. Anjum, F. Vermoortele, A.L. Khan, B. Bueken, D.E. De Vos, I.F. Vankelecom, Modulated UiO-66-based mixed-matrix membranes for CO_2 separation, ACS Appl. Mater. Interfaces 7 (45) (2015) 25193–25201.
[112] S. Sorribas, P. Gorgojo, C. Tellez, J. Coronas, A.G. Livingston, High flux thin film nanocomposite membranes based on metal-organic frameworks for organic solvent nanofiltration, J. Am. Chem. Soc. 135 (40) (2013) 15201–15208.
[113] M. Etxeberria-Benavides, T. Johnson, S. Cao, B. Zornoza, J. Coronas, J. Sanchez-Lainez, A. Sabetghadam, X. Liu, E. Andres-Garcia, F. Kapteijn, J. Gascon, O. David, PBI mixed matrix hollow fiber membrane: influence of ZIF-8 filler over H_2/CO_2 separation performance at high temperature and pressure, Sep. Purif. Technol. 237 (2020).
[114] Y. Cheng, X. Wang, C. Jia, Y. Wang, L. Zhai, Q. Wang, D. Zhao, Ultrathin mixed matrix membranes containing two-dimensional metal-organic framework nanosheets for efficient CO_2/CH_4 separation, J. Membr. Sci. 539 (2017) 213–223.
[115] B. Wang, J. Xu, J. Wang, S. Zhao, X. Liu, Z. Wang, High-performance membrane with angstrom-scale manipulation of gas transport channels via polymeric decorated MOF cavities, J. Membr. Sci. 625 (2021).
[116] Y. Cheng, Y. Ying, S. Japip, S.-D. Jiang, T.-S. Chung, S. Zhang, D. Zhao, Advanced porous materials in mixed matrix membranes, Adv. Mater. 30 (47) (2018), 1802401.
[117] V. Nafisi, M.-B. Hägg, Development of dual layer of ZIF-8/PEBAX-2533 mixed matrix membrane for CO_2 capture, J. Membr. Sci. 459 (2014) 244–255.
[118] T. Yang, T.-S. Chung, High performance ZIF-8/PBI nano-composite membranes for high temperature hydrogen separation consisting of carbon monoxide and water vapor, Int. J. Hydrogen Energy 38 (1) (2013) 229–239.
[119] P.D. Sutrisna, J. Hou, H. Li, Y. Zhang, V. Chen, Improved operational stability of Pebax based gas separation membranes with ZIF-8: a comparative study of flat sheet and composite hollow fibre membranes, J. Membr. Sci. 524 (2017) 266–279.
[120] M. Barooah, B. Mandal, Synthesis, characterization and CO_2 separation performance of novel PVA/PG/ZIF-8 mixed matrix membrane, J. Membr. Sci. 572 (2019) 198–209.
[121] J. Sánchez-Laínez, L. Paseta, M. Navarro, B. Zornoza, C. Téllez, J. Coronas, Ultrapermeable thin film ZIF-8/polyamide membrane for H_2/CO_2 separation at high temperature without using sweep gas, Adv. Mater. Interfac. 5 (19) (2018), 1800647.
[122] A. Guo, Y. Ban, K. Yang, W. Yang, Metal-organic framework-based mixed matrix membranes: synergetic effect of adsorption and diffusion for CO_2/CH_4 separation, J. Membr. Sci. 562 (2018) 76–84.
[123] S. Kanehashi, G.Q. Chen, L. Ciddor, A. Chaffee, S.E. Kentish, The impact of water vapor on CO_2 separation performance of mixed matrix membranes, J. Membr. Sci. 492 (2015) 471–477.
[124] C. Jiao, Z. Li, X. Li, M. Wu, H. Jiang, Improved CO_2/N_2 separation performance of Pebax composite membrane containing polyethyleneimine functionalized ZIF-8, Sep. Purif. Technol. 259 (2021), 118190.
[125] Y. Wang, J. Wang, X. Zhang, J. Li, L. Li, Polyvinylamine/ZIF-8-decorated metakaolin composite membranes for CO_2/N_2 separation, Sep. Purif. Technol. 270 (2021), 118800.
[126] X. Li, S. Yu, K. Li, C. Ma, J. Zhang, H. Li, X. Chang, L. Zhu, Q. Xue, Enhanced gas separation performance of Pebax mixed matrix membranes by incorporating ZIF-8 in situ inserted by multiwalled carbon nanotubes, Sep. Purif. Technol. 248 (2020), 117080.
[127] J. Shen, G. Liu, K. Huang, Q. Li, K. Guan, Y. Li, W. Jin, UiO-66-polyether block amide mixed matrix membranes for CO_2 separation, J. Membr. Sci. 513 (2016) 155–165.
[128] M. Mozafari, R. Abedini, A. Rahimpour, Zr-MOFs-incorporated thin film nanocomposite Pebax 1657 membranes dip-coated on polymethylpentyne layer for efficient separation of CO_2/CH_4, J. Mater. Chem. A 6 (26) (2018) 12380–12392.
[129] R. Xu, Z. Wang, M. Wang, Z. Qiao, J. Wang, High nanoparticles loadings mixed matrix membranes via chemical bridging-crosslinking for CO_2 separation, J. Membr. Sci. 573 (2019) 455–464.
[130] S. Ashtiani, M. Khoshnamvand, D. Bouša, J. Šturala, Z. Sofer, A. Shaliutina-Kolešová, D. Gardenö, K. Friess, Surface and interface engineering in CO_2-philic based UiO-66-NH_2-PEI mixed matrix membranes via covalently bridging PVP for effective hydrogen purification, Int. J. Hydrogen Energy 46 (7) (2021) 5449–5458.
[131] F. Guo, B. Li, R. Ding, D. Li, X. Jiang, G. He, W. Xiao, A novel composite material UiO-66@HNT/Pebax mixed matrix membranes for enhanced CO_2/N_2 separation, Membranes 11 (9) (2021) 693.
[132] J. Yuan, H. Zhu, J. Sun, Y. Mao, G. Liu, W. Jin, Novel ZIF-300 mixed-matrix membranes for efficient CO_2 capture, ACS Appl. Mater. Interfaces 9 (44) (2017) 38575–38583.
[133] Z. Wang, J. Yuan, R. Li, H. Zhu, J. Duan, Y. Guo, G. Liu, W. Jin, ZIF-301 MOF/6FDA-DAM polyimide mixed-matrix membranes for CO_2/CH_4 separation, Sep. Purif. Technol. 264 (2021), 118431.
[134] J. Qian, E. Song, H. Lian, J. Jiang, C. Wang, Y. Pan, High-performance ZIF-302 mixed-matrix membranes for efficient CO_2 capture, Kor. J. Chem. Eng. 39 (4) (2022) 1020–1027.
[135] L. Xiang, L. Sheng, C. Wang, L. Zhang, Y. Pan, Y. Li, Amino-functionalized ZIF-7 nanocrystals: improved intrinsic separation ability and interfacial compatibility in mixed-matrix membranes for CO_2/CH_4 separation, Adv. Mater. 29 (32) (2017), 1606999.
[136] J. Sun, Q. Li, G. Chen, J. Duan, G. Liu, W. Jin, MOF-801 incorporated PEBA mixed-matrix composite membranes for CO_2 capture, Sep. Purif. Technol. 217 (2019) 229–239.
[137] W. Chen, Z. Zhang, L. Hou, C. Yang, H. Shen, K. Yang, Z. Wang, Metal-organic framework MOF-801/PIM-1 mixed-matrix membranes for enhanced CO_2/N_2 separation performance, Sep. Purif. Technol. 250 (2020), 117198.
[138] S. Xu, H. Huang, X. Guo, Z. Qiao, C. Zhong, Highly selective gas transport channels in mixed matrix membranes fabricated by using water-stable Cu-BTC, Sep. Purif. Technol. 257 (2021), 117979.
[139] C. Wu, H. Guo, X. Liu, B. Zhang, Mixed matrix membrane comprising glycine grafted CuBTC for enhanced CO_2 separation performances with excellent stability under humid atmosphere, Sep. Purif. Technol. 295 (2022), 121287.
[140] Q. Qian, A.M. Wright, H. Lee, M. Dincă, Z.P. Smith, Low-temperature $H_2S/CO_2/CH_4$ separation in mixed-matrix membranes containing MFU-4, Chem. Mater. 33 (17) (2021) 6825–6831.
[141] S.J. Datta, A. Mayoral, N.M.S. Bettahalli, P.M. Bhatt, M. Karunakaran, I.D. Carja, D. Fan, P.G.M. Mileo, R. Semino, G. Maurin, O. Terasaki, M. Eddaoudi, Rational design of mixed-matrix metal-organic framework membranes for molecular separations, Science 376 (6597) (2022) 1080–1087.
[142] B. Wang, Z. Qiao, J. Xu, J. Wang, X. Liu, S. Zhao, Z. Wang, M.D. Guiver, Unobstructed ultrathin gas transport channels in composite membranes by interfacial self-assembly, Adv. Mater. 32 (22) (2020), 1907701.
[143] X. Liu, N.K. Demir, Z. Wu, K. Li, Highly water-stable zirconium metal–organic framework UiO-66 membranes supported on alumina hollow fibers for desalination, J. Am. Chem. Soc. 137 (22) (2015) 6999–7002.
[144] X. Liu, H. Jin, Y. Li, H. Bux, Z. Hu, Y. Ban, W. Yang, Metal–organic framework ZIF-8 nanocomposite membrane for efficient recovery of furfural via pervaporation and vapor permeation, J. Membr. Sci. 428 (2013) 498–506.

[145] X. Wang, L. Zhai, Y. Wang, R. Li, X. Gu, Y.D. Yuan, Y. Qiao, Z. Hu, D. Zhao, Improving water-treatment performance of zirconium metal-organic framework membranes by postsynthetic defect healing, ACS Appl. Mater. Interfaces 9 (43) (2017) 37848–37855.

[146] Z. Dai, V. Loining, J. Deng, L. Ansaloni, L. Deng, Poly(1-trimethylsilyl-1-propyne)-Based hybrid membranes: effects of various nanofillers and feed gas humidity on CO_2 permeation, Membranes 8 (3) (2018) 76.

[147] H. Jiang, L. Bai, Z. Wang, W. Zheng, B. Yang, S. Zeng, X. Zhang, X. Zhang, Mixed matrix membranes containing Cu-based metal organic framework and functionalized ionic liquid for efficient NH3 separation, J. Membr. Sci. 659 (2022).

[148] C.H. Lau, P.T. Nguyen, M.R. Hill, A.W. Thornton, K. Konstas, C.M. Doherty, R. J. Mulder, L. Bourgeois, A.C.Y. Liu, D.J. Sprouster, J.P. Sullivan, T.J. Bastow, A. J. Hill, D.L. Gin, R.D. Noble, Ending aging in super glassy polymer membranes, Angew. Chem. Int. Ed. 53 (21) (2014) 5322–5326.

[149] A.A. Shamsabadi, R.M. Behbahani, F. Seidi, M. Soroush, Physical aging of polyetherimide membranes, J. Nat. Gas Sci. Eng. 27 (2015) 651–660.

[150] A. Husna, I. Hossain, O. Choi, S.M. Lee, T.H. Kim, Efficient CO_2 separation using a PIM-PI-functionalized UiO-66 MOF incorporated mixed matrix membrane in a PIM-PI-1 polymer, Macromol. Mater. Eng. 306 (10) (2021).

[151] C. Geng, Y. Sun, Z. Zhang, Z. Qiao, C. Zhong, Mitigated aging in a defective metal–organic framework pillared polymer of an intrinsic porosity hybrid membrane for efficient gas separation, ACS Sustain. Chem. Eng. 10 (11) (2022) 3643–3650.

[152] Z. Wang, Y. Tian, W. Fang, B.B. Shrestha, M. Huang, J. Jin, Constructing strong interfacial interactions under mild conditions in mof incorporated mixed matrix Membranes for Gas Separation, ACS Appl. Mater. Interfaces 13 (2021) 3166–3174.

[153] M.Z. Ahmada, T.A. Petersd, N.M. Konnertze, T. Vissere, C. Téllezc, J. Coronasc, V. Filaa, W.M.d. Vosb, N.E. Benes, High-pressure CO_2/CH_4 separation of Zr-MOFs based mixed matrix membranes, Sep. Purif. Technol. 230 (2020), 115858.

[154] M. Rubio-Martinez, C. Avci-Camur, A.W. Thornton, I. Imaz, D. Maspoch, M. R. Hill, New synthetic routes towards MOF production at scale, Chem. Soc. Rev. 46 (11) (2017) 3453–3480.

[155] Q. Min Wang, D. Shen, M. Bülow, M. Ling Lau, S. Deng, F.R. Fitch, N.O. Lemcoff, J. Semanscin, Metallo-organic molecular sieve for gas separation and purification, Microporous Mesoporous Mater. 55 (2) (2002) 217–230.

[156] N. Stock, S. Biswas, Synthesis of metal-organic frameworks (MOFs): routes to various MOF topologies, morphologies, and composites, Chem. Rev. 112 (2) (2012) 933–969.

[157] Y.-K. Seo, J.W. Yoon, J.S. Lee, U.H. Lee, Y.K. Hwang, C.-H. Jun, P. Horcajada, C. Serre, J.-S. Chang, Large scale fluorine-free synthesis of hierarchically porous iron(III) trimesate MIL-100(Fe) with a zeolite MTN topology, Microporous Mesoporous Mater. 157 (2012) 137–145.

[158] A.U. Czaja, N. Trukhan, U. Müller, Industrial applications of metal–organic frameworks, Chem. Soc. Rev. 38 (5) (2009) 1284–1293.

[159] S.H. Jhung, J.-H. Lee, J.-S. Chang, Microwave synthesis of a nanoporous hybrid material, chromium trimesate, Bull. Kor. Chem. Soc. 26 (6) (2005) 880–881.

[160] S.H. Jhung, J.-H. Lee, J.W. Yoon, C. Serre, G. Férey, J.-S. Chang, Microwave synthesis of chromium terephthalate MIL-101 and its benzene sorption, Ability 19 (1) (2007) 121–124.

[161] Z. Ni, R.I. Masel, Rapid production of Metal−Organic frameworks via microwave-assisted solvothermal synthesis, J. Am. Chem. Soc. 128 (38) (2006) 12394–12395.

[162] J.-S. Choi, W. J. Son, J. Kim, W.-S. Ahn, Metal–organic framework MOF-5 prepared by microwave heating: factors to be considered, Microporous Mesoporous Mater. 116 (1–3) (2008) 727–731.

[163] P.P. Bag, X.-S. Wang, R. Cao, Microwave-assisted large scale synthesis of lanthanide metal–organic frameworks (Ln-MOFs), having a preferred conformation and photoluminescence properties, Dalton Trans. 44 (26) (2015) 11954–11962.

[164] M. Taddei, P.V. Dau, S.M. Cohen, M. Ranocchiari, J.A. van Bokhoven, F. Costantino, S. Sabatini, R. Vivani, Efficient microwave assisted synthesis of metal–organic framework UiO-66: optimization and scale up, Dalton Trans. 44 (31) (2015) 14019–14026.

[165] Y. Xin, S. Peng, J. Chen, Z. Yang, J. Zhang, Continuous flow synthesis of porous materials, Chin. Chem. Lett. 31 (6) (2020) 170–177.

[166] X. Liu, Metal-organic framework UiO-66 membranes, Front. Chem. Sci. Eng. 14 (2) (2019) 216–232.

[167] R. Ameloot, F. Vermoortele, W. Vanhove, M.B. Roeffaers, B.F. Sels, D.E. De Vos, Interfacial synthesis of hollow metal-organic framework capsules demonstrating selective permeability, Nat. Chem. 3 (5) (2011) 382–387.

[168] M. Gimeno-Fabra, A.S. Munn, L.A. Stevens, T.C. Drage, D.M. Grant, R. J. Kashtiban, J. Sloan, E. Lester, R.I. Walton, Instant MOFs: continuous synthesis of metal–organic frameworks by rapid solvent mixing, Chem. Commun. 48 (86) (2012) 10642–10644.

[169] A.S. Munn, P.W. Dunne, S.V.Y. Tang, E.H. Lester, Large-scale continuous hydrothermal production and activation of ZIF-8, Chem. Commun. 51 (64) (2015) 12811–12814.

[170] M. Rubio-Martinez, T.D. Hadley, M.P. Batten, K. Constanti-Carey, T. Barton, D. Marley, A. Monch, K.S. Lim, M.R. Hill, Scalability of continuous flow production of metal-organic frameworks, ChemSusChem 9 (9) (2016) 938–941.

[171] P.M. Schoenecker, G.A. Belancik, B.E. Grabicka, K.S. Walton, Kinetics study and crystallization process design for scale-up of UiO-66-NH_2 synthesis, AIChE J. 59 (4) (2013) 1255–1262.

[172] M. Taddei, D.A. Steitz, J.A. van Bokhoven, M. Ranocchiari, Continuous-flow microwave synthesis of metal–organic frameworks: a highly efficient method for large-scale production, Chem. Eur J. 22 (10) (2016) 3245–3249.

[173] H. Reinsch, S. Waitschat, S.M. Chavan, K.P. Lillerud, N. Stock, A facile "green" route for scalable batch production and continuous synthesis of zirconium MOFs, Eur. J. Inorg. Chem. 27 (2016) 4490–4498, 2016.

[174] A. Laybourn, A.M. López-Fernández, I. Thomas-Hillman, J. Katrib, W. Lewis, C. Dodds, A.P. Harvey, S.W. Kingman, Combining continuous flow oscillatory baffled reactors and microwave heating: process intensification and accelerated synthesis of metal-organic frameworks, Chem. Eng. J. 356 (2019) 170–177.

[175] A. Carne-Sanchez, I. Imaz, M. Cano-Sarabia, D. Maspoch, A spray-drying strategy for synthesis of nanoscale metal-organic frameworks and their assembly into hollow superstructures, Nat. Chem. 5 (3) (2013) 203–211.

[176] C. Avci-Camur, J. Troyano, J. Pérez-Carvajal, A. Legrand, D. Farrusseng, I. Imaz, D. Maspoch, Aqueous production of spherical Zr-MOF beads via continuous-flow spray-drying, Green Chem. 20 (4) (2018) 873–878.

[177] A. Pichon, A. Lazuen-Garay, S.L. James, Solvent-free synthesis of a microporous metal–organic framework, CrystEngComm 8 (3) (2006) 211–214.

[178] D. Crawford, J. Casaban, R. Haydon, N. Giri, T. McNally, S.L. James, Synthesis by extrusion: continuous, large-scale preparation of MOFs using little or no solvent, Chem. Sci. 6 (3) (2015) 1645–1649.

[179] S. Karak, S. Kandambeth, B.P. Biswal, H.S. Sasmal, S. Kumar, P. Pachfule, R. Banerjee, Constructing ultraporous covalent organic frameworks in seconds via an organic terracotta process, J. Am. Chem. Soc. 139 (5) (2017) 1856–1862.

[180] C. Echaide-Górriz, C. Clément, F. Cacho-Bailo, C. Téllez, J. Coronas, New strategies based on microfluidics for the synthesis of metal–organic frameworks and their membranes, J. Mater. Chem. A 6 (14) (2018) 5485–5506.

[181] A. Polyzoidis, T. Altenburg, M. Schwarzer, S. Loebbecke, S. Kaskel, Continuous microreactor synthesis of ZIF-8 with high space–time yield and tunable particle size, Chem. Eng. J. 283 (2016) 971–977.

[182] C. McKinstry, R.J. Cathcart, E.J. Cussen, A.J. Fletcher, S.V. Patwardhan, J. Sefcik, Scalable continuous solvothermal synthesis of metal organic framework (MOF-5) crystals, Chem. Eng. J. 285 (2016) 718–725.

[183] L. Garzón-Tovar, M. Cano-Sarabia, A. Carné-Sánchez, C. Carbonell, I. Imaz, D. Maspoch, A spray-drying continuous-flow method for simultaneous synthesis and shaping of microspherical high nuclearity MOF beads, React. Chem. Eng. 1 (5) (2016) 533–539.

[184] B. He, M.M. Sadiq, M.P. Batten, K. Suzuki, M. Rubio-Martinez, J. Gardiner, M. R. Hill, Continuous flow synthesis of a Zr magnetic framework composite for post-combustion CO_2 capture, Chem. Eur J. 25 (57) (2019) 13184–13188.

[185] L. Yan, H. Jiang, Y. Wang, L. Li, X. Gu, P. Dai, D. Liu, S.-F. Tang, G. Zhao, X. Zhao, K.M. Thomas, One-step and scalable synthesis of Ni_2P nanocrystals encapsulated in N,P-codoped hierarchically porous carbon matrix using a bipyridine and phosphonate linked nickel metal–organic framework as highly efficient electrocatalysts for overall water splitting, Electrochim. Acta 297 (2019) 755–766.

[186] Y. Wang, L. Li, L. Yan, L. Cao, P. Dai, X. Gu, X. Zhao, Continuous synthesis for zirconium metal-organic frameworks with high quality and productivity via microdroplet flow reaction, Chin. Chem. Lett. 29 (6) (2018) 849–853.

[187] C. McKinstry, E.J. Cussen, A.J. Fletcher, S.V. Patwardhan, J. Sefcik, Scalable continuous production of high quality HKUST-1 via conventional and microwave heating, Chem. Eng. J. 326 (2017) 570–577.

[188] G.H. Albuquerque, R.C. Fitzmorris, M. Ahmadi, N. Wannenmacher, P. K. Thallapally, B.P. McGrail, G.S. Herman, Gas–liquid segmented flow microwave-assisted synthesis of MOF-74(Ni) under moderate pressures, CrystEngComm 17 (29) (2015) 5502–5510.

[189] M. Gaab, N. Trukhan, S. Maurer, R. Gummaraju, U. Müller, The progression of Al-based metal-organic frameworks – from academic research to industrial production and applications, Microporous Mesoporous Mater. 157 (2012) 131–136.

[190] M. Mubashir, Y.Y. Fong, C.T. Leng, L.K. Keong, Issues and current trends of hollow fiber mixed-matrix membranes for CO_2 separation from N_2 and CH_4, Chem. Eng. Technol. 41 (2) (2018) 235–252.

[191] W. Quan, H.E. Holmes, F. Zhang, B.L. Hamlett, M.G. Finn, C.W. Abney, M. T. Kapelewski, S.C. Weston, R.P. Lively, W.J. Koros, Scalable Formation of diamine-appended metal-organic framework hollow fiber sorbents for postcombustion CO_2 capture, J. Am. Chem. Soc. Au 2 (6) (2022) 1350–1358.

[192] A.K. Zulhairun, Z.G. Fachrurrazi, M. Nur Izwanne, A.F. Ismail, Asymmetric hollow fiber membrane coated with polydimethylsiloxane–metal organic framework hybrid layer for gas separation, Sep. Purif. Technol. 146 (2015) 85–93.

[193] H. Demir, G.O. Aksu, H.C. Gulbalkan, S. Keskin, MOF membranes for CO_2 capture: past, present and future, Carbon Capture Sci. Technol. 2 (2022).

[194] Q. Ma, T. Zhang, B. Wang, Shaping of metal-organic frameworks, a critical step toward industrial applications, Matter 5 (4) (2022) 1070–1091.

[195] N. Sunder, Y.Y. Fong, M.A. Bustam, N.H. Suhaimi, Development of amine-functionalized metal-organic frameworks hollow fiber mixed matrix membranes for CO_2 and CH_4 separation: a review, Polymers (Basel) 14 (7) (2022).

[196] Q.-C. Xia, M.-L. Liu, X.-L. Cao, Y. Wang, W. Xing, S.-P. Sun, Structure design and applications of dual-layer polymeric membranes, J. Membr. Sci. 562 (2018) 85–111.

[197] Y. Tian, Z. Wang, L. Wang, Hollow fibers: from fabrication to applications, Chem. Commun. 57 (73) (2021) 9166–9177.

[198] A.L. Ahmad, T.A. Otitoju, B.S. Ooi, Hollow fiber (HF) membrane fabrication: a review on the effects of solution spinning conditions on morphology and performance, J. Ind. Eng. Chem. 70 (2019) 35–50.

[199] W. Li, P. Su, Z. Li, Z. Xu, F. Wang, H. Ou, J. Zhang, G. Zhang, E. Zeng, Ultrathin metal–organic framework membrane production by gel–vapour deposition, Nat. Commun. 8 (1) (2017).

[200] S. Basu, A. Cano-Odena, I.F.J. Vankelecom, MOF-containing mixed-matrix membranes for CO_2/CH_4 and CO_2/N_2 binary gas mixture separations, Sep. Purif. Technol. 81 (1) (2011) 31–40.

[201] J. Hu, H. Cai, H. Ren, Y. Wei, Z. Xu, H. Liu, Y. Hu, Mixed-Matrix-Membrane-hollow-fibers-of-$Cu_3(btc)_2$-mof-and-polyimide-for-gas-separation-and-adsorption.pdf&gt, Ind. Eng. Chem. Res. 49 (2010) 12605–12612.

[202] P.D. Sutrisna, J. Hou, M.Y. Zulkifli, H. Li, Y. Zhang, W. Liang, M. Deanna, D'Alessandro, V. Chen, Surface functionalized UiO-66/Pebax-based ultrathin composite hollow fiber gas separation membranes, J. Mater. Chem. A 6 (3) (2018) 918–931.

[203] G. Li, W. Kujawski, K. Knozowska, J. Kujawa, Thin film mixed matrix hollow fiber membrane fabricated by incorporation of amine functionalized metal-organic framework for CO_2/N_2 separation, Materials (Basel) 14 (12) (2021).

[204] Y. Dai, J.R. Johnson, O. Karvan, D.S. Sholl, W.J. Koros, Ultem®/ZIF-8 mixed matrix hollow fiber membranes for CO_2/N_2 separations, J. Membr. Sci. 401–402 (2012) 76–82.

[205] B. Sasikumar, S. Bisht, G. Arthanareeswaran, A.F. Ismail, M.H.D. Othman, Performance of polysulfone hollow fiber membranes encompassing ZIF-8, SiO_2/ZIF-8, and amine-modified SiO_2/ZIF-8 nanofillers for CO_2/CH_4 and CO_2/N_2 gas separation, Sep. Purif. Technol. 264 (2021).

[206] N. Widiastuti, T. Gunawan, H. Fansuri, W.N.W. Salleh, A.F. Ismail, N. Sazali, P84/ZCC hollow fiber mixed matrix membrane with PDMS coating to enhance air separation performance, Membranes (Basel) 10 (10) (2020).

[207] O.E.M. Ter Beek, M.K. van Gelder, C. Lokhorst, D.H.M. Hazenbrink, B. H. Lentferink, K.G.F. Gerritsen, D. Stamatialis, In vitro study of dual layer mixed matrix hollow fiber membranes for outside-in filtration of human blood plasma, Acta Biomater. 123 (2021) 244–253.

[208] R. Kamaludin, M. Xuefeng, M.H.D. Othman, A. Imtiaz, M. Hafiz Puteh, S.H.S. A. Kadir, ZIF-8-based dual layer hollow fiber mixed matrix membrane for natural gas purification, Fuel 354 (2023).

[209] M.-L. Liu, Z.-J. Fu, S.-P. Sun, Chapter 12 - hollow fiber spinning of dual-layer membranes, in: T.-S. Chung, Y. Feng (Eds.), Hollow Fiber Membranes, Elsevier, 2021, pp. 253–274.

[210] D. Li, T.-S. Chung, R. Wang, Morphological aspects and structure control of dual-layer asymmetric hollow fiber membranes formed by a simultaneous co-extrusion approach, J. Membr. Sci. 243 (1–2) (2004) 155–175.

[211] L. Jiang, Fabrication of Matrimid/polyethersulfone dual-layer hollow fiber membranes for gas separation, J. Membr. Sci. 240 (1–2) (2004) 91–103.

[212] C. Echaide-Górriz, J.A. Zapata, M. Etxeberría-Benavides, C. Téllez, J. Coronas, Polyamide/MOF bilayered thin film composite hollow fiber membranes with tuned MOF thickness for water nanofiltration, Sep. Purif. Technol. 236 (2020).

[213] G.-K. Gao, Y.-R. Wang, H.-J. Zhu, Y. Chen, R.-X. Yang, C. Jiang, H. Ma, Y.-Q. Lan, Rapid production of metal–organic frameworks based separators in industrial-level efficiency, Adv. Sci. 7 (24) (2020), 2002190.

[214] A. Knebel, A. Bavykina, S.J. Datta, L. Sundermann, L. Garzon-Tovar, Y. Lebedev, S. Durini, R. Ahmad, S.M. Kozlov, G. Shterk, M. Karunakaran, I.D. Carja, D. Simic, I. Weilert, M. Kluppel, U. Giese, L. Cavallo, M. Rueping, M. Eddaoudi, J. Caro, J. Gascon, Solution processable metal-organic frameworks for mixed matrix membranes using porous liquids, Nat. Mater. 19 (12) (2020) 1346–1353.

[215] D. Poloneeva, S.J. Datta, L. Garzon-Tovar, S. Durini, M. Rueping, M. Eddaoudi, A. Bavykina, J. Gascon, Toward liquid phase processable metal organic frameworks: dream or reality? Acc. Chem. Res. 2 (12) (2021) 1133–1140.

[216] C.S. Diercks, O.M. Yaghi, The atom, the molecule, and the covalent organic framework, Science 355 (6328) (2017) 1585.

[217] N. Huang, P. Wang, D. Jiang, Covalent organic frameworks: a materials platform for structural and functional designs, Nat. Rev. Mater. 1 (10) (2016), 16068.

[218] L.M. Lanni, R.W. Tilford, M. Bharathy, J.J. Lavigne, Enhanced hydrolytic stability of self-assembling alkylated two-dimensional covalent organic frameworks, J. Am. Chem. Soc. 133 (35) (2011) 13975–13983.

[219] Y. Du, K. Mao, P. Kamakoti, B. Wooler, S. Cundy, Q. Li, P. Ravikovitch, D. Calabro, The effects of pyridine on the structure of B-COFs and the underlying mechanism, J. Mater. Chem. A 1 (42) (2013) 13171–13178.

[220] Y. Du, K. Mao, P. Kamakoti, P. Ravikovitch, C. Paur, S. Cundy, Q. Li, D. Calabro, Experimental and computational studies of pyridine-assisted post-synthesis modified air stable covalent-organic frameworks, Chem. Commun. 48 (38) (2012) 4606–4608.

[221] B.P. Biswal, S. Chandra, S. Kandambeth, B. Lukose, T. Heine, R. Banerjee, Mechanochemical synthesis of chemically stable isoreticular covalent organic frameworks, J. Am. Chem. Soc. 135 (14) (2013) 5328–5331.

[222] S.Y. Ding, J. Gao, Q. Wang, Y. Zhang, W.G. Song, C.Y. Su, W. Wang, Construction of covalent organic framework for catalysis: Pd/COF-LZU1 in Suzuki-Miyaura coupling reaction, J. Am. Chem. Soc. 133 (49) (2011) 19816–19822.

[223] Z. Li, Y. Zhang, H. Xia, Y. Mu, X. Liu, A robust and luminescent covalent organic framework as a highly sensitive and selective sensor for the detection of Cu^{2+} ions, Chem. Commun. 52 (39) (2016) 6613–6616.

[224] H. Xu, J. Gao, D. Jiang, Stable, crystalline, porous, covalent organic frameworks as a platform for chiral organocatalysts, Nat. Chem. 7 (11) (2015) 905–912.

[225] X. Guan, H. Li, Y. Ma, M. Xue, Q. Fang, Y. Yan, V. Valtchev, S. Qiu, Chemically stable polyarylether-based covalent organic frameworks, Nat. Chem. 11 (2019) 587–594.

[226] Z. Kang, Y. Peng, Y. Qian, D. Yuan, M.A. Addicoat, T. Heine, Z. Hu, L. Tee, Z. Guo, D. Zhao, Mixed matrix membranes (MMMs) comprising exfoliated 2D covalent organic frameworks (COFs) for efficient CO_2 separation, Chem. Mater. 28 (5) (2016) 1277–1285.

[227] Y. Zhang, L. Ma, Y. Lv, T. Tan, Facile manufacture of COF-based mixed matrix membranes for efficient CO_2 separation, Chem. Eng. J. 430 (2022), 133001.

[228] Y. Cheng, L. Zhai, Y. Ying, Y. Wang, G. Liu, J. Dong, D.Z.L. Ng, S.A. Khan, D. Zhao, Highly efficient CO_2 capture by mixed matrix membranes containing three-dimensional covalent organic framework fillers, J. Mater. Chem. A 7 (9) (2019) 4549–4560.

[229] R. Zhao, H. Wu, L. Yang, Y. Ren, Y. Liu, Z. Qu, Y. Wu, L. Cao, Z. Chen, Z. Jiang, Modification of covalent organic frameworks with dual functions ionic liquids for membrane-based biogas upgrading, J. Membr. Sci. 600 (2020), 117841.

[230] C. Zou, Q. Li, Y. Hua, B. Zhou, J. Duan, W. Jin, Mechanical synthesis of COF nanosheet cluster and its mixed matrix membrane for efficient CO_2 removal, ACS Appl. Mater. Interfaces 9 (34) (2017) 29093–29100.

[231] H. Fan, J. Gu, H. Meng, A. Knebel, ü. Caro, High-Flux membranes based on the covalent organic framework COF-LZU1 for selective dye separation by nanofiltration, Angew. Chem. Int. Ed. 57 (15) (2018) 4083–4087.

[232] X. Shi, A. Xiao, C. Zhang, Y. Wang, Growing covalent organic frameworks on porous substrates for molecule-sieving membranes with pores tunable from ultra- to nanofiltration, J. Membr. Sci. 576 (2019) 116–122.

[233] S. Yuan, X. Li, J. Zhu, G. Zhang, P.V. Puyvelde, B.V.d. Bruggen, Covalent organic frameworks for membrane separation, Chem. Soc. Rev. 48 (10) (2019) 2665–2681.

[234] R. Wang, X. Shi, A. Xiao, W. Zhou, Y. Wang, Interfacial polymerization of covalent organic frameworks (COFs) on polymeric substrates for molecular separations, J. Membr. Sci. 566 (2018) 197–204.

[235] C. Fan, H. Wu, J. Guan, X. You, C. Yang, X. Wang, L. Cao, B. Shi, Q. Peng, Y. Kong, Y. Wu, N.A. Khan, Z. Jiang, Scalable fabrication of crystalline COF membranes from amorphous polymeric membranes, Angew. Chem. Int. Ed. 133 (33) (2021) 18199–18206.

[236] J. Fu, S. Das, G. Xing, T. Ben, V. Valtchev, S. Qiu, Fabrication of COF-MOF composite membranes and their highly selective separation of H_2/CO_2, J. Am. Chem. Soc. 138 (24) (2016) 7673–7680.

[237] S. Das, T. Ben, S. Qiu, V. Valtchev, Two-Dimensional COF-Three-Dimensional MOF dual-layer membranes with unprecedentedly high H_2/CO_2 selectivity and ultrahigh gas permeabilities, ACS Appl. Mater. Interfaces 12 (47) (2020) 52899–52907.

[238] H. Fan, A. Mundstock, A. Feldhoff, A. Knebel, J. Gu, H. Meng, J. Caro, Covalent organic framework-covalent organic framework bilayer membranes for highly selective gas separation, J. Am. Chem. Soc. 140 (32) (2018) 10094–10098.

[239] Y. Ying, S.B. Peh, H. Yang, Z. Yang, D. Zhao, Ultrathin covalent organic framework membranes via a multi-interfacial engineering strategy for gas separation, Adv. Mater. 34 (25) (2022), 2104946.

[240] Y. Ying, M. Tong, S. Ning, S.K. Ravi, S.B. Peh, S.C. Tan, S.J. Pennycook, D. Zhao, Ultrathin two-dimensional membranes assembled by ionic covalent organic nanosheets with reduced apertures for gas separation, J. Am. Chem. Soc. 142 (9) (2020) 4472–4480.

[241] H. Fan, M. Peng, I. Strauss, A. Mundstock, H. Meng, J. Caro, High-Flux vertically aligned 2D covalent organic framework membrane with enhanced hydrogen separation, J. Am. Chem. Soc. 142 (2020) 6872–6877.